

DOT/FAA/AR-97/2, I

Office of Aviation Research
Washington, D.C. 20591

**Proceedings of the
FAA-NASA Symposium on the Continued
Airworthiness of Aircraft Structures**

FAA Center of Excellence in Computational Modeling of Aircraft Structures
Atlanta, Georgia
August 28-30, 1997



July 1997

This document is available to the U.S. public
through the National Technical Information
Service, Springfield, Virginia 22161



NOTICE

This document is disseminated under the sponsorship of the U.S. Department of Transportation in the interest of information exchange. The United States Government assumes no liability for the contents or use thereof. The United States Government does not endorse products or manufacturers. Trade or manufacturer's names appear herein solely because they are considered essential to the objective of this report.

1. Report No. DOT/FAA/AR-97/2, I		2. Government Accession No.		3. Recipient's Catalog No.	
4. Title and Subtitle PROCEEDINGS OF THE FAA-NASA SYMPOSIUM ON THE CONTINUED AIRWORTHINESS OF AIRCRAFT STRUCTURES				5. Report Date July 1997	
				6. Performing Organization Code	
7. Author(s) Compiled by Catherine A. Bigelow, Ph.D.				8. Performing Organization Report No.	
9. Performing Organization Name and Address Federal Aviation Administration Airport and Aircraft Safety Research and Development Division William J. Hughes Technical Center Atlantic City International Airport, NJ 08405				10. Work Unit No. (TRAIS)	
				11. Contract or Grant No.	
12. Sponsoring Agency Name and Address U.S. Department of Transportation Federal Aviation Administration Office of Aviation Research Washington, DC 20591				13. Type of Report and Period Covered Proceedings August 28-30, 1996	
				14. Sponsoring Agency Code AAR-400	
15. Supplementary Notes Edited by Catherine A. Bigelow, Ph.D, Federal Aviation Administration, William J. Hughes Technical Center					
16. Abstract This publication contains the fifty-two technical papers presented at the FAA-NASA Symposium on the Continued Airworthiness of Aircraft Structures. The symposium, hosted by the FAA Center of Excellence for Computational Modeling of Aircraft Structures at Georgia Institute of Technology, was held to disseminate information on recent developments in advanced technologies to extend the life of high-time aircraft and design longer-life aircraft. Affiliations of the participants included 33% from government agencies and laboratories, 19% from academia, and 48% from industry; in all 240 people were in attendance. Technical papers were selected for presentation at the symposium, after a review of extended abstracts received by the Organizing Committee from a general call for papers.					
17. Key Words Corrosion, Crack detection, Nondestructive inspection, Residual strength, Fatigue, Crack growth			18. Distribution Statement Document is available to the public through the National Technical Information Service, Springfield, Virginia 22161		
19. Security Classif. (of this report) Unclassified		20. Security Classif. (of this page) Unclassified		21. No. of Pages 329	22. Price

CONTENTS

Volume I

Executive Summary	vii
Airframe Life Extension Through Quantitative Rework Inspections, W. H. Sproat	1
Analysis of a Composite Repair, C. Duong and J. Yu	17
Analysis of Safety Performance Thresholds for Air Carriers by Using Control Charting Techniques, A. Y. Cheng, J. T. Luxh•j, and R. Y. Liu.....	25
Analytical Approaches and Personal Computer (PC)-Based Design Package for Bonded Composite Patch Repair, Y. Xiong, D. Raizenne, and D. Simpson.....	37
Analytical Fatigue Life Estimation of Full-Scale Fuselage Panel, J. Zhang, J. H. Park, and S. N. Atluri.....	51
Analytical Methodology for Predicting the Onset of Widespread Fatigue Damage in Fuselage Structure, C. E. Harris, J. C. Newman, Jr., R. S. Piascik, and J. H. Starnes, Jr.	63
Application of Acoustic Emission to Health Monitoring of Helicopter Mechanical Systems, A. F. Almeida, W. D. Martin, and D. J. Pointer	89
Applying United States Air Force Lessons Learned to Other Aircraft, G. D. Herring, R. D. Giese, and P. Toivonen.....	93
Automated Evaluation of Residual Strength in the Presence of Widespread Fatigue Damage, W. T. Chow, H. Kawai, L. Wang, and S. N. Atluri	101
Controlling Fatigue Failures by Means of a Trade-Off Between Design and Inspection Parameters, A. Brot.....	109
Controlling Human Error in Maintenance: Development and Research Activities, W. B. Johnson and W. T. Shepherd	117
Coordinated Metallographic, Chemical, and Electrochemical Analyses of Fuselage Lap Splice Corrosion, M. E. Inman, R. G. Kelly, S. A. Willard, and R. S. Piascik.....	129
Designing for the Durability of Bonded Structures, W. S. Johnson and L. M. Butkus.....	147
The Effect of Crack Interaction on Ductile Fracture, C. T. Sun and X. M. Su	161
The Effect of Environmental Conditions and Load Frequency on the Crack Initiation Life and Crack Growth in Aluminum Structure, H.-J. Schmidt and B. Brandecker.....	171

Effects of Combined Loads on the Nonlinear Response and Residual Strength of Damaged Stiffened Shells, J. H. Starnes, Jr., C. A. Rose, and C. C. Rankin.....	183
Elasto-Plastic Models for Interaction Between a Major Crack and Multiple Small Cracks, K. F. Nilsson	197
An Energetic Characterization of the Propagation of Curved Cracks in Thin Ductile Plates, H. Okada and S. N. Atluri.....	225
Engineering Fracture Parameters for Bulging Cracks in Pressurized Unstiffened Curved Panels, J. G. Bakuckas, Jr., P. V. Nguyen, and C. A. Bigelow	239
Evaluation of Closure-Based Crack Growth Model, C. Hsu, K. K. Chan, and J. Yu.....	253
Failure Analysis of Aircraft Engine Containment Structures, S. Sarkar and S. N. Atluri	267
Fatigue and Damage Tolerance of Aging Aircraft Structures, G. I. Nesterenko.....	279
Fatigue Growth of Small Corner Cracks in Aluminum 6061-T651, R. L. Carlson, D. L. Steadman, D. S. Dancila, and G. A. Kardomateas.....	301
Fatigue Studies Related to Certification of Composite Crack Patching for Primary Metallic Aircraft Structure, A. Baker.....	313

Volume II

Executive Summary	vii
Fatigue-Life Prediction Methodology Using Small-Crack Theory and a Crack-Closure Model, J. C. Newman, Jr., E. P. Phillips, and M. H. Swain.....	331
Full-Scale Glare Fuselage Panel Tests, R. W. A. Vercammen and H. H. Ottens	357
A Graphic User Interface (GUI) Front-End for Parametric Survey and its Application to Composite Patch Repairs of Metallic Structure, H. Kawai, H. Okada. and S. N. Atluri	369
Implementation and Application of a Large-Rotation Finite Element Formulation in NASA Code ZIP2DL, X. Deng and J. C. Newman, Jr.....	377
Implications of Corrosion Pillowing on the Structural Integrity of Fuselage Lap Joints, N. C. Bellinger and J. P. Komorowski	391
Improved Nondestructive Inspection Techniques for Aircraft Inspection, D. Hagemaiier and D. Wilson	403

Improving the Damage Tolerance of Bonded Structures Via Adhesive Layer Barriers, J. C. Brewer	417
In Search of the Holy Grail—The Deterministic Prediction of Damage, D. D. Macdonald and J. Magalhaes.....	425
Investigation of Fuselage Structure Subject to Widespread Fatigue Damage, M. L. Gruber, K. E. Wilkins, and R. E. Worden.....	439
Numerical Investigations into Viability of Crack Tip Opening Displacement as a Fracture Parameter for Mixed-Mode I/II Tearing of Thin Aluminum Sheets, M. A. Sutton, W. Zhao, X. Deng, D. S. Dawicke, and J. C. Newman, Jr.....	461
A Numerical Study of the Interactions Between Multiple Longitudinal Cracks in a Fuselage (Multiple Discrete-Source Damages), W. T. Chow, L. Wang, H. Kawai, and S. N. Atluri	473
On-Aircraft Analysis of F-14 Aircraft Wing Bearings Using Acoustic Emission Techniques, D. J. Pointer, W. D. Martin, and A. F. Almeida.....	481
Operator Concerns About Widespread Fatigue Damage and How it May Be Handled and Regulated in the Commercial Environment, D. V. Finch.....	487
Predictions of Stable Growth of a Lead Crack and Multiple-Site Damage Using Elastic-Plastic Finite Element Method (EPFEM) and Elastic-Plastic Finite Element Alternating Method (EPFEAM), L. Wang, F. W. Brust, and S. N. Atluri.....	505
Predictions of Widespread Fatigue Damage Threshold, L. Wang, W. T. Chow, H. Kawai, and S. N. Atluri	519
Probability and Statistics Modeling of Constituent Particles and Corrosion Pits as a Basis for Multiple-Site Damage Analysis, N. R. Cawley, D. G. Harlow, and R. P. Wei	531
Probability-Based Cost-Effective Inspection Frequency for Aging Transport Structures, V. Li	543
Residual Strength Predictions Using a Crack Tip Opening Angle Criterion, D. S. Dawicke.....	555
A Review of Rotorcraft Structural Integrity/Airworthiness Approaches and Issues, D. P. Schrage	567
Rivet Bearing Load Considerations in the Design of Mechanical Repairs for Aging Aircraft, H. Chickermane and H. C. Gea	577

The Role of Fretting Crack Nucleation in the Onset of Widespread Fatigue Damage: Analysis and Experiments, M. P. Szolwinski, G. Harish, P. A. McVeigh, and T. N. Farris	585
The Role of New-Technology Nondestructive Inspection (NDI) Techniques, A. Q. Howard	597
Simulation of Stable Tearing and Residual Strength Prediction with Applications to Aircraft Fuselages, C.-S. Chen, P. A. Wawrzynek, and A. R. Ingraffea.....	605
A Study of Circumferential Cracks in the Presence of Multiple-Site Damage in an Aircraft Fuselage, L. Wang, W. T. Chow, H. Kawai, J. Zhang, and S. N. Atluri.....	619
A Study of Fatigue Crack Generation and Growth in Riveted Alcaid 2024-T3 Specimens, Z. M. Connor, M. E. Fine, and B. Moran	631
T*ε Integrals for Curved Crack Growth, P. W. Lam, A. S. Kobayashi, H. Okada, S. N. Atluri, and P. W. Tan	643
Use of Neural Networks for Aviation Safety Risk Assessment, H.-J. Shyur, J. T. Luxhøj, and T. P. Williams	655
Widespread Fatigue Damage Threshold Estimates, I. C. Whittaker and H. C. Chen	665

EXECUTIVE SUMMARY

The Federal Aviation Administration (FAA) and the National Aeronautics and Space Administration (NASA) jointly sponsored the Symposium on Continued Airworthiness of Aircraft Structures in Atlanta, Georgia, August 28-30, 1996. The Symposium was hosted by the FAA Center of Excellence for Computational Modeling of Aircraft Structures at Georgia Institute of Technology.

Technical papers were selected for presentation at the symposium, after a review of extended abstracts received by the Organizing Committee from a general call for papers. Keynote addresses were given by Dr. George L. Donohue, Associate Administrator of Acquisition and Research of the Federal Aviation Administration, and Dr. Robert W. Whitehead, Associate Administrator for Research and Acquisition, National Aeronautics and Space Administration.

Full-length manuscripts were requested from the authors of papers presented; these papers are included in the proceedings.

The members of the Conference Organizing Committee are as follows:

Chris C. Seher, Conference Chairman, Federal Aviation Administration
Charles E. Harris, Conference Co-Chairman, NASA Langley Research Center
Satya N. Atluri, Georgia Institute of Technology
Amos W. Hoggard, Douglas Aircraft Company
Roy Wantanabe, Boeing Commercial Airplane Group
John W. Lincoln, US Air Force
Thomas Swift, Federal Aviation Administration
Aubrey Carter, Delta Airlines
Jerry Porter, Lockheed Martin Aerospace
Catherine A. Bigelow, Federal Aviation Administration
James C. Newman, NASA Langley Research Center
Andres Zellweger, Federal Aviation Administration

Approximately 240 people attended the conference. The affiliations of the attendees included 33% from government agencies and laboratories, 19% from academia, and 48% from industry.

Chris C. Seher
FAA Technical Center

AIRFRAME LIFE EXTENSION THROUGH QUANTITATIVE REWORK INSPECTIONS

William H. Sproat
Measurement Systems Incorporated
2262 Northwest Parkway, Suite B
Marietta, GA 30067

SUMMARY

Averting widespread fatigue damage to attain structural life extension requires analytical tools to predict the nature and extent of physical degradation. Inspections and tests are then applied to validate and refine predictive models. The next critical step is to take action on decisions formed through modeling and condition assessment. In many cases, the decision is to effect rework. Confidence in rework for life extension is highly dependent on fastener fit and surface condition of materials. This presentation discusses how to quantitatively assess rework fastener hole condition, critical fastener fit, and surface microprofiles.

There are two technologies practically applied in these measurements: capacitance gaging for fastener hole size/condition and fastener dimensioning and optical profiling to measure fastener head protrusion and surface condition. Capacitance gaging is accomplished with the Capacitance Measurement System and the Fastener Measurement System. Laser optical profiling is performed with the Scratch Measurement System, an instrument originally developed for airframe skin and panel surface condition measurements.

In this paper, fatigue life enhancements with fastener installations to specified levels of interference are correlated with capacitance measurements. Tapered- and straight-shank fastener joint fatigue test data are compared. Economically preferred straight-shank fastener installations are shown to be equivalent in fatigue to tapered configurations. However, dependence on the positive attributes of interference fit with both straight and tapered fasteners must be based on the quantitative physical measurements as revealed by test data.

Laser optical profiling augments the capacitance measurement technology in quantitative assessment of dimensional features and attributes for fatigue life enhancement. This is a new instrument, developed into a portable hand-held unit. Presentations of its performance in this paper focus on initial trials regarding accuracy and resolution limits. Its versatility in a wide range of practical application continues to expand.

INTRODUCTION

Air vehicle life extension is effected through detailed condition assessment combined with predictive modeling of strength and fatigue life under specified service conditions. Reliable, cost-effective condition assessment is a key element in this process. Capacitance gaging and laser profiling, originally developed for production quality determinations, are emerging as excellent condition assessment tools. Both technologies are now affording major contributions to maintenance, repair, rework and modification programs.

This presentation first discusses the developed methodology surrounding fastener interference and then proceeds to the evolving technology of quantitative surface condition assessment.

FATIGUE LIFE AND FASTENER INTERFERENCE

A recent series of tests has been conducted by Douglas Aircraft Company (Materials and Processes Engineering Lab Report No. LR-15503, dated 11-28-94, Reference 1) to compare the durability of Hi-Shear pull pin and Taper-Lok interference bolts. Tests simulated MD-11 lower wing spar cap-to-panel joints. The objective was to determine whether the straight shank Hi-Shear system can provide equivalent (or better) joint durability compared with the more costly and time consuming installation of Taper-Loks. The test specimen design (Figure 1) represents a total joint thickness of 2.0 inches; 0.750-inch-thick 2024-T351 aluminum and 1.250-inch-thick 7075-T651 aluminum, with 0.375-inch-diameter 6Al-4V Titanium fasteners. This corresponds to the wing panel-to-spar cap joint in a critical region.

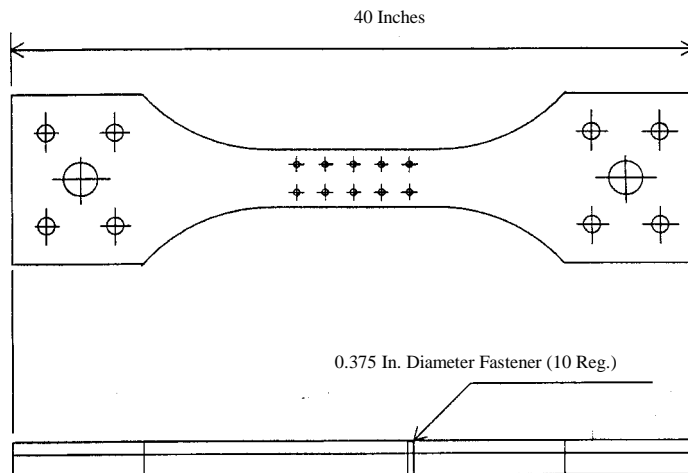


Figure 1. McDonnell Aircraft Company Specimen Design for Fatigue Life Comparison of Taper-Lok and Hi-Shear Interference Fasteners.

Fastener interference and fastener type (straight shank compared to taper) were the controlled variables in the test, given the test conditions of 22 Ksi gross stress, R factor of +0.2, and a cyclic rate of 3 Hz. Interferences were targeted in the range of 0.0020 to 0.0075 inch for straight shank fasteners and 0.0031 to 0.0054 inch for tapered fasteners. Actual fit of straight shank fasteners, as determined by the Measurement Systems Incorporated capacitance measurement system described later in this presentation, ranged from an 0.0008 inch average diameter oversize hole to 0.0086 inch interference. It is important to note that specimen design called for three interference dimensions with the straight shank fasteners; 0.0020, 0.0045, and 0.0075 inch. Target and capacitance measured actual dimensions are different. Interference calculated from measured protrusion of the comparison set of tapered fasteners ranged from 0.0031 to 0.0054 inch.

Test results (Figure 2) show that interference fit straight shank fasteners are capable of providing fatigue life comparable to the more costly tapered interference fasteners, provided their interference is in the range of 0.0040 to 0.0075 inch used in these tests. Cycles to failure for the full complement of specimens ranged from 95,900 for the low (and negative)-interference specimens to 947,300 for the high-interference specimens; near one order of magnitude. Specimen failures showed no bias to either the simulated spar cap or panel.

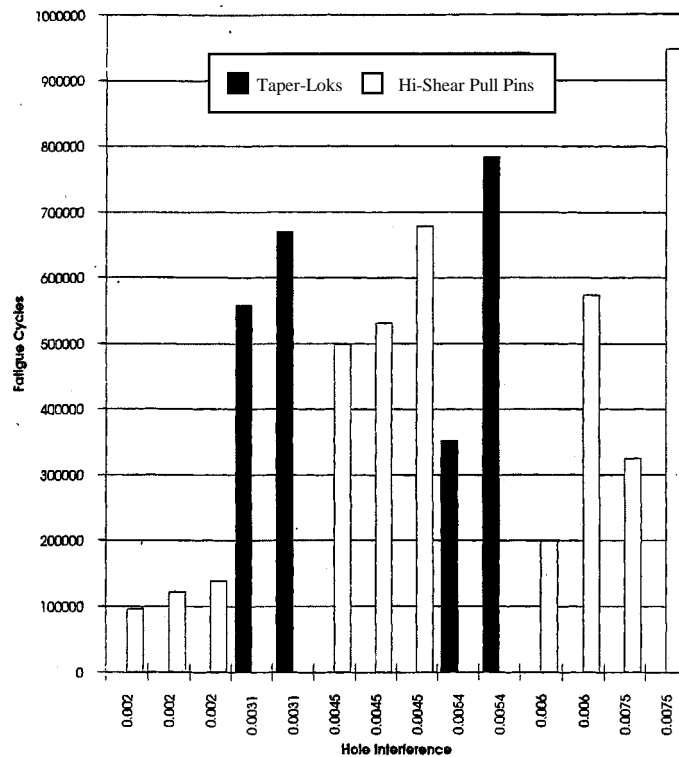


Figure 2. Graphic Comparison of Fatigue Life Related to Tapered- and Straight-Shank Fastener Interferences, McDonnell Aircraft Lab Tests.

If straight-shank fastener interference is to be proven a major factor in durability, then fatigue cycles should correlate especially well with fastener interference at failure sites. Fastener interferences plotted for the straight-shank primary failure sites range from 0.0000 to 0.0050 inch (Figure 3). Overall, the specimen fatigue life trends upward with increasing fastener interference. Specimen numbers 6 and 19, two in an experimental group of 10 Hi-Shear types, did not exhibit the expected results. Specimen No. 6 showed the fatigue damage origin at the faying surface but no evidence of pre-existing damage. Specimen No. 19 showed hole surface fretting, grooves in one fastener hole, and evidence of lack of hole fill; nonuniform interference. Nonuniform interference may be significant in reducing durability but we have no quantity of data to support this.

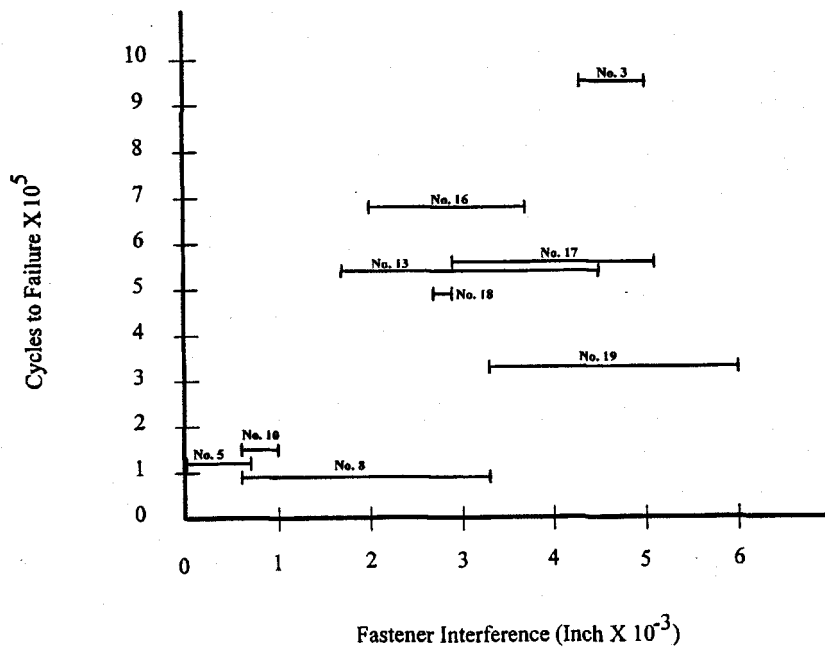


Figure 3. Measured Preinstallation Fastener Interference at Specimen Failure Sites Identified by Specimen Number, McDonnell Aircraft Lab Tests.

FATIGUE LIFE AND FASTENER HOLE QUALITY

As discussed briefly above, structural teardown inspections have qualitatively evidenced fatigue damage at fastener sites where fit was inadequate (nonuniform load transfer), flaws were present in hole surfaces, or design features imposed excessive stress levels. Quantitative evidence has been best presented with laboratory data from a 1977 report by Metcut Research Associates (Reference 2).

This Metcut project, “Verification of Production Hole Quality” for the Air Force Materials Laboratory in conjunction with the Lockheed C-5 Project, had objectives as follows:

1. To establish quantitative hole quality data for an extruded aluminum alloy.
2. To identify the ranking or order of hole quality characteristics as a function of the effect on fastener life of fatigue critical interference fit fastener systems and joints.
3. To evaluate the performance of a tapered blade cutter in producing tapered holes suitable for fastener installation in a single operation.
4. To develop, fabricate, and test specimens for an ongoing AGARD program.

This project used a variety of dogbone and strap specimens with tapered fasteners to evaluate both hole geometry and surface condition variables on fatigue life. The material was 5/16-inch-thick 7175-T73511 shot peened, anodized, and coated aluminum alloy extrusion. Fasteners were 5/16-inch-diameter 8740 alloy steel Taper-Loks. Fatigue loading was applied a 900 to 1800 cycles/minute with gross maximum stress in the 22 to 25 Ksi range and R ratios of +0.1 and -0.33. Fastener interferences ranged from 0.0005 to 0.0060 inch. Hole preparation influence on fatigue life was as follows:

- Specimens with hole wall surface roughness of 125 microinches or better yielded similar fatigue behavior.
- Burrs on the nut side of the hole do not have a detrimental effect.
- Hole axis perpendicularity within 3 degrees is tolerable.
- Hole ovality is a serious concern.
- Bellmouthing and barreling are of concern, but less than ovality.
- Rifling, axial scratches, chatter, plastic deformation, tears, and laps (within the range of severity explored in this project) have minimal effect with fasteners installed but are detrimental with open holes.

Holes were primarily checked for bearing, ovality, bellmouthing, barreling, rifling, and roughness with a bluing pin. Hole contour was checked with a multiple orifice tapered air gage probe. Bearing was also measured with an emerging capacitance gaging technology. Tapered fastener interference effects on fatigue life observed in the 1970s was similar to the contemporary findings with four Taper-Lok comparison specimens used by Douglas Aircraft. Twenty Metcut tapered fastener specimens had interference in the range of 0.0005 to 0.0060 inch and resulting fatigue life over an order of magnitude from 100,000 to 1,000,000 cycles (Figure 4). The Metcut report noted the following fastener interference effect:

“Specimens in which the fastener interference was 0.0035 inch or 0.0048 inch demonstrated maximum fatigue life. The 0.0060 inch level of interference, which is excessive of the (Lockheed) specification, showed a small but statistically insignificant drop in fatigue strength.”

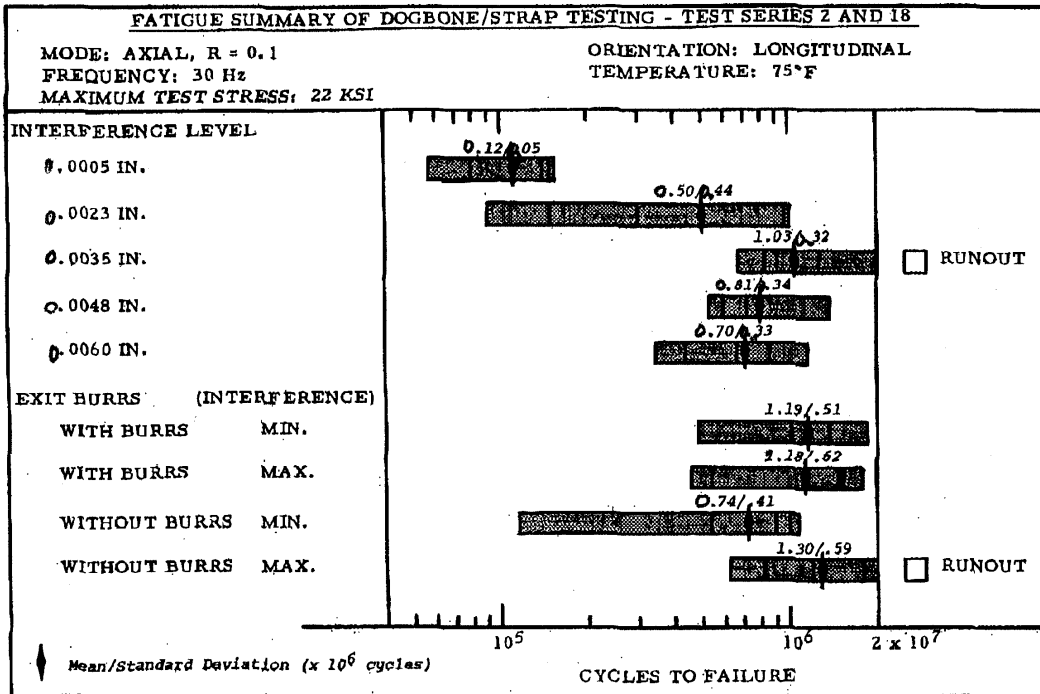


Figure 4. Fatigue Summary of Taper-Lok Fastener Interference Level, Metcut Lab Test.

GENERAL OBSERVATIONS

Evidence derived from the Douglas and Metcut tests provide the following general observations:

1. Durability of airframe joints is markedly influenced by degree of fastener interference and dimensional uniformity of holes.
2. The practical and effective interference range for fasteners is 0.0035 to 0.0050 inch.
3. Production flaws such as rifling, gouges, and roughness are mitigated with appropriate fastener interference.

These observations emphasize the necessity for efficient, precise, and thorough fastener hole dimensional measurement to assure desired fatigue properties. The practical means to do this had U S Air Force development origins in the 1970s. The technology has matured since then into the present day Capacitance Measurement System (CMS).

CAPACITANCE MEASUREMENT SYSTEM OVERVIEW

This technology uses electrical capacitance as a transducer function to measure distance. Two basic physical principles are employed by the CMS. The first principle is the behavior of a parallel plate capacitor, where the capacitance is proportional to plate separation. The second principle involves a capacitor discharge rate dependence on the resistance-capacitance time constant (Figure 5). The CMS transducer has a fixed capacitance plate area and circuit resistance, leaving the plate separation as the time dependent variable. A cylindrical probe capacitor plate placed into a hole which is the opposing electrically grounded capacitor plate provides for space measurement related to discharge time. Extending this concept to a precise multicapacitor probe (Figure 6) enables a detailed characterization of fastener hole features.

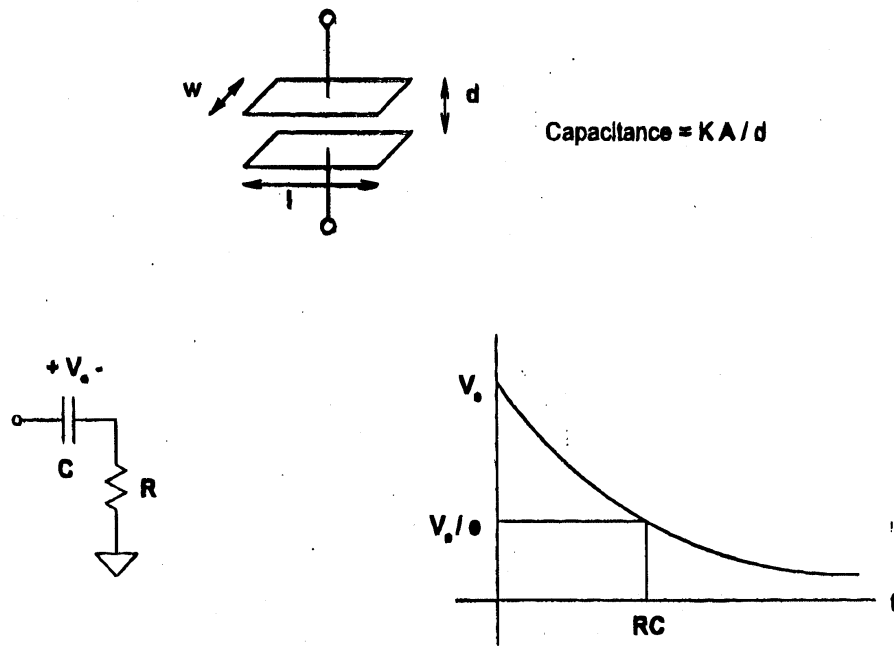
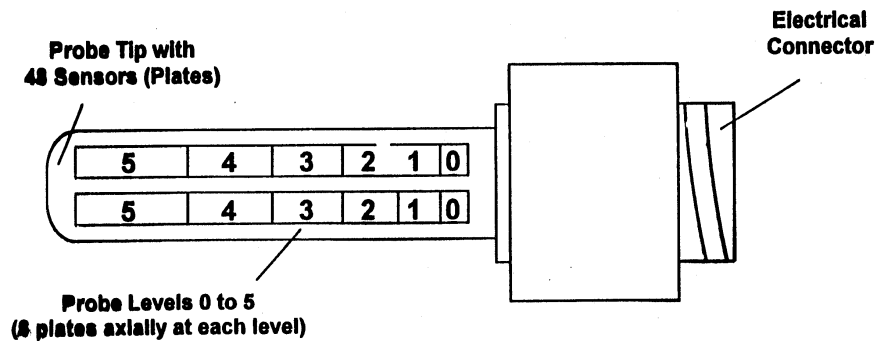


Figure 5. Physical Principles of Capacitance Measurement Use Electrical Discharge Rate as a Measure of Space Between Plates.

- **Probe Layout and Construction**



- **System Calibration**

Measure the Capacitance of 2 ring gauge standards. The diameters of the standards are traceable to NIST to within +/- 20 microinches

Figure 6. The Capacitance Measurement System (CMS) Hole Probe Uses Multiple Capacitor Plates to Characterize Hole Quality.

The CMS (Figure 7) consists of four major components which are:

1. The capacitor probe which is inserted into the hole.
2. An electronics unit with circuitry to measure capacitance.
3. A microcomputer for capacitance data processing, storage, and display.
4. A hand-held device for operator control of system operation.

System accuracy for a typical 5/16-inch-diameter probe is to within less than 0.00015-inch measurement uncertainty (Figure 8). Calibration provides resolution to within +/-20 microinches, traceable to NIST. Data acquisition time is approximately 1 second per hole in contrast to 5 minutes per hole for conventional inspection.

The microcomputer affords convenient diskette data storage and graphical readout. User information options include both axial profiles and section views at selected depths and tabulated numerical records (Figures 9 and 10).



Figure 7. The Four Major Components of the Capacitance Measurement System.

Accuracy Analysis - Measurement Uncertainty

- Total Uncertainty = Calibration Error + Measurement Uncertainty
- Worst Case Calibration Error Is Typically Bounded by $\pm 0.0001''$
- Total Uncertainty = $\pm (0.0001'' + \text{Measurement Uncertainty})$
- For a 0.1" by 0.1" Plate (Typical 5/16" Probe) the Total Uncertainty Over a 0.003" Specification Range Is $\leq 0.00015''$

Figure 8. The Capacitance Measurement System Accuracy Provides Radial Dimensions to 0.00015 Inch.

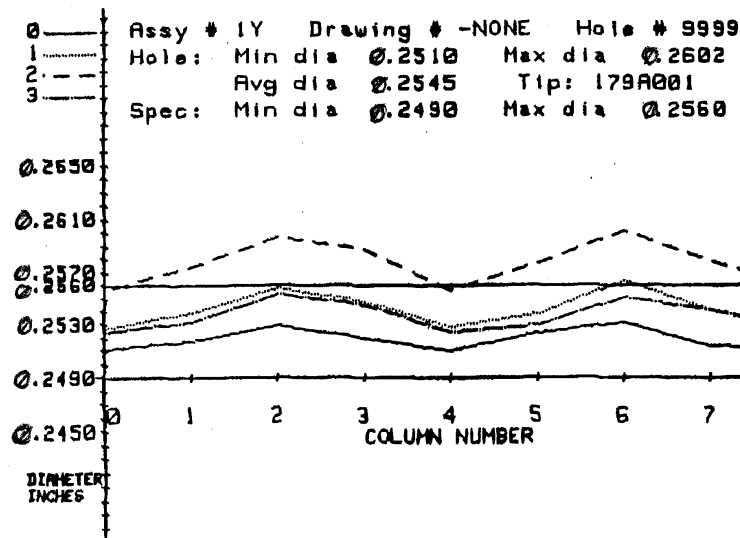


Figure 9. The Capacitance Measurement System Axial Profiles of a Fastener Hole Surface.

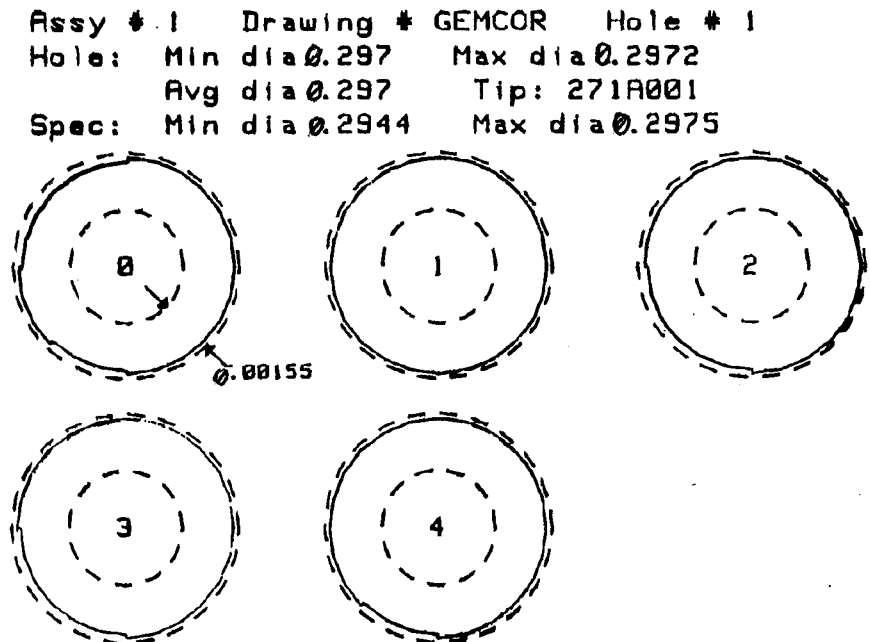


Figure 10. Capacitance Measurement System Section Profiles of a Fastener Hole Surface.

SURFACE DISCONTINUITIES

Scratches, skin mismatch, and fastener head protrusion are discontinuities encountered in both production and rework environments. Remedial action for scratches commonly involves blending with abrasives. Mismatch and fastener head protrusion require disassembly, machining and reassembly. These processes rely on quantitative assessments. Determining severity or out-of-tolerance conditions can be costly, time consuming, and of suspect accuracy, e.g., fingernail catch on a scratch.

The in-service environment adds to the picture with environmental degradation including corrosion and abrasion. Quantifying corrosion depth in structure and scratch/erosion depth in windshields is a challenge faced daily. Conservative design margins are commonly drawn from in blending out these surface discontinuities. Again, quantitative assessment of damage must be available to properly effect remedial action.

SCRATCH MEASUREMENT SYSTEM OVERVIEW

The Boeing Commercial Airplane Group Quality Assurance R & D organization addressed the surface discontinuity quantification challenge with optical technology. A portable machine vision instrument was developed for “out-of-laboratory” use. Identified as the Scratch Measurement System (SMS), the instrument shown in Figure 11 applies class I or class II laser illumination and a charge coupled device camera as source and sensor in a digital vision system. The illumination is positioned for normal incidence to the surface. The camera is oriented at a 45-degree angle to the surface, providing spatial distribution of reflected light which can be related to discontinuity depth. Certain applications are improved with a light diffusing paint on the surface.

Digitized spatial distribution and intensity of reflected light is passed through front end gate arrays for dedicated signal conditioning. The array outputs are then transferred to a central processor for user selected readout formats. A function block diagram of the system is provided in Figure 12.



Figure 11. Scratch Measurement System is a Machine Vision Instrument, Packaged for Portability and Ease of Use in a Production and In-Service Environment.

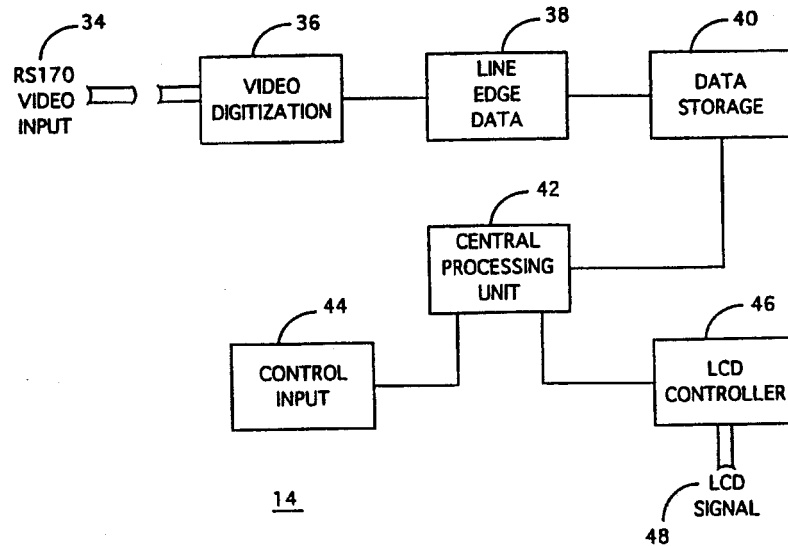


Figure 12. Sensor/User Interface Components of the Scratch Measurement System Depicted in a Function Block Diagram.

Typical readouts are presented in Figure 13. Filtering and edge enhancement features provide options for data format and image content on a liquid crystal display. Output hard copy and digital records are provided for both immediate action and archiving. Performance of the Scratch Measurement System has been established as outlined in Figure 14.

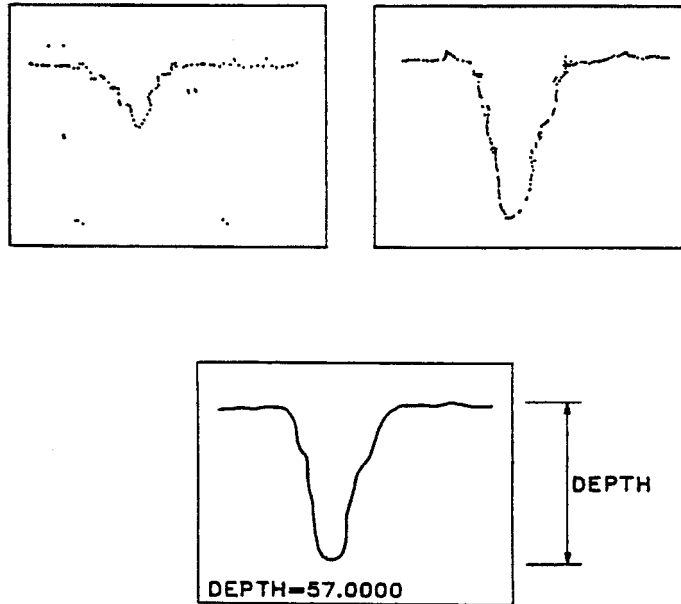


Figure 13. Typical Scratch Measurement System Graphic Scratch Cross Section Profile Displays Unfiltered, Enhanced, and Referenced to Calibrated Value.

- Accuracy of ~ 1% Field of View (F.O.V.) from 0.0005 inch
- 0 - 0.20 inch dynamic depth resolution for small F.O.V.
- 0 - 0.100 inch dynamic depth resolution for large F.O.V.
- Small Head F.O.V. - 0.055 inch
- Large Head F.O.V. - 0.148 inch
- Currently developing 0.500 inch F.O.V. Sensing Head

Figure 14. Scratch Measurement System Performance Characteristics.

CONCLUDING REMARKS

Capacitance Measurement System

Fastener hole quality levels for ever increasing structural endurance demands continue to challenge both new aircraft production and maintenance rework operations. Demonstrated options for replacement of costly tapered interference fasteners and tedious close tolerance hole quality measurements have been discussed. Required levels of durability have been demonstrated with straight-shank Hi-Shear interference fasteners. The fastener installation process has been complemented with precise and efficient hole quality determinations employing the Capacitance Measurement System (CMS). Increasing numbers of CMS users in both military and commercial environments are applying this cost-effective interference fastener hole quality tool (Figure 15).

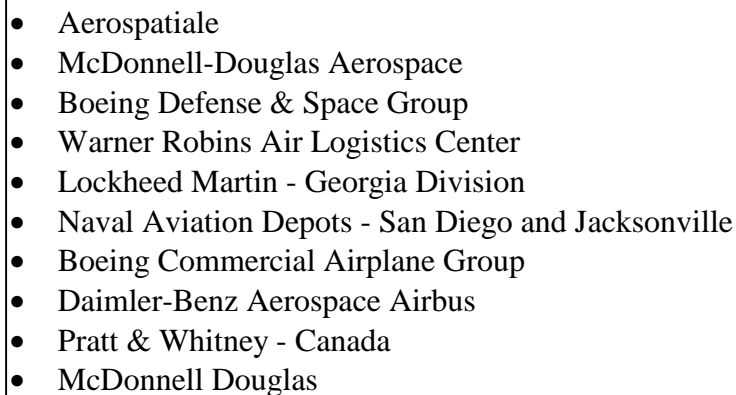
- 
- Aerospatiale
 - McDonnell-Douglas Aerospace
 - Boeing Defense & Space Group
 - Warner Robins Air Logistics Center
 - Lockheed Martin - Georgia Division
 - Naval Aviation Depots - San Diego and Jacksonville
 - Boeing Commercial Airplane Group
 - Daimler-Benz Aerospace Airbus
 - Pratt & Whitney - Canada
 - McDonnell Douglas

Figure 15. Users of the Capacitance Measurement System.

Scratch Measurement System

The Scratch Measurement System is an innovation which is experiencing a rapid growth in a wide range of applications. Originally developed for quantifying skin depth of scratch in the production environment, the spectrum of use is extending to include in-service corrosion damage quantification. This enabling technology is affordable, has demonstrated a number of capabilities to date, and is experiencing continued expansion in a wide range of practical applications.

REFERENCES

1. LR-15503, MD-11 Wing Box Fatigue Tests - Taperlocks and Hi-Shear Pull- Stem Pins, R. C. Lewis, et. al., Douglas Aircraft Materials & Processes Engineering Report, November 1994.
2. AFML-TR-77-185, Verification of Production Hole Quality, William P. Koster, John B. Kohls, and John T. Cammett, Metcut Research Associates, Inc., Cincinnati, Ohio, and B. L. Cornell, Lockheed - Georgia Company, Marietta, Georgia, November 1977.
3. Engineering Report 03/002/0001, Measuring Results of the 6AL-4V Titanium Alloy "2NSA5092V07" - Pins Manufactured by Voi-Shan/Diessel GMBH, Voi-Shan/Diessel GMBH Aerospace Fasteners, 31113 Hildesheim, 13 August 1993.
4. Project No. 95-5577, Robins Laboratories Metallurgical Analysis Team, Warner Robins Air Logistics Center, Robins AFB, GA, 16 June 1995.
5. F-16 Tapered Fastener Installation Process, presentation by G. J. Melven, Lockheed Fort Worth Company, 27 April 1993.
6. LG81WP7254-002, Capacitance Technique for Quantitative Inspection of Fastener Holes - A New NDE Technology, H. S. Gibson and W. H. Lewis, Lockheed - Georgia Company, Marietta, Georgia, September 1981.
7. AFWAL-TR-82-4041, Fastener Hole Inspection for New Aircraft: Capacitance Hole Probe System, H. S. Gibson, Jr., P. E. Goodman, S. R. Glidewell, and W. H. Lewis, Lockheed - Georgia Company, Marietta, Georgia, May 1982.
8. Capacitance - A Better and Cheaper Hole Inspection Method, W. H. Lewis, 14th. Symposium on Nondestructive Evaluation, April 19-21, 1983, Nondestructive Testing Information Analysis Center, Southwest Research Institute, San Antonio, Texas.
9. IEEE Transactions, Vol. IM-32, No. 2, Design of Algorithms to Extract Data from Capacitance Sensors to Measure Fastener Hole Profiles, J. L. Hammond, Jr. and S. R. Glidewell, June 1983.
10. MR84-900, Society of Manufacturing Engineers 1984 Aerospace Engineering Conference, Anaheim, California, Capacitance - A Better and Cheaper Hole Inspection Method, W. H. Lewis and C. T. Ratcliffe, Lockheed - GETEX, Atlanta, Georgia, January 1984.
11. Hole Probe System Inspects Northrop Jet Fighter Assemblies Fast at Less Cost, Nat Wood, CNC/West, October 1986.

12. Scratch Measurement Apparatus and Method, United States Patent Number 5,283,642, Dennis P. Sarr; Assignee: The Boeing Company, February 1994.
13. 777 Engine Nacelle Gap Mismatch System - Interim 1, Dennis P. Sarr - Boeing Company Operations Technology Development Report No. NG401C, 11 November 1995.

ANALYSIS OF A COMPOSITE REPAIR

Cong Duong and Jin Yu
McDonnell Douglas Aerospace
Long Beach, CA

SUMMARY

This paper presents analysis results for the problem of a composite patched stiffened panel containing a skin crack. The solution method used here is described in Ref. 7 which makes use of complex variables and Fourier transform techniques within the framework of linear elasticity. The repaired stiffened panel considered is under uniaxial tension load along with uniform temperature change. Also included in the formulation were the problem of disbond along the crack faces and the case of failed stiffeners. Effects of patch boundaries, thermally-induced stresses and debonding on the crack tip behavior were evaluated through examples of common repairs. It is found that the stiffener effect is relatively insignificant while the disbond along the crack faces should not be neglected if it exists.

INTRODUCTION

It is known that a composite patched repair offers an effective way to arrest the crack in the sheet because of the relative high stiffness in composite material and continuous bond provided in the interface.

Theoretical developments intended to address various aspects of issues in composite repairs can be found in References 1-6. In the earliest works [1, 3], the patch was modeled as an infinite orthotropic sheet. An approximate analysis for an elliptical patch without the effect of disbond was given in [4, 5]. The repair problem of an infinite composite strip parallel to the skin crack without the effects of disbond and thermal stresses was considered in [6]. Recent work by Duong and Yu [7] takes into account several issues in the formulation, including the effects of a disbond, stiffeners, temperature changes, finite patch boundaries, and asymmetrical configurations. The purpose of this paper is to present the results obtained by the method in Ref. 7 and discuss the implications on the damage tolerance of composite repairs. A brief summary of the approach will be given below.

ANALYTICAL FORMULATION

The problem under consideration involves a cracked stiffened sheet adhesively bonded by a composite patch under remote tension. The sheet was assumed infinite and isotropic and the patch an infinite orthotropic strip normal to the crack. Further, the sheet is reinforced by a set of stiffeners discretely fastened to the sheet normal to the crack. The patched panel is under uniaxial tension loaded remotely in such a manner that strain compatibility prevails. Also included in the formulations are the mismatch in thermal expansion as the panel undergoes temperature changes and the debonding along the crack surfaces. The cracked sheet and the patch are assumed under a generalized plane stress state. The stiffeners are modeled by one-dimensional axial members, and the adhesive is idealized by two-dimensional shear springs.

As described in [7], the problem was first decomposed into two parts. Part I considers an uncracked sheet with intact stiffeners under remote tension and temperature variation. The stress in the stiffened sheet at the prospective location of the crack is readily determined. In Part II, a crack with a prescribed disbond region surrounding it is introduced into the sheet. Applied on the surfaces of the crack are tractions as obtained from the Part I but in the opposite direction. This will induce shear forces in the adhesive as well as in the fasteners in the vicinity of the crack.

To evaluate the disturbance, the sheet and the patch were divided into finite number of regions in exactly the same manner. The compliances for the patch and sheet were derived using the complex variable within the theory of two-dimensional elasticity. For the finite-width patch, the traction free condition along the edges are satisfied by superposing the tractions, equal but opposite in sign to the stresses at the same locations in an infinite domain. Fourier transform techniques were used to obtain the stresses and displacements in the strip.

Thus, a set of equations can be set up with the transferring shear forces as unknowns by requiring that the displacement between the sheet and patch be compatible. In addition, another set of equations for fastener forces were assembled by enforcing that displacement between the sheet and stiffeners be compatible at each fastener location. In the latter case, the coefficients contain the compliance of a stiffener, which can be considered either intact or a broken one-dimensional rod. It should be noted that the perturbation in terms of interface shear and fastener loads only pertain to the vicinity of the crack. The stress intensity factors at the two crack tips due to the fastener forces and the interfacial shear tractions are then numerically computed using the quadrature formula.

RESULTS AND DISCUSSION

Two problems were selected and solved by the present method for the purpose of assessing the merit of the method. The materials and their mechanical properties used in these examples are given below:

Sheet Material	Aluminum Alloy $E = 72.4 \text{ GPa}$, $\nu = 0.33$, $\alpha = 22.7 \times 10^{-6} \text{ }^\circ\text{C}$
Composite Patch	Boron/Epoxy $E_y = 210 \text{ GPa}$, $\nu_y = 0.1677$, $\alpha_y = 4.5 \times 10^{-6} \text{ }^\circ\text{C}$ $E_x = 25 \text{ GPa}$, $G_{xy} = 20.7 \text{ GPa}$, $\alpha_y = 20 \times 10^{-6} \text{ }^\circ\text{C}$
Adhesive	AF-163-2 $G_a = 406 \text{ MPa}$, $t_a = 0.13 \text{ mm}$, $T_{\text{curing}} = 120^\circ\text{C}$

The first problem consists of an unstiffened aluminum sheet 1.75 mm thick. The sheet contains a crack 7 mm long and is under a remote tension load of 71.3 MPa. An infinite composite strip 80 mm wide is patched over the crack and there is no disbond. The thermal stress resulted from the curing temperature of 120°C and cruising at an altitude of 7652 m is also evaluated. The results in terms of stress-intensity factors as a function of patch thickness are presented in Fig. 1. Also shown in Fig. 1 are the results from [5].

Before we compare the two results, a few differences between the current model and that used in [5] should be pointed out. The patch in [5] is an ellipse 160 mm long and 80 mm wide and under a remote biaxial stress field ($\sigma_x = 35.6 \text{ MPa}$). Approximate scheme was used in [5] to compute the stress intensity factor solutions using a semi-infinite crack model. In calculating the thermal stresses, only a small area of the skin underneath and in the vicinity of the patch is cooled from T_{curing} to room temperature in [5]. This local cooling is then followed by a uniform (global) cooling from room temperature to the cruising temperature of about -34.5°C, however. Finally, the correction for the out-of-plane bending effect is included the results of [5].

From Figure 1, the present results are in very good agreement with those obtained by Fredell for the case without thermal consideration. This indicates that, without thermal effect, the bending has a small influence in the crack behavior. On the other hand, when thermal effect is included, there is a large discrepancy between the two solutions. This may be attributed to the facts that [5] assumes localized cooling from curing temperature and accounts for out-of-plane bending, while the present model uses the global cooling model and ignores the bending effect. As mentioned in [5], for boron/epoxy patches, local cooling curing results in only small thermal stresses. By neglecting the thermal stresses due to curing in our model, the results are in better agreement with solutions in [5] as shown in Figure 1. There is, however, still significant differences between the two solutions. This may be primarily due to out-of-plane bending which is amplified in the presence of thermal cooling as noted in [8].

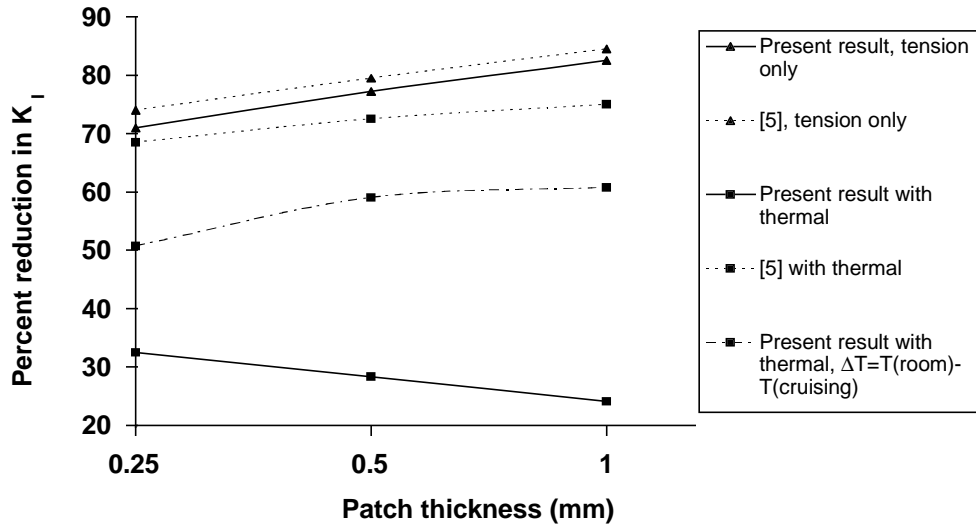


Figure 1. Comparison of Results for a Typical Repair in an Unstiffened Cracked Sheet ($a=70$ mm).

The second problem consists of a stiffened aluminum panel containing a symmetric two-bay crack. The sheet is 1.6 mm thick and loaded remotely at 50 MPa. The stiffeners are made of the same materials as the sheet and have an identical cross-sectional area of 200 mm². They are mechanically attached to the sheet at a constant pitch of 25 mm and oriented normal to the crack at 400 mm apart. The fastener hole size is 4.8 mm and its flexibility is accounted for, see [7]. The thermal stresses are computed based on global cooling of the patch and the skin at $\Delta T = -154^\circ\text{C}$. Three crack lengths of 20, 64 and 110 mm are considered to study the edge effect of the patch. An elliptical disbond is assumed to exist along the crack faces with its tip coincident with the crack tip. The ratio of minor axis of the ellipse to the major axis is set to be 0.1 in light of [2]. The effect of disbond on the stress intensity factor is assessed.

The effects of the disbond, the patch finite width, and the crack length on the stress intensity factor solutions for this example problem are illustrated in Figures 2 and 3. For clarity, the results for the remote tension are presented in Figure 2 and for the thermal stresses, in Figure 3. The corresponding “infinite patch” solutions are also included there for comparison. Since the analysis methods are within the limit of linear elasticity, the results for the case of combined thermo-mechanical loads can be obtained by superposition. From Figures 2 and 3, the effect of the disbond on K_I is about 10 percent higher for a short crack and about 20% for a longer crack. To study the influence of the stiffeners on K_I , the corresponding solutions for the unstiffened cracked sheets are also generated and they are found to be very close to the results shown in Figures 2 and 3 for the stiffened panel. The later results are therefore omitted from the paper.

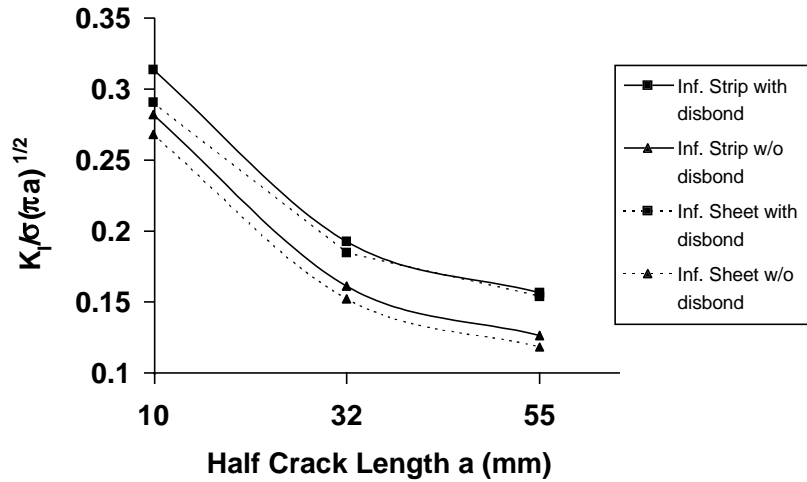


Figure 2. Normalized Stress Intensity Factor for a Repair in a Stiffened Sheet as a Function of Crack Length Due to the Remote Tension.

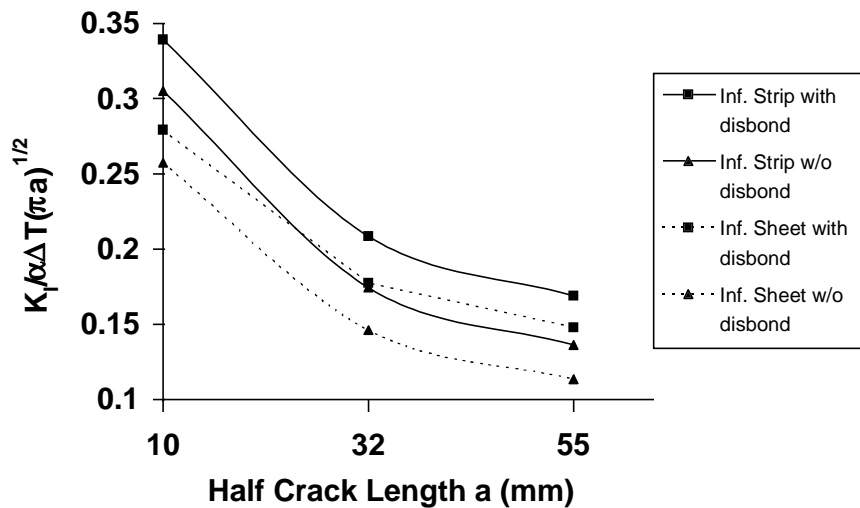


Figure 3: Normalized Stress Intensity Factor for a Repair in a Stiffened Sheet as a Function of Crack Length Due to Thermal Stresses.

The difference in K_I between the infinite sheet patch and the infinite strip is less than 5 percent in the absence of the thermal stresses for all three crack sizes, but it becomes more pronounced when the thermal stresses are included in the calculation. To further understand the interaction between the crack and the patch's edge, one should re-examine the solution procedure mentioned in the previous section. As outlined in that section, the repair problem is dealt with in two steps. First, starting with an uncracked stiffened sheet, the stress at the prospective location of the crack is determined in close form. The second step is to introduce a crack into the stiffened sheet. If the interaction between the crack and the patch boundary is negligible, the problem in the second step for an infinite strip repair can be estimated by

using an infinite orthotropic sheet model. The results from the approximate analysis for all cases considered agree very well with the more rigorous results except for the case of a very long crack surrounding it by a disbond and approaching the patch boundary, see Figures 4 and 5. Nevertheless, the approximate analysis still yields a reasonably good result for the mentioned extreme case of crack length.

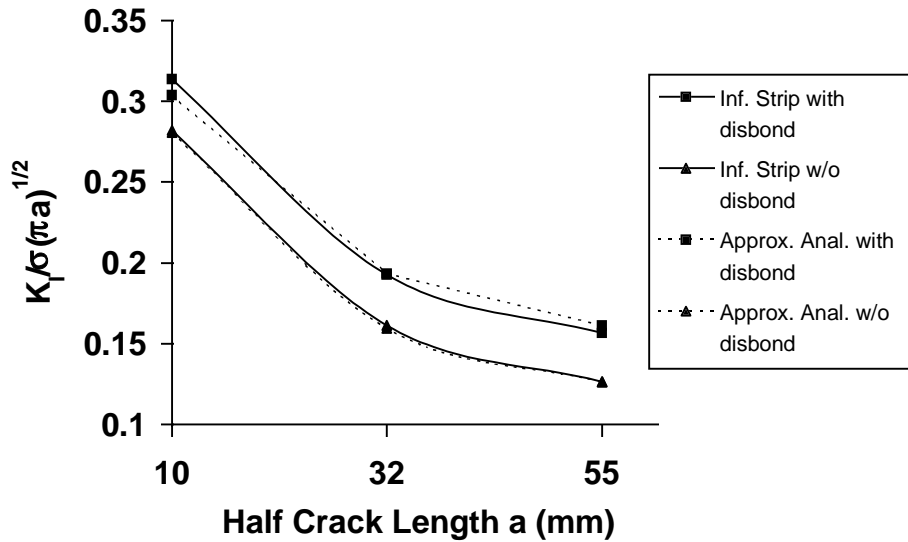


Figure 4: Results From the Approximate Analyses Based on Rose's Approach for a Repair in a Stiffened Sheet Due to the Remote Tension.

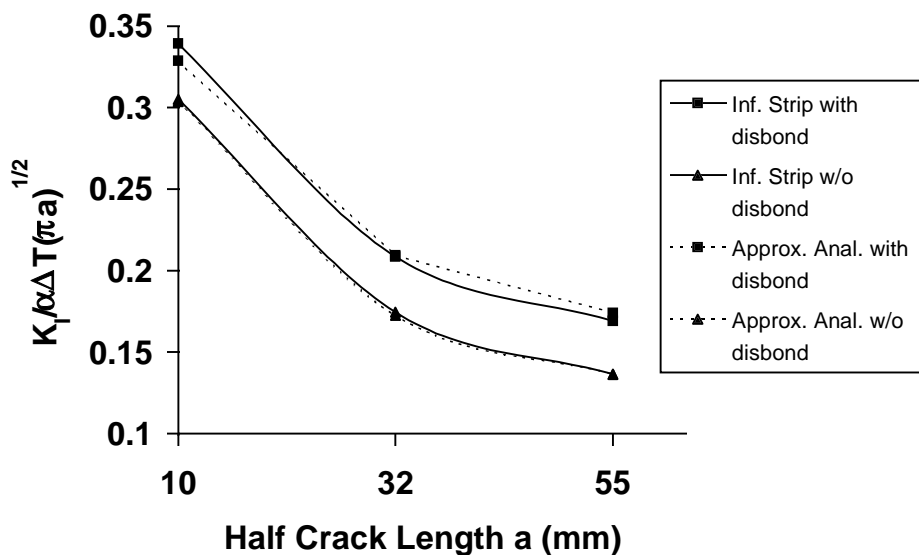


Figure 5: Results From the Approximate Analyses Based on Rose's Approach for a Repair in a Stiffened Sheet Due to Thermal Stresses.

CONCLUSIONS

Analysis results intended for the damage tolerance assessment of a composite patched skin crack repair is presented. The analysis method makes use of linear elasticity solution for the stress and displacement in the sheet and patch. The solution formulation also accounts for the disbond between the skin and patch and the thermal stresses induced by temperature variations. Numerical results for the example problems show that thermal stress is important on the crack tip behavior. The influence of disbond can be significant in some cases and should not be overlooked. The present analysis also reveals that the presence of stiffeners has little influence on the near tip distribution. It should be noted that the present methodology can be applied to the problem of a crack growing beyond the patch boundary and can be easily modified for the repairs by an infinite strip parallel to the crack. The out-of-plane bending effect is currently incorporated into the analytical model based on the simple beam theory. The present work has been funded by McDonnell Douglas Independent Research and Development.

REFERENCES

1. Erdogan, F. and Arin, K.: A Sandwich Plate With a Part-Through and a Debonding Crack. *Eng. Fract. Mech.*, vol. 4, 1972, pp. 449-458.
2. Ratwani, M.: Analysis of Cracked Adhesively Bonded Laminated Structures. *AIAA*, vol. 17, 1974, pp. 988-994.
3. Ratwani, M. M. and Kan, H. P.: Development of Composite Patches to Repair Complex Cracked Metallic Structures. Final Report NADC-80161-60, U.S. Navy, Naval Air Development Center, vol. I, 1982.
4. Rose, L. R. F., Baker, A. A., and Jones, R., eds: *Bonded Repair of Aircraft Structures*, Kluwer Academic Publisher, 1988.
5. Fredell, R. S.: Damage Tolerant Repair Techniques for Pressurized Aircraft Fuselages. Ph.D. Thesis, Delft Technical University, The Netherlands, 1994.
6. Atluri, S. N.: Composite Repairs of Cracked Metallic Aircraft Structures. DOT/FAA/CT-92/93, 1992.
7. Duong, C. and Yu, J.: The Stress Intensity Factor For a Cracked Stiffened Sheet Adhesively Bonded by a Composite Patch. Submitted for publication.
8. Sun, C. T. et al.: Analysis of Cracked Aluminum Plates Repaired With Bonded Composite Patches. *AIAA*, vol. 34, 1996, pp. 369-374.

ANALYSIS OF SAFETY PERFORMANCE THRESHOLDS FOR AIR CARRIERS BY USING CONTROL CHARTING TECHNIQUES*

Andrew Y. Cheng

James T. Luxh•j

Department of Industrial Engineering
Rutgers University, Busch Campus
Piscataway, NJ 08855

Regina Y. Liu

Department of Statistics
Rutgers University, Busch Campus
Piscataway, NJ 08855

SUMMARY

The rapid growth of air transport and air traffic density has long demanded that the FAA develop an effective safety inspection system. Well-defined thresholds are essential for the inspection system since they provide standards for both monitoring and regulating purposes. In this paper, we use control charting techniques to derive thresholds for inspection measures and to provide charts for monitoring them continuously. Our thresholds are justified statistically and safeguarded by probabilities of errors. This procedure has been applied to an FAA sample data set of operational surveillance results of ten air carriers and yielded promising results.

INTRODUCTION

An expected increase in usage of domestic flights in the next few years coupled with an aging aircraft population has led the Federal Aviation Administration (FAA) to initiate new air safety research efforts. Domestic passenger enplanements increased from 250 million to 450 million annually between 1977 and 1987 [*FAA Plan*¹]. The FAA anticipates that domestic enplanements will reach 800 million in the year 2000 and exceed a billion by 2010 for a 128 and 272 percent increase [*FAA Plan*¹]. This steady growth of air transport and air traffic density places increasing pressure on safety inspection activities.

* This article is based on research carried out at Rutgers University. The contents of this paper do not necessarily reflect the official view or policy of the Federal Aviation Administration. They reflect the view of the authors, who are solely responsible for the accuracy of the facts, analysis, conclusions, and recommendations presented herein.

One of the safety research efforts is to define new safety indicators which will enable inspectors to identify air carriers that present a greater safety risk and warrant heightened surveillance. The FAA has recently developed the Safety Performance Analysis System (SPAS) [SPAS^{2,3}]. It is designed as a decision support system by enabling inspectors to access existing FAA maintenance databases and identify the high-risk airlines. In each area of inspection, SPAS² defines a performance measure, which is a gauge of the performance of a specific carrier as compared to the performance of its peers. Thresholds for each performance measure are then derived and used to characterize meaningful performance levels of air carriers under surveillance. The meaningful performance levels include *expected*, *advisory*, *alert*, and *informational* [SPAS³]. Their definitions within the context of inspection system are:

- *Expected* is the normal range for a performance measure;
- *Advisory* indicates a performance measure is worse than the normal range;
- *Alert* indicates a performance measure is “significantly” worse than the normal range;
- *Informational* indicates a performance measure is better than the normal range.

An arbitrary choice of the range that defines the thresholds cannot sufficiently distinguish the carriers with somewhat worse performance from the ones with significantly worse performance. This paper presents a procedure to determine thresholds by control charting techniques. These thresholds are justified statistically in terms of false alarm rate and the average run length of the performance change and can distinguish different levels of performance efficiently.

Although this procedure can be applied on all performance measures, this analysis focuses on the operational surveillance results of ten air carriers. These carriers are of similar service type. The data set was provided by the FAA William J. Hughes Technical Center at Atlantic City International Airport, NJ. For confidentiality, the carriers’ names are masked as Carrier 1, Carrier 2, etc. The operations surveillance result is a general assessment of the inspection results from all operations surveillances for an air carrier. Its performance measure is defined as the unfavorable rate and is calculated as the fraction of the unfavorable records over the actual surveillance records in each month [SPAS²]. The data set consists of inspection records of a 66-month period from October 1989 to March 1995. Each record includes the number of unfavorable records, the number of total records, and the fleet size at the end of each month for each carrier.

THRESHOLDS BASED ON STATISTICAL CONTROL CHARTS

Control charts are commonly used in statistical process control for detecting significant process change, and then signaling for corrective actions [Montgomery⁴]. The construction of a control chart is equivalent to continuous plotting of the acceptance regions of testing two hypothesis: the null hypothesis, indicating that the process is in statistical control (only chance causes are present) and the observations are consistent with the preset

standard and the alternative hypothesis, indicating the opposite. Since a control chart is a graphical tool to detect significant process change, the charting techniques can help in monitoring the performance measures, and properly chosen control limits for the chart would yield a set of meaningful thresholds for the assessment of each carrier's performance.

There are different types of control charts for monitoring different types of data. A p-chart is designed to monitor the fraction of nonconforming measures observed from a process. This chart is considered appropriate in monitoring the operational surveillance since an unfavorable rate is viewed as a nonconforming fraction observed from the surveillance process. A typical p-chart consists of a center line and a set of control limits: *UCL* and *LCL*. The observed unfavorable rates, \hat{p} 's, then plot on the chart over consecutive observations. When a \hat{p} falls outside of the control limits, it is considered that a significant process change has occurred and assignable causes should be sought. Besides, the chart also allows us to detect any trend or pattern formation by visualizing the whole sequence of observations. The number of nonconforming measures, e.g., the number of unfavorable records, follows a binomial distribution with parameter n (the number of inspections) and p (the true unfavorable rate) when the inspection results are independent. If n is sufficiently large so that $np \geq 10$, the unfavorable rate follows approximately a normal distribution with parameters $\mu = p$ and $\sigma = \sqrt{p(1-p)/n}$ by applying the Central Limit Theorem. Therefore, the center line is set at p as the standard and the conventional 3-sigma control limits for a p-chart are defined as

$$UCL = p + 3\sqrt{p(1-p)/n}, \quad LCL = p - 3\sqrt{p(1-p)/n}. \quad (1)$$

The 3-sigma control limits are chosen so that the probability of false alarm, α , is at most 0.0027. As the inspection size in our data set changes from time to time, the control limits should be adjusted accordingly. If the number of inspections of the j th month is n_j , the control limits for that month should be:

$$UCL_j = p + 3\sqrt{p(1-p)/n_j}, \quad LCL_j = p - 3\sqrt{p(1-p)/n_j}. \quad (2)$$

Since similar carriers are expected to exhibit similar performance over a period of time under stable inspection conditions, their performance can be monitored with a common standard. Ideally, the standard should represent the perfect performance measure of a peer group. In practice, such perfect performance is unrealistic and we must face the problem of identifying an attainable standard. When the standard is unknown, it is generally estimated by the aggregate mean of all nonconforming fractions. The aggregate mean represents the average value of the performance or quality measures and is computed by

$$\bar{p} = \frac{\sum_i \sum_j D_{ij}}{\sum_i \sum_j n_{ij}}, \quad (3)$$

where D_{ij} and n_{ij} are, respectively, the number of unfavorable records and the number of inspections of carrier i in month j . However, it is arguable to use an average value of all

observations as the standard for monitoring the performance of individual carriers. Cheng et al.⁷ proposed that an aggregate mean of a medium cluster of a peer group is more appropriate for an attainable standard in terms of robust analysis. The medium aggregate mean, \bar{p}_m , is defined as

$$\bar{p}_m = \sum_{i \in * } \sum_j D_{ij} / \sum_{i \in * } \sum_j n_{ij}, \quad (4)$$

where * indicates the collection of the medium cluster. When a standard is specified, p in (1) and (2) should be replaced by the specified standard. For example, if \bar{p}_m is used as the standard, the center line of the p-chart is at \bar{p}_m and the control limits are

$$UCL_j = \bar{p}_m + 3\sqrt{\bar{p}_m(1 - \bar{p}_m) / n_j}, \quad LCL_j = \bar{p}_m - 3\sqrt{\bar{p}_m(1 - \bar{p}_m) / n_j}. \quad (5)$$

The use of 3-sigma control limits in (1) and (4) stems from the normal approximation of a binomial distribution, with the hope that the expected false alarm rate of 0.0027 be evenly distributed on both ends. That is, the probabilities $\Pr\{\hat{p} \leq LCL\} \cong \Pr\{\hat{p} \geq UCL\} \cong 0.00135$. However, the approximation errors are noticeable when p of the binomial distribution is small, even though the condition $np \geq 10$ is satisfied. Since the distribution function of a binomial random variable with small p is positively skewed, the symmetric normal approximation tends to underestimate the real upper tail probabilities and overestimate the lower ones. Note that the nonconforming fractions are very small in most safety inspection data sets, including ours. Consequently, if we use the conventional control limits in a p-chart to monitor the operational performance, the observed false alarm rate above UCL will be higher and that below LCL will be lower than expected. The approximation errors can be remedied by several methods. Johnson and Kotz⁵ presented an arcsine transformation such that the transformed binomial variable is normally distributed. Although the transformation does lead to more accurate control limits for a p-chart, the calculations are rather complicated. Ryan⁶ proposed a simpler method by adding a modified term to the conventional control limits. However, there are no clear rules for how to choose the best one. Cheng et al.⁷ suggested a simple guideline for the control limits to monitor observations with small nonconforming fractions:

1. If $p > 0.1$ and $np > 10$, use the conventional control limits (as in (2) and (4));
2. If $p \leq 0.1$ and $np > 10$, use Ryan's modified control limits:

$$\begin{aligned} UCL &= p + \sqrt{\frac{p(1-p)}{n}} + \frac{1.15}{n}, \\ LCL &= p - \sqrt{\frac{p(1-p)}{n}} + \frac{1.25}{n}; \end{aligned} \quad (6)$$

3. If $p \leq 0.1$ and $np < 10$, use the arcsine transformed control limits:

$$\begin{aligned} UCL &= \frac{1}{n} \left[\left(n + \frac{3}{4} \right) \sin^2 \left(\sin^{-1} \sqrt{p} + \frac{3}{2\sqrt{n}} \right) - \frac{3}{8} \right], \\ LCL &= \frac{1}{n} \left[\left(n + \frac{3}{4} \right) \sin^2 \left(\sin^{-1} \sqrt{p} - \frac{3}{2\sqrt{n}} \right) - \frac{3}{8} \right]. \end{aligned} \quad (7)$$

In this analysis, we use the control chart in two levels: (1) Monitor the overall performance of the whole group by charting the monthly aggregate unfavorable rates; and (2) Evaluate the performance of individual carriers by charting the individual unfavorable rates. The monthly aggregate unfavorable rate is defined as

$$\hat{P}_j = \sum_i D_{ij} / \sum_i n_{ij}, \quad (8)$$

which represents the performance of the whole group in month j . They are charted to test the stability of the inspection conditions since a standard represents the target performance under stable conditions. The control limits for charting the individual unfavorable rates are chosen to yield meaningful thresholds for evaluating the individual performance. Here, we consider the following definitions for the thresholds:

- *Alert*: the unfavorable rate is equal to or greater than 3 standard deviations above the grand aggregate mean rate;
- *Advisory*: the unfavorable rate is equal to or greater than 2 standard deviations above the medium aggregate mean rate, but is below the alert threshold;
- *Expected*: the unfavorable rate is within 2 standard deviations of the medium aggregate mean rate;
- *Informational*: the unfavorable rate is below the expected threshold.

The *alert* threshold intends to call for special attention on the alarmingly poor performance and is hence designed to detect the performance that is significantly worse than the average performance. On the other hand, the *expected* threshold is to identify a range of normal performance that is worry-free in the safety considerations. A medium aggregate mean rate provides an attainable but more stringent standard than an average value to assure such a worry-free state. Although the false alarm rate for using 2-sigma control limits is slightly higher than using 3-sigma control limits, the sensitivity of detecting an out-of-control observation is improved by trading with the α -risk. Two-sigma control limits are thus used to determine the *advisory* and *informational* levels for their warning purposes. The effectiveness of the thresholds in terms of the measures of the average run length (*ARL*) will be discussed in the Analysis section.

ANALYSIS OF THE DATA

It is important to establish standards or thresholds based on data that are representative of normal performance. We use a trimming scheme based on boxplots to screen the potential “wild” data or outliers (see, e.g., Hoaglin et al.⁸ for detailed justifications for this approach). Figure 1 displays the multiple boxplot of the observed unfavorable rates for the ten individual carriers. There are 22 observations outside the cutoff points, indicated by dots. They are viewed as outliers and are thus removed from estimating the standards. The remaining data form a representative data set and are used in monitoring the aggregate performance of the whole group. The monthly aggregate rates as described in (8) are calculated from the representative data set and are then charted as in Figure 2. The center line is set at the grand average of the representative data, which is 0.044. Since it is less than 0.1 and the aggregate inspection sizes are sufficiently large, we use (6) to compute the control limits by following the guideline described in Section 2. Some observations are found out of the control limits; therefore, the stability of the overall performance is somewhat questionable. Further analyses of the stability are to be discussed later.

An attainable standard for individual carriers is obtained from the medium aggregate mean as defined in (4). The selection of the medium cluster is based on the individual average performance of each carrier as listed in Table 1. They are computed by

$$\bar{p}_i = \sum_j D_{ij} / \sum_j n_{ij}. \quad (9)$$

The medium cluster should be homogeneous and large enough to be representative. Since the performance of Carriers 7, 9, and 10 seems sufficiently far apart from the remaining ones, we choose the remaining seven carriers as the medium cluster. Then the medium aggregate mean is calculated as 0.038. Note that the medium aggregate mean is slightly lower than the grand aggregate mean, the former then satisfies the requirement for a more stringent standard to ensure the worry-free state.

The safety thresholds for monitoring the individual performance are derived from standards of \bar{p} and \bar{p}_m as outlined in Section 2. However, the number of inspections for an individual carrier in our data set is usually not large enough to satisfy the condition $np \geq 10$ when p is around 0.04 or 0.038. We therefore use the arcsine transformed control limits as described in (7) to determine the thresholds. The individual observed unfavorable rates are monitored by these thresholds. The result of Carrier 1 in Figure 3 gives an example of a carrier with normal performance: most of the performance measures fluctuate within the *expected* level and no observation is found in the *alert* level. On contrast, Carrier 10 displays an opposite example in Figure 4: approximately a third of the observations are in the *alert* level. As for Carrier 10, only two observations fall in the *expected* level from September 1990 to December 1992, which indicates that the performance is alarmingly poor during that period. Outside of that period, Carrier 10 seems to have performed rather normally. Such dramatic shift in a long period may be affected by external factors and heightened surveillance is recommended. In practice, assignable causes should be sought for all

observations which fall in the levels other than *expected*. Some of those might just be false alarms, but others might originate from serious flaws.

Since the thresholds are derived from various one-sided control limits, the effectiveness of the thresholds can be demonstrated by the *ARL*. The *ARL* is the average number of observations charted before an observation falls outside of the control limits. An effective control limit is expected to have small *ARL* to detect a significant process change for a quick detection. On the other hand, the *ARL* is desired to be as large as possible when the process remains in control and the false alarm would not occur often. The *ARL* is calculated by $1/\alpha$ when the process is in control and $1/(1-\beta)$ when the process is out-of-control, where α and β are, respectively, the false alarm rate and the power of the test. Table 2 lists the *ARL*'s for the thresholds under different inspection sizes and different actual unfavorable rates. Note that the standard for the *Alert* level is set at 0.044 and that for the other levels is set at 0.038. The *ARL*'s for all levels are large enough when the performance is consistent with these standards. For example, the *Alert* level is expected to be mislabeled only once in 741 months. However, if a serious performance change has occurred, e.g. the unfavorable rate jumps to 0.074, the *Alert* threshold would take little time to spot the change. If the performance change is less serious, e.g., the unfavorable rate has risen to 0.05, the *Advisory* threshold would warn of this change in a short time although it is almost impossible to be spotted with the *Alert* threshold. The detection is more efficient with increasing inspection size.

Note that our thresholds are designed to effectively detect performance that is not consistent with a standard under stable inspection conditions. However, the result in Figure 2 shows that the performance of the whole group is not stable throughout the entire period. Instead, they appear to be considerably stable when they are monitored separately within each of the following three time intervals as shown in Figure 5: (1) October 1989 to June 1990, (2) July 1990 to February 1992, (3) March 1992 to March 1995. This seems to indicate that some changes, such as in inspection policy, have been made near the separation points of the time intervals and the performance measures were affected significantly. If the causes of the changes can be identified, the thresholds should be derived separately for these disjoint time intervals to reflect the performance pattern. The time-breaking scheme we used is, however, somewhat ad hoc since it is a result of trial-and-errors and visualization. It would be further improved by implementing some dynamic adjustments.

In conclusion, our procedure is a general approach to determine the thresholds for safety performance. Even though only p-charts are discussed in this paper, the principle of control charts can be applied to other types of data as well. For instance, the \bar{X} -charts would be used for continuous observed measures. Furthermore, many performance measures are currently monitored simultaneously in the FAA inspection system. It should be more economical and efficient when all relevant measurements are monitored simultaneously. Several multivariate control charts have been proposed (see, e.g., Alt⁹ for a short survey). A nonparametric method introduced in Liu¹⁰ is currently investigated in this project.

ACKNOWLEDGMENT

The authors would like to acknowledge the support by the FAA William J. Hughes Technical Center and the Center for Computational Modeling of Aircraft Structures at Rutgers University.

REFERENCES

1. *The Federal Aviation Administration Plan for Research, Engineering, and Development, Vol. I: Program Plan* (1989), U.S. Department of Transportation, Report # 100-591.
2. *Safety Performance Analysis System: Functional Description Document* (1992), U.S. Department of Transportation, Report # VS FSIS-D-1106, Volpe National Transportation System Center, Cambridge, MA.
3. *SPAS Performance Measure Definitions Ver. 1.0* (1995), Department of Transportation, Report # VR FSIS-D-1134, Volpe National Transportation System Center, Cambridge, MA.
4. D. C. Montgomery (1991), *Introduction to Statistical Quality Control*, 2nd ed., Wiley, New York.
5. Johnson, N. L., and Kotz, S. (1969), *Discrete Distributions: Vol. 1 of Distributions in Statistics*, Wiley, New York.
6. Ryan, T. P. (1989), *Statistical Methods for Quality Improvement*, Wiley, New York.
7. Cheng, A. Y., Liu, R. Y., and Luxh•j, J. T., (1996), Thresholds for Safety Inspection Measurements Based on Control Charts, *Technical Working Paper # 96-113*, Dept. of I.E., Rutgers University. (Submitted to *Int'l J. Reli., Qual., & Safety Eng.*)
8. Hoaglin, D. C., Monsteller, F., and Tukey, J. W., (1983), *Understanding Robust and Exploratory Data Analysis*, Wiley, New York.
9. Alt, F., (1982), Multivariate Quality Control Charts, *Annual Quality Congress Transactions*. pp. 886-893
10. Liu, R. Y., (1995), Control Charts for Multivariate Processes, *J. Amer. Stat. Asso.* pp. 1380-1387.

Table 1. Average Performance of Individual Carriers.

Carrier	Avg. Performance, \bar{p}_i	Avg. Fleet Size
Carrier 7	0.02074	133
Carrier 5	0.03375	527
Carrier 1	0.03466	623
Carrier 3	0.04000	94
Carrier 4	0.04035	331
Carrier 6	0.04284	350
Carrier 2	0.04285	63
Carrier 8	0.04474	200
Carrier 9	0.06031	502
Carrier 10	0.06823	444

Table 2. Average Run Length (Month).

Threshold Type	Unfavorable Rate	Number of Inspection			
		200	400	600	800
<i>Alert</i>	0.044	741	741	741	741
	0.050	215	132	96	72
	0.056	76	9	20	13
	0.062	32	12	7	4
	0.068	16	5	3	2
	0.074	8	3	2	1
<i>Advisory</i>	0.038	44	44	44	44
	0.044	17	12	10	8
	0.050	8	5	3	3
	0.056	5	3	2	2
	0.062	3	2	1	1
	0.068	2	1	1	1
<i>Informational</i>	0.074	2	1	1	1
	0.038	44	44	44	44
	0.032	16	11	9	7
	0.026	7	4	3	2
	0.020	3	2	1	1

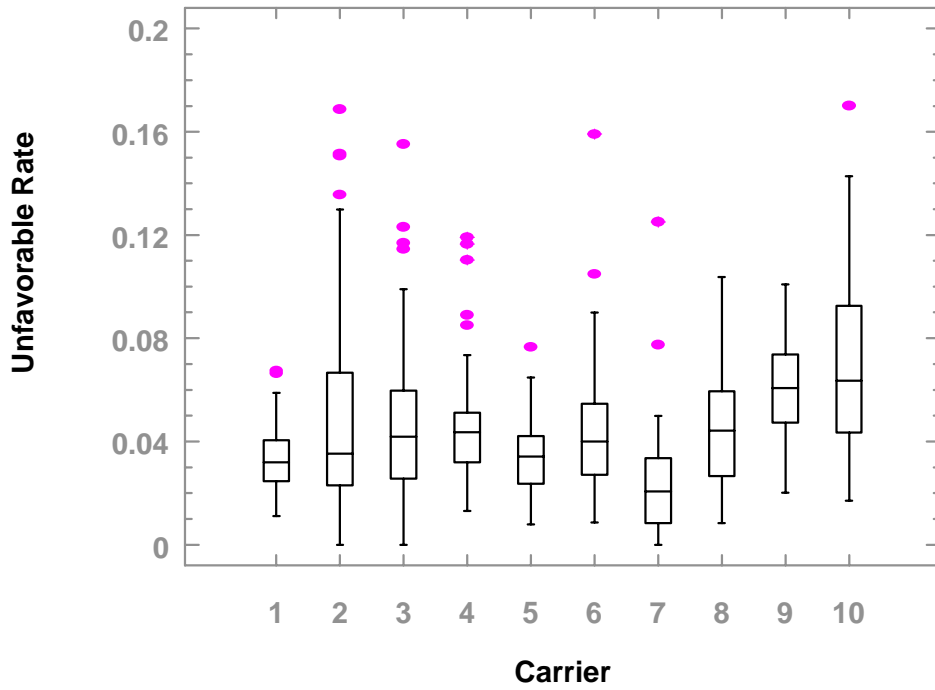


Figure 1. Multiple Boxplot of Individual Observed Unfavorable Rates.

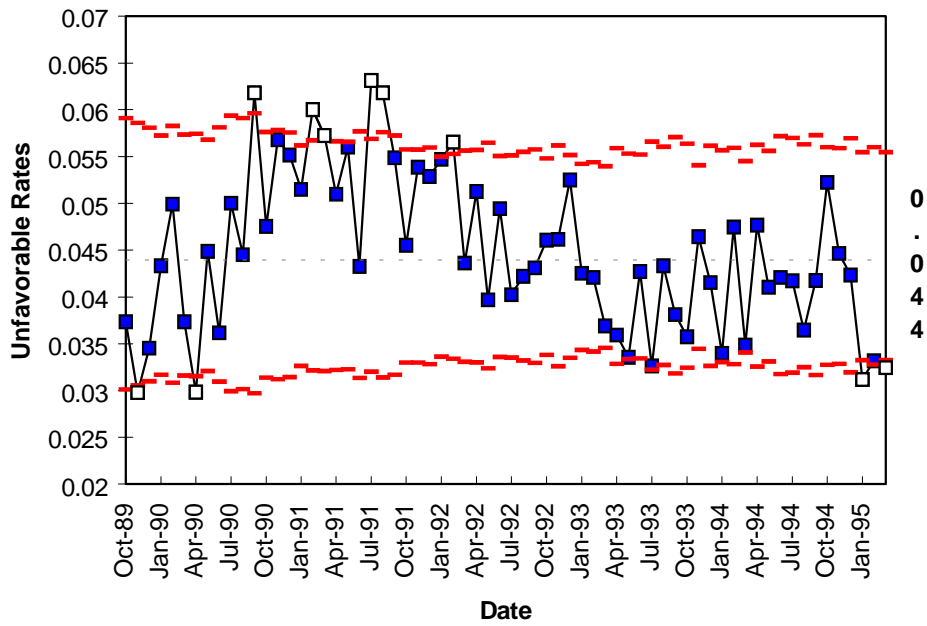


Figure 2. Control Chart of Aggregate Rates.

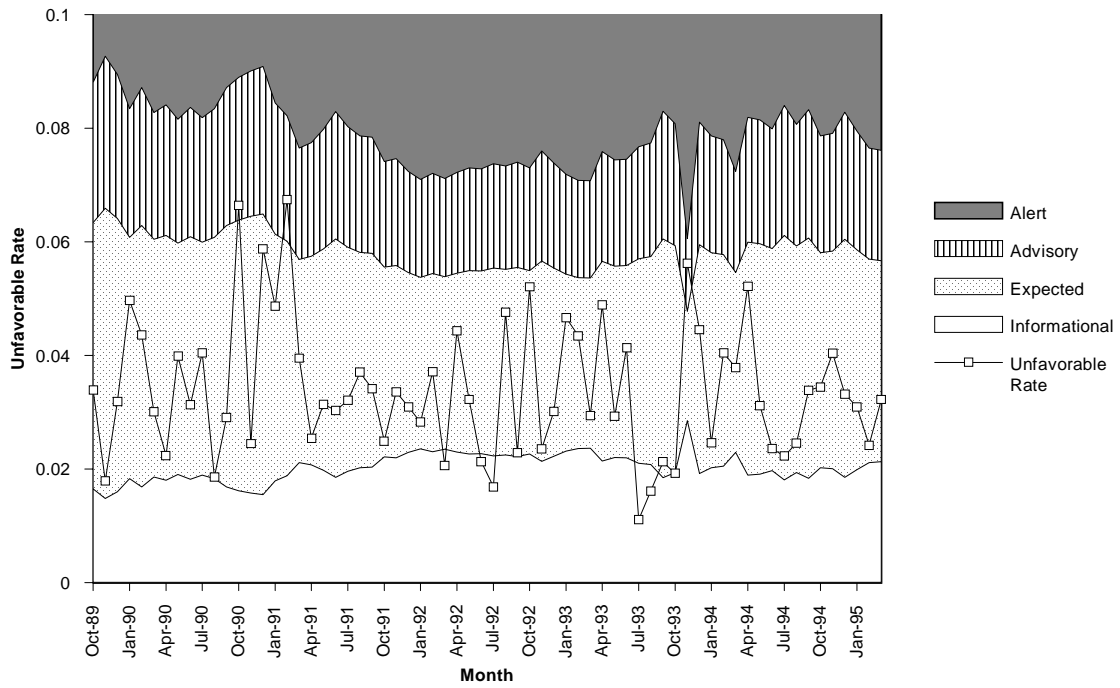


Figure 3. Threshold Levels for Carrier 1.

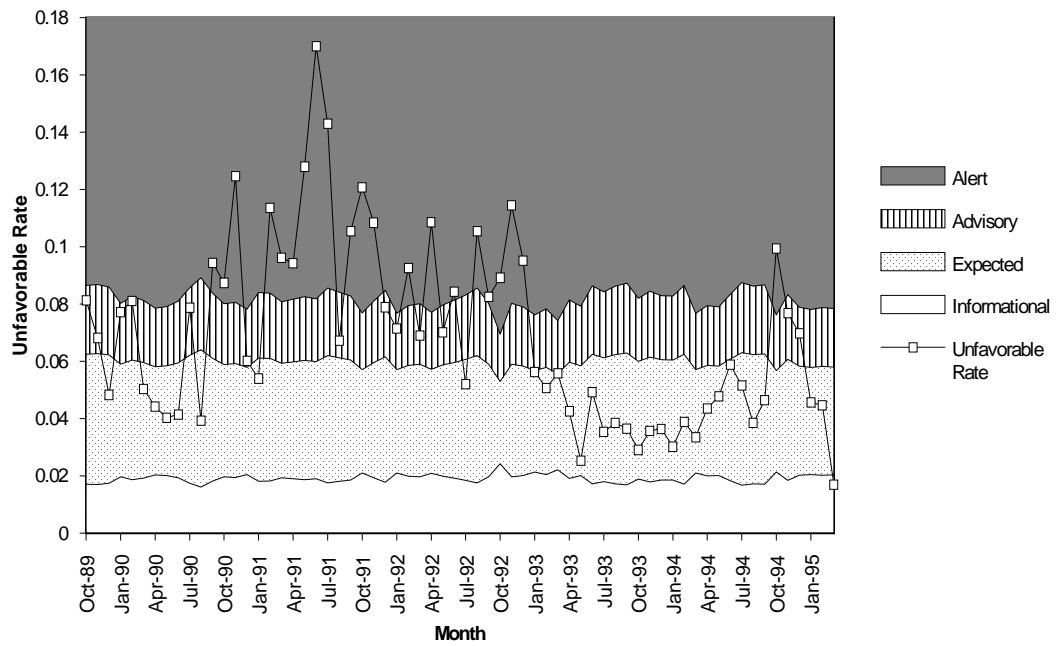


Figure 4. Threshold Levels for Carrier 10.

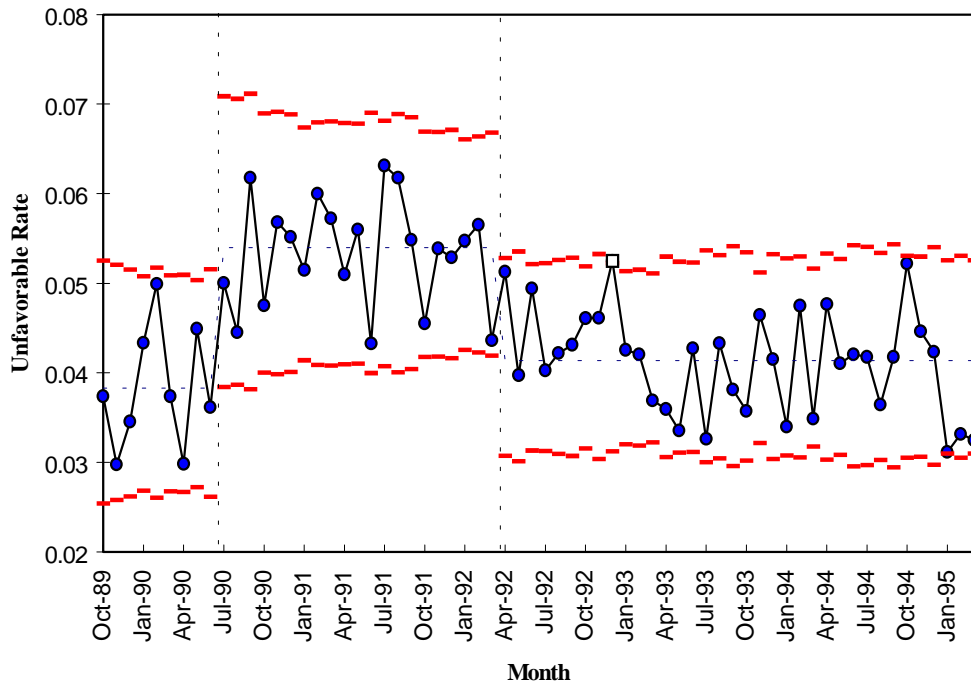


Figure 5. Control Chart of Aggregate Rates in Three Disjoint Time Intervals.

ANALYTICAL APPROACHES AND PERSONAL COMPUTER (PC)-BASED DESIGN PACKAGE FOR BONDED COMPOSITE PATCH REPAIR

Y. Xiong, D. Raizenne, and D. Simpson
Structures, Materials, and Propulsion Laboratory
Institute for Aerospace Research
National Research Council Canada
Ottawa, Canada K1A 0R6

SUMMARY

Analytical approaches for bonded composite patch repair of aircraft structures are discussed. A PC-based program has been developed based on the analytical approaches. Three types of bonded repairs are considered by the software: fatigue enhancement, crack patching, and composite impact damage repair. The issues being addressed are the global stress redistribution and the stress intensity or concentration factor reduction after patching, the local stresses along the bondline, and the prediction of failure strengths and failure modes of the repair. The residual stresses after curing due to thermal mismatch between the substrate and patch are taken into account in the joint stress analysis. A demonstration of the features of the software is presented.

INTRODUCTION

The current economic climate has resulted in the operation of both military and civilian aircraft well beyond their original design lives. Various forms of damage and cracks have inevitably occurred in the aging aircraft structures. To maintain airworthiness, innovative repair techniques using advanced composite materials have been explored, e.g., [1, 2]. Mechanical fastening and adhesive bonding involving composite patches are the two most common kinds of repair techniques. The discussion of the present paper is devoted to bonded composite patch repair. This is a developing technology that has been used for the purpose of enhancing the fatigue resistance of structures and restoring the stiffness and strength of damaged/cracked structures. The focus of the present work is on the detailed design and analysis of the bonded repair to meet the defined performance requirements. The performance requirements for the repair, usually in terms of reductions of strain level, stress intensity factor, or stress concentration factor, are set by the more general structural analysis which addresses the static, fatigue, and damage tolerance performance of the original structure.

There is a considerable range of capability in the design and analysis of bonded repairs from simple stiffness matching to complex three-dimensional (3D) finite element

analysis [3]. While numerical procedures are versatile and able to deal with complex geometry, they are not ideal for parametric studies or design optimization. Particularly, some special elements or modeling approaches are required to simulate the thin layer of adhesive and to avoid the stress singularities at the bonding edges. Analytical approaches such as Rose's Model for crack patching, which are based on some simplifying assumptions, have been shown to be useful for preliminary design [4, 5]. The work by Hart-Smith on bonded joints [6, 7], with closed-form solutions and the associated software A4EI [8], although not dealing with repairs directly, have been widely used in the aerospace industry for joint failure analysis in repair problems.

Currently there is a strong need for simple and efficient analytical approaches and integrated design packages for use in a PC environment [9, 10]. Such a package would greatly benefit the technology by allowing secondary and tertiary airframe manufacturers to develop bonded repair schemes which would be accepted by certification authorities. The National Research Council of Canada has developed expertise in design, analysis, testing, and actual applications over the last fifteen years [11, 12] relevant to this issue. Based on this experience, analytical approaches are proposed in this paper for bonded patch repair. Three types of repairs are dealt with: fatigue life enhancement of under-designed metallic substrates, crack patching of centrally cracked metallic substrates, and impact damage repair of composite substrates. A PC-based design software has been developed consisting of five stages: substrate data input, prerepair assessment, preliminary repair design, repair analysis and design optimization, and results output. In the following sections, a statement of the problems under consideration is given and the analytical approaches proposed are outlined. The features of the PC software developed are illustrated through an example problem of bonded patch repair. Some conclusions are made and further research work of this project is discussed.

STATEMENT OF PROBLEM

Bonded patch repairs are used where the performance of a structure is degraded. This structural degradation may be caused by corrosion and multisite damage in a metallic structure, delamination and impact damage in a composite structure, and face-sheet disbonding in a sandwich structure. In this paper, the patch repair is idealized as a rectangular metallic or composite plate which is bonded by an elliptical composite patch. The substrate is assumed to be under a uniaxial load.

Fatigue Enhancement

Fatigue enhancement refers to the repair of under-designed metallic components by externally bonded patches to increase the original stiffness and reduce the strain levels to enhance the fatigue life. The unrepaired structure may or may not have any damage or cracks

and a stiffness analysis is conducted for the prerepair assessment. The effects of the patch on the static and fatigue performance of the repaired structure are examined in order to design an appropriate patch. The behavior of the bond-line and its failure characteristics are also examined. The geometric configuration for fatigue life enhancement is shown in Figure 1. Fatigue related issues to be addressed are listed below:

- stresses in substrate, patch, and adhesive before and after patching,
- failure in substrate, patch and adhesive,
- effect of the patch dimensions (A and B), thickness (t_p), and lay-up on the strength enhancement.

Crack Patching

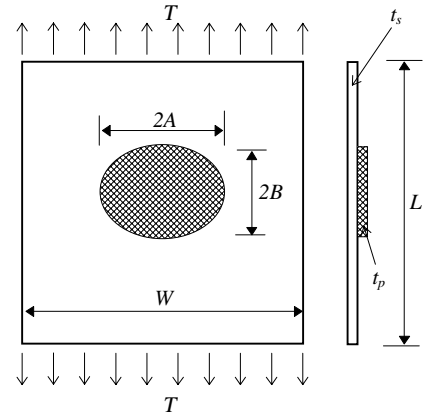


Figure 1. Fatigue Enhancement.

Crack patching refers to the repair of cracked structure by bonding an external composite patch to stop or retard the growth of cracks. The substrate is metallic with either a central crack, an edge crack, or cracks from a hole. Only a central crack is considered in this paper. One of the key parameters in determining the crack growth rate is the stress intensity factor. Therefore, a fracture analysis is conducted before and after repair. The general geometric configuration for crack patching is shown in Figure 2 and issues to be addressed are listed below:

- fracture analysis of centrally cracked plate
- stresses in substrate, patch, and adhesive after patching
- reduction of the stress intensity factor due to patching
- failure in substrate, patch, and adhesive
- effect of the patch dimensions (A and B), thickness (t_p), and lay-up on the reduction of the stress intensity factor

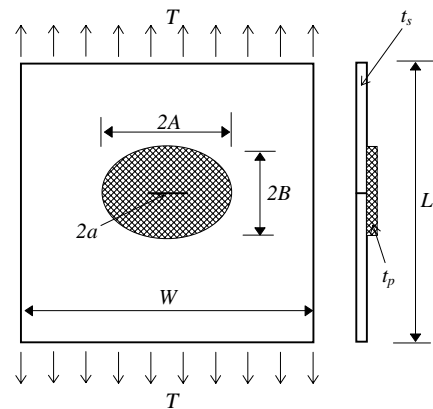


Figure 2. Patching on a Central Crack.

Impact Damage Repair of Composite Substrate

Only the case of a composite laminate with delamination dominant impact damage is considered and the applied load is in compression. It has been realized that the local buckling of delamination can degrade the material properties of the damaged area by as much as 40%. A delamination buckling based approach developed in [15] is employed for the prerepair

assessment before and after repair. The key parameter in this assessment is the stress concentration factor at the edge of the damaged area. The geometric configuration for damage repair is shown in Figure 3 and issues to be addressed are listed below:

- prediction of compression-after-impact strength
- stresses in substrate, patch, and adhesive before and after patching
- failure in substrate, patch, and adhesive
- effect of the patch dimensions (A and B), thickness (t_p), and lay-up on the reduction of the stress concentration factor at the damaged area

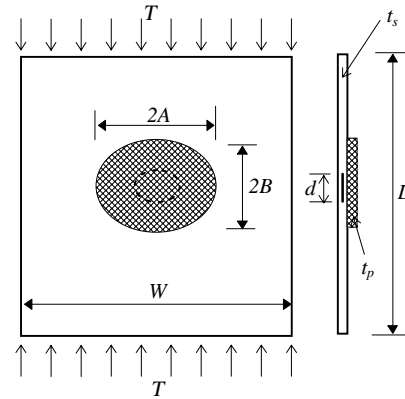


Figure 3. Patching on Impact Damage.

ANALYTICAL APPROACHES FOR REPAIRED STRUCTURES

The analysis of a bonded patch repair involves three steps: determination of the global stress redistribution after patching and the reduction of stress intensity/concentration factor, calculation of the bondline stresses, and predictions of the failure strength and mode. The global stress analysis is conducted using a hard inclusion analogy proposed by Rose [4] and the bondline stresses are calculated using the conventional one-dimensional model following Hart-Smith [6]. The failure strength of a repair is determined against the strength allowables of the materials used in the repair.

Global Stress Distribution After Patching

Hard Inclusion Analogy

Assuming that the repair patch is perfectly bonded to the plate, the repaired region behaves like a laminated plate and thus it is simulated as a hard inclusion in the plate for all three types of repairs under consideration (Figure 4). Closed-form solutions for an infinite anisotropic plate with an elliptical inclusion can be obtained from Lekhnitskii [13]. When the dimensions of the inclusion are not small compared with the width of the plate, a finite width correction factor is required [14]. For an isotropic plate with a centrally located orthotropic elliptical inclusion, the stress component in the loading direction, which is of major concern, is derived as

$$\begin{aligned}
T_y = M_h \left\langle T + \operatorname{Re} \left\{ \frac{A+B}{(z+s)s} \left[\frac{r(ys+yz-iB^2)}{(z+s)s} \right. \right. \right. \\
\left. \left. \left. + \frac{(yz-iB^2)r}{s^2} - \frac{T_y^i(t_s+t_p)A}{t_s} + TA \right] + \frac{irB}{(z+s)s} \right\} \right\rangle
\end{aligned} \quad (1)$$

where the geometry quantities are displayed in Figures 1-3, i is the imaginary unity, $z = x + iy$ is the complex coordinate variable, and M_h is the finite width correction factor from [14]. In the discussion below, the subscript s , p , and a represent the substrate, patch, and adhesive, respectively, and the superscript i represents the inclusion. The two constants in Eq. 1 are defined as

$$\begin{aligned}
r &= i[(T_x^i B - T_y^i A)(t_s + t_p) / t_s + TA] \\
s &= \sqrt{z^2 - A^2 + B^2}
\end{aligned} \quad (2)$$

where T_x^i and T_y^i are the stress components in the inclusion which are obtained by solving a set of complex algebraic equations and are written explicitly as

$$\begin{aligned}
T_x^i &= T t_s A a_{22} [(a_{22} - a_{22}^i) B \\
&\quad + (a_{12} - a_{12}^i)(2A + B)] / [(t_s + t_p) H]
\end{aligned} \quad (3)$$

$$\begin{aligned}
T_y^i &= T t_s a_{22} [a_{11}(A + 2B)B + a_{11}^i(2A + B)A \\
&\quad + (a_{12} + a_{66} + a_{12}^i)AB] / [(t_s + t_p) H]
\end{aligned} \quad (4)$$

where

$$H = [(a_{11} a_{22} + a_{11}^i a_{22}^i) + a_{22} (a_{12} + a_{66} + a_{12}^i) - (a_{12} - a_{12}^i)^2] AB + 2(a_{11} a_{22}^i B^2 + a_{22} a_{11}^i A^2) \quad (5)$$

and a_{jk} and a_{jk}^i ($j, k = 1, 2, 6$) are the in-plane compliance coefficients for the plate and inclusion, respectively.

The stress determined by Eq. 1 is demonstrated in Figure 5. The stress concentration in the substrate is shown at the boundary of the patched area because of the introduction of additional stiffness. This maximum tensile or compressive stress is

$$T_o = T_y(\mathbf{0}, \pm B) \quad (6)$$

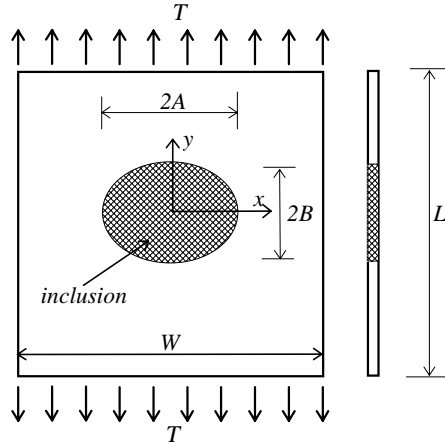


Figure 4. Hard Inclusion Analogy.

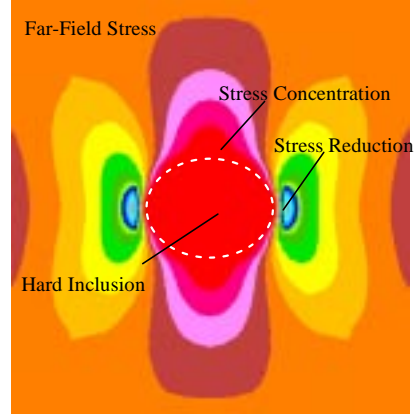


Figure 5. Stress Around Hard Inclusion.

Reduction of Stress Intensity Factor in Crack Patching

Fracture analysis is conducted for the cracked substrate under the patch (Figure 6). Following Rose [5], a modified approximate equation for the stress intensity factor after patching is derived as

$$K_I^r = M^r T_y^{rs} \sqrt{\pi a \Lambda / (a + \Lambda)} \quad (7)$$

where

$$T_y^{rs} = T_y^i E_s (t_s + t_p) / (E_s t_s + E_p t_p) \quad (8)$$

and

$$M^r = 1 / \sqrt{1 - (2a / 2A)^2}$$

$$\pi \Lambda = \sqrt{\frac{t_a E_s t_s}{G_a E_p t_p} (E_s t_s + E_p t_p)} \quad (9)$$

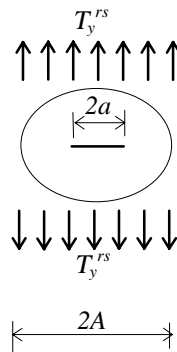


Figure 6. Crack Under Patch.

Reduction of Stress Concentration Factor in Damage Repair

Stress redistribution around the damage under the patch can be predicted (Figure 7). In this case, the repaired region is treated as an anisotropic plate. The damaged area inside the region is simulated as a soft inclusion after the delamination buckles. Following the approach proposed in reference 15 based on delamination buckling analysis, an equation for the stress in the repaired region along the loading direction is derived as

$$\mathbf{T}_{ys} = \mathbf{M}_s \left\langle \mathbf{T}_y^{rs} + 2 \operatorname{Re} \{ d\phi_1(z_1)/dz_1 + d\phi_2(z_2)/dz_2 \} \right\rangle \quad (10)$$

where $z_k = x + \mu_k y$, $k=1,2$, is the complex coordinate variables with μ_k being the two complex roots of the characteristic equation of the laminate, \mathbf{M}_s is the finite width correction factor for soft inclusion from [14], and ϕ_k are two complex stress potentials, see reference 15 for details.

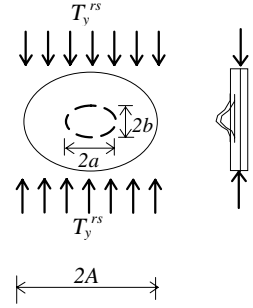


Figure 7. Damage Under Patch.

Bondline Stress Analysis

For the stress analysis along the bondline, a strip of the bonded region with unit width is considered which is under a far field tensile or compressive load, \mathbf{T}_o . The joint is single-lap in configuration and symmetric with respect to the mid-span. Therefore only half of the joint needs to be modeled (Figure 8). For damage repair of composite substrates, the length of the half joint is $\mathbf{B}-\mathbf{b}$ where \mathbf{b} is the minor axis of the impact damage ellipse. The distinctions in the boundary conditions between various repair types are:

for fatigue enhancement	$\mathbf{T}_p + \mathbf{T}_s = \mathbf{T}_o$,	$\mathbf{T}_p(-y) = \mathbf{T}_p(y)$	
for crack patching	$\mathbf{T}_p = \mathbf{T}_o$,	$\mathbf{T}_s = \mathbf{0}$	(11)
for damage repair	$\mathbf{T}_p + \mathbf{T}_s = \mathbf{T}_o$,	$\mathbf{T}_s = \mathbf{T}_{ys}^i$	

where \mathbf{T}_{ys}^i is the stress in the damaged area determined from the analysis for a damaged laminate under compression. Using the conventional one-dimensional model, closed-form solutions for the stresses along the bondline are obtained and they are listed below for the fatigue enhancement application:

$$\begin{aligned} \sigma_p(y) &= \eta [1 - \operatorname{Cosh}(\beta y) / \operatorname{Cosh}(\beta B)] / t_p \\ \sigma_s(y) &= \{T_o - \eta [1 - \operatorname{Cosh}(\beta y) / \operatorname{Cosh}(\beta B)]\} / t_s, & 0 \leq y \leq B \\ \tau_a(y) &= -\beta \eta \operatorname{Sinh}(\beta y) / \operatorname{Cosh}(\beta B) \end{aligned} \quad (12)$$

where

$$\beta = \frac{G_a}{t_a} \left(\frac{1}{E_s t_s} + \frac{1}{E_p t_p} \right), \quad \eta = \frac{\sigma_o}{E_s t_s} - (\alpha_s - \alpha_p) \Delta T \quad (13)$$

where α_s and α_p are the thermal coefficients of the substrate and patch, respectively, and ΔT is the temperature difference between the curing and operating conditions.

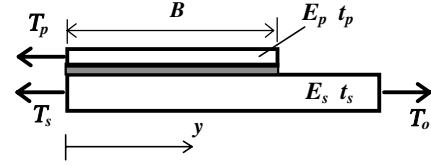


Figure 8. A Half of Joint

Failure Strengths and Modes

To predict the failure load and mode of the bonded joint, three maximum stress components are considered: axial normal stresses in the substrate and patch and shear stress in the adhesive. The failure criteria for the three failure modes are written as:

$$\begin{aligned} \text{for substrate yielding} & \quad (\sigma_s)_{\max} = T_o / t_s \leq \sigma^y \\ \text{for patch fiber failing} & \quad X' \leq (\sigma_p)_{\max} = T_p / t_p \leq X \\ \text{for adhesive shearing} & \quad (\tau_a)_{\max} = \text{Max} \{ \tau_a(0), \tau_a(B) \} \leq \bar{\tau}_a \end{aligned} \quad (14)$$

where σ^y , X , X' , and $\bar{\tau}_a$ are strength allowables for the substrate, patch, and adhesive, respectively.

PC-BASED DESIGN SOFTWARE BondRep

Based on the analytical approaches discussed above, a five-phase design package, BondRep, has been developed for use in a PC Microsoft-Windows™ environment. To demonstrate the features of the program, an example problem of crack patching is presented. The substrate is made of Aluminum 2024-T3 with a central crack which is to be repaired by bonding an elliptical composite patch. The patch material is Boron/5521-4 prepreg with unidirectional lay-up in parallel with the applied load. The adhesive is FM73. Design requirements are set for the stress in the substrate, strain level in the patch, and the stress intensity factor. The program will determine if the design meets all these requirements.

Figure 9 shows the starting or main window of BondRep in the form of a typical Windows™ application software. The program can be used for multiproject purposes at the same time and each project has a file name specified by the user. In running the program, the user can start a new project, open a previous project to check results, or modify an existing project. Five buttons on the top bar are to be clicked for respective phases of work. For a new project, these five phases of work must be conducted sequentially. Each phase of work

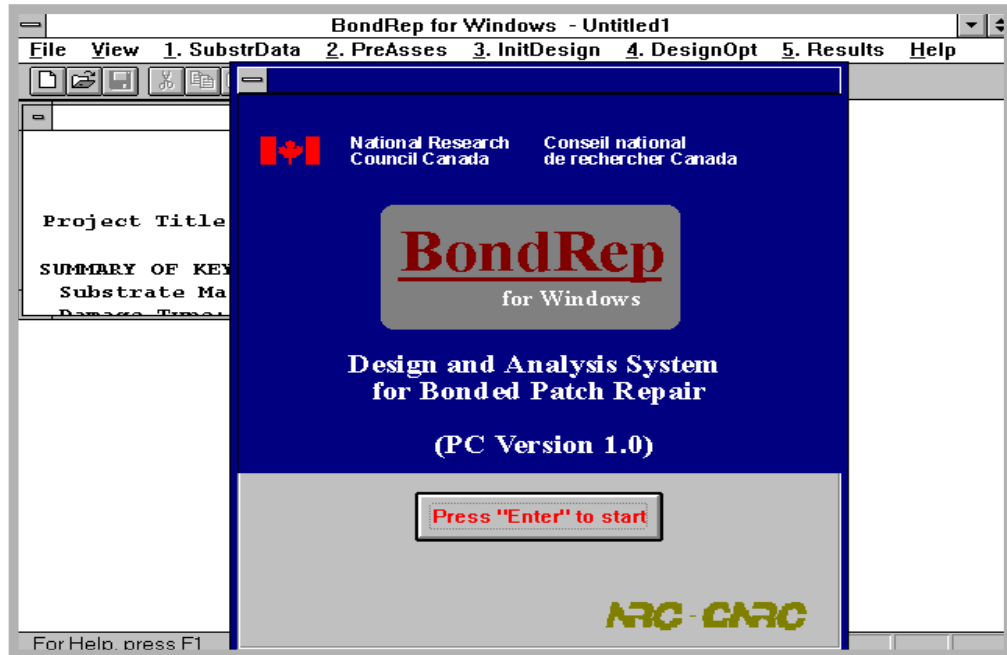


Figure 9. Main Window of BondRep.

can be activated from either the main window or the window for the previous phase of work. For a completed project, the results of any phase of work can be checked and modified by clicking appropriate buttons. All input data and results can be saved to the project file at any time.

Phase I. Substrate Data Input

Phase I is activated when the button “1.SubstrData” in the main window is clicked. In this phase of work, the user is asked to specify the material and geometry data for the substrate (Figure 10). There are two selections for the substrate material: metallic and composite materials. A material database is established which contains the properties of some commonly used materials. The user can either specify a material from the existing material list or input a new one and save the data into the database. The data in the material database can be modified by the user during the running of the program or by using any text editors outside the program (existing format must be strictly followed). Four geometric configurations can be selected: under-designed, central crack, edge crack, and impact damage. Features for the last two configurations are under development. Geometric and load data of the substrate are to be entered by the user. Once the substrate data input is completed, the next phase of work, damage assessment, can be activated from the current window or from the main window.

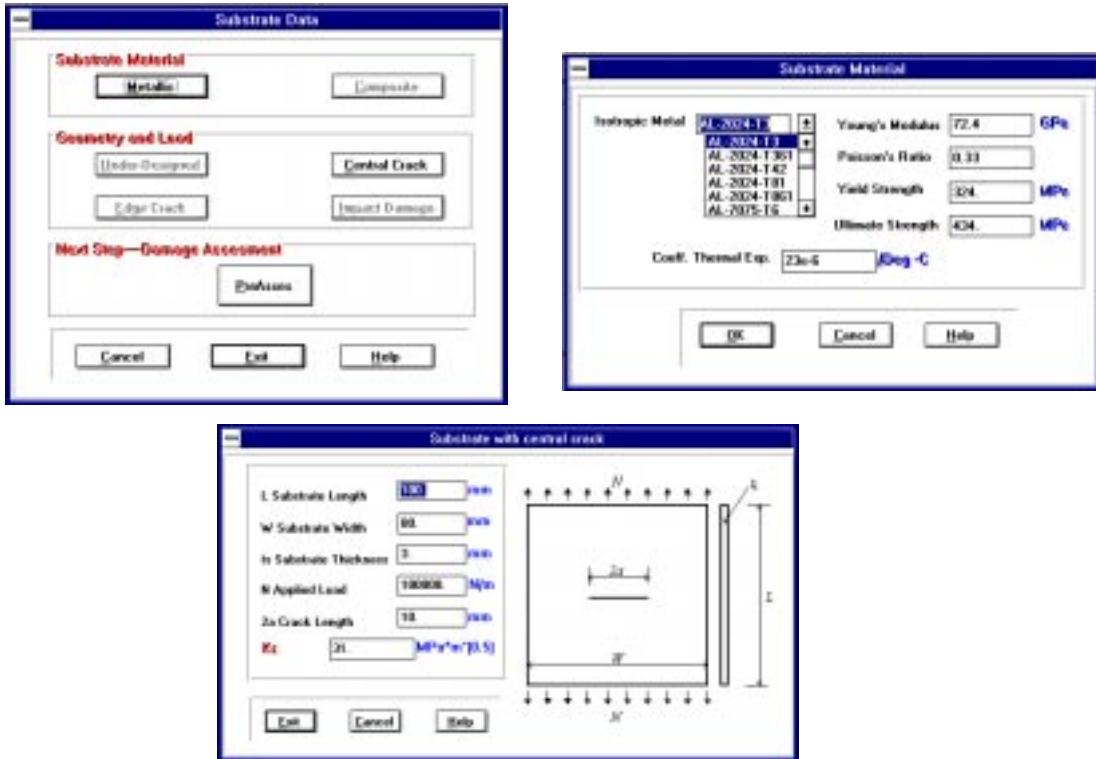


Figure 10. Windows for Phase I.

Phase II. Prerepair Assessment

The next phase following the substrate data input is an assessment of the unrepaired structure. In this phase, the actual strain and stress in the substrate and the stress intensity or concentration factor are calculated and displayed on the screen. The material yield and ultimate strain and strength are also shown for reference (Figure 11). To proceed, press the button “InitDesign” or go back to the main window and start Phase III for defining a preliminary design of the repair.



Figure 11. Window for Phase II

Phase III. Preliminary Repair Design

Phase III is for preliminary repair design (Figure 12(a) and (b)). In this phase, the user specifies the design requirements regarding the performance of the repair based on the general structural analysis. Also, the user must define an initial design of the repair including the material selection and geometric data for the patch and adhesive. The materials for the patch and adhesive can be selected from an integrated material database and the related material properties will be shown in the windows. Modifications of the material database and new material definitions are allowed.



Figure 12(a). Windows for Phase III.

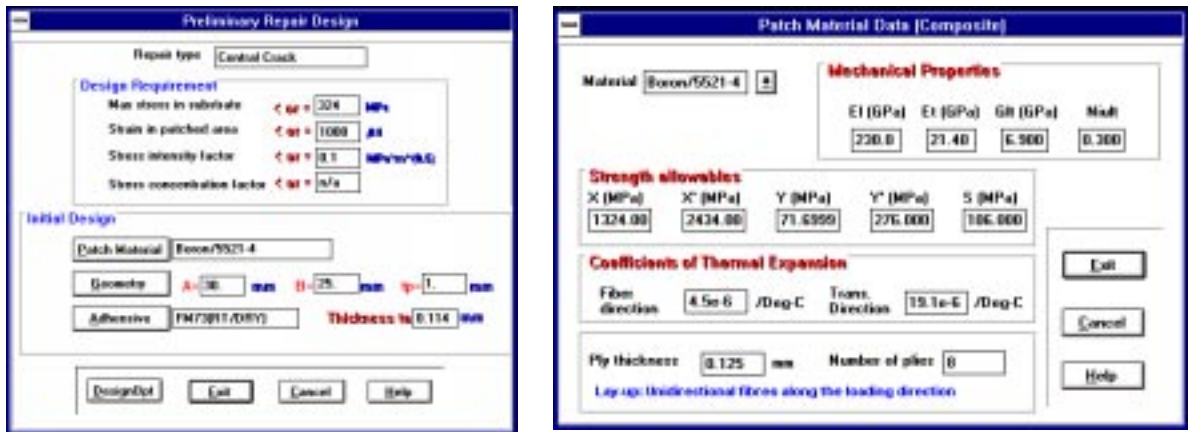


Figure 12(b). Windows for Phase III.

Phase IV. Repair Analysis and Design Optimization

Repair analysis and design optimization are conducted during this phase (Figure 13). Three analysis options can be chosen by the user: mechanical stresses only, thermal stresses only, and combination of mechanical and thermal stresses. In addition, there are four design options in the program with respect to the design requirements specified: analysis only, material selection, patch geometry design, and patch thickness design. For the option of

analysis only, the program calculates the stresses in the repair members and examine the satisfaction of the specified design requirements. For the other three design options, the user must specify the design variables and their ranges of variation. The design iterations, with the maximum strength being the objective, will be automatic amongst the ranges specified for the design variables (these features are being developed). An optimal repair design, which satisfies all the design requirements and has the maximum strength, will be determined. For the present example, only stress analysis under applied load is conducted.

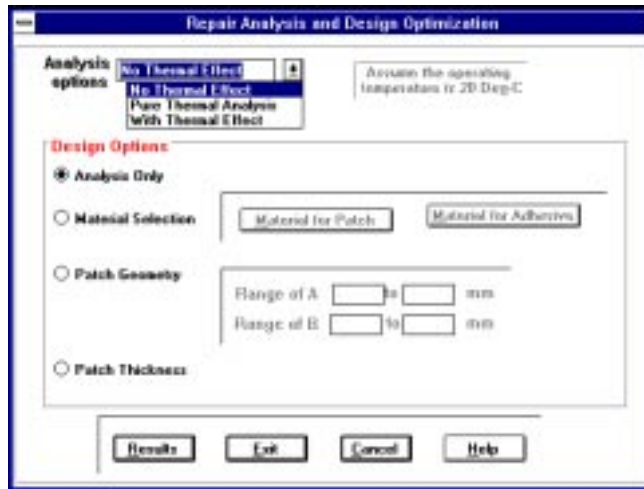


Figure 13. Window for Phase IV.

Phase V. Results Output

Final results are shown in this phase in different forms (Figure 14). The Final Design Window presents some key data about the performance of the repair against the initial design requirements specified by the user. Bondline stress distributions are shown graphically in a separate window and the maximum values of the stresses in the substrate, patch, and adhesive are displayed beside the curves. A project report which contains detailed information can be viewed on the screen and printed as a hard copy for the purpose of documentation. Various design charts can be shown for the design option selected. At this stage, the user can either modify the current design and obtain new results or save the project file and quit the program.



Figure 14. Windows for Phase V.

CONCLUSIONS

Analytical approaches have been proposed in this paper for bonded composite patch repair in aircraft structures. Three types of bonded repair were discussed: fatigue enhancement, crack patching, and composite impact damage repair. A PC-based design package has been developed and the features of the software were shown through an example problem of crack patching. Further work is being carried out to examine the effect of such factors as tapered patch thickness, adhesive elastic-plastic behavior, and secondary bending due to load eccentricity on the performance of bonded repair.

ACKNOWLEDGMENT

This work has been carried out under IAR Program 3G3, Aerospace Structures, Structural Dynamics and Acoustics, Project JGN-00, Composite Repair Techniques for Primary Aircraft Structures.

REFERENCES

1. Baker, A. A. and Jones, R., eds.: *Bonded Repair of Aircraft Structures*, Martinus Nijhoff Publishers, 1988.
2. Jones, R. and Miller, N. J., eds: *Proceedings of International Conference on Aircraft Damage Assessment and Repair*, The Institution of Engineers, Australia, 1991.
3. Xiong, Y. and Raizenne, M. D.: On Design and Analysis of Composite Bonded Repair in Aircraft Structures, LTR-ST-2014, IAR/NRCC, 1995.
4. Rose, L. R. F.: An Application of the Inclusion Analogy for Bonded Reinforcement, *Int. J. Solids Structures*, Vol. 17, 1981, pp. 827-838.
5. Rose, L. R. F.: Theoretical Analysis of Crack Patching, *Bonded Repair of Aircraft Structures* (eds. Baker, A. A. and Jones, R.), Martinus Nijhoff Publishers, 1988.
6. Hart-Smith, L. J.: Analysis and Design of Advanced Composite Bonded Joints, NASA-CR-2218, 1974.
7. Hart-Smith, L. J.: Design Methodology for Bonded-Bolted Composite Joints, Vol. 1 Analysis Derivations and Illustrative Solutions, AFWAL-TR-81-3154-Vol-1, 1982.
8. Hart-Smith, L. J.: A4EI Bonded Joint Program, Douglas Report A8372, 1983.
9. Fredell, R. S. and Vlot, Ad.: An Engineering Approach to the Design and Analysis of Fuselage Crack Patching With CalcuRep for Windows, *Proc. of the Symp. on Composite Repair of Aircraft Structures*, Vancouver, BC, 1995,
10. Xiong, Y. and Raizenne, M. D.: A Design Methodology and PC-Based Software for Bonded Composite Repair in Aircraft Structures, *Proc. of the Symp. on Composite Repair of Aircraft Structures*, Vancouver, BC, 1995.
11. Raizenne, M. D., Simpson, D. L., Zgela, M. B., and Bateman, G.: CF116 Upper Wing Skin Compression Induced Fatigue Cracking --A Case Study, Presented at ICAF, Stockholm, 1993.
12. Raizenne, M. D., Benak, T. J., and Heath, J. B. R.: Bonded Composite Repair of Thin Metallic Materials: Variable Load Amplitude/Temperature Cycling Effects, LTR-ST-1979, IAR/NRCC, 1994.
13. Lekhnitskii, S. G.: *Anisotropic Plates*, Gordon and Breach Science Publishers, 1968.
14. Xiong, Y.: On the Finite Width Correction Factor in Composite Laminates With Elliptical Inclusion, *Advanced Composites Letters*, Vol. 3, 1994, pp. 203-207.
15. Xiong, Y. and Poon, C.: Failure Prediction of Composite Laminates Containing Impact Damage, LTR-ST-1898, IAR/NRCC, 1992.

ANALYTICAL FATIGUE LIFE ESTIMATION OF FULL-SCALE FUSELAGE PANEL

J. Zhang, J. H. Park, and S. N. Atluri
FAA Center of Excellence for Computational Modeling of Aircraft Structures
Georgia Institute of Technology
Atlanta, GA 30332-0356

ABSTRACT

This paper presents the analytical fatigue life estimation of the curved full-scale fuselage panel which was tested by Foster-Miller, Inc. In the analysis, a hierarchical finite element based on global-intermediate-local modeling strategy has been used for determining the stress state in the crack area. The relevant crack tip parameters that govern the onset of fracture and crack growth are evaluated using the finite element alternating method (FEAM) in the local analysis. Then the load cycles from the initial cracks to local failure are estimated. This analytical result was verified against the result obtained from the full-scale testing of fuselage panel. It is found that the analytical results were in good agreement with the test results.

INTRODUCTION

The fatigue life of an undamaged structure subjected to a repeated external load can be divided into two periods. The first period is the fatigue crack initiation period. This period is dependent on the design, material, manufacture, and operating environment of structure. The structure of aging flight vehicles after years of service may have the detectable initial fatigue cracks. This situation is called as multisite damage (MSD). The first period of fatigue life can be obtained from the service record of aging flight vehicles. The second period is the initial fatigue crack growth period. In this period, the initial fatigue cracks (MSD) grow and propagate to local failure. Estimating the second period is significant for aging flight vehicles in economy and safety. In this paper, the focus is on the estimation of the second period of fatigue life. The fatigue life of structure can be obtained from the first and second period.

The computational fatigue analysis of aging aircraft structures has been developed for more than 10 years (Atluri, 1986). The structure usually is at a large-scale level and has complex geometry, but the cracks exist at a smaller scale level. A repeated computation of stress state and fracture parameters with different crack size is required for the fatigue analysis. These make the computational fatigue analysis very complex, difficult, and expensive in terms of computational cost. To obtain the stress distribution in the area containing cracks, a fine mesh has to be used in the finite element modeling. For a complex

geometry fuselage structure, it is very difficult. Starnes and Britt (1991) suggested a hierarchical modeling strategy, which consists of a series of models at different scales. Atluri (1995) has presented a three-level analysis scheme that consists of the global analysis, the intermediate analysis, and the local analysis. At different levels of scale, the structure is modeled by different finite element. This three level hierarchical strategy reduces the computational cost and satisfies the requirement to obtain the correct stress state.

One significant achievement in the past 10 years is the finite element alternating method (FEAM). In local analysis, an accurate evaluation of the fracture parameter and the stress-intensity factor (SIF) at the crack tip is required for fatigue analysis. To obtain the stress-intensity factor accurately, a fine element mesh at the area around the crack tip is needed (Atluri, 1988). This makes the computation very expensive especially in the case of MSD with stiffeners and lap joints. An alternating method (Atluri, 1986) can be used to compute the stress-intensity factor for multiple cracks sheet using a coarse finite mesh. Sequentially, the finite element alternating method (FEAM) has been developed (Atluri, 1992) for stiffened panel with MSD. In the same time, several computer codes using the FEAM have been developed at the FAA Center of Excellence for Computational Modeling of Aircraft Structures, Georgia Institute of Technology (Atluri, 1994, 1995).

In this paper, three-level scale modeling and analysis, global analysis, intermediate analysis, and local analyses are used. The FEAM is used in the local analysis for evaluating the SIF at the crack tip. Stress-intensity factor history with crack growth is found for estimating the fatigue life. The Full-Scale Fuselage Panel 12, tested in fatigue at Foster-Miller, Inc., is considered as an example. The geometry, material, load, and boundary condition of the model are based on the fatigue test fuselage panel 12. The analytically estimated fatigue life is in good agreement with the test results. The residual strength and fatigue estimation methodology is verified in this case.

THE BACKGROUND OF FULL-SCALE FUSELAGE PANEL TEST

The test and analysis of full-scale curved aircraft fuselage panel has been completed by Foster-Miller, Inc. The testing included the panel residual strength test and fatigue test. The final report was presented in April 1992 (Samavedam). The fatigue test was performed on the test fuselage panel 12.

This test fuselage panel is designed to represent critical construction features of the aging commercial aircraft. The panel has a 2.7-in.-wide lap joint. All through-skin rivets are 5/32 in. diameter, low profile, shear head 100° countersunk rivets. The minimum diameter of rivet bucktail of panel lap is 1.26d, where d is the rivet diameter. The maximum diameter of rivet bucktail of panel lap is 1.48d. The three-dimensional fuselage test panel 12 is shown in Figure 1. The fatigue load was cyclic pressure. The pressure was applied at 0.2 Hz over a pressure range of 8.5 psi with a loading ratio of 0.11.

At 75,000 loading cycles, cracks were found on the underside of the panel along the lower rivet line at lap joint 27, 28, and 29 in inner skin. The rivet number and fatigue damage are denoted in Figure 2. The test report shows that the cracks between rivet holes 27 and 28 linked up after 114938 cycles of loading.

MODELING AND ANALYSIS

The hierarchical modeling and analysis strategy consists of global analysis, intermediate analysis, and local analysis. At different levels of scale, the structure is modeled by different finite elements. The global analysis and the intermediate analysis are used to find the stress distribution in the crack area. The displacement at the location of intermediate model in global model is used to connect the global analysis and the intermediate analysis. The local analysis is used to evaluate the stress-intensity factor (SIF) at the crack tip. The interface between the intermediate analysis and the local analysis is the stress on the local model boundary. Then, crack propagation and fatigue analyses are carried out for estimating the fatigue life. In this fatigue life period, the cracks grow from the initial fatigue cracks (MSD) to a local linkup. The analysis procedure is illustrated in Figure 3. The hierarchical model relationship between the global model, intermediate model, and local model of the full-scale fuselage panel is shown in Figure 4.

Global Model and Global Analysis

The fuselage panel consists of outer skin, inner skin, 22 tear straps, 106 fillers, 6 stringers, 6 frames, and 24 stringer ties and rivets. The longitudinal length of the global model is $L = 112$ in. and the circumferential width is $B = 53$ in. (circular angle $\alpha = 40.49^\circ$ skin radius $R = 75$ in.). The outer and inner skins are modeled by three-dimensional (3D) 4-node doubly curved shell element. The tear straps and fillers also are modeled by 3D 4-node doubly curved shell element. The stringers and frames are modeled by the 3D 2-node linear beam element. The rivets between the tear straps and the frames, between the tear straps and the stringers, between the filler and the stringer, and between the stringer and the frames are modeled by beam element, but the rotations of two ends of this beam are constrained to be the same. The boundary conditions are fixed except the rotation about the longitudinal axis on the longitudinal boundary and the rotation about the circumferential axis on the circumferential boundary. The cracks are considered in the global model. The crack size in the global model increases by moving the crack tip node. The mesh in the crack area is refined to satisfy the requirement of elements. The pressure load on the skin is 8.5 psi. The total number of nodes is 10798. The total number of elements is 14161. The global analysis was carried out using the finite element structure analysis code ABAQUS version 5.3. The analysis was completed on a HP 735 workstation. The global analysis CPU time was about 714 seconds.

The rivets between the outer skin and inner skin at lap joints, between the skin and tear strap, and between the skin and filler are modeled by the spring model. The spring model consists of three spring elements. They are shown in Figure 5. When the membrane stresses are considered as the dominating stresses of the stress-intensity factor at the crack tip, the spring model can provide the transverse reaction force of the rivet. The stiffness of the rivet in the transverse plane of the rivet is presented by the spring element stiffness K_1 , K_2 . They are given by following equation (Swift, 1984):

$$K_{1,2} = \frac{E_{sh}D}{\left[A + C \left(\frac{D}{B_1} + \frac{D}{B_2} \right) \right]}$$

The K_3 is the stiffness of the rivet in the direction of the rivet axis.

$$K_3 = \frac{ED^2\pi}{2(B_1 + B_2)}$$

where

E_{sh} = modulus of skin material

E = modulus of rivet material

D = rivet diameter

B_1 and B_2 = thickness of joined sheets

$A = 5.0$ for aluminum rivet

$C = 0.08$ for aluminum rivet

Intermediate Model and Intermediate Analysis

The intermediate model contains the detail of the structure around the areas of MSD. The longitudinal length of the intermediate model is $L = 35$ in. and the circumferential width $B = 16.7$ in. (circular angle $\alpha = 12.77^\circ$, skin radius $R = 75$ in.). Intermediate model consists of outer skin, inner skin, eight tear straps, four fillers, one stringer, two frames, and two stringer ties and rivets. The outer skin, inner skin, tear straps, fillers, stringers, frames, and stringer ties are modeled by 3D 4-node doubly curved shell element. At the crack area, a fine mesh was used. The shell elements near to the cracks are about 0.13 by 0.1125 in. All rivets are modeled by the spring model. The boundary condition are the displacements, which are provided by the global analysis. The displacement of nodes on the boundary of the intermediate model are produced by an interface code. The displacement of nodes on the boundary of the intermediate model are determined by the displacement obtained from the global analysis. The external load is 8.5 psi on the skin. The crack growth can be modeled by moving the node at the crack tip. The number of nodes of intermediate model is 6180. The total number of elements is 6685. The intermediate analysis was completed using the finite element structure analysis code ABAQUS version 5.3. The intermediate analysis provided the

stresses for the local analysis. The CPU time for analysis was about 207 seconds on a HP 735 workstation.

Local Model and Local Analysis

The local analysis evaluates the fracture parameters, stress-intensity factors at the crack tips. The local model is two-dimensional. In this analysis, the local model is a piece of inner skin, which contains the rivets holes 26, 27, 28, 29, and 30. The local model consists of the 8-node plane finite elements. The boundary condition is a stress boundary condition. The methodology for evaluating the stress-intensity factor (SIF) is the finite element alternating method (FEAM). The FEAM (Atluri, 1986, Atluri and Tong, 1991, and Atluri and Park, 1992) is briefly described as follows.

Consider the local model, a finite size sheet of panel with multiple cracks. First, the finite size sheet without cracks subjected to the fastener reaction and external membrane stress is solved using finite element method with a very coarse finite element mesh to find the stress at the crack location. Then, an infinite sheet containing a central crack is considered, that is subject to an arbitrary crack face traction and its analytical solution is used to erase the traction at the locations of the cracks in the uncracked sheet (Figure 7).

The length of the local model = 5 in., height = 0.9 in., and is 0.04 in. thick. The rivet reaction forces are applied on the surface of the rivet hole and normal stresses are on the boundary of the local model. It is illustrated in Figure 6. The number of nodes is 1605. The number of elements is 480.

Crack Propagation and Fatigue Analysis

To estimate the fatigue life, the stress-intensity factor history is required. A repeated computational procedure was used to obtain the stress-intensity factor history. In this analysis, the repeated computational procedure consists of six global analyses, 42 intermediate analyses, and 42 local analyses from the initial fatigue cracks to the linkup of cracks at rivets 27 and 28. The normalized stress-intensity factor histories of the cracks at the right side of rivet hole 27 and at the left side of rivet hole 28 are shown in Figure 8. In Figure 8, b = crack length a + rivet hole radius R . To estimate the fatigue life, the Paris model is used. The Paris model is

$$\frac{da}{dN} = \left(\frac{\Delta K}{C} \right)^n$$

where

a = the length of crack
 $n = 6.0$
 $C = 0.364 \times 10^{-11}$
 $\Delta K = K$
 N = the number of external load cycles

When the crack length grows from the initial fatigue crack length a_0 to the linkup crack length a_f , the fatigue life can be calculated by the following equation:

$$n = \int_{a_0}^{a_f} \frac{C^n da}{(\Delta K)^n}$$

or approximately

$$n = \sum_{j=1}^m \frac{C^n \Delta a_j}{(\Delta K_j)^n}$$

where Δa_j is the increment of crack length from initial fatigue crack length a_0 to linkup crack length a_f

$$a_f - a_0 = \Delta a_1 + \Delta a_2 + \dots + \Delta a_j + \dots + \Delta a_m$$

RESULTS AND ANALYSIS

Before the test, the full-scale fuselage panel 12 did not contain any cracks. After 75,000 cycles of external loading, rivet holes 27, 28, and 29, at the lower row in the inner skin, were inspected for microcracks. The test report did not present the crack length. But the inspected microcrack length can be estimated from the rivet bucktail size. In the test report, the rivet bucktail diameters were manufactured to recommended 1.4d specifications. The rivet bucktail diameters have been controlled in the range between the minimum 1.26d and the maximum 1.48d in fatigue test panel 12, where d is the rivet diameter (= 5/32 in.). The microcrack length, i.e., the initial fatigue crack detectable length are estimated about 0.045 in. to 0.05 in. (see the Figure 9). At 98,782 cycles of loading, cracks at rivet holes 36-38 and 48-50 were inspected.

The test report shows that the cracks between rivet holes 27 and 28 were linked at 114,938 cycles of loading. The computational estimated loading cycles from the initial fatigue cracks of 0.045 in. (75,000 cycles) to local failure, 27-28 linkup, are 42,942 cycles by using the methodology presented in this analysis. Since cracks at rivet holes 36-38 and 48-50 were inspected at 98,782 cycles of loading, the cracks at rivet holes 36-38 and 48-50 are considered when the crack length at rivet holes 26-28 are 0.06 in. The fatigue life of the fuselage panel is 117,942 cycles. The difference from the test results is 2.6 percent (Figure 10). If the initial

fatigue crack length was considered to be 0.05 in., the estimated fatigue life is 113,389 cycles. The difference from the test results is 1.3 percent (Figure 11). Thus, the estimated fatigue life agrees well with the test results. It shows that the fatigue life estimation methods based on FEAM and computer codes are effective.

Another case in which the cracks length at rivet holes 26-28, 36-38, and 48-50 started at 0.045 in. is considered in this analysis. In this case, the estimated fatigue life is 108,339 cycles. The fatigue life reduce 8 percent from the above estimated fatigue life of 117,945 cycles. This result shows that more initial fatigue cracks will reduce the fatigue life of structure.

CONCLUSIONS

The analytical fatigue results show that fatigue estimation methodology using the hierarchical scheme, the FEAM, and the Paris model fatigue estimation methodology are effective for predicting the fatigue life of structures with MSD. The initial fatigue cracks (the cracks inspected at 75,0000 loading cycles), i.e., MSD, are formed not only by the imperfection of structure and material but also by the bending. The bending load accelerated the growth of the microcracks at the sharp knife edges between the rivet hole surface and the outer surface of the lower skin. In this analysis, the result of computational estimation shows an important fact. After the initial fatigue cracks are formed, the main role governing the crack growth at the lap joint is the membrane stress in the skin and rivet reaction force.

ACKNOWLEDGMENT

The authors are grateful for the financial support from Federal Aviation Administration to the Center of Excellence for Computational Modeling of Aircraft Structures, Georgia Institute of Technology. It is a pleasure to thank Mr. Freeman Lin for his assistance in preparing this paper.

REFERENCES

- Atluri, S. N. (1986): *Computational Methods in the Mechanics of Fracture*. Amsterdam: North Holland, also translated in Russian, Mir Publishers, Moscow.
- Atluri, S. N., Sampath, S. G., and Tong, P. (1991): *Structural Integrity of Aging Airplanes*, Berlin, Heidelberg, New York: Springer.
- Atluri, S. N. and Tong, P. (1991): *Computational Schemes for Integrity Analyses of Fuselage Panels in Aging Airplanes*, *Structural Integrity of Aging Airplanes*, Atluri, S. N., Sampath, S. G., and Tong, P. (eds.), Berlin, Heidelberg, New York: Springer.
- Atluri, S. N., Park, J. H., and Ogiso, T. (1992): *Analysis of Cracks in Aging Aircraft Structures, With and Without Composite Patch Repairs*, *Computational Mechanics*, 10, pp. 169-201.
- Atluri, S. N. and Park, J. H. (1993): *Fatigue Growth of Multiple-Cracks Near a Row of Fastener Holes in a Fuselage Lap Joint*, *Computational Mechanics*, 13, pp. 189-203.
- Atluri, S. N., Park, J. H., Ripudaman Singh, and Pyo, C. R. (April 1994): *Structural Integrity of Panels with Multisite Damage*, AIAA-94-1457-CP.
- Atluri, S. N., Ripudaman Singh, and Park, J. H.: *Residual Life and Strength Estimates of Aircraft Structural Components with MSD/MED*, Report Computational Mechanics Center, Georgia Institute of Technology.
- Atluri, S. N., Park, J. H., Sing, R., and Pyo, C. R. (1995): *Integrity of Aircraft Structural Elements with Multisite Fatigue Damage*, *Engineering Fracture Mechanics*, Vol. 51, No. 3, pp. 361-380.
- Samavedam, G., Hoadley, and D., Thomson, D. (1992): *Full-Scale Testing and Analysis of Fuselage Panels*, Foster-Miller, Inc.
- Swift, T. (1984): *Fracture Analysis of Stiffened Structures, Damage Tolerance of Metallic Structures*, ASTM STP 842, pp. 69-107.

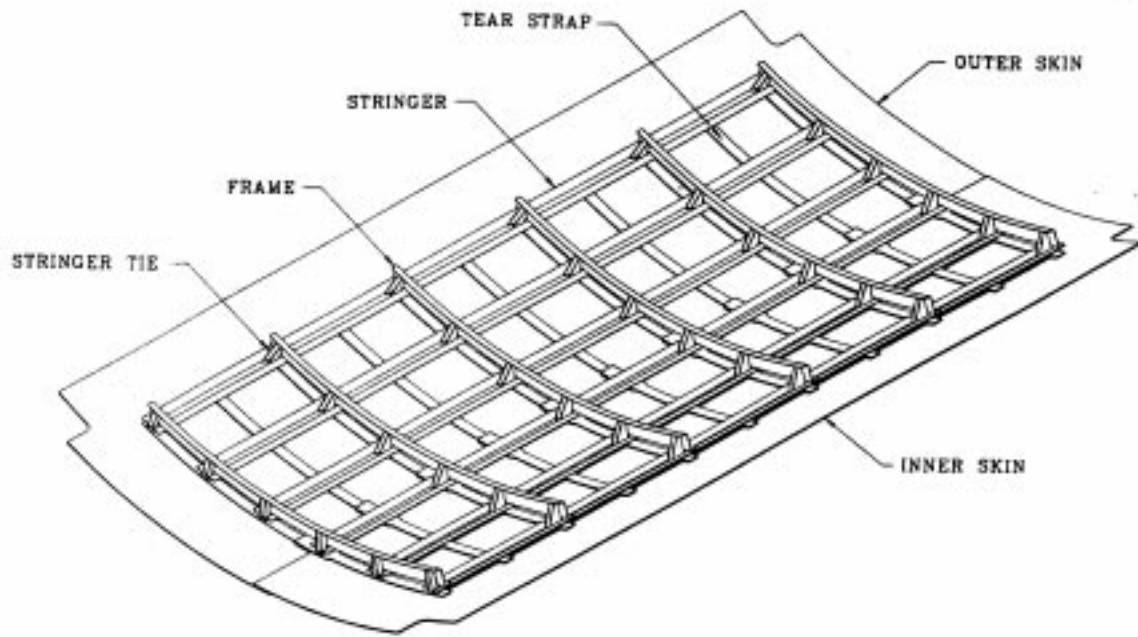


Figure 1. Full-Scale Fuselage Panel.

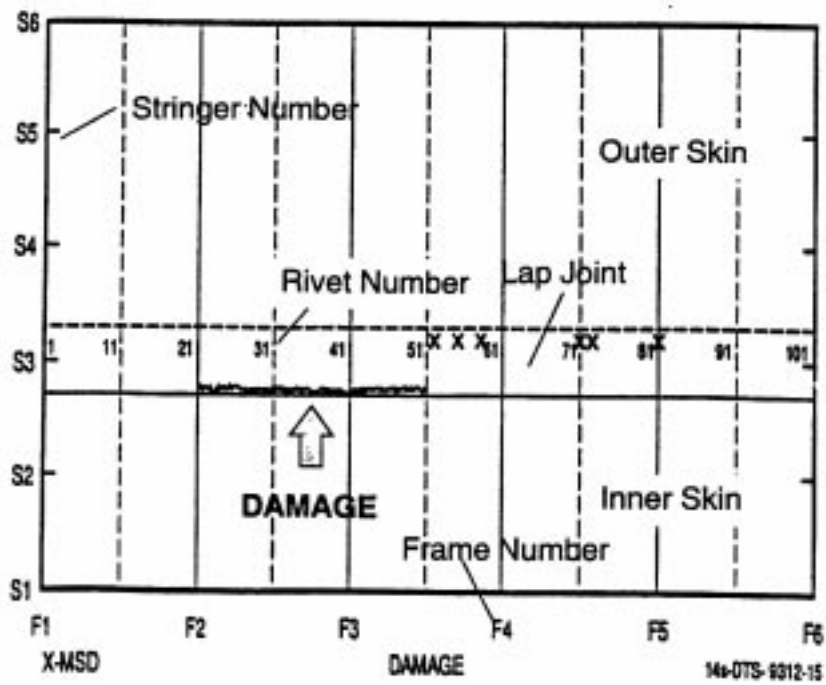


Figure 2. Fatigue Damage.

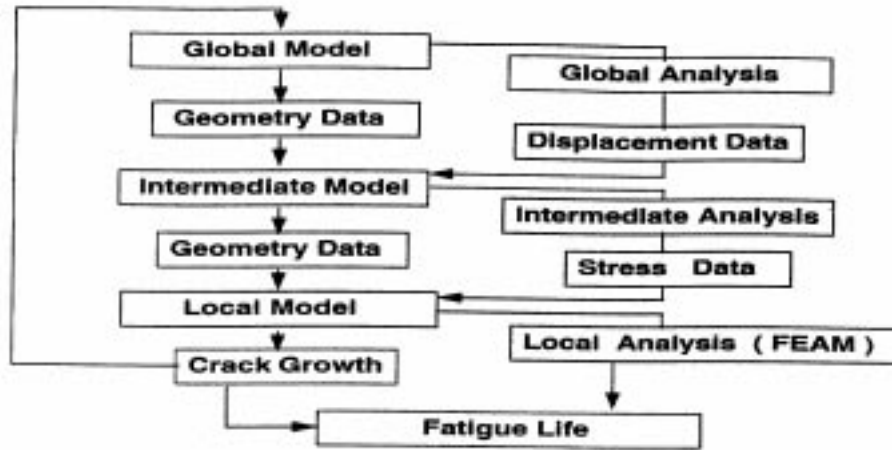


Figure 3. Fatigue Life Estimation Procedure.

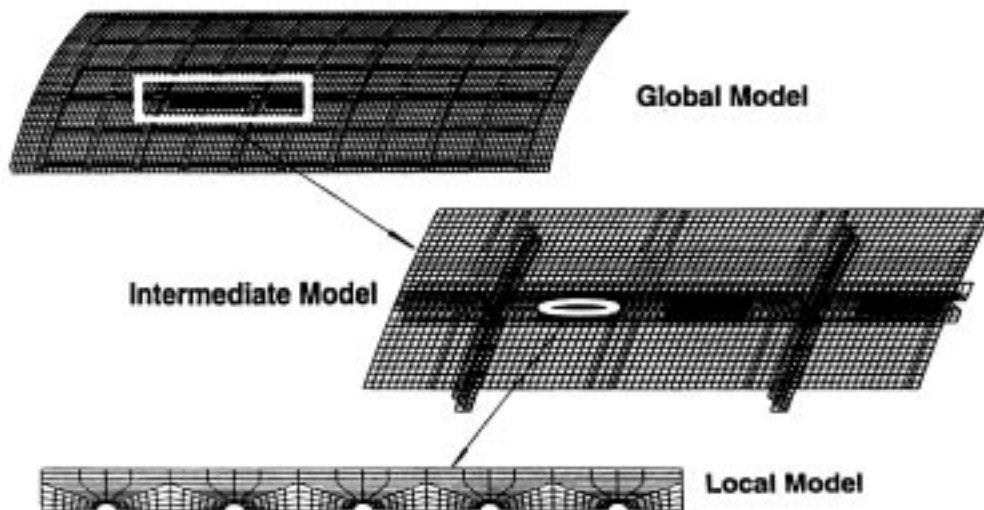


Figure 4. Global Model, Intermediate Model, and Local Model.

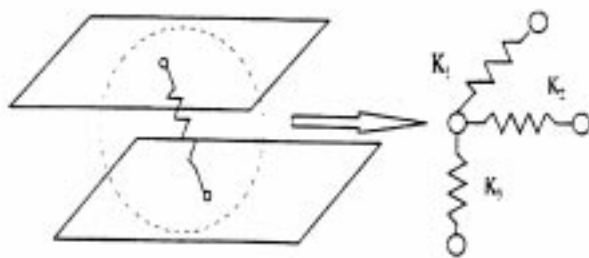


Figure 5. Spring Model.

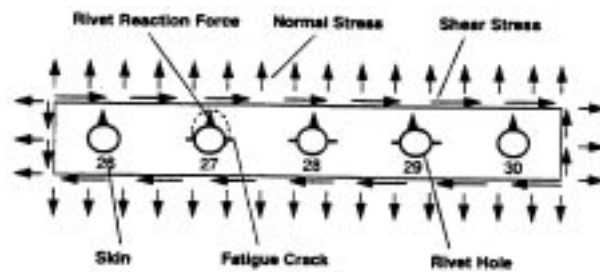


Figure 6. Force on Local Model.

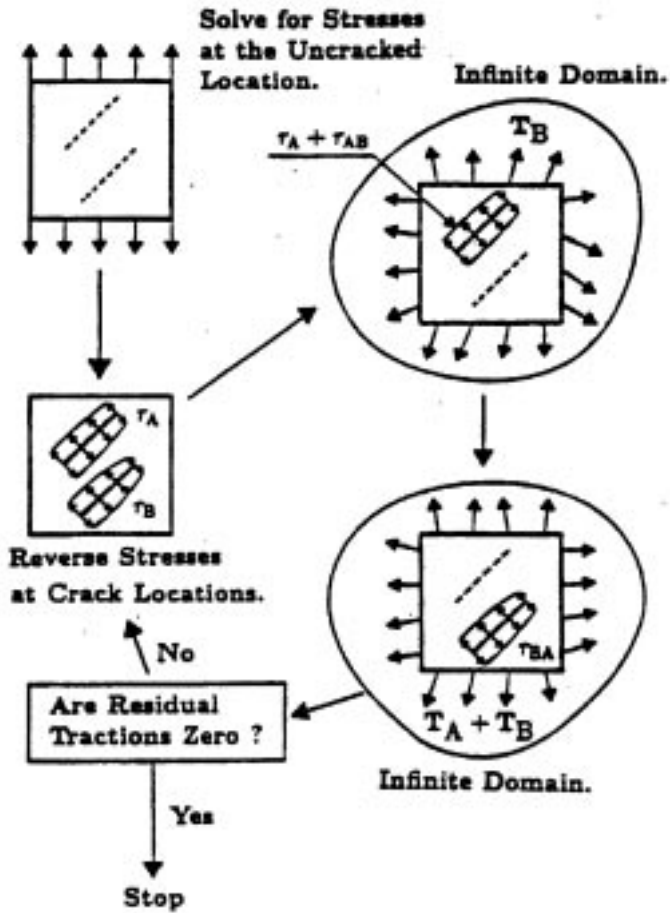
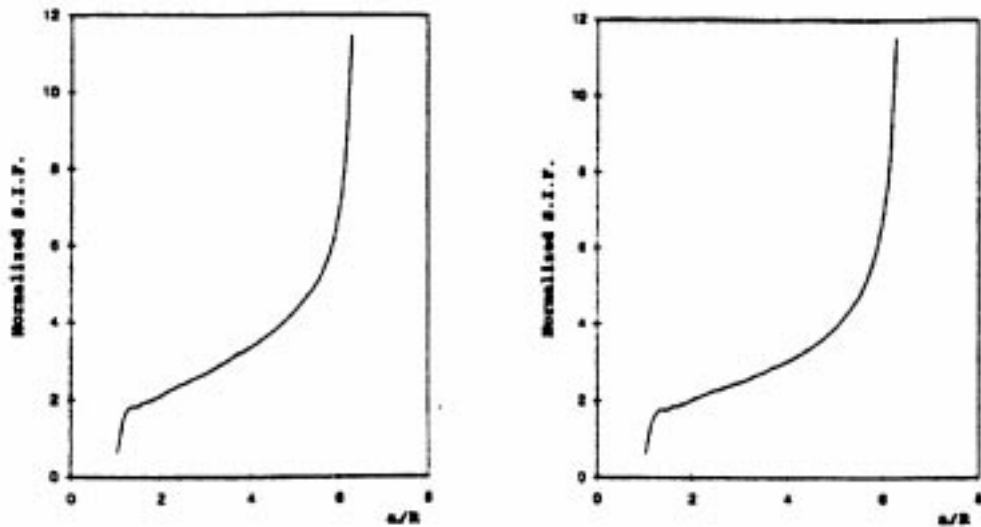


Figure 7. Finite Element Alternating Method.



At the Right Side of the Crack of Rivet Hole 27

At the Left Side of the Crack of Rivet Hole 28

Figure 8. Stress-Intensity Factor History of Cracks.

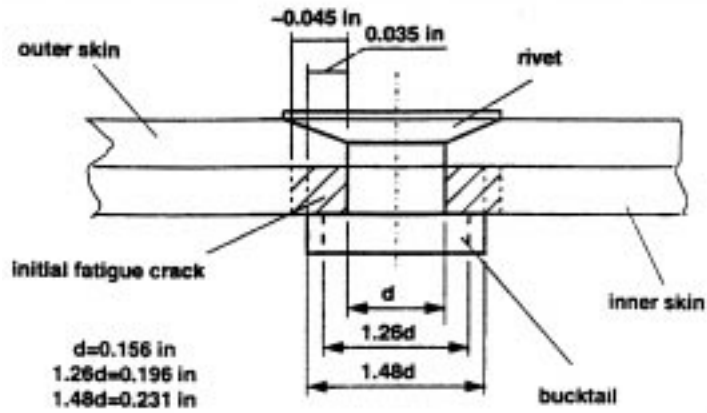


Figure 9. Initial Fatigue Crack in the Inner Skin.

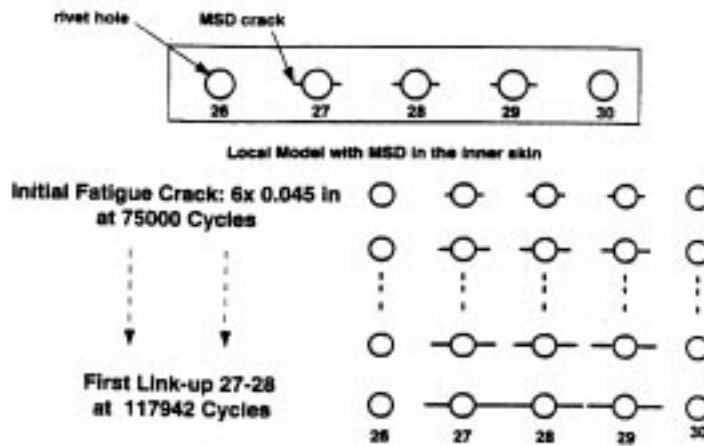


Figure 10. The Estimated Fatigue Life With Initial Fatigue Cracks 0.045 Inch.

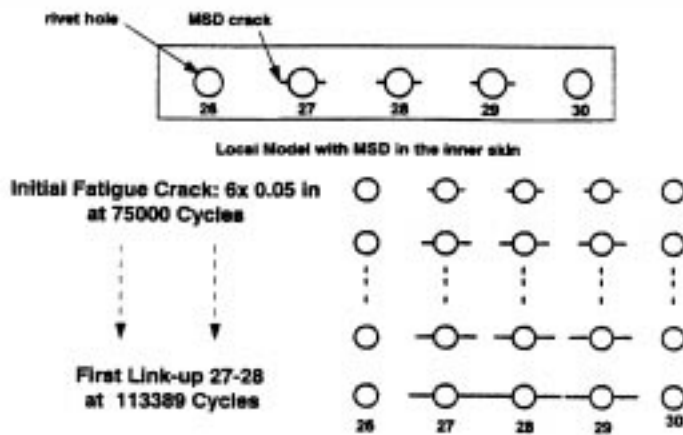


Figure 11. The Estimated Fatigue Life With Initial Fatigue Cracks 0.050 Inch.

ANALYTICAL METHODOLOGY FOR PREDICTING THE ONSET OF WIDESPREAD FATIGUE DAMAGE IN FUSELAGE STRUCTURE

Charles E. Harris, James C. Newman, Jr.,
Robert S. Piascik, and James H. Starnes, Jr.
Research and Technology Group
Langley Research Center
National Aeronautics and Space Administration (NASA)
Hampton, VA 23681

ABSTRACT

NASA has developed a comprehensive analytical methodology for predicting the onset of widespread fatigue damage in fuselage structure. The determination of the number of flights and operational hours of aircraft service life that are related to the onset of widespread fatigue damage includes analyses for crack initiation, fatigue crack growth, and residual strength. Therefore, the computational capability required to analytically predict the onset of widespread fatigue damage must be able to represent a wide range of crack sizes from the material (microscale) level to the global structural-scale level. NASA studies indicate that the fatigue crack behavior in aircraft structure can be represented conveniently by the following three analysis scales: small three-dimensional cracks at the microscale level, through-the-thickness two-dimensional cracks at the local structural level, and long cracks at the global structural level. The computational requirements for each of these three analysis scales are described in this paper.

INTRODUCTION

The ability to analytically predict the onset of widespread fatigue damage in fuselage structures requires methodologies that predict fatigue crack initiation, crack growth, and residual strength. Mechanics-based analysis methodologies are highly desirable because differences in aircraft service histories can be addressed explicitly and rigorously by analyzing different types of aircraft and specific aircraft within a given type. Each aircraft manufacturer has developed mature in-house durability and damage-tolerance design and analysis methodologies that are based on their product development history. To enhance these existing successful methodologies, NASA has adopted the concept of developing an analytical “tool box” that includes a number of advanced structural analysis computer codes which, taken together, represent the comprehensive fracture mechanics capability required to predict the onset of widespread fatigue damage. These structural analysis tools have complementary and specialized capabilities ranging from a nonlinear finite element-based stress-analysis code for two- and three-dimensional built-up structures with cracks to a

fatigue and fracture analysis code that uses stress-intensity factors and material-property data found in look-up tables or from equations. The development of these advanced structural analysis methodologies has been guided by the physical evidence of the fatigue process assembled from detailed teardown examinations of actual aircraft structure. In addition, NASA is conducting critical experiments necessary to verify the predictive capability of these codes and to provide the basis for any further methodology refinements that may be required. The NASA experiments are essential for analytical methods development and verification, but represent only a first step in the technology-validation and industry-acceptance processes. Each industry user of this advanced methodology must conduct an assessment of the technology, conduct an independent verification, and determine the appropriate integration of the new structural analysis methodologies into their existing in-house practices. NASA has established cooperative programs with U.S. aircraft manufacturers to facilitate this comprehensive transfer of this technology by making these advanced methodologies available to industry.

This paper presents the analytical framework for predicting the onset of widespread fatigue damage. After a discussion of the results of a thorough tear-down fractographic inspection of a five-bay fuselage lap splice joint containing widespread fatigue damage, the analytical fracture mechanics requirements to predict crack initiation, fatigue crack growth, and residual strength are presented. For each of these three fracture mechanics scales, example calculations will be compared to the results of experimental verification tests.

FRACTOGRAPHY OF WIDESPREAD FATIGUE DAMAGE (WFD) IN A STRUCTURAL FATIGUE TEST ARTICLE

Valid analytical methodology to predict the onset of widespread fatigue damage in fuselage structure must be based on actual observations of the physical behavior of crack initiation, crack growth, and fracture. The NASA methodology is based largely on the results of teardown fractographic examinations of aircraft fuselage components. A large section of a fuselage containing a longitudinal lap splice joint extending for five bays was provided to NASA by an aircraft manufacturer after conducting a full-scale fatigue test [1]. A photograph of the panel along with a schematic is shown in Figure 1. The fatigue test was terminated after reaching the number of fuselage pressurization cycles that equaled approximately three times the original economic design life goal of the aircraft established by the manufacturer. This section of the fuselage was selected because visual inspections made during the test had detected the growth of fatigue cracks extending from adjacent rivets which eventually linked up to form a long crack that extended completely across the bay. Further visual examinations of this section of the fuselage after completing the full scale fatigue test suggested that this section contained widespread fatigue damage. All rivet holes in each of the five bays of the panel were microscopically examined for fatigue cracks. The results of this examination form the physical basis for the analytical methodology developed by NASA to predict the onset of widespread fatigue damage.

There were three principal objectives of the fractographic examination of the fuselage panel. The first objective was to characterize widespread fatigue damage in a fuselage splice joint by assembling a database on the initiation and growth of fatigue cracks from rivets, including identifying the initiation mechanisms. The second objective was to provide a basis for comparing the crack growth behavior simulated in laboratory test specimens to the real behavior of an actual aircraft component. The third objective was to serve as a benchmark to verify the predictive capability of the fatigue crack growth portions of the widespread fatigue damage analytical methodology. This latter objective was achievable because the loading history of the full-scale fatigue test article was fully documented. Also, periodic underloads during the fatigue test were used to establish marker bands on the fatigue crack surfaces.

Achieving the above three objectives resulted in the development of a very large database. The contents of this database include:

- maps of cracks as a function of rivet locations in five consecutive bays;
- documentation of crack growth shapes and dimensions;
- identification of the crack initiation location and the initiating mechanisms such as high local stress, fretting, and manufacturing defects;
- analysis of fatigue marker bands;
- correlation between cycles and crack growth behavior; and
- indications of out-of-plane displacements and mixed-mode fracture behavior.

In addition to the extensive database assembled from the teardown fractographic examinations of the panel, sections of other retired aircraft and full-scale fatigue articles have also been examined to insure that the analytical methodology under development is sufficiently comprehensive to represent all fuselage assembly practices and design details.

Several general conclusions are obvious from the database. First, fatigue cracks were present at virtually every rivet hole in the top row of rivets. The cracks ranged in size from about 50 microns to several inches. Crack initiation mechanisms included high local stresses, fretting along mating surfaces, and manufacturing defects created during the riveting process. The cracking behavior in each bay was similar and the results of the fatigue marker bands were relatively independent of rivet hole location. An example of small cracks found in the panel is shown in Figure 2. A small crack initiating due to high local stresses within the rivet countersunk hole is shown in Figure 2 (a). The accompanying schematic shows the location of the crack in the outer skin of the lap splice joint. An example of a small crack initiating due to fretting is shown in Figure 2 (b) along with a schematic showing the interface where the fretting occurred. Examples of long cracks found at rivet holes are shown in Figure 3. Figure 3 (a, b, and c) shows a crack that initiated due to high local stresses and Figure 3 (d, e, and f) shows a crack in a different rivet hole that initiated by fretting. The higher magnifications of the cracks shown in Figure 3 (c and f) help to identify the location where the crack initiated and the initiation mechanism. Referring to Figure 3 (b), it is seen that the crack has grown completely through the thickness of the outer skin and has extended a considerable distance beyond the head of the rivet. Likewise, the crack shown in Figure 3 (e) has also extended a considerable distance from the head of the rivet but has not broken

through the outer surface of the skin. In both cases, the crack front is curved and indicates the existence of significant bending stresses across the lap splice joint. Figure 4 shows a large crack that has been formed by the link up of the small fatigue cracks that developed at adjacent rivet holes. As can be seen in the photograph, the crack extended into the tear strap region, changed crack growth directions, and grew into a rivet hole in the tear strap. The surfaces of the individual fatigue cracks between the rivets were clearly identifiable in the fractographic examination of the long crack surface. Close examination revealed several cracks that initiated due to high local stresses and other cracks that initiated due to fretting. However, the length of all of the fatigue cracks at link up were approximately the same. This observation suggests that the long crack behavior is somewhat independent of the initiating mechanism. Furthermore, this observation and the quantitative data obtained from the marker band analyses strongly suggest that the fatigue behavior of the long cracks is deterministic and predictable.

ANALYTICAL FRAMEWORK FOR THE METHODOLOGY TO PREDICT THE ONSET OF WIDESPREAD FATIGUE DAMAGE

It is obvious from the above described fractographic examinations that the computational capability required to predict analytically the onset of widespread fatigue damage must be able to represent a wide range of crack sizes from the material (microscale) level to the global structural-scale level. These studies indicate that the fatigue crack behavior in aircraft structure can be represented conveniently by the following three analysis scales: small three-dimensional crack geometries at the microscale level (Scale I: Crack Initiation); through-the-thickness two-dimensional crack geometries at the local structural level (Scale II: Fatigue Crack Growth); and long cracks at the global structural level (Scale III: Residual Strength). The computational requirements for each of these three analysis scales are described in the following paragraphs.

Scale I: Crack Initiation

The first analysis scale and corresponding computational capability represents the fracture mechanics of small cracks that exhibit three-dimensional crack-growth behavior. The existence and growth of these small cracks do not affect the global structural deformation states or internal load distributions. Examples of these cracks are surface and corner cracks that initiate at the edges of plates or at holes.

Criterion for Crack Initiation Based on Small Crack Behavior

Small fatigue cracks in some materials grow faster and at lower stress-intensity factor levels than is predicted from large-crack data which exhibits an apparent threshold for crack

growth [2]. The initiation and growth of these small cracks are affected by metallurgical features such as inclusion particles and grain-boundary interactions [3]. Typical large-crack results are obtained from tests with cracks greater than about 2 mm in length. The large-crack threshold is usually obtained from load-reduction tests. Some tests and analyses have shown that the development of the threshold may be caused by an increase in crack-closure behavior as the load is reduced. Small cracks that initiate at inclusion particles, voids, or weak grains do not have any prior plastic deformation to develop crack closure. If a small crack is fully open, then the stress-intensity factor range is fully effective and the crack growth rate for the small crack is faster than the rate exhibited by the large-crack data and at a lower stress-intensity factor range.

The concept of crack closure to explain crack growth acceleration and retardation was pioneered at NASA Langley almost two decades ago [4]. The closure concept is based on the postulate that the wake of plastically deformed material behind an advancing crack front may prevent the crack from being fully open during the complete loading cycle. Therefore, only part of the load cycle is effective in growing the crack. The crack closure concept has also been successfully used to explain the small-crack phenomenon exhibited by many aluminum alloys. The successful coupling of the closure methodology with the small-crack growth rate data base has resulted in a total life prediction methodology which treats initiation by predicting the growth of micron size cracks initiating at inclusion particles in the subgrain boundary microstructure [5].

Computational Methodology for Predicting Crack Initiation in Riveted Structure

Stress-intensity factor solutions are typically obtained from computational procedures such as the finite element analysis method. The ZIP3D computer code [6] has been developed to model three-dimensional crack configurations and to calculate the corresponding stress-intensity factors. This finite element analysis code uses an eight-node element and can be used to analyze stationary and growing cracks under cyclic elastic-plastic conditions, including the effects of crack closure. The FRANC3D code [7] also has solid modeling capabilities for three-dimensional geometries based on the boundary element method. For those crack configurations and general loading conditions that may occur for various structural components, weight-function solutions are being developed from the numerical results of parametric studies. These weight-function equations are particularly useful because the stress intensity factor solutions can be obtained from a stress analysis of the uncracked structure. Stress intensity factor solutions are currently being generated for cracks that initiate at countersunk rivet holes. Loading conditions include interference-fit stresses, clamp-up stresses, and loads transferred through a rivet. These stress-intensity factor solutions may then be used as input data for the FASTRAN II code [8] to predict fatigue crack growth. The FASTRAN II code is based on the mechanics of plasticity-induced crack closure. The effects of prior loading history on fatigue behavior, such as crack growth retardation and acceleration, are computed on a cycle-by-cycle basis. The code will predict the growth of cracks exhibiting the "small-crack effect" as well as two- and three-dimensional cracks exhibiting the classical Paris law crack growth behavior. The code has

been shown to be especially effective for predicting fatigue crack growth behavior in structures subjected to aircraft spectrum loads. The ZIP3D, FRANC3D, and FASTRAN II codes operate efficiently on engineering workstations, and FASTRAN II also operates on personal computers.

Experimental Verification of Crack Initiation Methodology

The small-crack effect and crack-closure analysis model, FASTRAN II, were used to calculate the total fatigue life (S-N) behavior of single-edge notched (SENT) specimens under constant amplitude and spectrum loads using an initial defect size based on microstructural data at initiation sites. Predicted results for aluminum alloy 2024-T3 were made using an initial semicircular crack size, 0.00024" (6 microns), that had an equal area to the average inclusion-particle sizes that were experimentally observed to initiate cracks [3]. Comparisons of experimental and predicted fatigue lives of the SENT specimens under the TWIST [10], FALSTAFF [11], and Gaussian [12] load sequences are shown in Figure 5. The specimens were cycled until a crack, length $2a$, had grown across the full thickness, B . The predicted lives are in very good agreement with the test data.

Scale II: Fatigue Crack Growth

The second analysis scale and corresponding computational capability represent the fracture mechanics of fatigue cracks that extend through the thickness of a skin or stiffener and are no longer three-dimensional in their crack-growth behavior.

Crack Closure Concept for Fatigue Crack Growth

As discussed in the previous section, the plasticity-induced crack closure model has been shown to be quite accurate in predicting the fatigue crack growth in aluminum alloys for a number of basic crack configurations for both constant amplitude and spectrum loads. The closure model is very accurate for a full range of R ratios and spike overload conditions provided the crack growth rate data are correlated with the effective stress-intensity factor range.

Computational Methodology for Fatigue Crack Growth in Riveted Structure

Two-dimensional analyses are typically quite adequate for predicting crack growth. However, accurate modeling of structural details is required to provide high-fidelity results for the local stresses in a structure so that the fracture mechanics calculations will be accurate. The FRANC2D finite element analysis code [13] has been developed for the analysis of two-dimensional planar structures, and the STAGS (Structural Analysis of

General Shells) nonlinear shell analysis code [14] has been developed for general shell structures. The FRANC2D code, developed by Cornell University, is a user-friendly engineering analysis code with pre- and postprocessing capabilities especially developed for fracture mechanics problems. The code operates on UNIX-based engineering workstations with X-Window graphics and is interactive and menu driven. A unique capability of the code is the ability to predict non-self-similar crack growth behavior. An automatic adaptive remeshing capability allows an engineer to obtain a history of the stress-intensity factors for any number of cracks in the structure and for any arbitrary crack growth trajectory. The STAGS finite element code, developed by Lockheed Palo Alto Research Laboratory, provides the capability to model any general shell structure and has both geometric and material nonlinear analysis capabilities. STAGS is particularly well suited for analyzing shells that have structural features such as frames, stiffeners, and cutouts. The code uses the Riks arc-length projection method and computes large displacements and rotations at the element level. The code has been developed especially for nonlinear stability and strength analyses. Both FRANC2D and STAGS can calculate the history of the stress intensity factors for a growing crack that are compatible with FASTRAN II so that fatigue crack growth analyses may be performed. Other crack growth models may also be used. STAGS and FRANC2D operate on engineering workstations and mainframe computers.

The advanced durability and damage-tolerance analysis capabilities developed in the NASA Airframe Structural Integrity Program will also be implemented in the NASGRO analysis code [15]. NASGRO is a general-purpose damage tolerance analysis code being developed by NASA Johnson Space Center. The code is based on fracture mechanics principles and may be used to compute stress intensity factors, fatigue crack growth, critical crack sizes, and the limit of safe life. An extensive library of stress intensity factors may be used with NASGRO or solutions may be obtained from a boundary element analysis capability using the FADD analysis code [16]. NASGRO also has an extensive material property library which includes most aluminum alloys, titanium alloys, and steels commonly used in the aerospace industry. Fatigue crack growth may be computed from a crack-closure mechanics model or from one of several empirical models commonly used by industry. NASGRO is used extensively throughout the aerospace industry. FADD was developed at the University of Texas and uses the distributed-dislocation method to compute stress intensity factors. This approach combines a highly accurate stress intensity factor analysis with the modeling simplicity of the boundary element analysis method. FADD is also available in a stand-alone version and is currently being tested by industry at beta-site locations. NASGRO operates on engineering workstations and personal computers. FADD is also available as a stand-alone code and operates on personal computers.

Experimental Verification of Fatigue Crack Growth Methodology

As part of the experimental verification of the fatigue crack growth methodology, fatigue tests on single shear riveted lap joint specimens were conducted to measure the growth of cracks from countersunk rivets holes [17]. The specimens were made from 0.040-inch-thick Alclad 2024-T3 sheet material and 5/16" rivets. A small EDM notch was used to

initiate the fatigue crack at the rivet hole. The EDM notch was placed in the countersunk hole before the rivet was expanded. Tension-tension fatigue tests ($R=0.02$) were conducted and the growth of the fatigue crack from the EDM notch was recorded throughout the test. The growth of the through-thickness cracks were recorded along the surface of the specimen using an optical microscope. Special restraints were used to prevent the large out-of-plane rotations caused by the eccentricity in the load path of the single shear specimen. The fatigue tests were terminated usually after appreciable crack growth was recorded. Several specimens were cut apart and the interference fit was estimated by measuring the size of the rivet hole after expanding the rivet relative to the original machined hole size.

The FRANC2D code was used to analyze the specimen and compute the crack growth rates. The analysis included the effects of interference fit stresses, bearing load distribution in the countersunk hole, and an approximation of the stress concentration produced by the three-dimensional geometry of the countersunk hole. The experimental measurements of the interference fit expansion was used to compute the interference fit stresses. The analytical reduction of the data recorded during the fatigue tests is shown in Figure 6. The measured crack growth rates are plotted against the computed stress-intensity factor range. The open symbols are the crack growth test data from the single shear specimens. The solid line is the baseline da/dn crack growth data for aluminum alloy 2024-T3 measured from standard crack growth tests. The length of the cracks growing from the rivet in the lap specimen were measured experimentally and the FRANC2D model was used to calculate the corresponding stress-intensity factors. The coalescence of the data from the single shear lap specimen around the baseline crack growth data confirms the accuracy of the FRANC2D analysis to properly account for the complex stress state at the countersunk rivet. The gray shaded area shows the values of the crack data if the stress intensity factors were computed without including interference fit stresses. Without the interference fit, the cracks grow at a faster rate for the same applied stress. The benefit in the crack growth rate is produced by the tensile residual stresses caused by the interference which results in a reduction to the stress intensity-factor range.

Scale III: Residual Strength

The third analysis scale and corresponding computational capability represent structures with long cracks that change the internal structural load distribution that exhibit behavior strongly affected by structural details and that affect the residual strength of the structure. In addition, the fracture mechanics of ductile materials such as 2024-T3 aluminum alloy often requires an elastic-plastic stress analysis capability that predicts stable tearing and fracture. Furthermore, nonlinear geometric effects, such as crack bulging in shell structures, also significantly affect residual strength predictions. All of these complexities are present in a fuselage shell structure and must be represented in a residual-strength analysis of the fuselage.

The structural analysis computer codes under development in the NASA Airframe Structural Integrity Program are being integrated into an analytical methodology for predicting the residual strength of a fuselage structure with one or more cracks. The analytical prediction of the residual strength of a complex built-up shell structure, such as a fuselage, requires the integration of a ductile fracture criterion, a fracture-mechanics analysis, and a detailed stress analysis of the structure. The crack tip opening-angle (CTOA) criterion has been experimentally verified to be a valid fracture criterion for mode I stress states in thin and moderately thick (0.5 inch thick or less) aluminum alloys. The CTOA criterion has been demonstrated to be valid for predicting the linkup of a long lead crack with small fatigue cracks ahead of the advancing lead crack. This fracture criterion has been implemented into the STAGS geometric and material nonlinear finite element-based shell analysis code to provide an integrated structural-integrity analysis methodology. The capability to model a growing crack that may extend in a non-self-similar direction has been added to the STAGS code along with an automated mesh refinement and adaptive remeshing procedure. The topological description of the growing crack is provided by the FRANC3D fracture mechanics code. The geometric nonlinear behavior of a stiffened fuselage shell is currently under study for internal pressure loads combined with fuselage body loads that produce tension, compression, and shear loads in the shell.

The CTOA Fracture Criterion for Residual Strength

The critical crack tip opening-angle (CTOA), or equivalently, the crack tip opening-displacement (CTOD), fracture criterion is a local approach to characterizing fracture. In contrast, the J-integral or J-R curve criterion is based on global deformations and has been found to be specimen and crack-size dependent for structures with large amounts of stable tearing. The constant CTOA (or CTOD) criterion has been used to predict the variations in J-R curves due to differences in crack sizes and specimen types. Therefore, a local crack tip displacement is a more fundamental fracture parameter than the J-integral representation for local strain-controlled fracture processes such as stable tearing and void coalescence.

Simple plastic-zone models that are based on linear-elastic stress intensity factors can be adjusted to fit experimental data and then used to predict crack linkup for relatively simple structural geometries. While these methods predict the correct trends in crack linkup behavior, they may be difficult to apply to analyses of complex structural details that are characteristic of a fuselage structure. The CTOA criterion can be effectively implemented into a finite element analysis code provided that the code has elastic-plastic deformation and crack-growth simulation capabilities. These capabilities exist in the STAGS geometric and material nonlinear shell analysis code, but analyses of large-scale problems must currently be conducted on a high-performance mainframe computer. After thorough experimental verification of the residual strength analysis methodology, it is anticipated that the methodology can be simplified by taking advantage of appropriate engineering approximations.

An extensive test program [18] has been conducted to interrogate experimentally the characteristics of the CTOA criterion and to establish its validity as a fracture criterion for thin-sheet aluminum alloy 2024-T3. A schematic of the four basic flat-panel geometries used to verify the elastic-plastic finite-element code and the CTOA criterion for mode I fracture is shown in Figure 7. The blunt-notch panel was used to verify the finite element analysis code used to compute plastic deformation fields and large displacements. Measurements of far-field displacements and the local displacements inside the open holes at the ends of the crack were accurately predicted by the finite element analysis for large-scale plastic deformations. The center-crack and three-hole-crack panels were used to measure the load (or far-field applied stress) as a function of crack extension and the CTOA during stable tearing. Because the tests were conducted at a specified controlled displacement rate, crack extension was measured well beyond the maximum load observed during the test. Stable tearing was quite extensive in the three-hole-crack specimen because the crack driving force is reduced as the crack approaches the two large open holes in a manner that is similar to the behavior of cracks in stiffened panels. A high-resolution long-focal-length microscope was used to record the stable-tearing results. The microscope image was videotaped, digitized, and recorded in a computer file. The tearing event was then analyzed on a frame-by-frame basis and the critical opening angle was measured throughout the fracture event. A typical CTOA measurement is shown in Figure 8. As can be seen in the figure, the opening angle is relatively insensitive to the length over which the angle is measured. The results of a three-hole-crack panel test are given in Figure 9. After an initial transition region, the CTOA is constant throughout the stable-tearing process. The initial transition region is caused by a three-dimensional effect that occurs as the crack tunnels and transitions from flat- to slant-crack growth. Over 63 mm (2.5 in.) of stable tearing was recorded and the CTOA values were nearly constant. Measurements such as these were also made for center-crack and three-hole-crack panels of various widths, crack lengths, and sheet thicknesses ranging from 1.0 mm (0.04 in.) to 2.3 mm (0.09 in.). Also, measurements of the CTOA were obtained for compact tension specimens. In all cases, the measured CTOA was approximately 6.0 degrees for cracks oriented in the LT direction of the sheet and 5.1 degrees for cracks oriented in the TL direction, where L designates the principal rolling direction of the sheet and T designates the direction transverse to the principal rolling direction. A complete description of these test results is given in reference 18.

A series of fracture tests were conducted by the National Institute of Standards and Technology (NIST) [19] on aluminum panels to characterize the fracture behavior and linkup of multiple cracks in very wide panels. Ten flat panel test specimens at 3988 mm (157.0 in.) long, 2286 mm (90.0 in.) wide, and 1.026 mm (0.040 in.) thick were fabricated from single sheets of bare 2024-T3 aluminum alloy. Three center-crack panels with a single long center crack and seven panels with a long crack and small multiple-site damage (MSD) cracks ahead of the single long crack were tested to failure. Saw cuts were used to simulate fatigue cracks. Specially designed grips and antibuckling guides were used to conduct the tests in the 1780-kN capacity universal testing machine at NIST. (One test, MSD #6, was conducted without antibuckling guides and the results from this test will be discussed later.) The load and displacement histories were recorded for each test and the fracture events were recorded on film, video tape, computer, magnetic tape, and occasionally optical microscopy. The first

three tests were used to measure basic material fracture properties such as the R-curve and critical crack tip opening angle (CTOA). The other six tests, with antibuckling guides, were linkup and fracture tests of panels with various multiple-site damage crack configurations.

NASA used the CTOA fracture criterion to analytically predict the fracture of the wide panels with MSD cracks. The center-crack panels with the single long crack were used to determine the value of the CTOA to be used in the MSD analyses. In order to match the load, displacement, and crack extension data recorded during the stable tearing and fracture of the single crack panels, a critical CTOA value of 3.4 degrees had to be used. In addition, an initial crack opening displacement of 0.0086 inch also had to be used in the analysis to properly simulate the initial stable tearing from the saw cuts. Using these values of CTOA and initial displacement, the applied load to crack linkup and final fracture were calculated for each MSD test prior to conducting the test. The crack configurations, experimental test loads at panel fracture, and the analytical predictions using the CTOA criterion are given in Table 1. As can be seen the predictions are within + or - 6% in all test but one which was off by 11%. It is interesting to note that MSD test number 10 is a repeat of MSD test number 7, with the identical crack configuration. This test is the only MSD test with multiple experimental failure loads. Note that the experimental failure loads varied by about 10%. Therefore, the analytical predictions are viewed to be within the experimental accuracy of the tests data.

It should be noted that the CTOA angle experimentally measured during the fracture tests was consistently about 5.5 degrees. This value is significantly higher than the value of 3.4 degrees required to analytically simulate the single-crack fracture test behavior. This difference is believed to be attributed to the ineffectiveness of the antibuckling guide to prevent out-of-plane displacements during the fracture tests. Visual observations made during the tests suggested that the panels did buckle even with the antibuckling guides. An additional test, MSD #6, was conducted without antibuckling guides to determine quantitatively the effect of panel buckling on the fracture load. The test resulted in about a 10% lower failure load than for the panel with the ineffective antibuckling plates. Subsequent fracture analyses conducted by NASA using the STAGS code and the CTOA fracture criterion have confirmed that the effects of flat panel buckling can result in the magnitude of the discrepancy between the measured CTOA and the value required in the analysis to predict the fracture test results.

The experimental and analytical results presented herein verify the CTOA fracture criterion for predicting the residual strength of flat panels with cracks undergoing mode I fracture behavior. Further testing is required to verify the criterion for predicting the residual strength of complex stiffened shell structures. The CTOA criterion must be extended to mixed-mode loading conditions. Also, numerical procedures for crack extension under mixed-mode loading conditions must be implemented into an elastic-plastic shell analysis code. And finally, the ability to predict crack trajectories accurately and to model curved crack growth must be developed. The next section describes the stiffened shell structural analysis methodology being developed for analyzing a fuselage structure and for predicting its residual strength accurately.

Computational Methodology for Residual Strength of Fuselage Structure

NASA has developed a unique capability that integrates the fracture topology modeling capabilities of FRANC3D with the general shell analysis capabilities of STAGS into an integrated FRANC3D/STAGS analysis procedure [20]. The automatic adaptive remeshing capability of FRANC3D and the geometric nonlinear stress-analysis capability of STAGS provides the analysis basis required to predict the crack-growth, crack-turning and crack-arrest behavior exhibited by pressurized shell structures in damage-tolerance tests. This capability is described in greater detail in the following paragraphs. For simple two-dimensional plane-stress or plane-strain fracture mechanics problems, the ZIP2D special-purpose finite element code [21] has proven to be very accurate and computationally efficient. The integrated FRANC3D/STAGS analysis procedure currently operates on high-level workstations or on mainframe computers, and ZIP2D operates on workstations.

The STAGS nonlinear finite element analysis code has been modified to include the capability of conducting crack growth and residual strength analyses for stiffened fuselage shell structures subjected to combined internal pressure and mechanical loads. STAGS was originally developed to predict the strength, stability, and nonlinear response of non-axisymmetric or general shells and includes analyses for both geometric and material nonlinear behavior. The nonlinear solution algorithm used in STAGS is based on Newton's method and includes both the modified and full versions of Newton's method. Large rotations are represented by a co-rotational algorithm at the element level, and the Riks arc-length projection method is used to integrate past limit points. The finite element library includes nonlinear beam, plate, and shell elements. Complex stiffened shell structures can be modeled to include as many finite elements as required to represent accurately the response of each structural member in the stiffened shell of interest. The computational efficiency of the code allows nonlinear analyses of models with over 100,000 degrees of freedom to be conducted in a reasonable amount of computer time. Both self-similar and non-self-similar crack-growth prediction capabilities have been added to STAGS for predicting crack growth in a shell that is in a nonlinear equilibrium state. The crack-growth analysis used in FRANC3D/STAGS is based on a virtual crack extension analysis that calculates the strain energy release rate for nonlinear shells with mixed-mode crack growth including shell wall bending. A load relaxation capability is used to represent the local load redistribution that occurs as a crack grows in the shell and Newton's method is used to maintain nonlinear equilibrium as the crack propagates. Nonlinear adaptive mesh refinement is used to determine the necessary finite element model changes as the crack propagates.

The general strategy for developing the nonlinear structural analysis methodology for predicting residual strength of stiffened shells with cracks is shown in Figure 10. Large-scale global models of a stiffened fuselage shell of interest are developed and nonlinear analyses are conducted to determine the internal load distribution and general response of the shell as shown in the upper left of the figure. A hierarchical modeling approach is used to provide more highly refined local models which are developed based on the global model results. The local models provide the higher-fidelity solutions that are necessary to predict stress and displacement gradients near the crack discontinuity in the shell as shown in the upper right of

the figure. Several local models are generated as required and analyzed to provide the detailed stress and deflection results necessary to predict crack growth and residual strength for any structural detail feature such as the longitudinal lap splice shown in the lower right of the figure.

An example [22] of the hierarchical modeling strategy for nonlinear stiffened shell analysis using STAGS is shown in Figure 11. The nonlinear hoop stress and radial deflection results for the global shell model of a frame and stringer stiffened aluminum shell are shown on the left of the figure. The shell has a longitudinal crack at the top of the fuselage and is loaded by 55.2 KPa (8 psi) of internal pressure. The longitudinal crack in the skin is next to a stiffener and the frame at the crack location is also broken. A curved stiffened panel model was developed with five frames and five stringers to generate the 36-skin-bay local model as shown in the upper right of the figure. This model provides more detailed stress- and deflection-gradient results near the cracked region as shown in the figure. The results shown are for a 0.508-m (20.0-in.) -long skin crack with the center of the crack at the broken frame. The frames are located at the dark circumferential regions in the figure. The boundary conditions for this local model are based on the results of the global model analysis, and both equilibrium and compatibility with the nonlinear global shell solution are maintained at the panel boundaries. A more refined stiffened panel model was developed with two frames and three stringers to generate the six-skin-bay local model shown in the lower right of the figure. The hoop stress and radial deflection results shown are for a 1.016-m (40.0-in.) -long crack that has grown to the frames on either side of the broken frame. The boundary conditions for this more refined local model are based on the results of the 36-skin-bay stiffened panel model and both equilibrium and compatibility with the nonlinear 36-skin-bay panel solution are maintained at the six-skin-bay panel boundaries. This hierarchical modeling and analysis approach provides the high-fidelity nonlinear stress- and deflection-gradient results needed to represent the shell behavior near the crack to the level of accuracy required to predict crack growth and residual strength accurately.

An example of the fracture mechanics analysis capability using FRANC3D/STAGS is shown in Figures 12 and 13. Using the initial STAGS finite element model shown in Figure 12, stable tearing is simulated for a 6-inch-, 8-inch- and 10-inch-long skin crack centered over a broken tear strap. The FRANC3D fracture analysis is performed using the local two-bay by two-bay geometry model with the edge displacements determined from an intermediate six-bay by six-bay model. As illustrated schematically in both Figures 12 and 13, the boundary conditions for the local and intermediate models were determined from the full-scale fuselage cylinder model shown in Figure 11. The full-scale fuselage model was subjected to an internal pressure of 55.2 KPa (8 psi) plus shear and bending loads simulating down forces acting on the empennage. The stress contour plot in the upper right of Figure 13 shows the hoop stress resultants for the initial crack length of 6 inches as modeled by the finite element mesh shown in Figure 12. Using the FRANC3D adaptive remeshing capability, the crack is extended to 8.0 inches and then to 10 inches as shown in the two lower stress contour plots in Figure 13. The direction of the crack extension was determined by a FRANC3D algorithm using a simple maximum principle stress criterion. Then the new finite element meshes for the 8-inch and 10-inch crack geometries were automatically

developed by the FRANC3D adaptive remeshing algorithms. The crack growth increments for this stable tearing simulation were arbitrarily chosen for illustrative purposes only. As is clearly evident from the stress contour plot, the effect of the shear force results in a nonsymmetric and non-self-similar crack extension.

Experimental Verification of Residual Strength Methodology

The methodology to analytically predict the residual strength of a fuselage structure with widespread fatigue damage and discrete source damage will be experimentally verified. NASA will be conducting verification tests of curved stiffened panels simulating sections of the fuselage geometry subjected to internal pressure loads only and subjected to combined loads. Plans call for two tests to be conducted under internal pressure loads only. The first test will be a residual strength test on a panel with a midbay skin crack oriented in the longitudinal direction with the damage located away from a splice joint. The second test will be a residual strength test of a panel with simulated widespread fatigue damage in a longitudinal lap splice joint and with a certification size lead crack simulating discrete source damage. The third and fourth verification tests will be conducted on panels with the same crack configurations as the first two tests but with combined internal pressure, shear, and bending loads simulating fuselage stresses created by the empennage loads. Two special test facilities, a pressure box for internal pressure loads, and a D-box for combined internal pressure and mechanical loads at NASA Langley Research Center will be used to conduct these tests of the built-up shell structures. In addition to the tests to be conducted at Langley, NASA will also use test data available from industry and other Government funded test programs as benchmarks to verify the accuracy of the analytical prediction methodology. This experimental verification test program will be completed during the next calendar year.

SUMMARY

NASA has developed a comprehensive analytical methodology for predicting the onset of widespread fatigue damage in fuselage structure. The determination of the aircraft service life that is related to the onset of widespread fatigue damage includes analyses for crack initiation, fatigue crack growth, and residual strength. Therefore, the computational capability required to predict analytically the onset of widespread fatigue damage must be able to represent a wide range of crack sizes from the material (microscale) level to the global structural-scale level. NASA studies indicate that the widespread fatigue damage behavior in aircraft structure can be represented by the following three analysis scales: small three-dimensional cracks at the microscale level, through-the-thickness two-dimensional cracks at the local structural level, and long cracks at the global structural level.

NASA has adopted the concept of developing a computational tool box that includes a number of advanced structural analysis computer codes which, taken together, represent the comprehensive fracture mechanics capability required to predict the onset of widespread

fatigue damage. These structural analysis tools have complementary and specialized capabilities ranging from a nonlinear finite element-based stress-analysis code for two- and three-dimensional built-up structures with cracks to a fatigue and fracture analysis code that uses stress-intensity factors and material-property data found in look-up tables or from equations. The development of these advanced structural analysis methodologies has been guided by the physical evidence of the fatigue process assembled from detailed tear-down examinations of actual aircraft structure. In addition, NASA is conducting critical experiments necessary to verify the predictive capability of these codes and to provide the basis for any further methodology refinements that may be required. The NASA experiments are essential for analytical methods development and verification but represent only a first step in the technology-validation and industry-acceptance processes. Each industry user of this advanced methodology must conduct an assessment of the technology, conduct an independent verification, and determine the appropriate integration of the new structural analysis methodologies into their existing in-house practices. NASA has established cooperative programs with the U.S. aircraft manufacturers to facilitate the comprehensive transfer of this advanced technology to industry.

REFERENCES

1. Piascik, R. S., Willard, S. A., and Miller, M., "The Characterization of Widespread Fatigue Damage in Fuselage Structure," FAA/NASA International Symposium on Advanced Structural Integrity Methods for Airframe Durability and Damage Tolerance, NASA CP 3274, Charles E. Harris, editor, 1994, pp. 563-580.
2. Ritchie, R. O. and Lankford, J., editors, Small Fatigue Cracks, Metallurgical Society, Warrendale, PA, 1986.
3. Newman, J. C., Jr. and Edwards, R. R., Short-Crack Growth Behavior in an Aluminum Alloy—An AGARD Cooperative Test Programme, AGARD R-732, 1988.
4. Elber, W., "The Significance of Fatigue Crack Closure," Damage Tolerance in Aircraft Structures, American Society for Testing and Materials, ASTM STP 486, Philadelphia, PA, 1971, pp. 230-242.
5. Newman, J. C., Jr., "A Review of Modeling Small-Crack Behavior and Fatigue-Life Predictions for Aluminum Alloys," Fatigue & Fracture of Engineering Materials and Structures, Vol. 17, No. 4, 1994, pp. 429-439.
6. Shivakumar, K. N. and Newman, J. C., Jr., "ZIP3D - An Elastic and Elastic-Plastic Finite-Element Analysis Program for Cracked Bodies," NASA TM 102753, 1990.
7. Potyondy, D. O., "A Software Framework for Simulating Curvilinear Crack Growth in Pressurized Thin Shells," Ph.D. Thesis, Cornell University, Ithica, NY, 1993.

8. Newman, J. C., Jr., "FASTRAN II - A Fatigue Crack Growth Structural Analysis Program," NASA TM 104159, February 1992.
9. deJonge, J. B., D. Schutz, H. Lowak, and J. Schijve, "A Standardized Load Sequence for Flight Simulation Tests on Transport Wing Structures-TWIST. National Lucht-en Ruimtevaart-Laborium, NLR TR-73029 U., 1973.
10. van Dijk, G. M. and deJonge, J. B., "Introduction to a Fighter Aircraft Loading Standard for Fatigue Evaluation FALSTAFF. National Lucht-en Ruimtevaart - Laborium, NLR MP-75017 U., 1975.
11. Huck, M., Schutz, W., Fischer R., and Kobler, H., A Standard Random Load Sequence of Gaussian Type Recommended for General Application in Fatigue Testing. Industrieanlagen Betriebsgesellschaft (IABG) TF-570, 1976.
12. Wawrzynek, P. A. and Ingraffea, A. R., "FRANC2D: A Two-Dimensional Crack Propagation Simulator Version 2.7 User's Guide," NASA CR 4572, March 1994.
13. Brogan, F. A., Rankin, C. C., and Cabiness, H. D., "STAGS User Manual," Lockheed Palo Alto Research Laboratory, LMSC Report P032594, 1994.
14. Forman, R. G., Shivakumar, V., and Newman, J. C., Jr., "Fatigue Crack Growth Computer Program NASA/FLAGRO," Version 2.0, NASA JSC-22276A, May 1994.
15. Chang, C. C., "A Boundary Element Method for Two-Dimensional Linear Elastic Fracture Analysis," Ph.D. Dissertation, The University of Texas, Austin, Texas, December 1993.
16. Dawicke, D. S., Phillips, E. P., Swenson, D. V., and Gondhalekar, S., "Crack Growth from Countersunk Rivet Holes," Durability of Metal Aircraft Structures, S. N. Atluri, C. E. Harris, A. Hoggard, N. Miller, and S. G. Sampath, editors, Atlanta Technology Publications, Atlanta, GA, 1992, pp. 75-90.
17. Newman, J. C., Jr., Dawicke, D. S., Sutton, M. A., and Bigelow, C. A., "A Fracture Criterion for Widespread Cracking in Thin-Sheet Aluminum Alloys," Proceedings of the ICAF 17th Symposium, 1993, pp. 443-467.
18. deWit, Roland, Fields, Richard J., Mordfin, Leonard, Low, Samuel R., and Harne, Donald, "Fracture Behavior of Large-Scale Thin-Sheet Aluminum Alloy," FAA/NASA International Symposium on Advanced Structural Integrity Methods for Airframe Durability and Damage Tolerance, NASA CP 3274, National Aeronautics and Space Administration, September 1994, pp. 963-984.

19. Potyondy, David. O., Wawrzynek, Paul A., and Ingraffea, Anthony R., "Discrete Crack Growth Analysis Methodology for Through Cracks in Pressurized Fuselage Structures," NASA CP 3274, C. E. Harris, editor, September 1994, pp. 581-602.
20. Harris, C. E., Starnes, J. H., Jr., and Newman, J. C., Jr., "Development of Advanced Structural Analysis Methodologies for Predicting Widespread Fatigue Damage in Aircraft Structures," FAA-NASA Sixth International Conference on the Continued Airworthiness of Aircraft Structures, DOT/FAA/AR-95/86, Catherine A. Bigelow, editor, 1995, pp. 139-164.

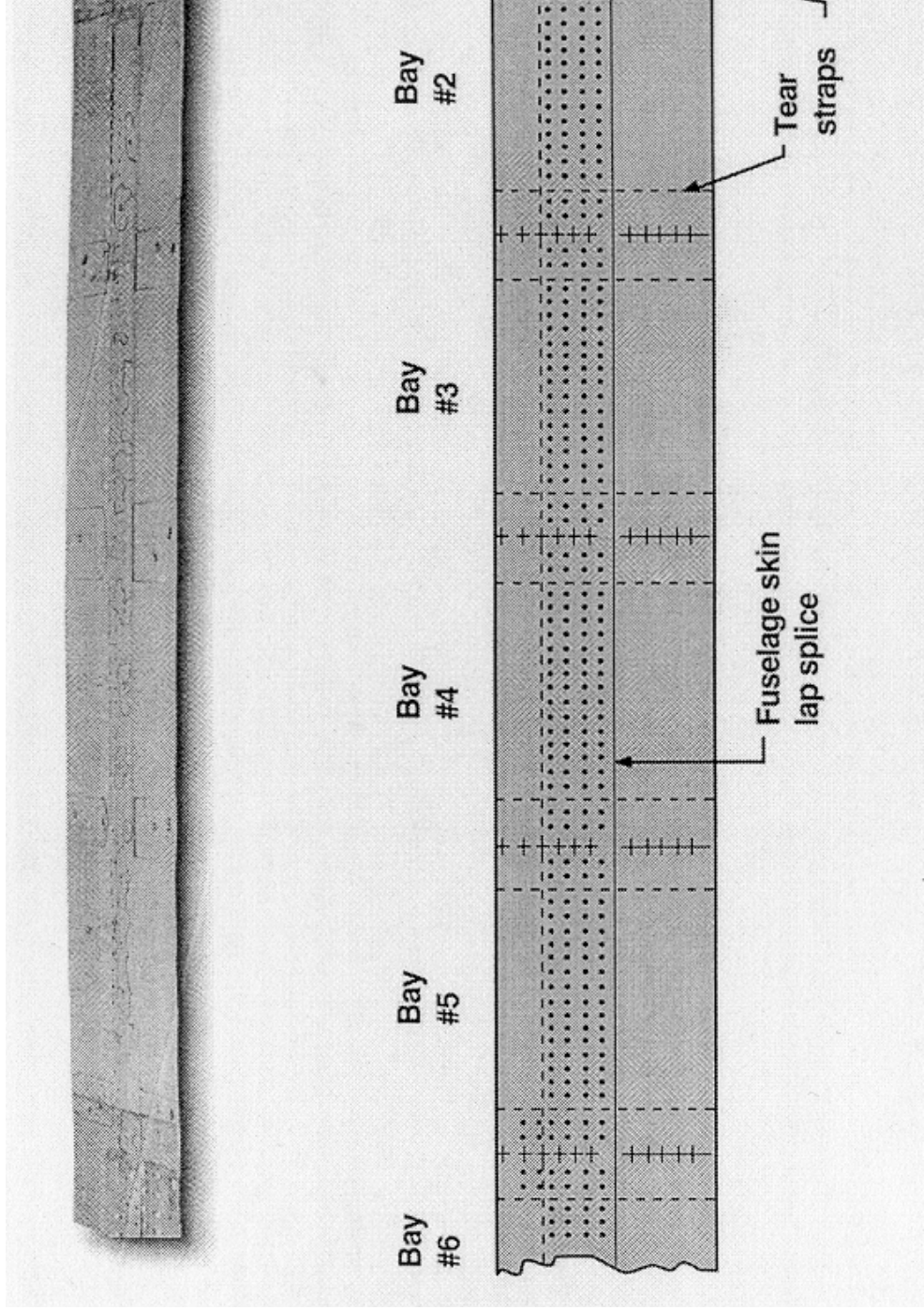


Figure 1. Fractography of WSFD in Structural Fatigue Test Article.

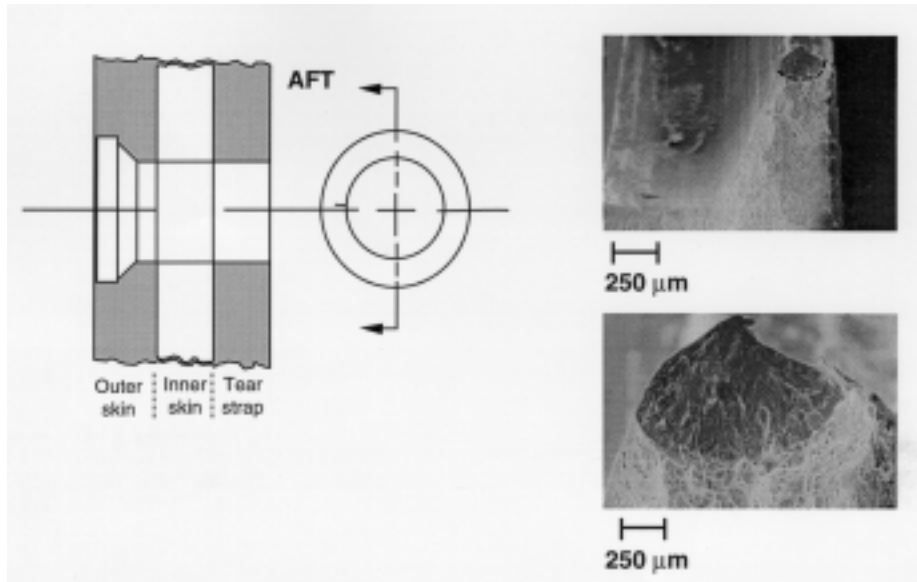


Figure 2(a). Small Fatigue Cracks at Rivets.

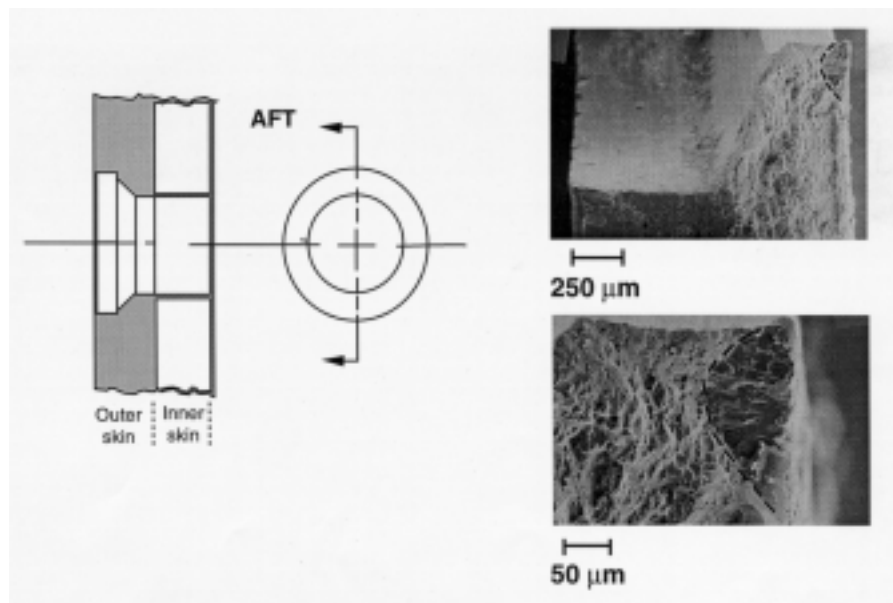


Figure 2(b). Small Fatigue Cracks at Rivets.

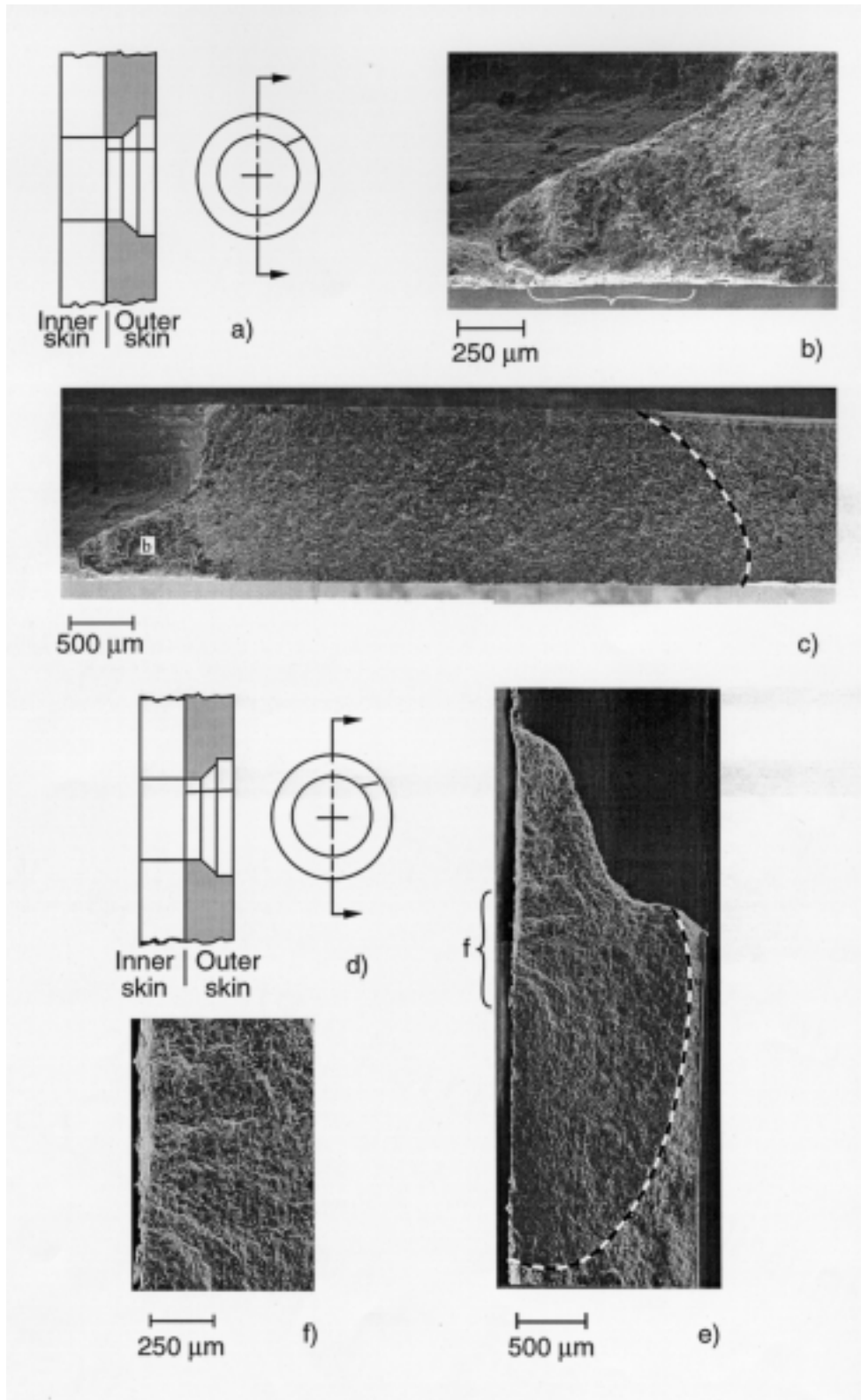


Figure 3. Long Cracks at Rivets.

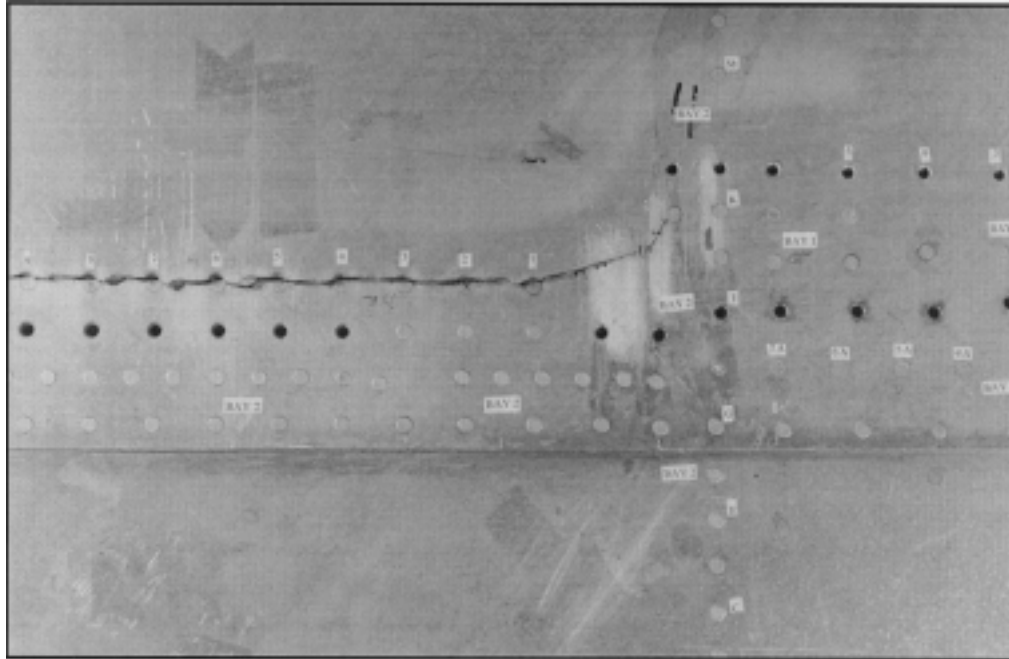


Figure 4. Fatigue Crack in a Fuselage Splice Joint of a Transport Aircraft.

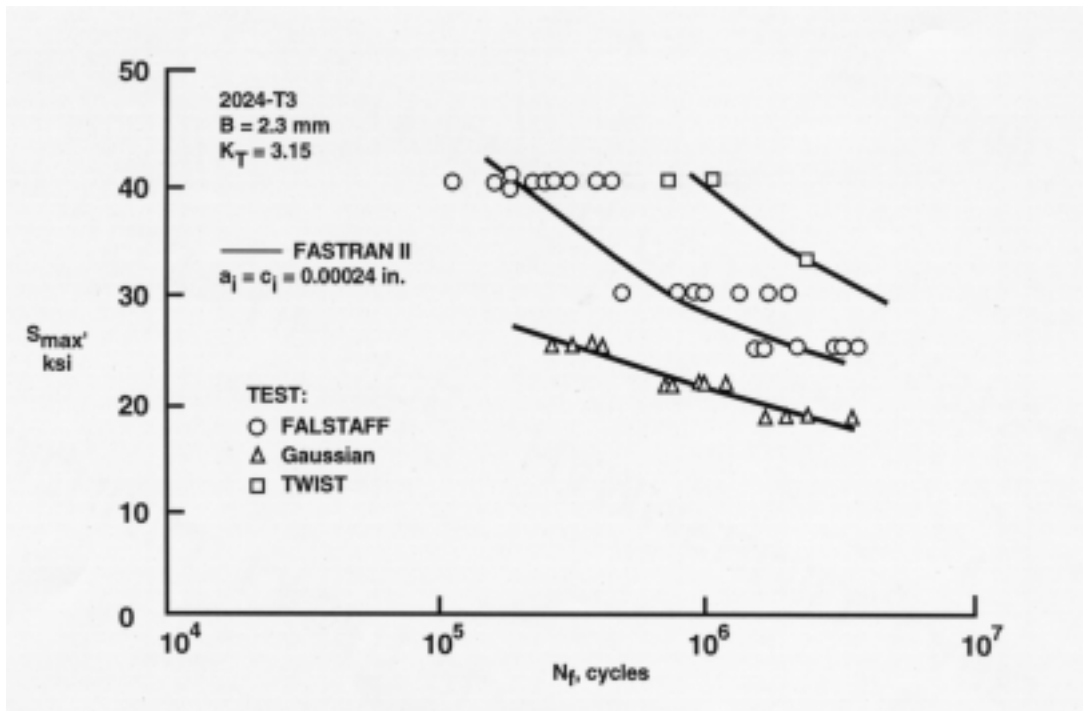


Figure 5. Comparison of Test and Predicted S-N Behavior.

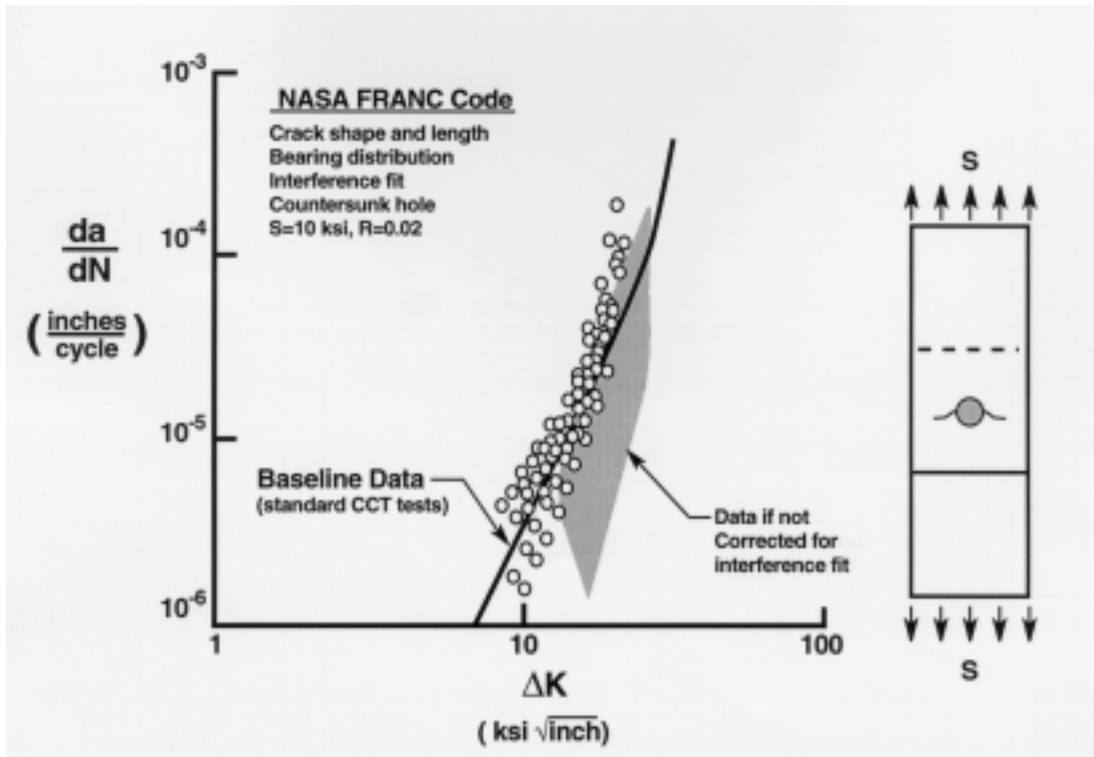


Figure 6. Fracture Mechanics of Cracks Extending From Rivets.

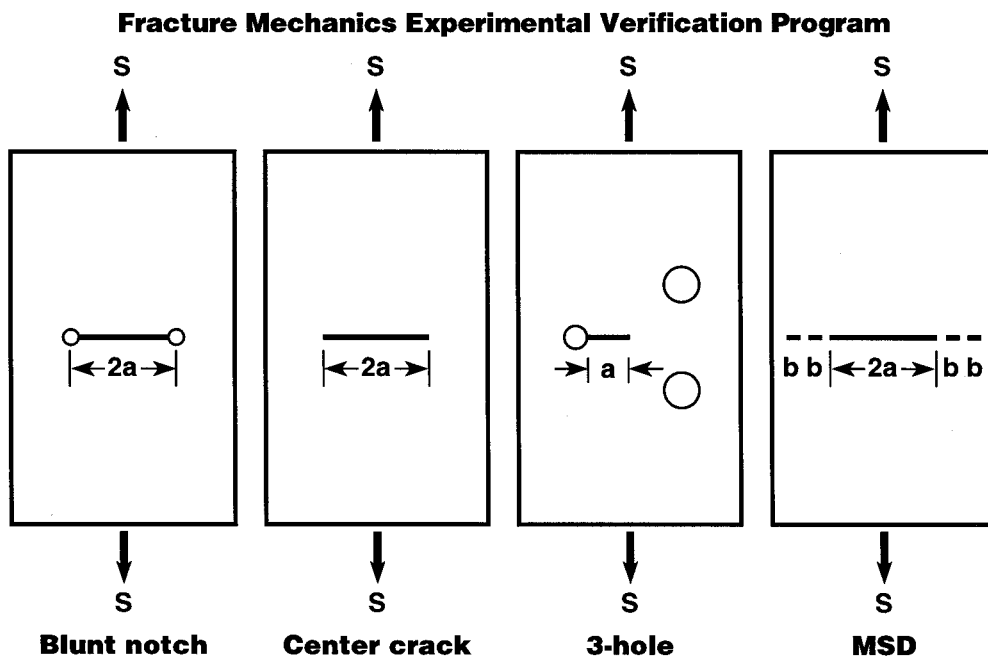


Figure 7. CTOA Fracture Criterion for Residual Strength.

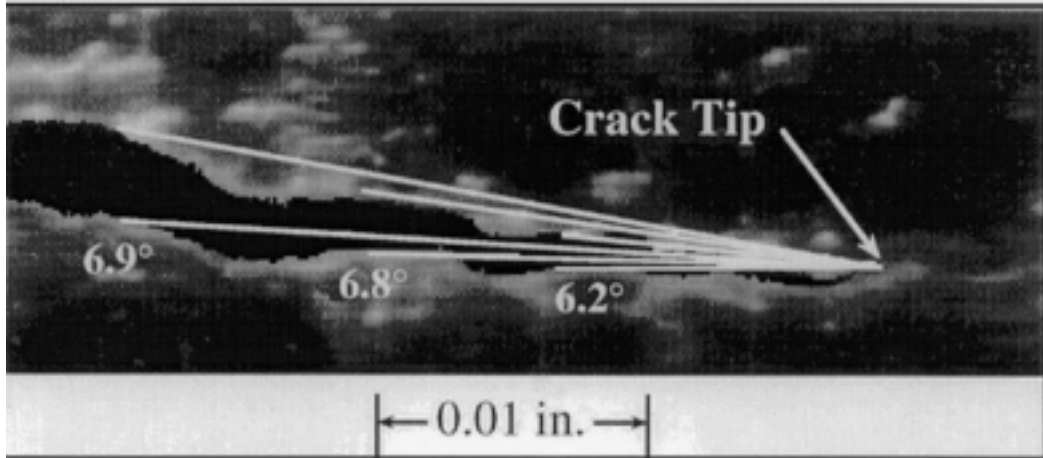


Figure 8. Crack Tip Opening Angle (CTOA) Measurements.

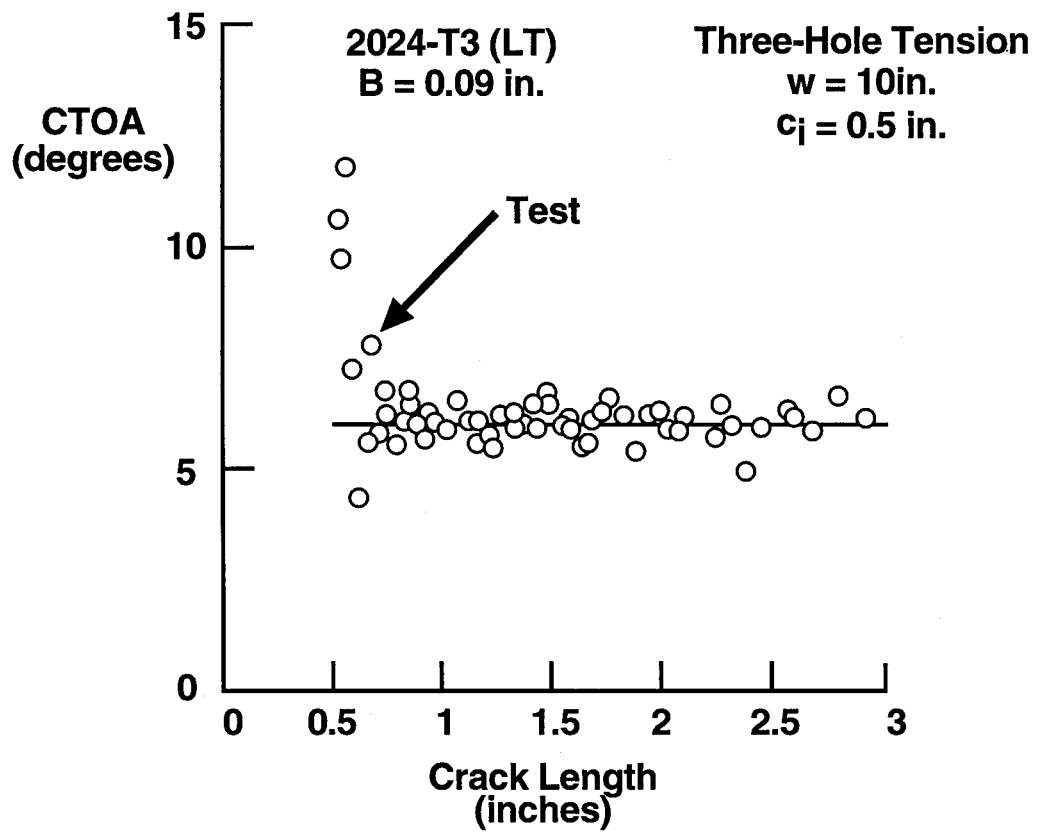


Figure 9. Experimental Measurements of CTOA.

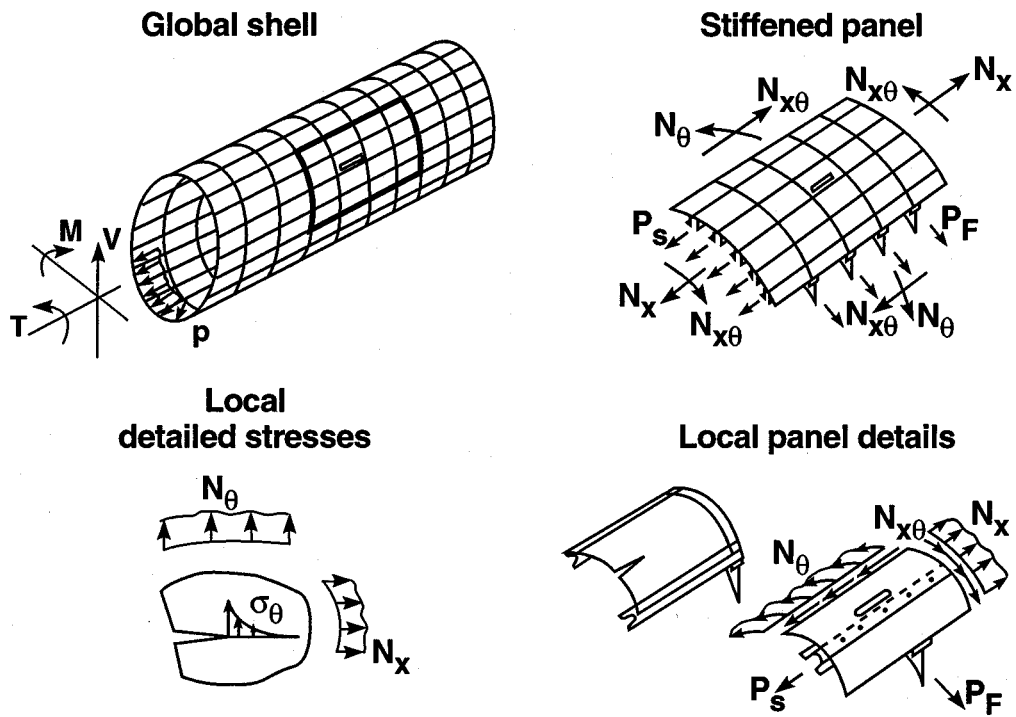


Figure 10. Hierarchical Nonlinear Stiffened Shell Models.

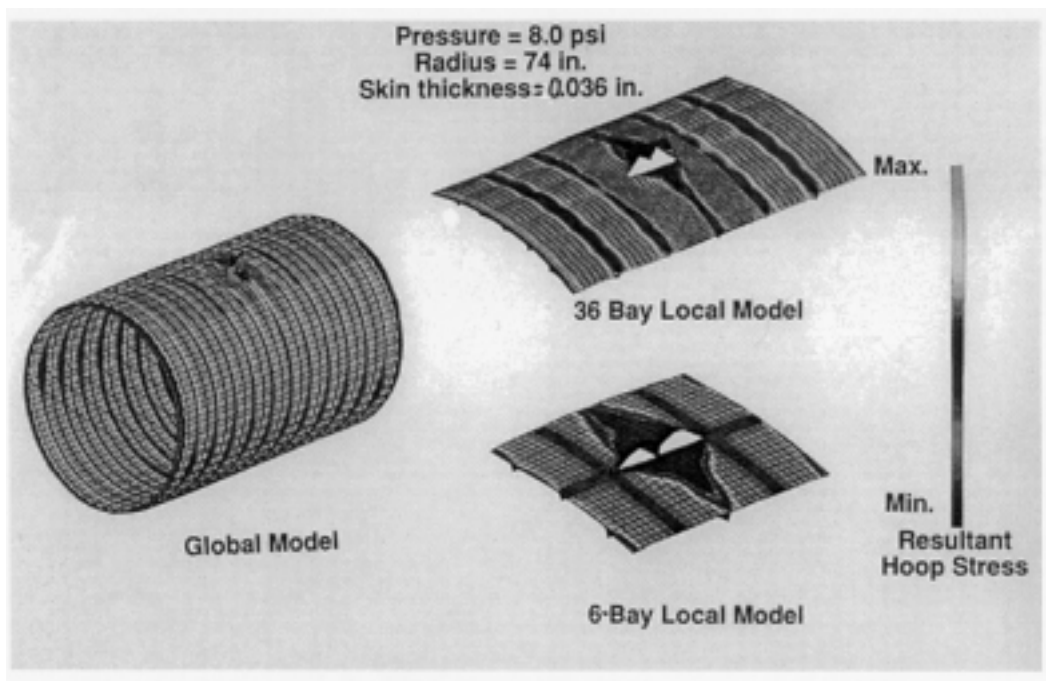


Figure 11. Stiffened Aluminum Fuselage Shell With 20'' Skin Crack and Broken Frame.

- **Hierarchical Models: Internal Pressure, Bending, Vertical Shear**
- **Local 2-Bay by 2-Bay Model, Edge Displacements From 6-Bay by 6-Bay Mode**

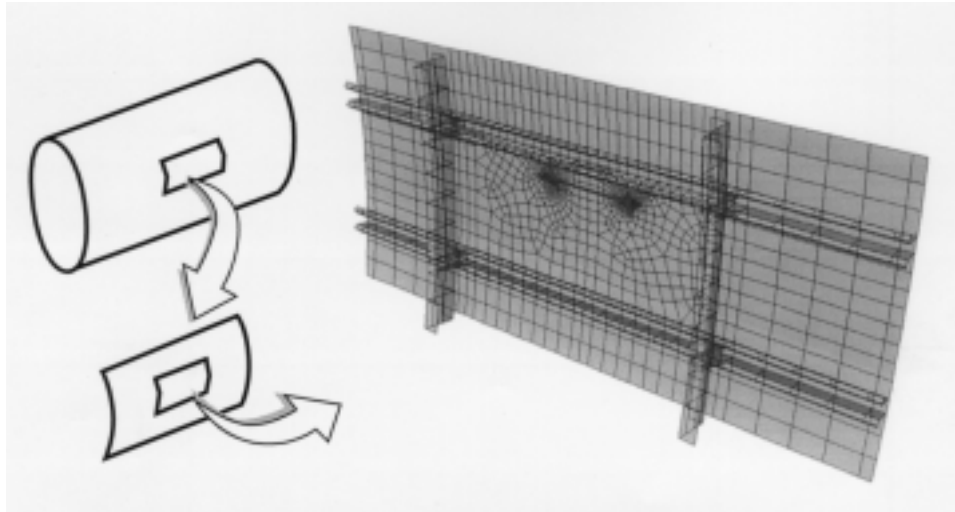


Figure 12. Curvilinear Crack Analysis Using FRANC3D/STAGS.

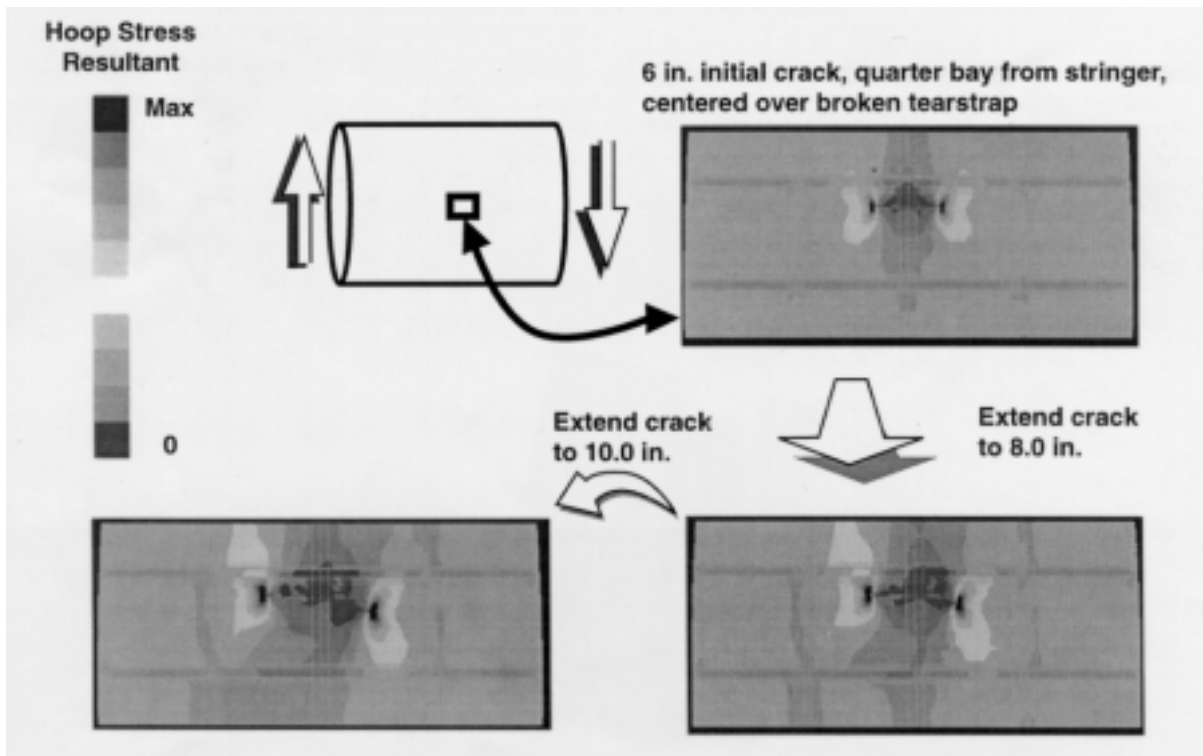


Figure 13. Curvilinear Crack Extension: Internal Pressure + Shear.

Table 1. Comparison of Measured and Predicted Failure Loads on NIST Multiple-Site Damage Fracture Tests.

Panel	Number of Sawcuts	Test Load kips	Predicted Load kips	Percent Error
MSD #1	1	77.0	76.8 (a)	-0.3
MSD #2	1	96.3	96.0	-0.3
MSD #3	1	64.9	65.6	+1
MSD #4	7	69.1	67.0	-3
MSD #5	7	91.2	80.9	-11
MSD #7	11	48.2	49.8	+3
MSD #8	21	47.5	50.6	+6
MSD #9	21	79.2	74.8	-6
MSD #10 (b)	11	52.2	49.8	-5

(a) Fitted to test (CTOA=3.4 deg.; δ_i = 0.0085 in.)

(b) MSD #10 was repeated of MSD #7

APPLICATION OF ACOUSTIC EMISSION TO HEALTH MONITORING OF HELICOPTER MECHANICAL SYSTEMS*

Adriano F. Almeida, W. Drew Martin, and Donald J. Pointer
Physical Acoustics Corporation
Princeton, NJ

SUMMARY

Early detection of mechanical failure in helicopter gearboxes is a key safety and economical issue with both military and civil sectors of aviation. The capability to continuously monitor gearbox operation in-flight is required in order to ensure that in-service defects are found before they cause catastrophic failure. On-line fault detection in gearboxes has been demonstrated using vibration sensors and metal chip detectors, but these methods alone are limited mainly because they cannot detect fatigue cracking. A helicopter gear component may develop a fatigue crack at the root of a gear tooth due to cyclic stresses caused by tooth bending. In some cases, the root crack may propagate through the gear web instead of the tooth itself, resulting in catastrophic gearbox failure and the possible loss of lives. The initiation and early stages of fatigue crack propagation do not usually change the component vibration response or cause any other form of detectable change in the operation of the gearbox, but the sound generated by crack growth can be detected using externally mounted Acoustic Emission (AE) sensors. Acoustic emission also has the potential of providing real-time detection and location of internal discontinuities caused by excessive wear, spalling, or pitting of bearings and gears.

INTRODUCTION

While vibration accelerometers generally monitor frequencies below 10 kHz, AE sensors respond to very rapid displacement waves containing energy in the kilohertz frequency range (10 - 1000 kHz). Since crack detection is one of the most important capabilities of acoustic emission, extensive research has been conducted over the years to allow the detection of cracks in noisy environments. For quite some time, it has been known that fatigue cracking in high strength steels produces relatively large acoustic emission bursts which can be detected even in the presence of high background noise. When crack growth burst signals are detected in the presence of other less-relevant emissions, the ability to perform signal discrimination becomes crucial since irrelevant mechanisms may cause larger signal bursts than those caused by crack growth. Because crack emission signals have characteristic features, it is possible to apply techniques from speech recognition technology

* Work done under DoD Phase I SBIR Contract DAAJ02-96-C-0038

to detect the presence of cracking among continuous streams of data. Performing this task in real-time is a challenge which requires efficient processing algorithms and the use of the fastest, latest-generation digital processing hardware.

A structurally sound gearbox generates less acoustic emission than one which is defective. This is because inside a gearbox, high frequency acoustic emission bursts occur as a result of a rapid release of strain energy generated by mechanisms such as sudden contact between metal surfaces. Near the source, these acoustic emission events resemble distinct short duration pulses with a broad frequency content. As the energy propagates from gearbox components to a sensor on the housing, the resulting stress waves undergo multiple reflections and mode conversions which modify the signal, making it more difficult to discriminate between different source mechanisms and their origin. By using specific time and frequency domain signal features to describe each burst emission, it is possible to implement a neural network to automatically distinguish between different mechanisms and their location.

EXPERIMENTAL VERIFICATION

The system employed during this research effort consisted of high frequency acoustic emission sensors, 40 dB preamplifiers, and a digital transient recorder with sophisticated front-end triggering logic. With this hardware, it was possible to detect discrete burst emissions in the presence of high background noise. Whenever a burst type emission triggered the system, a transient was digitized and later processed to extract relevant features for pattern recognition. Each transient record was written to a hard disk with a high resolution time-of-trigger reading and the current measurement of the Average Signal Level (ASL).

In order to prove the feasibility and effectiveness of our approach, we performed a series of controlled laboratory experiments, as well as full-scale tests on actual helicopter gearboxes. The first set of tests were performed onboard a BK-117 helicopter during hover flight. These tests helped characterize the gearbox in-service signal levels and the requirements for real-time signal discrimination during flight. While the BK-117 gearbox was in operation, several burst-type signals were detected by the acoustic emission system. These signals were generated as a result of internal moving parts and were associated with baseline gearbox operation. While the helicopter was hovering, we injected simulated pulses into the gearbox housing using a surface mounted pulser (Figure 1). The pulser generated waves propagated along the housing and were detected by an acoustic emission sensor 2 feet away. By recording the exact time each pulse was fired and matching it with the corresponding time-of-trigger in the AE sensor data, it was possible to separate pulser generated signals from those caused by baseline gearbox operation. With this data, we demonstrated the capability of discriminating between signals from induced pulses and signals from normal gearbox operation.

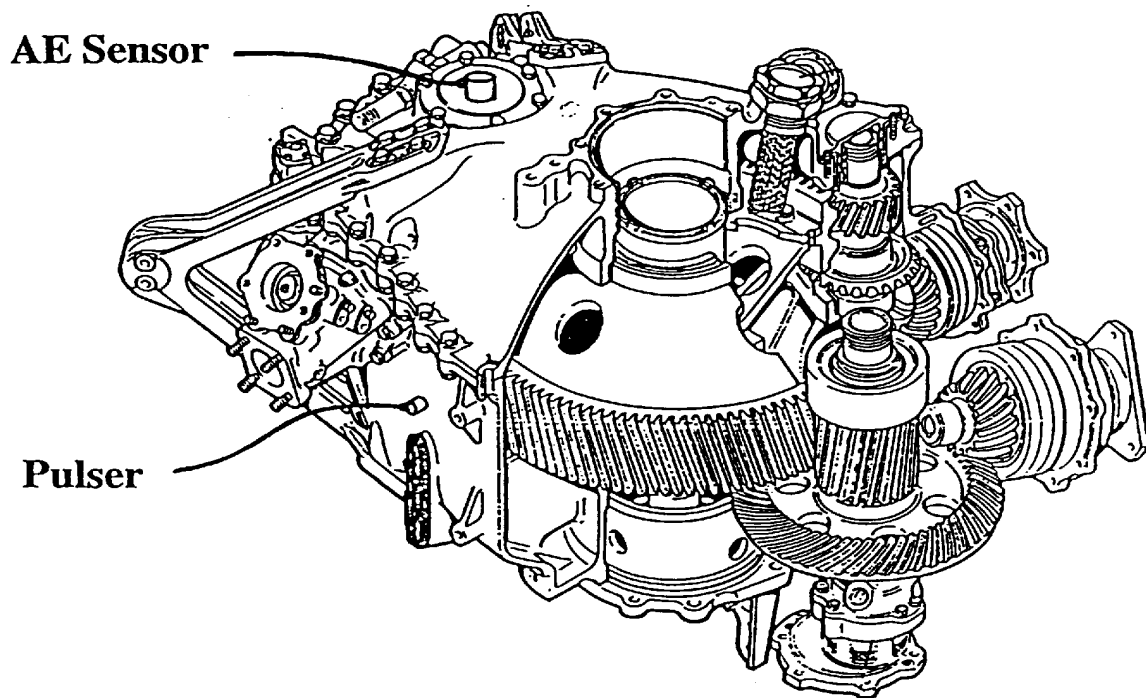


Figure 1. Sensor and Pulser Locations Used for Tests on BK-117 Helicopter.

The next set of tests were conducted on a subscale gearbox which was constructed specifically for this project. By generating simulated sources at different locations on the inside and outside of the gearbox, we proved that our approach provides accurate source discrimination and location in the absence of gearbox operating noise. We then proved that these techniques also worked when the gearbox was in operation. This was done by simulating different sources on the gearbox housing while it was running and showing that the pattern recognition algorithm was robust enough to perform accurate discrimination of individual in-coming bursts. We also ran the gearbox with a seeded fault and performed accurate detection and discrimination of the fault related emissions. It is important to note that although the classifier was trained with sample signals from each mechanism, the performance results were obtained using a different set of data, which was collected at a different time and which the classifier had never seen during training. With a single sensor bonded to the top surface of this gearbox (Figure 2) it was possible to determine with 95% accuracy whether incoming bursts were generated by an input gear fault (missing teeth), background noise, or simulated crack-like mechanisms generated at bolt locations on the gearbox feet.

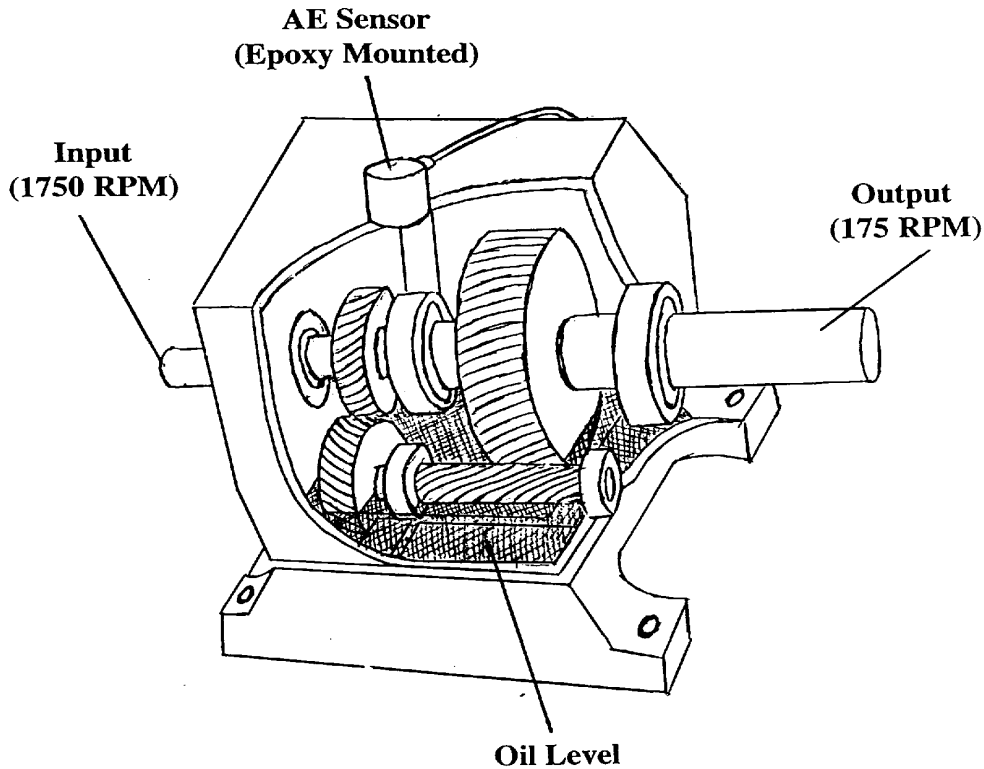


Figure 2. Gearbox Used for Laboratory Verification.

Another set of tests was performed on a full-scale SH-60 gearbox at the Naval Air Warfare Center (NAWC) located in Trenton, NJ. These tests confirmed that the acoustic emission Average Signal Level (ASL) measurement (which monitors the level of the signal floor) can be used to detect changes in continuous-type emissions generated by excessive component wear, or continuous contact between spalled components. We also learned that changes in engine torque levels did not effect the ASL level significantly, that the burst data rates were manageable during normal operating conditions, and that the acoustic attenuation levels from internal components to the housing were not excessive. On five different test occasions, we demonstrated that our sensors are robust enough to resist the high temperature and vibration environments encountered without significant change in response. The SH-60 test cell is a very sophisticated setup which closely resembles the environment encountered in an actual helicopter.

The results obtained during this Phase I research are very encouraging since they support the requirements for reliability, detectability, and real-time processing. As part of the Phase II contract, which was recently awarded to our company by the US Army, we will build a stand-alone prototype system to monitor helicopter mechanical systems in real time.

APPLYING UNITED STATES AIR FORCE LESSONS LEARNED TO OTHER AIRCRAFT

Grant D. Herring
Ogden Air Logistics Center
Hill Air Force Base, UT

Robert D. Giese
Scientech, Inc.
Ogden, UT

Paul Toivonen
McDonnell Douglas
St. Louis, MO

SUMMARY

This paper provides the history and background of the engineering efforts of the F-4 System Program Manager (SPM) to ensure the structural integrity of the fleet throughout the course of its life. These efforts to insure the fleet's integrity were based on the implementation of an Aircraft Structural Integrity Program (ASIP) and Damage Tolerance Analysis (DTA) principles. This paper will outline the data requirements, collection process, and the problems encountered with that process. It will go on to describe the evaluation and validation of the data and the software tools developed to make the job more efficient.

INTRODUCTION

The goal of an aircraft fleet manager is to field, fully utilize, and retire the fleet without a single catastrophic structural failure at minimum cost. Damage tolerant analysis tools were designed to achieve this goal. The F-4 was originally designed prior to damage tolerant analysis tools. This paper describes how the F-4 SPM implemented DTA concepts approximately 10 years after initial production and the lessons learned from this implementation.

MIL-STD-1530A - Aircraft Structural Integrity Program Requirements.

The F-4 SPM is responsible for the structural health of the operational F-4 fleet. This requires engineers to conduct analysis on repairs, track those repairs, and identify areas needing structural modifications. The structural modifications could be driven by any

number of reasons, such as flight safety, increased maintainability, or physical reconfiguration requirements as a result of changes in usage of the aircraft. To make these decisions, engineers need a clear picture of the current structural condition of the fleet, as well as any trends that may be occurring. In MIL-STD-1530A, paragraph 4.1.1b requires the SPM to acquire, evaluate, and utilize operational usage data to provide a continual assessment of the in-service integrity of individual airplanes. This is the fundamental direction given to the fleet manager to maintain the structural integrity of the aircraft. To implement the damage tolerant approach, the F-4 SPM developed a plan of in-service gathering (acquire), managing (evaluate), and utilizing the data. This data was used on a continual basis to assess the current structural health of the fleet, detect potential negative trends, and to proactively make corrections to insure future structural integrity. We will address each of the three primary areas focused on in MIL-STD-1530A.

Acquire the Data

The Original Equipment Manufacturer (OEM) data provided the static strength analysis and full-scale fatigue test of the baseline configuration airframe. These two pieces of information are used to determine initial trouble spots and areas to monitor. The in-service data is necessary to validate the original full-scale test and identify any additional fatigue hot spots that were not predicted by the analysis. Both the OEM and in-service data are essential for the user to maintain the structural integrity of the fleet. This implies that the user must have access to the original design data and that the OEM and user have an open interchange of this data. Neither the OEM nor in-service data can, by themselves, insure the structural integrity of a fleet of aircraft. The F-4 program was successful in large part because of the sharing of information between U.S. Air Force and McDonnell Douglas Aerospace engineers.

The data and decisions made from the in-service data which effect the aircraft structure are essentially independent of the OEM. Fleet management fundamentally is the responsibility of the using authority (the people flying the aircraft). Development of the baseline data is the responsibility of the OEM, and the using authority must build on this initial database.

Both in-service and historical data must be in a form that allows new personnel to easily learn from it. This is essential in maintaining a corporate knowledge base. Also, fleet managers must provide for a continuity of data, fleet history, and expertise (as noted above).

The first step is to decide what data must be acquired. If possible, determine and record only the driving variable and use it to extrapolate other dependent variables. To accomplish this, the fleet manager must determine what affects the structural integrity of an aircraft in service. This list must include:

- Loads/environmental spectra
- Structural repairs applied to the aircraft
- Modifications accomplished on the aircraft

Results of Programmed Depot Maintenance (PDM)
Results of Analytical Condition Inspections (ACI)

We will examine what each of these data contributes to the overall analysis.

Loads/Environmental Spectra.

This type of data includes output from the flight loads data recorder. In the case of the F-4, aircraft velocity, g-level, and altitude were recorded. These recorders were present on only a statistical sampling (approximately 10%) of the fleet due to the cost of the units. The entire F-4 fleet also had counting accelerometers which measured hits at 3, 4, 5, and 6 g's. This data represents how the aircraft is being flown and is the primary source for information to determine how much of the aircraft's fatigue life has been expended.

Structural Repairs Applied to the Aircraft

These are nonstandard repairs. They may come from such incidents as bird strikes, maintenance induced damage, atypical damage, corrosion, etc. They must be documented as part of the aircraft's historical records so that future users, maintainers, and analyzers are aware of the logic applied to the design of the repair. This also allows for the determination of inspection intervals if necessary. Corrosion data may also be included here and is essential to determine how to modify life predictions. These may vary for aircraft in more benign environments, such as an aircraft based in Colorado versus an aircraft based in Hawaii.

The actual physical condition and configuration and details of the aircraft are required since each aircraft is an individual due to manufacturing and repair variances. Inspections during repair and rework often help to reveal these conditions. Field units or depot teams often called in odd or serious findings. These may have been as a result of disassembly associated with the maintenance being performed or something that less trained personnel might not have detected.

Modifications Accomplished on the Aircraft

Any structural modification to the aircraft must be documented in the database. This will aid future personnel associated with the aircraft in determining the physical configuration of the aircraft. Since reasons for modifying the structure might vary, analyses associated with the modification must also be documented in the database so that assumptions made can be verified as well as fatigue life enhancements incorporated into fleet management plans.

Results of Programmed Depot Maintenance

Data gathered from PDM results give the fleet manager information concerning recurring defects, corrosion trends, and evidence of fleet-wide problems. Since the aircraft is disassembled to a larger degree than in normal periodic maintenance, it also allows for inspections of previous repairs and modifications to verify that assumptions used in design were correct.

PDM and other maintenance on F-4 aircraft was accomplished worldwide by independent commercial contractors and even foreign contractors and airlines (e.g. Korean Airlines, Messerschmitt, etc.). It is important that the different maintainers have access to the database so that data pertaining to an aircraft which might have been maintained or modified at another facility or contractor can be examined and/or updated.

Results of Analytical Condition Inspections (ACI)

These are one-time statistical inspections of areas not normally looked at, and usually occur at PDM while the aircraft is opened up. They are used to give the manager and analyst an idea of the condition of the fleet. They are also used to identify areas which may require structural modification but were not identified in the original analyses and tests of the aircraft. As is obvious, results of these inspections must be included in the database for not only determination of the need for modification, but also so that a future manager could direct additional inspections in the same area.

Data Collection Problems

There were problems associated with gathering the data. Some of the data was bad from things such as forms which had been "pencil whipped" or lost data as a result of electronic recorder failures or forms which had been incorrectly or incompletely filled out. Also, many of the forms were completely filled out but were illegible.

When gathering data, simple types are best. Automation of the data gathering process can greatly ease the problems noted, both of the mechanic in the field as well as the analyst.

While enhancing the database, there is an essential need for a central repository for all data which is accessible by all engineers working on the aircraft, as well as fleet managers. It is imperative that this data remain intact as individuals that are the users, managers, and maintainers change. The database is also constantly expanding, and the manager must keep aware of these changes to detect trends which may require action.

Evaluate the Data

When the F-4 SPM began implementing DTA concepts, the engineers observed that several problems hindered analysis efforts. New engineers required a great deal of training to do effective analyses. Frequently repairs required a quick analysis response to meet depot or field team schedules. Also, since the F-4 fleet was approximately 3500 aircraft at its peak, there was a tremendous amount of in-service data. The data was in paper form, was poorly organized, and finding the information required to conduct a good analysis was difficult and time consuming.

In the early days of accomplishing structural analysis the computer user interface was complex and cryptic. Files were scattered about and output from one analysis program could not be directly used as input to the next program in the sequence. This led to user frustration and required engineers to develop high levels of computer language and operation skill. This took away from time available to accomplish structural analysis and make engineering decisions.

These problems with storing, evaluating, and using large amounts of data caused the F-4 SPM to develop an integrated analysis tool that was effective and easy to use.

A microcomputer-based software package was developed to assist engineers and fleet managers in their daily work. It is an accumulation of the tools necessary to accomplish the tasks required under the ASIP concept. These tools include:

- Crack Growth Analysis
- Test Correlation
- Spectrum Development
- Fleet Damage Tracking
- Individual Aircraft Tracking
- FEM Loads Retrieval
- Static Stress Analysis Tools
- DTA Training

A brief description of each of these tools follows.

Crack Growth Analysis

The F-4 software system uses the modified Wheeler crack growth load interaction model. This model was used in the original analysis and is used to accomplish all repair analyses. The software also has the ability to use stress intensity parameters as investigated by Newman, Grandt, and others. Since historical material data is resident in the database, comparisons between new materials is possible. Also, spectra comparisons among historical and in-service data and the results can be displayed in either tabular or graphic form.

Test Correlation

The software contains results of the original full-scale fatigue and coupon tests in the database. These data are available to the user to help verify results of new crack growth analyses against historical test data to ascertain that correct assumptions were used. It also allows the user to do “what if” test runs to see how they would compare to the historic tests.

Spectrum Development

This section of the software is used to develop spectra for fleet tracking and analyses using the current fleet flying conditions. In this manner, the software is also used to detect fleet usage changes. Different mission mixes and aircraft mission profiles can be compared in “what if” mission change scenarios to determine the effect on fleet life.

Fleet Damage Tracking

This is used to monitor consumption of the fatigue life of critical areas of the aircraft. This aids the fleet manager in planning modifications to the structure to enhance the fatigue life when necessary.

Individual Aircraft Tracking

This section of the software records critical information for each aircraft in the fleet. The critical information includes current fatigue status, special repairs applied, dates and flying hours at the time of modification installation, and other pertinent data about a particular aircraft.

FEM Loads Retrieval

This allows the user to obtain gross aircraft loads from the full airframe model for usage in fatigue calculations and static strength analysis. Since this is a data retrieval system, it does not require the user to have expertise in the actual finite element analysis software. It allows the user easy access to loads data when a more detailed FEM is not necessary for a part or area of particular interest.

Static Stress Analysis Tools

This is a collection of static strength tools for analyzing such items as fastener layouts, bolt loading, buckling problems, residual stresses due to interference-fit fastener installations, etc. These provide the analyst with information necessary to size repairs and

fasteners. Results from these calculations can then be applied to fatigue calculations where necessary.

DTA Training

Since the software is much more user friendly than the mainframe programs, it allows for new personnel to be trained quite rapidly in performing DTA. As noted above, it allows multiple runs to be compared in a variety of fashions so that sensitivity studies can be performed and allow the trainee to observe how even small changes in variables effect analyses. Since the software has multiple levels of security access, trainees can be allowed to make mistakes and comparisons without the danger of corrupting the database while still allowing them full access to all of the information contained in it.

The Microcomputer-Based Integrated Analysis System (MBIAS) was developed by the USAF under contract with McDonnell Douglas. The present form of MBIAS represents a substantial software system. Current users of the system include all users of the F-4. The incorporation of these modern programming methods and data management engines provides efficient storage and retrieval of fleet data.

Utilize the Data

Repair lives/Inspection intervals must be determined prior to repair installation. Results of Finite Element Analyses (FEA) are used in determining life as well as sizing components, fastener layouts, etc. Engineering judgment allows for lessons learned to be applied to the problem at hand.

The function of the ASIP manager is to collect and analyze the information, and guide the system engineers in developing modifications, repairs, etc. Proper utilization and interpretation of the data can spot trends or future long term problems in the fleet. In a mature fleet, very few critical problems are new.

The data can be used to relate the aircraft in question to other aircraft. This must include historical knowledge, different models of the same basic airframe, and the different missions which the aircraft is being used for. Also, it must be determined if this aircraft is one which leads the fleet and should thus be used as a basis for decisions relating to the entire fleet. Decisions must be based on historical/initial test results such as (1) full-scale tests, (2) element tests, and (3) coupon tests. New models must be matched to these test results for the new results to be considered valid.

The fundamental reason for developing the MBIAS software was the requirement to maintain the structural integrity of the airframe. This ASIP methodology is described in MIL-STD-1530A and describes the requirements and processes of managing a fleet of aircraft. A very important aspect of effective fleet management is preserving all pertinent data and gathering and preserving the service history and the life of the airframe. Secondly,

gathering and preserving data is useless if it is not easily retrieved, catalogued, organized, and visualized. In the past, F-4 fleet problems were often buried in large amounts of paper data or unorganized service data.

By storing and analyzing service data, the usage of the aircraft from a fatigue damage aspect can be tracked. In monitoring the fatigue accumulation and results of inspections, necessary structural changes and modifications can be identified and planned for. Also, individual aircraft with major structural repairs can be monitored on an individual basis to insure the integrity of that aircraft. Also, by monitoring service data, fleet trends can be detected. These trends may involve changes in mission and aircraft usage, development of corrosion problem areas, or unexpected fatigue problems.

Some of the tools necessary in support of ASIP include crack growth analysis and verification of analysis using test data. To accomplish crack growth analysis, a spectrum for the area under consideration must be developed. Also, by studying the flying spectra, the fatigue damage accumulation of the fleet can be tracked. MBIAS allows comparison between historic and new data so that possible trends may be evaluated.

In addition to engineering analysis tools, MBIAS is a powerful data management engine. To provide efficient use by a group of engineers, the system provides for a multi-user environment where numerous users can access and update the database. It also allows the ASIP or fleet manager to make recommendations on modifications, repairs, inspections, and inspection intervals.

CONCLUSION

The user, not the OEM, is ultimately responsible for the continued structural integrity of the airplane in service. However, the user cannot build an in-service database to protect his fleet without access to the historical baseline analysis from the OEM. The simpler the database collection methods, the more accurate the resulting database is. Long term fleet problems are usually seen first in routine fleet inspection results. The basic philosophy used on the F-4 was to protect the single worst aircraft in the fleet against catastrophic failure. If this is accomplished, the rest of the fleet will then be protected as a matter of course. A single point of contact for structural integrity problems in a given fleet is vitally important for DTA to assist the fleet manager in achieving the overriding goal.

The F-4 program was successful in large part due to the excellent working relationship between U.S. Air Force and McDonnell Douglas Aerospace engineers. This relationship provided for a free flow of information between the two entities. It was also successful because of a concentrated effort to protect the corporate knowledge base and utilize new technologies to affect this effort.

AUTOMATED EVALUATION OF RESIDUAL STRENGTH IN THE PRESENCE OF WIDESPREAD FATIGUE DAMAGE

W. T. Chow, H. Kawai, L. Wang, and S. N. Atluri
FAA Center of Excellence for
Computational Modeling of Aircraft Structures
Georgia Institute of Technology
Atlanta, GA

SUMMARY

This paper describes a software package with a user-friendly Graphical User Interface (GUI), which can efficiently perform the fatigue and fracture analysis of multiple-site damage (MSD) in fuselages with various designs of frames and stiffeners. This software has been implemented in Windows NT for personal computers as well as in different UNIX-based X-Window systems for workstations. In order to substantially reduce the cost of computing, the modeling of the MSD cracks in the fuselage is based on the global-intermediate-local hierarchy. The software will automatically generate the finite element mesh of the skins, stiffeners, frames, and rivets for each level of modeling using the data provided through the GUI interface. Having generated the mesh, the global and intermediate analyses are carried out using a commercial finite element package, wherein the cracks are modeled explicitly, to obtain the load flow pattern around the damage zone near the MSD cracks. This is followed by a local analysis based on the elastic-plastic finite element alternating method (EPFEAM) and the fracture criteria using the T^* integral. In the local analysis, there is no need to model the cracks explicitly. At the end of the analysis, the software will provide the graphical output of the residual life and strength estimates for the fuselage with MSD in the presence of a discrete source damage.

INTRODUCTION

Structural integrity evaluation of aging aircraft structures is extremely important in ensuring the safety of the operation of these structures. A fuselage of an aircraft would typically undergo a cycle of pressurization for every single flight operation. These cycles of pressurization would result in fatigue cracking near the rivet holes of the fuselage panel and may lead to widespread fatigue damages (WFD). With the formation of widespread fatigue damage on the fuselage panel as shown in Figure 1, the fuselage structure may no longer meet the damage tolerance requirement. Under the current damage tolerance philosophy, the inspection program of a fuselage panel is established on the basis that a single lead crack, propagating between detectable and critical size at limit load, will be detected before failure. This single lead crack is intended to represent a discrete source damage from fatigue,

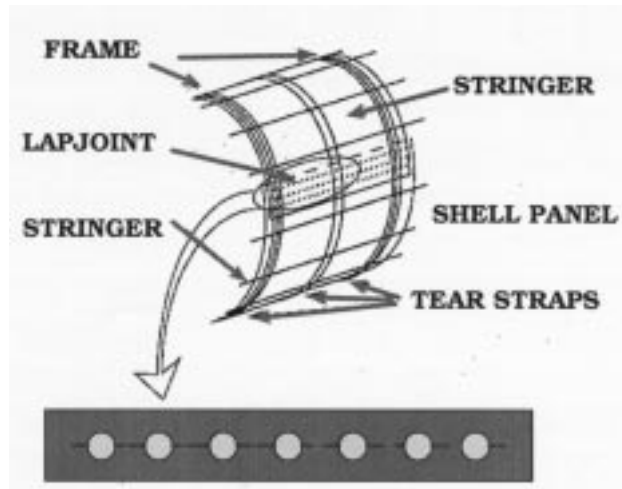


Figure 1. Widespread Fatigue Damage on a Fuselage Panel.

accident, or corrosion in service. However, when widespread fatigue damages exist on the fuselage panel, the interaction of the lead crack with WFD has to be studied and the damage tolerance requirement of this structure needs to be changed accordingly, in order to ensure that the structure with WFD would meet the same safety requirements of a structure without WFD. Some preliminary analyses performed by Swift [1], based on two-dimensional solutions, have shown that the residual strength of a fuselage can be degraded below the required levels when small cracks (with size of the order 0.05 inch) exist ahead of the lead crack. Furthermore, based on experiments of flat panels, Maclin [2] has found that cracks as small as 0.05 inch ahead of the lead crack can reduce the residual strength by more than 30%.

In order to provide the regulatory agencies as well as aircraft manufacturers with the ability to evaluate the effect of WFD on a model-by-model basis, an automated analytical method has been developed to model a full-scale fuselage panel with WFD, rather than relying on the approximations based on flat panels. This would allow a fundamental understanding on the behavior of WFD and help engineers in developing structural designs capable of containing WFD. This paper presents a software package with user-friendly Graphical User Interface (GUI), which can efficiently perform the fatigue and fracture analysis of multiple-site damage (MSD) in fuselages of various designs of frame and stiffener. This automation process would allow substantial savings in the human resources required to perform these analyses.

FUNCTIONALITY OF THE SOFTWARE PROGRAM

In order to capture the interaction of the lead crack with MSD cracks, it is important that the elastic-plastic material behavior of the skin panel be taken into account in the numerical analysis. It is generally found [4] that numerical fracture simulations of a panel with multiple cracks based on linear-elastic assumption tend to be anticonservative especially when

the cracks are close together. Therefore, one of the most important features of this software tool is its ability to calculate elastic-plastic fracture parameters for multiple cracks efficiently and accurately using elastic-plastic finite alternating method.

The summary of the functionality of this software tool is listed in Figure 2. In addition to being able to perform the residual strength analysis with MSD interactions, this software tool can also perform the analysis of multiple cracks of similar size. This feature is important in analyzing the damages that can occur when engine fragments of high velocity are to impact on a fuselage panel during an engine failure. During such circumstances, a large region of damage would be formed on the fuselage panel which is usually modeled as a single large crack. However, with this automated tool, the region of damage induced by engine disintegration can be modeled as a lead crack followed by a series of smaller cracks. Furthermore, in order to make the residual strength analysis more accurate, the software tool can account for the nonlinear flexibility behavior of the fasteners as well as the nonlinear geometric behavior of the shell structure.

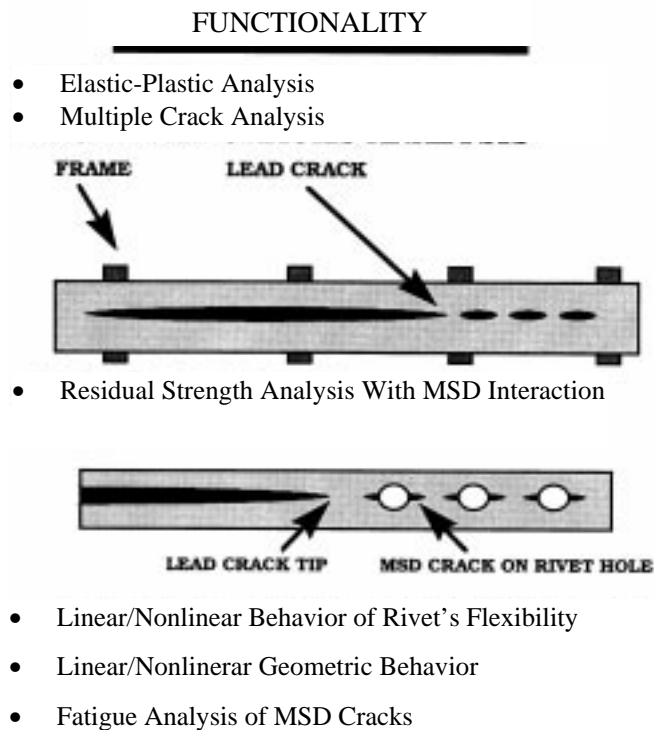


Figure 2. List of Functionality of the Software Tool.

For example, in the residual strength analysis for a large circumferential crack, it has been found that the ability to model the nonlinear flexibility behavior of the fasteners is important in correlating the analysis with experiment [5]. Also, it has been generally found that accounting for the nonlinear geometric behavior of the shell structure is important for the residual strength analysis of narrow-body aircraft where the skin panel is relatively thin.

Besides the ability to perform residual strength analysis, this automated tool can also perform the fatigue analysis of the fuselage panel using a complete three-dimensional shell model. In these analyses, the effect of residual stress at the rivet holes due to rivet misfit as well as coldworking are also included.

STRUCTURE OF PROGRAM

In order to substantially reduce the cost of computing, the modeling of the MSD cracks in the fuselage is based on the global-intermediate-local hierarchy. The software will automatically generate the finite element mesh of the skins, stiffeners, frames, and rivets for each level of modeling using the data provided through the GUI interface. In the global analysis, conventional linear elastic finite element analysis of the multibay stiffened shell panel is performed. The fuselage skin is modeled by 8-noded shell elements with 5 degrees of freedom per node while the frame, stringer, and tear strap are modeled by 3-noded beam elements. The fasteners on the fuselage panel are modeled using spring elements and multiple point constraints. The linear behavior for the fastener stiffness is represented by the empirical relation developed by Swift [3]:

$$K_F = \frac{ED}{A + C \left(\frac{D}{t_1} + \frac{D}{t_1} \right)} \quad (1)$$

with $A = 5.0$ and $C = 0.8$ for aluminum rivets. D and E are the diameter and elastic modulus of the rivet and t is the thickness of the skin. Whenever there is a crack, the stiffness of the fasteners along the crack length becomes zero as the fasteners will not be able to bear the load in that direction. A typical global model, shown in Figure 3a, has 7 frames and 20 stringers with approximately 3,000 elements.

Having performed the global analysis (here the cracks are modeled explicitly using disconnected finite element nodes) to capture the overall load flow of a large section of a fuselage panel, the displacement boundary conditions of a smaller section is then transferred to an intermediate analysis. This intermediate model will be sufficiently large to contain the entire lead crack of the fuselage panel. In the intermediate analysis, the frames, stringers, and fasteners are modeled in greater detail; each of the fasteners would be properly positioned according to the physical model, while the frames and the stringers are modeled with 4-noded shell elements as shown in Figure 3b. In this intermediate analysis, the options of nonlinear fastener behavior as well as nonlinear geometric behavior are carried out. To capture the interaction of the lead crack with much smaller MSD cracks, a local analysis of smaller sections of the fuselage skin is carried out. Here, the rivet holes are meshed in detail as shown in Figure 3c and the elastic-plastic material behavior is assumed.

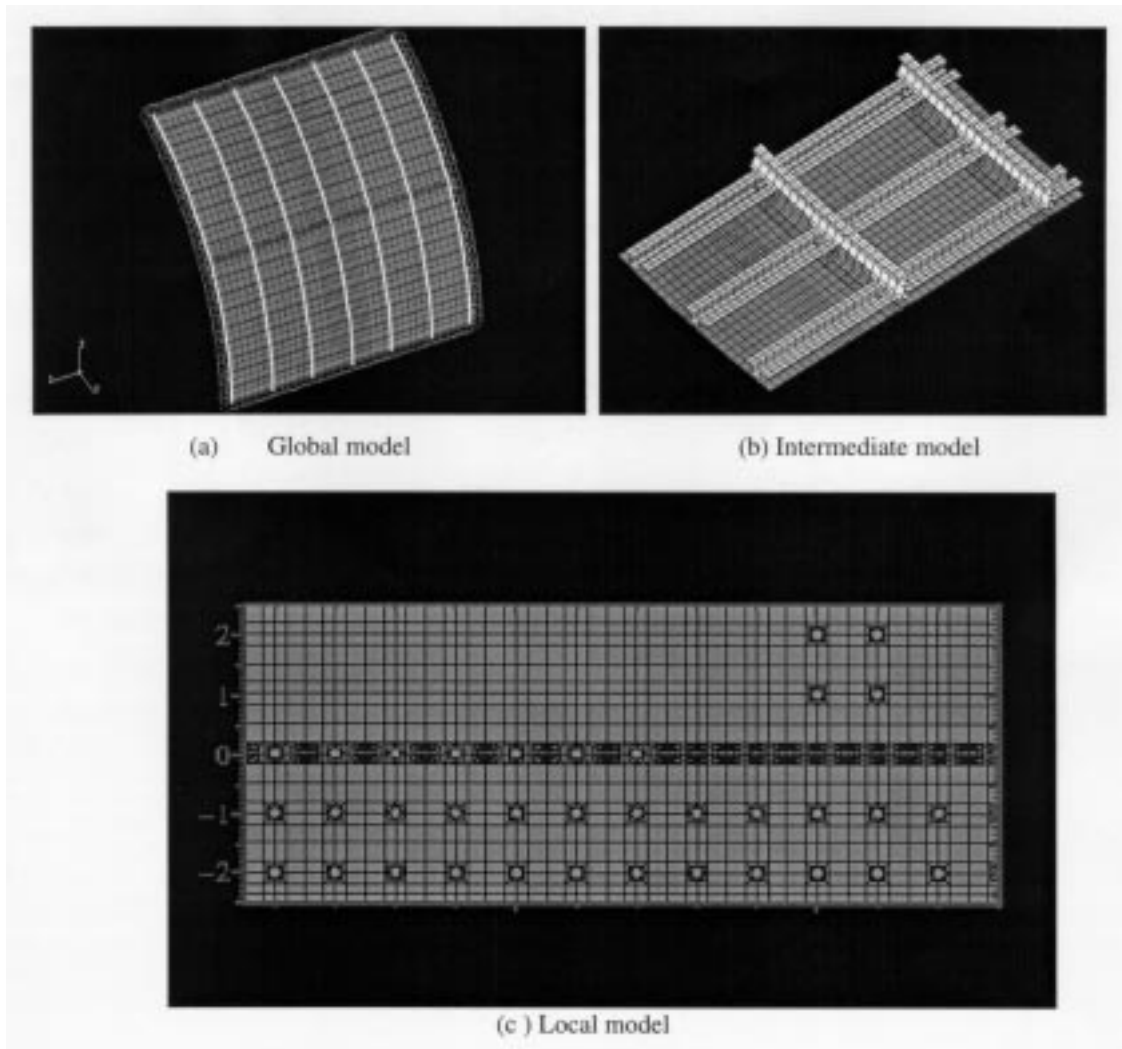


Figure 3. Global-Intermediate-Local Hierarchical Process.

To automate this hierarchical process of global-intermediate-local analysis, this software program can be separated into four major components: (1) main module, (2) mesh generator, (3) finite element method, and (4) finite element alternating method. The main module provides the detail of the geometric data as an input to the mesh generator. The mesh generator not only generates the mesh for the fuselage panel but also allows the proper positioning of the fasteners as well as the meshing of the cracks on the fuselage skin. With the mesh generated for the global and intermediate model, the global and intermediate analyses are performed using a commercial finite element package. The stress and displacement results are then transferred to the local analysis to be performed by an in-house elastic-plastic finite element alternating method (EPFEAM). The finite element alternating method (FEAM) solves for the cracks in finite bodies by iterating between an analytical solution for an embedded crack in the infinite domain and a finite element solution for the uncracked finite body. The FEAM is extended for elastic-plastic analysis by using the initial stress method, by decomposing the elastic-plastic analysis into a series of elastic analysis, in which the principle of superposition holds. The EPFEAM would evaluate the elastic-plastic stresses for given

strain increments using efficient and accurate algorithms based on the generalized midpoint radial return for three-dimensional constitutive laws and the stress subspace method [5]. The elastic-plastic analysis of the local model would accurately capture the effect of multiple-crack interactions on the residual strength of the fuselage panel.

To perform the fatigue crack growth analysis for MSD problem, linear-elastic material behavior is assumed. This analysis can be carried out efficiently with FEAM where the MSD cracks do not have to be meshed explicitly. To take into account of the effect of stress ratio, the Forman's crack growth equation is used. The effect of the initial radial pressure induced near a hole in the skin due to a rivet misfit and the effect of the plastic deformation near the hole due to rivet misfit are both considered [6]. These effects can alter the range of the stress intensity factor imposed on a crack tip during cyclic loading and thus affect the fatigue crack growth rates. It has been shown that these effects are responsible for a phenomenon whereby the shorter cracks near a row of fastener holes may grow faster than longer cracks.

DEMONSTRATION OF SOFTWARE

The program begins with the option of performing either a residual strength analysis or a fatigue crack growth analysis. It assumes that the details of the fuselage panel are provided by the OEM or can be easily obtained from a database. For the residual strength analysis, the user can choose the orientation of the cracks either in the longitudinal or circumferential direction as shown in Figure 4. The program can also allow the user to change the center of the lead crack with respect to the frame or stringer position to study the effect of the crack location on the residual strength of the fuselage panel. In order to obtain the residual strength curve, the user would be asked to input the initial and final crack length. For a longitudinal crack, the user will also be given an option on whether the tear strap is broken, and for a circumferential crack, the user will be given an option on whether the stringer is broken. Having completed the software input, the program will automatically generate the appropriate global-intermediate-local models for the analysis.

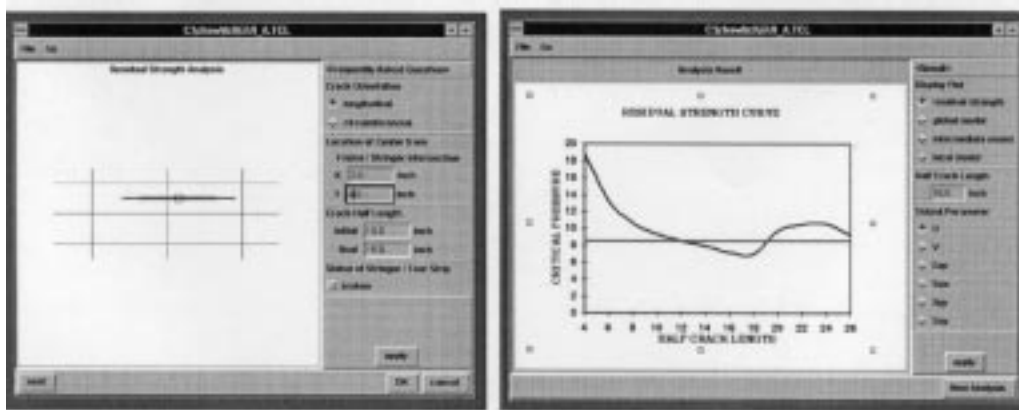


Figure 4. GUI for Residual Strength Analysis.

For the fatigue analysis shown in Figure 5, the user can input the MSD crack sizes for each of the fastener holes between two frame sections. These fastener holes are located on the first row of fasteners for the upper panel of a lap joint. As an additional safety feature, the program accepts a minimum MSD crack size input in which a MSD crack with a minimum size would be assumed on both sides of all the rivet holes. The program allows two options in which the fatigue growth analysis is carried out. It can calculate the number of fatigue cycles it takes for (1) a first crack link up between two rivet holes or (2) any cracks to reach a maximum crack size. At the end of the residual life analysis, the program will output the estimated fatigue life and the final crack size for all the MSD cracks.

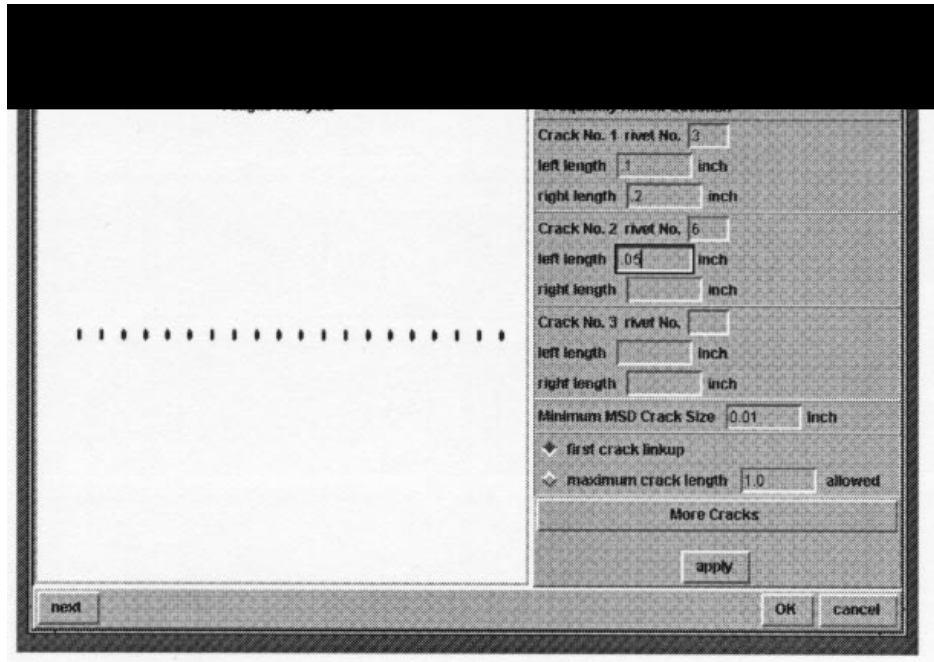


Figure 5. GUI for Fatigue Growth Analysis.

CONCLUSION

In conclusion, an automated tool to study the residual strength in the presence of widespread fatigue damage has been developed. The functionality of the program includes

- Residual strength analysis on (1) multiple cracks and (2) interaction of a lead crack with MSD on rivet holes using elastic-plastic finite alternating method.
- Residual life analysis for MSD cracks.

ACKNOWLEDGMENTS

The support of this work by the Federal Aviation Administration through a work grant to the Center of Excellence for Computational Modeling of Aircraft Structures at the Georgia Institute of Technology is sincerely appreciated.

REFERENCES

1. Swift, T.: Widespread Fatigue Damage Monitoring - Issues and Concerns. *Proceedings of the 5th international Conference on Structural Airworthiness of New and Aging Aircraft*, DGLR-Beicht 93-02, pp. 133-150, 1993.
2. Maclin, J. R.: Performance of Fuselage Pressure Structure. *1991 International Conference on Aging Aircraft and Structural Airworthiness*, NASA Conference Publication 3160, pp. 67-74.
3. Swift, T.: Fracture Analysis of Stiffened Structures. *ASTM STP 842*, 1984, pp. 171-183.
4. Wang, L., Brust, F. W., and Atluri, S. N.: Predictions of Stable Growth of a Lead Crack and MSD, Using EPFM and Elastic-Plastic Finite Element Alternating Method. *FAA-NASA Symposium on Continued Airworthiness of Aircraft Structures*, August 1996.
5. Wang, L., Brust, F. W., and Atluri, S. N.: The Elastic-Plastic Finite Element Alternating Method and the Prediction of Fracture Under WFD Conditions in Aircraft Structures. *FAA Center of Excellence Report by Georgia Institute of Technology*, August 1995.
6. Park, J. H. and Atluri, S. N.: Fatigue Growth of Multiple Cracks Near a Row of Fastener Holes in a Fuselage Lap Joint, *Proceedings of the International Workshop on Structural Integrity of Aging Airplanes*, edited by Atluri et al., pp. 91-116, 1992. Also *Computational Mechanics*, 13, pp. 189-203, 1993.

CONTROLLING FATIGUE FAILURES BY MEANS OF A TRADE-OFF BETWEEN DESIGN AND INSPECTION PARAMETERS

A. Brot
Engineering Division
Israel Aircraft Industries
Ben-Gurion Airport, Israel

ABSTRACT

A simulation method is described which allows the fatigue analyst to rationally trade-off specific design details and nondestructive inspection (NDI) methods in order to achieve an optimum degree of safety. The effects of remote stress, load transfer, and NDI method on the probability of failure of a typical splice structure is presented. The civilian and military damage-tolerance regulations are examined to determine whether their imposed trade-offs achieve the optimum degree of safety. The simulation method is shown to be also applicable to design trade-offs between multisite damage design parameters.

INTRODUCTION

The fatigue analyst has three lines of defense to protect his structure against fatigue failures:

1. Provide a long crack initiation life.
2. Insure that crack growth will be slow.
3. Specify suitable nondestructive inspection (NDI) methods and intervals to detect cracks before failure.

The first two items are controlled by the specific design parameters selected while the third item is set by the inspection parameters. The fatigue analyst can *trade-off* better design details with less effective NDI or worse design details with more effective NDI and achieve a satisfactory fatigue life.

The *INSIM* computer program, which is described in detail in References 1-3, has been developed in order to simulate the entire fatigue environment that a structure must withstand. *INSIM* simulates, in a probabilistic manner, service life variation, service load severity, time to crack initiation, crack growth history, and NDI detection capability.

Cracks often initiate at critical locations of aircraft structures. These cracks propagate and, unless detected and repaired, will eventually result in a failure. There are three, mutually exclusive, outcomes of the fatigue process:

1. The aircraft may reach the end of its operational life and be retired from service. The retired aircraft may or may not have undetected cracks at critical locations.
2. A crack may be detected during maintenance operations. The affected part is usually repaired or replaced.
3. A crack reaches its critical size undetected and the structure fails in service.

INSIM performs a simulation of a single critical location in an entire fleet of aircraft. Cracks initiate at various times and grow at variable rates in each aircraft. Inspections are performed according to a predetermined schedule, using as many as six different NDI methods. Cracks are detected during these inspections according to the statistical expectation of detection. As the simulation proceeds from aircraft to aircraft, cracks are detected, aircraft are retired from service, or failures occur. The computer acts as a scorekeeper, amasses the statistics, and summarizes the results. In order to provide statistically significant results, a large number of simulations must be performed. In a typical simulation, 300,000 inspections will be performed for a fleet of 100,000 aircraft, taking less than 1 minute on a Pentium equipped computer.

Based on these simulations, *INSIM* calculates the probability that the *three lines of defense* have been breached, and failure occurs.

SIMULATION OF A TYPICAL SPLICE

INSIM has been used to simulate a typical aircraft splice structure and to determine the probability of failure for various design parameters and inspection details. Figure 1 describes the 2024-T3 splice configuration that was selected for analysis. As is shown in Figure 1, the remote stress and the degree of load transfer were left variable in order to allow trade-off studies against inspection intervals. An *aging aircraft* scenario was assumed, in which the mean retirement life is the design life (20,000 flights) and the high-time aircraft is retired after 150% of the design life, in order to account for extreme conditions.

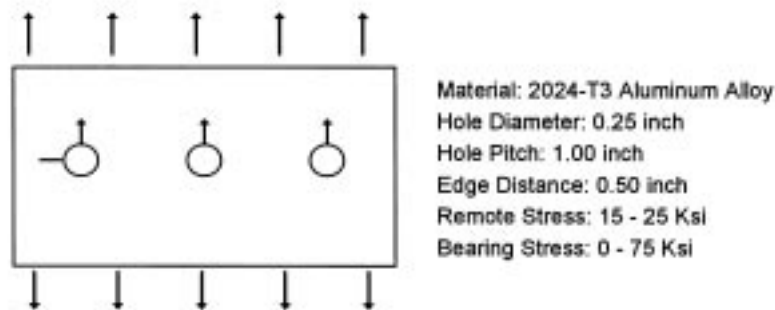


Figure 1. Schematic Representation of a Typical Splice Configuration.

Effect of Remote Stress on the Probability of Failure

Figure 2 describes the probability of failure of the splice defined in Figure 1, as a function of the remote stress and inspection interval, as determined by *INSIM*. As expected, increasing stress and increasing inspection intervals result in higher probabilities of failure. However, Figure 2 also indicates the possibilities for trading-off higher stresses with shorter inspection intervals, while maintaining a constant probability of failure. For example, a remote stress of 16 ksi coupled with a liquid-penetrant inspection interval of 5000 flights results in a probability of failure of about 0.07%. If the stress level is increased to 20 ksi (25% increase), the inspection interval must drop fivefold to 1000 flights *in order to maintain the same degree of safety*.

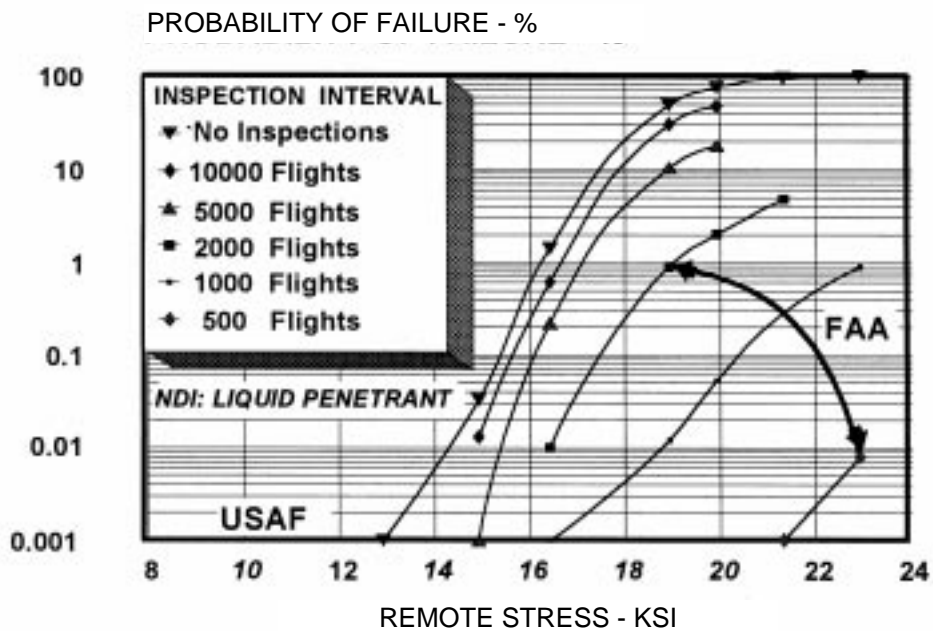


Figure 2. The Effect of Remote Stress Level on the Probability of Failure. (Bearing Stress/Remote Stress =3).

We can examine how the civilian and military damage-tolerance regulations deal with this trade-off. Basically, for damage-tolerance substantiation, inspection intervals are set as 50% of the time that a crack will grow from a detectable size until it is critical. However, the civilian (FAR-25) and military (MIL-A-83444 and MIL-A-87221) regulations contain important differences. For example, the “noninspectable option” of MIL-A-83444 encourages eliminating inspections completely by decreasing stresses to achieve a two-lifetime crack growth period. The FARs (Federal Aviation Regulations) require inspections at all critical locations, but the intervals can be selected to be as short as economically practical, thereby allowing stress levels to be raised.

We can analyze the degree of safety, that the damage tolerance regulations will impart to the structure, by the use of *INSIM*. Figure 2 designates a region as “USAF.” This represents a damage-tolerance analysis performed under the noninspectable option of MIL-A-83444. The region marked “FAA” on Figure 2 represents the same damage-tolerance analysis, performed to the requirements of FAR-25 for various stress levels. The FAA results indicate probabilities of failure ranging from 0.008% to 0.9% corresponding to inspection intervals ranging from 500 to 2000 flights. The USAF results indicate a probability of failure of about 0.001% *with no inspections*. The results indicate, for the configuration selected, that the USAF approach will result in a *significantly lower* probability of failure than the FAA approach. However, the reduced probability of failure for the USAF approach is due to significantly reducing the stress level – thereby increasing weight. This case demonstrates a common phenomenon, that reducing the stress level *more than compensates for the total lack of inspections*.

The results of Figure 2 also illustrate that the basic damage-tolerance philosophy does not result in a constant degree of safety. In the example shown, probabilities of failure ranged from 0.008% to 0.9% for the combinations of stress level and inspection intervals that were analyzed, all to the same damage-tolerance requirements.

Effect of Load Transfer on the Probability of Failure

The splice configuration shown in Figure 1 was analyzed for crack initiation and growth for various degrees of load transfer. Figure 3 indicates the effect of load transfer on crack initiation time, growth of relatively small cracks (0.01-0.13 inch), and growth of larger cracks (0.13 inch to critical size). These results clearly indicate, as expected, that load transfer has a large influence on crack initiation, a moderate influence on the growth of small cracks, and virtually no influence on the growth of large cracks. (0.13 inch represents a 63.2% probability of detection with liquid penetrant NDI.)

Figure 4 describes, for the same typical splice, the effect of load transfer on the probability of failure, as determined by *INSIM*. According to the damage-tolerance criteria, inspection intervals are set as 50% of the time a crack will grow from a detectable size until it is critical. Since the detectable crack size is relatively large (taken as 0.13 inch for a liquid-penetrant inspection), the degree of load transfer will have virtually no effect on the inspection interval. For the typical splice configuration of Figure 1, a 1500 flight inspection interval will meet FAA damage-tolerance requirements for ratios of bearing stress to tensile stress ranging from zero to three, as is shown in Figure 4 by the designation “FAA.” But the increased load transfer increases the probability of failure *very significantly*, as is shown in Figure 4, from less than 0.001% to about 0.6%. Clearly, the damage-tolerance regulations are unable to provide a constant degree of safety under conditions of varying load transfer.

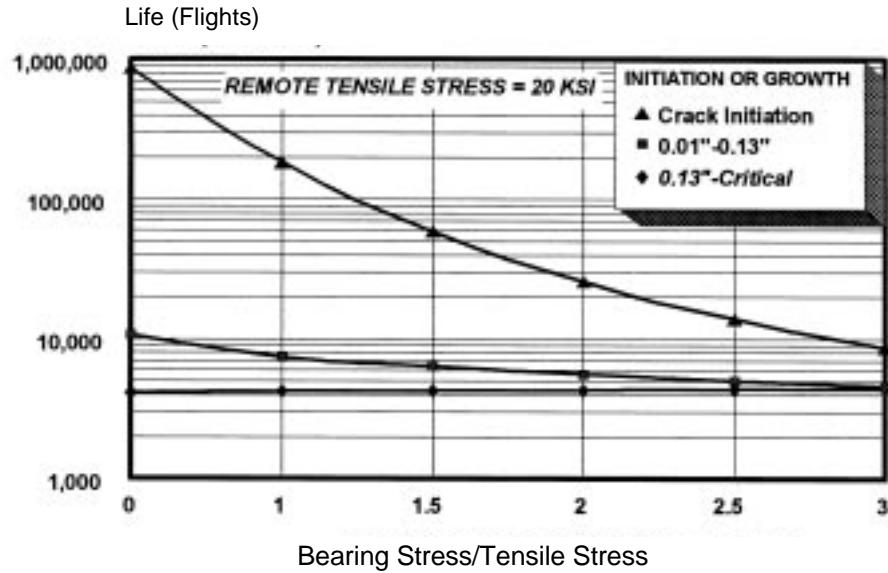


Figure 3. The Effect of Load Transfer on Crack Initiation and Growth.

Reference 4 sees the need to minimize load transfer and states “... the single most important feature for insuring a long fatigue life in metallic structures is the need for a low bearing stress on all fasteners at critical locations in the structure.” Clearly, the damage-tolerance regulations do not encourage the minimization of load transfer. As such, optimum safety cannot be achieved.

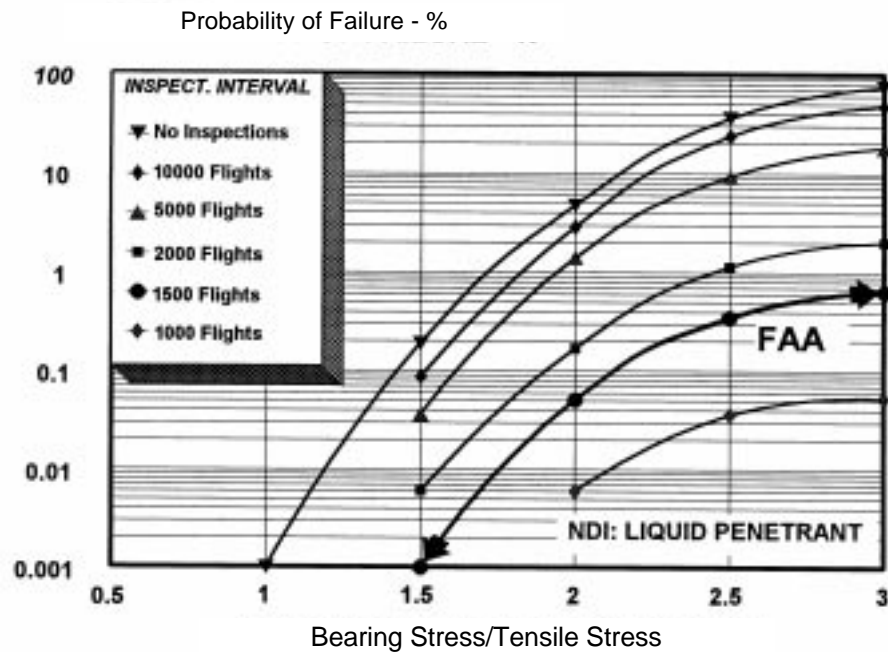


Figure 4. The Effect of Load Transfer on the Probability of Failure. (Remote Stress = 20 ksi.).

The results of Figure 4 suggest that the trade-off between load transfer and inspection interval can be performed using *INSIM* in order to achieve a constant degree of safety. For example, all the combinations of load transfer and inspection interval listed below will result in a probability of failure of approximately 0.05%:

<u>Bearing Stress/Tensile Stress</u>	<u>Inspection Interval</u>
1.5	5000 flights
2.0	1500 flights
3.0	1000 flights

Clearly, this approach yields more rational inspection intervals than the damage-tolerance regulations which would require an interval of 1500 flights in all the above cases.

Effect of NDI Method

Figure 5 indicates the effect of the NDI method on the probability of failure. The results indicate that the superior eddy-current method results in lower probabilities of failure than the liquid penetrant method. Simulations performed by *INSIM* allow the analyst to perform rational trade-off studies between the NDI method and the inspection interval.

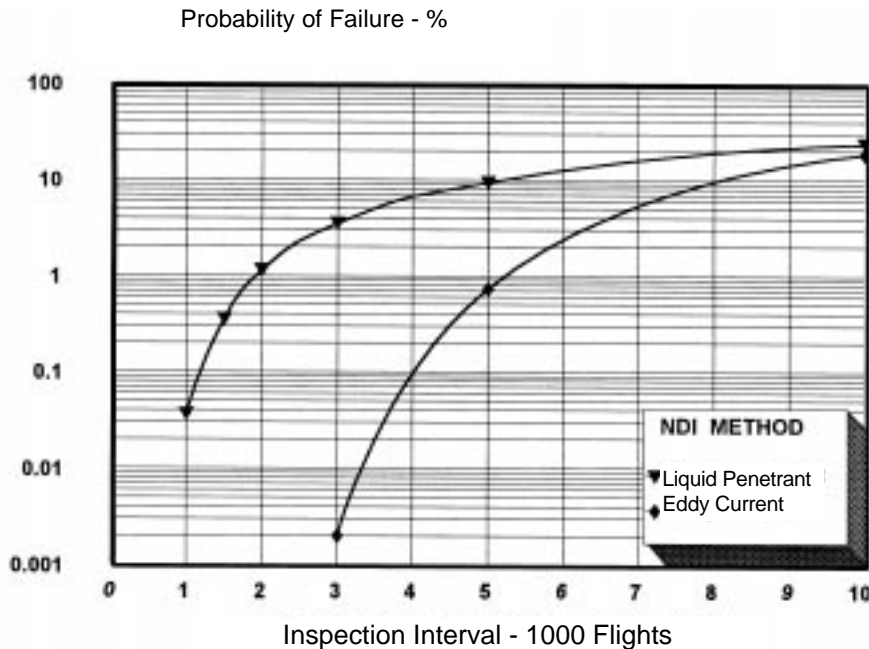


Figure 5. The Effect of the NDI Method on the Probability of Failure. (Remote Stress = 20 ksi; Bearing Stress = 50 ksi.)

MULTISITE DAMAGE DESIGN TRADE-OFFS

INSIM can simulate multisite damage in an approximate manner, as was described in References 1 and 2. Figure 6 examines the trade-off between design parameters for a typical multirow splice, multisite damage configuration. The crack growth analysis of the multiple cracks was performed using the methods described in Reference 5. As the hole pitch distance is decreased, less load transfer occurs at each hole, thereby reducing the probability of failure, as was described previously. On the other hand, as the hole pitch distance is increased, the load transfer at each hole is increased but inspection detection capability is *greatly enhanced* due to the longer critical crack size associated with the larger hole pitch distance. Under conditions where several cracks are likely to exist, the probability of detecting *at least one crack* is dramatically increased as the number of cracks increase, as was explained in References 1 and 2. The result, shown in Figure 6, indicates that favorable conditions exist for both *short and long* pitch distances and unfavorable conditions exist at an intermediate pitch distance. At the short pitch distance, crack initiation life is very long due to the low degree of load transfer. At the long pitch distance, cracks may occur early in the service life but they will be detected easily by the enhanced NDI detection capability provided by the multiple crack sites and their relatively long critical crack size. *INSIM* can be used to trade-off the various design and NDI parameters in order to achieve a reasonable degree of safety .

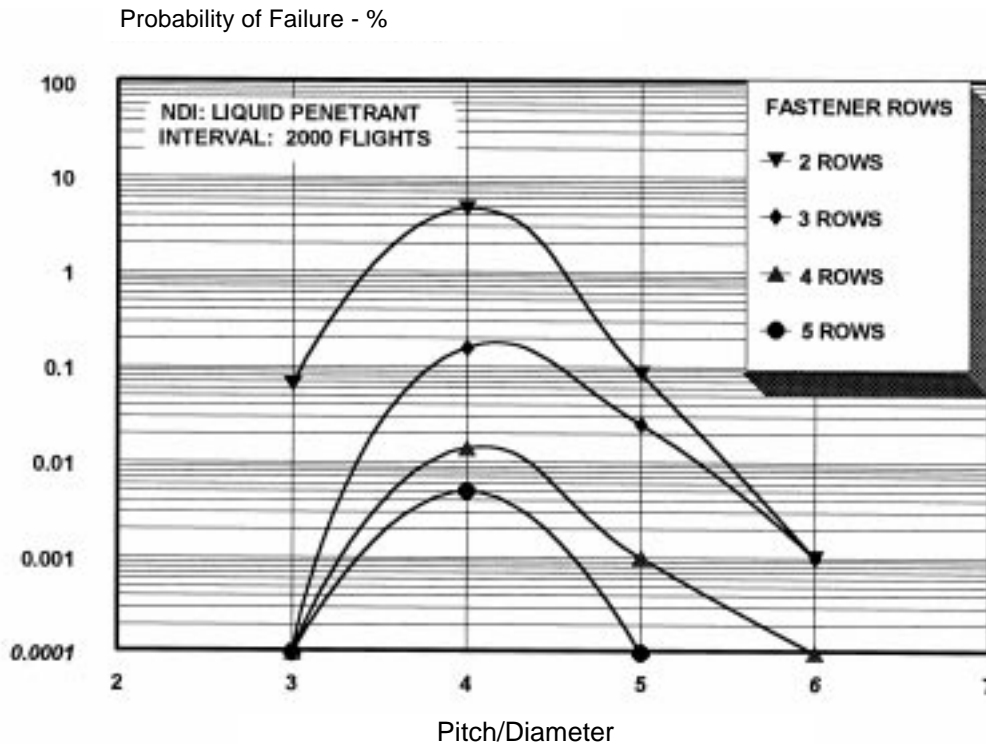


Figure 6. The Effect of Multisite Damage Design Trade-Offs on the Probability of Failure.

SUMMARY

It was demonstrated that *INSIM* can be used to perform trade-off studies between design and NDI parameters in order to achieve optimum safety by minimizing the probability of failure. The effects of remote stress, load transfer, and NDI method on the probability of failure of a typical splice structure were presented. It was shown that damage-tolerance regulations do not always achieve an optimum degree of safety because they do not account for large variations in crack initiation life that arise from load transfer considerations. The simulation method was applied to a multisite damage configuration and it was shown that optimum safety can be achieved with either short or long hole pitch distances, but not for intermediate pitch distances.

REFERENCES

1. Brot, A.: Developing Inspection Strategies to Enhance Structural Reliability of MSD Structures. *Proceedings of the 18th Symposium of the International Committee on Aeronautical Fatigue (ICAF)*, Melbourne, Australia, 1995.
2. Brot, A: Probabilistic Inspection Strategies – A Key to Controlling Multi-Site Damage. *Proceedings of the 1994 USAF Structural Integrity Program Conference*, San Antonio, TX, USA, 1994.
3. Brot, A: Probabilistic Inspection Strategies for Minimizing Service Failures. NASA CP-3274, September 1994.
4. Hart-Smith, L. J.: Easily Assembled Structurally Efficient Joints in Metallic Aircraft Structures. *Proceedings of the 18th Symposium of the International Committee on Aeronautical Fatigue (ICAF)*, Melbourne, Australia, 1995.
5. Nathan, A. and Brot, A.: An Analytical Approach to Multi-Site Damage. *Proceedings of the 17th Symposium of the International Committee on Aeronautical Fatigue (ICAF)*, Stockholm, Sweden, 1993.

CONTROLLING HUMAN ERROR IN MAINTENANCE: DEVELOPMENT AND RESEARCH ACTIVITIES*

William B. Johnson, Ph.D.
Galaxy Scientific Corporation
Atlanta, Georgia

William T. Shepherd, Ph.D.
FAA Office of Aviation Medicine
Federal Aviation Administration
Washington, DC

SUMMARY

Human error is the major contributor to airline incidents and accidents. Therefore, reduction of human error, throughout the air transportation system, has the highest potential to impact safety statistics. This paper considers the “human factors” related to airline maintenance by showing development activities addressing error reduction and maintenance human performance enhancement. The paper discusses a variety of research as well as various applied activities with the goal of identifying, limiting, and mitigating human error. The paper also describes technology-based solutions to enhance human performance in maintenance and inspection.

HUMAN ERROR: A LEADING ACCIDENT CAUSE

It is universally quoted that 80% of airline accidents and incidents are a result of human error. Such error includes the actions of pilots, air traffic controllers, dispatchers, technicians, engineers, and others. Improper maintenance follows Controlled Flight Into Terrain (CFIT) as the second highest cause of aviation fatalities between 1982 and 1991 (See Figure 1) (Phillips, 1994).¹ While better engines, airframes, navigation, and other systems have improved the overall safety of aviation over the past few decades, there are still opportunities to improve the performance of humans in the aviation system. Therefore, attention to maintenance and to maintenance human factors is an important and viable means to achieve the “Zero Accident” goal set forth by the US Department of Transportation.

* Work done on contract at Galaxy Scientific Corporation, DTFA01-94-Y01013.

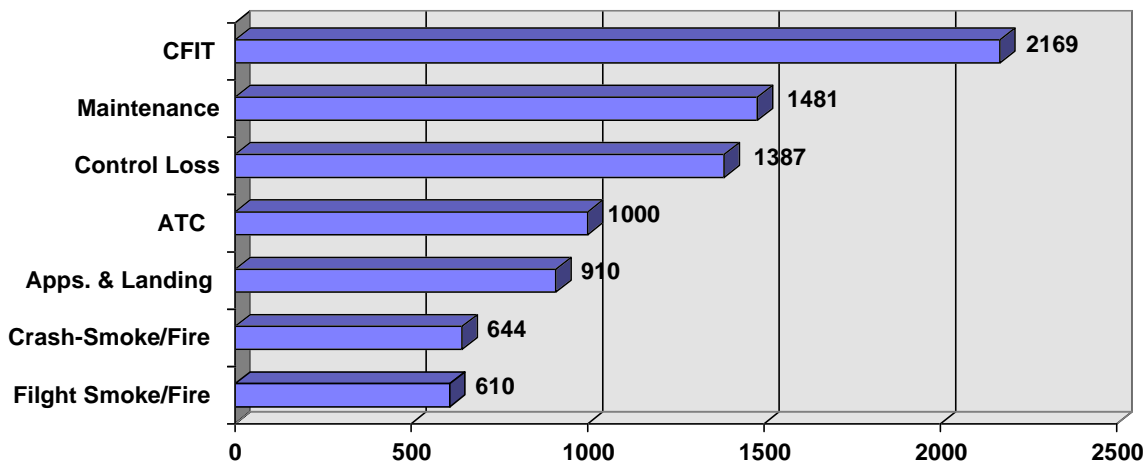


Figure 1. Safety Issues Versus Onboard Fatalities Worldwide (1982-1991).

HUMAN FACTORS DEFINED

The term “Human Factors in Aviation” elicits a variety of definitions (Johnson and Shepherd, 1993, 1994).^{2,3} Many airline operations and maintenance managers equate human factors with crew resource management (CRM). CRM has captured the attention of the airline industry because it has made major strides in enhancing communication and decision making in flight operations. CRM has increased safety, efficiency, and job satisfaction among flight crews. However, CRM is only a very small segment of the field of aviation human factors. Human factors affect all aspects of airline operations including, but not limited to, airline and airport security, reservations, ticketing and gate control, cabin service, flight operations, maintenance, and engineering.

The term “Human Factors” is synonymous with the term “Ergonomics.” The latter term is more widely used in Europe. However, most practitioners now do not differentiate between the two terms. As evidence, the largest human factors professional society recently changed its name from the Human Factors Society to the Human Factors and Ergonomics Society.

There are a variety of disciplines that affect human factors in maintenance. Each of these multiple disciplines add their perspective as the term human factors is defined. For example, the Clinical Psychologist, shown in Figure 2, might equate human factors with the study of personality traits, individual stressors, or personal psychological matters. An Anthropometric Specialist, also shown in Figure 2, may tie most human factors to the design of equipment “knobs and dials,” to seat design, and to other features associated to the physical characteristics of the human in the system. The Organizational Psychologist is likely to equate human factors with communication within or between groups, as with CRM. The

Experimental Psychologist is likely to view of human factors from the perspective of stimuli and response, or from the controlled study of experimental vs. control groups. Other specialties, shown in Figure 2, help communicate the fact that human factors in aviation is indeed a multidisciplinary effort.

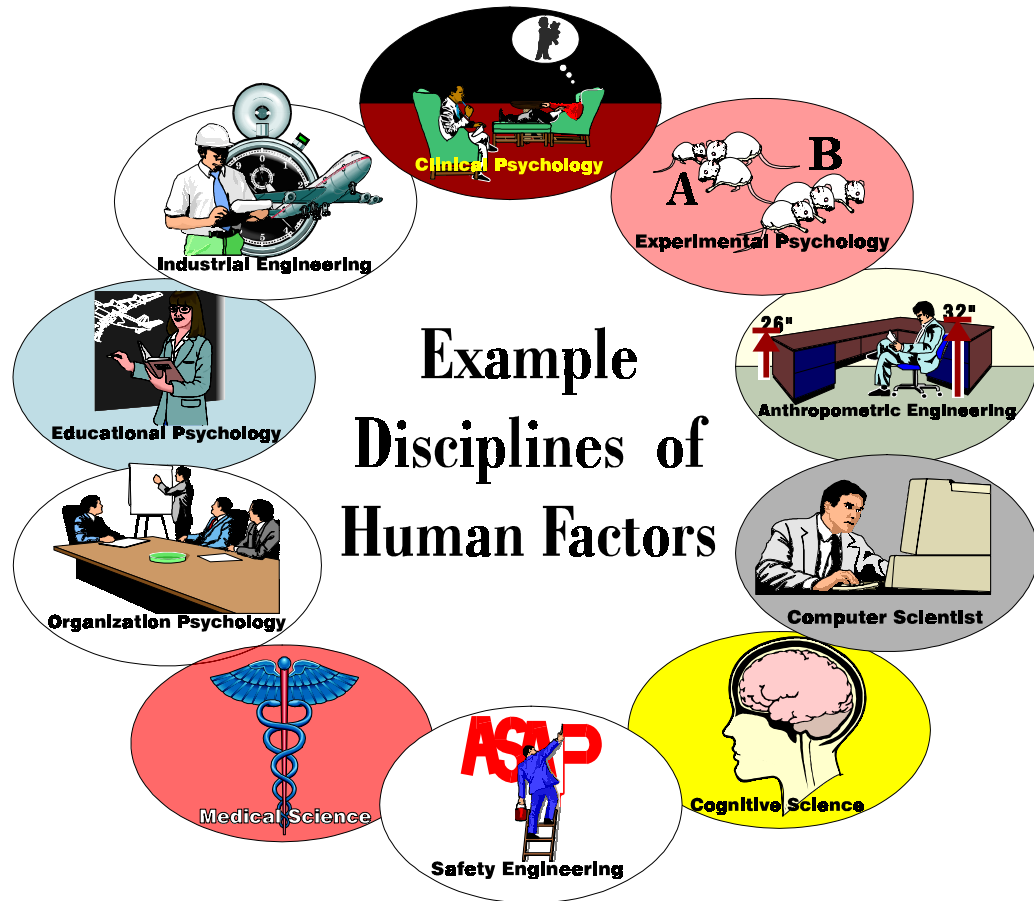


Figure 2. Example Disciplines of Human Factors.

In summary, the term human factors applies to a variety of factors that affect human performance. Human Factors pays attention to the human as the central and critical component necessary for the most effective, efficient, and safe operation of any system. The study of human factors identifies the best capabilities of the human in the system. Human factors also identifies the prominent limitations of the human in a system and makes appropriate compensation.

Incidents, Accidents, and Maintenance Human Factors

Airline safety continues to improve. Advances in system design, hardware manufacturing techniques, software design and development, flight crew deck design, maintenance equipment, and procedures are only a few example aspects of the evolving airline system that contribute to increased safety.

A recent study in the US found that 18% of accidents are related to maintenance factors (Phillips, 1994).¹ Table 1 lists several accidents where the probable cause was maintenance-related. In each of these cases, a change in some aspect of the organization, related to human performance, most likely would have prevented the accident. Examples of human factors interventions include: improved inter-airline communications; adherence to maintenance procedures and/or manufacturer specifications; an increased diligence in maintenance, repair and final inspection procedures; and improved maintenance training. One such example from Table 1 is the Continental Express accident in 1991. A failure to communicate information about an incomplete repair to the subsequent work shift resulted in a revenue flight before the fix was completed. Attention to human factors in maintenance can minimize such human error and/or mitigate the consequences.

Table 1. Examples of Maintenance Error.

Carrier	Location	Initiating Failure	Date
American Airlines DC-10	Chicago	Engine separation	5/25/79
Eastern Airlines L-1011	Bahamas	O-rings	5/05/83
JAL 747	Japan	Bulkhead	8/12/85
Aloha Airlines 737	Hawaii	Fuselage failure	4/28/88
BM AirTours 737	Manchester	Burner can	1/08/89
United Airlines DC-10	Iowa	Fan disk failure	7/19/89
Continental Express	Texas	Deicing boot	9/11/91
Northwest Airlines	Norita	Engine separation	3/01/94

Figure 3 shows the percentage growth in the US airlines for an 11-year period ending in 1993 (Air Transport Association, 1994).⁴ Maintenance costs, passenger miles flown, and the number of aircraft have all exceeded the overall growth of the aviation maintenance technician (AMT) workforce. This growth pattern is representative of airlines worldwide. This chart leads to an obvious conclusion - that the AMT must raise efficiency to match the increasing work load. The work load is compounded by the combination of new skill and knowledge requirements for advanced technology aircraft and increasing labor demands necessary to provide continuing airworthiness to the existing fleet. To accomplish these goals, individual technician responsibilities and skill levels must increase. The industry must

work together to ensure that *either* workers become more qualified *or* that maintenance tasks and procedures become adapted to meet human capability. Attention to human factors in maintenance will ensure continuing performance enhancement of the technician workforce.

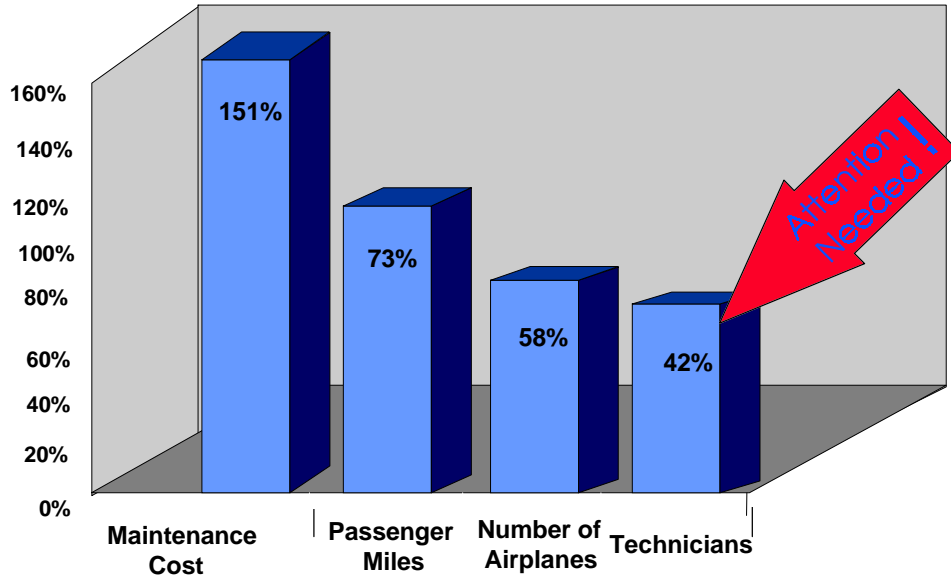


Figure 3. Examples of Maintenance Error.

IDENTIFYING MAINTENANCE ERROR: PROACTIVE APPROACHES

The sections above have defined maintenance human factors and set the stage for the development, implementation, and test of applications-oriented hardware, software, and procedures for human performance enhancement in maintenance. This section shows a few examples.

United Airline's Non-Routine Write-Ups

United Airline's (UAL) Oakland Modification Center conducts heavy maintenance for the airline and for numerous contract customers. The detection, documentation, planning, and completion of non-routine maintenance is a logistical effort of significant magnitude. There can be as many as 5000 non-routine write-ups on a large high-cycle aircraft. Efficiency in documentation and planning is critical to meeting production schedules.

In an effort to control/reduce maintenance cycle time, to expedite planning and scheduling, to reduce data errors, and improve tracking, United created the Electronic Non-routine Write-up system. Following good systems design practices UAL conducted appropriate front-end analyses and system design. These human-centered procedures ensured that the completed system was designed to meet the specific needs of the maintenance

technician and inspector. A series of software and hardware rapid prototypes were used for iterative evaluations of the system with maintenance personnel. Figure 4 shows representative screens of the software displays. The system operates on small portable computers using a stylus (like a pen) input. Data can be transferred to a client-server system via wireless or hard wired Local Area Network connections.

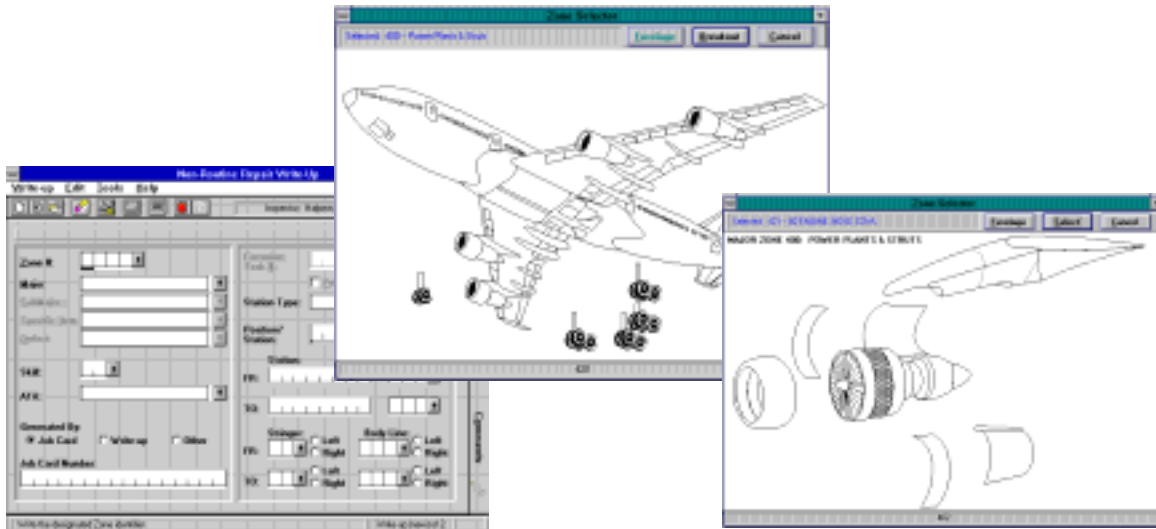


Figure 4. United Non-Routine Write-Up Sample Screens.

Initial evaluations of the United Non-routine Write-up systems are positive. Users like the interface and data errors are being reduced. The airline is currently wrestling with the logistical problems of attaining integration between the new system and the many legacy systems. The decision to create a small system that is compatible with existing systems was intentional. United felt that waiting to “fix everything at once” would mean years of development that could be outdated before it is implemented. So far the decision was a wise one.

Boeing’s MEDA With Galaxy’s TEAM

Boeing Commercial Airplane Group reinforced its reputation as an industry leader in maintenance human factors development with the introduction of the Maintenance Error Decision Aid (MEDA) system. MEDA is the first system to promote a structured error investigation process to identify factors that contribute to maintenance error (Rankin and Allen, 1996).⁵ The MEDA system identifies such error contributing factors as: information, communication, job design, environmental conditions, organizational factors, and others. Boeing has delivered MEDA classes to nearly 40 airlines worldwide and currently offers MEDA via its Customer Service network.

The Boeing MEDA system is supplemented by a software system called Tools for Error Analysis in Maintenance (TEAM). Created in cooperation with Boeing, Galaxy Scientific created the TEAM system for easy data recording and analysis. Figure 5 shows an example TEAM data entry screen and data analysis screen. TEAM uses standard Windows interface conventions like pull-down menus and pop-up screens for information and assistance.

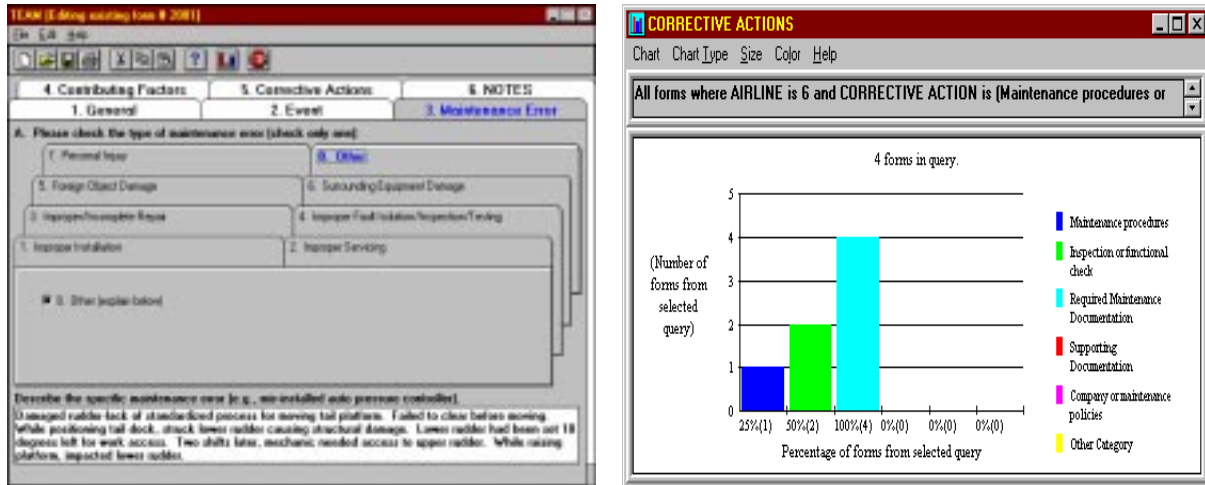


Figure 5. TEAM Sample Screens.

FAA's On-Line Aviation Safety Inspection System

The FAA has over 2000 Aviation Safety Inspectors (ASIs) responsible for safety and compliance inspections related to flight operations, avionics, and air worthiness. In an attempt to meet the in-the-field data collection and reporting requirements of the ASIs the On-line Aviation Safety Inspection System (OASIS) was specified and created. The project started as a research effort studying the working habits and software support requirements of FAA inspectors. The project escalated to delivery of OASIS. The system objectives included the following: increased speed of data collection, increased quality of safety data, standardized access to national safety data bases, and overall efficiency improvement afforded by portable computers and software tools. An example of OASIS applications is shown in Figure 6. Currently, OASIS is fielded in selected FAA District Offices and International Field Offices. FAA has a plan for full implementation of OASIS over the next 3 years.

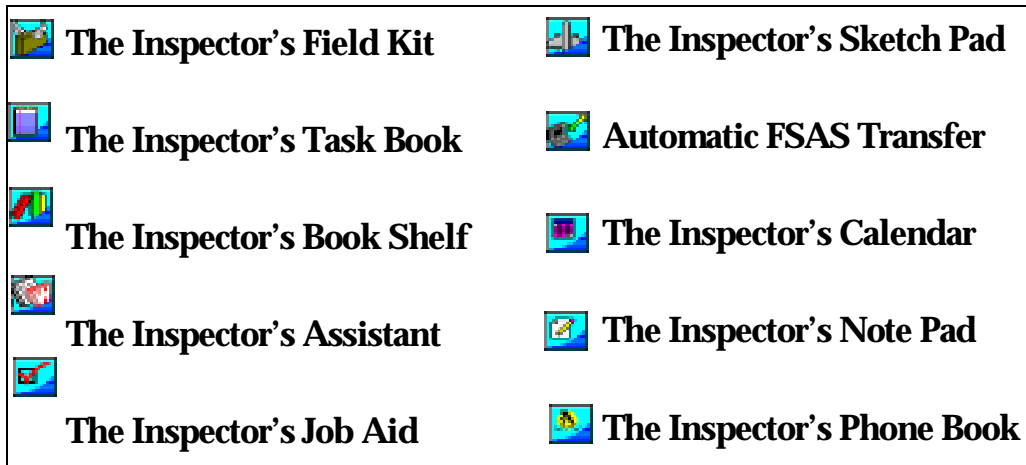


Figure 6. OASIS Applications.

FAA HUMAN FACTORS RESEARCH

The FAA Office of Aviation Medicine has operated a very large human factors in maintenance research and development program since 1988. That project has involved a multidisciplinary team of applied engineers and psychologists to conduct pragmatic human factors studies and develop useable products to promote enhanced maintenance performance. Example research includes the following: workplace illumination, human performance in restricted work environments, redesign and test of maintenance work cards, speed accuracy trade-offs in inspection performance, development of maintenance supervisor job aid, design of a paperless documentation system for a component overhaul shop, and the evaluation of simplified English for maintenance procedures. The research program has also developed and tested software tools to audit human factors mismatches in aviation maintenance working environments. All of the FAA research can be found on the World Wide Web at: <http://www.hfskyway.com>.

Here are a few more examples of human factors projects that are related to training and information dissemination.

Training Projects

Training has been an important discipline in human factors since the term human factors and ergonomics originated (FAA, 1995 a, b; Wiener and Nagel, 1988).^{6,7,8} There has always been the tendency to adapt the human to a system by providing training. For example, if a system is difficult to use, either by its complexity or by design usability features, the solution is to “provide more training.” Systems with excellent design also often require some training.

Training/education researchers and professionals are tasked to find the optimal training methods to ensure maximum human performance. Approaches vary from the straight forward textbook and instructor lecture to computer-based distance education transmitted via satellite or other networked systems. Two recently developed training systems that showcase advanced technology approaches to aviation maintenance training are described the FAA Boeing 767 Environmental Control System tutor (ECS) and the multimedia System for Training Aviation Regulations (STAR).

Environmental Control System Tutor

The FAA Environmental Control System tutor was built in cooperation with Delta Air Lines, with many other US and international carriers as advisors. Shown in Figure 7, the goal of the ECS training development project was to demonstrate the combination of simulation and individualized intelligent feedback. The result was an intelligent tutoring system to provide simulation-based practice and instruction for a modern jet liner environmental control system (ECS). The project showed that computer-based training can be delivered on standard 80x86 computers to provide simulation and, most importantly, individualized, intelligent feedback and advice. The training system was evaluated in an airline maintenance training department and a college aviation maintenance training department. The system was shown to have advantages over traditional instruction (FAA, 1993).⁹ The ECS trainer has been distributed to over 50 airlines and nearly 150 aviation maintenance technician schools.

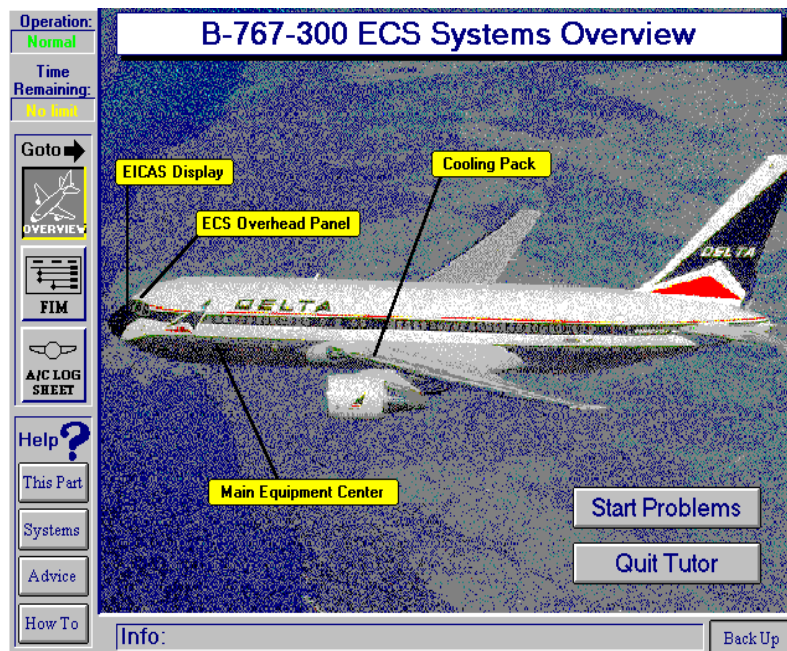


Figure 7. Display From Intelligent Training Simulation.

System for Training Aviation Regulations

All aviation maintenance technicians must be familiar with the Federal Aviation Regulations (FARs) to ensure compliance and safety. The traditional methods to teach or learn the FARs are boring. Typically, new trainees are instructed on these rules, which are written in the modified language of lawyers. New technicians seldom fully understand the context of the FARs and are motivated only by the requirement to complete a required number of hours in training.

The System for Training Aviation Regulations (STAR) has the goal of applying advanced technology training to the topic of FARs. STAR capitalizes on multimedia, like audio and video, to present the student with scenarios from actual maintenance environments. The software permits the student to explore the FARs, take different solution paths, and to learn the regulations by using them. User acceptance has been positive. Students like the stand-alone and self-paced nature of STAR. Instructors like STAR as a vehicle to stimulate discussion and show video clips for example. The STAR system was distributed, on CD-ROM, by the FAA in early 1996.

A Source for Human Factors Information

Most human factors information is published for the scientific community or for trained human factors professionals. As a result, airline maintenance managers must call in a human factors consultant when there is a perceived need for such expertise. In most cases, the consultant has minimal experience with aviation maintenance, which affects the rate at which relevant human factors information can be provided.

The FAA Office of Aviation Medicine, recognizing the need for applied maintenance human factors information, created and published the *Human Factors Guide for Aviation Maintenance* (FAA, 1995 a)⁶ (*Guide*), shown in Figure 8.



Figure 8. The Human Factors Guide for Aviation Maintenance.

The *Guide* was designed and developed using the very human-centered approach that characterizes human factors studies. The authors began the project by polling a variety of aviation managers regarding the critical issues in maintenance. An advisory committee was established to steer the document design and the information content. The *Guide* was extensively reviewed by aviation maintenance personnel and by senior human factors professionals. The *Electronic Human Factors Guide* has been distributed to *over* 2000 users worldwide. The industry-wide positive acceptance has been overwhelming.

The Guide is available in hardcopy from the US Government Printing Office (FAX: 202-512-2250), on CD-ROM from the FAA Office of Aviation Medicine (FAX 202-366-7105), or on the INTERNET at: <http://www.hfskyway.com/hfg.html> .

HUMAN FACTORS TRAINING

One final trend worthy of mention is the flurry of human factors training that is emerging within airlines, from various training companies, and from consulting firms. Since there is a demand many organizations, as well as some self-appointed Human Factors gurus, are stepping forward to offer “The Solution.” While it is not a goal of this paper to present a human factors training curriculum, we can offer a few cautions. First, human factors training must not be unidimensional. It must contain more than crew resource management materials. It must be more than psycho-babble lectured by an eloquent Ph.D. Human factors training must be based on scientific principles and an understanding of aviation maintenance. Human factors must do more than make the student feel good about him/herself. Human factors training must provide concrete information and guidance about how to work safer, how to communicate better, how to recognize personal and peer performance limitations, and where to obtain more information. There is no single magic credential necessary for the human factors course instructor/facilitator. However, the instructor must acknowledge the multidisciplinary nature of human factors in maintenance. Armed with that acknowledgment and the right instructional resources, like the *Human Factors Guide*, there are many qualified personnel who can deliver a quality human factors course.

CONCLUSIONS

The conclusion from this paper is quite straight forward. First, proper attention to human factors in aviation maintenance has the potential to improve air transportation safety statistics. Second, attention to human factors can also enhance human performance, lower error rate, and improve the bottom line. This paper has described how the FAA and the industry has created programs and products to address human factors in maintenance. The paper has also emphasized that there are many opportunities for improvement related to such areas as error reduction, job aiding, training, and information dissemination are currently the primary research and development areas. Because our air transportation is so safe it is

difficult to show significant statistical safety improvements. However, the control of human error remains as one of the few frontiers for improving airline safety.

REFERENCES

1. Phillips, E. H.: (August 29, 1994). Focus on accident prevention key to future airline safety. *Aviation Week and Space Technology*, pp. 52-53.
2. Johnson, W. B. and Shepherd, W. T.: (1993). The impact of human factors research on commercial aircraft maintenance and inspection. *Proceedings of the Flight Safety Foundation 46th Annual International Air Safety Seminar Kuala Lumpur*, Malaysia, Arlington, VA: Flight Safety Foundation (ISSN 0270-5176), November, 1993, 187-200.
3. Johnson, W. B. and Shepherd, W. T. (1994). Human factors in aviation maintenance and inspection: progress report on the US-FAA research program. Report on the Seventh *ICAO Flight Safety and Human Factors Regional Seminar*, Addis Ababa, Ethiopia, October, 1994, (pp. 400-409). Montreal: International Civil Aviation Organization.
4. Air Transport Association (1994). *The annual report of the U.S. scheduled airline industry* [Brochure]. Washington, DC: Air Transport Association. (Also see <http://air-transport.org/ata/home.htm>).
5. Rankin, B. and Allen, J. (1996). Boeing introduces MEDA maintenance error decision aid. *Airliner*, Apr-Jun, 1996.
6. Federal Aviation Administration (1995 a). *Human factors guide for aviation maintenance* (GPO No. 050-007-01098-2). Washington, DC: U.S. Government Printing Office. (Also see <http://hfskyway.com>).
7. Federal Aviation Administration (1995 b). *Electronic human factors guide for aviation maintenance*. Washington, DC: FAA Office of Aviation Medicine. (Also see <http://hfskyway.com>).
8. Wiener, E. L. and Nagel, D. C. (Eds.) (1988), *Human factors in aviation*. San Diego, CA: Academic Press, Inc.
9. Federal Aviation Administration and Galaxy Scientific Corporation. (1993, August). Results of the environmental control system tutor experiment. In *Human Factors in Aviation Maintenance - Phase Three, Volume 1 Progress Report* (Report No. DOT/FAA/AM-93/15). Washington DC: Federal Aviation Administration.

COORDINATED METALLOGRAPHIC, CHEMICAL, AND ELECTROCHEMICAL ANALYSES OF FUSELAGE LAP SPLICE CORROSION

M. E. Inman and R. G. Kelly
Department of Materials Science and Engineering
University of Virginia
Charlottesville, VA

S. A. Willard
Lockheed Engineering and Sciences Co.
Hampton, VA

R. S. Piascik
NASA Langley Research Center
Hampton, VA

SUMMARY

The development of improved airframe corrosion prevention practices (coatings, replacement structural materials, etc.) and accurate life prediction methods require laboratory corrosion test protocol(s) that simulates airframe corrosion environments. Further fundamental understanding of aging aircraft corrosion damage modes and environments are necessary for the development of the corrosion test protocol(s).

The results of this investigation suggest that condensate and ionic contaminants (Na^+ , Ca^{2+} , NO_3^- , SO_4^{2-} , Cl^- , and F^-) combined in the lap splice to form a corrosive electrolyte. Supporting cathodic reactions within the joint produced hydroxyl which promoted an increase in the local pH, further accelerating the corrosion. Precipitation of corrosion products drew in additional water by capillary action allowing the attack to continue. As the corrosion accelerated, the precipitated corrosion products along the faying surface stressed the lap splice skin and rivets leading to the observed pillowing, skin cracking, and rivet failure.

INTRODUCTION

Aluminum alloys used for aircraft airframe structures are susceptible to a wide range of environmentally induced degradation phenomena including pitting, crevice corrosion, exfoliation, and environment assisted cracking under constant and fatigue loading [1]. Although rare, fatigue cracking of corroded airframe structure does occur and can lead to major damage and loss of life. On August 22, 1981, a commercial aircraft experienced a fuselage explosive decompression failure in Taiwan [2]. Here, severe, undetected fuselage

skin corrosion over an 8-foot region led to fatigue cracking and failure of a large portion of the fuselage. In Hawaii, on April 1988, the ALOHA incident again revealed that fatigue cracking can occur in corroded fuselage structure [2]. More recently, on March 4, 1996, a high-cycle (82,000 flights) U.S. commercial transport was found to contain a 0.98-m (3.2-ft) crack in the fuselage skin with corrosion close to the damage [3]. These incidents occurred along riveted structures, such as the lap splice joint, which form occluded regions that are difficult to inspect and are susceptible to crevice corrosion.

Corrosion of structural aluminum alloys can obviously pose limitations on the service life of aircraft. The physical design of aircraft requires the formation of many regions that have an occluded geometry in which water and corrosive species can be trapped. For example, the lap splice joint studied in this work contained several such regions. The areas of overlap between the inner and outer skins form an occluded site, as do the regions between the rivets and the outer skin. During service, moisture is drawn into these sites by capillary action. Pollutant gases, such as SO_2 and NO_x , dissolve in the water, forming a corrosive solution which attacks the protective oxide on the material [4]. Takeoffs and landings near the ocean can lead to Cl^- ingress, acid rain can cause pH effects, and simple maintenance procedures (wash and deicing solutions) may lead to harmful crevice effects over the life of the aircraft.

As the aircraft ages, the occluded environments become more aggressive and tend to overcome the corrosion protection measures as paint cracks, sealant degrades, and crevices tend to open. Once corrosion initiates inside crevice regions, the trapped solution becomes increasingly aggressive due to the hydrolysis of metal cations produced by dissolution [5-7]. The process can become autocatalytic and thereby result in rapid loss of load-bearing capacity of the structure due to a reduction in the thickness of the component. In addition, the buildup of voluminous corrosion product can eventually create high local stresses in the creviced region. These induced stresses, in conjunction with lost component structural integrity, can lead failure by environmental fatigue or stress corrosion cracking.

Little is known about the corrosion environment contained in airframe creviced structure and test protocols that truly simulate these aggressive environments are lacking. The chemistry inside occluded sites such as crevices, cracks, and pits can become substantially different than the bulk environment. The local creviced solutions are typically more aggressive than the bulk environment, containing significantly higher levels of both metal ions and aggressive ions such as H^+ , Cl^- , SO_4^{2-} , and NO_3^- [8]. However, two hurdles have prevented the determination of the composition of solutions from corroded occluded joints. Accessing the very small volumes present in such joints can be experimentally challenging. More importantly, until very recently, there has not been an analytical technique which can detect and quantitatively analyze all of the ions expected in such a solution.

Due to the lack of understanding available concerning occluded site chemistry, simple analogues are often used as simulants for localized corrosion site chemistries. For example, salt water (typically 3.5 wt.% NaCl) is commonly used for the environment in the measurement of the corrosion and environment assisted cracking behavior of aluminum alloys used in aircraft. In the absence of direct measurements of the actual occluded solutions, the relevance of data generated from experiments in these simple analogue

environments cannot be determined. Thus, lifetime prediction models based upon data generated in these simple analogues are also subject to questions of relevance. Some progress in this area has been made, but it has not been based upon a full analysis of the occluded site chemistry coupled with measurements to verify that the extent and nature of the attack in the simulant matches that observed in service joints.

The work reported here involves two thrusts: (a) metallographic examination characterizing a portion of a retrieved fuselage lap splice joint that contains severe crevice corrosion and (b) a rehydration of the corroded occluded surfaces and analysis of the collected solutions for ionic content via capillary electrophoresis (CE). The goals of this proof-of-concept effort are to determine (a) the types of corrosion occurring in lap splice joints and (b) the capabilities of CE for identifying airframe crevice corrosion chemistry so that a definitive laboratory corrosion test protocol can be developed in the future.

EXPERIMENTAL

Metallographic Analysis

A section (approximately 0.61 x 0.56 m) of severely corroded horizontal fuselage lap splice was removed from a B707-320C aircraft fuselage. This aircraft was delivered to its first owner on 11/22/68 and was retired on 8/1/87 after 46,685 flight hours and 19,967 landings. The fuselage skin is constructed of clad aluminum alloy 2024-T3, the three rivet row lap splice joint faying surface is painted, and the inboard surface of the lap splice joint outer skin was not clad. The rivets are anodized aluminum alloy 2017-T4. A section (10 x 9.5 cm) of the corroded sample was removed from the lap splice panel for metallographic examination and occluded site analysis. Great care was taken not to contaminate the samples during all cutting operations. The metallographic samples were mounted in a vacuum fixture so that the friable corroded specimen was impregnated with epoxy mounting. This technique prevented material fall-out during subsequent specimen cross sectioning. Etching of the cross sections was accomplished with Keller's etchant.

Occluded Site Analysis

Rehydration solutions (referred to hereafter as "soak solutions") were produced from the exterior surface of the outer skin and the interior surface of the inner skin. During aircraft service or storage the corrosive solutions contained in the lap joint had dried, the corrosive species became trapped within the corrosion products that precipitated. By rehydrating these corrosion products and then analyzing the ionic content of the reformed solution, identification of the corrosive species present during service is possible [9]. After removal of the metallographic specimen, the remaining portion of the (10 x 9.5 cm) lap splice joint sample was used for the faying surface chemical analysis. The corroded faying surface was exposed by carefully removing the rivets by milling (no lubricant) the bucked portion of the

rivet and pushing out the countersink rivet head. Again, great care was taken not to contaminate the sample as the outer and inner skin of the lap splice joint were separated, thus exposing the faying surface. The faying surface was rehydrated by immersion in 50 ml of high-purity water from a Milli-Q UV™ (Waters) purification system for 9 days before analysis. Analyses of the ionic content of this soak solution were achieved via capillary electrophoresis (CE).

Capillary electrophoresis is a solution analysis technique that allows the ionic speciation of small volumes (on the order of 1 μ l or less) [10] with high sensitivity (on the order of 100 ppb) [10-12]. It involves the differential separation of ions during migration through a narrow bore, fused silica capillary upon the application of a large electric field. Detection is generally accomplished via either indirect or direct ultraviolet (UV) absorbance. The resulting plot of absorbance vs. migration time is referred to as an electropherogram. Comparison of migration times with standard injections as well as spiking of the sample solutions with standards was used for confirmation of the identification of the ions. Quantitation is achieved by comparing the magnitude of UV absorbance to that of standard solutions of the ionic species detected. The solution was analyzed for hard acid anions, organic acids, chromate, alkali, alkali earth cations, and transition metals by capillary electrophoresis using a Waters Quanta 4000 equipped with either a positive or negative power supply, dependent upon the type of analysis. The capillary was a 60-cm x 75- μ m I.D. fused silica capillary (Polymicro Technologies, Phoenix, AZ). Six different carrier electrolytes were used to identify all the ionic species present in the solution. Analysis for hard acid anions (*e.g.*, Cl^- , SO_4^{2-}) was achieved using a 0.5-mM CrO_4^{2-} electrolyte containing 0.5 mM of the osmotic flow modifier tetradecyltrimethyl ammonium bromide (TTAB). Analysis for organic acids was performed using 5-mM phthalate with 0.5-mM TTAB. Analysis for chromate was accomplished using an electrolyte containing 25-mM phosphate with 0.5-mM TTAB. Indirect photometric detection was used for all three electrolytes at a wavelength of 254 nm. Analysis for alkali and alkali earth cations and transition metals was conducted using 5-mM UV-Cat 1 + 6.5-mM HIBA. The presence of K^+ was distinguished from that of NH_4^+ using an electrolyte containing 5-mM UV-Cat 1 with additions of 6.5-mM HIBA and 2-mM 18-crown-6 ether. Analysis for Al^{3+} was done using UV-Cat 2 electrolyte. Indirect photometric detection was used for all three electrolytes at a wavelength of 185 nm. Samples were introduced into the capillary using a 30 s hydrostatic injection, from a height of 10 cm. The separation voltage in all cases was 20 kV. Data were collected with a LAC/E interface card and analyzed using Millenium Version 2.10 software.

Electrochemical Analysis

Based on the CE results, electrochemical tests were conducted to initiate protocol test development. When conducted in a relevant environment, electrochemical measurements allow quantitative assessments of the dissolution rate of a material during service. Potentiodynamic polarization measurements were conducted in several solutions which were designed to mimic the occluded site solutions determined by the capillary electrophoresis analyses. All solutions were made with reagent grade chemicals and were deaerated with nitrogen for 45 minutes before the initiation of the polarization measurement. All testing was

performed at room temperature. All electrochemical studies were performed on AA2024-T3. Polarization curves were generated using a EG&G Princeton Applied Research Model 253 potentiostat controlled by a personal computer with Model 352 software. Scans were initiated at 100 mV below the open circuit potential, and the potential was scanned anodically at a rate of 0.5 mV/s.

RESULTS

Metallographic Examination

A portion of the corroded lap splice joint panel is shown in Figure 1. The photograph shows the outer surface of the three rivet row lap splice joint which is oriented longitudinally along the fuselage. The riveted lap joint forms an occluded region bounded by an inner and outer skin. Figure 1 shows severe lap splice corrosion, several rivet heads are missing, and the outer skin appears to be pushed out of plane. This phenomenon, termed “pillowing,” is a result of internal pressure produced by voluminous corrosion products that form along the lap splice faying surface.

The metallographic cross section shown in Figure 2 consists of a montage of photomicrographs along a line between rivets and perpendicular to the rivet line. The figure reveals that faying surface corrosion has completely penetrated the outer skin while the inner skin exhibits corrosion at localized regions. The nature of the attack indicates exfoliation corrosion [13] in which the grain boundary areas are preferentially corroded, leaving the pancake-shaped grains of the sheet behind. The precipitated corrosion products are extremely voluminous causing a wedging stress to develop along the grain boundary, allowing further attack of the grain boundaries. As a result of the faying surface corrosion products, the outer skin has been pushed outward (pillowed) forming a crack on the outer skin surface located approximately 15 mm from the left edge of the specimen. The inner skin exhibits much less corrosive attack compared to the outer skin. A detailed examination of this region revealed that the inboard surface of the outer skin was painted and contained no clad layer. Examination of Figure 2 suggests that the outboard surface of the inner skin also contained no cladding along the faying surface. Further metallography revealed that the outboard surface did contain clad earlier in life and, as intended, the clad layer sacrificially corroded during the crevice corrosion process.

Figure 3 shows a second cross section along a line perpendicular to the rivet line which intersected two of the rivets. The separation of the inner and outer skins reached almost 2.5 mm at the point halfway between the two rivets. Complete penetration of the outer skin occurred in several locations. The build-up of corrosion products pushed the outer skin away from the rivet head located on the left of Figure 3a. The micrograph in Figure 3b reveals the intergranular and intersubgranular corrosion morphology of exfoliation damage process. Figure 3c shows the location (bracket) noted in Figure 3b using polarized light. The bright lines correspond to the edges of the original paint layer which has completely delaminated from the faying surface of the outer skin. Figure 3d shows the large pit that

formed below the rivet head shown in Figure 3a. Close inspection reveals the attack to be predominantly intergranular.

A number of rivets were removed and examined metallographically. Figure 4a shows a typical rivet containing a crack located at the head-shank transition region. An intergranular crack grew from the point of high stress concentration and propagated approximately 220 μm as shown at high magnification in Figure 4b. The majority of rivets removed from this region contained similar environment assisted intergranular cracking in the identical head-shank region.

Occluded Site Analysis

The species that are present during corrosion are often trapped in the resulting corrosion products. The rehydration of the corroded areas thereby allows an analysis of the ionic constituents that were responsible for the corrosion during service. Four anions were detected in the soak solution from the interior of the joint as shown in Figure 5 and Table 1. In order of predominance, sulfate, chloride, nitrate, and fluoride were present. Separate analyses by CE showed that neither chromate nor small organic acids (i.e., acetate, formate,...) were present at levels above the detection limits (250 ppb for chromate, 680 ppb for acetate, ...) in the soak solution. Four cations were detected in the soak solution as shown in Table 2. Figure 6 shows electropherograms of the alkali, alkali earth, and transition metals found within the corroded lap splice as well as a standard. Neither copper nor ammonium was measured above the detection limits (130 ppb for copper, 110 ppb for ammonium) in the soak solution.

Electrochemical Analysis

The electrochemical behavior of aluminum alloy (AA) 2024-T3 was determined in three solutions having compositions based upon the analysis of the soak solution from the interior joint as shown in Table 3. The composition shown in Table 3 is influenced by the volume of water used to rehydrate the corrosion products. The volume of solution originally present in the lap splice joint during service is unknown; thus, the degree of dilution during the rehydration process is unknown. In order to take the volume uncertainty into account, three solutions were studied all of which had the same ratio of ions as the soak solution. The three solutions differed in the total concentration of ions present as a means of taking into account the uncertainty concerning the active volume that was present during the corrosion.

In addition, two pH values were studied, the natural pH of the soak solution (10.5) and an acidic pH of 3.2. Under different conditions, occluded corrosion regions of aluminum alloys can develop either alkaline or acid pH values [14,15]. The composition of Solution A was that of the soak solution as analyzed. The combination of the salts used resulted in chloride and sulfate levels three times that of the measured soak solution. The natural pH of this solution was 10.5. Solution B consisted of the same salts as Solution A but at

concentrations ten times higher. The pH was 10.5. The composition of the Solution C was, like Solution B, ten times that of the original soak solution, but the pH was 3.2 due to the use of AlCl_3 , CaSO_4 , and MgSO_4 , rather than hydroxides of these metals. Note that this combination led to sulfate concentrations twice that of Solution B and chloride concentrations twenty times higher.

Figure 7 shows the electrochemical behavior observed in the three solutions. In Solution A, the alloy is spontaneously passive and dissolves at very low rates ($< 10 \mu\text{m/y}$) over a wide range of potentials. The solution of lower pH (Solution C) shows very similar behavior. Despite the higher concentration of chloride, no pitting or localized attack was observed after polarization. Solution B shows dramatically different behavior. A small active/passive transition is observed, and a passive current density corresponding to a uniform penetration rate of almost $100 \mu\text{m/y}$ is observed before localized attack of the surface occurs above a potential of $+0.1 \text{ V(SCE)}$.

DISCUSSION

This work combines extensive metallographic examination and occluded site solution analysis from a retired aircraft with electrochemical measurements to lay the foundation for the development of a protocol for identifying the relevant solution compositions to be used in the development of input data for lifetime prediction models of aging aircraft.

Metallographic Analysis

There is a clear correlation between the severe corrosion of the outer skin observed in the cross-sectional photomicrographs and the observation of pillowing on the external surface. The corrosion products which eventually precipitate along the faying surface force the outer skin outwards, leading to the characteristic pillowed appearance. The transformation of elemental aluminum into alumina (Al_2O_3) leads to a volume expansion of approximately 34%, assuming that the corrosion products form with the atomic density of pure Al_2O_3 . Calculations considering other possible corrosion products (e.g., Al(OH)_3) lead to similar qualitative conclusions. The stresses that can develop due to corrosion product formation in restricted sites can be extremely large, as evidenced by the complete fracture of rivet heads noted in Figure 1. As the lap splice joint deforms, ingress into the joint by corrosive agents via the mechanisms described above becomes increasingly easy. The corrosion products will tend to be somewhat porous, which will also increase the tendency to draw in and retain moisture. Thus, once initiated, the physical structure of the environment will favor continued corrosion attack.

Microscopically, exfoliation corrosion is the primary mode of corrosion attack of the outer skin as shown in Figures 2 and 3. Precipitation hardened aluminum alloys in wrought form are well known to be susceptible to exfoliation in certain tempers [13]. The deformation during the thermomechanical processing leads to the formation of elongated,

pancake-shaped grains. Under certain environmental conditions, the grain boundaries are preferentially attacked. For AA2024-T3, the generally accepted mechanism involves the dissolution of copper-depleted regions near Al_2CuMg (S-phase) particles which nucleate and grow at the grain boundaries during thermomechanical processing. As these regions corrode, voluminous corrosion products precipitate, forcing the grains apart. In an analogous manner to the macroscopic effects observed in pillowing, the regions between the particles of corrosion product formed during exfoliation act as capillaries, drawing in additional solution which allows the corrosion process to continue.

In the lap splice joint studied, it appears that some of the rivets suffered intergranular, stress-corrosion cracking. The chemistry of the water that was drawn into the rivet head/outer skin crevice was modified by the corrosion processes as discussed above. This solution led to the initiation and propagation of the intergranular crack shown in Figure 4. Environmental assisted cracking (EAC) of the rivet head was a result of the combination of rivet clamping force and outer skin pillowing force evidenced in Figure 3. The head/shank transition is the most susceptible region due to the simultaneous presence of maximum stress concentration and the aggressive environment of the occluded faying surface. The susceptibility of this region is highlighted by the preferential dissolution of the head/shank transition coincident with the faying surface shown in Figure 3d.

In the cross-sectional views shown in Figures 2 and 3, the extent of attack of the outer skin was much greater than that of the inner skin. Detailed metallography in a region of the lap splice joint that contained little corrosion revealed that the inner surface of the outer skin was painted with no clad layer and the inner skin outer surface was protected by an aluminum clad layer as shown in Figure 2. The initiation of corrosion on the inner surface of the outer skin is expected once corrosion penetrated and subsequently undercut the painted surface shown in Figure 3. The inner skin remained nearly intact except for the inner clad which has sacrificially corroded away. It should be noted that the inner skin was attacked severely at some sites, although the outer skin was more severely attacked in general.

At several locations, the 1.2-mm-thick outer skin was completely penetrated by corrosion. Although accurate assessments of the rate of attack are impossible due to the lack of information regarding the time to the initiation of attack, some estimates can be made. Based upon the known service life of the aircraft of 19.75 years and assuming that the corrosion occurred at the midpoint of the service life, the average penetration rate would be on the order of $100 \mu\text{m}/\text{y}$. Although the attack could have initiated somewhat earlier or later, this estimate provides a reasonable value for assessment of the corrosion conditions required.

Occluded Site Solution Analysis

The rehydration of the corroded lap splice joint allowed the analysis of the major ionic species present. Some reasonable speculation of the sources of the Na^+ , Ca^{2+} , NO_3^- , SO_4^{2-} , Cl^- , and F^- can be made without a complete service history of the aircraft. The NO_3^- and SO_4^{2-} most likely come from the ingress of pollutant gases, and moisture, followed by oxidation of NO_x and SO_2 . The Cl^- can have multiple sources, including moist coastal environments and chlorinated tap water. The F^- may have been trapped in the oxide of alloy

during surface treatments (e.g., desmutting) as also seen by others [16]. Cations such as Al^{3+} and Mg^{2+} originated in the alloy. Cations such as Na^+ and Ca^{2+} are ubiquitous in the natural environment.

The relative concentrations of the ions should be considered carefully. The finding shown in Figure 5 that suggests sulfate was the dominant anion (concentrations an order of magnitude higher than chloride) has important implications for the design of test solutions relevant to aging aircraft lifetime prediction studies. These results clearly show that the use of simple simulants such as 3.5% NaCl in corrosion testing for this application is inappropriate. Any correlation between corrosion behavior measurements in such simulants and the performance of the tested materials in aircraft would be fortuitous.

Although the focus of developments in test solutions will be on the species detected, the absence of certain species in the soak solution can also give insight into the evolution of the corrosion within the joint. The lack of chromate indicates either the absence or exhaustion of any chromate reservoir. The Cr^{3+} cation (if present) would support ideas of Brown et al. related to reduction of chromate and precipitation of $\text{Cr}(\text{OH})_3$ in conversion coating as protection mechanism [17]. The lack of measured small organic acids indicates that chemical degradation of the coating was not likely responsible for onset of attack.

Estimation of Occluded Site Chemistry

Because corrosion is an electrochemical process, electrochemical techniques can be used to determine the kinetics of dissolution reactions as a function of solution chemistry and other variables. Through Faraday's second law, the dissolution rate (in units of $\mu\text{A}/\text{cm}^2$) can be translated to a uniform penetration rate (in units of $\mu\text{m}/\text{y}$). In order to use electrochemical data for life prediction, the test environment must well simulate the service environment.

Lap splice joint corrosion chemistry can be estimated. The relative abundance (peak area) of the species identified in Figures 5 and 6 was used to determine the ionic concentration in the soak solutions. Knowing the injection volume, the masses of each of the species can be calculated. Converting these data into estimates of the concentrations present during the corrosion process requires estimation of the active volume. Estimates of the active volume are difficult, particularly for cases such as the lap splice joint in which all of the water has evaporated. Rather than attempt to estimate the volume, concentration factors can be used. In the present case, the problem of active volume can be handled by assuming that the solution is saturated. Such an assumption is reasonable based upon the exfoliation nature of the attack which relies on the precipitation of corrosion products within the attacked region for continued propagation. In order to determine the proper concentration factor, solutions with the ionic concentrations found by the capillary electrophoresis were cycled up until saturation was reached. For the present investigation, two concentration factors were examined, 1x and 10x. At the higher concentration factor, slight precipitation occurred, indicating that saturation had been reached. Higher concentration factors were not considered because such solutions could not accurately reflect the ionic ratios measured.

In addition to the solution concentrations, the pH of the localized corrosion site must also be carefully considered. Because Al is amphoteric, the pH of the localized corrosion site can be either acid or alkaline. The work of Wall [14] as well as Holroyd et al. [15] indicate that when a boldly exposed cathode is present, the pH within localized corrosion sites fall to approximately 3.5, whereas in the absence of a boldly exposed cathode, the pH rises due to the formation of hydroxyl within the occluded site by water reduction. In a lap/splice, we would therefore expect an alkaline pH. The pH measurements of simulated corrosion sites with no boldly exposed cathode showed pH levels of 9.5-11 [14,15]. Charge balance of the retrieved solutions supports this idea (i.e., the sum of the charge from the anions measured was less than the sum of the charge from the cations measured). However, both acidic and alkaline pH solutions were studied for completeness.

Electrochemical Behavior of AA2024-T3 in Occluded Site Simulants

The electrochemical behavior of AA2024-T3 in simulated lap splice joint occluded environments shown in Figure 7 demonstrates the importance of both concentration factor and pH on the corrosion rate. At 1x (Solution A, the solution composition found by the capillary electrophoresis), the material is spontaneously passive with low (5-10 m/yr) dissolution rates. A solution with a concentration factor of 10 (Solution B, solution concentrations ten times higher than the original soak solution, but with the same pH = 10.5), the material undergoes an active/passive transition, with much higher (ca. 100 $\mu\text{m}/\text{yr}$) dissolution rates. The solution pH was also key. Solution C, the pH 3.2 solution, even with a concentration factor of 10, shows very low corrosion rates. The penetration of the skin during service cannot be rationalized with the rates from the pH 3.2 data.

In a lap/splice joint, we would expect the material to be at or very near its open circuit potential due to the lack of a boldly exposed cathode to polarize it anodically. Assuming that no boldly exposed cathode was available to polarize the localized corrosion site within the lap splice joint, estimates of the corrosion rate can be made for each of the site simulants. Although the open circuit corrosion rates for AA2024-T3 exposed to Solutions A and C were on the order of $< 1 \mu\text{m}/\text{y}$, the dissolution rate of the alloy in Solution B was much higher, with open circuit corrosion rates which can rationalize the observed attack. Although such estimates assume uniform dissolution, they provide a means of comparison for the different site solutions.

CONCLUDING REMARKS

The combination of metallographic and occluded site analyses allowed an in-depth investigation of the nature of the corrosion within the lap splice joint from a retired commercial aircraft. The metallographic analysis showed that the nature of attack was predominantly exfoliation corrosion which caused massive thinning of the fuselage skin. The large volume change associated with the corrosion products build-up led to the lap splice joint pillowing and the build-up of extremely high local stresses in the fuselage skin. This

damage mode led to the failure of rivets by stress induced environment-assisted cracking and the eventual loss of structural integrity of the lap splice joint.

The rehydration of corroded areas of lap/splice joints removed from retired aircraft with subsequent analysis by CE provided a means to assess the chemical conditions which led to the observed attack. Sulfate was the dominant anion present, existing at a 10:1 ratio over chloride. Small amounts of nitrate and fluoride were also found. Both solution analysis and electrochemical measurements in occluded site simulants indicated that the occluded site solution that developed during service had an alkaline pH. The electrochemical measurements in bulk simulants designed on the basis of the CE analysis were able to rationalize the extent of the attack observed.

Results support the following description of the corrosion in aging aircraft lap splice joints. Initially, condensate and ionic contaminants (Na^+ , Ca^{2+} , K^+ , NO_3^- , SO_4^{2-} , Cl^- , and F^-) combined in the lap splice to form a corrosive electrolyte. Supporting cathodic reactions within the joint produced hydroxyl which promoted an increase in the local pH, further accelerating the corrosion. Precipitation of corrosion products drew in additional water by capillary action allowing the attack to continue. As the corrosion accelerated, the precipitated corrosion products along the faying surface stressed the lap splice skin and rivets leading to the observed pillowing, skin cracking, and rivet failure.

ACKNOWLEDGMENTS

This research is supported by a joint NASA-U.S. Air Force effort under Grant No. NAG-1-1841. The authors wish to recognize the program support of Donald E. Neiser, Tinker AFB and Clare A. Paul, Wright Laboratory. Equipment support from Waters Corporation and E.G.& G. Princeton Applied Research is also gratefully acknowledged.

REFERENCES

1. Corrosion Control For Aircraft, Advisory Circular 43-4A, US Dept. of Transportation, Federal Aviation Administration, July 1991.
2. NTSB Aircraft Accident Report, 89/03 (1989).
3. Aviation Week & Space Technology, March 18, 1996.
4. Sinclair, J. D.: in *Manual on Corrosion Tests and Standards*, R. Baboian, ed., ASTM, Philadelphia, pp. 166-175 (1995).
5. Turnbull, A.: in *Advances in Localized Corrosion*, H. S. Isaacs, U. Bertocci, J. Kruger, and S. Smialowska, eds., NACE, Houston, 359 (1990).
6. Fontana, M. G. and Greene, N. D.: *Corrosion Engineering*, McGraw-Hill, New York, 41 (1967).
7. Szlarska-Smialowska and J. Mankowski, *Corros. Sci.*, 18, 953 (1978).
8. Turnbull, A., in *Embrittlement by the Localized Crack Environment*, R. P. Gangloff, ed., TMS-AIME, Warrendale, PA, p. 3 (1984).
9. Kelly, R. G., Scully, H. S., and Stoner, G. E.: "Corrosion of Packaged Galvanized Steel Analyzed by Capillary Electrophoresis," *British Corrosion Journal*, 28, No. 3, pp. 1-4 (1993).
10. Olefirowicz, T. M. and Ewing, A. G.: *Anal. Chem.*, 62, 1872 (1990).
11. Jones, W. R. and Jandik, P.: *American Laboratory*, 22, 51 (1990).
12. Jandik, P. and Bonn, G.: *Capillary Electrophoresis of Small Molecules and Ions*, VCH Publishers, New York (1993).
13. Sprowls, D. O.: in *Corrosion Tests and Standards: Application and Interpretation*, R. Baboian, ed., Amer. Soc. for Testing and Materials, Philadelphia, 218 (1995).
14. Wall, F. D.: "Environmental Assisted Cracking of Al-Li-Cu Alloys 2090 and 2095," Ph.D. Dissertation, University of Virginia, (1996).
15. Holroyd, N. J. H., Scamans, G. M., and Hermann, R.: in *Corrosion Chemistry within Pits, Crevices, and Cracks*, A. Turnbull, ed., Her Majesty's Stationery Office, London, 495 (1987).
16. Cooper, K. R.: "A Development of a Quantitative Test for the Exfoliation Resistance of Aluminum Alloy 7075," M.S. Thesis, University of Virginia, (1995).
17. Brown, G. M., Shimizu, K., Kobayashi, K., Thompson, G. E., and Wood, G.C.: *Corrosion Sci.*, 34, 1045 (1993).

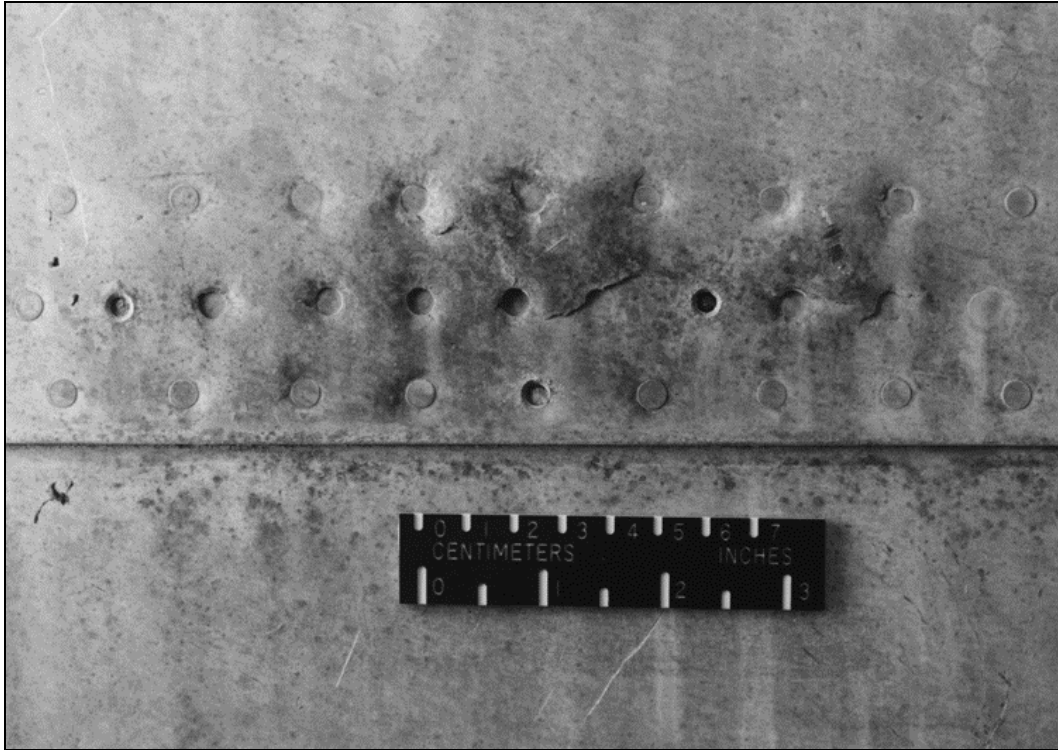


Figure 1. Macro photograph of lap splice joint removed from the retired aircraft. Note the pillowed appearance of the skin just above the joint. Several rivet heads had failed during service. The scale on the top of the ruler is in centimeters.

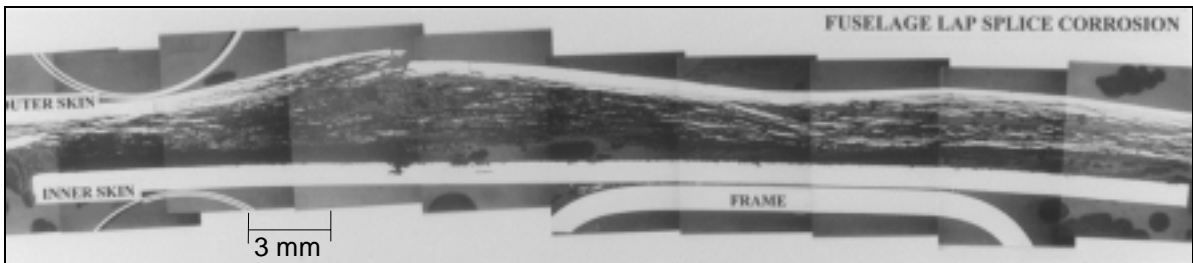


Figure 2. Montage of photomicrographs from a cross section of the lap splice joint which did not intersect any rivets. Outer skin, inner skin, and frame are indicated. The massive exfoliation attack of the outer skin is apparent. Note the complete penetration of the outer skin by corrosion in one region.

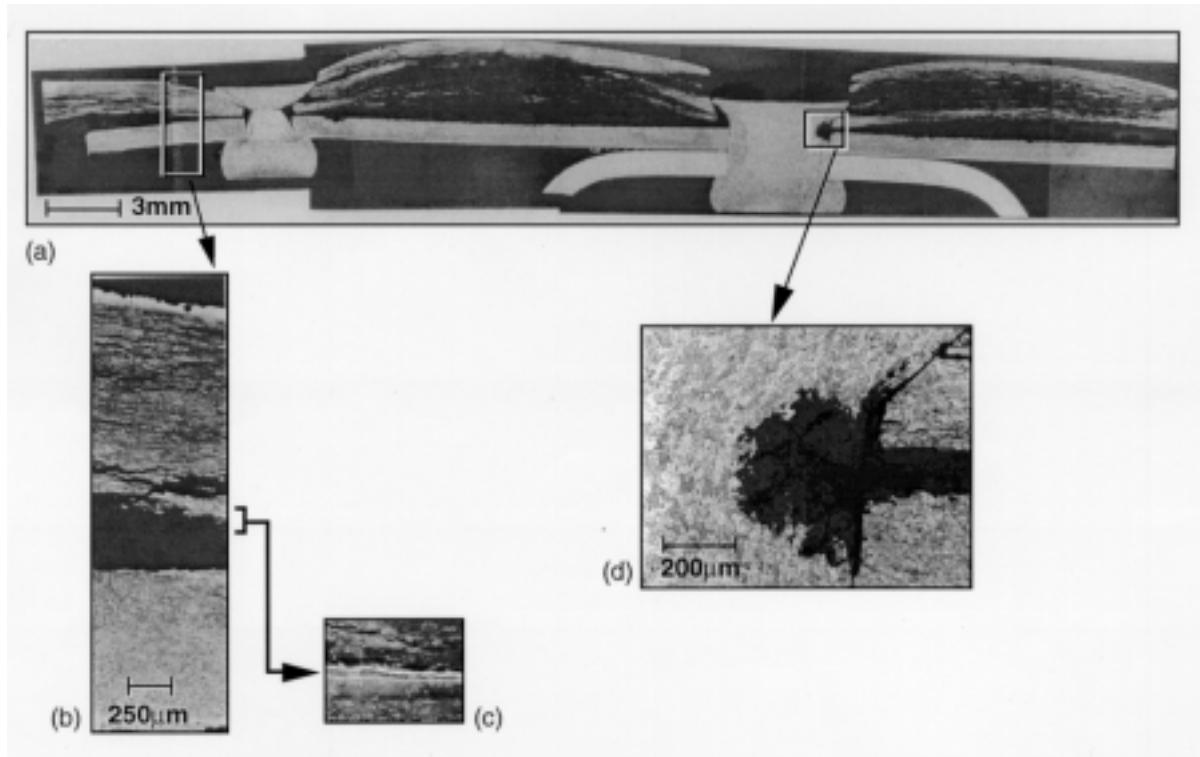


Figure 3. (a) Montage of photomicrographs from a cross section of the lap splice joint which intersected two rivets. Note the separation of the outer skin from the rivet heads in several places. (b) Photomicrograph showing higher magnification of exfoliation attack. (c) Photomicrograph using polarized light to highlight the surface coating which was undercut by the corrosion on the inner surface of the outer skin. (d) Photomicrographs showing the extensive rivet corrosion at the faying surface interface.

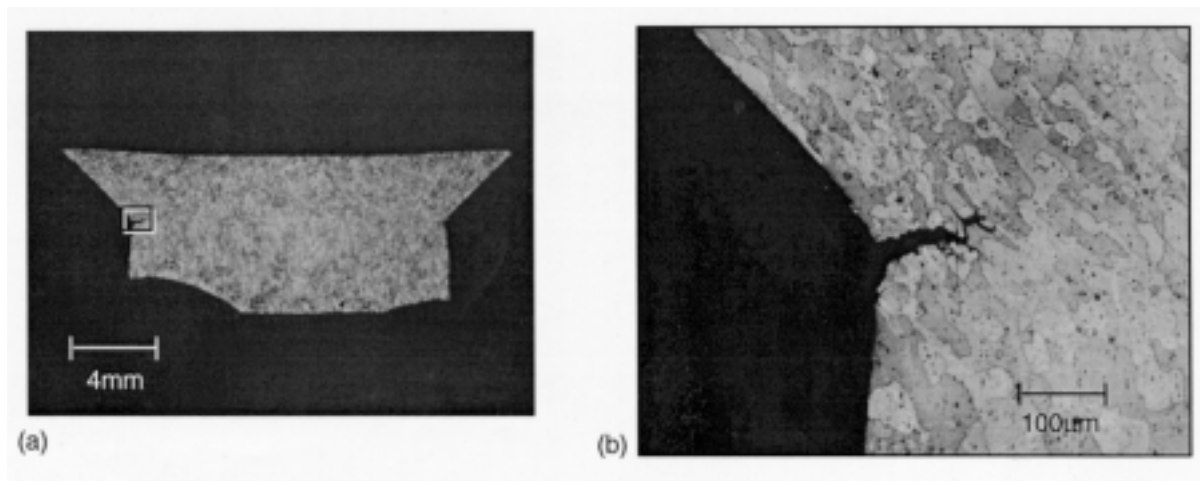


Figure 4. (a) Overview showing location of a rivet crack. (b) Photomicrograph showing the intergranular crack at head/shank transition region.

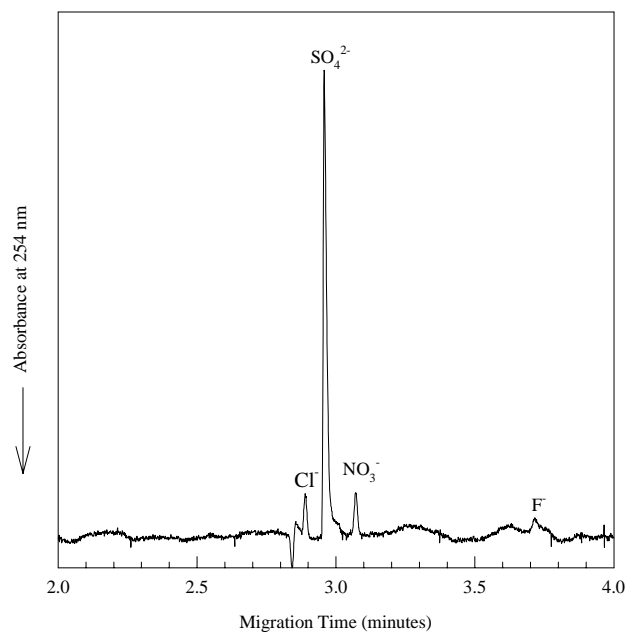


Figure 5. Electropherogram of anions in soak solution from interior of retrieved lap splice joint showing the presence of Cl^- , SO_4^{2-} , NO_3^- , and F^- . Chromate electrolyte used.

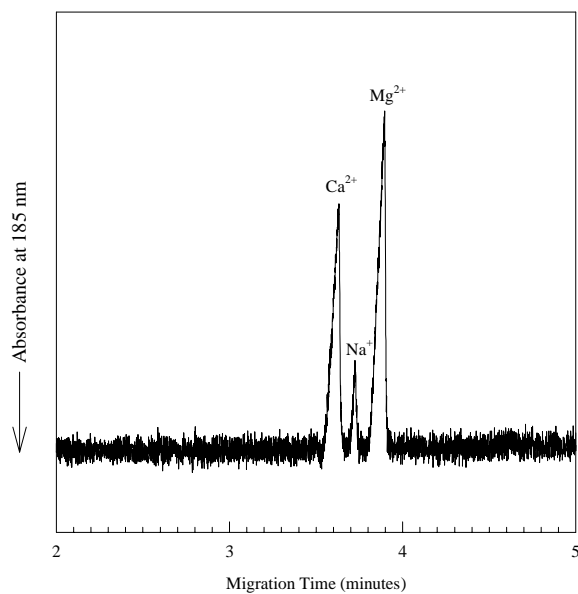


Figure 6. Electropherogram of alkali, alkali earth, and transition metal cations in soak solution from interior of retrieved lap splice joint showing the presence of Na^+ , Ca^{2+} , and Mg^{2+} .

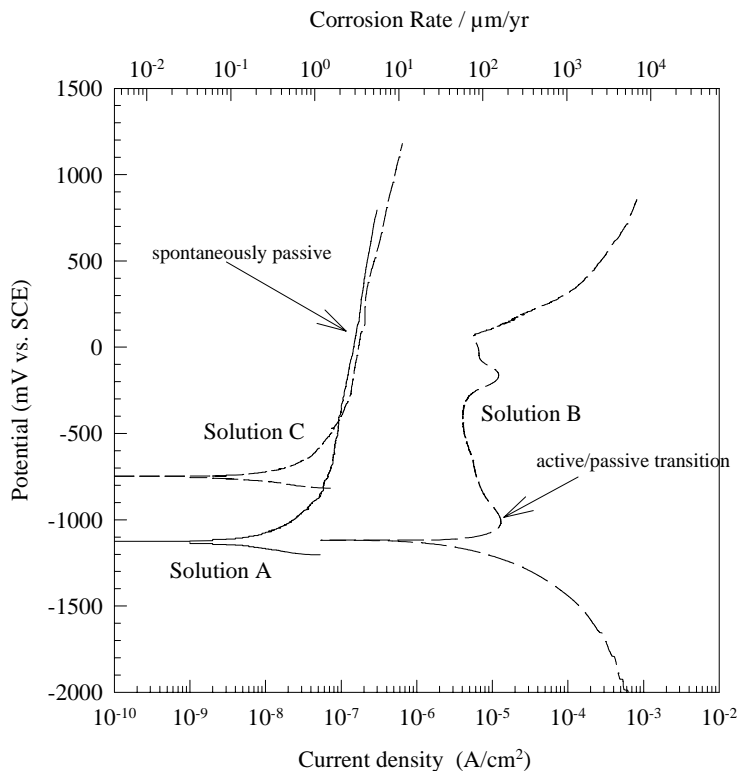


Figure 7. Electrochemical behavior of AA2024-T3 in bulk simulants of occluded site solutions. Spontaneous passivity and accompanying low-rate dissolution were observed for the material exposed to either Solution A (pH 10.5, concentration factor of 1) and C (pH 3.2, concentration factor of 10). An active/passive transition and high dissolution rates were observed in Solution B (pH 10.5, concentration factor of 10). All solutions were deaerated and the tests were conducted at room temperature.

Table 1. Concentrations of cations detected by capillary electrophoresis of soak solution from rehydration of corrosion products on interior of the retrieved lap splice joint.

Species	Soak Solution Concentration (mM)
Cl ⁻	0.007
SO ₄ ²⁻	0.077
NO ₃ ⁻	0.0108
F ⁻	0.0047

Table 2. Concentrations of anions detected by capillary electrophoresis of soak solution from rehydration of corrosion products on interior of the retrieved lap splice joint.

Species	Soak Solution Concentration (mM)
Ca ²⁺	0.197
Na ⁺	0.002
Mg ²⁺	0.251
Al ³⁺	0.142

Table 3. Concentrations of salts used to generate different simulated occluded site solutions for electrochemical testing of AA2024-T3.

Species	Concentrations (mM)		
	Solution A	Solution B	Solution C
Al(OH) ₃	0.142	1.42	
Ca(OH) ₂	0.197	1.97	
CaSO ₄	-	-	1.97
MgCl ₂	0.011	0.11	
MgSO ₄	0.240	2.40	2.51
NaNO ₃	0.0108	0.108	0.108
NaF	0.0047	0.047	0.047
AlCl ₃			1.42
pH	10.5	10.5	3.2

DESIGNING FOR THE DURABILITY OF BONDED STRUCTURES*

W. Steven Johnson
School of Materials Science & Engineering
Georgia Institute of Technology
Atlanta, GA 30332-0245

Lawrence M. Butkus
School of Mechanical Engineering
Georgia Institute of Technology
Atlanta, GA 30332-0405

SUMMARY

The continued airworthiness of aging aircraft and long-term durability of new airframes depends, in part, on the integrity of adhesive bonds used for repairs and in joining structural components. Additionally, the advent of composite materials and advanced repair techniques have increased the number of adhesively bonded joints specified for use in aerospace structures. Traditionally, adhesive bonds have been analyzed and designed using a dependable and rigorous stress-based approach. However, the need to address the effect of bondline flaws and to understand the fatigue characteristics of bonded joints has led to the adoption of an analysis already common in the design of metallic components - fracture mechanics. To further understand the durability of bonded structures, however, it is also necessary to examine the effect of environmental exposure on the performance of the adhesive bondline. This paper will briefly discuss the attributes of the two main forms of bonded joint analysis and will also provide a broad outline of a design philosophy that combines fracture mechanics with an assessment of environmental effects. A summary of recent results from a study of the effect of environmental exposure on the Mode I fracture toughness and fatigue crack growth characteristics for an aluminum/epoxy bonded system is also included.

BACKGROUND

Adhesive bonding of aerospace components is a fabrication technique which, though over 70 years old, has increased markedly in popularity during the last two decades and is currently a focal point in many studies regarding aging aircraft. Military applications of adhesive bonding began in the early days of flight and during the First World War. Significant breakthroughs such as the use of phenolic resins in wood and wood-to-metal joints occurred during the World War II era on aircraft such as the RAF's *Mosquito*.

* Research performed at Georgia Institute of Technology under FAA William J. Hughes Technical Center Grant #95G023, Technical Monitor: Dr. Don Oplinger

Building upon these advances, engineers at Fokker began bonding structural metal components on the successful F-27 and F-28 series in the late 1940's and early 1950's.^{1,2} Military use of bonded metal structures occurred almost simultaneously on aircraft like the USAF's B-58 *Hustler*.³

A highly successful program investigating bonding for use in joining metal aircraft components was the Primary Adhesively Bonded Structures Technology (PABST) program^{4,5} sponsored by the USAF in the late 1970's. This program's results confirmed and expanded the list of advantages offered by properly manufactured adhesive bonds over riveted assemblies including reduced weight, increased fatigue resistance, improved sealing capabilities, more efficient aerodynamics, and, often, reduced costs.

These advantages, combined with the increase of structural composite assemblies, have expanded the number of adhesive bonds used in primary and secondary aircraft structures. For example, the amount of adhesively bonded honeycomb construction on commercial airliners is extensive. In addition, military aircraft such as the F-16, F-18, and the future F-22 employ significant amounts of adhesively bonded polymer matrix composite laminates for wing skins and control surfaces.

Coincident with this rise in popularity of bonds for structural fabrication, advances in repair technology and an increased emphasis on extending the lifetimes of aging aircraft, have focused a great deal of interest on the use of adhesives for repairs. Pioneering work in Australia⁶ and the US⁷ resulted has in broad usage of bonded repairs on military and commercial aircraft. Although carbon fiber reinforced composites⁸ and GLARE™ laminates⁹ have been employed, the most common bonded repair system consists of a boron-epoxy composite laminate bonded to an aluminum airframe using a modified epoxy adhesive. Though no exhaustive survey exists of all bonded aircraft repairs, an estimated 6500 boron-epoxy patches are in use on military aircraft and over 200 have been applied to commercial aircraft worldwide.¹⁰ The most prevalent use of this technique has been the repair of nearly 500 fatigue cracks emanating from wing skin fuel transfer holes ("weep holes") on the USAF C-141 fleet.¹¹ The primary advantage offered by these repairs is a significant reduction in crack growth in the underlying metallic structure. This problem has been studied extensively,^{12,13,14} with the reduction in stress levels and ΔK at the crack tip and an increase in patched component life being well-documented.

Despite prior successes in wood, metal, and composite bonded joints and repairs, questions still remain regarding the durability and damage tolerance of the adhesive bondline, the critical region upon which the integrity of the bonded repair or assembly depends. Though dimensionally small compared to the adherends, the bondline contains not only the adhesive but interphase regions and is the complex and crucial component of any bonded structure. Thus, understanding the affect of defects and service environments on the adhesive is necessary to assess the long-term performance of bonded structures. This issue is of critical importance in the current climate of extending the lives of existing aircraft and of creating new designs intended for operational periods measured in decades rather than in years.

PREVIOUS RESEARCH

Previous research of bonded joint analysis and design may be grouped into two major areas of emphasis. The first, a stress-based approach, was initiated by Goland & Reissner,¹⁵ and has been used extensively by Hart-Smith,⁵ Hart-Smith & Thrall,¹⁶ and others. This approach has focused on determining the distribution of shear and normal (or “peel”) stresses within the adhesive bondline under static loading conditions. In their seminal work, Goland & Reissner investigated single lap shear joints with thin (inflexible) and thick (flexible) adhesive layers. Their results indicated that both shear and normal stresses approach maximums at or near the free edge of the joint. Adams¹⁷ confirmed this observation and, using a finite element analysis, proposed that failure of the adhesive layer occurs in tension due to the high peel stresses rather than in shear as suggested by the lap shear joint’s name. The importance of peel stresses, therefore, has been incorporated into bonded joint design, and current criteria call for their elimination or drastic reduction.^{4,5,17} The presence of stress concentrations at the edges of a joint combined with a lightly loaded though useful region of adhesive at the center has led to techniques that reduce the magnitude of the near-edge stresses such as increased overlaps and tapered adherends. To date, the stress-based approach to bonded joint design has functioned well, has been incorporated into computerized design programs used in the aerospace industry, and has contributed to the success of the USAF’s PABST program and subsequent adhesively bonded designs.

However, in order to more accurately evaluate the effects of bondline flaws and fatigue, a second, parallel approach to the examination of bonded joints based on the principles of fracture mechanics has emerged. Founded upon the basic theories developed by Griffith and Irwin, the use of fracture mechanics for bond analysis was first proposed by Ripling, Mostovoy, & Patrick.¹⁸ At the time of their research, the stress intensity factor, K , had become accepted for describing fracture in homogeneous metals. However, recognizing the inhomogeneity of bonded systems, Ripling *et al.* proposed the use of the strain energy release rate, G , to describe fracture in adhesive joints. More recent research by Shaw¹⁹ explored the restriction of the plastic zone within the adhesive layer by the adherends and reinforced the logic of choosing an energy (G) approach. A number of specimens have since been developed to investigate the Mode I, II, and/or III fracture and fatigue behavior of adhesively bonded joints. The most common is the double cantilever beam (DCB) which tests the resistance to Mode I cracking. Realistic mixed-mode behavior may be addressed using specimens such as the cracked lap shear (CLS) developed by Brussat *et al.*²⁰ and the mixed mode bending (MMB) test designed by Reeder and Crews.²¹

The DCB and CLS specimens were used by Johnson & Mall^{22,23} to examine the fracture toughness and fatigue crack growth characteristics of bonded composite joints. In fatigue tests on graphite reinforced composites bonded with various epoxies, the authors developed da/dN vs. G_{total} curves similar to the da/dN vs. ΔK relationships used to describe fatigue in metals. Other key conclusions from their work include observations that fatigue cracks in the bondline may propagate in the absence of peel stresses and at applied strain energy release rate (G) levels lower than the fracture toughness (G_C).

A FRACTURE MECHANICS APPROACH TO DURABILITY

Design of metal aerospace components has successfully integrated a static or yield strength analysis with fracture mechanics to accommodate various philosophies ranging from safe-life to fail-safe to durability and damage tolerance. The design of adhesively bonded structures can also benefit from a similar and deliberate pursuit of stress-based and fracture mechanics analyses. However, in order to fully understand the durability of adhesively bonded joints, the effect of operating environments on the fatigue and fracture properties must also be known. Though groundwork has been laid by the investigators previously mentioned and by studies of the effects of various environments on some adhesive properties, needs still exist to address the performance of specific adherend-adhesive combinations and to combine environmental, fatigue, and fracture studies of bonded systems.

For example, it is known that moisture absorption results in varying degrees of plasticization, strength loss, and increased ductility of some epoxy adhesives. However, the effect of moisture on the fatigue and fracture properties of bonded joints employing these adhesives is still not fully understood. In addition, since adhesive joints are systems comprised of adhesives and interphase regions, the performance of both may strongly affect the performance of the joint as a whole. Thus, knowledge of the behavior of adhesives exposed to various environments must be supplemented by knowledge of the behavior of specific bonded systems.

In reviewing some of the trends observed by Johnson, Mall, and Mangalgi²²⁻²⁴ for room temperature behavior of as-received specimens, it appears that environmental exposure may affect the behavior of bonded joints in several ways that can be highlighted using fracture mechanics analyses. Figure 1 illustrates some possible effects on the static and cyclic properties of adhesive joints. As shown (Figure 1a.), environmental exposure may affect the fracture behavior of bonded joints by changing the fracture toughness in general or by preferentially changing the fracture toughness in one mode compared to another. Such changes in the fracture toughness may translate into effects on the fatigue behavior in the form of a shift in the locus of da/dN vs. G_{total} data (Figure 1b.), indicating a change in the threshold level and rate of crack growth. Alternatively, the effect on fatigue behavior may be manifested by a change in the slope of the da/dN vs. G_{total} data, indicating a change in the sensitivity of the crack growth rate to changes in applied load or strain energy release rate. Figure 1 reflects the changes as detrimental, but there is no reason to doubt that exposure to some environments may enhance bonded joint performance.

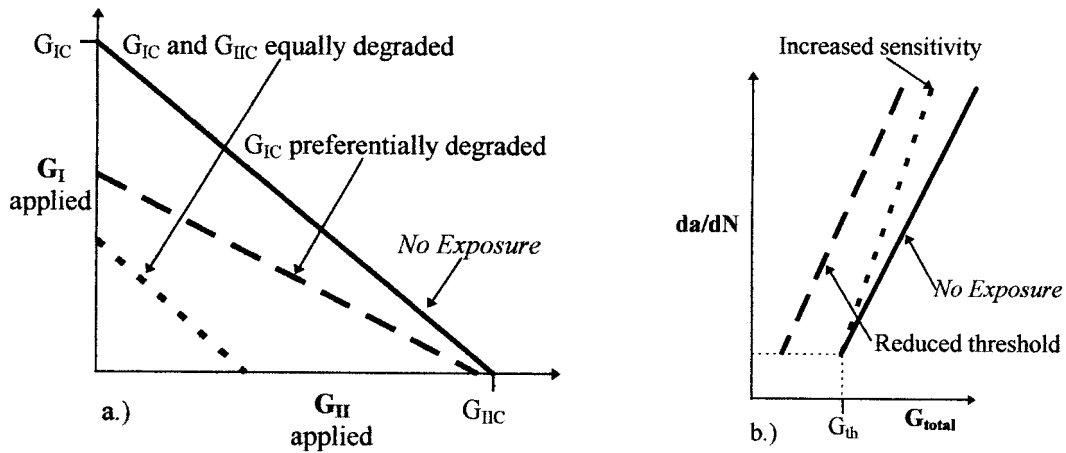


Figure 1. Possible Environmental Effects on the a.) Fracture Toughness and b.) Fatigue Crack Growth Behavior of Adhesively Bonded Joints.

The importance of these possible trends is crucial to designers for it is their task to ensure a bonded joint's integrity over the life of the structure. Knowledge of these trends may result in so called "knockdown" factors to limit the loads applied to affected joints or alterations in the geometric designs of the joints. Figure 2 shows, for a case where exposure has shifted the crack growth threshold, that environmental effects may also force geometric modifications to be made in order to achieve a desired design lifetime for a given cyclic stress level. Such modifications may reduce the applied total strain energy release rate (G_{total}) perhaps though changes in the adherend taper angle. For the case where one mode of toughness is preferentially attacked, other design changes may permit a bonded joint to be loaded in a manner that better exploits its less-degraded properties. In any case, knowledge of the way in which the environment affects a joint's fatigue and fracture properties will lead to improved designs.

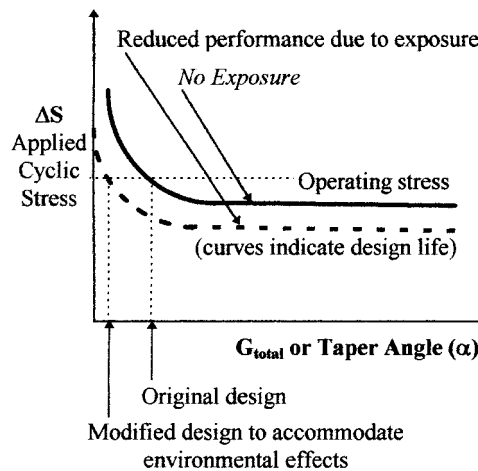


Figure 2. Environmental Exposure Effects May Require Design Changes to Meet Operating Requirements.

Thus, to design efficient, effective, and durable bonded joints, it is necessary to determine the effect of service environments on the properties examined by stress-based and fracture mechanics approaches. Changes in strength, preferred mode of fracture, and crack growth behavior during long-term exposures will affect the design of adhesive joints used for structural and repair purposes. Through the use of stress analyses to ensure adequate static strength, fracture mechanics, and fatigue analyses to ensure adequate damage tolerance, and environmental studies to ensure adequate long-term durability, adhesively bonded aircraft joints, and repairs can be designed and fabricated to meet the increasingly stringent requirements for extended aircraft lifetimes.

RECENT EXPERIMENTAL INVESTIGATIONS

In research at the Georgia Institute of Technology, the behavior of several bonded joint systems is being investigated using fracture mechanics and the philosophies previously described. These systems include aluminum/epoxy and aluminum/epoxy/boron-epoxy in support of the USAF C-141 transport program, graphite-bismaleimide/epoxy for the new F-22 fighter, and titanium/polyimide from the High Speed Civil Transport program. The Mode I, Mode II, and mixed-mode behavior of these systems will be examined using double cantilever beam (DCB), end notched flexure (ENF), and cracked lap shear (CLS) geometries, respectively. The aim of this study is to apply fracture mechanics concepts in evaluating the durability of bonded systems used in repair and construction of aerospace structures. Thus, the intent is to examine the behavior of cracks in the bondline rather than to investigate the fracture and fatigue characteristics of cracks in an aluminum structure repaired or reinforced with a bonded doubler. A major objective is to identify trends in the fracture toughness, critical strain energy release rate (G_C) and fatigue threshold (G_{th}), caused by environmental exposure. A short synopsis of results from the Mode I fracture and fatigue testing of environmentally exposed specimens comprised of the same aluminum/epoxy system used in the PABST program is presented in the following sections.

Specimen Geometry, Materials, and Fabrication. The DCB specimens used for this research were nominally 25 mm (1 in) wide and 305 mm (12 in) long (Figure 3). Adherends consisted of 9.26-mm (0.375-in)-thick bare 7075-T651 aluminum. Lockheed Martin Aeronautical Systems Co. (Marietta, GA) fabricated the specimens using standard manufacturing procedures with FM-73M (1.42 kg/m² [0.06 lb/ft²]), a toughened epoxy adhesive containing a random polyester mat (Cytec, Havre de Grace, MD).

Prebond surface preparation of the aluminum involved an Al₂O₃ grit blast, a sodium dichromate (Forest Products Lab, "FPL") etch, and the application of a protective BR127 primer.

A 102- μ m (4-mil)-thick TeflonTM release film was used to prevent bonding of a nominal 57.15 mm (2.25 in) region at one end of each specimen. These initially debonded regions served as initiation sites from which cracks in the adhesive layer were grown.

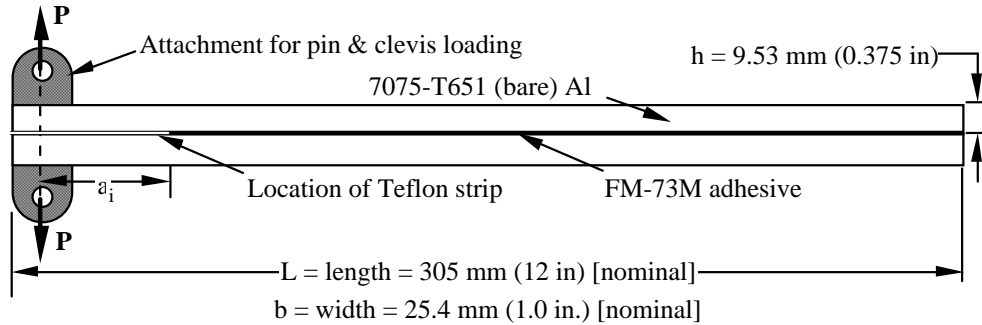


Figure 3. Geometry for the Aluminum/Epoxy (Al/FM-73/Al) Double Cantilever Beam Specimens.

Specimens were vacuum bag cured at 116°C (240°F) and 1 atm. for 150 minutes. The resulting bondline thickness was approximately 125 μm (4.9 mils).

Environmental Exposure. Based upon discussions with the specimen manufacturer, common test procedures used by major airframe manufacturers and defense laboratories and transport aircraft service conditions, two forms of environmental exposure were employed: 1) 5,000 hours of exposure to a hot/wet environment of 71 \pm 0.6°C (160 \pm 1°F), 94 \pm 3% rh, and 2) 100 cycles between -54°C (-65°F) and 71°C (160°F) following premoisturization in the hot/wet environment.

Moisture absorption by the adhesive resulted in weight gains by the exposed specimens. Bondline saturation, revealed by an approximate 0.06% weight gain in the Al/FM-73/Al specimens, occurred in roughly 200 hours. Exposed specimens were stored at room temperature and >90% rh prior to testing.

Specimens which were to be tested following thermal cycling (performed at WR-ALC/TIECD, Robins AFB, GA) were aged for 320 hours in the hot/wet environment prior to thermal cycling. During thermal cycling, a thermocouple placed between two adherends monitored bondline temperatures. An average ramp rate of 11°C/min (21°F/min) was used during the thermal cycling (Figure 4). Thermally cycled and as-received specimens were stored in laboratory conditions (22 \pm 2°C [72 \pm 3°F], 50 \pm 5% rh).

General Testing Procedures. Mechanical testing was performed on a 89 kN (20 kip) screw-driven machine or a 22 kN (5 kip) servohydraulic machine in a laboratory environment (22 \pm 2°C [72 \pm 3°F], 50 \pm 5% rh). Loads, displacements and cycle counts were collected automatically using a digital data acquisition system. Load transfer to the Al/FM-73/Al specimens was accomplished by means of a pin-and-clevis attachment bolted to the adherends (Figure 3). Crack growth within the adhesive layer was measured using a 20X magnification traveling microscope. To further assist in tracking crack growth, one edge of each specimen was painted white and imprinted with a scale consisting of 0.5 mm gradations. Crack length was monitored on the painted edge. Selected fracture surfaces revealed that the crack front in the interior of the specimens advanced at only a slightly faster rate than at the edges.

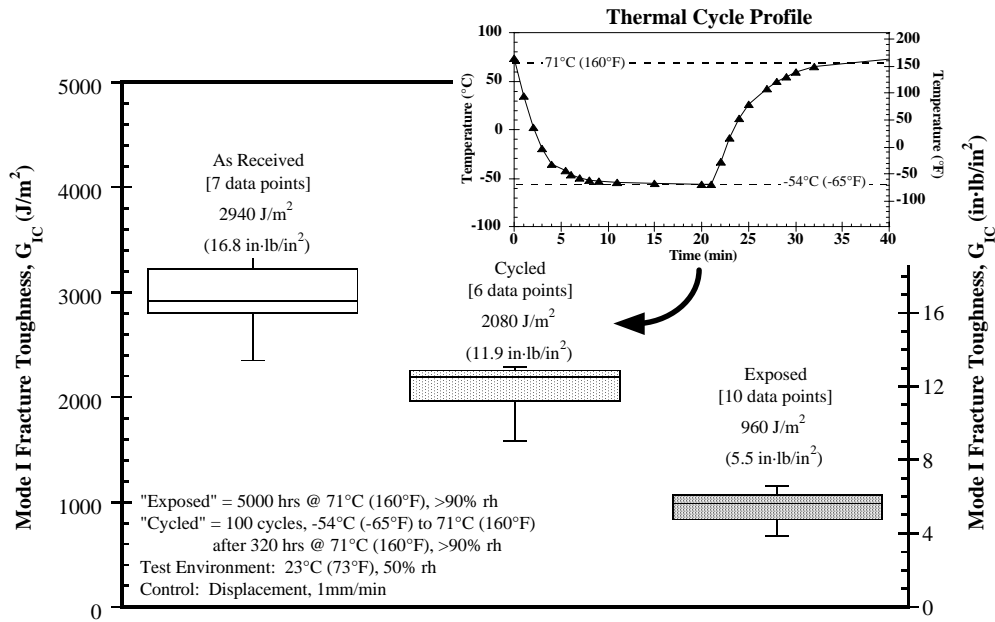


Figure 4. Effect of Environmental Exposure on Mode I Fracture Toughness.

Monotonic Testing Procedures. Monotonic testing, using ASTM D3433-75²⁵ and D5228-94a²⁶ as guidelines, was conducted to obtain a fracture toughness or critical strain energy release rate (G_{IC}) for the FM-73M adhesive. A crosshead displacement rate equal to a crack mouth opening rate of 1.0 mm/min (0.04 in/min) was used. Deviation from linearity of a load vs. displacement trace indicated the onset of crack growth in the bondline region. This was confirmed by optical observations. Several runs, permitting the calculation of multiple G_{IC} values, were performed on each specimen.

Fatigue Testing Procedures. Fatigue testing was carried out under displacement control at a frequency of 10 Hz using a displacement R ratio ($\delta_{min}/\delta_{max}$) of 0.1. Maximum displacements varied between 1.0 and 4.0 mm (0.04 and 0.16 in) and induced crack growth rates at various applied strain energy release rates. Periodic cycles conducted at 0.1 Hz captured peak/valley load and displacement values used in compliance calculations and in estimates of crack length and G_I .

Analysis Determination of the applied strain energy release rate may be performed using

$$G_I = \frac{P^2}{2b} \frac{dC}{da} \quad (1)$$

where

P = load

C = specimen compliance (δ/P)

b = specimen width
 a = crack or debond length
 δ = crosshead or crack mouth opening displacement

Using beam theory, (1) reduces to

$$G_I = \frac{3P\delta}{2ba} \quad (2)$$

Equation 2 may be further modified^{27,28} to account for the relationship between specimen compliance and observed crack length using

$$G_I = \frac{3P\delta}{2b(a + |\Delta|)} \quad (3)$$

where Δ is the intercept of the a-axis obtained from a linear relationship between $C^{1/3}$ and a .

Critical strain energy release rates (G_{IC}) were obtained using this Modified Beam Theory, equation 3, the visually observed crack length, and the load, P , at which crack growth began and the load vs. displacement trace deviated from linearity.

Results: Mode I Fracture Toughness. Figure 4 shows a comparison of the critical strain energy release rate (G_{IC}) or fracture toughness values for specimens tested in the as-received, exposed, and thermally cycled conditions. Each box in Figure 4 represents multiple G_{IC} values obtained from one specimen and encloses data between the 25th and 75th percentiles. Maximums and minimums on Figure 4 are indicated by outlying horizontal lines. Medians are indicated by horizontal lines within each box, and means are listed numerically.

Results: Fatigue Crack Growth. For fatigue tests, applied strain energy release rates were determined using equation 3. Crack growth rates were determined either by visual observation or by using specimen compliance and the $C^{1/3}$ vs. a relationship. A threshold crack growth rate (da/dN) was chosen as 1×10^{-6} mm/cycle (4×10^{-8} in/cycle). Figure 5 depicts the results of fatigue tests carried out on specimens in the as-received, exposed, and thermally cycled states.

Discussion The significant effects of environmental exposure on the fracture and fatigue characteristics of the specimens bonded with FM-73M toughened epoxy adhesive is evident in Figures 4 and 5. Exposure to a hot/wet environment for 5,000 hours is the most severe, degrading the fracture toughness by 60% and the threshold $G_{max,th}$ by nearly 50%. The effect of thermal cycling on G_{IC} values is significant, but not as severe. Cycling did not appear to appreciably affect fatigue behavior.

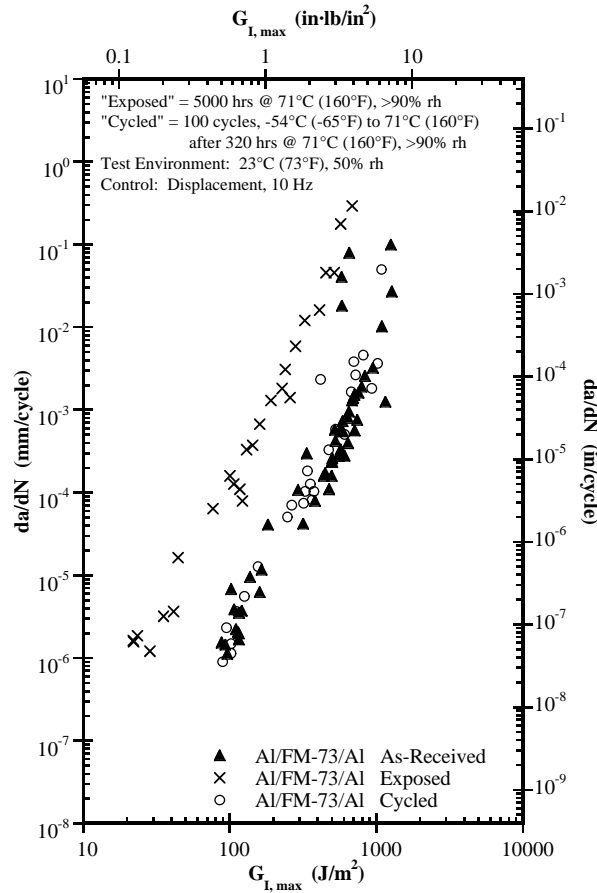


Figure 5. Effect of Environmental Exposure on Mode I Fatigue Behavior.

The relatively steep slopes of the da/dN vs. G_{max} data suggest that crack growth in bonded joints is much more sensitive to changes in applied loads or strain energy release rates than in monolithic metals. Also, the sensitivity of the crack growth rate to changes in G_{max} levels (slopes of the data) appeared to be relatively unaffected by the form of environmental exposure.

It must be understood that these results are for exposure to specific and somewhat arbitrary environments and some concern exists as to their applicability. For example, the long-term exposure to the hot/wet environment may be too severe. However, the conditions employed in this study are based on actual service environments and, therefore, the general trend of these effects should not be discounted.

CONCLUSIONS

Stress-based analyses of adhesive joints have proven valuable for the design of bonded aircraft structures using static strength considerations. However, to better

comprehend the damage tolerance in the presence of bondline flaws and durability under cyclic loading and environmental exposure, fracture mechanics offers a supplemental method. The long-term integrity of bonds in repairs to aging aircraft and the full realization of the structural efficiencies possible with adhesive joints depends on a thorough understanding of their behavior that fatigue and fracture studies can provide. A small investigation of a popular bonded system has identified the need to address the effect of the operating environment and to consider bonded joints as systems rather than focusing solely on the adhesive.

The trends of degraded durability should encourage designers and engineers to carefully consider environmental factors in determining the intended lifetimes of bonded structures. In addition, the observed fatigue behavior indicates that the crack growth rate for these joints is extremely sensitive to changes in the applied strain energy release rate. Therefore, in the design and use of these bonded joints, continued operation below identified threshold conditions, a safe-life approach, is most conservative and, perhaps, imperative.

REFERENCES

1. Schliekelmann, R.J.: "Past, Present, and Future of Structural Adhesive Bonding in Aero-Space Applications," *Transactions of the Japanese Society of Composite Materials*, vol. 5, no. 1/2, Dec. 1979.
2. *Ciba-Geigy Technical Notes. 3/1977*. Ciba-Geigy Plastics and Additives, Co., Cambridge, UK, 1977.
3. Blomquist, R.F.: "Adhesives - Past, Present, and Future," Adhesion, ASTM STP 360, American Society for Testing and Materials, Philadelphia, PA, 1963.
4. Potter, D.L.: *Primary Adhesively Bonded Structure Technology (PABST), Design Handbook for Adhesive Bonding*. Douglas Aircraft Co., Long Beach, CA, for the Air Force Flight Dynamics Laboratory, AFFDL-TR-79-3129, Jan. 1979.
5. Hart-Smith, L.J.: "Adhesive Bonding of Aircraft Primary Structures," High Performance Adhesive Bonding, G. DeFrayne, ed., Society of Manufacturing Engineers, Dearborn, MI, 1983.
6. Baker, A.A.: "Bonded Composite Repair of Metallic Aircraft Structures," Composite Repair of Military Aircraft Structures: Proceedings of the 79th Meeting of the AGARD Structures and Materials Panel, Seville, Spain, 1994.

7. Sandow, F.A. and Cannon, R.K.: *Composite Repair of Cracked Aluminum Alloy Aircraft Structure*. Air Force Flight Dynamics Laboratory, AFWAL-TR-87-3072, Sept. 1987.
8. Elkins, C.A.: "Use of Composite Materials to Repair Metal Structures," Proceedings of the 14th Symposium of the International Committee on Aeronautical Fatigue, Ottawa, Canada, 8-12 Jun 1987.
9. Fredell, R.; Van Barneveld, W.; and Vogelesange, L.B.: "Design and Testing of Bonded GLARE Patches in the Repair of Fuselage Fatigue Cracks in Large Transport Aircraft," Proceedings of the 39th International SAMPE Symposium, Society for the Advancement of Material and Process Engineering, Covina, CA, 1994.
10. Belason, E.B.: "Fatigue and Static Ultimate Tests of Boron/Epoxy Doublers Bonded to 7075-T6 Aluminum with a Simulated Crack," Proceedings of the 18th Symposium of the International Conference on Aeronautical Fatigue, Melbourne, Australia, May 1995.
11. Elliott, W.R.: "WR-ALC Aging Aircraft - Structures and Corrosion Programs," Proceedings of the 2nd Annual Air Force Aging Aircraft Conference, Air Force Office of Scientific Research, Washington, D.C., May 1994.
12. Baker, A.A.; Callinan, R.J.; Davis, M.J.; Jones, R.; and Williams, J.G: "Repair of Mirage III Aircraft Using the BFRP Crack-Patching Technique." *Theoretical and Applied Fracture Mechanics*, Elsevier Science Publ., Holland, vol. 2, 1984.
13. Pipkins, D.S. and Atluri, S.N.: "A FEAM-Based Methodology for Analyzing Composite Patch Repairs of Metallic Structures," Composite Repair of Military Aircraft Structures: Proceedings of the 79th Meeting of the AGARD Structures and Materials Panel, Seville, Spain, 1994.
14. Ruschau, J.J. and Coate, J.E.: "The Effectiveness of an Adhesively Bonded Composite Patch Repair as Applied to a Transport Aircraft Lower Wing Skin," Proceedings of the 41st International SAMPE Symposium. Society for the Advancement of Material and Process Engineering, Covina, CA, 1996.
15. Goland, M. and Reissner, E.: "The Stresses in Cemented Joints." *Journal of Applied Mechanics*, American Society of Mechanical Engineers, New York, NY, vol. 11, March 1944.
16. Hart-Smith, L.J. and Thrall, Edward W.: "Structural Analysis of Adhesive-Bonded Joints," Adhesive Bonding of Aluminum Alloys, E.W. Thrall and R.W. Shannon, eds., Marcel Dekker, Inc., New York, NY, 1985.

17. Adams, R.D.: "Testing of Adhesives - Useful or Not?" Adhesion 15: Proceedings of the 28th Annual Conference on Adhesion and Adhesives, K.W. Allen, ed., Elsevier Applied Science Publishers, London, UK, 1991.
18. Ripling, E.J.; Mostovoy, S.; and Patrick, R.L.: "Application of Fracture Mechanics to Adhesive Joints." in Adhesion, ASTM STP 360, American Society for Testing and Materials, Philadelphia, PA, 1963.
19. Shaw, S.J.: "Adhesive Joint Failure - A Fracture Mechanics Approach," Adhesion 7: Proceedings of the 20th Annual Conference on Adhesion and Adhesives. K.W. Allen, ed., Elsevier Applied Science Publishers, London, UK, 1983.
20. Brussat, T.R.; Chiu, S.T.; and Mostovoy, S.: *Fracture Mechanics for Structural Adhesive Bonds - Final Report*, Lockheed Co., Burbank, CA, for the Air Force Materials Laboratory, AFML-TR-77-163, July 1987.
21. Reeder, J.R. and Crews, J.H., Jr.: "Mixed-Mode Bending Method for Delamination Testing," *IAA Journal*, vol. 8, no. 7, American Institute of Aeronautics and Astronautics, New York, NY, 1988.
22. Johnson, W.S.; and Mall, S.: "A Fracture Mechanics Approach for Designing Adhesively Bonded Joints," in Delamination and Debonding of Materials, ASTM STP 876, W.S. Johnson, ed., American Society for Testing and Materials, Philadelphia, PA, 1985.
23. Mall, S.; and Johnson, W.S.: "Characterization of Mode I and Mixed-Mode Failure of Adhesive Bonds Between Composite Adherends," Composite Materials: Testing and Design (Seventh Conference), ASTM STP 893, J.M. Whitney, ed., American Society for Testing and Materials, Philadelphia, PA, 1986.
24. Johnson, W.S. and Mangalgiri P.D.: "Influence of the Resin on Interlaminar Mixed-Mode Fracture." Toughened Composites, ASTM STP 937, N.J. Johnston, ed., American Society for Testing and Materials, Philadelphia, PA, 1987.
25. ASTM D3433-75: "Standard Practice for Fracture Strength in Cleavage of Adhesives in Bonded Joints." Annual Book of ASTM Standards, American Society for Testing and Materials, Philadelphia, PA, 1994.
26. ASTM D5528-94a: "Standard Test Method for Mode I Interlaminar Fracture Toughness of Unidirectional Fiber-Reinforced Polymer Matrix Composites." Annual Book of ASTM Standards, American Society for Testing and Materials, Philadelphia, PA, 1994.

27. Hashemi, S.; Kinloch, A.J.; and Williams, J.G.: "Corrections Needed in Double-Cantilever Beam Tests for Assessing the Interlaminar Failure of Fibre-Composites." *Journal of Materials Science Letters*, vol. 8, 1989.
28. O'Brien, T.K. and Martin, R.H.: "Round Robin Testing for Mode I Interlaminar Fracture Toughness of Composite Materials." *Journal of Composites Technology and Research*, vol. 15, no. 4, Winter 1993.

THE EFFECT OF CRACK INTERACTION ON DUCTILE FRACTURE¹

C. T. Sun and X. M. Su
School of Aeronautics and Astronautics
Purdue University
West Lafayette, IN 47907-1282

SUMMARY

The interaction of a major crack and a small crack is analyzed by using a simple ductile fracture criterion based on critical equivalent stresses at the crack tip. To account for the three-dimensional effect at the crack tip of cracked plates, a plane strain strip is used. With commercial finite element code ABAQUS, the crack interactions are analyzed for two materials with different hardening and yielding behaviors. The numerical results indicate that when the plastic zone of the major crack and that of the small crack coalesce, the small crack would extend rapidly toward the major crack, producing a drop in applied load.

INTRODUCTION

Interaction between a major crack and small cracks is of great concern in aircraft safety [1]. A large number of aging airplanes are in service beyond the lifetime they were designed for. Multiple site damages (MSD) in the aging aircraft, involving a large number of small fatigue cracks, may reduce the residual strength of the aircraft in the presence of a major crack.

In a series of papers, Swift [1-3] approached the problem of the interaction of a major crack and small cracks by postulating that the major crack and a small crack would coalesce once the yield zones of the major crack and the small crack overlap. Swift based his analysis on elastic fracture mechanics and a crude estimation of the plastic zone. Its validity remains to be verified especially for ductile materials such as aluminum alloys used in aircraft structures.

Specimens under static monotonic loading and fractured with large-scale yielding are noted to go through the stage of initial crack growth and the stage of steady-state crack growth. Many parameters have been suggested to characterize the two stages. The J integral [4] and the J-R curve were very popular in earlier studies. It was later found, however, that the J integral and the J-R curve are specimen size dependent [5]. Other parameters, such as plastic dissipation energy at the crack tip [6], CTOA [7], etc., have also been suggested.

¹ This work was supported by the Air Force Office of Scientific Research through a University Research Initiative Grant Number F49620-93-0377 to Purdue University. Dr. Water Jones was the grant monitor.

By simulating more than 15 ductile fracture tests on grooved specimens performed by three different groups of researchers, Su and Sun [8] have recently found that stresses, especially equivalent stresses, at a point within a critical distance from the crack tip remain constant during crack growth and are specimen size independent for fractures under plane strain deformation. Stresses, especially equivalent stresses, can be used as the parameter to characterize ductile fracture.

For ductile fracture of flat plates without side grooves, three-dimensional effects at the crack tip must be considered. Recent analytical solution of three-dimensional stresses at the crack tip for a cracked plate showed that singular stresses at the crack tip are plane strain throughout the plate thickness for elastic materials [9]. In other words, a plane strain core region exists around the crack tip where singular stresses dominate. Away from the crack tip, a state of plane stress prevails. The plane strain condition in ductile fracture has been investigated by Newman, et al [10], Narasimhan and Rosakis [11], and Nakamura and Park [12], among others. A moving plane strain core model, which accounts for plane strain deformation at the crack tip and plane stress deformation away from the crack tip has been developed successfully [13]. By using the moving plane strain core model, stresses, especially equivalent stresses at the crack tip, remain constant during steady static crack growth [13]. Stresses at the crack tip can be used together with the moving plane strain core model to characterize ductile fracture of flat plates.

In the present paper, the above mentioned ductile fracture criterion is used together with a simple version of the plane strain core model to study crack interactions in cracked plates under in-plane loading.

THE DUCTILE FRACTURE CRITERION

Recently, Su and Sun [8] simulated fifteen ductile fracture tests performed by three different research groups on grooved specimens to study local parameters during plane strain ductile fracture. The tests, reported by Hiser and Terrel [14], Joyce, Hackett, and Roe [15], and Joyce and Link [16], used three different materials, i.e., A302B, HY100, and A533B, respectively. The specimens for A302B are standard compact tension specimens, with sizes ranging from $1/2T$ to $6T$. The specimens for HY100 and A533B include single-edge notched bending, single-edge notched tension, and double-edge notched tension specimens.

Figure 1 gives the stresses at the first Gaussian point of the first element ahead of the current crack tip (referred to as G1-F1 later) for A302B. In the simulation, the same element size is used along the entire line of crack growth for every specimen. The stresses of G1-F1 are thus the stresses of a point with fixed position relative to the current crack tip. Figure 1 shows that stresses, especially equivalent stresses, are independent of specimen size and thus, can be used to characterize ductile fracture. This is also true for HY100 and A533B.

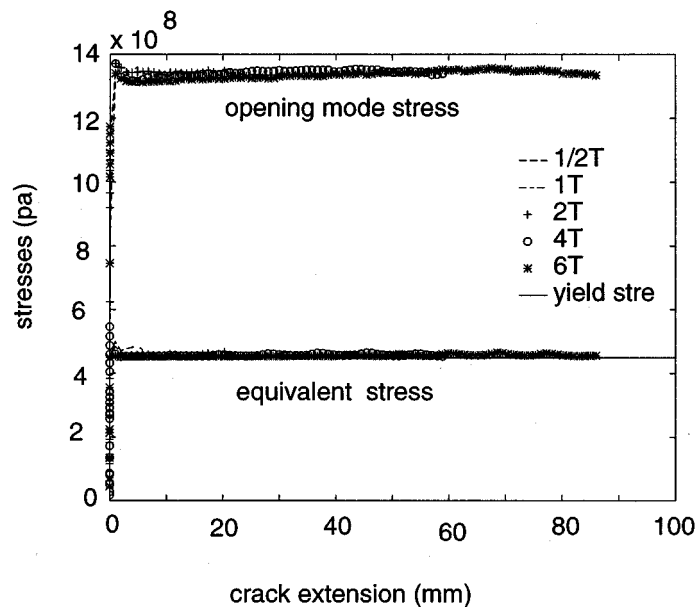


Figure 1. Stresses at G1-F1 From Numerical Simulations.

Stresses at a critical distance from the crack tip remain constant during steady static crack growth. A transition region exists before crack growth reaches the steady state. However, the transition is very short if equivalent stress is used to characterize ductile fracture. Here, a simple ductile fracture criterion is adopted which states that when the equivalent stress at a critical distance from the current crack tip (say, G1-F1 for a specific mesh) reaches a critical value, the crack would grow. In using this criterion in cracked flat plates, the plane strain nature of the near tip stresses must be accounted for. This is accomplished by using a plane strain core that encompasses and moves with the crack tip. Beyond the plane strain core region, a state of plane stress is assumed.

To realize the moving plane strain core model using the commercial finite element code ABAQUS, user material subroutines must be used. Unfortunately, ABAQUS cannot be used to plot contours of plastic deformation when user material subroutines are used. Instead, a simplified version of the plane strain core model, i.e., plane strain strip model which was first suggested by Dawicke, et al. [17] is used in this study. For the plane strain strip model, a strip which spans the crack line is assumed to be in plane strain and the rest of the plate in plane stress. Although not precise, the plane strain strip model captures the plane strain characteristics of singular stresses at the crack tip.

THE NUMERICAL MODEL

The problem considered in this study is a flat plate under remote uniform tensile displacement. The two sides of the panel are traction free. A major crack of initial length 20 cm is at the center of the plate. Two smaller cracks, each of length 1.5 cm, are symmetrically

located 5 cm away from the major crack on the crack line, as shown in Figure 2. Only a quarter of the plate needs to be analyzed. The finite element mesh used is shown in Figure 3. The thickness of the structure is assumed to be 2 cm and the width of the plane strain strip used is 0.6 cm. The element size is 1 mm along the crack line.

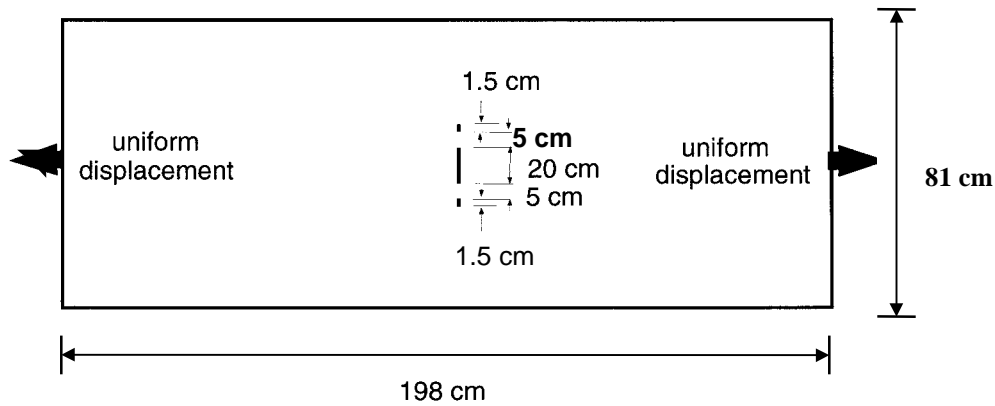


Figure 2. A Panel With a Major Crack and Two Small Cracks.

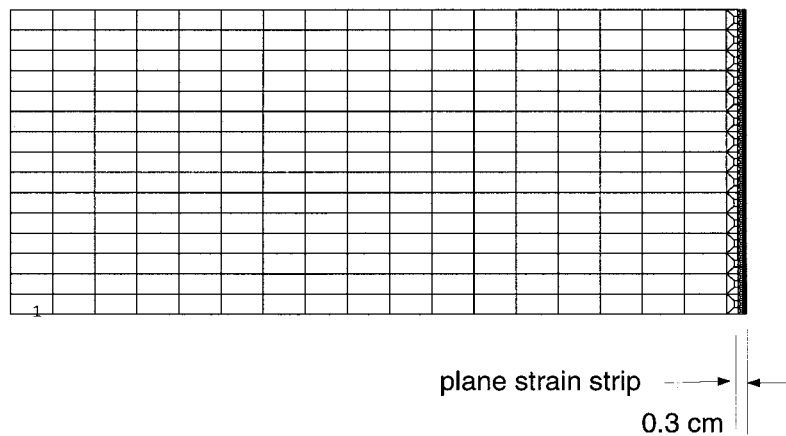


Figure 3. The Mesh Used in the Analysis.

The commercial finite element code ABAQUS (1994) is used in the study with four-nodal plane strain element CPE4 in the plane strain strip and four-nodal plane stress element CPS4 for the rest of the plate. J_2 flow theory is the constitutive model. Crack growth is modeled by nodal release. Using the ductile fracture criterion to predict crack growth is an interactive process that requires consecutive redefining boundary conditions in accordance with the current crack length, which itself is being determined by the results from current calculations. This interactive calculation is realized by using user subroutines “uel” and “uvarm.” The user subroutine “uvarm” is used to read the equivalent stress at the first Gaussian point of the first element ahead of current crack tip. The user subroutine “uel” is the subroutine to define the user element. It is used here to define two-nodal spring elements which lie below the line of crack growth. A shadow node is defined with the same coordinates but with a different nodal number for each of the nodes along the line of crack

growth. Each of the spring elements connects a node along the crack growth line to its shadow which is rigidly supported. The spring element possesses an almost infinite stiffness before breaking; it breaks only when it is at the current crack tip and the equivalent stress at the first Gaussian point of the first element ahead of it reaches critical value.

In the ABAQUS execution, the equivalent stress at the first Gaussian point of the first element ahead of current crack tip is read by “uvarm” for each increment of loading and is compared with the given critical stress for crack growth. If the equivalent stress is equal to or larger than the critical stress, a signal is sent to the subroutine “uel” so that the spring element below the current crack tip will break in the following calculations.

RESULTS OF CRACK INTERACTION

Two different materials are studied, i.e., A302 steel and 2024-T3 aluminum alloy. The stress and strain relations for the two materials are shown in Figure 4. The aluminum alloy has a lower yield stress and does not harden as much as A302. The critical equivalent stresses for fracture at G1-F1 for crack growth with the element size of 1 mm are 390 MPa and 455 MPa for 2024-T3 and A302, respectively. The critical equivalent stresses are obtained from numerical simulations.

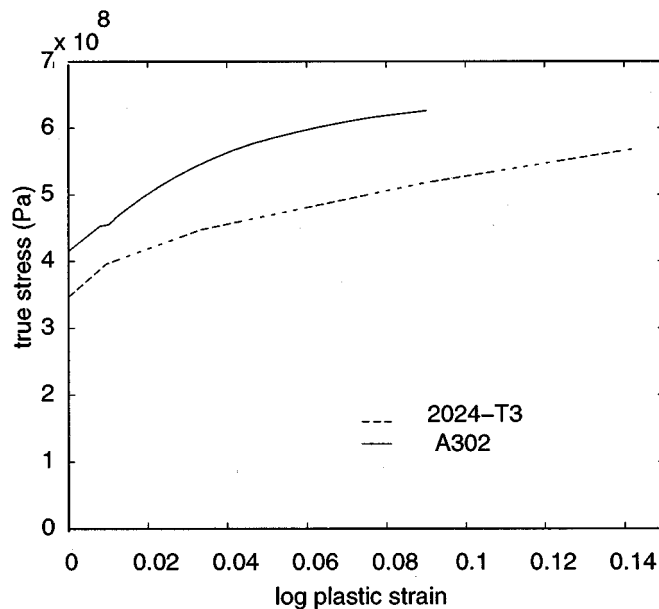


Figure 4. Stress and Strain Curves for A302 and 2024-T3.

Figure 5(a) gives the load and displacement relations for A302. Initially, only the major crack grows, and the yielding zone of the major crack extends quickly, as shown in Figure 5(b). At the load level indicated by a circle in Figure 5(a), the yielding zone of the major crack begins to join with that of the left crack tip of the small crack, as shown in Figure

5(c). As soon as the two yield zones overlap, the small crack grows towards the major crack. The speed of the growth of the small crack picks up quickly, and would surpass that of the major crack. The combined yield zone of the major crack and left tip of the small crack extends with loading and finally joins the yielding zone of the right tip of the small crack, as shown in Figure 5(d). The load at which the two yield zones coalesce is depicted by a star in Figure 5(a). After the yielding zone of the right tip of the small crack coalesces the combined yielding zone of the major crack and left tip of the small crack, the right tip of the small crack begins to grow to the right. The coalescence of the major crack and small crack is accelerated with further loading, and the load and displacement curve has a jump when the major crack and small crack meet.

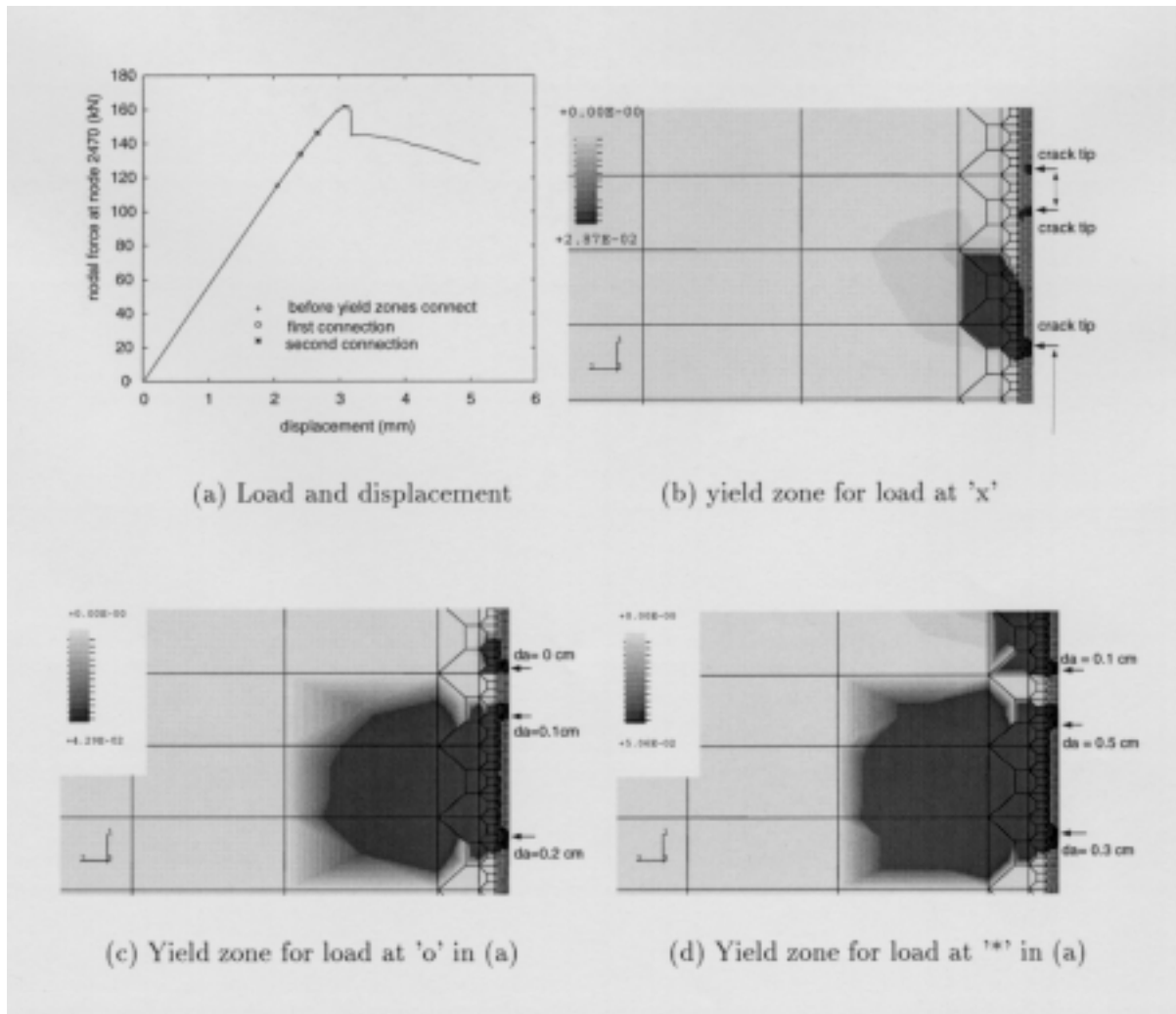


Figure 5. Yield Development During Crack Interaction for A302.

Obviously, for material A302, overlap of the yielding zone of the major crack and that of the small crack does not mean the two cracks will coalesce. Load can still increase after the overlapping.

Before turning to the results of 2024-T3, we need to elaborate the definition of crack length. For fracture tests carried out on 2024-T3, very severe tunneling effects are found, as shown in Figure 6 for a 1T one-inch-thick specimen. When tunnelings are there, crack length measured on specimen surface or inferred by compliance calculation leads to overestimation of the load capacity of a structure [18]. An equivalent crack length, the average of crack length through the plate thickness has to be used in such cases. As shown in Figure 7, by using the equivalent crack length and plane strain core, fracture tests on 2024-T3 can be accurately simulated. In the following discussion, the crack length for 2024-T3 refers to the equivalent crack length.

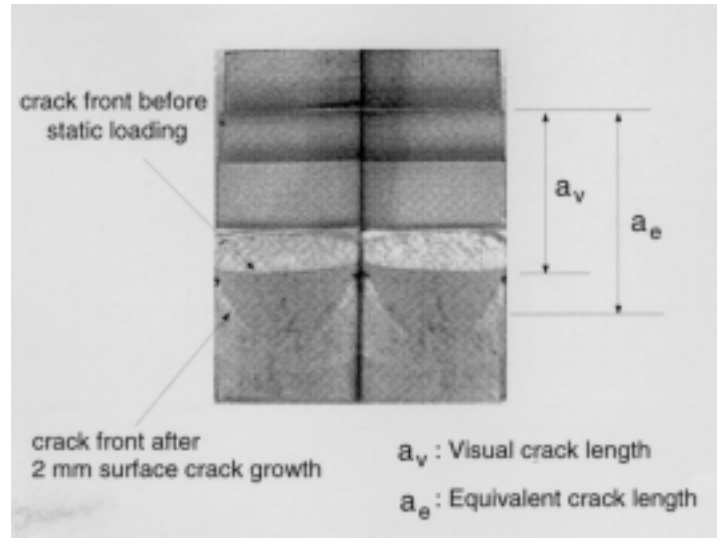


Figure 6. Fracture Tests Showing Tunneling.

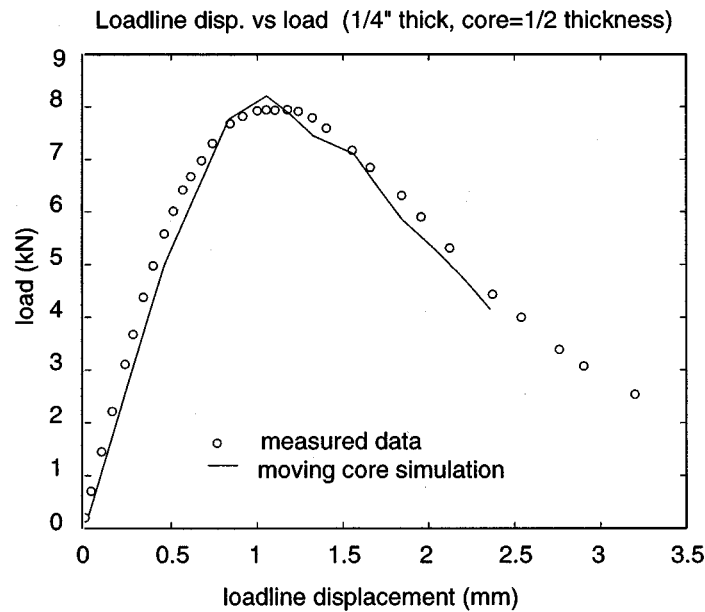


Figure 7. Load and Loadline Relation by Using Equivalent Crack Length.

Figure 8(a) presents the load and displacement relation for the material 2024-T3. The initial load-displacement relation is basically linear where only the major crack grows stably. When the load reaches the value denoted in Figure 8(a) by a circle, the yielding zones of the major crack and small crack overlap, as shown in Figure 8(c). By then the major crack has already extended for 1.0 cm. The small crack begins to grow towards the major crack as the yielding zones overlap. The small crack grows slowly initially, but picks up the pace very quickly. The right tip of the small crack starts growing as shown in Figure 8(d) when its yielding zone merges with the combined yielding zone of the major crack and the left tip of the small crack. The coalescence of the major crack and the small crack appears unstable as it is accompanied by an abrupt drop in loading. It is also noted that for 2024-T3, the coalescence of these cracks occurs almost immediately after the yielding zones overlap.

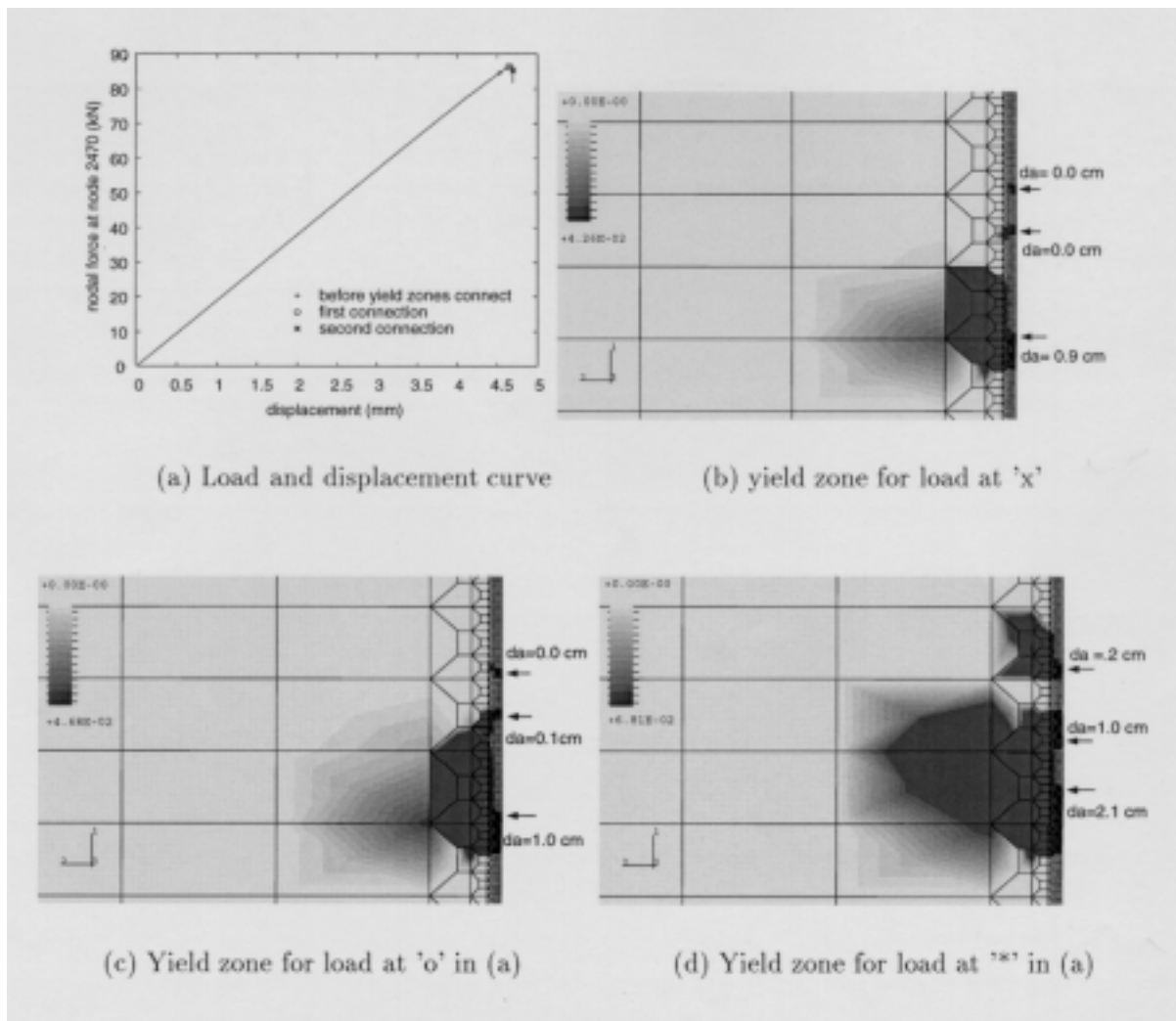


Figure 8. Yield Development During Crack Interaction for 2024-T3.

CONCLUSION

By comparing results for the two materials reported in the above sections, we conclude that plastic properties of materials, such as yielding and hardening, play an important role in the crack interactions in ductile materials. For 2024-T3 which exhibits little hardening, the merging of the crack tip plastic zone of the major crack and the small crack leads to almost immediate coalescence of the cracks and, correspondingly, a sharp drop in the applied load. The present numerical results appear to support Swift's postulation at least for aluminum alloys. Of course, to obtain accurate predictions using Swift's postulation, an accurate estimate of the crack tip plastic zone size should be used instead of the Irwin's model suggested by Swift.

REFERENCES

1. Swift, T.: Widespread Fatigue Damage Monitoring Issues And Concerns, in *Proc. Int. Conf. on Structural Airworthiness of New and Aging Aircraft*, Hamburg, 1993, pp. 113-150.
2. Swift, T.: Damage Tolerance in Pressurized Fuselages, *14th International Committee on Aeronautical Fatigue*, 1987. pp. 351-387.
3. Swift, T.: Damage Tolerance Capability, *Fatigue of Aircraft Materials, Proc. Specialists Conf.*, Delft, October 1992, pp. 351-387.
4. Rice, J. R.: Mathematical analysis in the mechanics of fracture, in *Fracture 2* (Edited by H. Liebowitz). Academic Press, New York, 1968.
5. Landes, J. D.: Extrapolation of the J-R Curve for Predicting Reactor Vessel Integrity, *NUREGCR-5652*, US Nuclear Regulatory Commission, Washington DC, 1992.
6. Saka, M. ; Shoji, T.; Takcheshi, H.; and Abe, H.: A Criterion Based on Crack Tip Energy Dissipation in Plane Strain Crack Growth under Large Scale Yielding, in; *Elastic-Plastic Fracture: second symposium, V.1-Inelastic Analysis, ASTM STP 803*, pp. I-130-I-158.
7. Newman Jr., J. C.; Booth, B. C.; and Shivakumar, K. N.: An Elastic Plastic Finite Element Analysis of the J Resistance Curve Using a CTOA Criterion, *Fracture Mechanics: Eighteenth Symposium, ASTM STP 945*, 1988, pp. 665-685.
8. Su, X. M. and Sun, C. T.: A Ductile Fracture Criterion Derived from Numerical Simulations, in *Proceedings of the 24th Midwest Applied Mechanics Conference*, Iowa State University, 1996, pp. 317-319.

9. Su, X. M. and Sun, C. T.: On Singular Stress at the Crack Tip of a Thick Plate under In-plane Loading, *International Journal of Fracture*, to appear.
10. Newman, Jr., J. C.; Bigelow, C. A.; and Shivakumar, K. N.: Three-Dimensional Elastic Plastic Finite Element Analysis of Constraint Variations in Cracked Bodies, *NASA TM-107704*, National Aeronautics and Space Administration, Washington DC, 1992.
11. Narasimhan R. and Rosakis, A. J.: Three-Dimensional Effects near a Crack Tip in a Ductile Three-Point Bend Specimen: Part I-A Numerical Investigation, *Journal of Applied Mechanics*, Vol. 57, 1990, pp. 607-617.
12. Nakamura, T. and Park, D. M.: Three-dimensional Crack Front Fields in a Thick Ductile Plate, *Journal of Mechanics Physics and Solids*, Vol. 38, 1990, pp. 787-812.
13. Su, X. M. and Sun, C. T.: A Plane Strain Core Model for Crack Growth in Ductile Materials, presented at the *Symposium on Fracture Mechanics for Ductile Materials*, ASME WAM, Atlanta, 1996.
14. Hiser, L. A. and Terrel, J. B.: Size Effects on J-R Curves for A302-B Plate, *NUREGCR-5265*, US Nuclear Regulatory Commission, Washington DC, 1989.
15. Joyce, J. A.; Hackett, E. M.; and Roe, C.: Comparison of J_{1c} and J-R Curves for Short Cracked Tensile Loaded Specimen Geometries of High Strength Structural Steel, *NUREGCR-5879*, US Nuclear Regulatory Commission, Washington DC, 1992.
16. Joyce, J. A. and Link, R. E.: Effects of Tensile Loading on Upper Shelf Fracture Toughness, *NUREGCR-6051*, US Nuclear Regulatory Commission, Washington DC, 1994.
17. Dawicke, D. S.; Sutton, M. A.; Newman, Jr., J. C; and Bigelow, C. A.: Measurement and Analysis of Critical CTOA for an Aluminum Alloy Sheet, in *Fracture Mechanics: 25th Volume, ASTM STP 1220*, F. Erdogan, Ed., American Society for Testing and Materials, Philadelphia, 1995.
18. Su, X. M.: Three-Dimensional Effects in Ductile Fracture, Ph.D. Thesis, School of Aeronautics and Astronautics, Purdue University, December 1996.

THE EFFECT OF ENVIRONMENTAL CONDITIONS AND LOAD FREQUENCY ON THE CRACK INITIATION LIFE AND CRACK GROWTH IN ALUMINUM STRUCTURE

H.-J. Schmidt and B. Brandecker
Fatigue and Fracture Mechanics Department
Daimler-Benz Aerospace Airbus
Hamburg, Germany

SUMMARY

The environmental conditions influence the crack initiation life (durability) and the damage tolerance behavior (crack growth) of the structure. The load frequency has an additional effect on the crack growth behavior of aluminum structure. These aspects play a major role during the material selection for a new Airbus aircraft generation. New materials are under consideration to reduce the manufacturing costs by simplifying the design and the assembly process and to comply with the forthcoming regulations. This paper describes the newest crack growth test results for several aluminum alloys which may be used for the skin of the pressurized fuselage of the next Airbus aircraft type.

INTRODUCTION

The present aircraft generation was designed for an economic operational life of at least 20 to 25 years and up to 90,000 flight cycles. These design goals will be exceeded by many operators of jet-powered airplanes and turboprops. Therefore corrosion of metallic materials is one of the most important issues affecting the life of the airplane structure with consequences to economic and airworthiness aspects. In general, the occurrence of corrosion damage depends on several parameters, such as the corrosion protection during the manufacturing and assembly process, the maintenance performed during the operational life, the environmental conditions during operation, and the type of cargo. Therefore the correct material choice is a major contribution to an adequate corrosion control. In addition, the environmental conditions (temperature and humidity) have an effect on the fatigue life (crack initiation life) and the crack growth in aluminum structure and consequently repercussions on the structural inspection program necessary to maintain the airworthiness of the airplanes. These effects have been investigated for present materials and those new materials which will probably be used for the skin of the pressurized fuselage of future transport aircraft. These investigations regarding the crack growth behavior consider the effects of environment, test frequency, spectrum shape, temperature, and application of cladding. The investigations of the crack initiation life are performed with respect to environmental conditions, surface treatment, assembly process, and frequency.

CRACK GROWTH TESTS

From the designer's point of view the static strength, the durability, the damage tolerance behavior, and the corrosion resistance are the major technical aspects for the material choice. These aspects have been fully considered for the present generation of transport aircraft, where the skin of the pressurized fuselage and the bottom wing skin, which are mainly dimensioned by durability and damage tolerance, are mainly made of 2024T3/T42/T351. The skin of the pressurized fuselage of the next Airbus generation may be made from new material, e.g., 6013 or 2524 (C188) instead of conventional 2024T3/T42. The reasons for the possible material change are to reduce manufacturing costs by changing the assembly process or by simplifying the design and to comply with the forthcoming Federal Aviation Regulations (FAR) §25.571.

One of the key issues is the crack growth behavior under real environment. Any new material for fuselage and bottom wing skin in areas where damage tolerance is the dimensioning case can only be accepted if the crack growth behavior under real environment and real frequency is not worse than the present 2024T3/T42 material. If the new material would not fulfill this requirement, either the skin thickness would have to be increased which is unacceptable due to weight reasons or more severe inspection programs have to be applied.

Comprehensive coupon tests have been carried out by Daimler-Benz Aerospace Airbus (DA) which are presented in the following as well as some investigations from other authors. For all DA tests the following conditions were applied: the 2024 specimens were cladded (except one test series to investigate the influence of cladding) as well as the 7475 specimens; all 6013 specimens were bare; the specimen geometry was: width 100 or 160 mm, thickness 1.6 mm; all specimens were manufactured without surface treatment and painting; the specimen direction was L-T; the tests were performed either in laboratory air or in 3.5 percent sodium chloride (NaCl) with inhibitors; and all tests were performed at room temperature except those to investigate a lower temperature.

Crack Growth Tests under Constant Amplitude Loading

To date the effect of corrosive environments on the crack growth behavior has been investigated by comparative coupon tests performed at a frequency of approximately 20 Hz and using either laboratory air or 3.5 percent sodium chloride (NaCl) which is the state of the art. Table 1 presents the crack growth behavior of different materials obtained by tests with center cracked tension (CCT) specimens performed at 20 Hz. The comparison for the two lower ΔK values reveals that, e.g., for 6013 and laboratory air the da/dn values are similar to the 2024T3 values. The same comparison for an environment of 3.5 percent sodium chloride shows significant differences.

Table 1. Crack Growth Data for a Frequency of 20 Hz.

Material	Environment	da/dn (mm · 10 ⁻³ /cycle)		
		$\Delta K = 13$ MPa√m	$\Delta K = 13$ MPa√m	$\Delta K = 13$ MPa√m
2024T3	laboratory air	0.20	0.65	2.40
6013T6	laboratory air	0.28	0.55	1.00
7475T76	laboratory air	0.45	1.00	1.90
2024T3	3.5 percent NaCl	0.27	0.65	2.30
6013T6	3.5 percent NaCl	0.65	0.80	1.50
747KT7	3.5 percent NaCl	0.85	1.50	2.20

Considering the above mentioned comparison it would not be recommended to use these new materials. However, the test conditions are quite different from reality, therefore new test procedures need to be developed and applied before a final decision is made. DA has accomplished crack growth tests using new test procedures. In general the effect of the frequency and the environment on the crack growth behavior has to be evaluated for longitudinal and circumferential cracks in a pressurized fuselage. The load spectra for these crack types are quite different, i.e., a constant amplitude spectrum due to internal pressure is driving the longitudinal cracks and a complex flight-by-flight spectrum due to internal pressure and external loading has to be considered for the circumferential cracks.

In test series 1 and 2, DA has analyzed the frequency and environmental effect for longitudinal cracks. Constant amplitude tests (R = 0.1) have been carried out with CCT specimens and the stress-time histories shown in Figure 1.

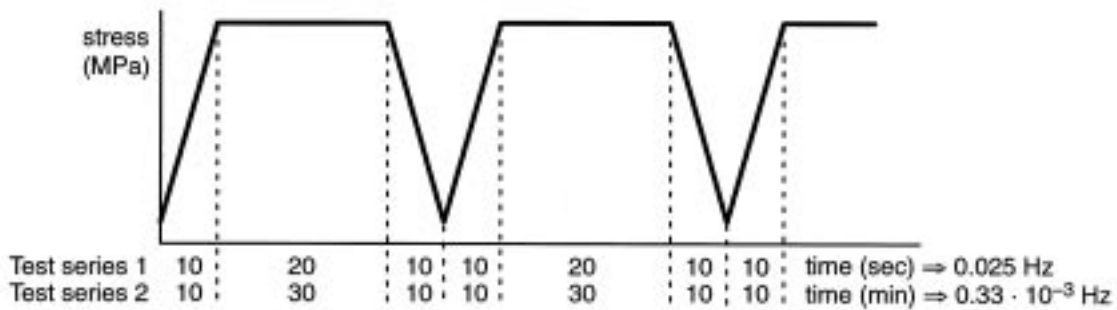


Figure 1. Stress-Time Histories for Crack Growth Tests.

Figures 2 a and b contain the results of the test series 1 compared with the data for the frequency of 20 Hz. The left-hand figures show the da/dn data obtained under laboratory air. Independent from the test frequency, material 6013 shows a better crack growth behavior than 2024. The right-hand figures for the environment of sodium chloride show different results: In case of a frequency of 0.025 Hz, the crack growth behavior of 6013 is better. For a frequency of 20 Hz and lower ΔK values ($\Delta K \leq 22$ MPa√m), the crack growth behavior of 2024 is significantly better. For higher ΔK values ($\Delta K > 22$ MPa√m), which are less important, 6013 is superior to 2024.

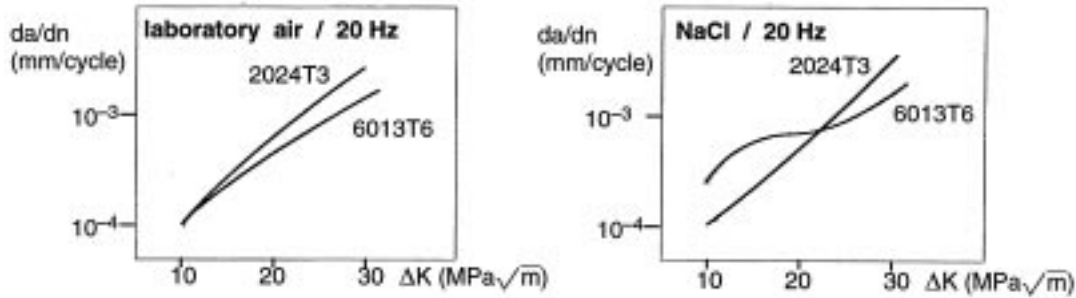


Figure 2a. Crack Growth Test Results for 2024T3 and 6013T6 at a Frequency of 20 Hz.

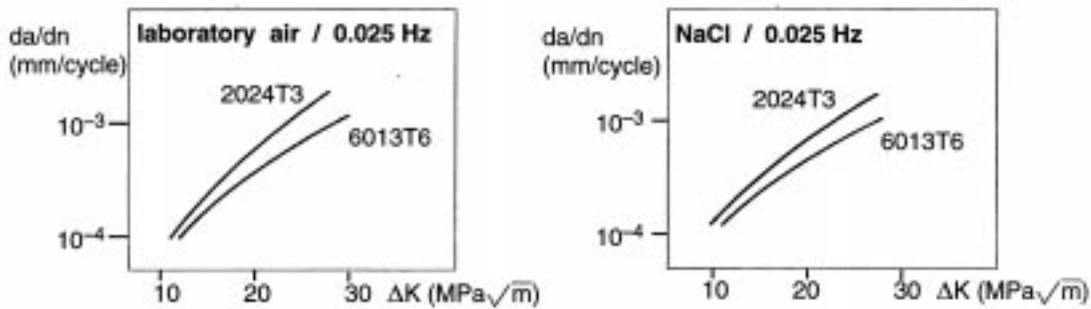


Figure 2b. Crack Growth Test Results for 2024T3 and 6013T6 at a Frequency of 0.025 Hz.

Test series 2 contains similar tests with a frequency of $0.33 \cdot 10^{-3}$ Hz, see Figure 3. As for test series 1, the material 6013 has a better crack growth behavior than 2024 for the frequency of $0.33 \cdot 10^{-3}$ Hz and 3.5 percent sodium chloride. The same behavior, i.e., 6013 better than 2024, is observed for laboratory air and the low frequency.

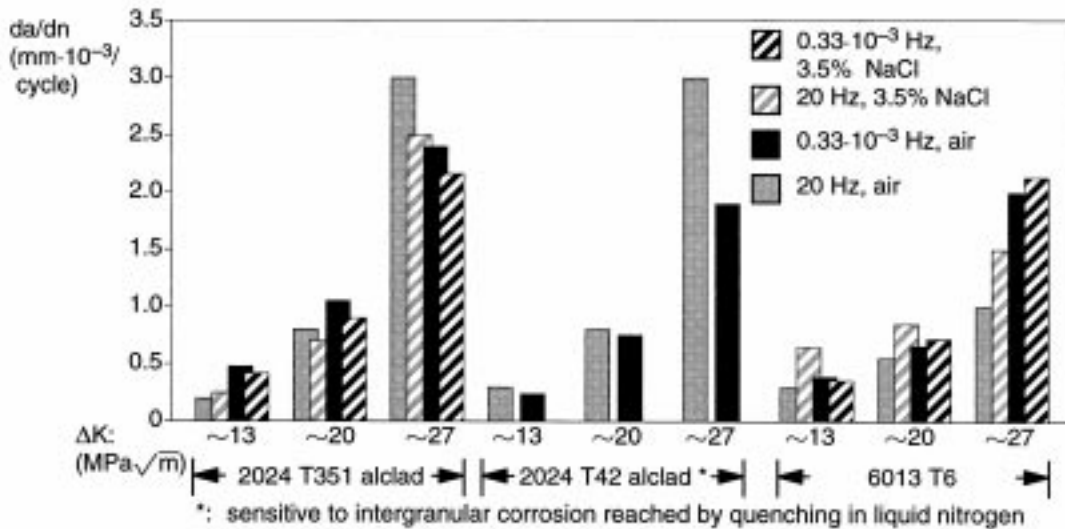


Figure 3. Crack Growth Test Results for 2024T351/T42 and 6013T6 at Frequencies of 20 Hz and $0.33 \cdot 10^{-3}$ Hz.

Furthermore some special effects such as temperature, application/deletion of cladding, and other frequencies have been investigated with the following results.

Figure 4 presents a comparison of crack growth test results for specimens tested at a low frequency of $0.33 \cdot 10^{-3}$ Hz in laboratory air and two temperatures (room temperature (RT) and -55°C). For the lower temperature of -55°C , the crack growth is less than that for RT for the two lower ΔK values of ~ 13 and ~ 20 $\text{MPa}\sqrt{\text{m}}$. For the highest ΔK value, no decrease is observed for 2024 or even an increase for 6013.

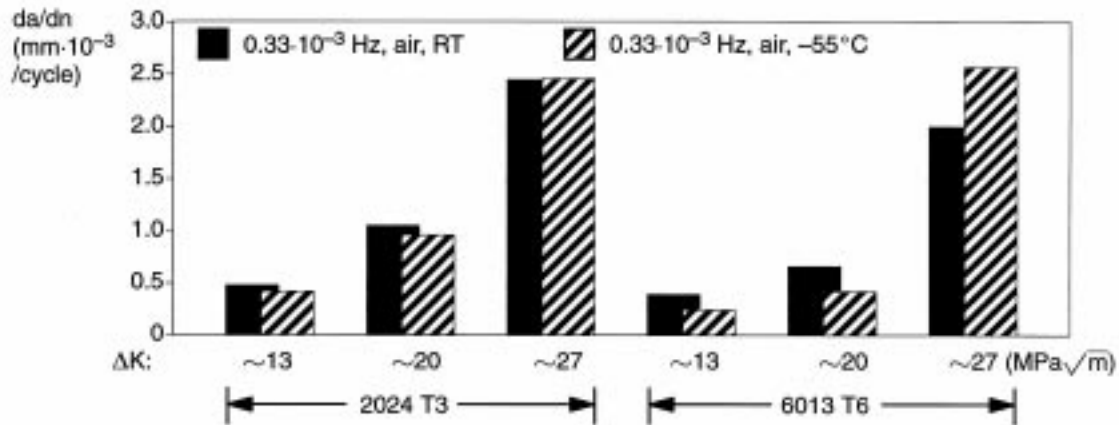


Figure 4. Crack Growth Test Results for 2024T3 and 6013T6 at a Low Frequency and RT/ -55°C .

Comparative crack growth tests with 2024 clad and bare specimens were performed at a frequency of 0.025 Hz and 3.5 percent sodium chloride, see Figure 5. The bare specimens show a slightly better crack growth behavior which can be explained by the thicker core material for the bare specimens.

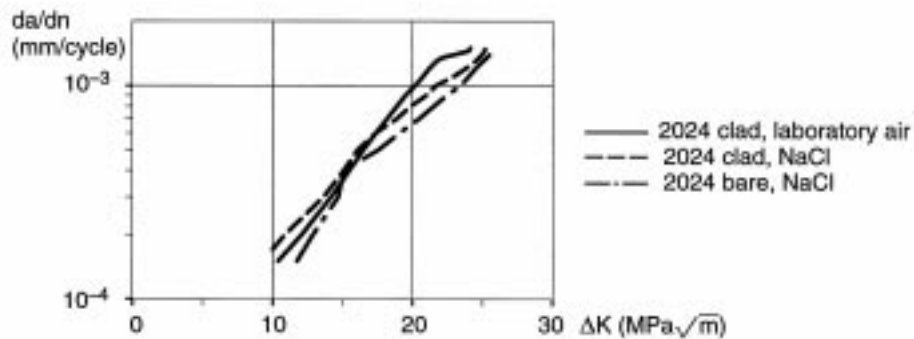


Figure 5. Crack Growth Test Results for 2024T3 Clad and Bare Specimens at 0.025 Hz and 3.5 Percent NaCl.

The Technical University of Hamburg-Harburg, Germany, has carried out similar tests (ref. 1) and investigated the crack growth versus the frequency for the materials 2024T351, 6013T6, and 7475 under aged at two ΔK values. In principle the test results correlate with

the DA investigations, but a maximum crack growth has been found at 1 Hz for all three materials and 3.5 percent sodium chloride environment with inhibitors, see Figure 6. It is assumed at present that a repassivation of the surface may be the reason.

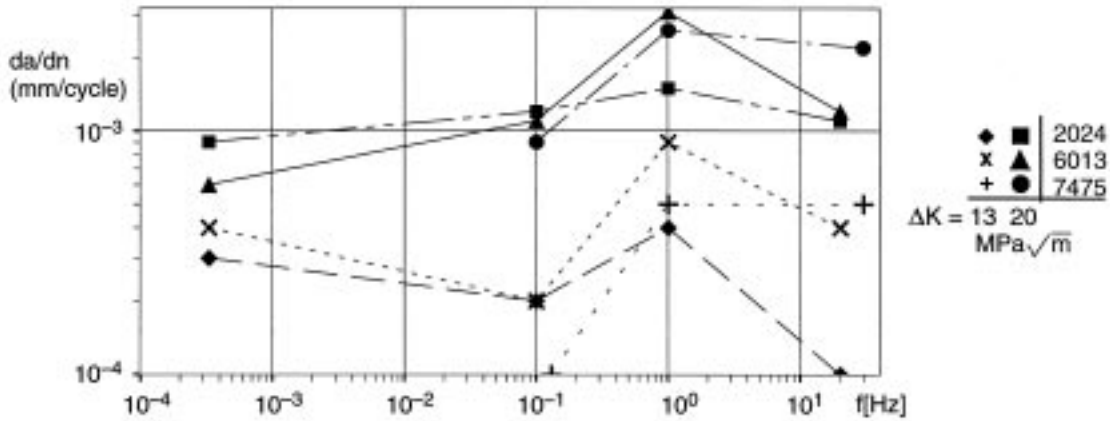


Figure 6. Influence of Frequency on 2024, 6013, and 7475 Alloys.

Crack Growth Tests Under Flight-By-Flight Loading

For assessing the behavior of circumferential cracks in the upper shell of the pressurized fuselage complex, flight-by-flight loading is necessary to comply with the in-service loading. Crack growth tests have been carried out using the stress-time history applied at the Airbus A330 full-scale fatigue test of the rear fuselage. This flight-by-flight test program consists of 3920 normal (revenue) and 80 crew training flight types applied in a block of 4000 flights by 12 different flight types which are split into more than 100 subflight types in test. The flight types presented as examples in Figure 7 occur 5 times (A) and 980 times (G) in a block (the stress time histories are given in different scales).

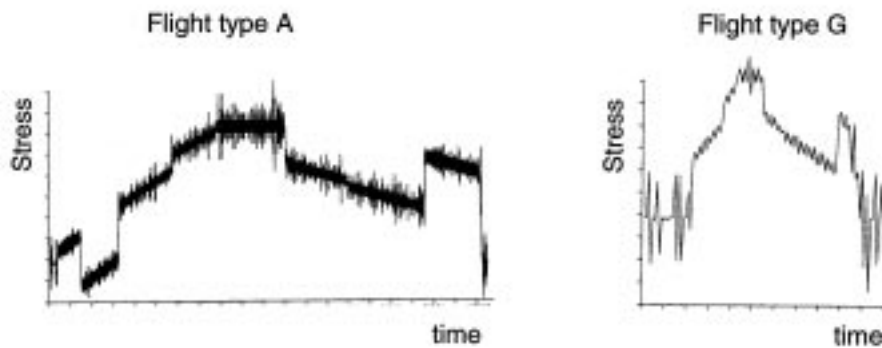


Figure 7. A330-300 Short Range Stress-Time Histories for Upper Shell of Rear Fuselage.

The tests with 2024T351 and 6013T6 specimens were performed at a frequency of approximately 15 to 20 Hz either in laboratory air or in 3.5 percent sodium chloride, see Figure 8. The crack growth behavior of 2024 for the two different environments shows small differences only, as expected from the experience with constant amplitude testing, see Table 1. In contrast 6013 shows an increased crack growth of factor 2 to 2.75 for the corrosive environment and the high test frequency. This result is also in line with the data presented in Table 1. However, the crack growth rates for 6013 and 3.5 percent NaCl are 2 factors higher than for 2024.

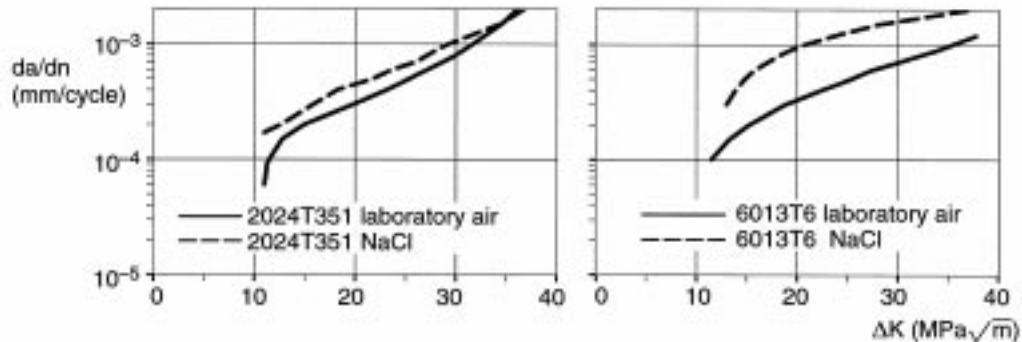


Figure 8. Crack Growth of 2024T351 and 6013T6 Under Airbus Fuselage Spectrum Loading (15 to 20 Hz).

Crack Growth Tests Under Simplified Flight-By-Flight Loading

To investigate the effect of the flight-by-flight loading systematically, simplified flight-by-flight stress-time histories were defined with major cycles of $R = 0.1$ and incremental cycles of $R = 0.8$, see Figure 9. The goal of this investigation is to understand the effect of incremental cycles during taxi and cruise (spectrum 1) and the effect of incremental cycles during climb, cruise, and descent (spectrum 2). For both spectra the test frequency is 0.025 Hz for one flight allowing the comparison with the results of the constant amplitude testing (test series 1).

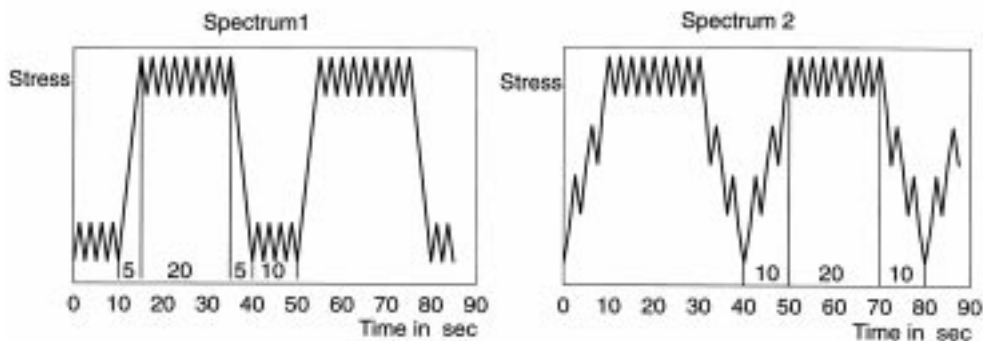


Figure 9. Simplified Flight-By-Flight Stress-Time Histories.

Figure 10 shows the results of the crack growth tests with spectrum 1. For 2024 no difference has been observed between the test conditions laboratory air and 3.5 percent NaCl which is in line with results presented in Figure 2. A similar behavior was observed for 6013 for ΔK values less than 17 MPa \sqrt{m} . Above this value the corrosive environment leads to an increased crack growth up to a factor of 2. The comparison of 2024 and 6013 under spectrum 1 loading and 3.5 percent NaCl reveals no difference in the crack growth rates.

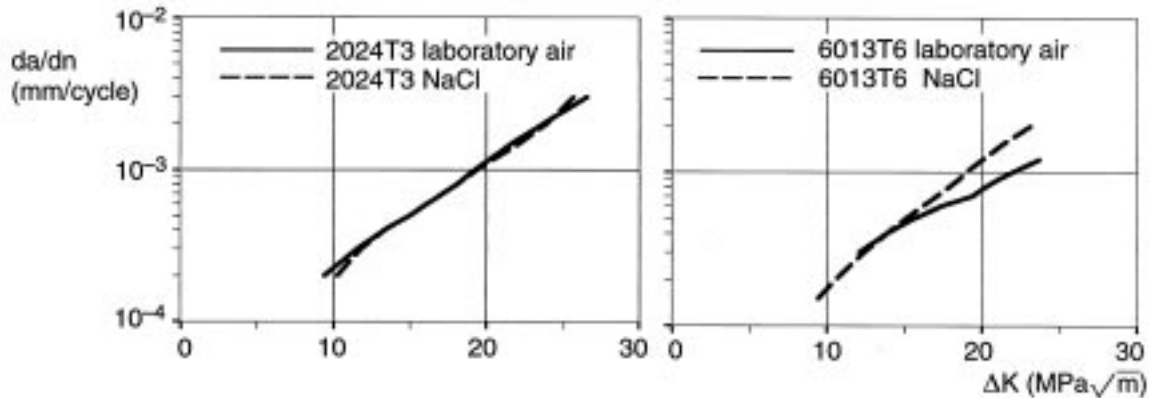


Figure 10. Crack Growth of 2024T3 and 6013T6 Under Simplified Spectrum Loading (Spectrum 1, 0.025 Hz).

The tests with spectrum 2 loading are not yet fully completed. However, the initial results show almost no differences in the crack growth rates under laboratory air and sodium chloride for both materials, see Figure 11.

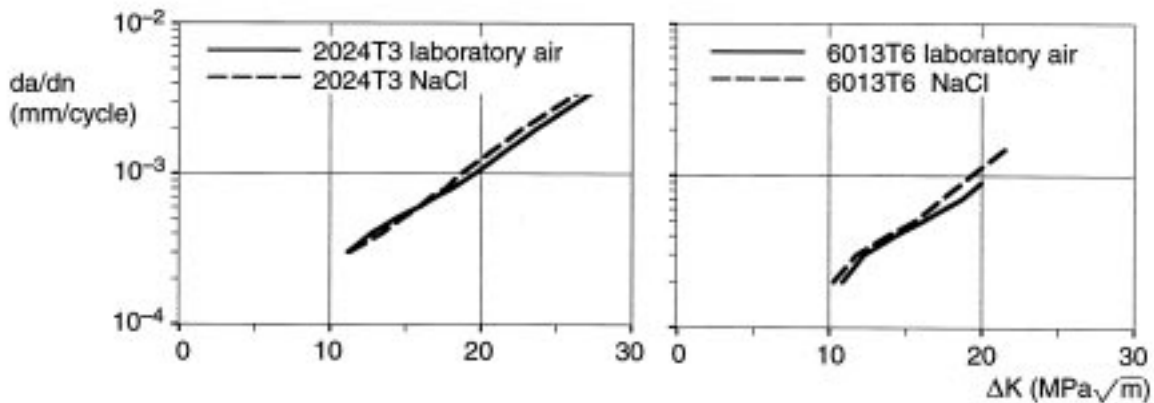


Figure 11. Crack Growth of 2024T3 and 6013T6 Under Simplified Spectrum Loading (Spectrum 2, 0.025 Hz).

Crack Growth Tests under Variable Amplitude Waveforms

The Technical University of Hamburg-Harburg, Germany, investigated the effect of frequency on crack growth behavior of 6013T6. Besides the sinusoidal waveform, a sawtooth and two different types of variable amplitude waveforms were applied (ref. 2). The major cycles of all of the waveforms were applied with an R value of 0.1 (in addition 0.8 for waveform A) and a frequency of either 1 Hz (waveform A) or 0.1 Hz (waveform A and B) or 0.303 Hz (waveform C and D). Waveforms B and D were superposition of the basic cycle and incremental cycles with $R = 0.8$ applied either at the maximum stress or during the climb flank, see Figure 12. The corrosive environment consists of 3.5 percent sodium chloride solution with an inhibitor. The specimens were 30 mm wide and 1.6 mm thick and tested in T-L direction.



Figure 12. Applied Waveforms and Corresponding Frequencies.

The left-hand diagram of Figure 13 presents results for the constant amplitude sinusoidal tests (waveform A) with either $R = 0.1$ and 0.1 Hz or $R = 0.8$ and 1 Hz and the variable amplitude trapezoidal tests (waveform B). The crack growth rates obtained for both waveforms are identical up to about $\Delta K = 10 \text{ MPa}\sqrt{\text{m}}$, above this stress intensity waveform B leads to increased crack growth rates. The right-hand diagram of Figure 13 compares test results for waveform A with the frequencies of 0.1 Hz and 1 Hz. The results are in line with data presented in Figure 6, i.e., increased crack growth rates for 1 Hz are observed. A further comparison between the sawtooth (waveform C) and the modified sawtooth by superposition of small cycles (waveform D) reveals slightly increased crack growth rates for waveform D. However, the increased crack growth rates do not exceed the data for waveform A with a frequency of 1 Hz.

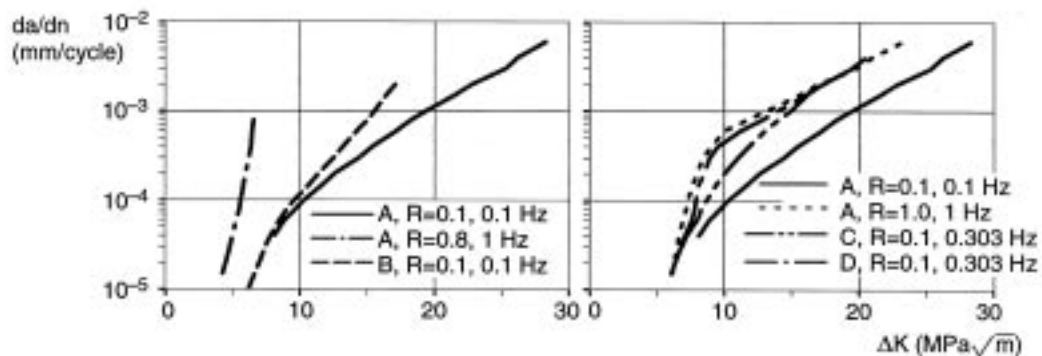


Figure 13. Crack Growth Rates for 6013T6 in NaCl.

CRACK INITIATION TESTS

Many investigations have been carried out to determine the effect of a corrosive environment on fatigue life (crack initiation). For example DA tested several coupons representing the longitudinal lap joint. The test specimens were manufactured according to the production standard, i.e., with surface treatment (CAA, primer, top coat), wet assembly, and wet riveting. The tests performed for two materials, the current skin material 2024T3 and the Al-Li alloy 8090T8, revealed no influence of the different environments, i.e., laboratory air and sodium chloride, see Figure 14.

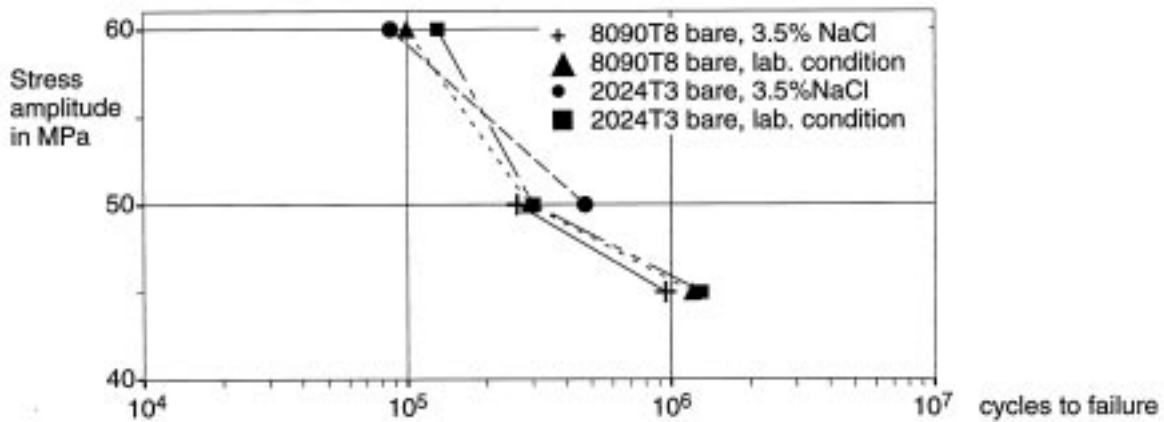


Figure 14. Influence of the Environment on the Fatigue Life of Longitudinal Lap Joints.

In contrast to the above mentioned results, corrosion has a significant effect on the fatigue life of lap joints investigated in ref. 3. It has to be recognized that these 2024T3 specimens were manufactured without surface treatment and dry assembled. The described results are nearly independent from the test frequency as shown in Figure 15.

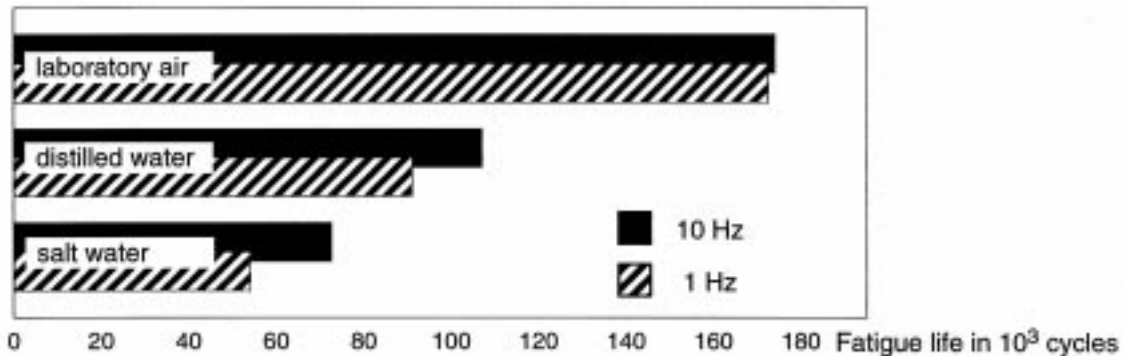


Figure 15. Influence of the Environment on the Fatigue Life of 2024T3 Lap Joints Without Surface Treatment.

These test series lead to the conclusion that no reduction of the fatigue life has to be expected for in-service aircraft as long as the surface protection system is intact.

CONCLUSIONS

The application of new materials to the next aircraft generation requires among others crack initiation and crack growth tests to verify that the new materials are not worse than the conventional 2024. Since this could not be concluded from the standard crack growth tests with 20 Hz in laboratory air or sodium chloride, DA has performed comparative crack growth tests with 2024 and 6013 specimens loaded by either constant amplitude or variable amplitude spectra and more realistic frequencies. The crack growth tests with the low frequencies in laboratory air or in a corrosive environment revealed that the crack growth rates for 6013T6 are as good as or better than those for 2024T3/T42/T351 except for low temperature and high ΔK values. This result leads to the conclusion that 6013 may be considered during the material choice for future aircraft as far as the crack growth aspect is concerned.

The crack initiation tests revealed that the surface protection plays the major role to prevent a fatigue life reduction in corrosive environment.

REFERENCES

1. Trockels, I.; Gysler, A.; and Lutjering, G.: Influence of Frequency on Fatigue Crack Propagation Behavior of Aluminum Alloys in Aggressive Environment. FATIGUE'96, The Sixth International Fatigue Congress; May 6-10, 1996; Berlin, Germany.
2. Trockels, I.; Lutjering, G.; and Gysler, A.: Effect of Frequency on Fatigue Crack Propagation Behavior of the Aluminum Alloy 6013 in Corrosive Environment. 5th International Conference of Aluminum Alloys; July 1-5, 1996; Grenoble, Switzerland.
3. Muller, R. P. G.: An Experimental and Analytical Investigation on the Fatigue Behavior of Fuselage Riveted Lap Joints. Ph. D. Thesis, Delft University of Technology, Faculty of Aerospace Engineering, Structures and Materials Laboratory, The Netherlands, 1995.

EFFECTS OF COMBINED LOADS ON THE NONLINEAR RESPONSE AND RESIDUAL STRENGTH OF DAMAGED STIFFENED SHELLS

James H. Starnes, Jr., and Cheryl A. Rose
NASA Langley Research Center
Hampton, VA 23681-0001

Charles C. Rankin
Lockheed Palo Alto Research Laboratory
Palo Alto, CA 94304-1191

ABSTRACT

The results of an analytical study of the nonlinear response of stiffened fuselage shells with long cracks are presented. The shells are modeled with a hierarchical modeling strategy and analyzed with a nonlinear shell analysis code that maintains the shell in a nonlinear equilibrium state while the crack is grown. The analysis accurately accounts for global and local structural response phenomena. Results are presented for various combinations of internal pressure and mechanical loads, and the effects of crack orientation on the shell response are described. The effects of combined loading conditions and the effects of varying structural parameters on the stress-intensity factors associated with a crack are presented.

INTRODUCTION

Transport fuselage shell structures are designed to support combinations of internal pressure and mechanical flight loads which can cause a geometrically nonlinear structural response. These fuselage shell structures are required to have adequate structural integrity so that they do not fail if cracks occur in service. The structural response of a stiffened fuselage shell structure with one or more cracks is influenced by the local stress and displacement gradients near the cracks and by the internal load distribution in the shell. Local displacements near a crack can be large compared to the fuselage skin thickness, and these displacements can couple with internal stress resultants in the shell to amplify the magnitudes of the local stresses and displacements near the crack. This nonlinear response must be understood and accurately predicted in order to determine the structural integrity and residual strength of a fuselage structure.

Recent studies (e.g., Refs. 1-3) have shown that the stiffness and internal load distributions in a stiffened fuselage shell will change as a long crack grows in the shell. These changes affect the local stress and displacement gradients near the crack in a manner

that may contribute to additional crack growth in the shell and, as a result, affect its structural integrity and residual strength. Refs. 1-3 show that the structural response and structural integrity of a stiffened fuselage shell with a crack can be studied analytically using a nonlinear structural analysis procedure that models crack growth in the shell. Results from a nonlinear analysis procedure more accurately represent the local and global responses of a thin stiffened shell with a crack than the results from a conventional linear analysis procedure for all loading conditions.

The present paper describes the results of an analytical study of the nonlinear response of a typical stiffened fuselage shell structure with long cracks and subjected to various combinations of internal pressure and mechanical loads. Both longitudinal and circumferential fuselage cracks are considered. The results illustrate the influence of the different loading conditions on the local stress and displacement gradients near a crack, on the magnitudes of the stress-intensity factors associated with the crack, and on crack-growth trajectories. The effects of varying structural parameters, such as fail-safe strap thickness and stiffener area, and varying crack orientation on the results are described. The effects of loading conditions and crack location relative to stiffening members on both self-similar and non-self-similar crack-growth trajectories are also presented.

NONLINEAR ANALYSIS PROCEDURE AND HIERARCHICAL MODELING STRATEGY

A nonlinear shell analysis procedure that is combined with a hierarchical modeling strategy is used in the present study to analyze the nonlinear response of a typical stiffened fuselage shell with long skin cracks. The analysis procedure models crack growth in a shell while the shell is in a nonlinear equilibrium state and determines local stress and displacement gradients in critical areas of a fuselage where cracks may be growing. In addition, the analysis procedure accurately models frame and stringer cross-sectional distortion and rolling and predicts the nonlinear interactions that occur between individual structural elements and larger subcomponents as a result of these deformations. The details of the analysis procedure and modeling strategy are discussed subsequently.

Nonlinear Analysis Procedure

The STAGS (SStructural Analysis of General Shells) nonlinear finite element analysis code⁴ is used in the present study to conduct the nonlinear analyses of stiffened fuselage shells with long cracks. STAGS is a finite element code for analyzing general shell structures and includes the effects of geometric and material nonlinearities in the analysis. STAGS is capable of conducting strength, stability, and collapse analyses for general shell structures with complex geometry and subjected to combined mechanical and thermal loads. The code uses both the modified and full Newton methods for its nonlinear solution algorithms and

accounts for large rotations in a shell by using a co-rotational algorithm at the element level. STAGS has static and transient analysis capabilities that can be used to predict local instabilities and modal interactions that occur due to destabilizing mechanical loads, such as an applied compression or shear load. The Riks pseudo arc-length path following method⁵ is used to continue a solution past the limit points of a nonlinear response. A boundary constraint function, based on a least-squares analysis, is used to apply equivalent beam loads to the boundary of a thin-shell finite element model without artificially distorting the shell wall. By using this least-squares constraint function, flight loads can be extracted from a lower fidelity global aircraft model and then applied as edge loads on the boundaries of a more refined finite element model of a fuselage shell section.

STAGS can also perform crack-propagation analyses. Cracks in simple unstiffened shells and in built up structures and structural elements, such as frames, stringers, and fail-safe straps, can be modeled. A node-release method and a load-relaxation technique are used to extend a crack while the shell is in a nonlinear equilibrium state.² The forces necessary to hold the nodes together along the path of new crack growth are calculated with this method. These forces are relaxed as the crack is extended, and a new equilibrium state is calculated which corresponds to the longer crack. The changes in the stiffness matrix and the internal load distribution that occur during crack growth are accounted for in the analysis, and the nonlinear coupling between internal forces and in-plane and out-of-plane displacement gradients that occurs in a shell are properly represented. Output from STAGS includes strain-energy release rates that can be used to determine stress-intensity factors. The stress-intensity factors^{2, 6} can then be used to estimate the residual strength of a damaged shell.

The FRANC3D (FRacture ANalysis Code for 3D surfaces) fracture analysis code⁷ has been interfaced with STAGS to predict curved or non-self-similar, crack-growth trajectories. STAGS results are transmitted to FRANC3D which computes the stress intensity factors at the crack tips using the modified crack closure integral method, and an estimate of the crack growth direction at each tip is computed by applying the maximum tangential stress criterion. Using these parameters, the crack is grown within FRANC3D by a user specified length. After the crack is grown, FRANC3D creates a new finite element mesh in the area of the crack. The STAGS results from the previous finite element mesh are mapped onto the new finite element mesh using a transformation subroutine that is compatible with STAGS. The nonlinear STAGS analysis can then be continued with the new finite element mesh results from FRANC3D.

Hierarchical Modeling Strategy

A hierarchical modeling strategy is used in the present study for the analysis of stiffened fuselage shell sections subjected to combined internal pressure and mechanical loads. The three hierarchical modeling levels used to obtain the analysis results presented in this paper are characterized by a global shell model, a 6x6 bay stiffened-panel model, and a

2x3 bay stiffened-panel model. Different modeling idealizations are employed in the three levels in the hierarchy.

The first level in the hierarchical modeling strategy uses a global stiffened fuselage shell model that is subjected to combined internal pressure and mechanical loads. The mechanical loads are applied as concentrated loads to one end of the global fuselage shell model using a least squares boundary constraint function. Symmetry conditions are imposed at the other end. The global stiffened shell model includes floor beams and stanchions, frames, stringers, fail-safe straps, and stringer clips. The skin is modeled with shell elements; the frames, which may have nonsymmetric cross sections, are modeled with shell and beam elements in order to represent accurately the cross-sectional bending and twisting of the frames; and the floor beams, stanchions, fail-safe straps, stringers, and stringer clips are modeled with beam elements. Damage is introduced in the global model in the form of longitudinal or circumferential skin cracks and may also include broken frames, stringers, and fail-safe straps. A geometrically nonlinear analysis of the global shell model provides the internal load distribution for the fuselage shell and kinematic boundary conditions for the 6x6 bay stiffened-panel model.

The 6x6 bay stiffened-panel model has a higher degree of mesh refinement and structural detail than the global model described above in order to represent more accurately the structural response around the crack and the distortion of the frames and stringers. Frames, stringers, and stringer clips are modeled as branched shells in the 6x6 bay stiffened-panel model, and the fail-safe straps are modeled using shell elements. In addition, the mesh is sufficiently refined around the crack tip for calculating crack-growth parameters.

Displacements obtained from the 6x6 bay stiffened-panel model are used as boundary conditions for the third modeling level, which consists of a more detailed, highly local 2x3 bay stiffened-panel model. The 2x3 bay stiffened-panel model differs from the 6x6 bay stiffened-panel model primarily in the degree of mesh refinement and may also include additional structural details such as lap joints and fasteners. The fasteners are modeled in STAGS with nonlinear spring elements. In addition, at this modeling level, the STAGS analysis is interfaced with FRANC3D to simulate general, curved, non-self-similar crack growth trajectories. Results from a nonlinear STAGS analysis of the original structural configuration are mapped into FRANC3D where the modified crack closure integral method is used to determine stress intensity factors at each crack tip and an estimate of the crack growth direction at each tip is computed by applying the maximum tangential stress criterion.⁷ Using these parameters, the crack is extended within FRANC3D, by an amount specified by the analyst, and the 2x3 bay model is remeshed in the area of the crack. The STAGS results from the previous finite element mesh are mapped onto the new finite element mesh. The new mesh is then employed for the next STAGS analysis. The steps described above are repeated to obtain a crack trajectory and stress-intensity factor history.

Generic Narrow-Body Transport Fuselage Model

The fuselage shell analyzed in this study is a typical generic narrow-body transport aluminum fuselage. The shell has a 74-inch radius and is 160 inches long. The shell consists of 0.036-inch-thick 2024-T3 clad aluminum skin, and is reinforced by nine frames that are spaced 20 inches apart and by fifty stringers that are spaced 9.3 inches apart. The stringers and frames are made of 7075-T6 aluminum. Fail-safe straps are located beneath each frame and stringer, and additional circumferential fail-safe straps are located midway between frames. The fail-safe straps are 0.036 inch thick, the stringers are 0.028-inch-thick hat sections, and the frames are 0.040-inch-thick Z-sections, unless otherwise noted. A Poisson's ratio equal to 0.33 is used for all structural components, a Young's modulus equal to 10.5E6 psi is used for the skin and tear straps and a Young's modulus equal to 10.7E6 psi is used for the frames, stringers, and stringer clips in all analyses. In addition, it is assumed that a perfect bond exists between all structural components along their entire area of overlap at all modeling levels. Circumferential and longitudinal cracks are located in the crown midway between the ends of the global fuselage shell model.

The loads considered in the present study include internal pressure, up and down bending, vertical shear, and torsion. The internal pressure is equal to 8 psi for all analyses which is the nominal operating pressure in the passenger cabin of a typical subsonic transport. Tensile axial stress resultants are applied to the model to represent the loads from the pressure bulkheads. The magnitudes of the bending and vertical shear loads used in this study are the maximum values of these applied loads that can be supported by an undamaged global shell model without buckling the skin. The applied bending moment is equal to 6,325,000 in-lbs, and the applied shear force is equal to 50,000 lbs., unless otherwise noted. Up-bending moments are applied to the model with a longitudinal crown crack so that the crack is loaded in compression. Axial compression has been shown³ to cause higher stress-intensity factors at the tips of longitudinal crown cracks than are caused by axial tension. Both up- and down-bending moments are applied to the global models with a circumferential crack so that the fuselage crown is loaded in either compression or tension, respectively.

RESULTS AND DISCUSSION

Results of the stiffened fuselage nonlinear analysis have been generated for seven loading conditions: internal pressure plus a bending load; internal pressure plus a vertical shear load; internal pressure plus a torsion load; internal pressure plus bending and torsion loads; internal pressure plus bending and vertical shear loads; internal pressure plus vertical shear and torsion loads; and internal pressure plus bending, vertical shear, and torsion loads. Results for these loadings are presented for both longitudinal and circumferential cracks to illustrate the effects of crack orientation and the applied loading condition on the structural response.

Results are presented in the form of stress-intensity factor versus crack-length plots, stress resultant contours and deformed shape plots, and crack growth trajectories. The stress-intensity factors presented were obtained from the 6x6 bay stiffened-panel models. To simulate crack growth in the 6x6 bay stiffened-panel models, the longitudinal cracks were grown from an initial length of 6.0 inches to a final length of 18.5 inches, and the circumferential cracks were grown from an initial length of 4.7 inches to a final length of 17.7 inches. Boundary conditions for the 6x6 bay stiffened-panel models with a longitudinal crack or a circumferential crack were obtained from a global model with a 6.0-inch-long longitudinal crack or a 4.7-inch-long circumferential crack, respectively. Crack-growth trajectories for a longitudinal crack were obtained using a 2x3 bay stiffened-panel model with an initial crack length of 6.0 inches. Boundary conditions for the 2x3 bay model were obtained from the 6x6 bay stiffened-panel model with a 6-inch-long crack.

6x6 Bay Stiffened Panels with a Longitudinal Crack

The stress-intensity factors K_I and K_{II} , which correspond to a crack-opening mode and a crack-shearing mode, are shown in figures 1a and 1b, respectively, as a function of longitudinal crack length for the seven combined loading conditions considered in this study. The legend in the figures identifies the loading conditions by combinations of the letters P, M, S, and T, which indicate the internal pressure, bending, vertical shear, and torsion loads, respectively. The solid lines represent results for internal pressure plus one mechanical load component, and the dashed lines represent results for internal pressure plus more than one mechanical load component. As shown in figure 1a, the loading conditions with bending (M) and vertical shear (S) have higher values of K_I than those with torsion (T). This trend is explained by the fact that in the bending and vertical shear loading cases, high axial compressive stresses are present in the crown panel that couple with the out-of-plane displacements along the edges of the crack. The loading conditions with torsion have high values of shear stress resultants in the crown panel and are not represented by a simple crack-opening response. Consequently, the panels subjected to torsion loading have higher values of K_{II} than those without a torsion load, as shown in figure 1b. In addition, the curves representing the change in K_I as the crack length increases in figure 1a are not linear, and the slope of the curves decreases as the crack length increases. The curves for K_{II} are mildly nonlinear. The decrease in slope of the K_I curves with increasing crack length is explained by noting that as the crack length increases, the loads in the skin are redistributed to the frames and fail-safe straps, and the cross sections of the stringers on either side of the crack distort enough to reduce the stiffnesses of the stringer.

Values of the stress-intensity factors are typically used to determine the residual strength of a stiffened shell structure as a crack grows. An example residual strength diagram for a stiffened shell with a longitudinal crack in the skin and a broken frame and subjected to pressure loading is shown in figure 2. The diagram shows a skin fracture curve, plotted as a solid line, and a frame yield curve for the next intact frame, plotted as a dotted line. The solid curve is a plot of the critical far-field hoop stress in the skin as a function of

crack length. The critical far-field hoop stress is determined from the pressure that would cause the dominant crack tip stress-intensity factor to become critical for each crack length. The curve for the frame is determined from the far-field hoop stresses that correspond to yielding in the frame for each crack length. In general, the curves in figure 2 indicate that the residual strength of the skin and the frame decreases as the crack grows. The residual strength of the skin decreases significantly at first, and then increases slightly as the crack approaches a fail-safe strap because some of the skin load is redistributed to the fail-safe strap. The residual strength of the frame decreases once the crack has grown past the fail-safe strap because some of the skin load is redistributed to the frame, which causes the frame to yield at a lower load. The crack in the skin will grow before the frame yields if the residual strength of the skin is less than the residual strength of the frame. In contrast, the frame will yield before the skin crack grows when the residual strength of the frame is less than the residual strength of the skin. The structure has no residual strength when the two curves have values less than prescribed allowable strength values.

The effects of varying fail-safe strap thickness, t , on the stress-intensity factor K_I for a panel with a longitudinal crack and subjected to internal pressure and a bending or a torsion load are shown in figure 3. Fail-safe strap thicknesses equal to 0.018, 0.036, and 0.054 inch were used. The solid curves are for internal pressure and bending loads and the dashed curves are for internal pressure and torsion load. The length of the crack varies from 6.0 to 18.5 inches. The results presented in figure 3 indicate that K_I increases as the fail-safe strap thickness decreases. In addition, as previously shown in figure 1, the loading with bending produces higher values of K_I than the corresponding loading in torsion. Moreover, the slope of the K_I curves decreases as the crack approaches the frames and the load in the skin is redistributed to the frames. The decrease in the slope of the K_I curves is more significant for the loading with bending. Similar results from the analysis for K_{II} indicate that K_{II} is not significantly affected by these changes in the fail-safe strap thickness; however, there is a slight increase in K_{II} as the fail-safe strap thickness decreases.

6x6 Bay Stiffened-Panels with a Circumferential Crack

Stress resultant distribution contour plots obtained from the nonlinear analyses of a 6x6 bay stiffened-panel with an 17.7-inch-long circumferential crack are shown on the corresponding deformed shapes in figures 4 and 5 for a stiffened panel subjected to combinations of internal pressure and bending loads and a stiffened panel subjected to internal pressure and torsion, respectively.

In a panel subjected to internal pressure only (not shown) the edges of the crack spread apart and the crack opens. The material line elements along the edges of the crack are in hoop tension because of the outward bulging deformations in the local crack region that are caused by the internal pressure. The outward bulging deformations near the crack are not symmetric for this crack location because the crack has a relatively stiff frame on one side and a relatively flexible fail-safe strap on the other side. The hoop stress resultant

distribution results in a panel that is subjected to internal pressure and a down-bending moment are shown in figure 4a. This loading condition also causes the edges of the crack to spread apart and open the crack, but the skin along the edges of the crack is in hoop compression except at the crack tips where a significant tensile stress resultant exists. Apparently, the compressive hoop stress resultant induced by the tensile axial stress resultant caused by the down-bending moment is large enough to dominate the tensile hoop stress resultant along the edge of the crack caused by the internal pressure. The down-bending moment causes a significant tensile axial stress resultant gradient near the crack, as shown in figure 4b, and a biaxial tension stress state exists at the crack tip for this loading condition. In a panel that is subjected to internal pressure and an up-bending moment, compressive axial stresses in the crown, resulting from the up-bending moment, cause the edges of the crack to approach one another and contact occurs at several locations (not shown). One edge of the crack contacts the webs of the broken stringer on the other edge of the crack, and the two edges of the crack contact each other at two other locations. The contact was not accounted for in the analysis and will be considered in future analyses. The skin along the edges of the crack is in hoop tension for this loading condition along the entire length of both crack edges. Apparently, the tensile hoop stress resultant induced by the compressive axial stress resultant caused by the up-bending moment increases the magnitude of the tensile hoop stress resultant along the edges of the crack caused by the internal pressure.

The axial stress resultant distribution results in a panel with a 17.7-inch-long circumferential crack and subjected to internal pressure and torsion loads are shown in figure 5a. The crown is primarily in axial tension because of the tension load induced by the pressure bulkhead. The outward bulging deformations near the crack are not the same on both sides of the crack for this loading condition, and the edges of the crack are displaced circumferentially or sheared relative to one another and significantly distorted. Therefore, the local displacements of the crack are not representative of a simple crack-opening mode. The hoop stress resultant distribution for this loading condition is shown in figure 5b and does not have reflective symmetry, due to the torsion load. The results indicate that the hoop stress resultant in the skin at the crack tips has a relatively high tensile value for this loading condition.

The stress-intensity factors K_I and K_{II} are shown as a function of circumferential crack length in figures 6a and 6b, respectively, for the seven combined loading conditions considered in this study. The legend convention used in figure 1 is also used in figure 6. One half of the values of the moment and vertical shear loads previously stated were used in the analysis for the loading conditions with both the bending (M) and vertical shear loads (S) to prevent the crack faces from contacting. The loading condition with internal pressure and a torsion load has the highest value of K_I , and all loading conditions with a torsion load have high values of K_{II} . For a torsion load only, there is no axial compression to close the crack which would cause a higher value of K_I . The torsion load causes one crack face to deform more than the other, which causes a higher value of K_{II} . The bending and vertical shear loads cause the crack to close which reduces the value of K_I . The curves representing the change in K_I and K_{II} as a function of crack length in figures 6a and 6b are not linear as the crack length increases because of the internal load redistribution that occurs. The redistribution of internal

loads changes the stress magnitudes in the skin and, as a result, changes the magnitudes of the stress-intensity factors.

The effects of varying the stringer cross-sectional area on the stress-intensity factor K_I for a panel with a circumferential crack and that is subjected to internal pressure and torsion are shown in figure 7. The area of the stringer is varied by changing the thickness, t , of all components of the stringer hat section. The results in the figures are for thicknesses, t , equal to 0.028, 0.036 and 0.040 inch. The length of the crack varies from 4.7 to 17.7 inches. The results in figure 7 indicate that K_I increases as the stringer area decreases and as the crack length increases, which suggests that the skin has higher axial stress resultants when the stringer is thinner. The results from the analysis indicate that K_{II} increases as the stringer thickness decreases for all crack lengths, which suggests that thicker stringers restrain the shear deformations near the crack and reduce the shear stress resultants in the skin. The values of K_I and K_{II} both decrease as the crack length increases beyond approximately 15.0 inches because the crack tips are approaching the stringers on either side of the broken stringer and the load in the skin is redistributed to the intact stringers.

Crack-Growth Trajectories

The effects of loading condition and crack location on crack growth trajectories were studied using a detailed 2x3 bay local-panel model that is centered around the crack. Displacements obtained from the 6x6 bay stiffened-panel model with a 6-inch-long longitudinal crack were applied as boundary conditions for the 2x3 bay local-panel model. Crack-growth trajectories are shown in figure 8 for three longitudinal crack locations and loading conditions. The initial crack length for these longitudinal crack configurations is 6.0 inches, and the crack is located either midway between two stringers or 1.2 inches from a stringer. The crack-growth trajectory for a crack located midway between two stringers in a panel that is subjected to internal pressure, bending, and vertical shear loads is shown in figure 8a for a crack length of 16.0 inches. The crack-growth trajectory for this case is self-similar due to the symmetry of the loading condition and geometry. The crack-growth trajectory for a crack located 1.2 inches from a stringer in a panel subjected to internal pressure, bending, and vertical shear loads is shown in figure 8b for a crack length of 16.0 inches. The crack-growth trajectory for this case is non-self-similar due to the asymmetry of the geometry. The crack-growth trajectory for a crack that is located midway between two stringers in a panel that is subjected to internal pressure and torsion shear loads is shown in figure 8c for a crack length of 16.0 inches. The crack-growth trajectory for this case is non-self-similar due to the nonsymmetry of the loading condition.

CONCLUDING REMARKS

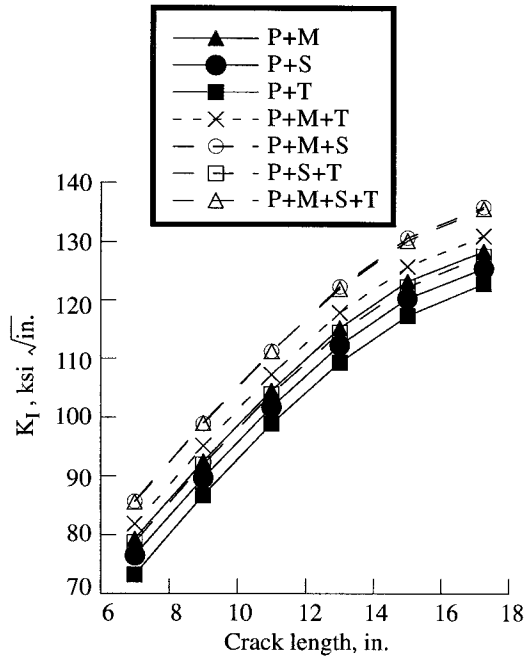
The results of an analytical study of the effects of long cracks on the nonlinear response of stiffened fuselage shells subjected to combined internal pressure and mechanical loads are presented. The nonlinear analysis predicts the large local stress and out-of-plane displacement gradients that exist near cracks in stiffened shells and accounts for the coupling that occurs between the in-plane stress resultants and the out-of-plane displacements in the neighborhood of the crack.

The results of the nonlinear analyses show that the response of a damaged stiffened shell subjected to combined internal pressure and mechanical loads is affected by both the load combination and the crack orientation. In the case of a longitudinal crown crack, the axial compressive stresses in the crown that are caused by bending and vertical shear loads can couple with the out-of-plane displacements in the crack region to amplify the magnitudes of the local stresses and displacements, thereby increasing the crack-opening, stress-intensity factor. On the other hand, compressive axial stress resultants can close a circumferential crack and reduce the crack-opening, stress-intensity factor associated with the crack. Tensile axial stress resultants can open a circumferential crack. Torsion loads can also significantly affect the local response of a shell with a circumferential crack by causing the edges of the crack to shear relative to one another and by increasing the crack-shearing, stress-intensity factor associated with the crack.

As a crack grows in a stiffened shell, the internal loads are redistributed from the fuselage skin to other structural elements such as frames, stringers, and fail-safe straps, and this internal load redistribution affects the magnitudes of the stress-intensity factors associated with a crack. Varying the thickness of the fail-safe straps or the area of the stringers can affect the magnitudes of the stress-intensity factors, which will affect residual strength. The crack-growth trajectory can be influenced by the crack location and by the loading condition. Nonsymmetric loading conditions or geometries can cause non-self-similar crack-growth trajectories.

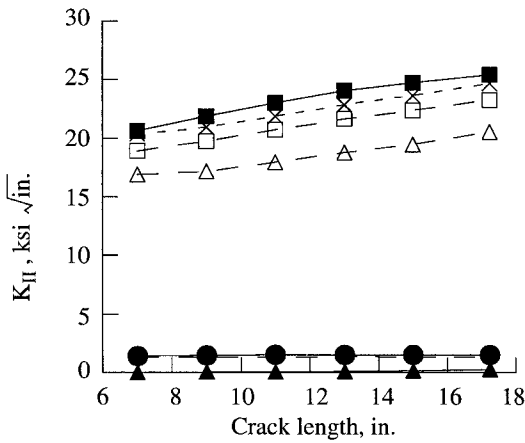
REFERENCES

1. Riks, E.: Bulging Cracks in Pressurized Fuselages: A Numerical Study. NLR MP 87058 U, NLR National Aerospace Laboratory, The Netherlands, September 1987.
2. Rankin, C. C., Brogan, F. A., and Riks, E.: Some Computational Tools for the Analysis of Through Cracks in Stiffened Fuselage Shells. *Computational Mechanics*, Springer International, Vol. 13, No. 3, December 1993, pp. 143-156.
3. Starnes, James H., Jr., Britt, Vicki O., and Rankin, Charles C.: Nonlinear Response of Damaged Stiffened Shells Subjected to Combined Internal Pressure and Mechanical Loads. AIAA Paper 95-1462, April 1995.
4. Brogan, F. A., Rankin, C. C., and Cabiness, H. D.: STAGS User Manual. Lockheed Palo Alto Research Laboratory, Report LMSC P032594, 1994.
5. Riks, E.: Some Computational Aspects of the Stability Analysis of Nonlinear Structures. *Computational Methods in Applied Mechanics and Engineering*, Vol. 47, pp. 219-259, 1984.
6. Riks, E., Brogan, F. A., and Rankin, C. C.: Bulging of Cracks in Pressurized Fuselages: A Procedure for Computation. In *Analytical and Computational Models of Shells*, Noor, A. K., Belytschko, T., and Simo, J. C., Editors, The American Society of Mechanical Engineers, ASME-CED Vol. 3, 1989.
7. Potyondy, D. O.: A Software Framework for Simulating Curvilinear Crack Growth in Pressurized Thin Shells. Ph.D. Dissertation, Cornell University, Ithaca, NY, 1993.



(a) K_I stress-intensity factor.

Fig. 1 Stress-intensity factors for a six-bay by six-bay stiffened fuselage crown panel with an 18.5-inch-long longitudinal crack subjected to internal pressure and mechanical loads.



(b) K_{II} stress-intensity factor.

Fig. 1 Concluded.

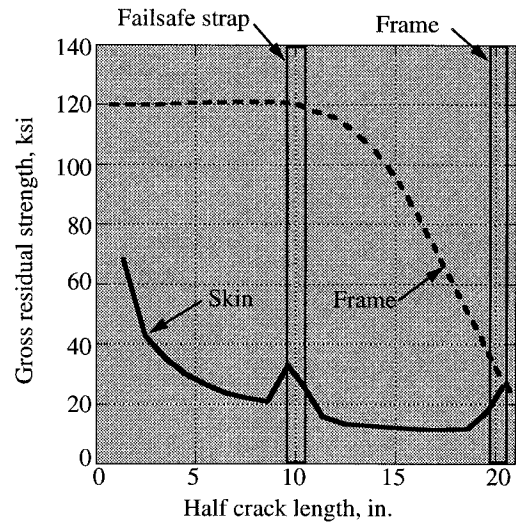


Fig. 2 Residual strength of a stiffened fuselage crown panel with a longitudinal skin crack and broken frame, and subjected to internal pressure.

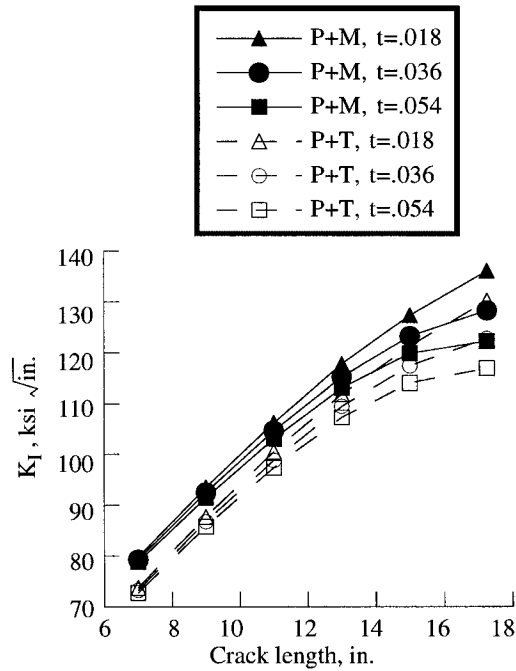
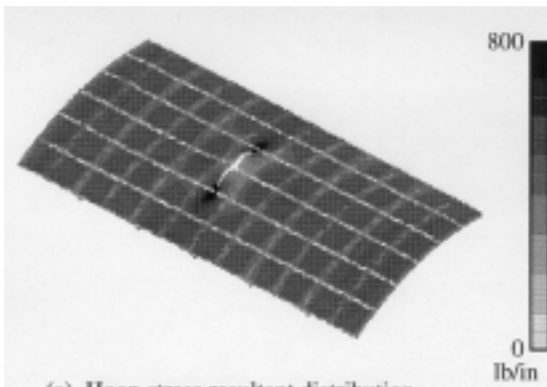
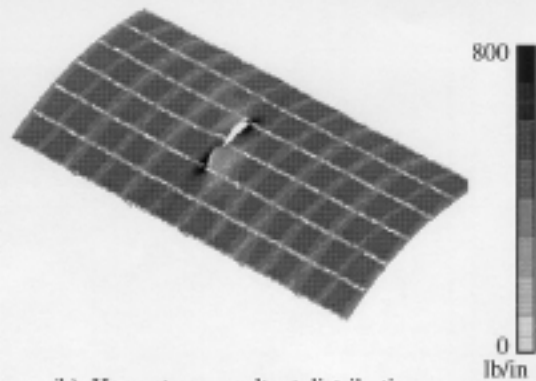


Fig. 3 Effects of varying fail-safe-strap thickness on the K_I stress-intensity factor for a six-bay by six-bay stiffened fuselage crown panel with an 18.5-inch-long longitudinal crack and subjected to internal pressure, bending and torsion loads.



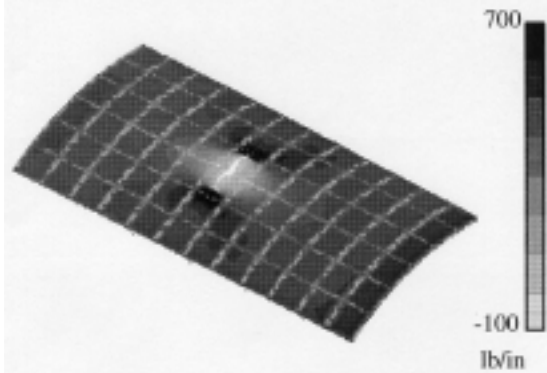
(a) Hoop stress resultant distribution.

Fig. 4 Stress resultant distributions in a six-bay by six-bay stiffened fuselage crown panel with a 17.7-inch-long circumferential crack and subjected to internal pressure and down-bending loads.



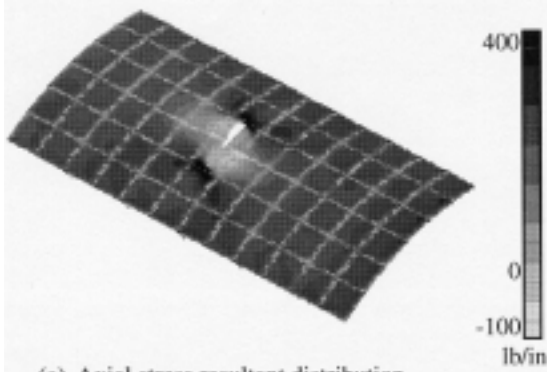
(b) Hoop stress resultant distribution.

Fig. 5 Concluded.



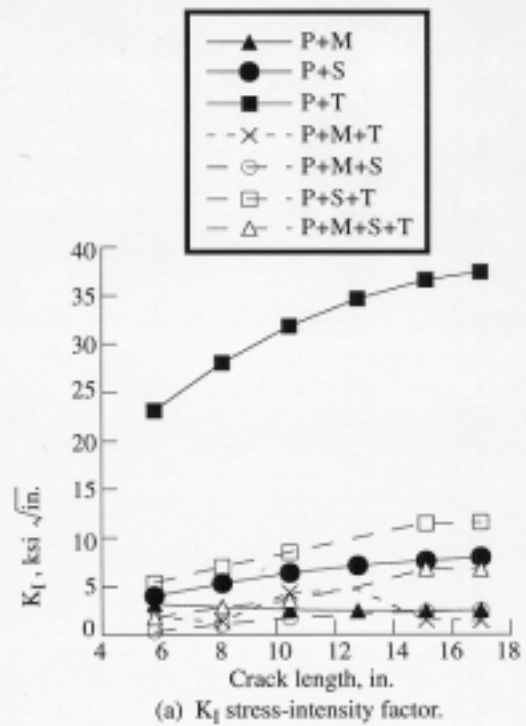
(b) Axial stress resultant distribution.

Fig. 4 Concluded.



(a) Axial stress resultant distribution.

Fig. 5 Stress resultant distributions in a six-bay by six-bay stiffened fuselage crown panel with a 17.7-inch-long circumferential crack and subjected to internal pressure and torsion loads.



(a) K_I stress-intensity factor.

Fig. 6 Stress-intensity factors for a six-bay by six-bay fuselage crown panel with an 17.7-inch-long circumferential crack and subjected to internal pressure and mechanical loads.

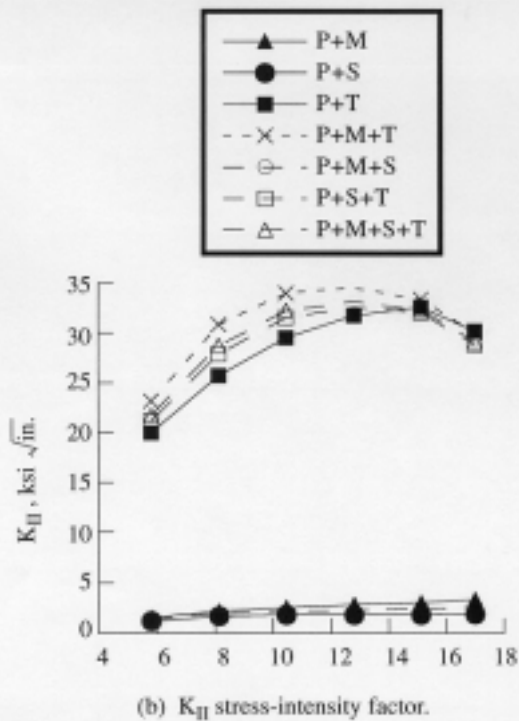


Fig. 6 Concluded.

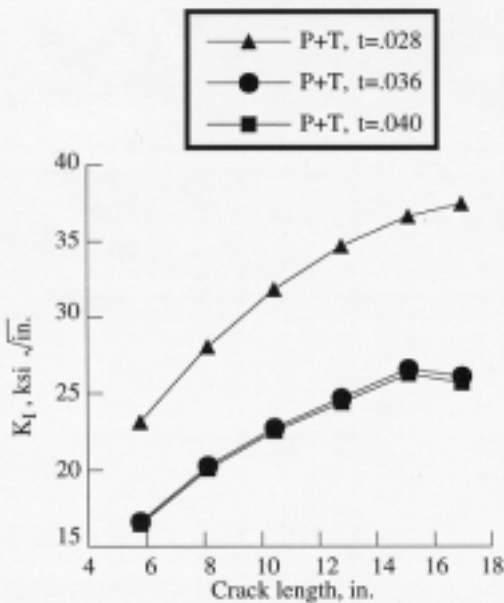
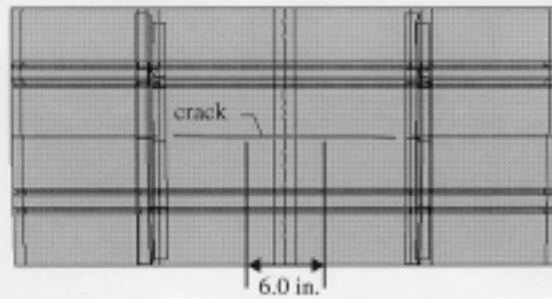
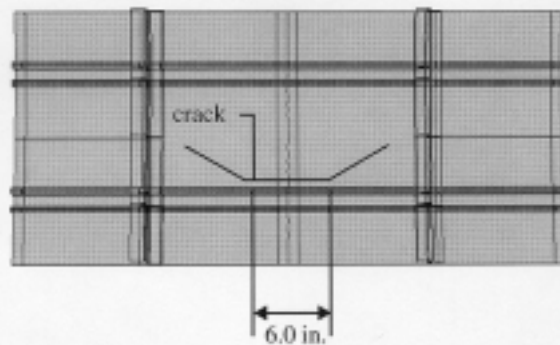


Fig. 7 Effects of varying stiffener thickness on the K_I stress-intensity factor for a six-bay by six-bay stiffened fuselage crown panel with a 17.7 inch-long circumferential crack and subjected to internal pressure and torsion loads.



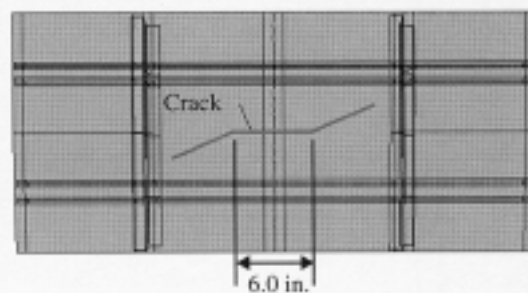
(a) 16-inch-long crack trajectory for internal pressure, bending and vertical shear loads with crack midway between two stringers.

Fig. 8 Crack growth trajectories for a two-bay by three-bay stiffened fuselage crown panel with a 6.0-inch-long initial crack.



(b) 16-inch-long crack trajectory for internal pressure, bending and vertical shear loads with crack 1.2 inches from a stringer.

Fig. 8 Continued.



(c) 16-inch-long crack trajectory for internal pressure and torsion loads with crack initially midway between two stringers.

Fig. 8 Concluded.

ELASTO-PLASTIC MODELS FOR INTERACTION BETWEEN A MAJOR CRACK AND MULTIPLE SMALL CRACKS

Karl-Fredrik Nilsson
The Aeronautical Research Institute of Sweden
Structures Department
PO Box 110 21, S-161 11
Bromma, Sweden

SUMMARY

Two-dimensional elasto-plastic analyses based on the yield-strip concept with different levels of complexity have been used to analyze the residual strength of flat sheets weakened by a central major crack amid small cracks. The predicted loads at crack linkup and failure were compared with reported test results. Three modeling aspects were investigated in some detail: elastic-plastic crack interaction, restart of crack growth after linkup, and the effect of modeling the propagation of the small cracks. The most advanced method gave predictions that were in excellent agreement with test results whereas the simpler methods gave reasonably good agreement.

INTRODUCTION

An increasing number of commercial airplanes are used beyond their original design life. Fatigue cracking at multiple rivet locations along the lap joint of the fuselage have been found during inspections of older aircraft. The phenomenon is known as multiple-site damage (MSD), and there is general concern that MSD may impair the tolerance of the fuselage to major cracks. A complete analysis of an MSD damaged lap joint with all the fine details becomes very complicated and there is definitely a need to first understand the basic mechanisms of the crack interaction as well as to derive simplified analysis methods that can account for the gross behavior of the crack interaction. It is apparent though that plastic interaction plays an important role since the rivet pitch is typically 25 mm whereas the small scale yield estimate of the plastic zone ahead of an advancing major crack in an aluminum alloy is typically 50 mm.

Basic tests have been carried out on flat panels with a major crack and a number of small cracks distributed across the ligaments of both sides of the major crack [1, 2]. The fracture behavior was registered and in particular loads at which the major crack linked up with small cracks. Some of these tests have been analyzed with methods of different levels of complexity and criteria for crack linkup. Newman et al. [3] used a crack opening angle criterion together with an elasto-plastic finite element analysis. Their predictions for crack

linkup and panel failure agreed well with the test results. A much simpler approach suggested by Swift [4] uses the load at which the ligament between the major crack and the small crack is fully yielded to predict linkup. This criterion has become popular due to its simplicity and has been adopted in [2] and [5] with small-scale yielding estimates for the plastic zone size to analyze the MSD problem. Nilsson and Hutchinson [6] proposed another simplified approach where plastic crack interaction is modeled approximately by reducing the yield stress of the material. The problem can then be analyzed using a standard Dugdale model. This approach was adopted in [7] to analyze the basic sets of tests [1].

The main objective of this paper is to analyze basic panels tests with yield-strip methods of different levels of complexity and thereby try to understand the dominant effects of crack interaction and to assess the various simplifying assumptions. The study includes: the effect of modeling plastic crack interaction exactly or in an average manner, restart criteria after linkup, and the effect of small crack growth. Crack growth resistance will be modeled in the spirit of Deng and Hutchinson [7] by accounting for the plastic stretch released behind the crack tip in the yield-strip model. The background to some modeling aspects are only very briefly described since they can be found elsewhere [6, 7, 8].

MODELING ASPECTS

Material Model

The uniaxial tensile curve for true stress, σ_t , vs. true strain, ε_t , for aluminum alloys used in aircraft can be relatively well represented by the formulae

$$\begin{aligned} \varepsilon_t &= \sigma_t/E & \sigma_t &\leq \sigma_0 \\ \varepsilon_t &= (\sigma_0/E) (\sigma_t/\sigma_0)^n & \sigma_t &\geq \sigma_0 \end{aligned} \quad (1)$$

where σ_0 , E , and n represent initial tensile yield stress, Young's modulus, and the strain hardening coefficient, respectively. A calibration of Eq. 1 with reported test results for 2024-T3 aluminum alloys given in [3] gives $\sigma_0 = 345$ MPa, $E = 71.4$ GPa, $n = 10$ for 2024-T3 bare and $\sigma_0 = 285$ MPa, $E = 71.4$ GPa, and $n = 8$ for 2024-T3 clad. The measured and computed stress-strain curves are shown in Figure 1. The plastic deformation in the Dugdale model is represented by a line ahead of the crack along which the yielded sheet transmits a constant nominal yield stress of σ_y . For materials described by Eq. 1, Deng and Hutchinson [7] suggest a constant nominal yield stress

$$\sigma_y = \frac{n \left[(n\varepsilon_0 e)^{\frac{n+1}{n}} - 1 \right]}{(n+1) \left[(n\varepsilon_0 e)^{-1} - 1 \right]} \sigma_0 \quad (2)$$

where e is the natural base of logarithms (2.71828....) and $\varepsilon_0 = \sigma_0/E$. This yield stress is based on J-integral equivalence for a material with constant flow stress and a material described by Eq. 1 and where the maximum strain equals the necking strain. Using the initial yield stress and hardening coefficient above, $\sigma_0 = 400$ MPa and 353 MPa for bare and clad, respectively.

Fracture Criterion

Initiation and Continuous Growth

A two-parameter crack growth criterion, (α, δ_0) , based on a constant near tip opening profile leads to crack growth resistance when used in conjunction with the Dugdale model [8]. Maintenance of a constant effective crack tip opening angle, α , is used as the propagation criterion and crack growth resistance is generated by accounting for the plastic stretch released by the crack tip. The model was adapted to the MSD problem in [7].

Referring to Figure 2, crack growth is initiated when the crack tip opening displacement reaches a critical value, δ_0 . Subsequent growth is modeled by advancing the crack in small increments r , requiring that the standard Dugdale opening a distance r behind the current tip attains the opening associated with the near tip angle criterion plus the plastic stretch, δ_s .

$$\delta(x = a-r) = 2r \tan(\alpha/2) + \delta_s \quad (3)$$

The subscript s denotes the stretch. The plastic stretch, δ_s , is the crack tip opening displacement of the previous increment. The two parameters, δ_0 and α , are determined by the values that best match the material crack growth resistance curve. The crack increment r depicted in Figure 2b will be 1 mm for all panels in this study.

Restart After Linkup

When the major crack breaks through the ligament and links up with the small crack, the crack propagation scheme above has to be restarted for the new extended crack [7] and is illustrated in Figure 3. In the limit of vanishing length of the small crack, continuity of the crack growth resistance requires that the restart opening is equal to the major crack's opening just prior to coalescence, δ_R . On the other hand, if the small crack is much larger than the ligament, we expect restart after linkup to be controlled by the small crack. In that case, if the small crack has not grown, the value for a virgin crack, δ_0 , is used; whereas if the small crack has grown, the crack tip opening displacement of the small crack prior to coalescence, δ_{MSD} , is adopted. A general formula for the critical opening after crack linkup, δ_{LU} , for all small crack lengths can be formulated as

$$\delta_{LU} = \begin{cases} \delta_0 + L(\delta_R = \delta_0) & \delta_{MSD} < \delta_0 \\ \delta_{MSD} + L(\delta_R - \delta_{MSD}) & \delta_{MSD} \geq \delta_0 \end{cases} \quad (4)$$

The transition value, L , is a function of loading, geometry, and material properties, and actual values used in the application should be determined by experiments.

Elastic-Plastic Crack Interaction Models

Exact Dugdale Model

In the Exact Dugdale Model (Figure 4(a)), zero traction conditions are enforced along the line of the small cracks embedded in the plastic zone and the yield stress, σ_Y , is applied on ligaments or portions of ligaments where yielding occurs. MSD-cracks in the elastic portion of the sheet are not modeled since elastic crack interaction is small [6].

Modified Dugdale Model

In the Modified Dugdale Model, a constant but damage reduced yield stress $\bar{\sigma}_Y$ is applied along the line of plastic deformation (Figure 4(b)). The reduced yield stress is

$$\bar{\sigma}_Y = \sigma_Y (1 - D_{MSD}) \quad 0 \leq D_{MSD} \leq 1 \quad (5)$$

where D_{MSD} denotes the damage factor. Thus, the Modified Dugdale Model treats the plastic interaction in an average sense and reduces the problem to the standard Dugdale problem.

To illustrate some differences and similarities between the two approaches, a wide panel with a major crack of 400 mm with five small 10 mm cracks with ligaments of 15 mm distributed on each side of the major crack is investigated. The material properties for 2024-T3 clad are assumed ($E = 71.4$ MPa, $\nu = 0.3$, $\sigma_Y = 353$ MPa). Figure 5(a) and 5(b) display the far-field stress, σ , and crack tip opening displacement of the major crack, δ_i , as a function of the plastic zone size, s , given by the Exact Dugdale Model and the Modified Dugdale Model with damage factors, 0, 0.2, 0.32, and 0.4. The dashed portions for the Exact Dugdale Model indicate plastic zone lengths for which the stress is lower than the stress at which the previous ligament was fully yielded and in a load controlled experiment the plastic zone would increase in jumps as given by the solid line. In the Modified Dugdale Model on the other hand, the stress and crack tip opening displacement increase monotonically with the plastic zone size. Figure 5c shows the crack tip opening displacement, δ_i , as a function of the far-field stress, σ . The small discontinuities in the crack tip opening displacements in the Exact Dugdale Model result from the jump in the plastic zone sizes at ligament yield. The main observation from Figure 5(a-c) is that the Modified Dugdale Model for a stationary crack fairly well reflects the plastic crack interaction by an appropriate choice of the damage factor.

It could be expected that $D_{MSD} = 0.32$ gives the closest approximation of the Exact Dugdale Model since the sum of the small cracks divided by the plastic zone length, s , is in average close to this number.

The Four Residual Strength Models

Four models with different levels of modeling complexity or fracture criterion will be used to predict linkup and failure of MSD-damaged panels.

Model 1, Exact Dugdale Model with Small Crack Growth Model adopts the Exact Dugdale Model outlined above for the elastic-plastic crack interaction. Propagation of the major crack is governed by the propagation law (Eq. 3) and restart after linkup by Eq. 4. The small cracks propagate according to the same propagation law as the major crack. Model 2, Exact Dugdale Model Without Small Crack Growth, is identical to Model 1 with the exception that the small cracks are not allowed to propagate. Model 3, Ligament Held Criterion, differs from Model 1 by the additional assumption that linkup will also occur when the ligament is fully yielded; linkup is triggered by the fracture criterion (Eq. 3) or the ligament yield condition, whichever occurs first. Model 4, Modified Dugdale Model, embraces the modified Dugdale concept for plastic crack interaction and initiation and crack growth governed by Eq. 3.

Numerical Model

The theory of complex potentials and singular integral equations [10] was used for all analyses. The plastic zone size was computed by requiring that stress singularities at the tip of the plastic zone should vanish and the finite-width effect was modeled by aid of the fundamental point force solution. A description of the numerical scheme is given in the Appendix. Thirty point force pairs were adopted for the most narrow panels (the NLR-panels), whereas 20 point force pairs were used for the other panels (Foster-Miller and NIST).

RESULTS

Description of Basic Tests

Twenty-four panels with the geometry detailed in Table 1 and with the geometry parameters defined in Figure 6 will be analyzed. These tests come from three institutes: Foster-Miller and NIST in the U.S. and NLR in the Netherlands. The first set, denoted

FM1-FM12, has been described in several papers, e.g., [1, 3, 5]. The second set, NIST1-5 and NIST7-10, is described in [2]. The third set has not been described in the open literature. All tests were load controlled and provided with antibuckling guides to prevent out-of-plane deflection. In particular the first but also the third set have significant finite-width effect.

Basic Fracture Tests of Panels With Only Central Crack

Panels with only a central crack (FM1-3, NIST1-NIST3 and NLR-R1) were used to determine the basic fracture parameters, δ_0 and α , for each set respectively. The fracture parameters were determined by an iterative procedure where computed residual strength curves for each set were compared with the corresponding experimental ones and with fracture parameters adjusted at each increment until a best (judged visually) overall fit between experimental and computed curves was attained. This resulted in $\delta_0 = 0.21$ mm, $\alpha = 0.55$ rad for FM1-3; $\delta_0 = 0.25$ mm, $\alpha = 0.45$ rad for NIST1-3; and $\delta_0 = 0.18$ mm, $\alpha = 0.85$ rad for the single test NLR-R1. The computed stress as a function of the crack growth with the fracture parameters, (δ_0, α) , given above together with the experimental values are shown in Figure 7(a-c) for the three sets of experimental data, respectively. The agreement between experimental curves and the computed ones is relatively good. The difference in the computed crack opening angle between the sets (particularly for the Foster-Miller and NLR tests) is larger than expected. This difference could be due to three-dimensional constraint effects which are not accounted for in the present investigation. Global constraint factors in the spirit of Newman et al. [9] could be an efficient way of accounting for constraint effects in the Dugdale Model.

Linkup and Maximum Load of Panels Weakened by Small Cracks

Measured Values

The applied load in all experiments expressed in stress at which the major crack links up with the first and second small crack and the maximum load the panel sustained are given in Table 2 along with the residual strength reduction due to small crack damage. This reduction is based on computed results for panels with only a central crack but otherwise of the same geometry and material as given in Table 1. Loads in parenthesis for second linkup indicates that the second ligament failed already at first linkup; whereas the parenthesis for the maximum load implies that the maximum load was attained already at first or second linkup. The mean value and standard deviation of the residual strength reduction due to small crack damage is around 30% as given at the bottom of Table 2.

Model 1—Exact Dugdale Model With Small Crack Growth

The computed stress required to drive the major crack, σ_c , as function of its length, a , for the panels FM8 and NIST10 using this model is shown in Figures 8(a) and 8(b) for transition values, $L = 0$ and 0.5. For reference, the corresponding stress for a panel without the small cracks is also shown. The initial position of the tips of the small cracks are depicted as filled circles. The first and second linkup and maximum load from the corresponding experiments are shown as dotted lines. When the major crack coalesces with a small crack the length of the central crack is immediately extended with the length of the small crack. This linkup extension of the crack is represented with a zero stress for σ_c in Figures 8(a) and 8(b). The small crack growth for each crack tip prior to linkup is represented by the distance between the filled circle and the point where the residual strength curve intersects the crack length curve.

The residual strength increases initially due to crack growth resistance, either until a ligament is fully yielded where after it drops slightly and increases again, or until onset of small crack growth where after it decreases as the ligament erodes from both sides. The maximum load along each ligament is attained either at onset of small crack growth or when a ligament is fully yielded. In Figures 8(a) and 8(b), first linkup of both cases and second linkup for FM8 coincided with onset of small crack growth whereas the second linkup for NIST10 tallied with ligament yield and linkup with the remaining cracks. The agreement between measured and computed linkup loads and maximum load is very good when the higher restart value, $L = 0.5$, is used. A higher transition value is partially balanced by earlier onset of small crack growth which explains the relatively small difference in result for the two transition values.

The computed linkup and maximum stress for all panels are given in Table 3 together with their relative deviation from the measured values. For all panels with more than two cracks, the remaining cracks failed at loads lower or very close to the load at first or second linkup. This pattern was also observed in the experiments. Apart from the first linkup of FM7, the computed loads met well with the measured ones and there is no particular trend; some are lower and some are higher. The mean value and standard deviation of the relative discrepancy between computed and measured loads are also given in Table 3. The mean value is of the order of 1% and the standard deviation is of the order of 5%. These numbers should be compared with residual strength reduction which was of the order of 30% or with the difference between the nominally identical panels NIST7 and NIST10, which was of the order of 10-15%.

Model 2—Exact Dugdale Model Neglecting Small Crack Growth

The significance of allowing for small crack growth can be appreciated if the computations above are repeated without allowing for small crack propagation. Figures 9(a) and 9(b) display the applied stress as function of the length of the central crack for the panels FM8 and NIST10 respectively for $L = 0$ and 0.5. For reference the corresponding curve with

small crack growth allowed and $L = 0.5$ is also given. The linkup and maximum loads are, as expected, generally higher and the result is also much more sensitive to the transition parameter than for Model 1. The computed values for linkup and the maximum load for all panels using this approach are given in Table 4. All computed values for the first linkup are higher than the measured ones except for the panels NIST5 and NIST9 and the mean value of the deviation is 8.5%. There is also a clear trend that the deviation from the small crack growth model is, due to the finite-width effect, more pronounced for the narrower panels.

In [7] the first and second linkups were predicted for the Foster-Miller panels using this method and their predictions were all slightly higher than the test results but the deviation was generally smaller than found in this study.

Model 3—Ligament Yield Criterion

The basic idea underlying the First Ligament Yield Criterion is that the major crack will link-up with the small crack shortly after the ligament has fully yielded. The simplicity of the criterion is appealing. Nevertheless, it is not based on fracture mechanics and it is obviously wrong in the hypothetical case with a major crack and small crack of vanishing size. However, when the ligament yields, the tip crack opening displacement will have a jump as illustrated in Figure 5(c), which in turn might be sufficient to cause linkup.

The choice of the yield stress to be adopted strongly influences the plastic zone size. This choice is not evident since the material is hardening. The stress for initial tensile yielding and the effective yield stress given by Eq. 2 should bound the range of values we are interested in.

Using the initial yield stress, σ_0 , the first ligament was fully yielded prior to crack initiation for all panels and the predicted linkup load was consistently lower than the result using the fracture mechanics approach embodied in Eq. 3. The result for first linkup for all panels is given in Table 4.

The result is better when the effective yield stress, σ_y , is used. In this case, the first linkup load given by the fracture law (Eq. 3) was in fact attained when the ligament yielded for the panels FM4, FM9, FM11, FM12, NIST8, NIST9, and NLR3, and accordingly the linkup load became the same as for Model 1. A common feature for these panels is that the ligament or the MSD crack is relatively large which results in a large additional crack opening when the ligament is fully yielded. The distance between cracks as well as the size of the cracks in the experiments were for most panels larger than one would expect in typical lap joints and the ligament yield criterion would for such geometries would probably consistently underestimate linkup loads also with the effective yield stress.

Model 4—Modified Dugdale Model

The selection of an appropriate damage factor, D_{MSD} , is a key issue in the application of the Modified Dugdale Model. The true damage factor (defined as the sum of all small cracks embedded in the plastic zone and divided by the length of plastic zone) varies as the major crack advances and links up with the small cracks and its plastic zone engulfs new MSD cracks and there is therefore no unique way to choose a constant damage factor to be used in analyses. A natural choice, however, for the damage factor in the case of equally spaced MSD cracks is

$$D_{MSD} = 2a_{MSD}/s_{MSD} \quad (6)$$

where s_{MSD} is the distance between MSD cracks defined in Figure 6. For many panels in the basic experiments, there was only one MSD crack or the first ligaments differed in size substantially from the remaining ones, and then the expression

$$D_{MSD} = a_{MSD}/(d_{MSD} - a_0) \quad (7)$$

emerges as a more natural choice for the damage factor at first linkup.

When the Modified Dugdale Model was first presented [6], crack growth resistance was not considered, and the idea was to account for crack interaction only by solving a standard Dugdale problem with a damage reduced yield stress. Figure 10(a) depicts the residual strength for the panel NIST10 using this approach with $D_{MSD} = 0, 0.33$ and 0.5 and where the latter damage factors correspond to Eq. 6 and 7 respectively. The crack growth resistance becomes more pronounced when the yield stress is lowered and consequently the residual strength may be larger after some growth when the lower yield stress is used as shown in Figure 10(a). This feature suggests that, although small cracks are not modeled explicitly, one should still invoke the restart concept for the Modified Dugdale Model. In a computational scheme that poses no additional computational complexity. Figure 10(b) displays the residual strength for NIST10 as given by the Modified Dugdale Model for the two damage levels $D_{MSD} = 0.5$ and 0.33 and the restart values $L = 0, 0.25,$ and 0.5 . In the Exact Dugdale Model with small crack growth, the linkup load was typically attained when the major crack had advanced half way through the ligament (see Figures 8(a) and (b)). To reflect this observation it seems more natural to read off the residual stress at the center of the ligament as illustrated with the filled triangles in Figure 10b for the case $D_{MSD} = 0.5$ and $L = 0.25$.

The prediction for first and second linkup for two different damage levels and restart values are presented in Table 6. The first three columns represent first linkup. The damage factor given by Eq. 7 is used in the first two and the load is read off when the major crack has advanced to the end of the ligament (first column) or at the center of the ligament (second column). We note that the linkup load is overestimated for all panels except NLR2. However, if we actually go back to the Exact Dugdale Model with small crack growth and verify the true damage factor at first linkup, it turns out to be typically 10%-35% larger than

what was given by the formula (Eq. 7). In the third column, the damage factor is therefore reduced an additional 25% and loads are read off at the center of the ligament, and we see that predicted linkup values are fairly close to the measured ones. The three last columns are predicted second linkup loads where the load is read off at the center of the ligament. The first two columns adopt the damage factor (Eq. 7) and restart parameters 0 and 0.25, and the last one uses the larger damage factor (1.25 times Eq. 7) and with $L = 0.5$.

No systematic study was carried out here on how to best select the damage factor and the restart parameter to predict linkup loads with the Modified Dugdale Model. However, the result in Table 6 suggests that it might be possible to arrive at fairly accurate predictions.

CONCLUDING REMARKS

The residual strength, and in particular the linkup loads, have been computed for elasto-plastic sheets with a central crack and small cracks using yield-strip methods similar to the Dugdale model and where crack growth resistance was modeled by accounting for the plastic stretch released behind the crack tip. These predictions have been compared with reported test results from three different investigations.

Three modeling aspects have been identified and assessed: elastic-plastic crack interaction, restart of crack growth procedure after crack linkup, and the effect of modeling growth of small cracks. The plastic crack interaction was modeled by two models; either by treating cracks as traction-free entities and with yielded ligaments loaded by the yield stress (Exact Dugdale Model) or in a more approximate manner, by adopting a constant but damage reduced yield stress along the line with plastic crack interaction (Modified Dugdale Model).

The most detailed model, Exact Dugdale Model with Small Crack Growth, gave excellent overall predictions for linkup loads as well as for the failure load. When small crack growth was not modeled, the predicted linkup loads were consistently somewhat higher and the result was also more sensitive to the restart condition.

The first ligament yield criterion to predict linkup was assessed with two levels of applied yield stress. When the initial yield stress was used the predictions were consistently and substantially lower than the test results. When the effective yield stress was adopted, the predictions coincided with the Exact Dugdale Model with Small Crack Growth for some cases when either the ligaments or small cracks were relatively large; whereas for other cases, predictions were consistently lower.

The Modified Dugdale Model gave relatively good and consistent predictions for first and second linkup. The choice of the Damage Factor, D_{MSD} , and restart parameter, L , is essential but more work is needed to determine how to apply damage factors in the applications. The main advantage of the Modified Dugdale Model is that cracks do not have to be modeled explicitly, and in particular for more complex geometries, such as damaged lap

joints, this feature gives a substantial simplification of the modeling. On the other hand, the choice of damage factors and restart values introduces additional complexities and also some arbitrariness into the modeling.

The accuracy and applicability of proposed models should be applied to more complex structures with MSD to see whether the models still retain consistency and accuracy in residual strength predictions.

ACKNOWLEDGMENTS

This work has been funded partly by the European Commission by the Grant BRITE-Euram BE-1053 and by the Swedish National Board for Industrial and Technical Development (NUTEK).

REFERENCES

1. Thomson, D., Hoadley, D., and McHatton, J.: Load Tests of Flat and Curved Panels with Multiple Cracks, Foster-Miller, Waltham, MA, Final Report, 1993.
2. deWit, R., Fields, R. J., Low III, S. R., Harne, D. E., and Foecke, T.: Fracture Testing of Large-Scale Thin-Sheet Aluminum Alloy, NISTIR 5661, US Dep. of Commerce, 1995.
3. Newman, J. C., Dawicke, D. S., Sutton, M. A., and Bigelow, C. A.: A Fracture Criterion for Widespread Cracking in Thin-Sheet Aluminum Alloys, in *Durability and Structural Integrity of Airframes*, Ed. A. F. Blom, EMAS Publications, London, pp. 443-467, 1993.
4. Swift, T.: Damage Tolerance in Pressurized Fuselages in New Materials and Fatigue Resistant Aircraft Design, From Proceedings, Ed. D. L. Simpson, EMAS Publications, London, pp. 1-78, 1987.
5. Broek, D.: The Effects of Multi-Site Damage on the Arrest Capability of Aircraft Fuselage Structures, FractuREsearch TR 9302, 1993, Ohio, USA.
6. Nilsson, K.-F. and Hutchinson, J. W.: Interaction Between a Major Crack and Small Crack Damage in Aircraft Sheet Material, *Int. J. Solids Structures*, 31, pp. 2331-2346, 1994.

7. Deng, X. and Hutchinson, J. W.: Approximate Methods for Analyzing the Growth of Large Cracks in Fatigue Damaged Aircraft Sheet Material and Lap-Joint, Harvard Univ., MECH-277, Cambridge, MA, USA.
8. Budiansky, B. and Sumner, Jr., E. E.: On Size Effects in Plane Stress Crack Growth Resistance, in Developments in Mechanics, 13, Proceedings of 19th Midwestern Mechanics Conference, Ohio State University, Columbus, Ohio, USA, 1985.
9. Newman, J. C., Crews, J. H., Bigelow, C. A., and Dawicke, D. S.: Variations of a Global Constraint Factor in Cracked Bodies Under Tension and Bending Loads, ASTM-STP- 1244, pp. 21-42, 1995.
10. Muskhelishvili, N. I.: Some Basic Problems of The Mathematical Theory of Elasticity, Noordhoff Int. Publishing, Leyden, The Netherlands, 1977.
11. Rooke, D. P. and Cartwright, D. J.: Compendium of Stress-Intensity Factors, Her Majesty's Stationary Office, London, United Kingdom, 1974.
12. Newman, J. C.: Prediction of Stable Crack Growth and Instability Using the VR-Curve Method, in Elastic-Plastic Fracture Mechanics Technology ASTM STP 896, Eds. Newman, J. C. and Loss, F. J., pp. 139-166, 1985.

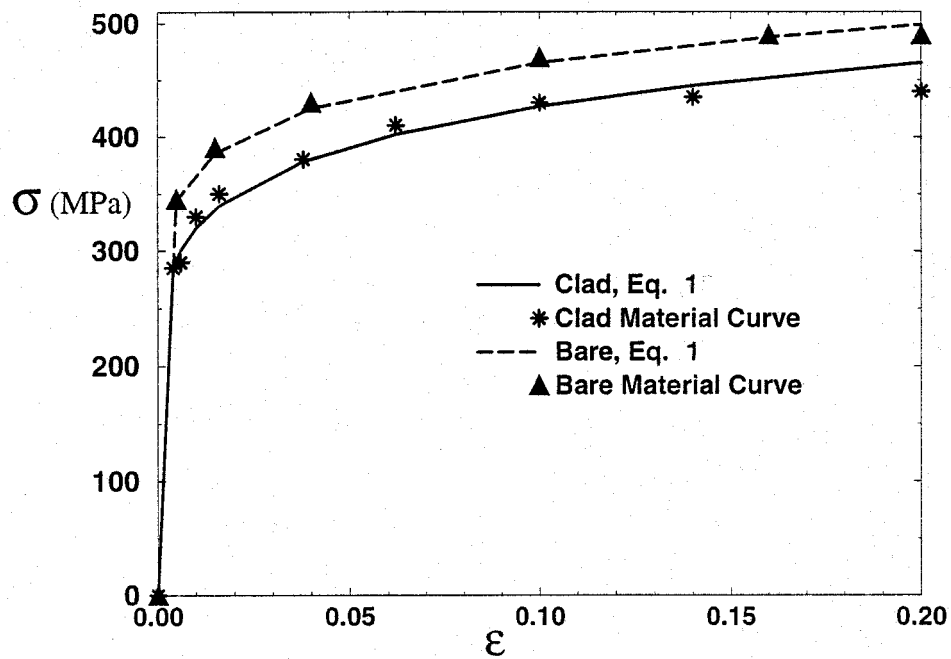


Figure 1. Measured Stress-Strain Curves and as Given by Equation 1 for 2025-T3 Bare and Clad

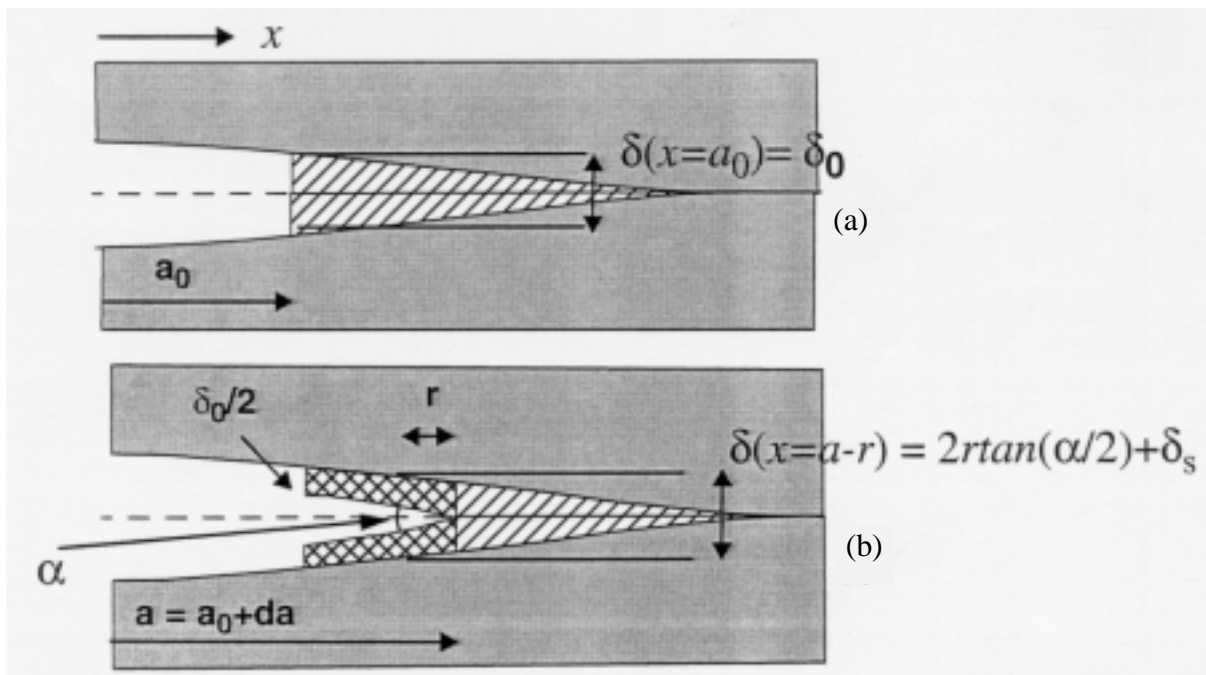


Figure 2. The Crack Profile at Initiation (a) and (b) at Propagation With Definition of Crack Growth Parameters, α and δ_0 . The Hatched Area Depicts the Plastic Stretch Behind the Crack Tip.

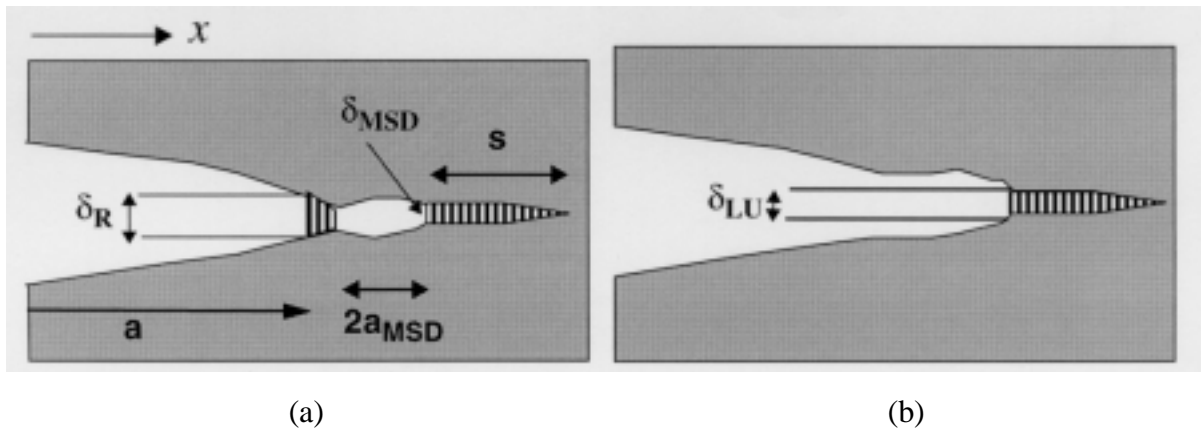


Figure 3. The Crack Tip Deformation With Definition of Crack Opening Displacements (a) Just Prior to Crack Linkup the Major Crack Has an Opening δ_R and the Right Tip of the Small Crack δ_{MSD} and (b) after Crack Linkup, the Extended Crack Restarts Propagation With the Critical Crack Tip Opening δ_{LU} .

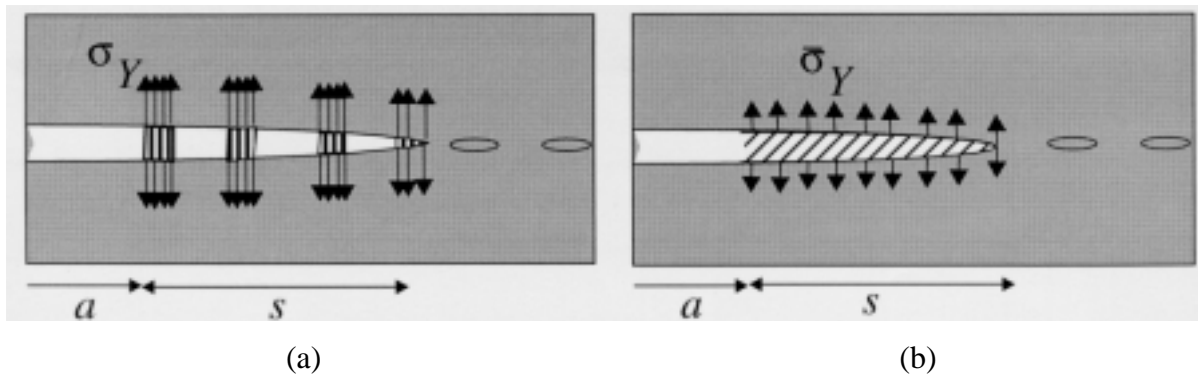


Figure 4. Illustration of the Two Basic Dugdale Models (a) Exact Dugdale Model (b) Modified Dugdale Model.

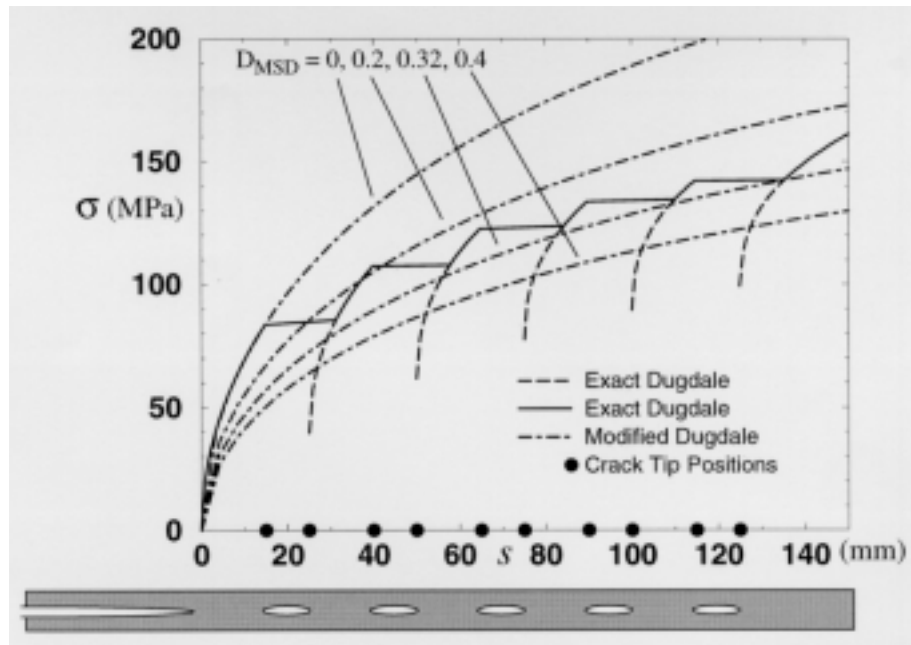


Figure 5a. Applied Stress, σ , Versus Plastic Zone Length, s , for Exact Dugdale and Modified Dugdale Model $D_{MSD} = 0, 0.2, 0.32, \text{ and } 0.4$.

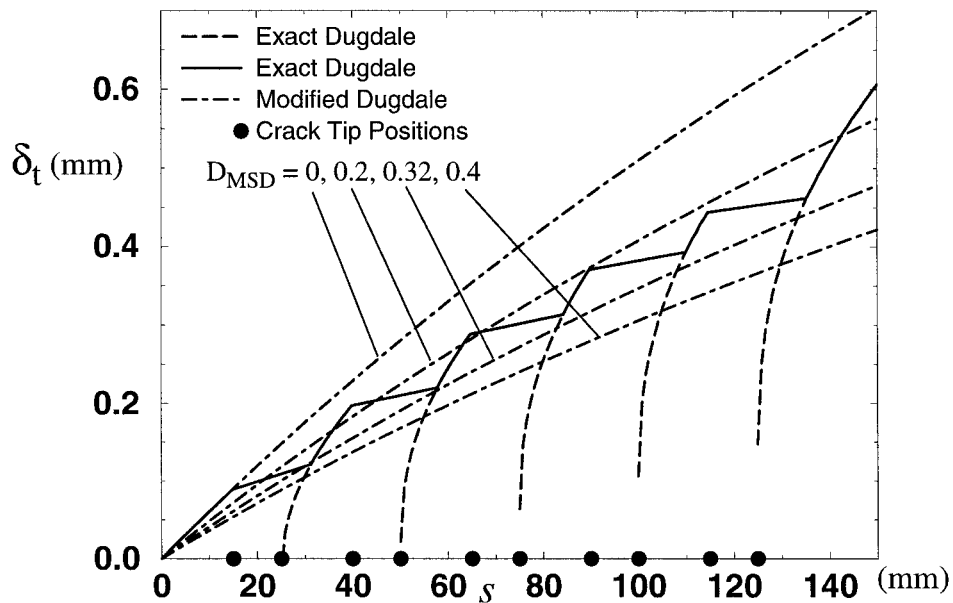


Figure 5b. Crack Tip Opening Displacement of the Major Crack, δ_t , Versus Plastic Zone Length, s , for Exact Dugdale and Modified Dugdale Model $D_{MSD} = 0, 0.2, 0.32, \text{ and } 0.4$.

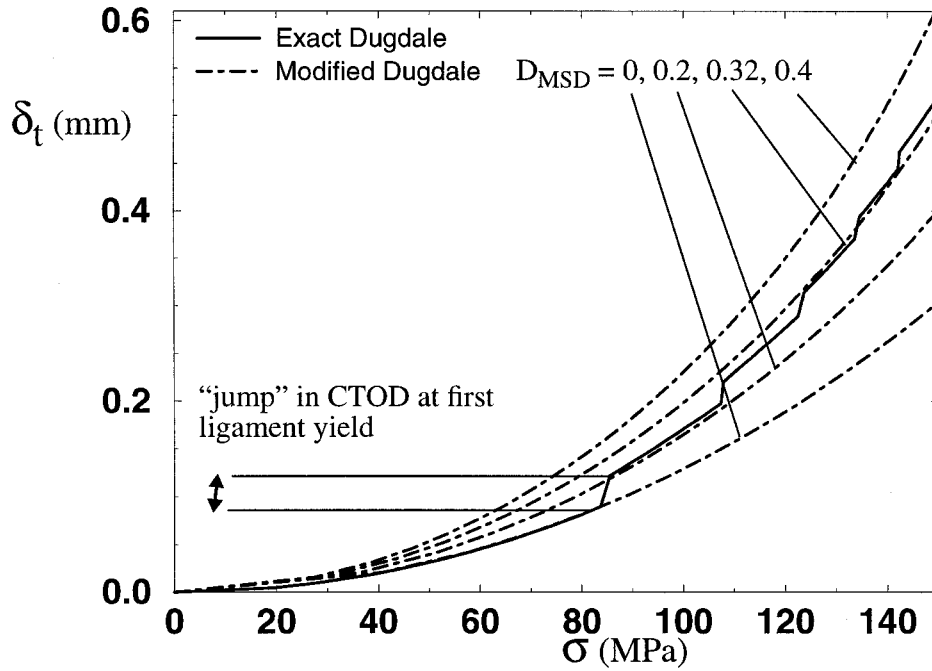


Figure 5c. Crack Tip Opening Displacement Versus Applied Load for Exact Dugdale and Modified Dugdale Model $D_{MSD} = 0, 0.2, 0.32,$ and 0.4 , Derived From 4(a) and 4(b).

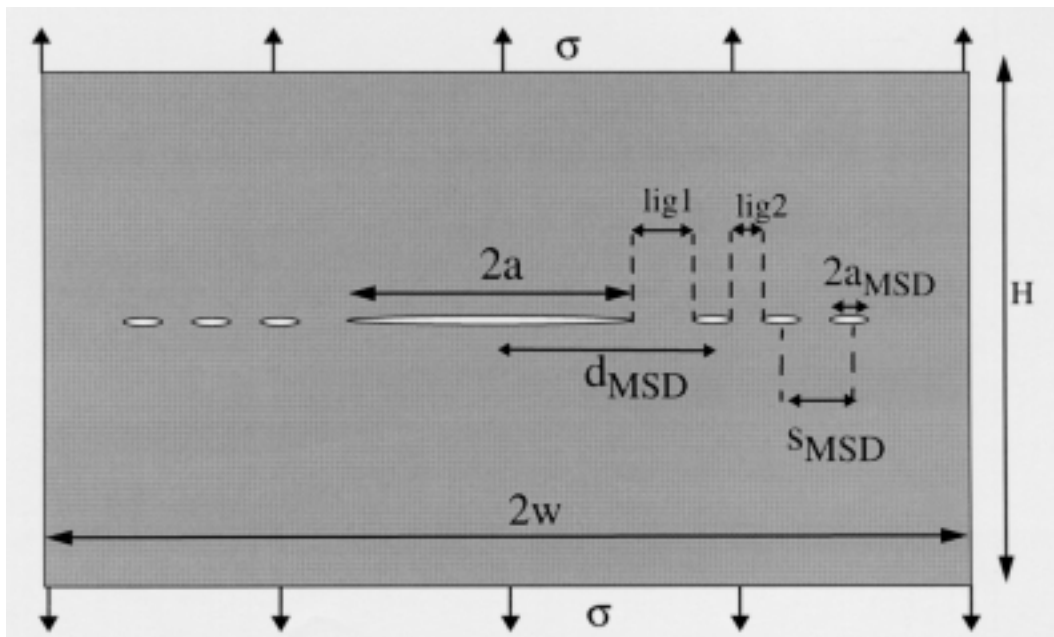


Figure 6. Description of Geometry Parameters for Damaged Sheets.

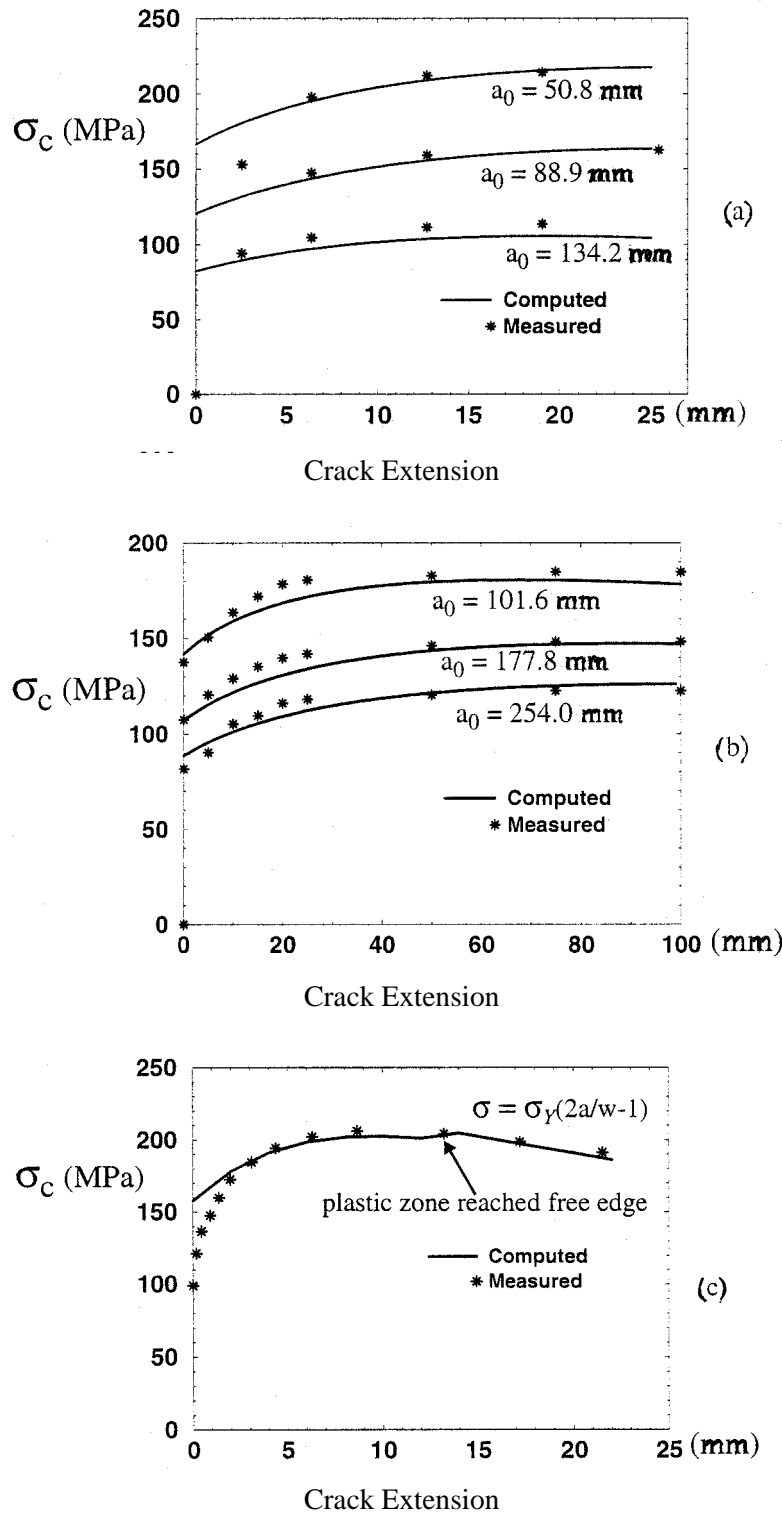
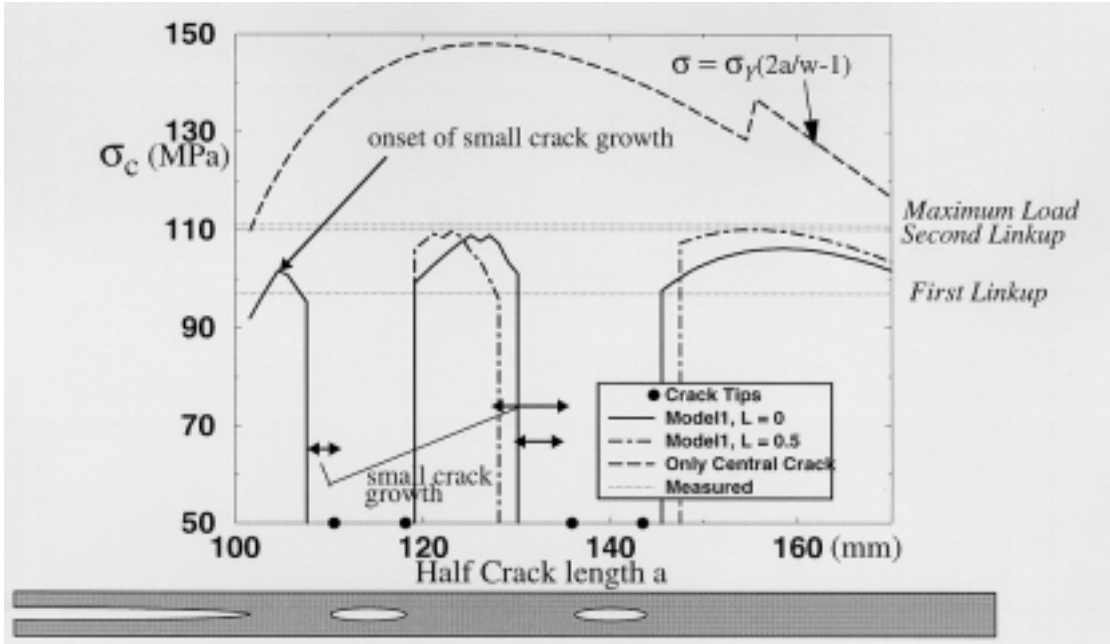
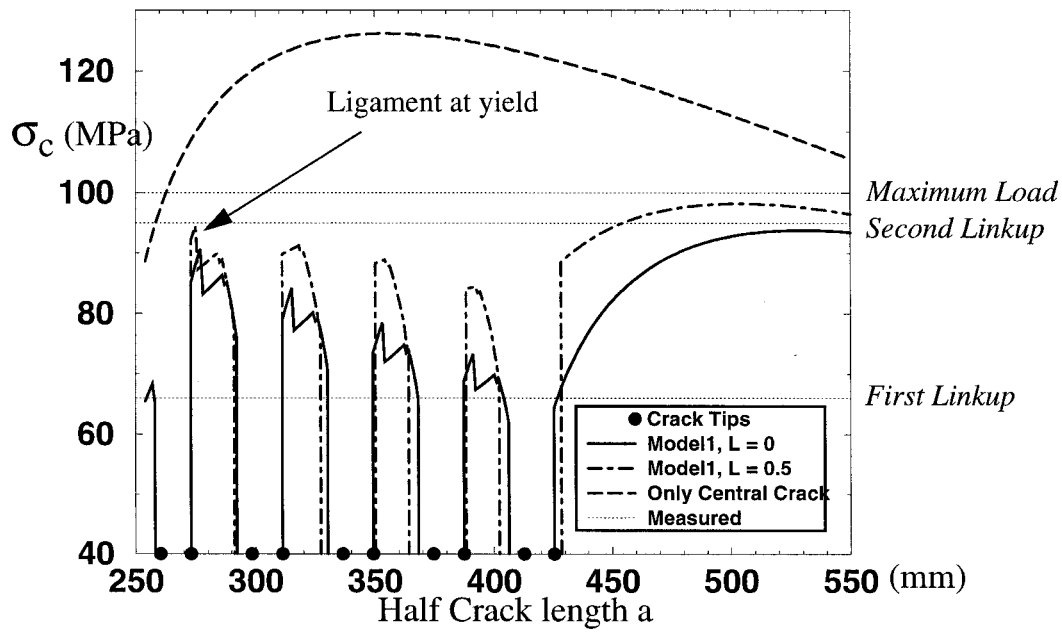


Figure 7. Applied Stress, σ_c , Versus Crack Growth for the Basic Fracture Tests With Crack Calibrated Growth Parameters (a) FM1-3, $\delta_0 = 0.21 \text{ mm}$, $\alpha = 0.55 \text{ rad}$, (b) NIST1-3 $\delta_0 = 0.25 \text{ mm}$, $\alpha = 0.45 \text{ rad}$ (c) NLR1 $\delta_0 = 0.18 \text{ mm}$, $\alpha = 0.85 \text{ rad}$.



(a)



(b)

Figure 8. The Applied Stress Needed to Drive the Crack, σ_c , as Function of the Major Crack Length, a , for the Panels (a) FM8 and (b) NIST10 (NIST7) from Exact Dugdale Model With Small Crack Growth, for Restart Values $L = 0$ and 0.5 Along With Residual Strength for Plate With Central Crack Only. Measured First and Second Linkup and Failure Load Also Shown.

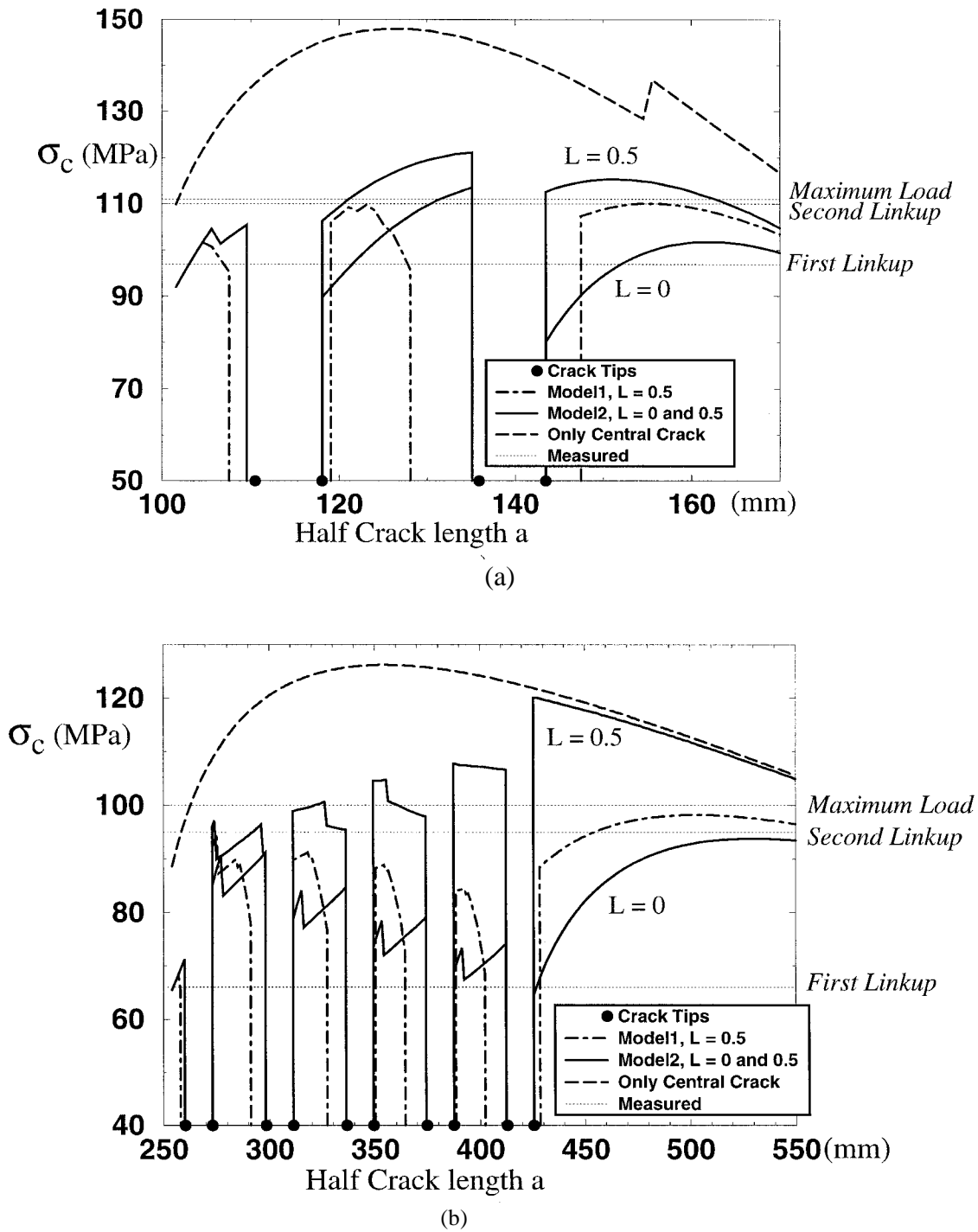


Figure 9. The Applied Load Needed to Drive the Crack, σ_c , as Function of the Major Crack Length, a , for the Panels (a) FM8 and (b) NIST10 from Exact Dugdale Model Without Crack Growth, (Model 2), $L = 0$ and 0.5 . Results for Model 1 with $L = 0.5$ and Central Crack Also Displayed.

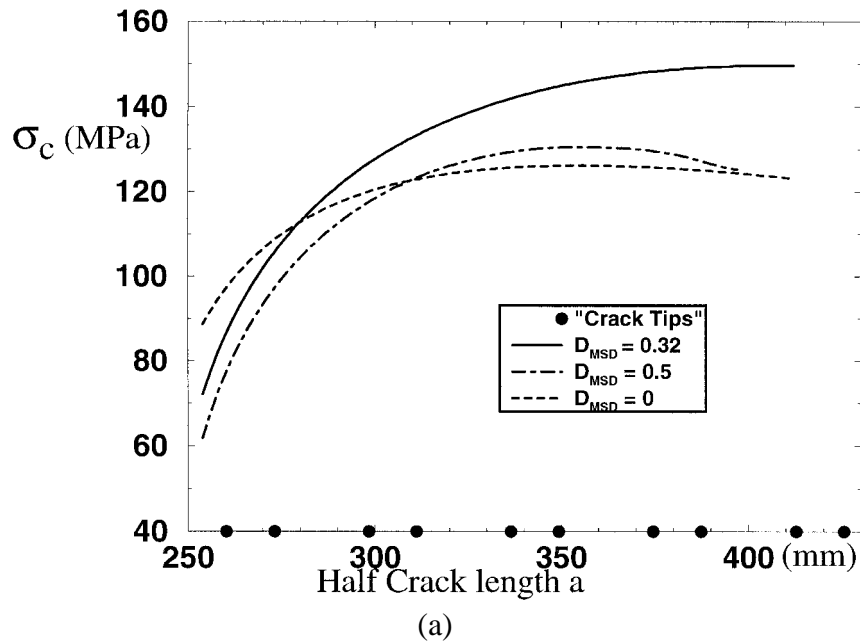


Figure 10(a) The Applied Load, σ_c , as Function of the Major Crack Length, a , for NIST 10 Using Modified Dugdale Model Without Restart. $D_{MSD} = 0, 0.32, \text{ and } 0.5$.

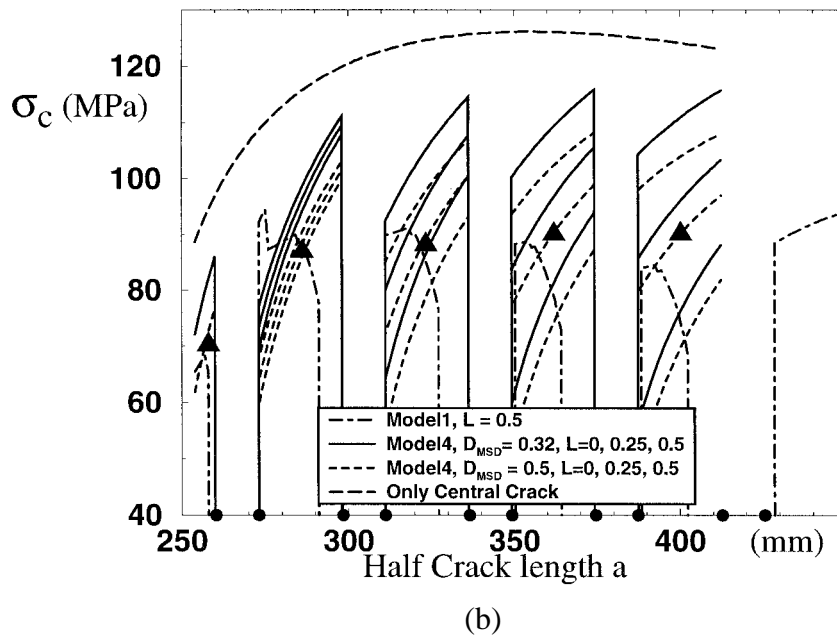


Figure 10(b) The Applied Load, σ_c , as Function of the Major Half Crack Length, a , for NIST 10 From Modified Dugdale Model $D_{MSD} = 0.32 \text{ and } 0.5$ With Restart $L = 0, 0.25, \text{ and } 0.5$. ▲ Denotes the Values Read Off at Center of Ligaments for $D_{MSD} = 0.5, L = 0, 0.25, \text{ and } 0.5$. Result for Model 1, $L = 0.5$ and Central Crack Only Also Displayed.

Table 1. Unstiffened Flat Sheet Geometry for Experiments with Geometry Description in Figure 6.

Test	2w (mm)	H (m)	a_0 (mm)	d_{MSD} (mm)	S_{MSD} (mm)	$2a_{MSD}$ (mm)	lig1 (mm)	lig2 (mm)	# per side	Mat
FM1	254	1.0	50.8	-	-	-		-		Clad
FM2	254	1.0	88.9	-	-	-		-		Clad
FM3	254	1.0	134.2	-	-	-		-		Clad
FM4	254	1.0	76.2	114.3	-	12.7	31.8	-	1	Clad
FM5	254	1.0	91.4	114.3	-	12.7	16.5	-	1	Clad
FM6	254	1.0	96.5	114.3	38.1	12.7	11.4	25.4	2	Clad
FM7	254	1.0	94.0	114.3	38.1	12.7	14.0	25.4	3	Clad
FM8	254	1.0	101.6	114.3	25.4	7.62	8.9	17.8	2	Clad
FM9	254	1.0	40.7	63.5	50.8	20.32	12.7	30.5	2	Clad
FM10	254	1.0	40.7	63.5	38.1	12.7	16.5	25.4	2	Clad
FM11	254	1.0	63.5	88.9	50.8	25.4	12.7	25.4	2	Clad
FM12	254	1.0	38.1	88.9	-	25.4	38.1	-	1	Clad
NIST-1	1143	3.8	177.8	-	-	-	-	-	-	Bare
NIST-2	1143	3.8	101.6	-	-	-	-	-	-	Bare
NIST-3	1143	3.8	254.0	-	-	-	-	-	-	Bare
NIST-4	1143	3.8	177.8	190.5	25.4	10.2	7.62	15.24	3	Bare
NIST-5	1143	3.8	71.12	88.9	38.1	15.2	10.1	22.86	3	Bare
NIST-7,10	1143	3.8	254.0	266.7	38.1	12.7	6.35	25.40	5	Bare
NIST-8	1143	3.8	241.3	266.7	38.1	12.7	19.35	25.40	10	Bare
NIST-9	1143	3.8	127.0	165.1	25.4	10.2	33.0	15.24	10	Bare
NLR-R1	304	0.7		-	-	-	-	-	-	Clad
NLR-R2	304	0.7	50.3	69.71	-	13.2	12.8	-	1	Clad
NLR-R3	304	0.7	24.9	44.4	26.3	11.94	13.5	14.4	2	Clad

Table 2. Measured Values for First and Second Linkup and Failure Load Together With Relative Reduction in Residual Strength Due to MSD Cracks at First Linkup and Failure. The Reduction is Based on Computed Values for Panel With Central Crack Only.

Panel ID	First Linkup (MPa)	MSD Reduction	Second Linkup (MPa)	Failure (MPa)	MSD Reduction
FM4	155	-14%	-	(155)	-14%
FM5	119	-24%	-	130	-19%
FM6	100	-31%	111	(111)	-28%
FM7	110	-27%	(110)	(110)	(-30%
FM8	97	-29%	110	111	-25%
FM9	145	-36%	(152)	(152)	-35%
FM10	171	-26%	(171)	(171)	-27%
FM11	106	-44%	110	(110)	-44%
FM12	195	-17%	-	(195)	-19%
NIST4	84	-29%	98	132	-10%
NIST5	138	-26%	161	174	-14%
NIST7	57	-41%	88	92	-27%
NIST8	89	-21%	91	(91)	-29%
NIST9	152	-5%	(152)	(152)	-9%
NIST10	66	-32%	95	100	-21%
NLR-R2	134	-35%	-	150	-27%
NLR-R3	174	-36%	(174)	(174)	-35%
Mean		-28%			-24%
St. Dev.		30%			27%

Table 3. Computed Stress Levels for First and Second Linkup and Maximum Load Predicted by Exact Dugdale With Small Crack Growth (Model 1) for All MSD Damaged Panels Together With Relative Deviation From the Experimental Values.

Panel ID	First Linkup (MPa)	Second Linkup (MPa) L=0	Second Linkup (MPa) L = 0.5	Failure (MPa) L=0	Failure (MPa) L=0.5
FM4	147 (-5.1%)	-	-	(147) (-5.2%)	(147) -5.2%)
FM5	114 (-4.2%)	-	-	127 (-2.3%)	134 ((3.1%)
FM6	100 (0%)	103 (-7.2%)	106 (-4.5%)	(103) (-7.2%)	(103) (-4.5%)
FM7	107 (-2.7%)	(107) (-2.7%)	108 (-1.8%)	(107)(-2.7%)	(108) (1.8%)
FM8	101 (4.1%)	109 (-0.9%)	110 (0%)	(109)(-1.8%)	(110)(-0.9%)
FM9	141 (-2.7%)	146 (-3.6%)	144 (-5.3%)	(146)(-3.9%)	(144) (-5.3%)
FM10	171 (0%)	(171) (0%),	(171) (0%)	(171)(0%)	(171)(0%)
FM11	107 (0.9%)	114 (3.6%)	108 (-1.8%)	(114)(3.6%)	(108) (-1.8%)
FM12	203 (4.1%)	-	-	(203)(4.1%)	(203) (4.1%)
NIST4	88 (4.7)	96 (-2.0%)	102 (-4.8%)	128 (-3.0%)	132 (0%)
NIST5	131 (-5.1%)	147 (-8.7%)	147 (-8.7%)	149 (-14.4%)	157 (-9.7%)
NIST7	68 (19.3%)	91 (3.4%),	94 (6.8%)	94 (2.2%)	98 (6.5%)
NIST8	87 (-2.2%)	91 (0%),	96 (5.5%),	(91) (0%)	(96) (5.5%)
NIST9	140 (-7.9)	(140)(-7.9%)	(140) (-7.9%)	(140) (-7.9%)	(140)(-7.9%)
NIST10*	68 (3.0%)	91 (-4.2%)	94 (-1.0%)	94 (-6%)	98 (-2%)
NLR-R2	143 (6.7%)	-	-	148 (-1.3%)	151 (0.67%)
NLR-R3	177 (1.7%)	(177) (1.7%)	(177) (1.7%)	(177) (1.7%)	(177)(1.7%)
Mean	0.8%	-2.2%	-1%	-2.6%	-1.0%
Std Dev	6.3%	4.7%	4.9%	5.4%	4.8%

Table 4. Computed Stress Levels for First and Second Linkup and Maximum Load Predicted by Exact Dugdale Without Small Crack Growth (Model 2) for All MSD Damaged Panels Together With Relative Deviation From the Experimental Values.

Panel ID	First Linkup (MPa)	Second Linkup (MPa) L=0	Second Linkup (MPa) L = 0.5	Failure (MPa) L=0	Failure (MPa) L=0.5
FM4	157 (1.2%)	-	-	(157) (1.3%)	(157) (1.3%)
FM5	129 (8.4%)	-	-	(129) (-0.8%)	138 ((6.1%)
FM6	112 (12%)	112 (0.9%)	115 (3.3%)	(112) (0.9%)	(115) (3.6%)
FM7	116 (5.4%)	(116) (5.4%)	116 (5.4%)	(116)(5.4%)	(116) (5.4%)
FM8	105 (8.3%)	113 (2.7%)	121 (10%)	(113)(1.8%)	(121)(9%)
FM9	160 (10.4%)	160 (5.3%)	160(-5.3%)	(160)(5.3%)	(160) (5.3%)
FM10	174 (1.8%)	(174) (1.8%),	(179) (4.7%)	(174)(1.8%)	(179)(4.7%)
FM11	123 (16%)	(123)(11.8%)	(123)(11.8%)	(123)(11.8%)	(123)(11.8%)
FM12	203 (4.1%)	-	-	(203)(4.1%)	(203) (4.1%)
NIST4	93 (10.7%)	98 (0%)	104 (6.1%)	128 (-3.0%)	139 (5.3%)
NIST5	136 (-1.4%)	147 (-8.7%)	153 (-5.0%)	149 (-14.4%)	175 (0.6%)
NIST7	71 (24.6%)	91 (3.4%),	96 (9.1%)	94 (2.2%)	120 (30.4%)
NIST8	92 (3.4%)	(92) (1.1%),	102 (12.1%),	(92) (1.1%)	110 (20.1%)
NIST9	140 (-7.9)	(140)(-7.9%)	(140) (-7.9%)	(140) (-7.9%)	151(-0.7%)
NIST10*	71 (7.6%)	91 (-4.21%)	96 (1.1%)	94 (-6%)	120 (20%)
NLR-R2	167 (24.6%)	-	-	(167)(11.3%)	(167)(11.3%)
NLR-R3	202 (16.1%)	(202)(16.1%)	(202)(16.1%)	(202)(16.1%)	(202)(16.1%)
Av. Dev	8.5%	2.1%	5.6%	1.8%	9%
Std Dev	12.3%	7.3%	8.9%	7.6%	12.6%

Table 5. Predicted First Linkup as Given by Ligament Yield Criterion With Initial Yield Stress, σ_0 , and Effective Yield Stress σ_Y .

Panel ID	First Linkup (MPa) σ_Y : Initial Yield stress $\sigma_Y = 281$ (Clad), 345 MPa (Bare)	First Linkup (MPa) σ_Y : Effective Yield stress $\sigma_Y = 353$ (Clad), 400 MPa (Bare)
FM4	130 (-16.1%)	147* (-5.1%)
FM5	90 (-24.4%)	111 (-6.7%)
FM6	73 (-27.0%)	91 (-9%)
FM7	82 (-25.5%)	100 (-9.1%)
FM8	63 (-35.0%)	79 (-18.6%)
FM9	113 (-22.1%)	140 (-3.4%)
FM10	131 (-23.4%),	162 (-5.2%)
FM11	92 (-13.2%)	107* (0.9%)
FM12	176 (-9.7%)	203* (4.1%)
NIST4	59 (-29.8)	68 (-19.0%)
NIST5	101 (-26.8%)	120 (-13.0%)
NIST7	44 (-22.8%),	51 (-10.6%)
NIST8	81 (-9.0%),	87* (-2.2%)
NIST9	140 (-14.5%)	140* (-7.9%)
NIST10*	44 (-33.3%)	51 (-22.7%)
NLR-R2	102 (-23.9%)	127 (-5.2%)
NLR-R3	143(-17.8%)	177* (1.7%)
Av. Dev	-22.0%	-7.7%
Std Dev	23.9%	10.9%

Table 6. Predicted First and Second Linkup by Modified Dugdale Model (Model 4).

Panel ID	First Linkup (MPa) D _{MSD} = (7) Result read off at end of ligament.	First Linkup (MPa) D _{MSD} = .(7) Result read off at centre of ligament.	First Linkup (MPa) D _{MSD} = (7) Result read off at centre of ligament.	Second Linkup (MPa) D _{MSD} = (7) L = 0 Result read off at centre of ligament	Second Linkup (MPa) D _{MSD} = (7) L = 0.25 Result read off at centre of ligament	Second Linkup (MPa) D _{MSD} = (7)1.25 L = 0.5 Result read off at centre of ligament
FM4	164 (5.8%)	160 (3.2%)	157 (1.3%)	-	-	-
FM5	133 (11.8%)	124 (4.2%)	118 (-0.8%)	-	-	-
FM6	117 (17.0%)	107(7.0%)	98 (-2.0%)	(107) (-3.6%)	(107) (-3.6%)	(98) (-11.7%)
FM7	126 (14.6%)	116 (5.4%)	109(-0.9%)	(116) (5.4%)	(116) (5.4%)	(109) (-0.9%)
FM8	115(18.6%)	102(5.2%)	99 (2.1%)	(102)(-7.3%)	105 (-4.5%)	100 (-9.1)
FM9	155 (6.9%)	153(5.5%)	127(-12.4%)	(153) (0.6%)	(153) (0.6%)	(127)(-16.4%)
FM10	190 (11.1%)	183(7.0%),	172 (0.5%)	(183)(7.0%)	(183)(7.0%)	(172) (0.6%)
FM11	121(14.2%)	119(12.3%)	94(11.3%)	(119)(8.2%)	(119)(8.2%)	(94) (-14.6%)
FM12	200(2.6%)	200 (2.6%)	187 (-4.1%)	-	-	-
NIST4	101 (20.2%)	92(9.5%)	86(2.4%)	97 (-1.0%)	100 (2.0%)	98 (0%)
NIST5	154 (11.6%)	141 (2.2%)	127 (-8.0%)	141 (-12.4%)	145 (-9.9%)	137 (-14.9%)
NIST7	77 (35.1%)	70 (22.8%),	61 (7.0%)	84 (-4.54%)	87 (-1.1%)	80 (-9.1%)
NIST8	110 (23.6%)	97 (9.0%),	95 (6.7%),	97 (6.6%)	102 (12.1%)	97 (17.6%)
NIST9	164 (7.9%)	148(-2.6%)	148 (-2.6%)	147(-3.3%)	147(-3.3%)	148 (-2.6%)
NIST10*	77 (16.7%)	70(6.1%)	61 (-7.6%)	84 (-11.6%)	87 (-8.4%)	80 (-15.8%)
NLR-R2	127 (-5.2%)	127 (-5.2%)	120 (-10.4)%	-	-	-
NLR-R3	190 (9.2%)	190 (9.2%)	175 (0.57%)	190 (9.2)	190 (9.2)	175 (0.6%)
Av. Dev	13.0 %	6.1%	-2.3%	-0.5%	1.0%	-5.9
Std Dev	16.2 %	8.7%	6.3%	7.4%	7.0%	11.4

APPENDIX

The elasto-plastic solution to the damaged problem depicted in Figure 6 was obtained by superposition of the three subproblems illustrated in Figure A1. Closed form solutions to each one of the subproblems can be derived using the theory of complex potentials and singular integral equations [10].

The finite width effect is approximated by applying N point force pairs (subproblem C) along a line a parallel, but a short distance outside the free edge, and requiring traction free conditions ($\sigma_x = 0$, $\sigma_{xy} = 0$) at N collocations points along the free edge. The plastic deformation is modeled by loading the ends of the crack faces, which represent the yield zone, with the damaged reduced yield strip, $\bar{\sigma}_Y$, (Modified Dugdale Model, Figure 5(b)) or with the effective yield stress, σ_Y , in the segments corresponding to the yielded ligaments (Exact Dugdale Model, Figure 5(a)).

For a given length of the yield zone, s , the stress and displacement fields are linear functions of the applied loads in each of the subproblems A-C. The total solution is obtained by adding the subsolutions in such a way that the amplitude of the square root stress singularity at the tip of the plastic zone vanishes and requiring traction-free conditions at the N collocations points along the line $x = w$. This determines the applied load, σ , and the $2N$ finite-width correction forces, P_N and Q_N . All other quantities of interest can then be determined, including the crack opening profile. A critical value, σ_c , of the applied load, σ , corresponding to the critical crack opening can then be determined in an iterative procedure where the length of the yield strip, s , is updated until the crack opening condition is satisfied. A convergence norm for the crack tip opening displacement of the order 10^{-3} typically requires three iterations.

The accuracy of the finite-width correction depends on the number of point forces used and their distribution. In order to verify the accuracy of the present finite-width correction, computed stress-intensity factors and plastic zone lengths for the case with only a major crack were compared with interpolation formulas. The stress-intensity factor as function of a/w was compared with the interpolation formula

$$K^i = \left(1 - 0.52 \frac{a}{w} + 0.326 \left(\frac{a}{w} \right)^2 \right) / \left(\sqrt{1 - \frac{a}{w}} \right) \quad (\text{A1})$$

which is accurate to 1% for all a/w [11]. The computed values for the stress-intensity factor differed from this interpolation formula by -2%, -0.15%, and 0.7% when $a/w = 0.7$ and by -6.6%, -2.6%, and -0.75% when $a/w = 0.9$ for 20, 30, and 40 point forces respectively. An interpolation formula for the plastic zone is

$$s^i = a \left\{ \frac{2w}{\pi a} a \sin \left(\frac{\pi a}{2w} \right) \sec \left(\frac{\sigma \pi}{2\sigma_Y} \left(1 + 0.22 \left(\frac{a}{w} \right)^2 \right) \right) \right\} \quad (\text{A2})$$

which is accurate within 1% for $(a+s)/w < 0.85$ [12]. The computed plastic zone size, s , was compared with Eq. A2 for a plate with $a/w = 0.5$ and loaded such that the plastic zone varied from 0.175 to 0.3 w . The computed plastic zone length differed by 0.78%, 0.37%, and 0.7% for $s^i/w = 0.175$, and by -2.8%, -1.4%, and -0.96% for $s^i/w = 0.3$ for 20, 30, and 40 point forces respectively.

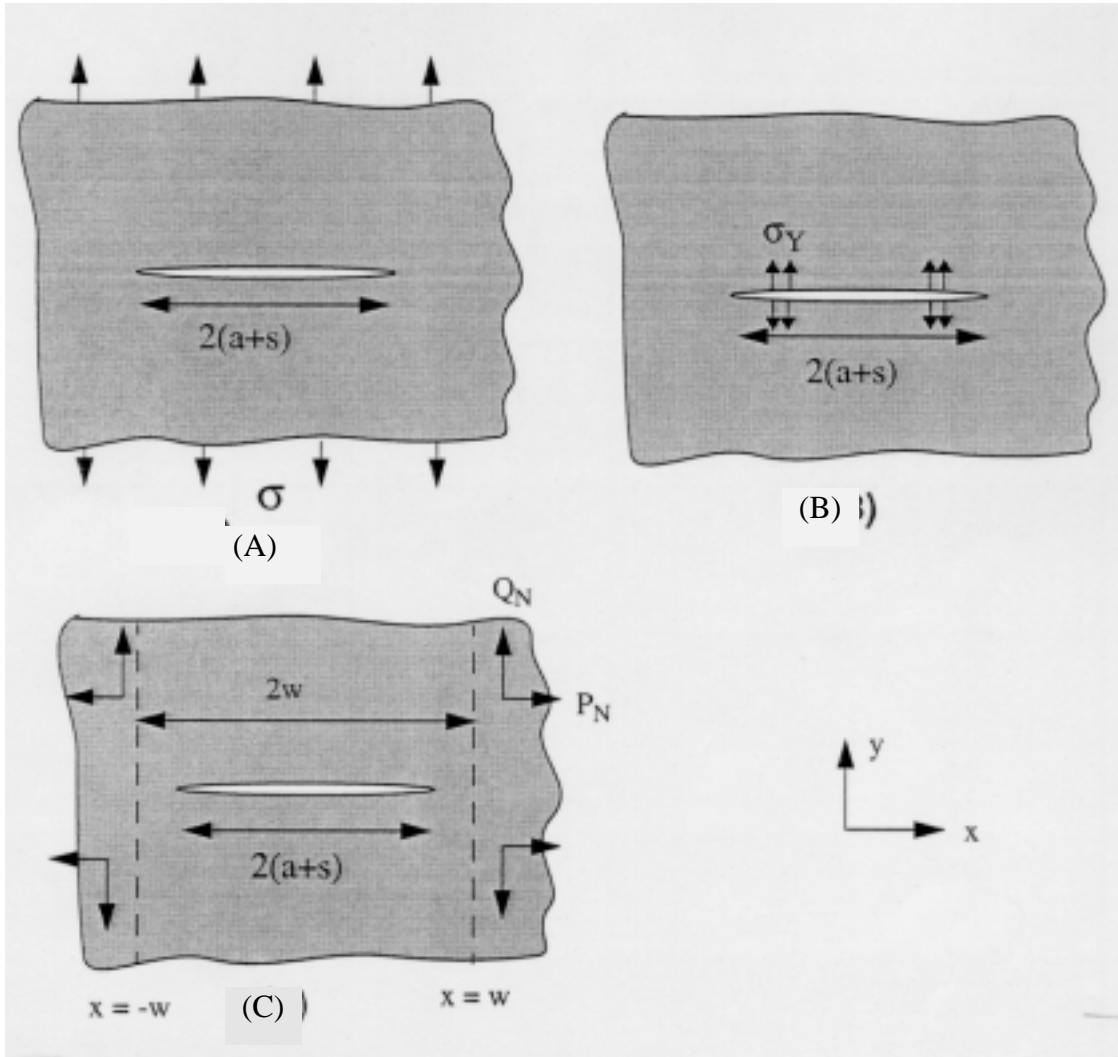


Figure A1. The Three Subproblems Used in the Numerical Procedure.

- (A) Infinite Plate With a Major Crack Loaded in Far-Field Tension.
- (B) Infinite Plate With a Major Crack and Loaded With Applied Yield Stress Along Crack Face Segments.
- (C) Infinite Plate With a Major Crack Loaded by a Quadruple of Point Force Pairs.

AN ENERGETIC CHARACTERIZATION OF THE PROPAGATION OF CURVED CRACKS IN THIN DUCTILE PLATES

Hiroshi Okada
Department of Mechanical Engineering, Faculty of Engineering
Kagoshima University
Kagoshima 890
Japan

Satya N. Atluri
Computational Modeling Center
Georgia Institute of Technology
Atlanta, GA 30332-0356

ABSTRACT

In this paper an energetic approach to characterize and predict the stable crack propagation in thin ductile metal along a smoothly curved crack path is presented. Though much investigation has been carried out for straight crack problems, not much has been done for curved cracks. The purpose of this paper is to show a research direction towards the development of a unified crack propagation criterion which can characterize the propagation for both curved and straight cracks.

INTRODUCTION

The objective of this investigation is to find a way to define a crack propagation, curving, and kinking criterion in a unified manner for all straight, curved, and kinked cracks. We often see a crack which initially propagates along straight and then follows a curved path as the length of crack increases. For example, a crack initiated at midposition of a stiffened plate follows a curved path as the crack front approaches the stiffeners, as shown in Figure 1. The cause of this phenomenon is that the problem naturally becomes a mixed one as the crack propagates and the resistance to the crack propagation increases. Therefore, a residual strength prediction for a stiffened plate under a Mode I condition may result in a very conservative one (the strength may be underestimated). For a correct (and economically sound) safety evaluation of a damaged stiffened plate, a methodology which includes the curved crack case as well as a straight one is needed (for the problems of structural integrity of aircraft, see Atluri, Sampath, and Tong (1991)).

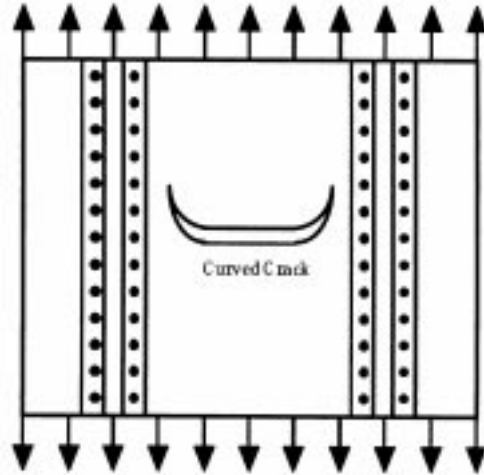


Figure 1. Stiffened Panel Under Tension With a Crack Curving as it Approaches the Stiffeners.

There are useful, energetic approaches for straight cracks, known as T_{ϵ}^* integral (see Atluri et al. (1984) and Atluri (1986)), stress-intensity factor K , and J-integral (see Rice (1968) and Paris et al. (1979) for the method of tearing modulus). For the case of elastic-plastic crack propagation problems, especially for long crack extension, the T_{ϵ}^* approach has been known to be quite effective, as discussed by various authors. (See Brust et al. (1985, 1986, 1995), Nishioka et al. (1986, 1987, 1989), Pyo et al. (1995a, 1995b), and Wang (1996). Though the T_{ϵ}^* approach has been proven to be very powerful, the application was limited to straight crack cases.

For curved and kinked cracks, there are several approaches to determine the direction of the crack extension and the crack propagation criterion. The most common approach is the so called $\sigma_{\theta\theta}$ approach in which the crack is assumed to extend along direction θ from the tangent to the crack path at the current crack tip position, giving the maximum θ value expressed in terms of a polar coordinate system whose origin is at the current crack tip. This one seems to be rather ad hoc. However, its prediction has been known to be quite reasonable. It is noted here that this approach is, most of the time, limited to linear-elastic materials for the reason that the detailed stress field around the current crack tip must precisely be known in this approach. In the linear-elastic problems, once the stress-intensity factors (i.e., K_I and K_{II}) are evaluated, the detailed stress distribution around the crack tip can be determined based on them. However, for elastic-plastic problems, in general, we must rely on some type of numerical method. The most popular one is the finite element method. Even with the finite element method, it will be quite difficult to accurately evaluate the stresses at the vicinity of the crack tip. This would be one of the reasons why energetic approaches such as J-integral and T_{ϵ}^* are so popular in elastic-plastic fracture mechanics, and they have been proven to be quite effective.

To predict the direction of crack kinking in brittle materials, a more elaborate approach which calculates the angle of the maximum $\sigma_{\theta\theta}$ value a characteristic distance from

the current crack tip (see Ramulu and Kobayashi (1983,1985)) has been shown to be accurate. The characteristic distance is assumed to be related with the microstructure of the material (i.e., the size and density of initially existing material defects). In this case also, once the stress-intensity factors are accurately calculated, the prediction can be carried out by superposing K -controlled singular field and nonsingular stress field.

For the case of elastic-plastic fracture problems with straight cracks, the crack-tip parameters such as J and T_{ϵ}^* have successfully been used. However, for curved crack and crack kinking problems, we still do not know an effective approach to characterize and predict the curvature or direction of crack extension and the angle of crack kinking.

One possible approach may be to extend the T_{ϵ}^* integral method so that the energy dissipation in the vicinity of the crack tip includes the terms responsible for crack curving. Possibly, the terms responsible for straight crack extension and the directional change of crack extension may be derived. Hence, the radius of crack path can be characterized by those two parameters. In the next section, we shall derive such parameters by accounting for energy flux to the region in the immediate vicinity of the crack. In the subsequent sections, the characteristics of the derived parameters and experimental-numerical analyses, which are necessary to evaluate the proposed parameters, are discussed.

NEAR TIP INTEGRAL PARAMETERS ACCOUNTING FOR ENERGY DISSIPATION RESPONSIBLE FOR THE STRAIGHT AND CURVED CRACK EXTENSION

In this section, we shall derive formulae which can account for the amount of deformation energy dissipating at the vicinity of propagating crack tip. As presented in Okada and Atluri (1996), the T_{ϵ}^* integral for an extending curved crack can be seen to measure the amount of deformation energy dissipating at the vicinity of the crack tip per unit crack extension. The same approach can be used even for the straight crack case. In the upper half of Figure 2, the region at the vicinity of the crack is surrounded by the integral contour. In the present investigation, we shall consider an extending crack tip whose directional change is angle $\Delta\theta$ while it propagates for length Δa . Thus, the radius of curvature of the crack path R is expressed by θ . One can establish an energy balance statement in the same manner as that presented in Okada and Atluri (1996), where the deformation energy given to the system always equals the internal energy stored in it. One may write the statement by the following expression.

$$W_{EXT} = W_{INT} + W_{\Omega_{\epsilon}} \quad (1)$$

where W_{EXT} , W_{INT} , and $W_{\Omega_{\epsilon}}$ are energy externally given to that stored in the region of the body $\Omega - \Omega_{\epsilon}$ and inside Ω_{ϵ} . Equation 1 is always true even if the region Ω_{ϵ} changed (i.e., translation, elongation, rotation, etc., inside A). Here we shall designate Ω_{ϵ} to be a small

region surrounding the crack tip. It elongates as the crack extends. The crack and the small region Ω_ϵ are schematically given in Figure 2.

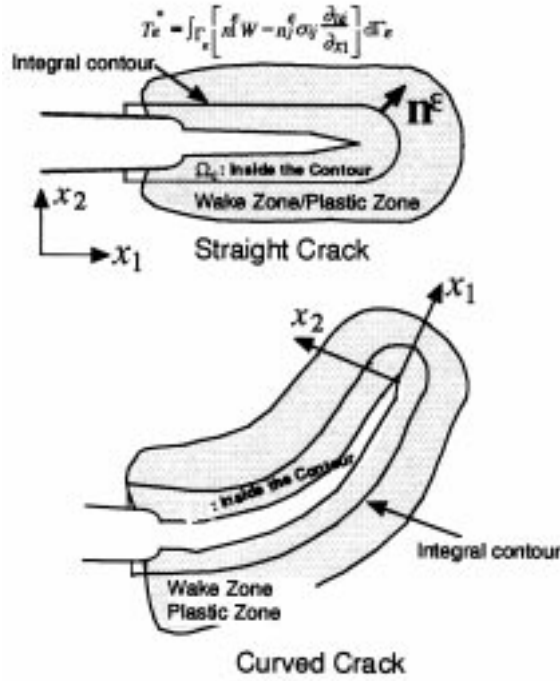


Figure 2. Straight and Curved Cracks With T_ϵ^* Integral for a Propagating Crack on a Straight Path.

Energy externally given to the system can be written as

$$W_{EXT} = \int_{\partial\Omega} \left[\int_0^{u_i} n_j \sigma_{ji}(p_1, p_2, p_3, \dots) d\bar{u}_i \right] d(\partial\Omega) \quad (2)$$

where $\partial\Omega$ designates the external boundary of the body, u_i are the displacements, n_j are the unit outward normal vectors on the external boundary, σ_{ij} are stresses, and (p_1, p_2, \dots, p_n) show the strain (deformation) history at a point. The energy stored in the body can also be expressed in a similar manner.

$$W_{INT} = \int_{\Omega - \Omega_\epsilon} \left[\int_0^{\epsilon_{ij}} \sigma_{ji}(p_1, p_2, p_3, \dots) d\bar{\epsilon}_{ij} \right] d\Omega \quad (3)$$

$$W_{\Omega_\epsilon} = \int_{\Omega_\epsilon} \left[\int_0^{\epsilon_{ij}} \sigma_{ji}(p_1, p_2, p_3, \dots) d\bar{\epsilon}_{ij} \right] d\Omega$$

where ϵ_{ij} are the strains.

The variation of W_{Ω_e} , with respect to the extension of the crack, shows the energy flowing into the region in the vicinity of the crack tip. It can be shown to be

$$\frac{DW_{\Omega_e}}{Da} = \frac{D}{Da} \left[\int_{\Omega_e} \int_0^{\epsilon_{ij}} \sigma_{ji}(p_1, p_2, p_3, \dots) d\bar{\epsilon}_{ij} \right] \quad (4)$$

where $D(\)/Da$ designates the total derivative of () with respect to the crack length. However, from the definition shown in equation 4, it will be quite difficult to accurately calculate such a quantity by using the results of the nonlinear finite element method. That is because the region near the crack tip may accumulate a large amount of numerical error in the stress and strain values. Therefore, one needs to consider an alternative way to calculate the quantity which is expressed by equation 4.

From equation 3, one can also write it in the following fashion.

$$\frac{DW_{\Omega_e}}{Da} = \frac{DW_{INT}}{Da} - \frac{DW_{EXT}}{Da} \quad (5)$$

The right-hand side of equation 5 can be evaluated without using quantities in the vicinity of the crack tip, unlike when the left-hand side is directly calculated. In the following, the evaluation of the right-hand side of equation 5 is presented.

The differentiation of W_{EXT} , with respect to the change of crack length a , can be given by

$$\begin{aligned} \frac{DW_{EXT}}{DA} &= \int_{\partial\Omega} \left(n_i \sigma_{ij} \frac{Du_j}{Da} \right) d(\partial\Omega) \\ &= \int_{\partial\Omega} \left(n_i \sigma_{ij} \left[\frac{\partial u_j}{\partial a} + \frac{\partial u_j}{\partial p_1} \frac{dp_1}{da} + \frac{\partial u_j}{\partial p_2} \frac{dp_2}{da} + \frac{\partial u_j}{\partial p_3} \frac{dp_3}{da} + \dots \right] \right) d(\partial\Omega) \end{aligned} \quad (6)$$

where the displacements u_i are considered to be the functions of the crack length a , and the deformation history parameters are $p_1, p_2, p_3, \dots, p_n$. Hence, one can write $[u_i - u_i(p_1, p_2, p_3, \dots, p_n)]$. Also, the history of deformation is a function of the crack length and applied load. Thus, we can write the total derivative of the displacements as

$$\left[\frac{Du_j}{Da} = \frac{\partial u_j}{\partial a} + \frac{\partial u_j}{\partial p_1} \frac{dp_1}{da} + \frac{\partial u_j}{\partial p_2} \frac{dp_2}{da} + \frac{\partial u_j}{\partial p_3} \frac{dp_3}{da} + \dots + \frac{\partial u_j}{\partial p_n} \frac{dp_n}{da} \right]$$

Likewise, the energy stored in the region $\Omega-\Omega_\epsilon$ can be shown to be

$$\begin{aligned}
\frac{DW_{INT}}{Da} &= \int_{\Omega-\Omega_\epsilon} \left(\sigma_{ij} \frac{D\epsilon_{ij}}{DA} \right) d(\partial\Omega) \\
&\quad - \frac{da_1}{da} \int_{\Gamma_\epsilon (Extending)} n_1^\epsilon W \Gamma_\epsilon - \frac{da_2}{da} \int_{\Gamma_\epsilon} n_2^\epsilon W \Gamma_\epsilon - \frac{d\theta}{da} \int_{\Gamma_\epsilon} e_{3ij} n_1 x_j W d\Gamma_\epsilon \\
&= \int_{\Omega=\Omega_\epsilon} \sigma_{ij} \left(\frac{\partial^2 u_i}{\partial x_j a} + \frac{\partial^2 u_i}{\partial x_j p_1} \frac{dp_1}{da} + \frac{\partial^2 u_i}{\partial x_j p_2} \frac{dp_2}{da} + \frac{\partial^2 u_i}{\partial x_j p_3} \frac{dp_3}{da} + \dots + \frac{\partial^2 u_i}{\partial x_j p_n} \frac{dp_n}{da} \right) d(\partial\Omega) \\
&\quad - \frac{da_1}{da} \int_{\Gamma_\epsilon (Extending)} n_1^\epsilon W \Gamma_\epsilon - \frac{da_2}{da} \int_{\Gamma_\epsilon (Extending)} n_2^\epsilon W \Gamma_\epsilon - \frac{d\theta}{da} \int_{\Gamma_\epsilon (Extending)} e_{3ij} n_1 x_j W d\Gamma_\epsilon
\end{aligned} \tag{7}$$

where the term $-\frac{da_1}{da} \int_{\Gamma_\epsilon (Extending)} n_1^\epsilon W \Gamma_\epsilon - \frac{da_2}{da} \int_{\Gamma_\epsilon (Extending)} n_2^\epsilon W \Gamma_\epsilon - \frac{d\theta}{da} \int_{\Gamma_\epsilon (Extending)} e_{3ij} n_1 x_j W d\Gamma_\epsilon$ appears

because of the elongation of the region Ω_ϵ as the crack extends with a curvature of $R = da/d\theta$. Since the differential length and angle of crack extension can be given by

$da_1 = R \sin \frac{\Delta a}{R}$, $da_2 = R \left(1 - \cos \frac{da}{dR} \right)$, and $d\theta = da/r$. Thus, the first order derivatives da_1/da ,

da_2/da , and $d\theta/da$ with respect to Δa , can be expressed by

$$\frac{da_1}{da} = 1, \quad \frac{da_2}{da} = 0, \quad \text{and} \quad \frac{d\theta}{da} = \frac{1}{R} \tag{8}$$

The term $\int_{\Omega=\Omega_\epsilon} \sigma_{ij} \left(\frac{\partial^2 u_i}{\partial x_j a} + \frac{\partial^2 u_i}{\partial x_j p_1} \frac{dp_1}{da} + \frac{\partial^2 u_i}{\partial x_j p_2} \frac{dp_2}{da} + \frac{\partial^2 u_i}{\partial x_j p_3} \frac{dp_3}{da} + \dots + \frac{\partial^2 u_i}{\partial x_j p_n} \frac{dp_n}{da} \right) d\Omega$ can be

converted to line integrals on Γ and on Γ_ϵ by applying the Gauss divergence theorem and the results can be shown to be

$$\begin{aligned}
&\int_{\Omega=\Omega_\epsilon} \sigma_{ij} \left(\frac{\partial^2 u_i}{\partial x_j a} + \frac{\partial^2 u_i}{\partial x_j p_1} \frac{dp_1}{da} + \frac{\partial^2 u_i}{\partial x_j p_2} \frac{dp_2}{da} + \frac{\partial^2 u_i}{\partial x_j p_3} \frac{dp_3}{da} + \dots + \frac{\partial^2 u_i}{\partial x_j p_n} \frac{dp_n}{da} \right) d\Omega \\
&= \int_{\Gamma} n_j \sigma_{ij} \left(\frac{\partial u_i}{\partial a} + \frac{\partial u_i}{\partial p_1} \frac{dp_1}{da} + \frac{\partial u_i}{\partial p_2} \frac{dp_2}{da} + \frac{\partial u_i}{\partial p_3} \frac{dp_3}{da} + \dots + \frac{\partial u_i}{\partial p_n} \frac{dp_n}{da} \right) d\Omega \\
&\quad - \int_{\Gamma} n_j^\epsilon \sigma_{ij} \left(\frac{\partial u_i}{\partial a} + \frac{\partial u_i}{\partial p_1} \frac{dp_1}{da} + \frac{\partial u_i}{\partial p_2} \frac{dp_2}{da} + \frac{\partial u_i}{\partial p_3} \frac{dp_3}{da} + \dots + \frac{\partial u_i}{\partial p_n} \frac{dp_n}{da} \right) d\Omega
\end{aligned} \tag{9}$$

Thus, the total derivative of W_{EXT} , with respect to the length of crack extension, can be given by the following expression.

$$\begin{aligned} \frac{DW_{INT}}{Da} &= \int_{\Gamma} n_j \sigma_{ij} \left(\frac{\partial u_i}{\partial a} + \frac{\partial u_i}{\partial p_1} \frac{dp_1}{da} + \frac{\partial u_i}{\partial p_2} \frac{dp_2}{da} + \frac{\partial u_i}{\partial p_3} \frac{dp_3}{da} + \dots + \frac{\partial u_i}{\partial p_n} \frac{dp_n}{da} \right) d\Omega \\ &\quad - \int_{\Gamma} n_j^{\varepsilon} \sigma_{ij} \left(\frac{\partial u_i}{\partial a} + \frac{\partial u_i}{\partial p_1} \frac{dp_1}{da} + \frac{\partial u_i}{\partial p_2} \frac{dp_2}{da} + \frac{\partial u_i}{\partial p_3} \frac{dp_3}{da} + \dots + \frac{\partial u_i}{\partial p_n} \frac{dp_n}{da} \right) d\Omega \\ &\quad - \int_{\Gamma_{\varepsilon}(Extending)} n_1^{\varepsilon} W \Gamma_{\varepsilon} - \frac{1}{R} \int_{\Gamma_{\varepsilon}(Extending)} e_{3ij} n_i x_j W d\Gamma_{\varepsilon} \end{aligned} \quad (10)$$

Combining equations 6 and 10, we can express $\frac{DW_{\Omega_{\varepsilon}}}{Da}$ as:

$$\begin{aligned} \frac{DW_{\Omega_{\varepsilon}}}{Da} &= \frac{DW_{INT}}{Da} - \frac{DW_{EXT}}{Da} \\ &= \int_{\Gamma} n_j^{\varepsilon} \sigma_{ij} \left(\frac{\partial u_i}{\partial a} + \frac{\partial u_i}{\partial p_1} \frac{dp_1}{da} + \frac{\partial u_i}{\partial p_2} \frac{dp_2}{da} + \frac{\partial u_i}{\partial p_3} \frac{dp_3}{da} + \dots + \frac{\partial u_i}{\partial p_n} \frac{dp_n}{da} \right) d\Omega \\ &\quad + \int_{\Gamma_{\varepsilon}(Extending)} n_1^{\varepsilon} W \Gamma_{\varepsilon} + \frac{1}{R} \int_{\Gamma_{\varepsilon}(Extending)} e_{3ij} n_i x_j W d\Gamma_{\varepsilon} \end{aligned} \quad (11)$$

Thus, the energy accumulated inside the near crack region, Ω_{ε} , can be calculated by the contour integrals on the right-hand side of equation 11. Though it may be possible to evaluate the term

$$\left[\int_{\Gamma} n_j^{\varepsilon} \sigma_{ij} \left(\frac{\partial u_i}{\partial a} + \frac{\partial u_i}{\partial p_1} \frac{dp_1}{da} + \frac{\partial u_i}{\partial p_2} \frac{dp_2}{da} + \frac{\partial u_i}{\partial p_3} \frac{dp_3}{da} + \dots + \frac{\partial u_i}{\partial p_n} \frac{dp_n}{da} \right) d\Omega \left(= \int_{\Gamma_{\varepsilon}} n_j^{\varepsilon} \frac{Du_j}{Da} d\Omega \right) \right]$$

by keeping track of deformation history at every point on the integral contour line, we shall seek a more convenient way to calculate this term.

We shall introduce a concept of ‘‘locally self-similar’’ crack extension that the distribution of the stresses, strains, displacements, etc., at the vicinity of the crack tip do not experience any sudden changes with the crack extension. This condition is retained as long as the crack extends in a straight or on a smoothly curved line.

By using the concept of self-similar crack extension, one can convert the integral, which includes the term Du_i/Da (see Atluri (1986)) for the concept of self-similar crack propagation):

$$\int_{\Gamma_\varepsilon} n_j^\varepsilon \sigma_{ij} \frac{Du_i}{Da} d\Gamma_\varepsilon \approx -\frac{da_1}{da} \int_{\Gamma_\varepsilon} n_j^\varepsilon \sigma_{ij} \frac{\partial u_i}{\partial x_1} d\Gamma_\varepsilon - \frac{da_2}{da} \int_{\Gamma_\varepsilon} n_j^\varepsilon \sigma_{ij} \frac{\partial u_i}{\partial x_2} d\Gamma_\varepsilon - \frac{d\theta}{da} \int_{\Gamma_\varepsilon} \varepsilon_{3ij} n_k^\varepsilon \sigma_{km} \frac{\partial u_m}{\partial x_j} x_i d\Gamma_\varepsilon \quad (12)$$

Here, the relationship $\left[\frac{Du_i}{Da} = -\frac{\partial u_i}{\partial x_1} - \frac{\partial u_i}{\partial x_2} - \frac{d\theta}{da} e_{3kj} \frac{\partial u_i}{\partial x_j} x_k \right]$ is used in equation 12.

This limits the applicability of equation 12 such that, for the curved crack case especially, the entire integral contour must be in the vicinity of the current crack tip.

So, we shall propose a use of a “locally extending integral contour,” as shown in Figure 3. In the following discussions we limit ourselves in the use of the locally extending contour path. Only the portion of the locally extending integral contour which is in front of the current crack tip is considered to move forward as the crack propagates. Also, the contour path is redefined as the current crack tip location moves forward. After the present crack tip location changes, the contour is redefined so that the entire path is always in the vicinity of the tip.

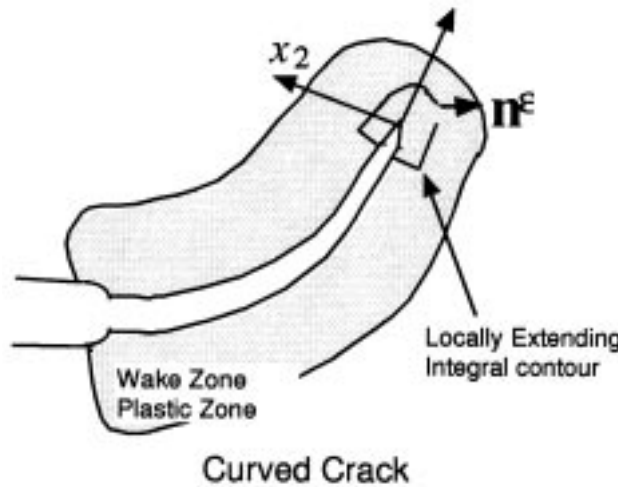


Figure 3. The Concept of a Locally Extending Integral Contour.

Therefore, equation 11 can be rewritten by using the result of equation 12 as

$$\begin{aligned}
\frac{DW_{\Omega_\epsilon}}{Da} &= \frac{DW_{INT}}{Da} - \frac{DW_{EXT}}{Da} \\
&= \int_{\Gamma_\epsilon(Extending)} n_1^\epsilon W d\Gamma_\epsilon - \int_{\Gamma_\epsilon} n_j^\epsilon \sigma_{ij} \frac{\partial u_i}{\partial x_1} d\Gamma_\epsilon \\
&\quad + \frac{1}{R} \left[\int_{\Gamma_\epsilon(Extending)} e_{3ij} n_i x_j W d\Gamma_\epsilon - \int_{\Gamma_\epsilon(Extending)} e_{3ij} n_k^\epsilon \sigma_{km} \frac{\partial u_m}{\partial x_j} x_i d\Gamma_\epsilon \right]
\end{aligned} \tag{13}$$

The above equation is composed of two parts: the energy flux responsible for straight crack extension and that for curved crack extension. Though the structure of the second term in equation 13 is very similar to the equation arising from the conservation law of Knowls and Steinberg (1972), there is a slight difference in that there is an additional term in the formula of Knowls and Steinberg (1972). The cause for this difference shall be a subject of further investigation.

Equation 13 gives the energy dissipating inside the small region at the vicinity of the crack tip. The first term can be considered to be the T_ϵ^* integral. The second one, which should be a parameter characterizing the crack curving phenomenon, shall be designated to be L_ϵ^* in this paper. Thus, one may write

$$\begin{aligned}
\frac{DW_{\Omega_\epsilon}}{Da} &= T_\epsilon^* + \frac{1}{R} L_\epsilon^* \\
T_\epsilon^* &= \int_{\Gamma_\epsilon(Extending)} n_1^\epsilon W d\Gamma_\epsilon - \int_{\Gamma_\epsilon} n_j^\epsilon \sigma_{ij} \frac{\partial u_i}{\partial x_1} d\Gamma_\epsilon \\
L_\epsilon^* &= \frac{1}{R} \left[\int_{\Gamma_\epsilon(Extending)} e_{3ij} n_i x_j W d\Gamma_\epsilon - \int_{\Gamma_\epsilon(Extending)} e_{3ij} n_k^\epsilon \sigma_{km} \frac{\partial u_m}{\partial x_j} x_i d\Gamma_\epsilon \right]
\end{aligned} \tag{14}$$

The basic characteristics of the integral, especially for L_ϵ^* , need to be explored to determine if it has good basic properties as a crack tip parameter of any means. In the subsequent section, we will see some of the important aspects of L_ϵ^* .

BASIC CHARACTERISTICS AND PROPERTIES OF
THE INTEGRAL PARAMETERS T_{ϵ}^* AND L_{ϵ}^*

In this section, some of the basic characteristics of the integral parameters T_{ϵ}^* and L_{ϵ}^* are presented. Here the relationships between the size of the near crack region Ω_{ϵ} (path independent property of the contour integrals) and the values of integral parameters T_{ϵ}^* and L_{ϵ}^* are presented.

When the T_{ϵ}^* integral is evaluated in the limit as the size of integral contour ϵ approaches zero, the value becomes nonzero and finite if its integrand had a $1/r$ type singularity. (For elastic and elastic-plastic stationary crack problems, this is the case, i.e., for linear-elastic problems $\sigma_{ij} \propto 1/\sqrt{r}$, $\epsilon_{ij} \propto 1/\sqrt{r}$, $W \propto 1/r$.) Here r is the distance between the current crack tip and a point apart from the tip. Therefore one may write a statement

$$\lim_{\epsilon \rightarrow 0} T_{\epsilon}^* = \lim_{\epsilon \rightarrow 0} \left[\int_{\Gamma_{\epsilon} (Extending)} n_1^{\epsilon} W d\Gamma_{\epsilon} - \int_{\Gamma_{\epsilon}} n_j^{\epsilon} \sigma_{ij} \frac{\partial u_i}{\partial x_1} d\Gamma_{\epsilon} \right] = \text{nonzero finite value} \quad (15)$$

if $\lim_{\epsilon \rightarrow 0} W \propto \frac{1}{\epsilon}$, $\sigma_{ij} \frac{\partial u_i}{\partial x_1} \propto \frac{1}{\epsilon}$

However, the L_{ϵ}^* integral becomes zero because its integrand has no singularity when the integrand of T_{ϵ}^* has a $1/r$ type behavior. Therefore, it can be concluded that

$$\lim_{\epsilon \rightarrow 0} L_{\epsilon}^* = \lim_{\epsilon \rightarrow 0} \frac{1}{R} \left[\int_{\Gamma_{\epsilon} (Extending)} e_{3ij} n_i x_j W d\Gamma_{\epsilon} - \int_{\Gamma_{\epsilon} (Extending)} e_{3ij} n_k^{\epsilon} \sigma_{km} \frac{\partial u_m}{\partial x_j} x_i d\Gamma_{\epsilon} \right] = 0 \quad (16)$$

when $\lim_{\epsilon \rightarrow 0} W \propto \frac{1}{\epsilon}$, $\sigma_{ij} \frac{\partial u_i}{\partial x_1} \propto \frac{1}{\epsilon}$

What the above equations means is that the L_{ϵ}^* integral component does not contribute to the energy release rate at all. The T_{ϵ}^* component is fully responsible for the energy release at the crack tip. However L_{ϵ}^* still measures the energy flowing into the crack tip region. This means that L_{ϵ}^* would have a secondary effect as the crack propagation driving force.

In the case of stable crack propagation in a ductile material, the order of singularity in the quantities such as W and σ_{ij} all are known to be lower than the $1/r$ type (see Rice (1982)). Therefore, in the limit $\epsilon \rightarrow 0$, even T_{ϵ}^* approaches zero. Thus, it was proposed that a finite ϵ be used to measure the rate of energy dissipation near the crack tip region (Okada and Atluri (1996)). For the same ϵ , T_{ϵ}^* may be the material constant measuring a resistance against crack propagation. In the same consideration, even for the curved crack case, the rate of energy dissipation at the vicinity of the crack tip may be the material constant.

A PROPOSED METHODOLOGY TO VALIDATE THE PRESENTLY PROPOSED ENERGETIC PARAMETERS FOR CURVED CRACK PROPAGATION

It will take a hybrid experimental-numerical investigation in which, as seen in Okada et al. (1995), experimentally determined boundary conditions drive crack propagation in the numerical analysis procedure. Then, the parameters T_{ϵ}^* and L_{ϵ}^* should be evaluated for different crack curving radius R . It may require a number of experiments. After enough experiments have been performed, one may fit curves to the data as shown in Figure 4(a) and 4(b). Figure 4(a) shows the relationship between the radius of curvature and the total crack propagation resistance. Figure 4(b) shows the relationship between the ratio of T_{ϵ}^* and L_{ϵ}^* and the radius of curvature. Once these relationships are established, then we will be able to predict the radius of curvature for stably propagating curved cracks.

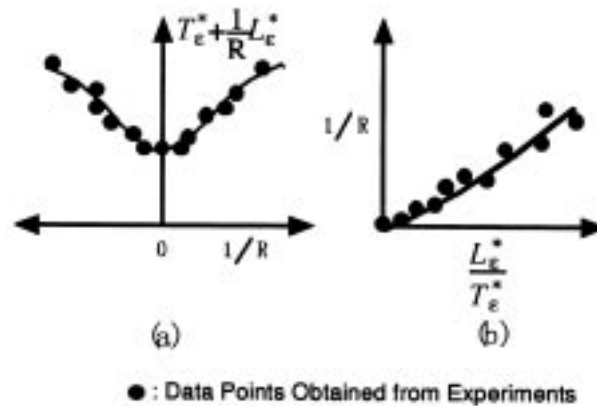


Figure 4. Expected Relationships Between the Curvature of the Crack Path.

Next, it is expected that the crack kinking occurs when the relationship shown in Figure 4(a) and 4(b) breaks down. How does it break down? The answer is that there may be a critical ratio of T_{ϵ}^* and L_{ϵ}^* , at which the stably smooth curved crack propagation jumps to a nonsmooth crack path (kinking). Thus, the occurrence of crack kinking may be predicted by the T_{ϵ}^* and L_{ϵ}^* parameters. However, the prediction of kink angle may not be possible because the parameters are derived under the assumption of a smoothly curved path. Thus, much further research would be needed to provide energetic crack tip integral parameters to characterize the phenomenon of crack kinking.

CONCLUDING REMARKS

The present paper provides a set of integral parameters to characterize stable and smoothly curved crack propagation phenomena in ductile material. The extension was made from the case of T_{ϵ}^* integral parameter in straight crack cases. The presently proposed method includes the case of straight crack propagation with T_{ϵ}^* integral, which is known to

perform well. Thus, at least, we can expect that the present method works for moderately curved crack cases.

Much investigation must be carried out experimentally and numerically to validate the presently proposed way of characterizing curved cracks. This paper shows guidelines for future research work.

ACKNOWLEDGMENTS

The authors would like to express their sincere thanks to the Federal Aviation Administration for their support. Also, appreciation is extended to Professor A. S. Kobayashi and Dr. Y. Omori of the University of Washington, Dr. L. Wang of Georgia Tech, and Dr. F. W. Brust of Battelle Memorial Labs for valuable discussions.

REFERENCES

- S. N. Atluri (1986): Energetic Approaches and Path Independent Integrals in Fracture Mechanics, in *Computational Methods in the Mechanics of Fracture*, S. N. Atluri, (ed.) North-Holland.
- S. N. Atluri, T. Nishioka, and M. Nakagaki (1984): Incremental Path-Independent Integrals in Inelastic and Dynamic Fracture Mechanics, *Engineering Fracture Mechanics*, 20, No.2, pp. 209-244.
- S. N. Atluri, S. G. Sampath, and P. Tong (Eds.) (1991): Structural Integrity of Aging Airplanes, Springer Verlag.
- F. W. Brust, J. J. McGowan, and S. N. Atluri (1986): A Combined Numerical-Experimental Study of Ductile Crack Growth After a Large Unloading, Using T^* , J and CTOA Criteria, *Engineering Fracture Mechanics*, 23, No. 3, pp. 537-550.
- F. W. Brust (1995): The T^* -Integral: Definition and Use for Predicting Damage Accumulation and Fracture, *Contemporary Research in Engineering Science*, R.C. Batra, Springer, (ed.) pp. 118-140.
- F. W. Brust, T. Mshioka, and S. N. Atluri (1985): Further Studies on Elastic-Plastic Stable Fracture Utilizing The T^* Integral, *Engineering Fracture Mechanics*, 22, No. 6, pp. 1079-1103.
- J. K. Knowles and E. Steinberg (1972): On a Class of Conservation Laws in Linearized and Finite Elastostatics, *Archives for Rational Mechanics Analysis*, pp. 187-211.

T. Mshioka and M. Kobashi (1986): Path Independent Integrals in Nonlinear Dynamic Fracture Mechanics, *Nihon Kikaigakkai Ronbun Shu A-hen 53 (JSME: Japan Society of Mechanical Engineers)*, pp. 271-277.

T. Mshioka and M. Kobashi (1987): Analysis of Path Independent T^* Integral in Elastoplastic Dynamic Fracture Testing, *Nihon Kikaigakkai Ronbun Shu A-hen 54 (JSME: Japan Society of Mechanical Engineers)*, pp. 301-306.

T. Mshioka, T. Fujimoto, and S. N. Atluri (1989): On the Path Independent T^* Integral in Nonlinear and Dynamic Fracture Mechanics, *Nuclear Engineering and Design*, 111, pp. 109-121.

P. C. Paris, H. Tada, A. Zahoor, and H. Ernst (1979): The Theory of the Tearing Mode of Elastic-Plastic Crack Growth, *Elastic-Plastic Fracture, ASTM STP 668*, pp. 5-36.

C.-R. Pyo, H. Okada, and S. N. Atluri (1995a): An Elastic-Plastic Finite Element Alternating Method for Analyzing Widespread Fatigue Damage in Aircraft Structures, *Computational Mechanics*, 16, pp. 62-68.

C.-R. Pyo, H. Okada, and S.N. Atluri (1995b): Residual Strength Prediction for Aircraft Panels with Multiple Site Damage, using the “EPFEAM” for Stable Crack Growth, *Computational Mechanics*, 16, pp. 190-196.

M. Ramulu and A. S. Kobayashi (1983): Dynamic Crack Curving-A Photoelastic Evaluation, *Experimental Mechanics*, 23, pp. 1-9.

M. Ramulu and A. S. Kobayashi (1985): Mechanics of Crack Curving and Branching - A Dynamic Fracture Analysis, *International Journal of Fracture*, 27, pp. 187-201.

J. R. Rice (1968): A Path Independent Integral and Approximate Analysis of Strain Concentration by Notches and Cracks, *Journal of Applied Mechanics*, 35, pp. 379-386.

J. R. Rice (1982): Elastic Plastic Crack Growth, in *Mechanics of Solids-The Rodney Hill 60th Anniversary Volume*, Eds. H.G. Hopkins and M.J. Sewell, Pergamon Press, Elmsford, NY, pp. 539-562.

L. Wang (1996): Elastoplastic Analysis of Multiple Cracks in Thin Sheets, and of Elliptical Cracks in 3-Dimensional Bodies, Ph.D. Thesis, School of Aerospace Engineering, Georgia Institute of Technology.

ENGINEERING FRACTURE PARAMETERS FOR BULGING CRACKS IN PRESSURIZED UNSTIFFENED CURVED PANELS

John G. Bakuckas, Jr.
Paul V. Nguyen
Catherine A. Bigelow

Federal Aviation Administration
William J. Hughes Technical Center
Airworthiness Assurance Research and Development Branch, AAR-430
Atlantic City International Airport, NJ 08405

ABSTRACT

A global-local hierarchical approach was developed and used to obtain engineering fracture parameters for bulging cracks in pressurized, unstiffened curved panels. In the first step of the global-local hierarchical approach, a global model using a geometric nonlinear shell finite element analysis to obtain displacement boundary conditions applied in the second step to a higher fidelity local model. A geometric nonlinear, three-dimensional solid finite element analysis was conducted for the local model to obtain the bulging factor defined as the ratio of the stress-intensity factor of a curved panel to that of the flat panel. The results generated using this global-local hierarchical approach were in excellent agreement with published results. Results from a parametric study are reported in which the effects of crack length, panel radius, thickness, modulus, and the applied pressure on the bulging factors were determined. Results showed that the bulging factor increases as the crack length and panel thickness increase and that the bulging factor decreases as the applied load and panel radius increase.

INTRODUCTION

Widespread fatigue damage (WFD) in aging aircraft has been the subject of vital concern since the Aloha Airlines accident in 1988 in which a large fuselage section of a B737 tore apart in flight due to the sudden link-up of small cracks emanating from multiple rivet holes in the fuselage lap splice joint. The load carrying capability of the aircraft was degraded below certification requirements due to WFD. Laboratory testing of flat and curved panels has demonstrated that residual strength can be reduced significantly by a lead crack accompanied by several smaller collinear cracks, compared to the case of a single lead crack only. The Federal Aviation Administration (FAA) has initiated several research programs to investigate the effect of WFD on the structural integrity of the aging fleet.

To better understand and quantify the effects of WFD on the structural integrity of aircraft, a study was undertaken to determine the mechanics governing the growth of cracks in pressurized fuselage structures. The development of cracks in a pressurized fuselage structure is a complex process due to the biaxial and internal pressure loads and the structural configuration. The response of such cracks is characterized by large out-of-plane deformations or bulging of the surfaces of the crack which develops local membrane and bending stresses. The bulging phenomena is often quantified in terms of a bulging factor defined as the ratio of the stress-intensity factor of a curved panel to the stress-intensity factor of a flat panel. The bulging factor is a nonlinear function of the applied pressure, material properties, and geometric parameters including the panel radius, panel thickness, and crack length. To accurately model bulging cracks, including the out-of-plane deformation, large displacement theory and geometric nonlinearities must be considered.

Many studies have been conducted to characterize bulging cracks, for example [1-8]; these studies can be divided into experimental correlations [1-2,7] and analytical formulations [3-8]. Experimental correlations have primarily concentrated on comparing fracture toughness and fatigue crack growth data for curved and flat panels to derive empirical relations for the bulging factors which are highly dependent on the material and specimen configurations. Consequently, these experimentally determined empirical relations are limited to specific configurations. More generalized characterizations of bulging cracks have been obtained using analytical formulations. Early work of Folias [3] provided the first analytical expressions for bulging factors based on linear elastic theory. Numerical analysis by Erdogen and Kibler [4] using linear elastic fracture mechanics support the expressions developed by Folias. However, later work conducted by Riks [5] and Ansell [6] using geometric nonlinear finite element analysis demonstrated that the bulging phenomena was a nonlinear problem and that large deformations needed to be considered in order to appropriately characterize bulging cracks. It was shown that the stress-intensity factor for a given crack configuration increased with applied pressure and the value was smaller than the value using linear elastic theory.

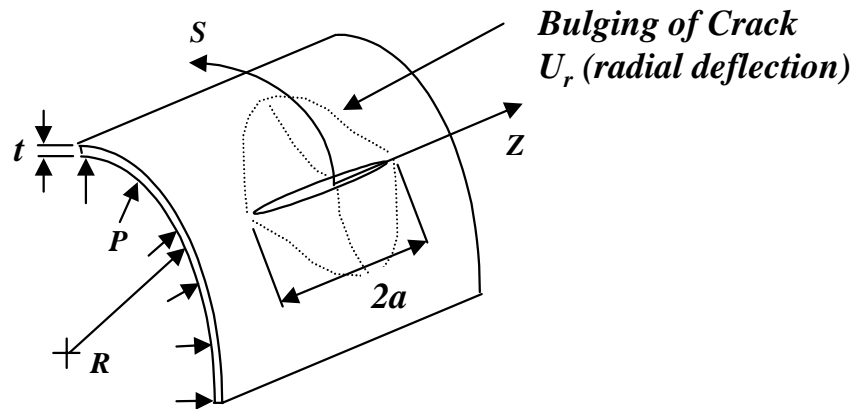
The work of Chen and Schijve [7] considered the problem from a fracture mechanics, energy balance approach accounting for the nonlinear deformation in the vicinity of the crack using a semiempirical formulation. By correlating with experiments, Chen and Schijve [7] developed an expression for the bulging factor which was in good agreement with the results published by Riks [5] and Ansell [6]. More recent and advanced work by Shenoy, et al. [8] used the T^* -integral which accounts for both geometric and material nonlinearity to study the nonlinear effects on the mechanics of bulging cracks. The material nonlinearity due to plasticity decreased the value of the T^* -integral when compared to the case of material linearity.

Due to the complexities of analyzing bulging cracks a wide range of the stress-intensity factors (SIF) for bulging cracks are not available. Without SIF, accurate damage tolerance assessments for a broad spectrum of crack configurations in aircraft fuselage structures are difficult. To address this need, a compendium of SIF for bulging cracks in unstiffened pressurized curved panels were generated using a geometric nonlinear finite element analysis. A global-local hierarchical approach was developed to obtain the SIF

solutions, the crack bulge shape, and the crack bulge profile. In the first step of the global-local hierarchical approach, a geometric nonlinear shell analysis is conducted for the global model. The global model defines the displacements of the boundary of the local model. In the second step, the boundary displacements from the global analysis are used in a geometric nonlinear, three-dimensional finite element analysis of the local model to obtain the bulging factor defined as the ratio of the stress-intensity factor of the curved panel to that of the flat panel. The results generated using this global-local hierarchical approach were compared with published results. Results from a parametric study are reported in which the effects of crack length, panel radius, panel thickness, modulus, and the applied pressure on engineering bulging factors were determined.

ANALYSIS MATRIX

In the current study, five parameters were considered: the crack length, $2a$, panel radius, R , panel thickness, t , panel modulus, E , and applied pressure, P . The analysis matrix is shown in Figure 1.



	$R = 60''$		$R = 80''$				$R = 100''$			$R = 120''$			
t (in)	0.036	0.048	0.036	0.048	0.060	0.072	0.048	0.060	0.072	0.048	0.060	0.072	0.084
$2a$ (in)													
4	31			1				33				35	
8	7	22	13	2	14	15	37	8	25	40	42	9	28
12	32			3				34				36	
16	10	23	16	4	17	18	38	11	26	41	43	12	29
20		24	19	5	20	21	39		27	44	45		30
30				6									

Figure 1. Analysis Matrix Used to Generate Engineering Fracture Parameters ($PR/t = 5, 10, 15, 20$ ksi; $E = 10.5 \times 10^6$ and 17.5×10^6 psi).

Two materials were considered in the analysis matrix, generic aluminum and generic titanium with moduli of 10.5×10^6 psi and 17.5×10^6 psi, respectively. The generic aluminum was used for all 45 cases, and the generic titanium was used only in cases 1-6.

GLOBAL-LOCAL HIERARCHICAL APPROACH

A global-local hierarchical finite element approach was used to obtain the engineering fracture parameters for bulging cracks in a pressurized, unstiffened panel. The commercially available finite element program, ABAQUS 5.5 [9] was used for the analysis. In the first step of the global-local hierarchical (GLH) approach, a geometric nonlinear shell analysis was conducted for the global model. The global model consisted of a capsule subjected to internal pressure. Due to symmetry in the load and geometry, one quarter of the capsule was modeled, as shown in Figure 2.

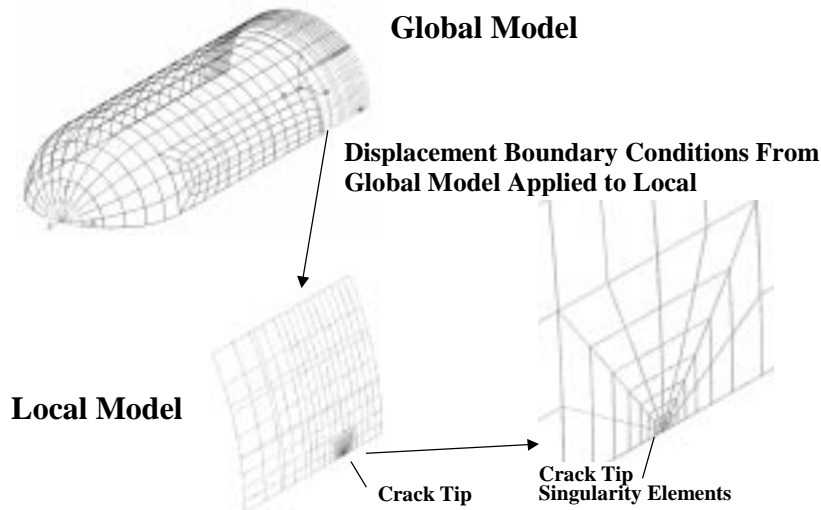


Figure 2. Global-Local Hierarchical (GLH) Approach.

The global model consisted of 8-noded shell elements. A total of 1000 elements were typically used in the global model. From the global model, the displacements defining the boundary of the local model were determined. In the second step, the boundary displacements were used in a geometric nonlinear, three-dimensional solid analysis for the local model. The local model consisted of two layers of 20-noded brick elements. A total of 2000 elements were typically used in the local model. The boundary displacements from the global model were applied to the local model using the submodeling features available in ABAQUS 5.5. The stress-intensity factors and bulging factors were determined from the local model.

A detailed view of a typical finite element mesh from the local model near the crack tip is shown in Figure 3. A ring of singularity elements was placed around the crack front. These singularity elements are 20-noded, isoparametric brick elements with one side collapsed along the crack front, with the mid-side nodes on the element sides adjacent to the

collapsed side shifted to the quarter point so that a $1/\sqrt{r}$ singularity was obtained. From the local model, the J-integral was calculated using the equivalent domain integral method at points a, b, c, d, and e along the crack front shown in Figure 3.

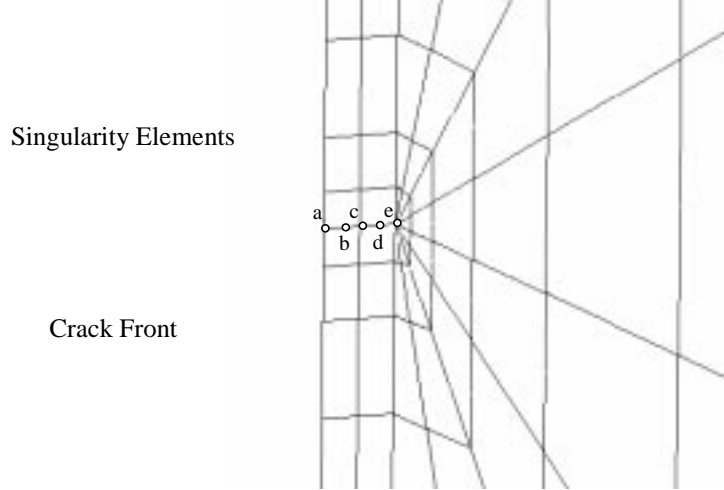


Figure 3. Finite Element Mesh in the Vicinity of the Crack.

With the singularity elements having the same length through the thickness along the crack front, the average J-integral was calculated by treating the J-integral values as equivalent nodal forces having units of forces per unit length:

$$J_{avg} = \frac{J_a + 4J_b + 2J_c + 4J_d + J_e}{12} \quad (1)$$

Assuming a plane stress elastic material response, the stress-intensity factor for the curved panel is

$$K_{curve} = \sqrt{J_{avg} E} \quad (2)$$

The bulging factor is defined as the ratio of the stress-intensity factor of the curved panel to that of the flat panel:

$$\beta = \frac{K_{curve}}{K_{flat}} \quad (3)$$

where:

$$K_{flat} = \frac{PR}{t} \sqrt{\pi a} \quad (4)$$

RESULTS

The global-local hierarchical approach was validated by comparisons with existing results. A parametric study was then conducted to determine the effect of various parameters on the calculated values of the bulging factor.

Comparison With Existing Results

The results generated using the global-local hierarchical (GLH) approach were compared with the results published by Riks [5], Ansell [6], and Chen and Schijve [7]. Chen and Schijve [7] derived the following expression for the bulging factor, β , from the energy balance approach and experimental data:

$$\beta = \sqrt{1 + \frac{5}{3\pi} \frac{Eta}{R^2 P} \frac{0.316}{\sqrt{1 + 18\chi}} \tanh\left(0.06 \frac{R}{t} \sqrt{\frac{Pa}{Et}}\right)} \quad (5)$$

where χ is the ratio of the circumferential stress to longitudinal stress and is equal to 0.5 for the current comparisons. Both Riks [5] and Ansell [6] obtained bulging factors using the strain energy release rate calculated from a geometric nonlinear finite element analysis.

Comparisons of the bulging factor as a function of half crack length calculated using the GLH approach and published results are shown in Figures 4 and 5. Results from the present approach (open circles) are in good agreement with the results of Riks [5], Ansell [6], and Chen and Schijve [7]. In these figures, the results of Chen and Schijve [7] were generated using Equation 5 (solid line).

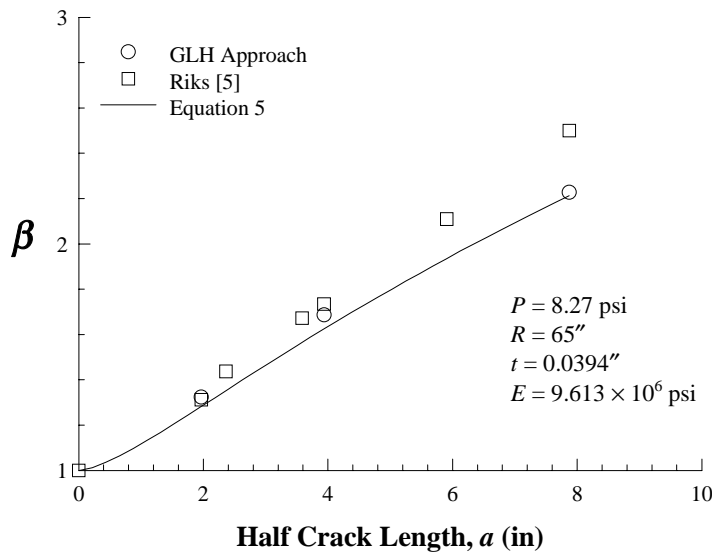


Figure 4. Bulging Factors as a Function of Half Crack Length.

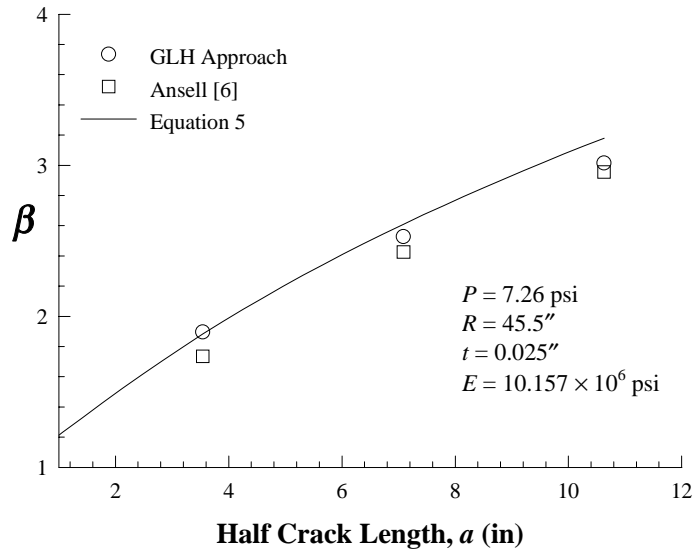


Figure 5. Bulging Factors as a Function of Half Crack Length.

The bulging factor as a function of the applied pressure was calculated using the GLH approach and compared with published results as shown in Figures 6 and 7. In these figures, the results of Chen and Schijve [7] were generated using Equation 5.

The results shown in Figure 6 were generated for a radius, $R = 65$ inches, thickness, $t = 0.0394$ inches, modulus, $E = 9.613 \times 10^6$ psi, and half crack length, $a = 3.937$ inches. As shown in this figure, excellent agreement was obtained between the results generated using the present approach (open circles), the results of Riks [5] (open squares), and the results of Chen and Schijve [7] using Equation 5 (solid line). As the pressure decreases, the value of β calculated using Equation 5 approaches infinity due to the pressure singularity term in the denominator of Equation 5.

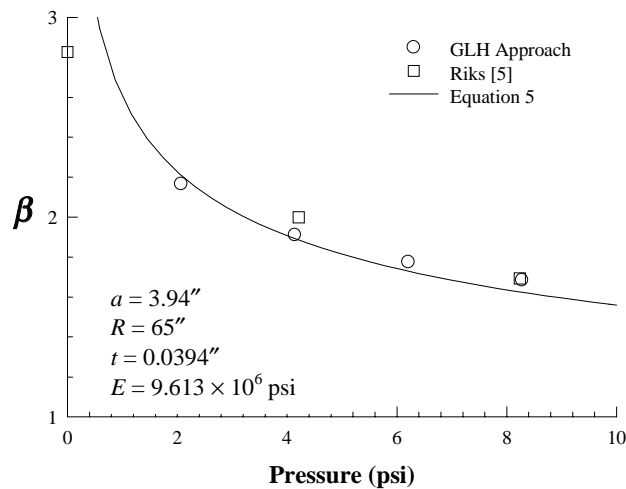


Figure 6. Bulging Factors as a Function of Applied Pressure.

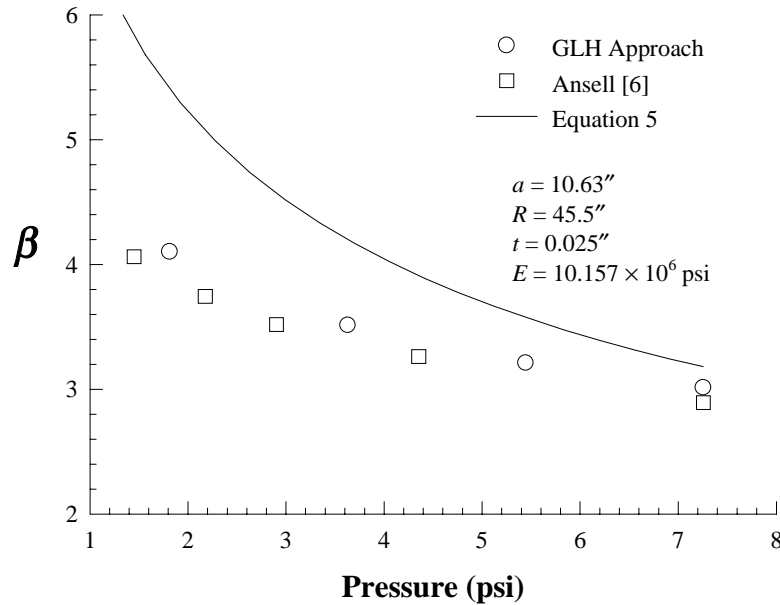


Figure 7. Bulging Factors as a Function of Applied Pressure.

The results shown in Figure 7 were generated for a radius, $R = 45.5''$, thickness, $t = 0.025''$, modulus, $E = 10.157 \times 10^6$ psi, and half crack length of $a = 10.63''$. As shown in this figure, excellent agreement was obtained between the results generated using the GLH approach (open circles) and the finite element results of Ansell [6] (open squares). The results of Chen and Schijve [7] from Equation 5 (solid line) give an upper bound solution. Again, as the pressure decreases, the value of β calculated using Equation 5 increases substantially due to the pressure singularity term in the denominator.

Parametric Study

Five parameters were varied to determine their effects on the calculated values of the bulging factor: the crack length, $2a$, applied pressure, P , panel radius, R , panel thickness, t , and panel modulus, E .

Effect of Crack Length on Bulging Factor

The bulging factor for varying half crack lengths was calculated using the GLH approach as shown in Figure 8. The results shown in Figure 8 were generated for a radius, $R = 80''$, thickness, $t = 0.048''$, modulus, $E = 10.5 \times 10^6$ psi, and applied pressure, $P = 12$ psi. As shown in this figure, the value of the bulging factor increases as the half crack length increases.

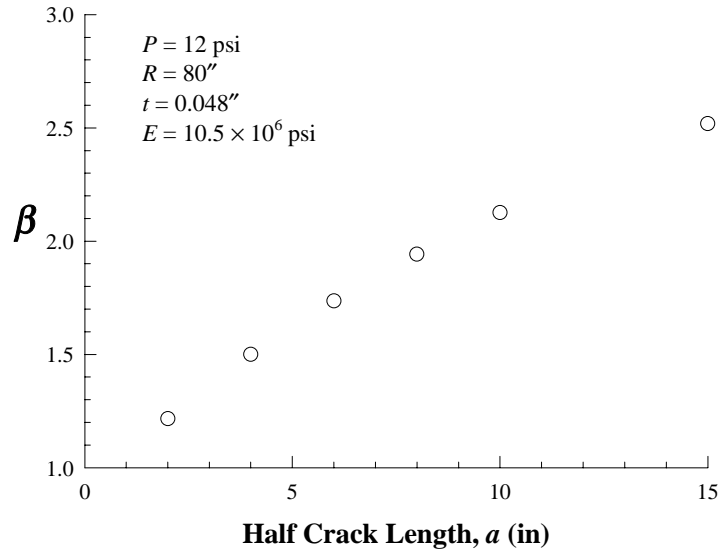


Figure 8. Bulging Factor as a Function of Half Crack Length.

Effect of Applied Pressure on Bulging Factor

The bulging factor for varying normalized pressure was calculated using the GLH approach as shown in Figure 9. The results shown in Figure 9 were generated for a radius, $R = 80''$, thickness, $t = 0.048''$, modulus, $E = 10.5 \times 10^6$ psi, and crack length, $a = 8''$. As shown in Figure 9, the value of the bulging factor decreases as the normalized applied pressure increases. This is a geometric nonlinear stiffening effect where the resistance to the bulging deformation increases as the pressure increases. The membrane stresses along the crack edge magnify the stiffening effect.

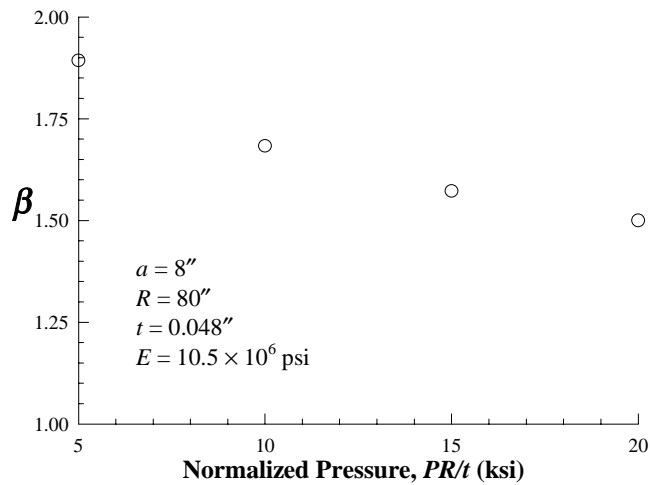


Figure 9. Bulging Factor as a Function of Normalized Applied Pressure.

Effect of Panel Radius on Bulging Factor

The bulging factor for varying panel radius was calculated using the GLH approach as shown in Figure 10. The results shown in Figure 10 were generated for a thickness, $t = 0.048''$, pressure, $P = 8$ psi, modulus, $E = 10.5 \times 10^6$ psi, and half crack length, $a = 8''$. As shown in Figure 10, the value of the bulging factor decreases as the radius increases.

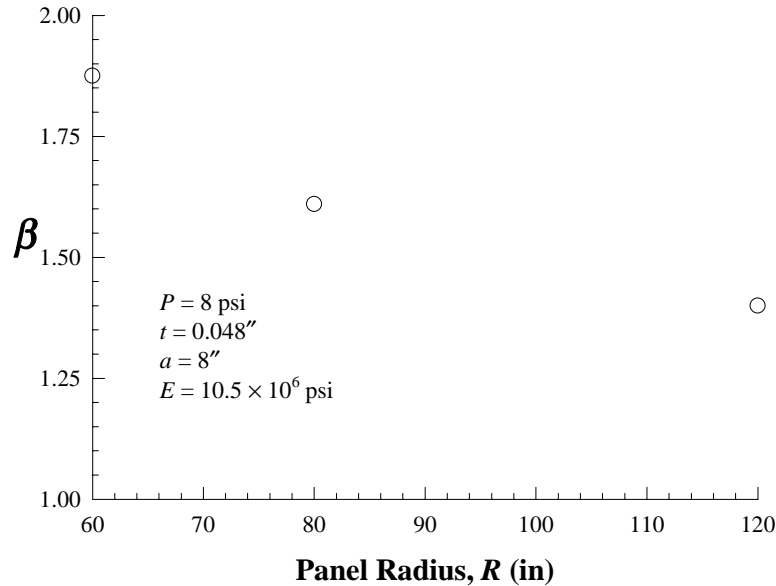


Figure 10. Bulging Factor as a Function of Panel Radius.

Effect of Panel Thickness on Bulging Factor

The bulging factor for varying panel skin thickness was calculated using the GLH approach as shown in Figure 11. The results shown in Figure 11 were generated for a radius, $R = 80''$, pressure, $P = 9$ psi, modulus, $E = 10.5 \times 10^6$ psi, and half crack length, $a = 8''$. As shown in Figure 11, the value of the bulging factor slightly increases as the thickness increases.

Effect of Panel Modulus on Bulging Factor

The bulging factor as a function of crack length normalized by the panel radius for a generic aluminum and titanium having modulus of 10.5×10^6 psi and 17.5×10^6 psi, respectively, is plotted in Figure 12. The results shown in Figure 12 were generated for a radius, $R = 80''$, pressure, $P = 3$ psi, and thickness, $t = 0.048''$. As shown in this figure, the value of the bulging factor is greater for the stiffer titanium compared with the aluminum.

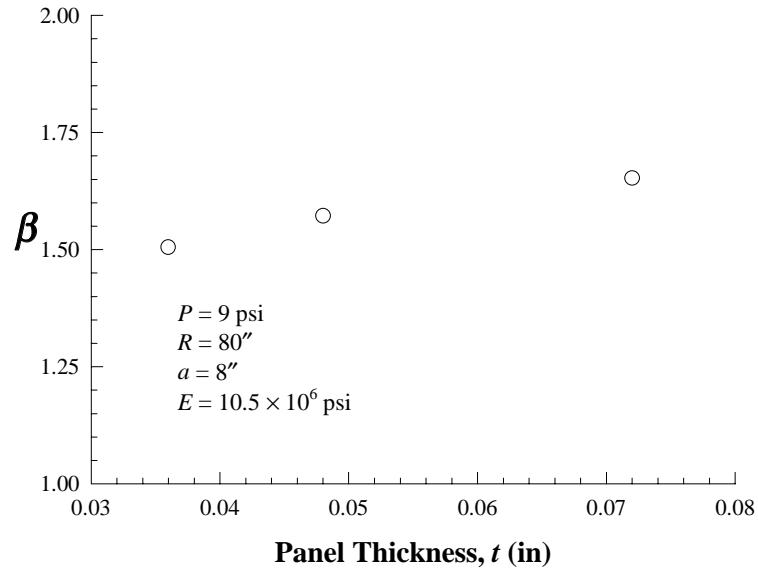


Figure 11. Bulging Factor as a Function of Panel Skin Thickness.

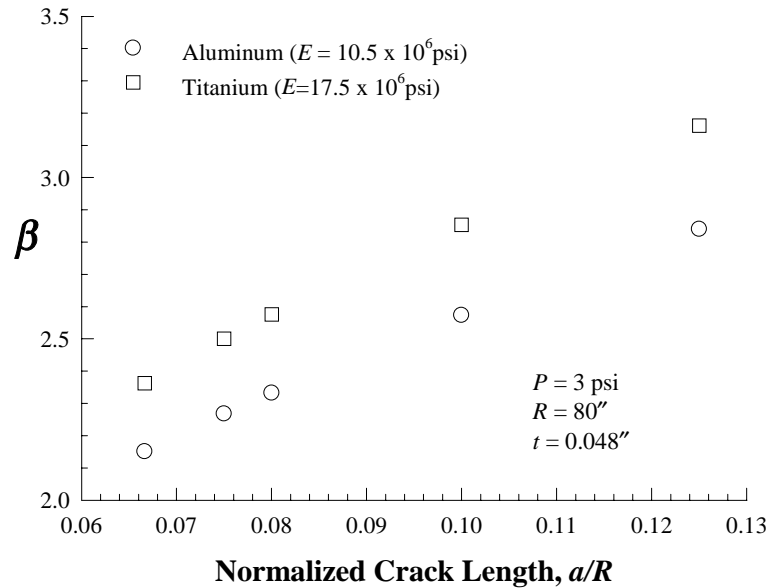


Figure 12. Effect of Modulus on Bulging Factor.

Summary of Bulging Factor Results

The bulging factors from the parametric study for the generic aluminum (modulus, $E = 10.5 \times 10^6$ psi) are plotted in Figure 13 and summarized in Table 1 as a function of the half crack length normalized by the panel radius. In general, the bulging factor increases as the crack length and panel skin thickness increase and also increases as the panel radius and pressure decrease. Similar trends were obtained for the generic titanium.

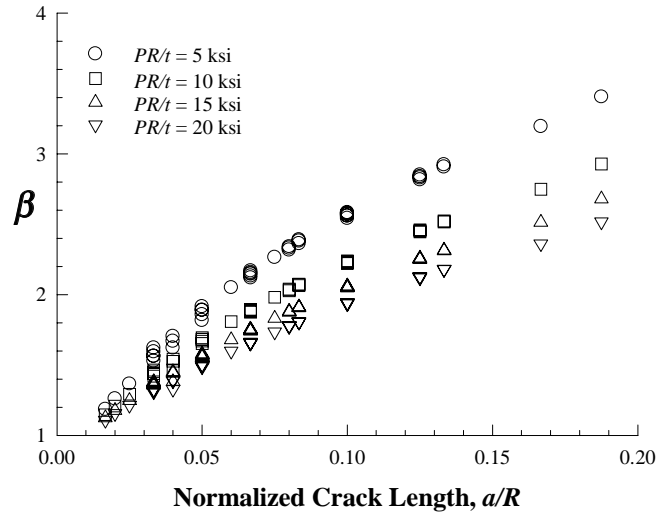


Figure 13. Summary of Results From Parametric Study for Generic Aluminum, $E = 10.5 \times 10^6$ psi.

Table 1. Summary of Bulging Factors for Generic Aluminum, $E = 10.5 \times 10^6$ psi.

a/R	β $PR/t = 5$ ksi	β $PR/t = 10$ ksi	β $PR/t = 15$ ksi	β $PR/t = 20$ ksi
0.0167	1.188	1.148	1.124	1.109
0.0200	1.262	1.209	1.177	1.156
0.0250	1.369	1.292	1.247	1.216
0.0333	1.576	1.443	1.369	1.320
0.0400	1.668	1.511	1.426	1.370
0.0500	1.876	1.676	1.568	1.498
0.0600	2.052	1.808	1.681	1.598
0.0667	2.149	1.886	1.749	1.660
0.0750	2.268	1.982	1.833	1.736
0.0800	2.332	2.034	1.879	1.778
0.0833	2.380	2.070	1.910	1.806
0.1000	2.569	2.231	2.055	1.940
0.1250	2.835	2.453	2.254	2.124
0.1333	2.916	2.520	2.314	2.179
0.1667	3.198	2.748	2.515	2.362
0.1875	3.407	2.927	2.680	2.518

In the engineering approach used in this study, material plasticity was not considered. Shenoy, et. al [8] accounted for nonlinearity due to material plasticity, which decreased the value of the T^* -integral. Although the trends in the results from the current study match those of Shenoy, et. al [8], the bulging factors would decrease if material plasticity were accounted for.

SUMMARY

The finite element approach was used to obtain the engineering fracture parameters for bulging cracks in pressurized, unstiffened curved panels. A global-local hierarchical approach was used to obtain the bulging factors defined as the ratio of the stress-intensity factor of the curved panel to that of the flat panel. The preliminary results generated using this global-local hierarchical approach were in good agreement with published results. A parametric study showed that the bulging factor increases as the crack length and panel skin thickness increase and that the bulging factor decreases as the applied load and panel radius increase.

REFERENCES

1. Peters, R. W. and Kuhn, P., "Bursting Strength of Unstiffened Pressure Cylinders with Slits," NACA TN 3993, 1957.
2. Anderson, R. B. and Sullivan, T. L., "Fracture Mechanics of Through-Cracked Cylindrical Pressure Vessels," NASA TN D-3252, February 1966.
3. Folias, E. S., "An Axial Crack in a Pressurized Cylindrical Shell," *International Journal of Fracture Mechanics*, Vol. 1, pp. 104-113, 1965.
4. Erdogan, F. and Kibler, J. J., "Cylindrical and Spherical Shells with Crack," *International Journal of Fracture Mechanics*, Vol. 5, pp. 229-237, 1969.
5. Riks, E., "Bulging Cracks in Pressurized Fuselages: A Numerical Study," NLR MP-87058-U, National Aerospace Laboratory, NLR, The Netherlands, 1987.
6. Ansell, H., "Bulging of Crack Pressurized Aircraft Structure," LUI-TEK-LIC-1988:11, Institute of Technology, Department of Mechanical Engineering, S-581 83 Linköping, Sweden.
7. Chen, D. and Schijve, J., "Bulging of Fatigue Cracks in a Pressurized Aircraft Fuselage," Report LR-655, May 1991, Faculty of Aerospace Engineering, Delft University of Technology, Delft, The Netherlands.
8. Shenoy, V. B., Potyondy, D. O., and Atluri, S. N., "A Methodology for Computing Nonlinear Fracture Parameters for a Bulging Crack in a Pressurized Aircraft Fuselage," *Computational Mechanics*, Vol. 14, pp. 529-548, 1994.
9. ABAQUS Version 5.5, Hibbit, Karlsson, and Sorensen (HKS), 1080 Main Street, Pawtucket, RI 02860, 1995.

EVALUATION OF CLOSURE-BASED CRACK GROWTH MODEL

C. Hsu, K. K. Chan, and J. Yu
McDonnell Douglas Aircraft Company
Long Beach, CA

SUMMARY

The closure stress was measured using center-cracked tension (CCT) specimens made from 7050-T76 aluminum plate under constant amplitude and repeated overloads. The behavior of crack-opening stress predicted by Newman's FASTRAN-II is consistent with the experimental results for repeated overload. It was also found that the program is capable of predicting crack growth under complex spectrum loading which consists of significant numbers of compression cycles.

INTRODUCTION

Since Elber's discovery of crack-closure in the wake of a fatigue crack [1,2], many attempts were made to analyze the crack-closure phenomena using finite element models [3,4], to quantitatively determine crack-opening stress experimentally for a variety of materials[5], or to develop analytical crack closure models using Dugdale-Barenblatt's ideally plastic model ahead of crack tip [6]. Most of these works were performed using simplified constant-amplitude loading which is not directly applicable to practical aircraft design problems that the engineers are facing every day. Newman [7] combined modified Dugdale-Barenblatt model into a simplified one-dimensional strip-yield model at the crack tip, which can be used to compute the crack-opening stress based on the plastic deformation on the crack surface as a result of the crack propagation under cyclic loading. The primary objective of this paper is to evaluate Newman's crack-closure model and its application program FASTRAN-II [8] using experimental results.

The evaluation was performed in three steps. The first step was to establish a technique that can be used to measure the crack-opening stress accurately. D. Gan and J. Weertman [9] had successfully employed strain gage and crack-opening-displacement (COD) gage techniques to measure the crack-closure stress of a thin and narrow 7050-T76 aluminum sheet from the plots of local strain against nominal stress during unloading. However, the accuracy of their method was highly dependent of whether the first deviation point from linearity to nonlinearity in the strain-stress plot can be clearly determined. In most cases, the deviation points were indistinguishable unless the strain gages were located just behind the crack tip. It also required a number of strain gages placed in the path of the crack in order to measure the closure stress while the crack was propagating. The present technique allows

more accurate measurement with fewer strain gages. The second step was to evaluate FASTRAN-II's crack-opening stress prediction under constant-amplitude loads with repeated overload. This would be used to assess FASTRAN-II for more complex spectrum loading. The third step was to compare FASTRAN-II's prediction using a realistic aircraft spectrum which consisted of a significant number of fully reversed cycles. It is commonly known that compression cycles can eliminate the overload retardation effects or cause acceleration in crack growth. However, many nonclosure-based crack growth models are incapable of giving reasonable predictions for such types of loading.

EXPERIMENTAL METHOD

Measurement of Crack-Opening Stress

Center-cracked tension (CCT) test specimens were used for the crack-opening stress measurement tests. The specimens were 3.25 inches wide by 14 inches long, made from a 1/4" thick 7050-T76 aluminum plate with the rolling direction parallel to the applied load. The subject material has a yield strength of 68.5 ksi and ultimate strength of 76.0 ksi. A 0.25" diameter hole was drilled at the center of the plate with EDM notches of 0.100" in length extended from both sides of the hole. The surfaces of the specimen, adjacent to the path of the crack, were polished and markers were inscribed at 0.100" intervals starting at 0.500" from the centerline such that the crack propagation can be accurately measured with a pair of 40-power travel microscopes located on both sides of the specimen. The tests were conducted in laboratory dry air at room temperature. Precracking was performed using constant-amplitude stress of 9.1 ksi maximum and a stress ratio of 0.05 until sharp crack tips were visible at both ends of notches. Following the precracking procedure, constant-amplitude cyclic loads consisted of blocks of 2500 cycles at maximum of 9.1 ksi and a stress ratio of 0.05 were applied. The test was paused at the end of each block to allow measurement of the crack length and application of overload. When the half crack length approaching 0.5", the specimens were removed from the test machine and strain gages were installed between 0.5" and 0.6" markers and also between 0.7" and 0.8" markers, just above the cracked plane. The strain gages were of the EA-13-125BZ-350 type and the grid area was approximately 0.062" wide by 0.062" long. The grid of the gage was normal to the crack surface. After the strain gage installations, the crack propagation test continued until the crack reached the desired length, at that point, one cycle of overload was applied gradually to the specimen and the readouts of the strain gages and the COD gage along with the applied loads were scanned and recorded continuously onto a computer diskette at a rate of 1000 samples per second. This stress survey procedure was conducted at several crack lengths and also before and after the overload. Figure 1 depicts the test specimen and test setup.

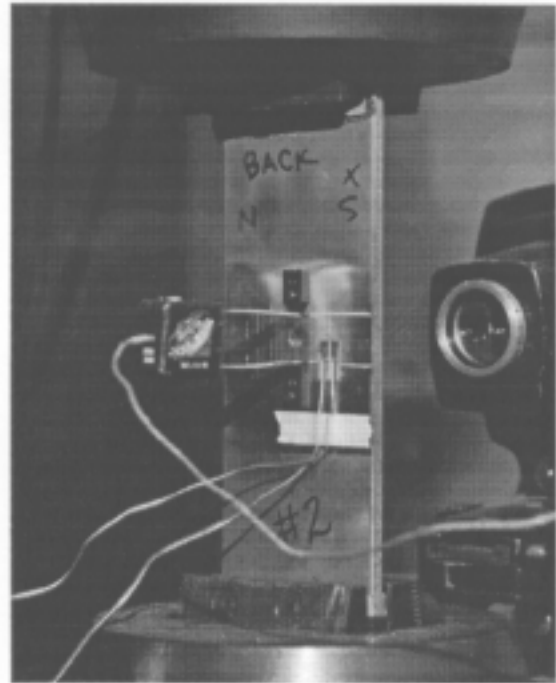
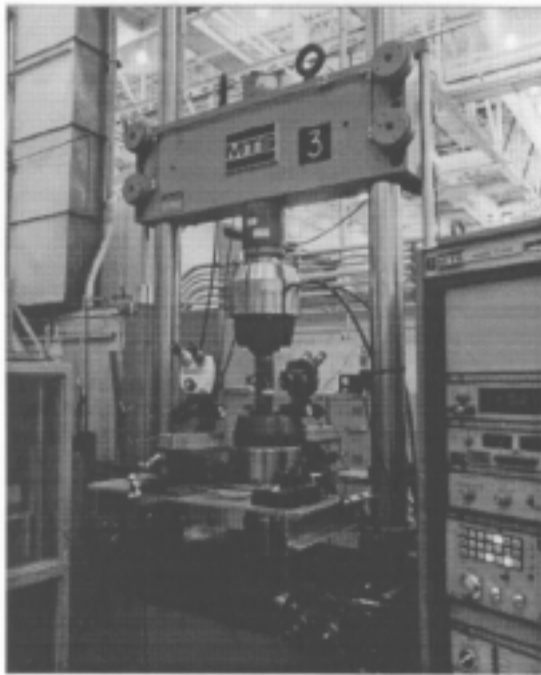


Figure 1. Test Setup and Test Specimen for Crack-Opening Stress Measurement.

Crack Growth Under Simulated Flight Loads

The specimen used in the crack propagation tests were 12" wide by 24" long CCT specimen machined from a 0.25" thick 7050-T74 aluminum plate with the rolling direction parallel to the applied load. A notch of 0.01" to 0.02" wide and 0.5" in total length was introduced at the center of the specimen via EDM. An antibuckling guide was used to prevent lateral deformation under compression, as shown in Figure 2. The specimen was precracked at maximum stress of 15 ksi until the crack tips were visible from both sides of the notch. Then, the pore-cracking procedure continued with reducing loads to avoid retardation effects from the large plastic zone ahead of the crack tip. Following the precracking procedure, a simulated flight spectrum was applied. The flight spectrum consisted of variable-amplitude cycles representing the stress sequence in an aircraft a structure that experiences a significant number of fully reversed loads. The crack propagation was measured periodically until failure of the specimen occurred.

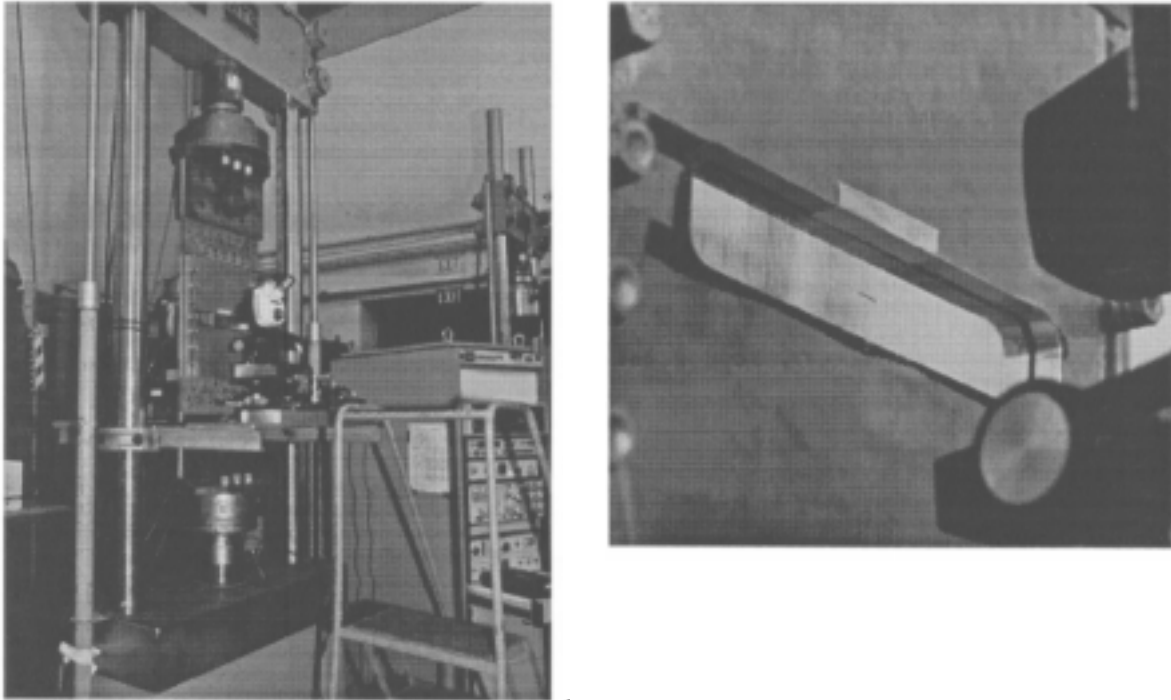


Figure 2. Test Setup and Test Specimen for Crack Growth Test.

EXPERIMENTAL RESULTS AND ANALYSIS

Measurement of Crack-Opening Stress

Crack-Opening Stress Under Constant Amplitude Loads

The test specimen was subject to a constant-amplitude cyclic load of maximum stress of 9.1 ksi and a stress ratio of 0.05. Three strain surveys were taken: 1) when the crack tip was approaching Gage A, 2) when the crack tip reached the center of Gage A, and 3) when the crack tip just passed Gage A. Similarly, three more surveys were taken when the crack tip propagated to Gage B. The strain-stress curves of the surveys are shown in Figures 3a and 4a. The deviation point from linearity to nonlinearity were not distinguishable in all cases, except when the crack tip was just ahead of the gage. However, from the plots of the $D_{\text{strain}}/D_{\text{stress}}$ (slope of the strain-stress curve) vs. nominal stress, Figures 3b and 4b, the deviation point of linearity became more pronounced. The deviation point is defined as the transition point at which $D_{\text{strain}}/D_{\text{stress}}$ becomes constant. The running averages of $D_{\text{strain}}/D_{\text{stress}}$ were used in the plots, instead of $D_{\text{strain}}/D_{\text{stress}}$ at a data point, to avoid the oscillation caused by the run-off errors in the recorded data. The results showed that this technique can be used to determine the crack opening and closure stress as long as the strain gage is near the crack tip. The effective stress ratios from the test results were compared with FASTRAN-II's

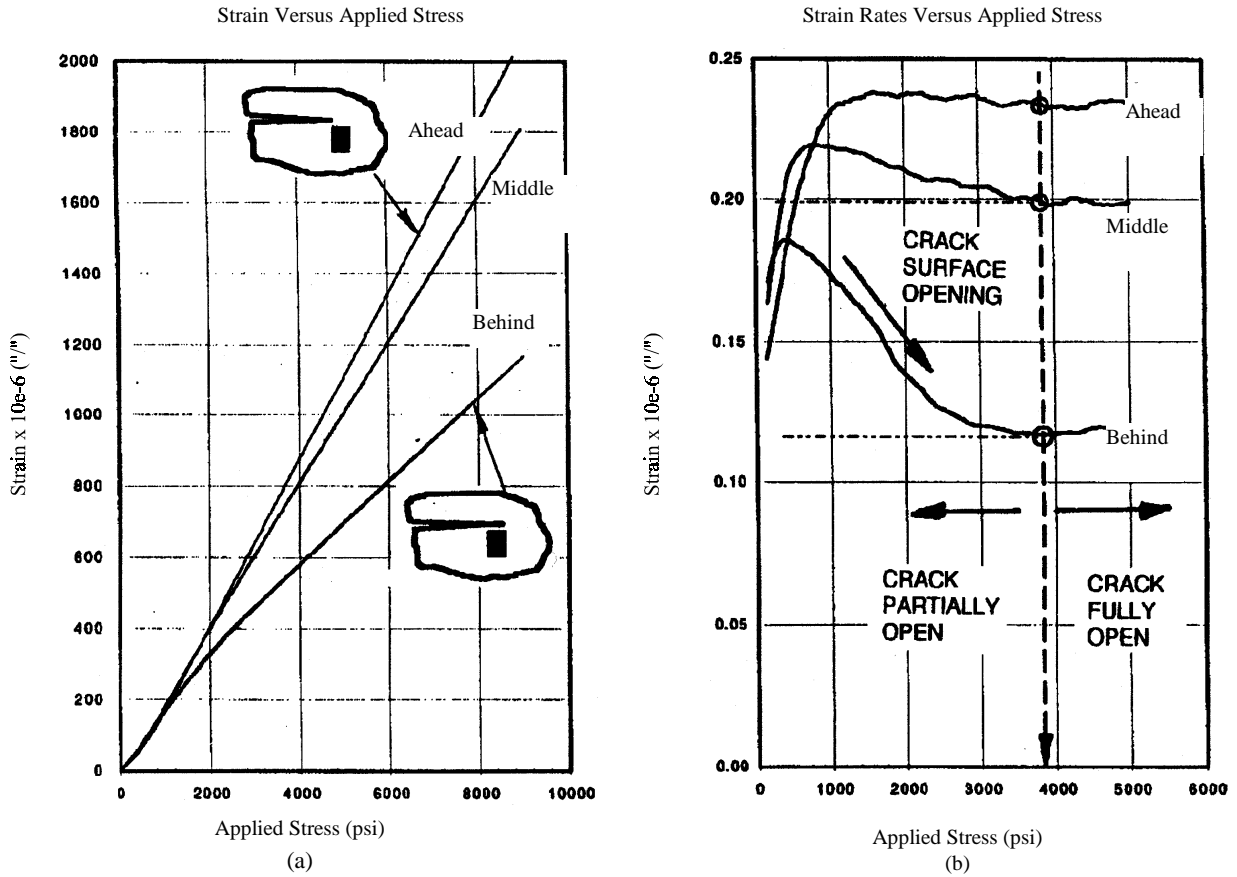


Figure 3. (a) Local Strain Versus Nominal Stress, (b) $\Delta_{\text{strain}}/\Delta_{\text{stress}}$ Versus Nominal Stress at Gage A.

prediction in Figure 5. A good correlation with FASTRAN-II for $a=1.6$ was shown there, which was consistent with the plane-stress condition measured by the gage. From Figures 3 and 4, the crack length or the plastic zone size did not have any effects on the present techniques. The plots of COD vs. applied stress did not show any sign of transition from nonlinearity to linearity. It is believed that the COD gage was too far away, more than 0.50" from the crack tip, to detect any crack closure effects.

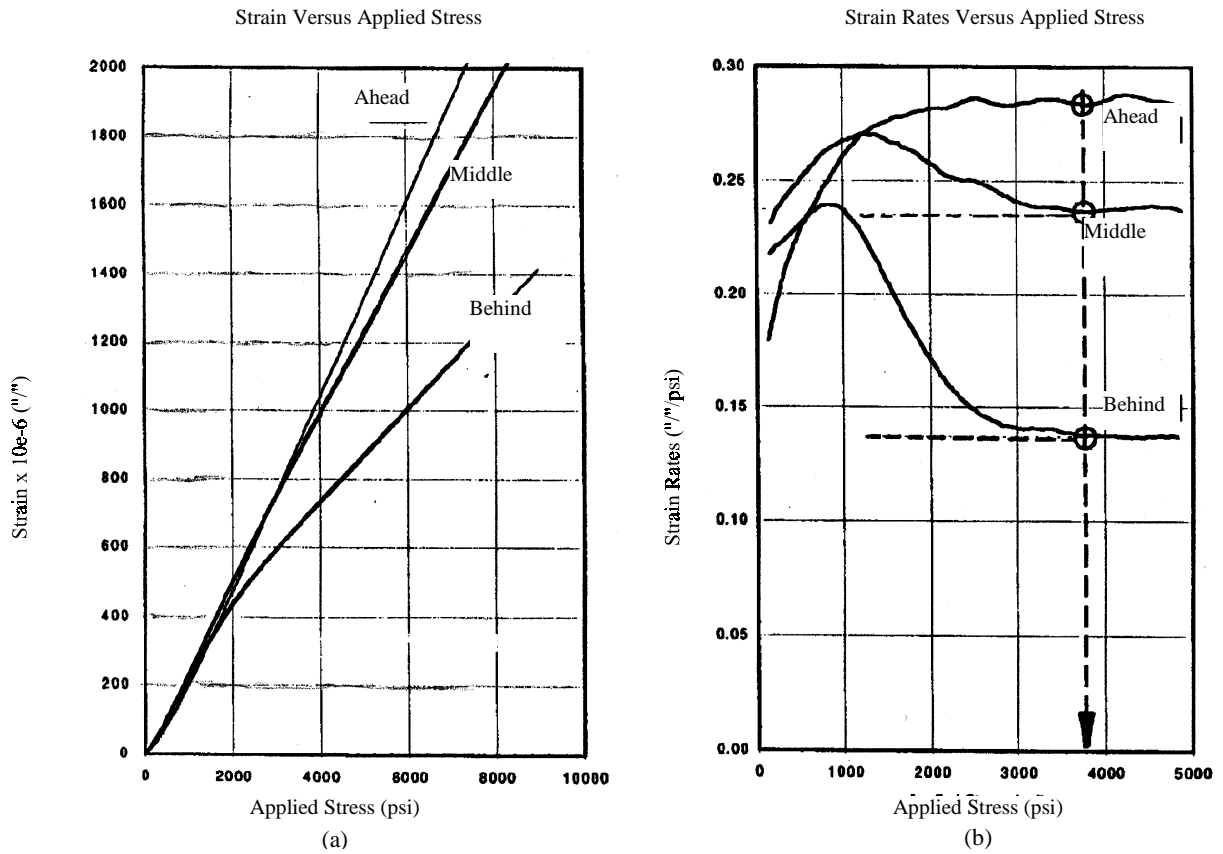


Figure 4. (a) Local Strain Versus Nominal Stress, (b) $\Delta_{\text{strain}}/\Delta_{\text{stress}}$ Versus Nominal Stress at Gage B.

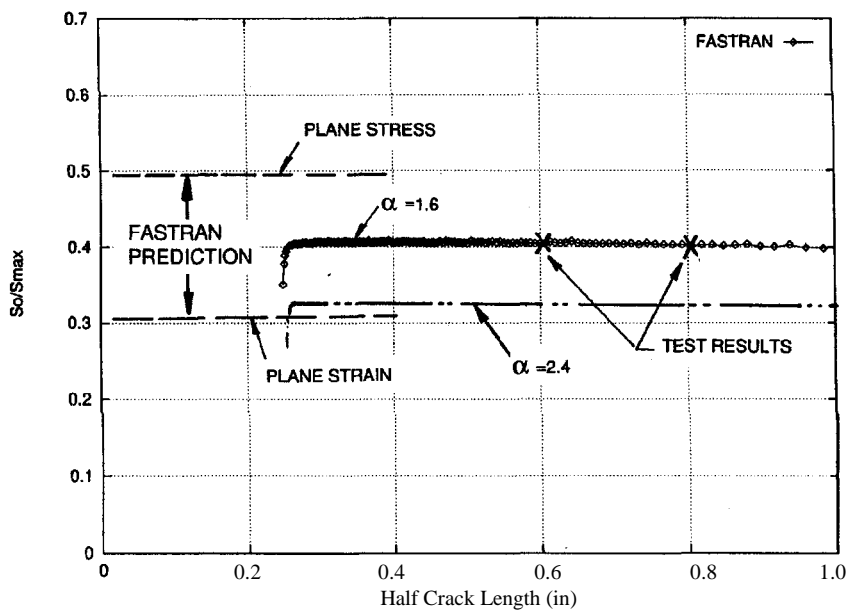


Figure 5. Comparison of Crack-Opening Stress, Experimental Results Versus FASTRAN-II Using $\alpha=2.4$.

The Effects of Overload

One cycle of 150% overload was applied periodically at every 2500 constant-amplitude cycles. The constant-amplitude loading has a maximum stress of 9.1 ksi and a stress ratio of 0.05. The percentage of overload is defined as s_{ol}/s_{ca} . Strain surveys were taken when the crack propagated near the strain gages. Strain surveys were performed before and after application of overload and subsequently at 500 cycle and 1000 cycles after the overload. The experimental results show that the overload caused an immediate drop in s_{op} , see Figure 6, which implied that DK_{eff} would increase and so would the crack growth rate following the overload. The decrease of the closure stress was also confirmed by the results of a nonlinear Finite Element analysis, which had shown that the crack surface could remain partially or completely open as a result of an overload. However, Gan and Weertman [9] could not detect any s_{op} due to crack tip blunting. The FASTRAN-II predictions were consistent with the experimental results for the trend of s_{op} for post overload crack propagation. They both showed that the s_{op} recovered rapidly to a level that was higher than the normal s_{op} and then decreased to normal level, as illustrated in Figure 7. The normal s_{op} is referred to here as the s_{op} under constant-amplitude loading only. The increase of s_{op} and the decrease of DK_{eff} caused an apparent slowdown in crack growth, which was consistent with the well known retardation effects after an overload. The experimental results were compared in Figure 8 with the FASTRAN-II's prediction based on $a=1.6$.

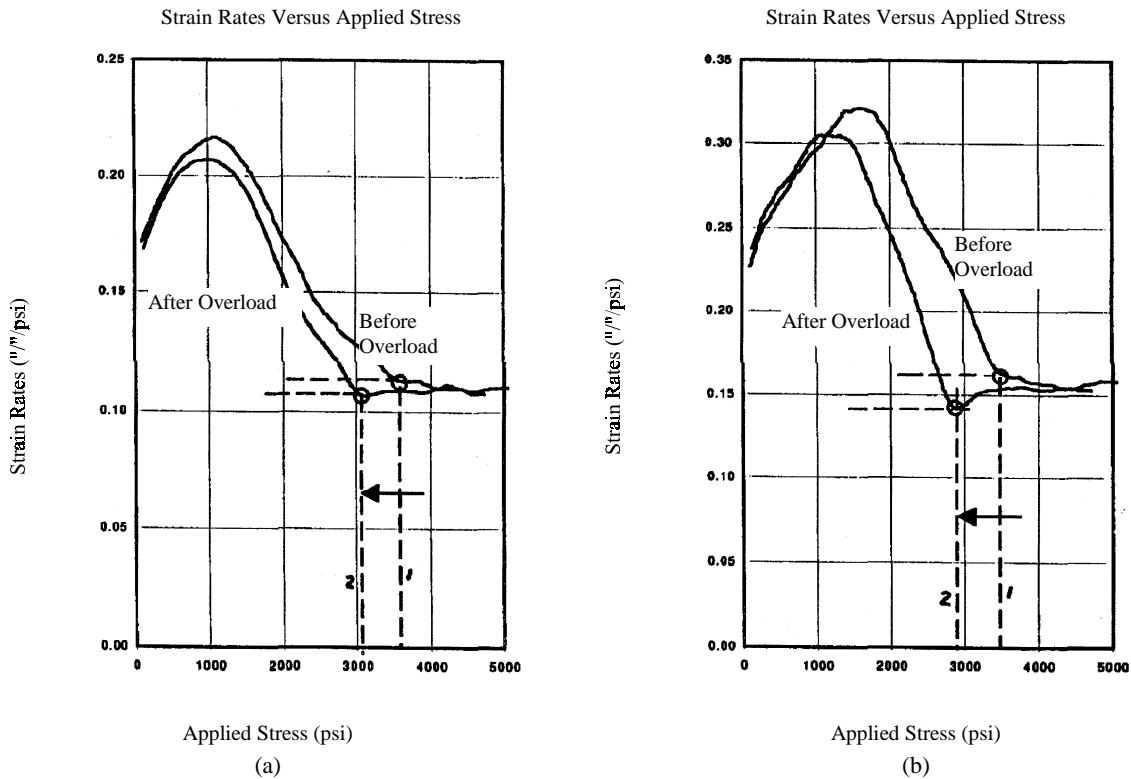


Figure 6. Comparison of Crack-Opening Stress Before and After Overload, (a) at Gage A, (b) at Gage B.

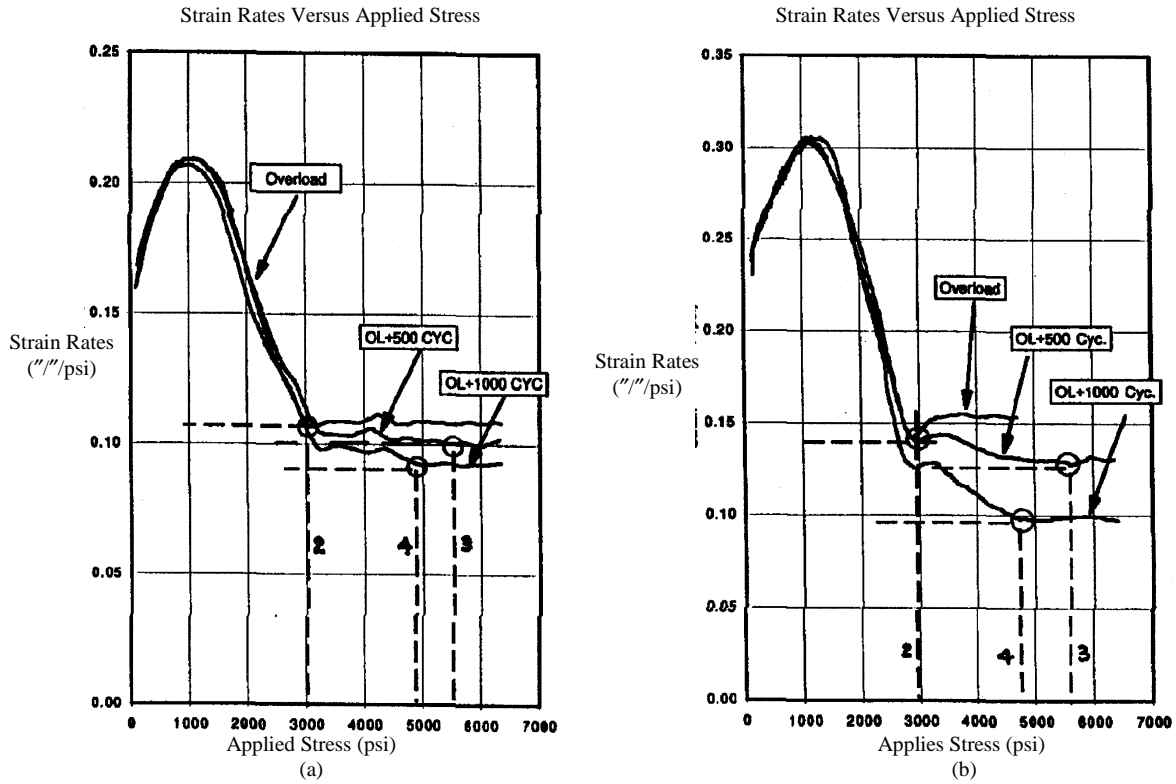


Figure 7. Comparison of Crack-Opening Stress After Overload, (a) at Gage A, and (b) at Gage B.

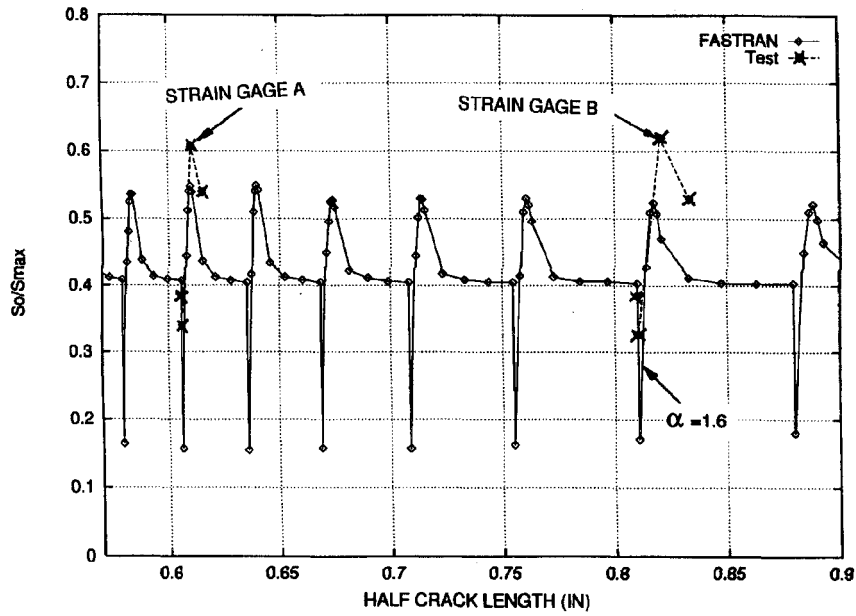


Figure 8. Comparison of Crack-Opening Stress, Experimental Results Versus FASTRAN-II.

Crack Growth Under Simulated Flight Loads

The experimental results of crack propagation under spectrum loading were plotted against the number of flights in Figure 9. The predictions made by FASTRAN-II with various constraint factors were also shown for comparison purposes. The raw fatigue crack growth rate (FCGR) data for 7050-T76 plates are shown in Figure 10a. These FCGR were converted from DK to DK_{eff} using computer program DKEFF [8] for a thickness constraint factor a ranging from 1.0 to 3.0; $a=1.0$ and $a=3.0$ corresponds to plane stress and plane strain conditions, respectively. The FCGR converged reasonably well into a narrow band between 1.2 to 2.4 as shown in Figure 10b. Average FCGR values were used in crack growth predictions.

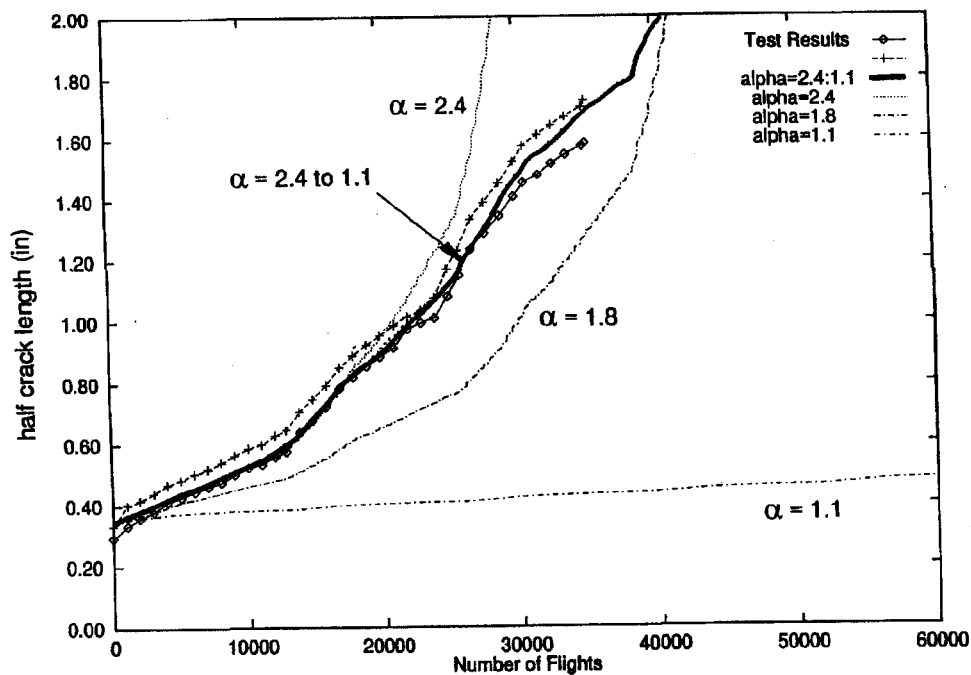


Figure 9. Crack Growth Comparison, Experimental Results Versus FASTRAN Using Fixed and Variable Thickness Constraint Factors.

FASTRAN-II was unable to match test results using constant a . However, they compared very well when a variable a was used. Using trial-and-error, the following variable a had the best correlation with the experimental results: for da/dn less than $5.0 \times 10^{-5} \text{ in}/\text{cyc}$, $a=2.4$, $DK_{\text{eff}}=9.1 \text{ ksi} \cdot \text{in}^{1/2}$; for da/dn greater than $4.0 \times 10^{-3} \text{ in}/\text{cyc}$, $a=1.10$ and $DK_{\text{eff}}=28.0 \text{ ksi} \cdot \text{in}^{1/2}$. The a and DK_{eff} were log-linearly interpreted for the FCGR between these two points, as indicated in Figure 11.

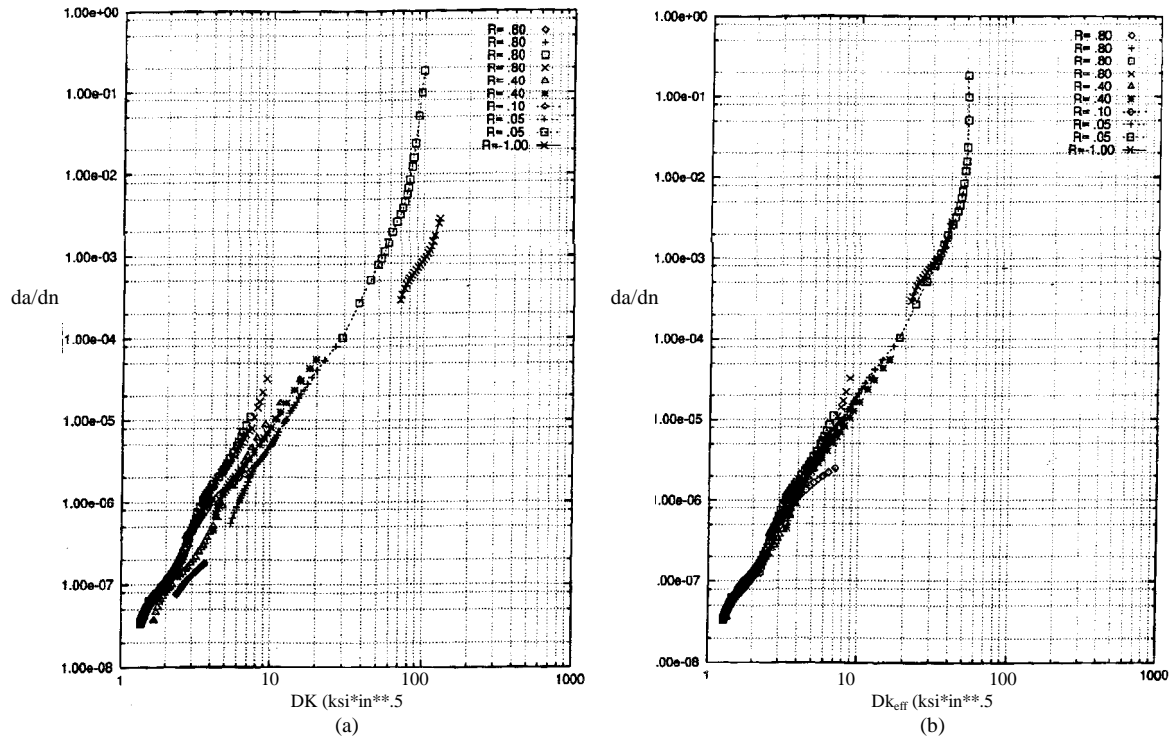


Figure 10. Fatigue Crack Growth Rate of 7050-T76 Plate, (a) FCGR Versus DK, (b) FCGR Versus ΔK_{eff} for $\alpha=1.7$.

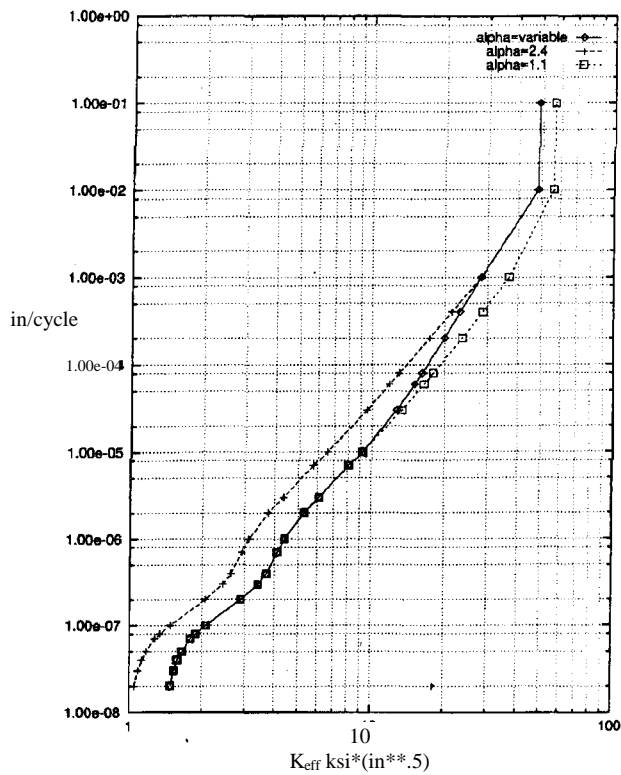


Figure 11. FCGR Versus ΔK_{eff} of 7050-T76 for Variable $\alpha=2.4$ to $\alpha=1.1$.

The need of using a variable a for spectrum loading is consistent with the analysis results obtained by Newman [10] and other researchers regarding the constraint variation associated with the flat-to-slant crack growth behavior or shear-lip development. Newman predicted the loss of constraint when a crack grows from a small size, a plane-strain prevailing condition to a size where the plastic-zone size becomes large compared to the plate thickness, plane-stress prevailing condition. Schijve[11] discovered that such a transition occurred at nearly the same FCGR over a wide range in stress ratios for aluminum alloys. From this phenomena, he proposed that such a transition should be controlled by DK_{eff} , since FCGR is a function of DK_{eff} . Based on this theory and experimental results, Newman derived an equation to determine the DK_{eff} at the transition point as follows:

$$(DK_{eff})_T = m s_o B^{1/2}$$

where s_o is the flow stress of the material, m is the transition coefficient determined from the test, and B is the plate thickness. Substitute the values of $s_o=72.25 \text{ ksi}\cdot\text{in}^{1/2}$, $m=0.50$ and $B=0.25''$ into the equation, we obtained $(DK_{eff})_T=18.06\text{ksi}\cdot\text{in}^{1/2}$ which coincided with the average value of the transition zone used in the FCGR, average $(DK_{eff})_T=(9.1+28.0)/2=18.5 \text{ ksi}\cdot\text{in}^{1/2}$. However, after close examination of the cracked surface of the test specimen, Figure 12, it only revealed a small amount of shear-lip near the edge of the crack surface. This experiment demonstrated the feasibility of using variable a and the capability of FASTRAN-II to predict crack growth for a wide specimen under a complex spectrum loading.

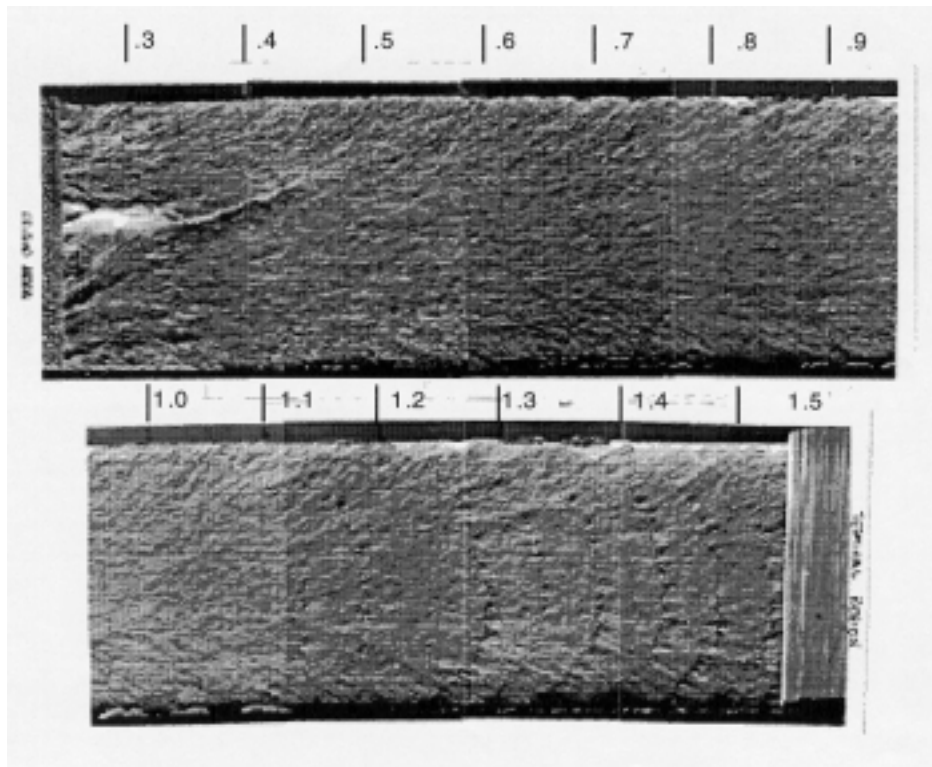


Figure 12. Crack Surface Under Spectrum Loading.

CONCLUSIONS

Based on the experimental results, the following conclusions are drawn:

1. The crack-opening and closure stress can be effectively measured from the $D_{\text{strain}}/D_{\text{stress}}$ vs. stress plots of strain gages near the crack tip.
2. The test has verified the trend of the crack-opening stress following an overload.
3. The overload can temporarily reduce the crack-opening stress, then causes the crack-opening stress to raise above the normal s_{op} leading to a crack growth retardation.
4. The thickness constraint factors used in the FASTRAN-II crack closure model requires an extensive test program to establish reliable values for practical applications.
5. A crack closure model to account for transition of plane strain to plane stress is a must for variable-amplitude spectrum loading. Using variable thickness constraint factors have proven to be a useful method.
6. The FASTRAN-II model is capable of predicting the crack growth under variable-amplitude spectrum loading containing a significant number of fully reversed loads with a reasonable degree of accuracy.

ACKNOWLEDGMENT

The authors would like to acknowledge Mr. Charles Thrash and his staff at the McDonnell Aircraft Company Material and Process Technology Laboratory for supporting and conducting tests for this project.

REFERENCES

1. Elber, W., "Fatigue Crack Closure Under Cyclic Tension," Engineering Fracture Mechanics, Vol. 2, No. 1, July 1970, pp. 37-45.
2. Elber, W., "The Significance of Fatigue Crack Closure," Damage Tolerance in Aircraft Structures, ASTM STP 486, 1971, pp. 230-242.

3. Newman, J. C. Jr., "A Finite Element Analysis of Fatigue Crack Closure," *Mechanics of Crack Growth*, ASTM STP 590, pp. 281-301.
4. Ogura and K. Ohji, "FEM Analysis of Crack Closure and Delay Effect in Fatigue Crack Growth Under Variable Amplitude Loading," *Engineering Fracture Mechanics*, Vol. 9, pp. 471-480, 1977 .
5. Katcher, M. and Kaplan, M., "Effects of R Factor and Crack Closure on Fatigue Crack Growth for Aluminum and Titanium Alloys," ASTM STP 559, pp. 264-282, 1974.
6. Budiansky, B. and Hutchinson, J. W., "Analysis of Closure in Fatigue Crack Growth," *Journal of Applied Mechanics*, ASME, 45, pp. 267-276, 1978.
7. Newman, J. C. Jr., *A Crack-Closure Model for Predicting Fatigue Crack Growth Under Aircraft Spectrum Loading*, 748, ASTM, 1981.
8. Newman, J. C. Jr., "FASTRAN-II, A Fatigue Growth Structural Analysis Program," NASA Technical Memorandum No. 104159, 1992.
9. Gan and J. Weertman, "Crack Closure and Crack Propagation Rates in 750 Aluminum," *Engineering Fracture Mechanics*, Vol. 15, No 1-2, pp. 87-106, 1981.
10. Newman, J. C. Jr., "Effects of Constraints on Crack Growth Under Aircraft Spectrum Loading," *The Specialist's Conference at Delft University of Technology*, 1992.
11. Schijve, J., "Shear Lips On Fatigue Fracture in Aluminum Alloy Sheet Material," *Delft University of Technology*, Report LR-287, Sept. 1979.

FAILURE ANALYSIS OF AIRCRAFT ENGINE CONTAINMENT STRUCTURES¹

S. Sarkar and S. N. Atluri
Computational Mechanics Center
Georgia Institute of Technology
Atlanta, GA

SUMMARY

The Johnson/Cook constitutive model is incorporated in failure analysis of a semicircular containment structure when subjected to impact by titanium projectiles. The failure criterion is based on the adiabatic shear localization model where material fails when the thermal softening caused by local plastic heating exceeds the combined effects of strain and strain rate hardening. Steel and aluminum are considered as the materials for containment structure and the results are compared with tests conducted in a gas gun testing facility.

INTRODUCTION

In the event of an aircraft engine rotor failure, high energy rotor fragments are often released that can lead to catastrophic failure of the aircraft. Such failures occur for a variety of reasons, the primary one being fatigue due to normal engine operation in a high temperature environment for a long period of time. They may also occur due to blade overheating, bird strikes, blade detachment, and material defects. The rotor fragments can generally be characterized in terms of their size, shape, mass, speed, and energy level. Rotor failure can lead to release of both high-energy disk fragments and relatively low-energy blade fragments. The central disk part of the rotor is much heavier than the blades attached to them along the periphery, and hence rotor fragments containing a portion of the disk can in general cause far more harm than the relatively lighter blade fragments. Currently, the FAA requires that all engines must be able to contain one blade from each of the fan, compressor, and turbine stages. The heavier disk fragments cannot be contained using current technology without incurring a high penalty in terms of weight and performance.

Rotor failure is a complex dynamic process that involves multiple interactions among different rotor parts, and once initiated, the process evolves along a cascade of events whose final outcome depends upon a host of factors. A number of investigators in the past have studied the rotor failure phenomena. Mangano (ref. 1) did a number of rotor burst

¹ The numerical analysis at the Georgia Institute of Technology is supported by the FAA Center of Excellence in Computational Modeling of Aircraft Structures.

experiments in a spin chamber to develop criteria and data for the design of optimum lightweight containment devices. Hagg and Sankey (ref. 2) identified two stages of rotor failure; stage 1 was failure due to compression and shearing of the material over the perimeter of the impact area, and stage 2 was due to tensile strain exceeding the failure limit over the extended volume of the material. Wu and Witmer (ref. 3) developed a spatial finite element method to study the response of containment rings that can undergo large elastic-plastic deformation. Mathis et al. (ref. 4) studied the response of flat and circular rings when subjected to impact by rigid projectiles. Stotler and Coppa (ref. 5) studied different configurations and lightweight materials to determine the optimum combination that had the best energy absorbing capability per unit weight. Sarkar and Atluri (ref. 6) performed a finite element-based analysis to study the impact of various types of rotor fragments on aircraft engine containment structures.

The success of computational and analytical methods in determining transient response and failure of materials depends on a properly validated material failure criterion. In reference 6, the failure criterion is based on large accumulated plastic strains and a cutoff failure limit has to be prescribed. Additionally, the plasticity model is based on isotropic strain hardening and does not take into account high strain rate and thermal softening effects that are characteristics of high-speed impact. In this study, the Johnson/Cook model (ref. 7) is used to incorporate the effects of strain rate hardening and thermal softening, and a new failure criterion is defined where the material is assumed to have failed when the thermal softening of the material exceeds the strain hardening effects.

ADIABATIC SHEAR LOCALIZATION

Narrow bands of intense shear strain are sometimes observed on cross sections of materials which have been subjected to sharp, impulsive loads. These zones of intense shear strain are called shear bands which form due to rapid local heating resulting from rapid plastic deformation. When plastic deformation occurs in a material, a large proportion of the work is converted into heat. If the plastic deformation occurs slowly, then the heat developed diffuses away into the surroundings; however, if the plastic deformation is very quick, then there is no time for the heat to diffuse away and as a result there is a sharp local increase in the temperature of the material. The increase in temperature causes a local thermal softening effect. If the strength loss due to increase in temperature becomes greater than the increase in strength due to strain and strain rate hardening, the plastic deformation becomes unstable and homogeneous plastic deformation gives way to a localized band like plastic deformation, which is known as the adiabatic shear bands.

In this work, adiabatic shear localization effects is modeled by the Johnson/Cook expression for yield stress which is given as

$$\sigma_y = \left[A + B(\epsilon^p)^n \right] \left[1 + C \ln(\dot{\epsilon}^p) \right] \left[1 + T^{*m} \right]$$

where T^* is defined as

$$T^* = \left(\frac{T - T_r}{T_m - T_r} \right)$$

A is the yield stress in quasi-static simple tension or compression test, B is the plastic modulus, n is the strain hardening exponent, C is the strain rate dependent coefficient, m is the temperature dependent exponent, ϵ^p is the effective plastic strain, and T_m and T_r are the melting and room temperatures, respectively. The first and second term in the product incorporate the strain hardening and strain rate hardening effects while the third term accounts for the thermal softening effect. The temperature rise is determined from the plastic work done and assuming no heat loss, can be written as

$$C_v \rho \Delta T = \sigma_{ij} \Delta \epsilon_{ij}^p$$

where C_v is the specific heat, ρ is the density, and ΔT denotes the increase in temperature.

Failure Criterion

The failure criterion is based on the adiabatic shear localization model and is defined when the thermal softening of the material overcomes the strain hardening. The product $[A + B(\epsilon^p)^n][1 - T^{*m}]$ is evaluated at each time step after plastic deformation has occurred and if the product decreases from the value evaluated at the previous time step, failure is assumed to have occurred. The failure criterion is applied at every integration point across the thickness of the shell elements and if the failure criterion is satisfied at any location, the whole element is deleted from the analysis.

GAS GUN TESTS ON SEMICIRCULAR CONTAINMENT STRUCTURES

The adiabatic shear failure criterion is validated with test data available from gas gun testing facilities. In the tests, projectiles are hurled against semicircular containment structures that are made of different materials such as aluminum, steel, and composites and utilized various geometrical configurations. The projectiles are accelerated inside a long tube and since spin could not be imparted in the gas gun testing, rotational kinetic energy is compensated by imparting additional translational energy to the projectiles. The projectiles

can also be prescribed an initial attitude angle to account for different angles of impact against the containment structure. The lateral edges of the semicircular test structure are supported by radial spokes which are secured at the other end to a heavy steel ring which is rigidly fastened. The most optimum configuration of the containment structure is obtained by carrying out a large number of tests in the gas gun testing facility. All such results are compared with the conventional containment system made of steel. The test results on steel are simulated by the finite element analysis to test the validity of the failure criterion.

Finite Element Model

The semicircular containment structure is modeled by bilinear quadrilateral shell elements. The radius of the structure is 10.9 inches and its length along the axial direction is 5.9 inches and the finite element model has 90 divisions along the circumferential direction and 12 along the axial direction. The thickness of the containment structure is 0.072 inch. The test projectile is constructed of titanium whose weight is 0.1281 lb. and is 2.0 x 5.0 inches in plan form and is tapered in thickness from 0.05 inch on the long edges to 0.1 inch in the center. Brick elements are used to model the projectile in the finite element analysis and the projectile is assumed to be rigid in the analysis. The spokes that support the lateral edges of the containment structure are modeled by beam elements. Twenty beam elements are used for each radial spoke. At the ends where the beam elements join the lateral edges of the containment structure, the six degrees of freedom of the beam nodes are merged with the six degrees of freedom of the shell nodes. The other end of the beam elements join the inner ring and are completely restrained.

RESULTS AND DISCUSSION

In the gas gun facility, two tests are performed on steel containment structures with titanium projectiles released at 850 and 912 fps. For both tests, the projectile produced a distinctive crease on the steel surface at the point of impact, and the containment structure deformed substantially. The projectile reoriented itself to a flat attitude with respect to the surface of the containment structure after impact and remained in the flat orientation in its subsequent motion. It exited with a high velocity in the reverse direction at the opposite end of the structure. In the finite element analysis, the simulations are performed for the two tests on steel containment structures. Additionally, analysis is also carried out on aluminum materials to compare its effectiveness with respect to structures made of steel.

The material properties and the coefficients appearing in the adiabatic shear localization model are shown in Table 1. The projectile is assumed to lie initially at a vertical distance of 9.265 inches from the center of the semicircular structure. Additionally, an attitude angle of 13.3 degrees is prescribed to it in the clockwise direction from the horizontal axis. The finite element simulation results for the steel structure is shown in Figure 1 when

the projectile speed is equal to 912 fps. Just as in the test results, the projectile oriented itself in a flat attitude with respect to the surface of the structure and exited from the opposite end. The crease and the local bulging in the containment structure where the projectile made initial contact can be observed. For the two tests performed in the gas gun facility at projectile speeds of 850 and 912 fps, the containment structure deformed significantly but did not fail, and the projectile was redirected in the opposite direction. The same outcome is predicted by the finite element analysis. The failure criterion used in the formulation is not met for the projectile speeds considered, and the material did not fail.

For the same projectile speeds, the analysis is repeated for containment structures made of aluminum. No test data is available for aluminum, and the overall results are the same as observed for steel containment structures. The projectile is redirected and the structure did not fail; however, it suffered far more deformation as compared to steel. The response of aluminum and steel containment structures due to impact by the titanium projectile at 912 fps is shown in Figure 2, and it can be observed that the aluminum structure undergoes considerably more deformation.

The gas gun test data is available for projectile speeds of 850 and 912 fps only. In the finite element analysis, the speeds are gradually increased to determine the onset and nature of material failure. The variation of the effective plastic strain for an element at the point of initial impact is plotted with respect to time for varying projectile speeds in Figure 3. The magnitude of the effective plastic strain increases with the increase in projectile speed. For the aluminum structure, the same trend is observed though the increase is relatively more as compared with the steel containment structure. The effective plastic strain history is compared in Figure 5 for steel and aluminum structures with a projectile speed of 912 fps. The rise in temperature due to plastic heating is shown in Figure 6. When the speed is increased to 2000 fps, adiabatic shear failure criterion is satisfied for two elements for the steel containment structure, and a small perforation is formed near the point of impact. At 2500 fps, a number of elements fail, and a small hole is observed though the projectile is still redirected in the opposite direction. For the aluminum containment structure, perforation is first observed when the projectile speed is 1200 fps. At 1500 fps, a big hole is formed, and the projectile is redirected. When the projectile speed is increased to 2000 fps, many elements fail near the vicinity of impact and instead of redirection, as observed at lower speeds, the projectile penetrates through the aluminum containment structure, as shown in Figure 7. The impact results are tabulated in Table 2 for different projectile speeds.

CONCLUSIONS

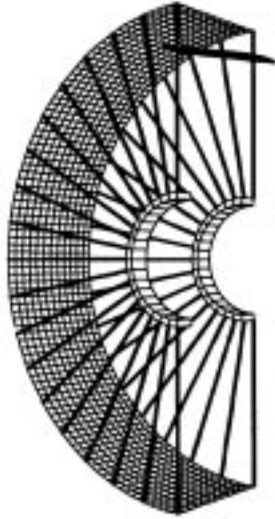
A failure analysis is performed on semicircular containment structures when subjected to impact by projectiles made of titanium. The Johnson/Cook constitutive model is used as the constitutive model, and the effects of strain rate hardening and thermal softening are included. Failure criterion is based on adiabatic shear localization model and failure is defined when the thermal softening of the material exceeds the strain hardening effects. Steel and

aluminum are the materials used for the containment structures. The analysis results are compared with the tests conducted on steel containment structures in the gas gun testing facilities. The steel containment structure did not fail for the projectile speeds used in the tests and the analysis results also show that the failure criterion is not met and the overall deformation of the structure and the motion of projectile are in good agreement with the test results. For higher projectile speeds than those used in the gas gun test facility, the failure criterion is satisfied and holes are formed near the vicinity of the impact; though, such results could not be validated with experimental data. In the future, the failure criterion needs to be validated with test results where actual perforation or penetration of the containment structure takes place. Some data are available from tests conducted in spin chamber test facilities to determine the critical failure speeds.

REFERENCES

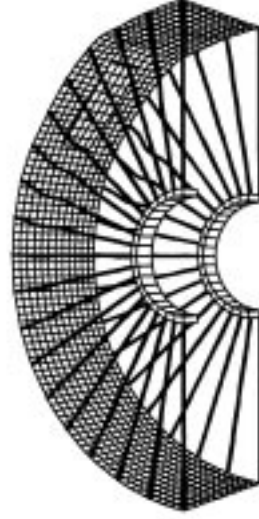
1. Mangano, G. J., "Studies of Engine Rotor Fragment Impact on Protective Structures," AGARD Conference Proceedings, No. 186, Specialists Meeting on Impact Damage Tolerance of Structures, 41st Meeting of the Structures and Materials Panel, Ankara, Turkey, September 28-October 3, 1975, pp. 10.1-10.23.
2. Hagg, A. C. and Sankey, G. O., "The Containment of Disc Burst Fragments by Cylindrical Shells," *Journal of Engineering and Power*, Transactions of the ASME, Vol. 96, 1974, pp. 114-123.
3. Wu, R. W. H. and Witmer, E. A., "Approximate Analysis of Containment/Deflection Ring Response to Engine Rotor Fragment Impact," *Journal of Aircraft*, Vol. 10, 1973, pp. 28-37.
4. Mathis, J. A., Parduhn, S. C., and Alvarez, P., "Analysis of Turbine Engine Rotor Containment and Shielding Structures," AIAA-93-1817 AIAA/SAE/ASME/ASEE 29th Joint Propulsion Conference and Exhibit, Monterey, CA, June 28-30, 1993.
5. Stotler, C. L. and Coppa, A. P., "Containment of Composite Fan Blades Final Report," NASA CR-159544, 1979, NASA Lewis Research Center.
6. Sarkar, S. and Atluri, S. N., "Finite Element Analysis of Rotor Fragment Impact on Containment Structures," *Computer Modeling and Simulation in Engineering*, Vol. 1, No. 3, 1996, pp. 391-427.
7. Johnson, G. R. and W. H. Cook, "A Constitutive Model and Data for Metals Subjected to Large Strains, High Strain Rates, and High Temperatures," Presented at the Seventh International Symposium on Ballistics, Hague, Netherlands, April 1983.

Projectile hitting a curved pa
time = 0.00000E+00



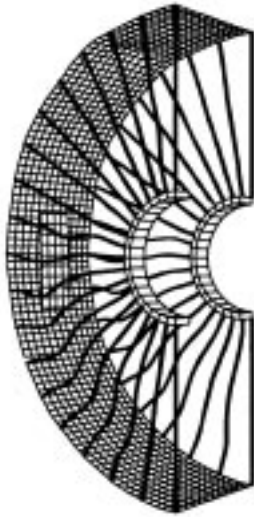
Disp. Scale factor 0.100E+01 (default)

Projectile hitting a curved pa
time = 0.79961E-03



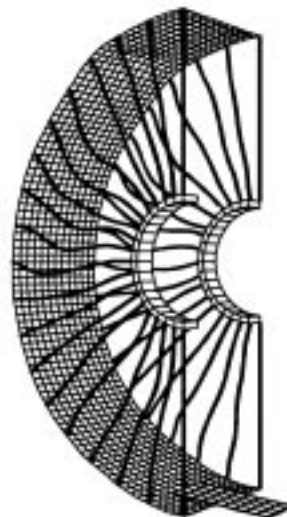
Disp. Scale factor 0.100E+01 (default)

Projectile hitting a curved pa
time = 0.17988E-02



Disp. Scale factor 0.100E+01 (default)

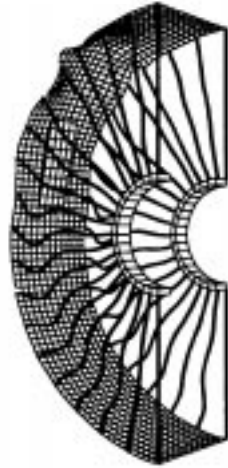
Projectile hitting a curved pa
time = 0.39992E-02



Disp. Scale factor 0.100E+01 (default)

Figure 1. Rigid Projectile Hitting a Semicircular Containment Structure (Weight = 0.1281 lb., Speed = 912 fps, Kinetic Energy = 19854 lb.-in, Thickness = 0.071 in.).

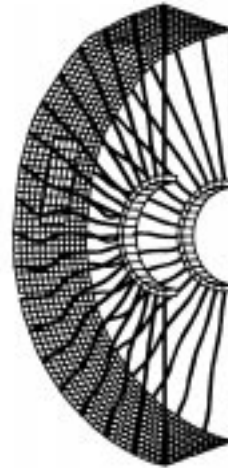
Projectile hitting a curved pa
time = 0.13999E-02



Disp. Scale factor 0.100E+01 (default)

(a)

Projectile hitting a curved pa
time = 0.13999E-02



Disp. Scl factor 0.100E+01 (default)

(b)

Figure 2. Impact Against Aluminum (a) and Steel (b) Containment Structures (Projectile Speed = 912 fps).

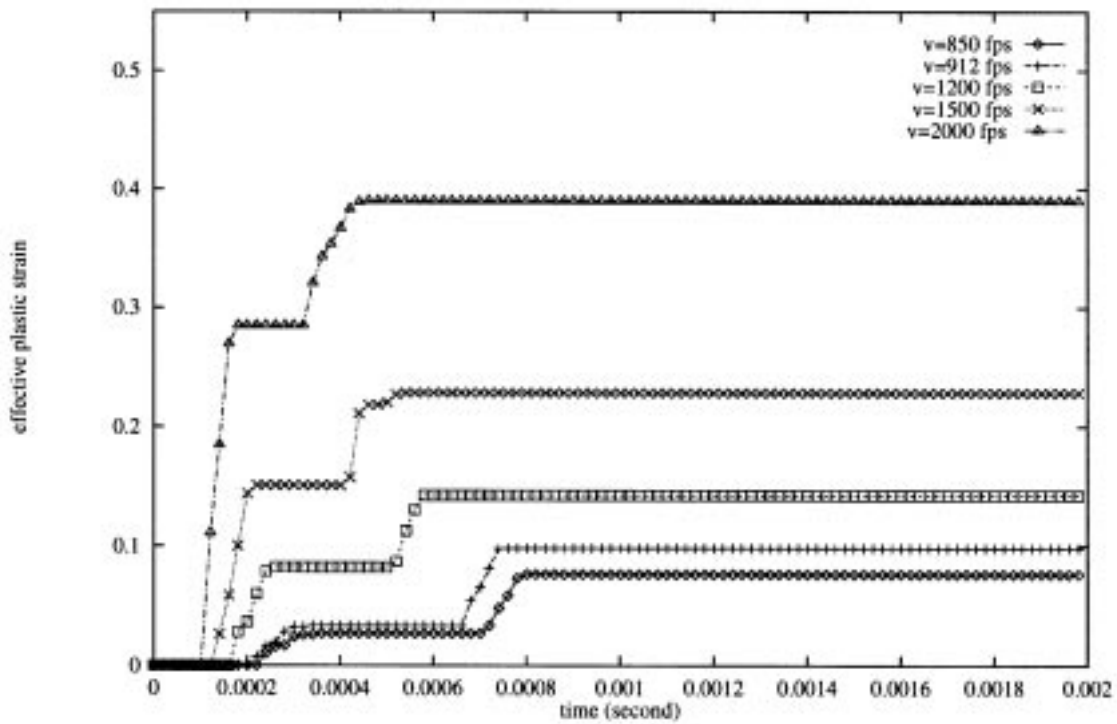


Figure 3. Effective Plastic Strain History for Different Projectile Speeds (Steel Containment Structure).

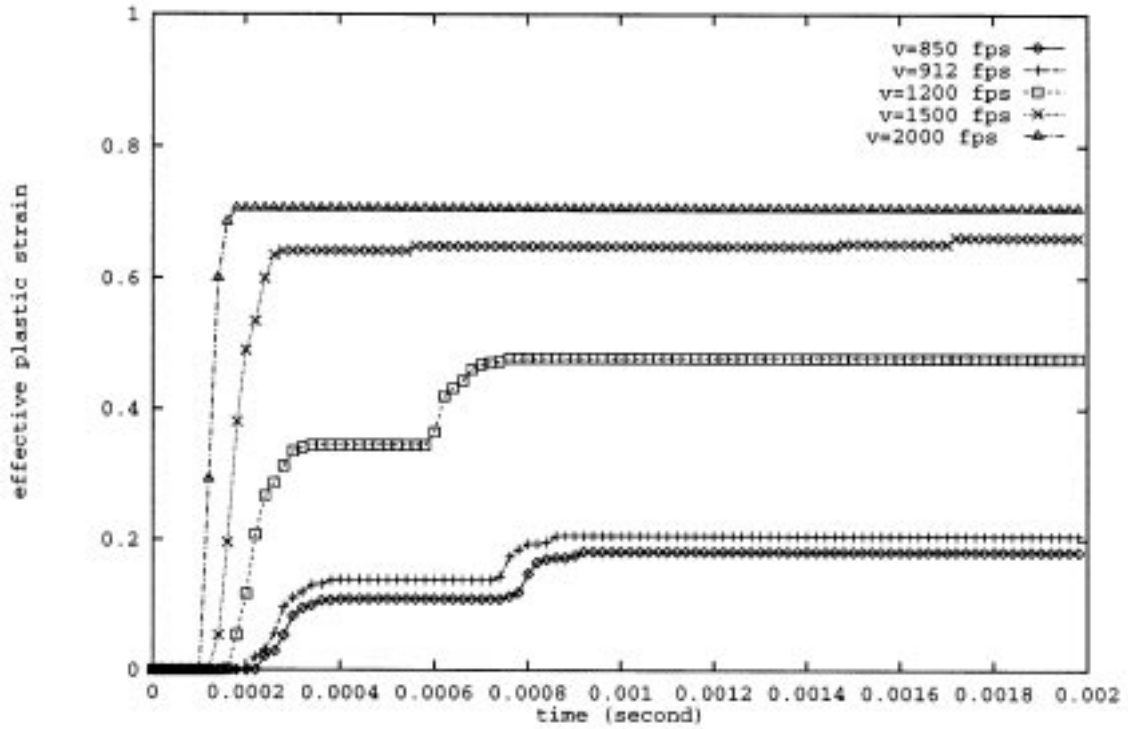


Figure 4. Effective Plastic Strain History for Different Projectile Speeds (Aluminum Containment Structure).

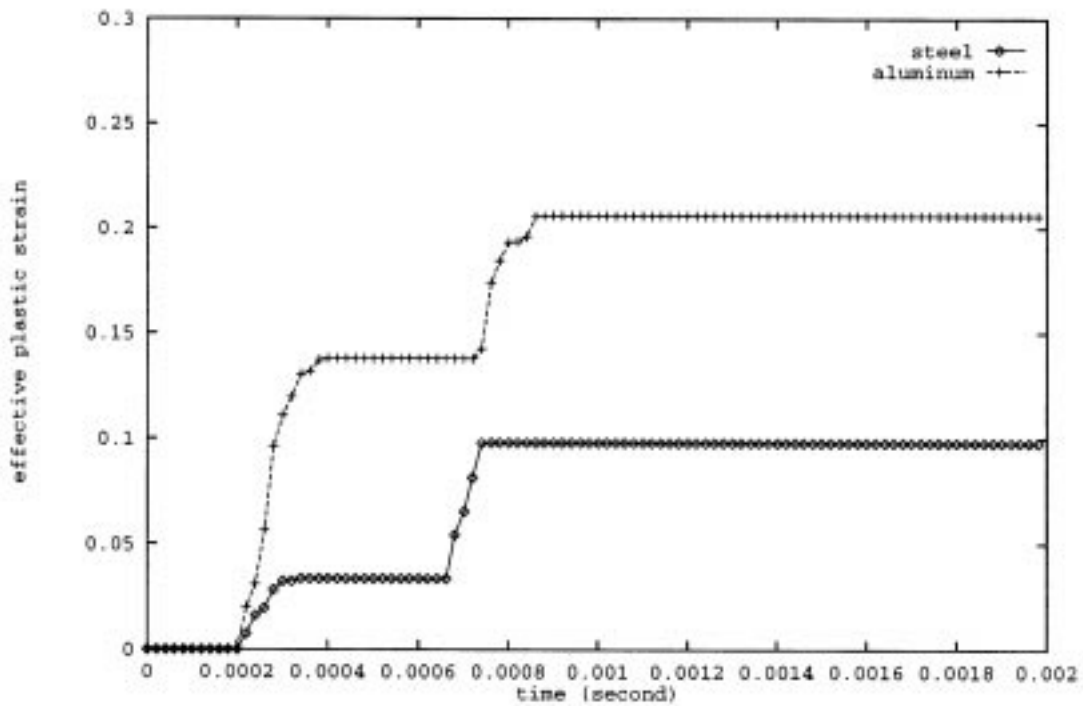


Figure 5. Effective Plastic Strain History for Steel and Aluminum Containment Structures (Projectile Speed - 912 fps).

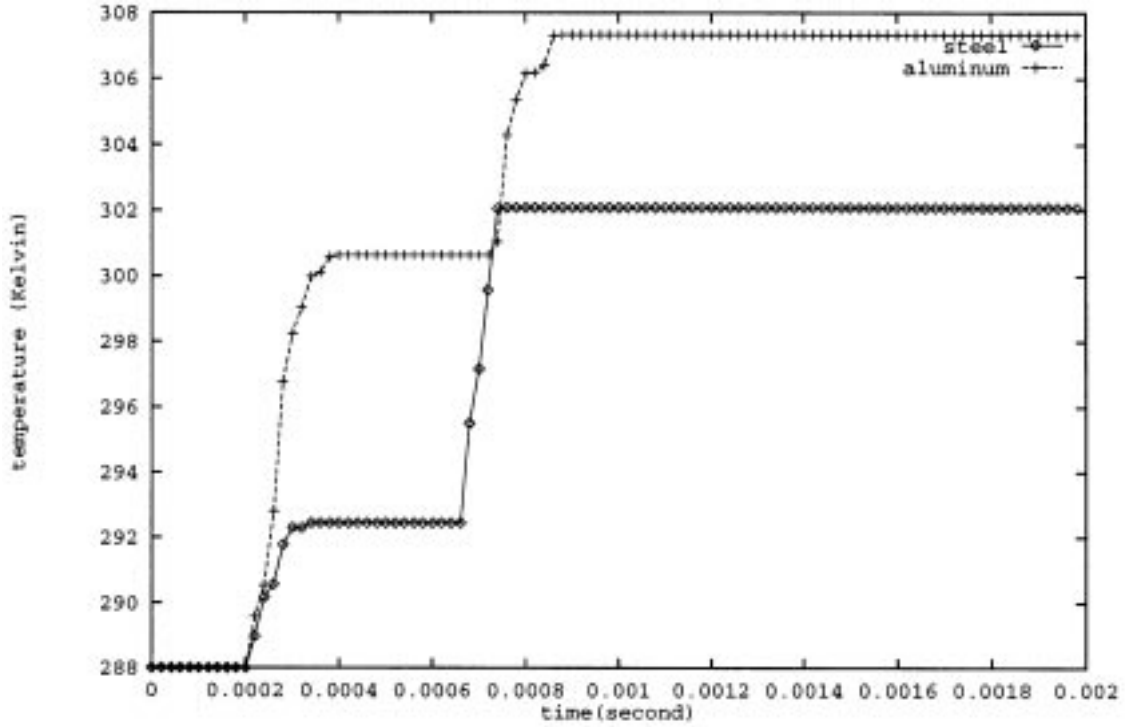
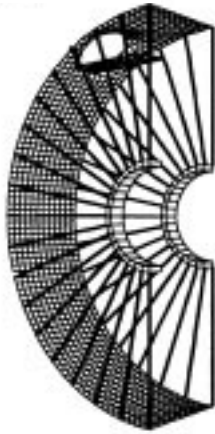


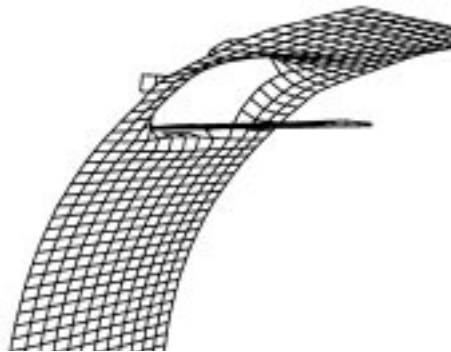
Figure 6. Temperature History for Steel and Aluminum Containment Structures (Projectile Speed = 912 fps).

Projectile hitting a curved pa
time = 0.22418E-03



Disp. Scale factor 0.100E+01 (default)

Projectile hitting a curved pa
time = 0.22418E-03



Disp. Scale factor 0.100E+01 (default)

Figure 7. Perforation of the Aluminum Containment Structure (Projectile Speed = 2000 fps).

Table 1. Material Properties for Steel and Copper.

Material Properties	Steel	Aluminum
A (yield stress)	114900 psi	38400 psi
B (Plastic modulus)	73900 psi	61800 psi
C (Strain rate coefficient)	0.014	0.015
C_v (specific heat)	$7.394 \times 10^5 \text{ in}^2/(\text{S}^2\text{-K})$	$1.356 \times 10^6 \text{ in}^2/(\text{S}^2\text{-K})$
n (strain hardening coefficient)	0.26	0.34
m (temperature exponent)	1.03	1.0
E (Young's modulus)	30 x 106 psi	10.5 x 106 psi
v (Poisson's ratio)	0.29	0.33
ρ (density)	$7.33 \times 10^{-4} (\text{lb-S}^2)/\text{in}^4$	$2.59 \times 10^{-4} (\text{lb-S}^2)/\text{in}^4$
T_m (melting temperature)	1793 K	775 K

Table 2. Containment Results for Different Projectile Speeds.

Speed (feet/sec)	Analysis Results	
	Steel	Aluminum
850	no failure, projectile redirected	no failure, projectile redirected
912	no failure, projectile redirected	no failure, projectile redirected
1200	no failure, projectile redirected	small perforation, projectile redirected
1500	no failure, projectile redirected	large perforation, projectile redirected
2000	small perforation, projectile redirected	penetration, noncontainment
2500	large perforation, projectile redirected	

FATIGUE AND DAMAGE TOLERANCE OF AGING AIRCRAFT STRUCTURES

G. I. Nesterenko
Central Aerohydrodynamic Institute (TsAGI)
140160, Zhukovsky, Moscow Region, Russia

SUMMARY

The experience in implementation of the safe-life, fail-safe, and damage tolerance concepts in Russian aircraft structures is summarized. The significance of fatigue and damage tolerance certification testing of full-scale aircraft structures is shown. The results of experimental evaluation of crack growth rate and residual strength of full-scale airframes having multisite fatigue cracks are given. Fatigue strength of new aircraft structures is compared to that of high-time aircraft. Test results on crack resistance of new materials and materials in high-time aircraft structures are analyzed.

APPLICATION OF SAFE-LIFE AND DAMAGE TOLERANCE CONCEPTS

In 1950-1970s the USSR Civil Aircraft Airworthiness Regulations [13] contained the only concept to ensure safety during long-time aircraft operation—the safe-life concept. However, there were notable doubts about the reliability of safe-life prediction, in the stabilization for decades of the operational conditions assumed at the prediction stage, and, finally, in the fatigue phenomenon being the only threat to safety. In response to these doubts, the system of safety margin factors were developed, and the number of full-scale structures to be tested for fatigue was increased (including those operated for some time). For example, four to six copies of full-size airframes were tested to check out such airplanes as Tupolev TU-104, Ilyushin IL-18, and Antonov AN-24. For the main passenger aircraft types the center-of-gravity load factor occurrence rate data were collected (proceeding from records of on-board emergency recorders) and analyzed comprehensively. In establishing the step-by-step approach the next specified periods of service within the design goal service life has been very effective. When establishing the next (prolonged) specified service period, the life and loading prediction for the next stage is refined, and the actual technical condition of the airframe fleet is analyzed.

In 1976 the term “damage tolerance” was introduced in Civil Aircraft Airworthiness Regulations [13] on par with the term “safe life.” To ensure structural safety, the designer has been free to choose any of these two concepts. It was a common practice in the USSR to use the damage tolerance concept including both the damage tolerance and fail-safe design philosophy. The application of this combined approach in some cases helped prevent

catastrophic aircraft failure when the requirements for the flaw detection service qualification and experience were too stringent for some airlines.

It was in 1994 that Aviation Regulations for Transport Aircraft (AC 25.571) were introduced. As these regulations stipulate, the safe-life concept is only applicable when the applicant proves that it is impossible to resort to the damage tolerance concept for his specific structure.

FULL-SCALE STRUCTURAL TESTS

Much attention was paid in the Civil Aircraft Airworthiness Regulations to the laboratory testing for fatigue strength of full-scale structures (including the determination of both the fatigue crack emergence time and the crack propagation path and duration). None of the Russian aircraft types has been left without full-scale structure fatigue testing over time intervals much longer than the design life goal.

In the new document “Means of Compliance” (MOS 25.571) that is similar to the US Advisory Circular (AC 25.571) the priorities are stated as follows. The first in significance is the direct testing of full-scale structures (or structural components reasonably close thereto), the second priority is the referencing of test results to other critical structural elements of the same airframe, and finally, the third is the purely theoretical analysis [13].

AGING AIRCRAFT OPERATION

The majority of the flying vehicle fleet in Russian civil aviation are airplanes manufactured in 1960-70s. By now this fleet has been operated in exceedance of its design fatigue life and service life. In the total air transportation, such aging airplanes fly more than 80% of the total cargo and passengers. It is impossible in the near future to replace the old types by newer ones (more comfortable and economically efficient), therefore the aviation industry has to prolong the service above the design figures for most aging aircraft. Such aging airplanes include Tupolev TU-134 and-154, Ilyushin IL-62 and-76, Antonov AN-12 and-24, as well as Yakovlev YaK-40. These have been designed for 15- to 20-year operation. Their service lives should be prolonged to 25 to 35 years. Operating the aging aircraft with cracks is permitted as an exception only, provided that the standardized requirements to damage tolerance are satisfied.

Today’s Russian civil aviation has a plan (coordinated with aircraft industry) to increase the service lives and lifetimes of aging airplanes. The planned lengths of service and lifetimes exceed the design figures by a factor of over 1.5. TsAGI together with some design bureaus and the State Research Institute of Civil Aviation (GosNIIGA) have resolved several R&D problems to support the prolongation of service. Adequate measures have been prepared for each type of aging airplanes as well as for major operation categories being

common to all aircraft and important from an aircraft operation safety standpoint. The studies showed that most concerns in aging aircraft are connected with multisite fatigue damage, corrosion, and crack-resistance degradation.

SOLUTION OF MULTISITE FATIGUE DAMAGE PROBLEM

The multisite fatigue damage term is intended to mean a set of fatigue cracks (or fractures of another kind) in a single structural component or in several components in a particular load transferring cross section of the structure. In Russian usage, multisite fatigue damage is similar to the term widespread fatigue damage (WFD) that includes multiple-site damage (MSD) and multiple-element damage (MED) [14]. Hereinafter, the multiple-site fatigue damage term is used.

The problem of multiple-site fatigue damage in aircraft structures was dealt with in the USSR by aircraft designers, fatigue experts, and scientists since the catastrophe with the Antonov AN-10A turboprop in 1972 [1]. During flight, the wing lower panels failed due to multiple-site fatigue damage in the stringers and skin. In the fracture zone the stiffeners had interface adapters, whereas the skin was a single sheet. Multiple cracks formed in both the stiffeners and the skin at the ends of the adapters. The damage was a multiple-site fatigue one due to structural features of the wing center section.

A uniform distribution of increased local stresses in stiffeners and skin at the ends of the adapters was a major cause of almost simultaneous initiation of several cracks. These cracks were growing at nearly equal rates. The service life of AN-10A airplanes had been established in accordance with the safe-life principle. For the wing area wherein the fatigue failure occurred, no in-service, flaw-detection measures had been prescribed because this area had not been found to be critical when fatigue testing the AN-10A airframe. In these tests the wing loading program was insufficiently close to in-service loading. After the catastrophe the same areas in other copies of AN-10A were inspected – many of them had multiple-site fatigue damages in stringers and skins.

To evaluate the airplane load at which the wing had broken, a special program of AN-10A wing residual strength determination was developed and implemented. This program included experimental study of skin sheet residual strength, residual strength, and crack growth rate for full-size stiffened panels of the wing and residual strength of two copies of AN-10A's that were flown for a long time and had multiple-site fatigue damages in the wing zone under study. The test data generated include residual strength of sheets made out of alloys D16ATNV (similar to 2024-T3 alloy) and V95ATV1 (similar to 7075-T6 alloy) and having transverse rows of fastener holes; each sheet was damaged with a large lead crack and a number of short cracks at the holes [2]. Features of fatigue crack growth and static fracture of stiffened structures with multiple-site damages were outlined [3]. Main points of a method for predicting the residual strength of built-up structures with multiple-site damages were formulated; the residual strength of the AN-10A wing was predicted [4].

Thereafter both the multiple-site fatigue crack growth rate and the residual strength of structures with multiple-site damages were estimated experimentally for full-size airplane structures tested for fatigue and damage tolerance in laboratory conditions. Note that the Russian principle “ekspluatatsionnaya zhivuchest” (operational survivability) incorporates simultaneously the fail-safe principle and the damage tolerance principle. However, for short, this more comprehensive principle will hereafter be denoted with the term “damage tolerance.” Methods for ensuring safety of an airframe with multiple-site fatigue damage are based on testing of full-size structures; this has been the main method because there exist many different patterns of multiple-site fatigue damage depending on design features. Without conducting the appropriate experiments on a full-size structure we cannot in most cases predict analytically a specific mode of multiple-site fatigue damage in a particular structure.

It is assumed that a cross section of a structure comprises some ten elements with identical fatigue life and a multiple-site fatigue damage exists in a structure if at least two elements show cracks. Probabilistic analysis indicates that these assumptions dictate the required amount of equivalent flight hours of the full-size structure in lab conditions to be three airplane service life goals in order for us to reveal the likelihood of in-service multiple-site fatigue damage [5].

In the USSR the tests for fatigue and damage tolerance have been conducted on full-size structures of almost all types of airplanes. The high-time structures of these types have also been tested for fatigue and damage tolerance. These structures were examined for at least three design service lives. At the last stage of evaluations the structures were tested for strength under a design limit load ($P^{\text{lim}} = 0.67 P^{\text{ult}}$). In some cases the structures failed under this load due to multiple-site fatigue damage. After the tests the structures were torn down and inspected to detect small cracks, including the multiple-site ones. Crack surfaces were examined fractographically and the crack evolution curves were plotted for crack lengths of over 0.3 mm (or 0.5 mm).

These experiments were the basis for determining growth rates and critical lengths of multiple-site cracks; inspection and repair intervals were established for the structural zones prone to multiple-site fatigue damage. Recommendations on ensuring damage tolerance were developed.

A survey of fatigue damage of structures showed that a high reliability of a structure is ensured when designers fulfill simultaneously the damage tolerance requirements [5] for the cases of multiple-site cracks in a single component (a stiffened panel) and multiple-site cracks in several components of one particular cross section of the structure. On the basis of this principle the designers are advised to ensure at the design stage the required residual strength of a wing in the following cases simultaneously [5]:

- a complete failure of one of the stiffened panels, no cracks in the other panels;
- one two-bay skin crack with center stiffener broken simultaneously in each of several panels of a particular cross section of the wing.

To ensure the residual strength of the structure with a two-bay skin crack and a broken center stiffener, the following opportunity is taken into account: after a long service, short cracks can originate in the skin from fastener holes for the intact side stiffeners at both sides of the broken center stiffener. This was accounted for by the evaluation of residual strength of the structure having the above mentioned standardized damage after testing the structure for three planned service lives and the propagation of the two-bay crack ends through the fastener holes for side stiffeners [6].

The critical multiple-site fatigue cracks in longitudinal joints in pressurized fuselage skin sheets are known to be very short and hardly detectable in service; therefore, recommendations are given to design these joints in compliance with the safe-life principle [6].

RESIDUAL STRENGTH OF STRUCTURES WITH MULTISITE DAMAGE

Ensuring the residual strength in structures with multiple-site fatigue damages is one of the primary concerns in the field of multiple-site fatigue damage in airframes. For the USSR airplanes this concern was dealt with on the basis of the survey and generalization of test data on residual strength of various types of airframes with multiple-site fatigue cracks. Figures 1 through 12 represent

- structures of airplane wings and bodies,
- types and locations of multiple-site fatigue damages in primary elements,
- structural alloys,
- relative values of net stresses $\sigma_{\text{fract net}}$, and
- stress-intensity factors K_{fract} at which the structures have failed.

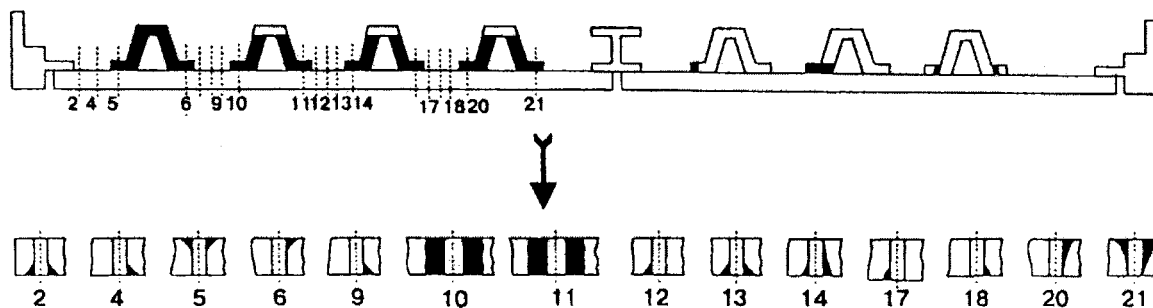


Figure 1. Damage of Skin and Stiffeners in Stiffener Interface Zone on Wing Lower Surface:
D16T Alloy; $\sigma_{\text{fract net}} = 0.8 \sigma_{0.2}$; $K_{\text{fract}} = 0.5 K_c^{\text{app}}$.

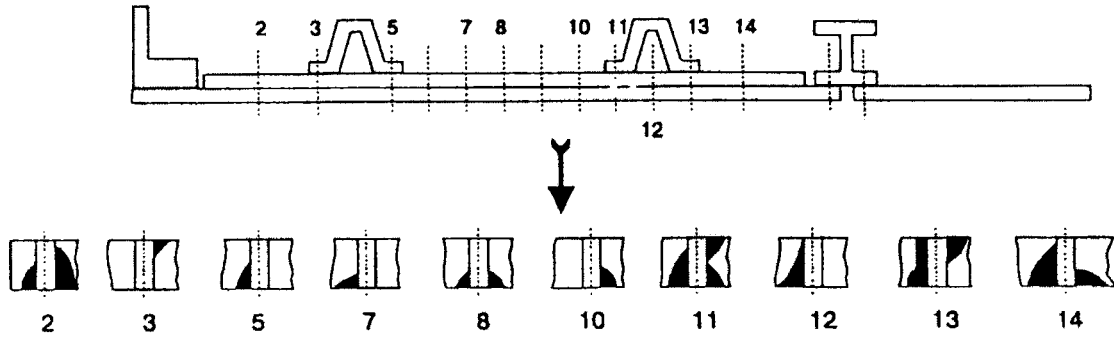


Figure 2. Damage in Strip Coupling the Skin Sheets on Wing Lower Surface:
 V95T1 Alloy; $\sigma_{\text{fract net}} = 0.4 \sigma_{0.2}$; $K_{\text{fract}} = K_{\text{Ic}} = 0.4 K_c^{\text{app}}$.

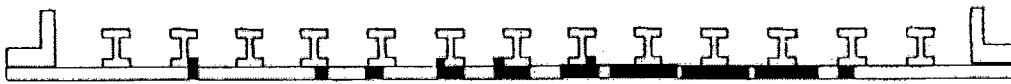


Figure 3. Damage of Skin and Stiffeners at the Doubler Edge on Wing Lower Surface:
 D16T Alloy; $\sigma_{\text{fract net}} = 0.9 \sigma_{0.2}$; $K_{\text{fract}} = 0.5 K_c^{\text{app}}$.



Figure 4. Damage of Skin at the Doubler Edge on Wing Lower Surface: V95T Alloy;
 $\sigma_{\text{fract net}} = 0.45 \sigma_{0.2}$; $K_{\text{fract}} = 0.5 K_c^{\text{app}}$.

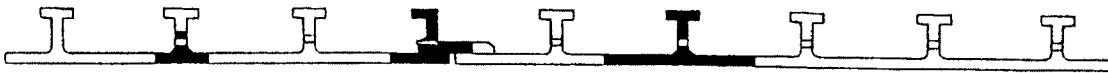


Figure 5. Damage of Skin and Stiffeners on Wing Lower Surface Near Fuel Holes in the
 Stringers: D16T Alloy; $\sigma_{\text{fract net}} = 0.7 \sigma_{0.2}$; $K_{\text{fract}} = 0.5 K_c^{\text{app}}$.

Surfaces of fatigue cracks are shown as black in these figures. The values of $\sigma_{\text{fract net}}$ and K_{fract} have been referred, respectively, to the yield strength $\sigma_{0.2}$ (F_{ty}) and to the fracture toughness K_c^{app} (in the case of plane stress state) or to a plane-strain fracture toughness K_{Ic} . The breaking net stresses $\sigma_{\text{fract net}}$ were calculated taking into account the component cross section reduction due to cracks and fastener holes. Crack longitudinal section areas were calculated on the basis of initial crack length a_0 . The length of the structure cross section where the net area and the stress $\sigma_{\text{fract net}}$ were computed was determined in the following way. The initial length equal to a span of the multiple-site fatigue damage zone was adopted. The cross section design length was assumed to be extended (in comparison with the initial value) to the left by two lengths of a leftmost crack and to the right by two lengths of a rightmost crack. The stress-intensity factor K was computed by conventional techniques. The stress-intensity factor $K = K_{\text{fract}}$ was computed for a crack with the maximum size,

accounting for interaction of this crack with neighboring ones. Experimental data show that the residual strength of a structure with multiple-site fatigue damage is influenced by a great number of various factors: structural design feature, bending stress, material plasticity, arrangement of the multiple-site cracks, stable growth of cracks under single static loading, holes, etc. There have been many instances of MSDs emerging on plain surfaces of thin plates rather than at holes and cutouts. A versatile criterion to evaluate residual strength of structures with MSDs appears not to exist.

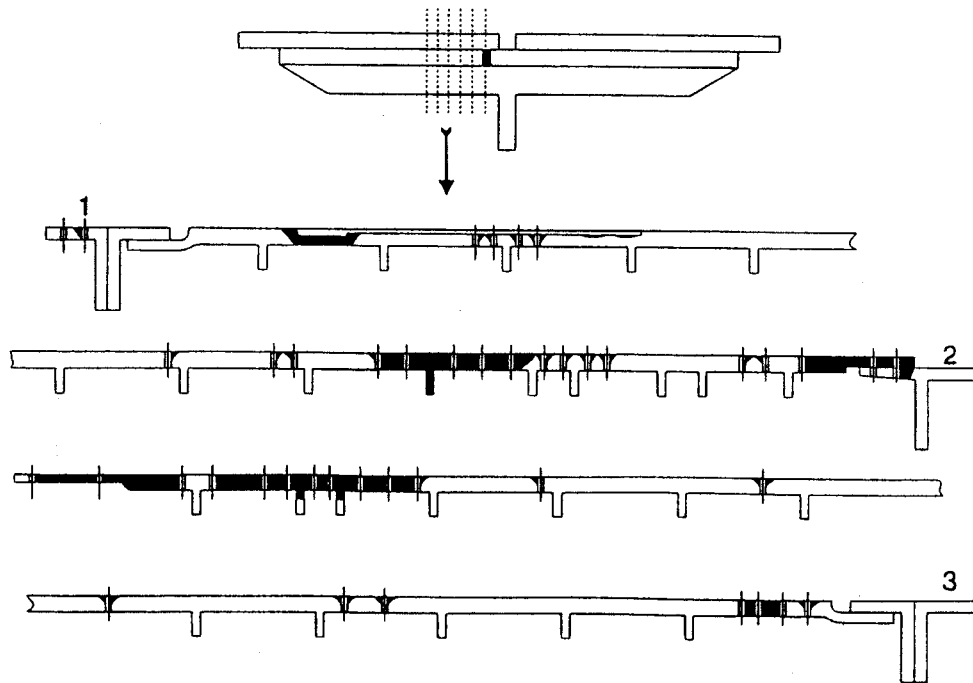


Figure 6. Damage to Spars and Panel Interface Component on Wing Upper Surface: D16T Alloy; $\sigma_{\text{fract net}} = 0.3 \sigma_{0.2}$; $K_{\text{fract}} = 0.5 K_c^{\text{app}}$.

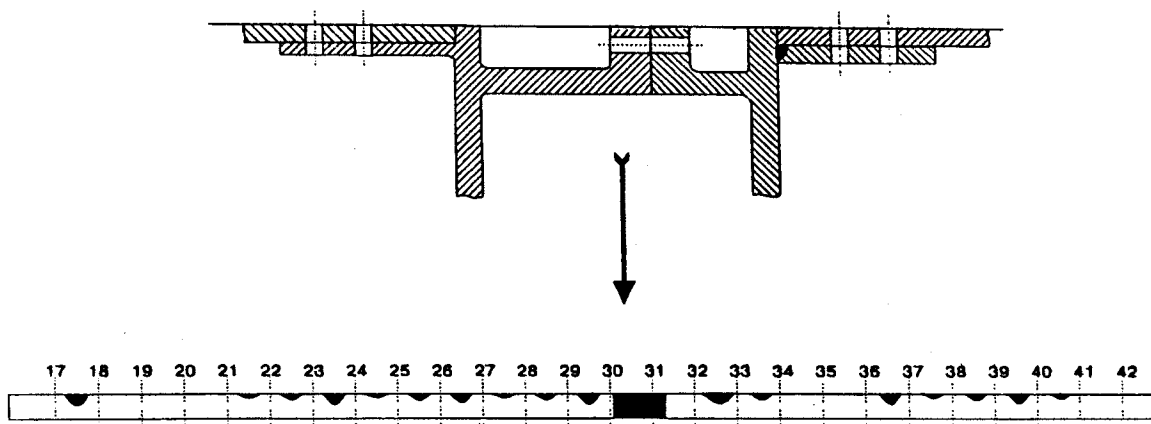


Figure 7. Damage of Panel Interface Component on Wing Upper Surface: D16T Alloy; $\sigma_{\text{fract net}} = 0.7 \sigma_{0.2}$; $K_{\text{fract}} = 0.75 K_c^{\text{app}}$.

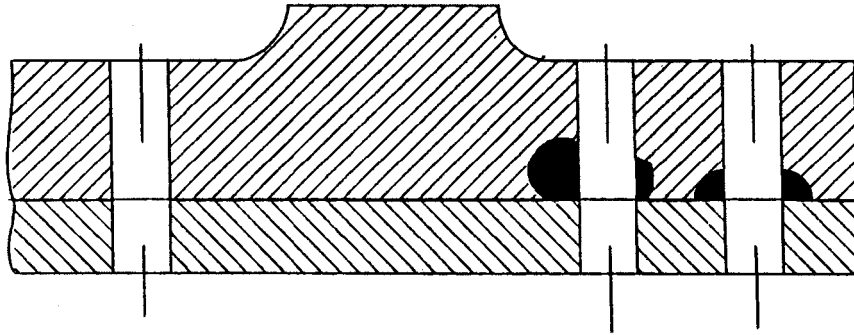


Figure 8. Damage in Wing Hinge Assembly; V93T1 Alloy; $\sigma_{\text{fract net}} = 0.4 \sigma_{0.2}$; $K_{\text{fract}} = K_{\text{ic}}$.

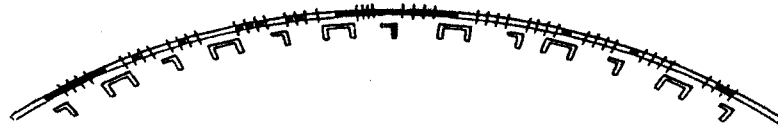


Figure 9. Damage of Stringer and Doubler on Circumferential Joint of Skin Around Pressurized Fuselage: D16T Alloy; $\sigma_{\text{fract net}} = 0.75 \sigma_{0.2}$; $K_{\text{fract}} = 0.5 K_c^{\text{app}}$.

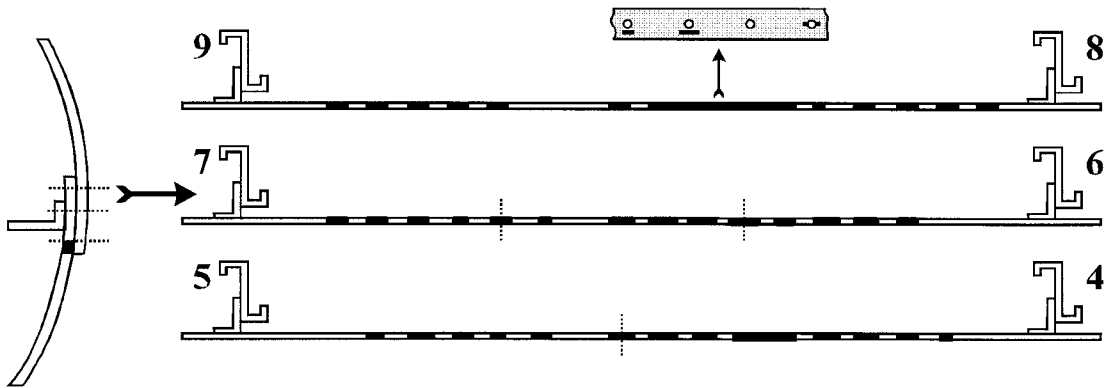


Figure 10. Damage of Pressurized Fuselage Skin Near Longitudinal Skin Joint: D16T Alloy; $\sigma_{\text{fract net}} = 0.57 \sigma_{0.2}$; $K_{\text{fract}} = 0.5 K_c^{\text{app}}$.

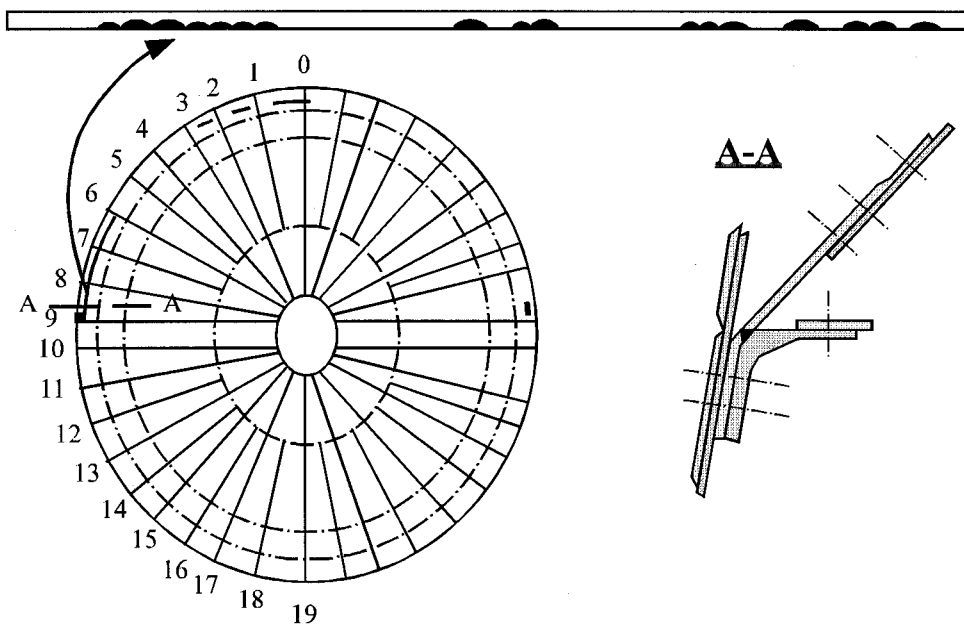


Figure 11. Damage in Strip Coupling Pressurized Fuselage Cylinder With Bulkhead:
 D 16T Alloy; $\sigma_{\text{fract netto}} = 0.16 \sigma_{0.2}$; $K_{\text{fract}} = 0.45 K_c^{\text{app}}$.

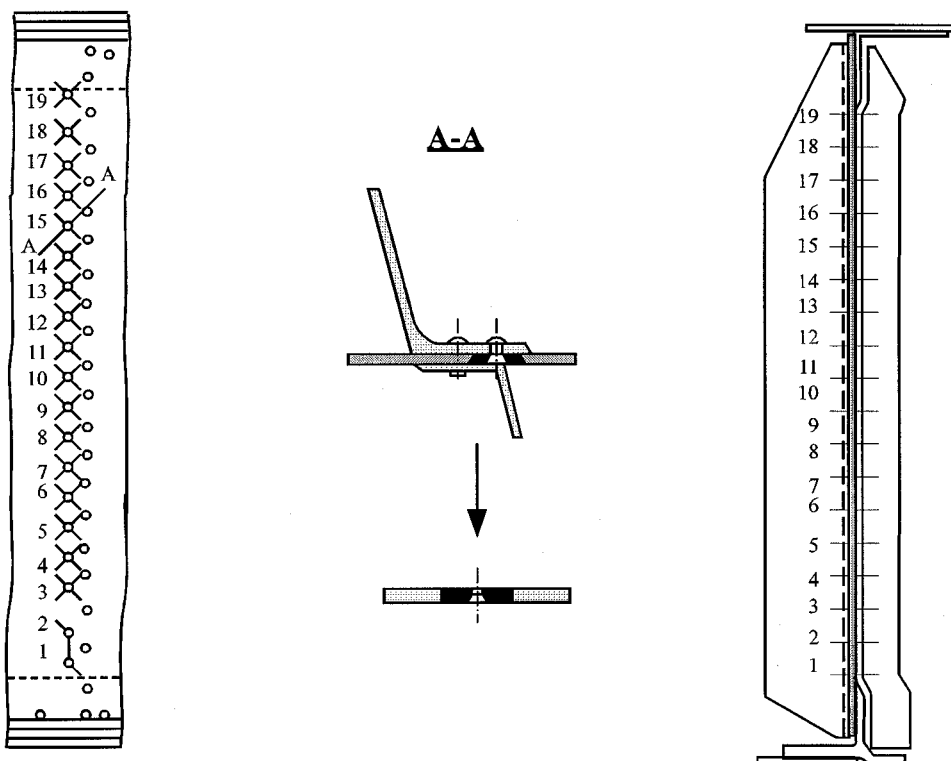


Figure 12. Damage of Wing Rear Spar Wall Near its Attachment to Rib;
 D16T Alloy.

A special-purpose experiment for evaluation of residual strength of a sheet with a single center through-crack showed the following implication: if both ends of the crack are at the holes, then the residual strength capability of the sheet with holes turns out to be higher than that of the sheet without holes at the crack ends. This increase in residual strength is as great as 5%-10% for plates about 5 mm thick made out of D16T alloy (similar to 2024-T3), 30%-35% for plates about 10 mm thick made of D16T, and 40%-45% for plates about 5 mm thick made of V95T1 alloy (similar to 7075-T6). It follows from Figures 1 to 12 that the values of the stress-intensity factors K_{fract} at which the structure fails are equal to K_{Ic} and $(0.4-1.0) K_c^{\text{app}}$; the breaking net stresses $\sigma_{\text{fract net}}$ were $(0.15-0.9) \sigma_{0.2}$.

After the multiple-site fatigue damage in the structure was detected during the fatigue tests (Figures 1 to 12), the airplanes were operated further. Damage tolerance of structural zones with multiple-site fatigue damage was analyzed to establish inspection intervals and deadlines for reworking these zones. When estimating damage tolerance, the allowable crack lengths were specified conservatively.

MULTISITE FATIGUE CRACK GROWTH

The multisite fatigue crack growth rate was determined on full-scale structures tested for fatigue and damage tolerance as well as on structures operated. Complete failure of the structures tested in laboratories resulted mainly from the failure of principal structural elements with multisite fatigue damage. With the tests completed, the surfaces of multisite cracks were analyzed using fractographic methods, thereafter the curves of multisite in-service crack growth rates were generated [15]. Crack growth rates for multisite cracks in operated structures were determined by the methods of mathematical statistics based on crack sizes measured during aircraft inspections [16].

Figures 13 through 25 present the results of evaluating multisite fatigue crack growth rates. The X-axis shows aircraft structure flight hours since the beginning of the tests or of the operation. These flight hours include the time before the crack initiation and crack growth duration. The relative operational time \bar{T} is the ratio of current operational time to the value at which failure occurred in the structure with multisite cracks during the tests, or to the operational time at which the crack propagating at an average in-service rate reaches its maximum size detected in operation. For those structures that had multisite damages in both laboratory and real service the crack growth duration data are presented only for the operation. The test crack growth duration data are for those structures that had no multisite cracks in operation. The figures presenting multisite crack growth during full-scale structure tests only show the curves corresponding to the maximum and minimum values of crack growth duration obtained by fractography [15]. The rest of the curves obtained by fractography and located between these two curves are not presented in the figures. The points in the figures presenting multisite crack in-service growth show the sizes of multisite cracks and operational time for those aircraft where the multisite cracks have been found. Here the curves of crack growth duration corresponding to the probability $P = 0.5, 0.05$, and

0.001 are also given. These curves were generated by the methods of mathematical statistics using the points from the figures [16]. When generating the curves, account was also taken of the copies having no cracks by the moment of inspection.

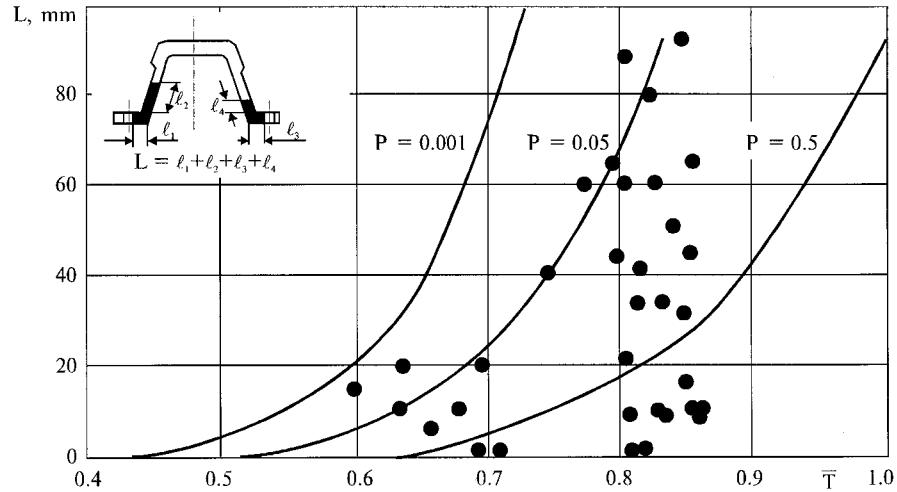


Figure 13. Relative Crack Growth Duration for Multisite Cracks in Stringers of Wing Lower Surface (Figure 1 in Service).

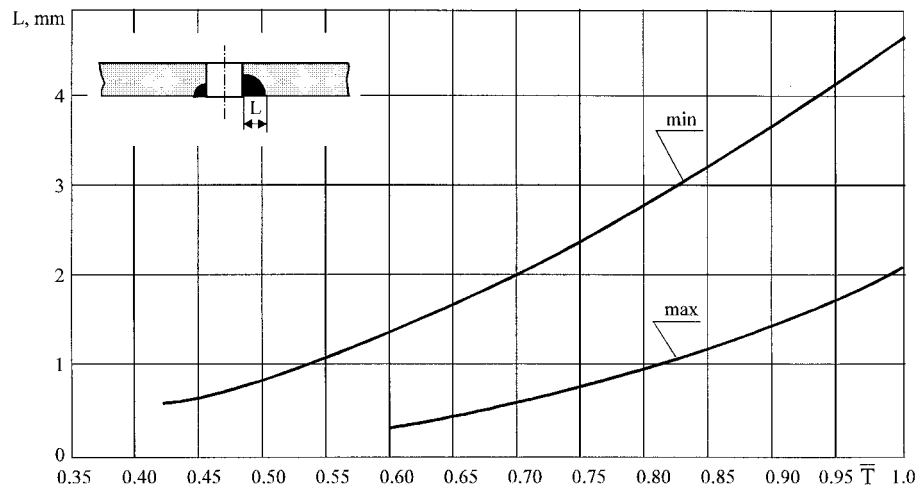


Figure 14. Relative Crack Growth Duration for Multisite Cracks in Doubler on Wing Lower Surface (Figure 2) During Aircraft Tests.

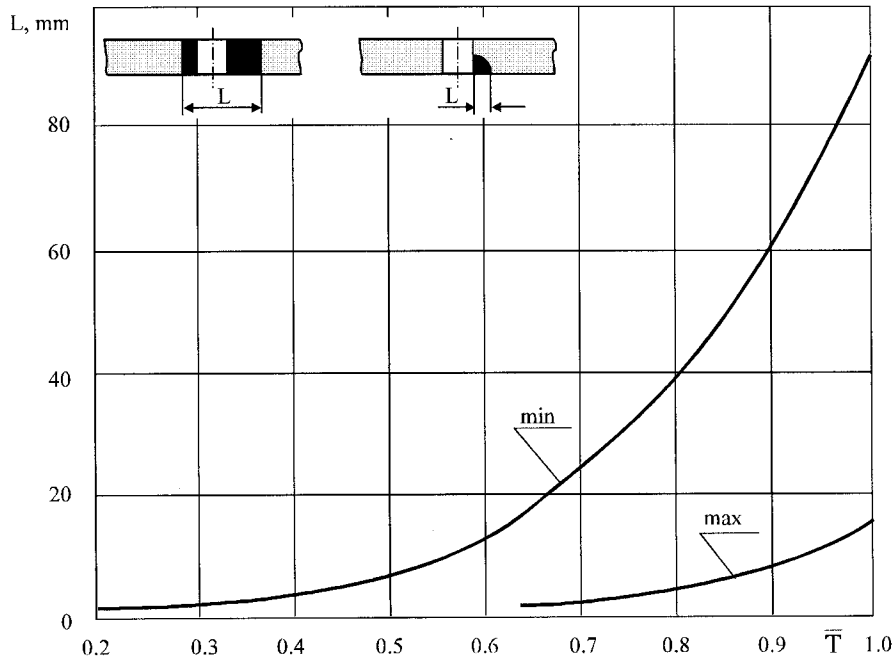


Figure 15. Relative Crack Growth Duration for Multisite Cracks in Wing Lower Surface Rear Panel Skin Near Reinforcing Doubler Edge (Figure 4) During Aircraft Tests.

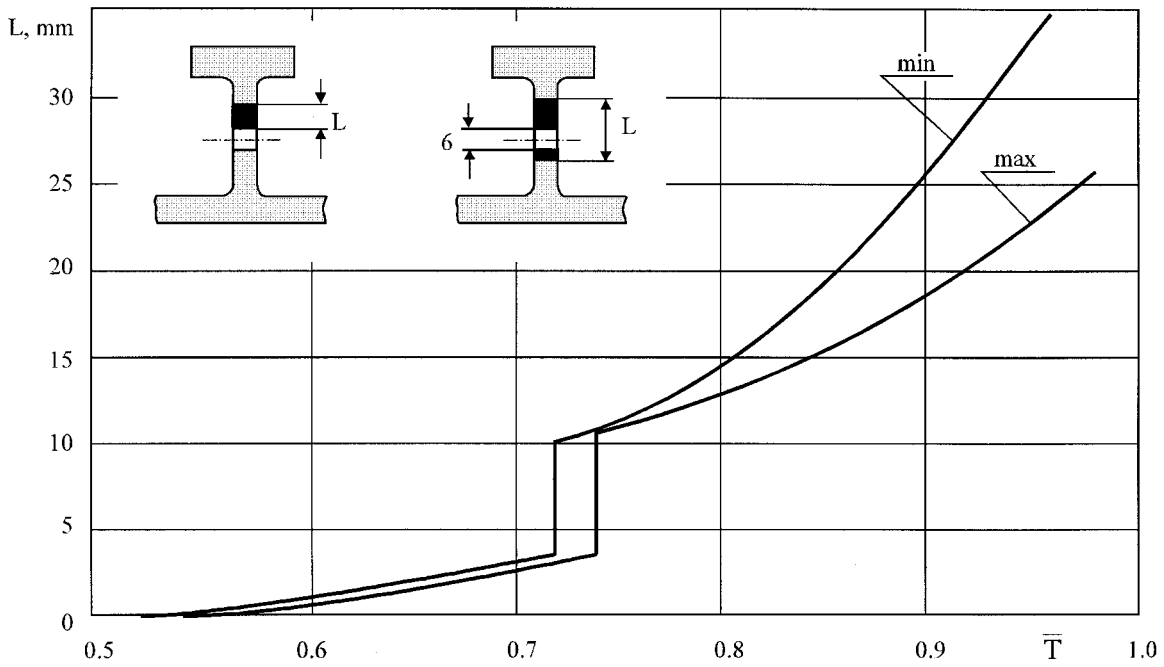


Figure 16. Relative Crack Growth Duration for Multisite Cracks in One-Piece Wing Lower Surface Panels Near Fuel Hole (Figure 5) During Aircraft Tests.

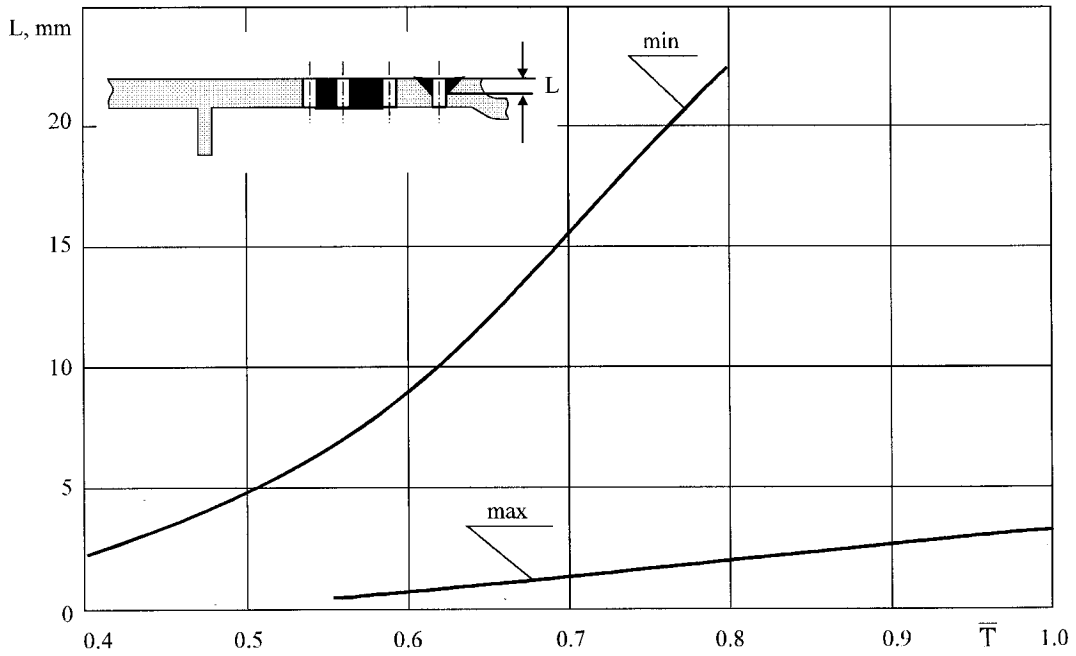


Figure 17. Relative Crack Growth Duration for Multisite Cracks in Spars and Attachment Part of Wing Upper Surface (Figure 6) During Aircraft Tests.

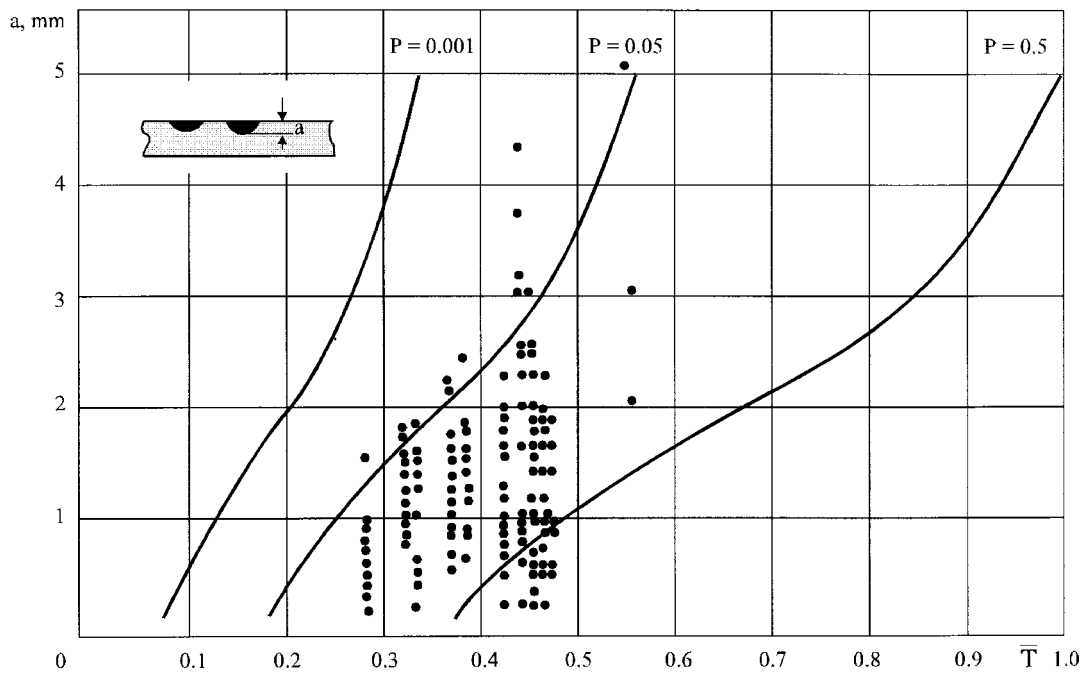


Figure 18. Relative Crack Growth Duration for Multisite Cracks in Panel Attachment Detail of Wing Upper Surface (Figure 7) in Service.

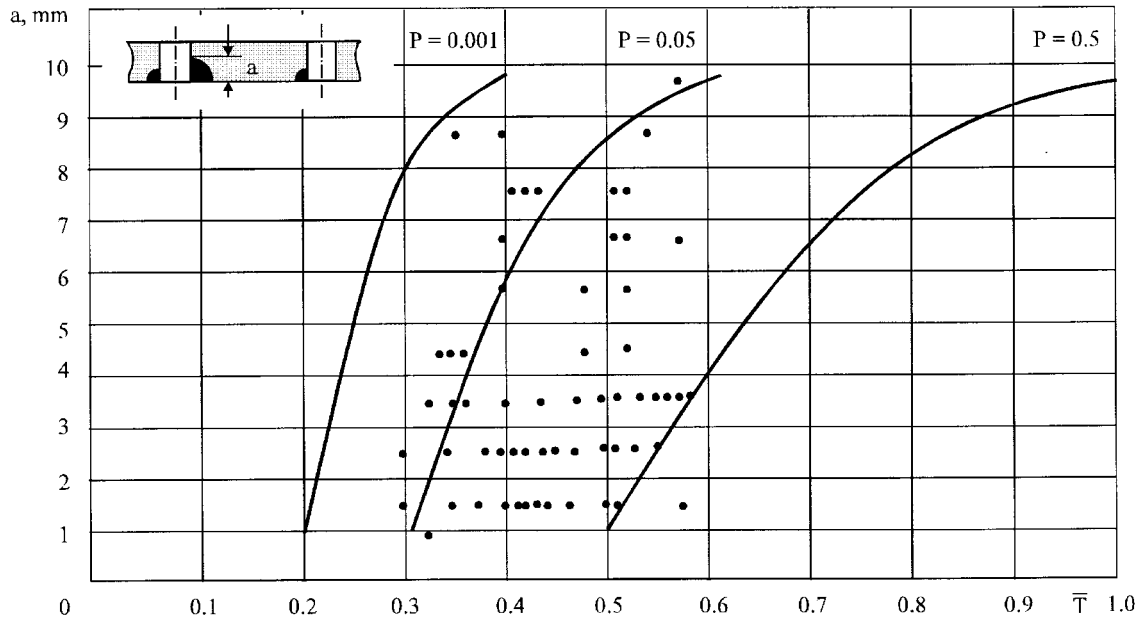


Figure 19. Relative Crack Growth Duration for Multisite Cracks in Wing Rotation Assembly. (Figure 8) in Service.

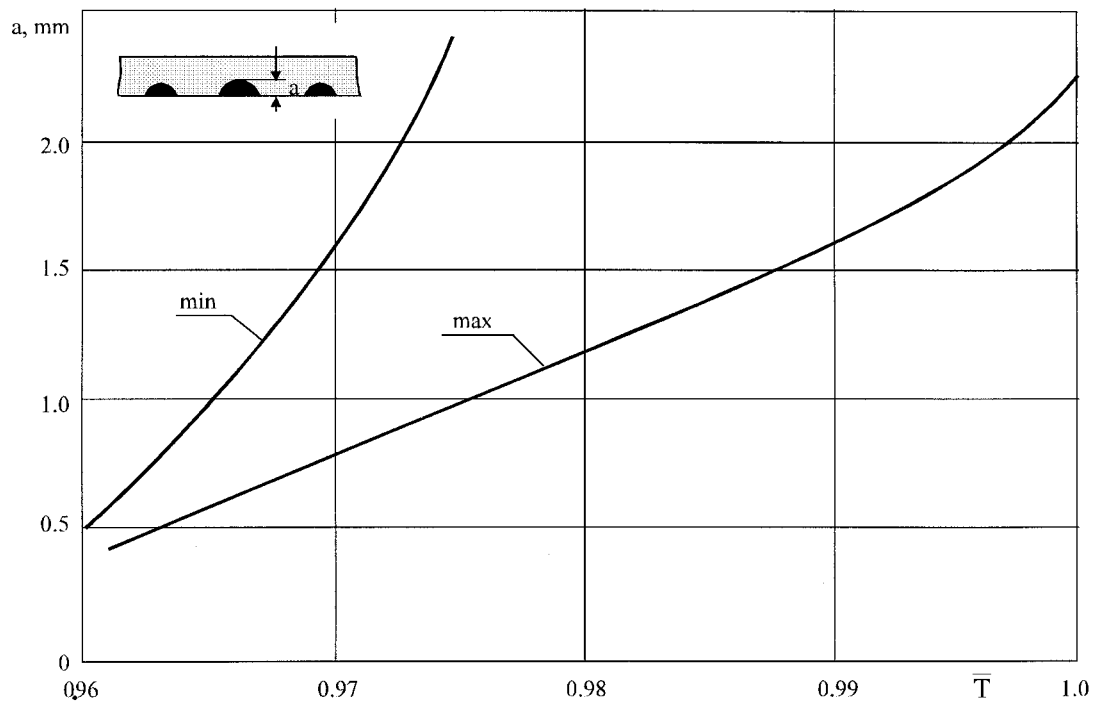


Figure 20. Relative Crack Growth Duration for Multisite Cracks in Strip Coupling Pressurized Fuselage Cylinder With Bulkhead (Figure 11) During Fuselage Box Tests.

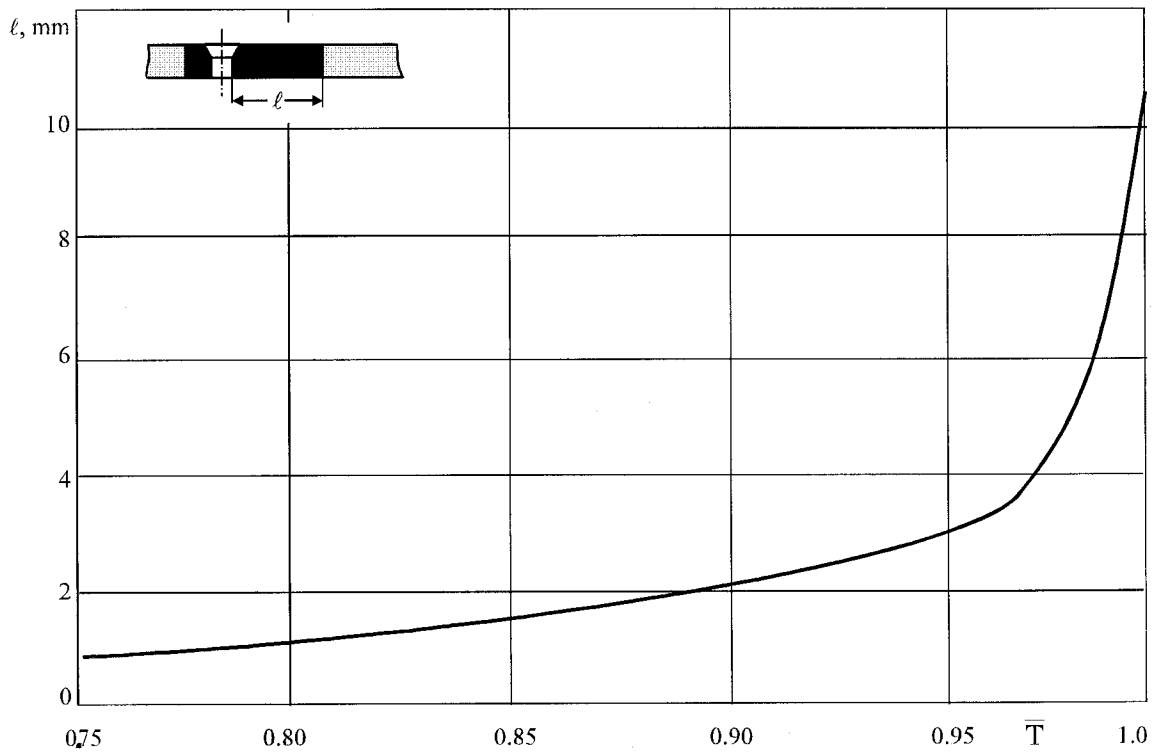


Figure 21. Relative Crack Growth Duration for Multisite Cracks in Wing Rear Spar Wall Near Its Attachment to Rib (Figure 12) in Service.

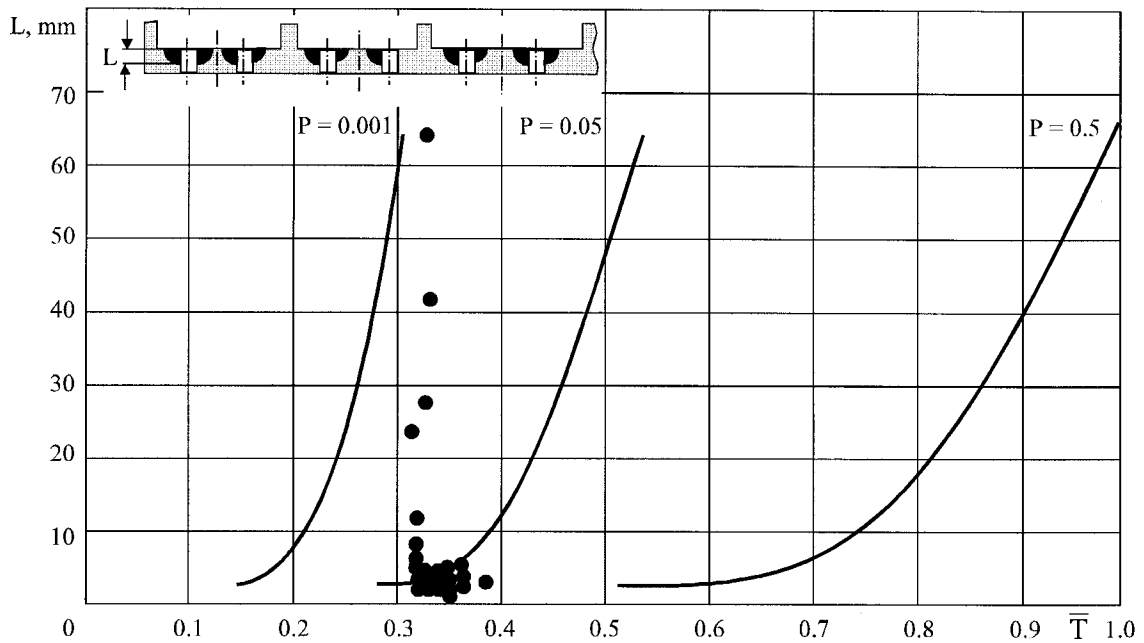


Figure 22. Relative Crack Growth Duration for Multisite Cracks in Panel Attachment Part on Wing Lower Surface in Service; B95T1 Alloy.

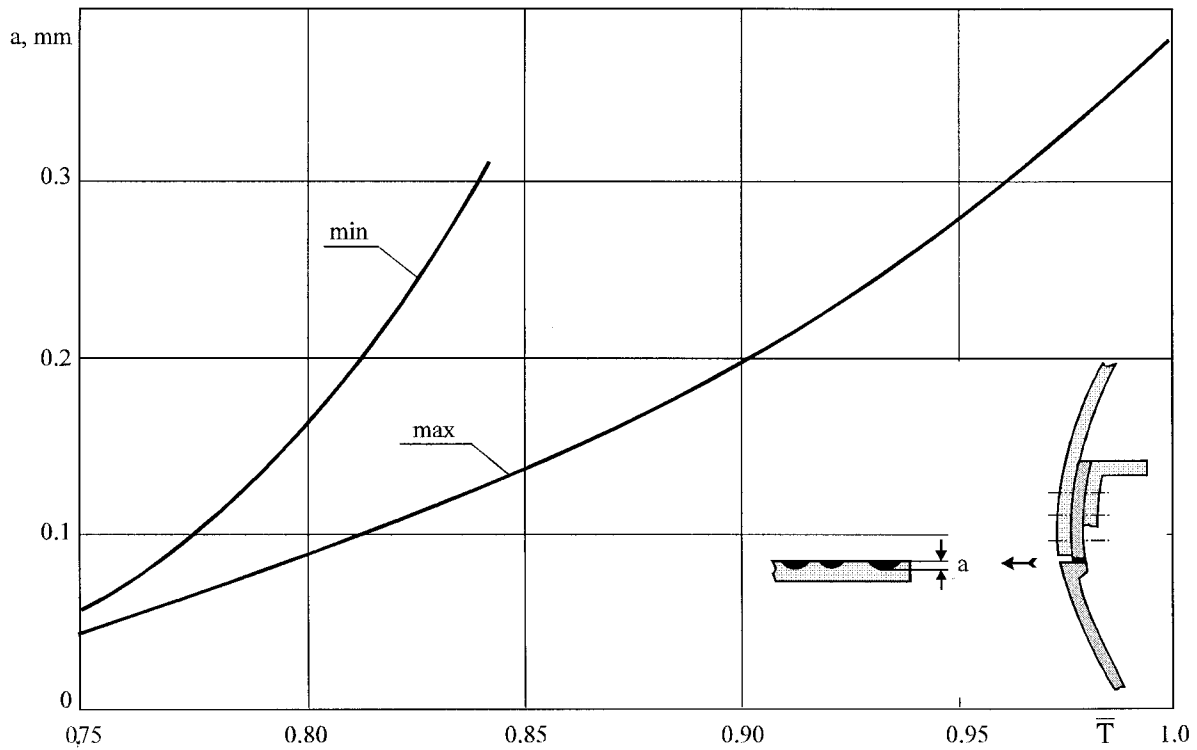


Figure 23. Relative Crack Growth Duration for Multisite Cracks in Pressurized Fuselage Skin Near Skin Sheet Longitudinal Splices in Service; D16T Alloy.

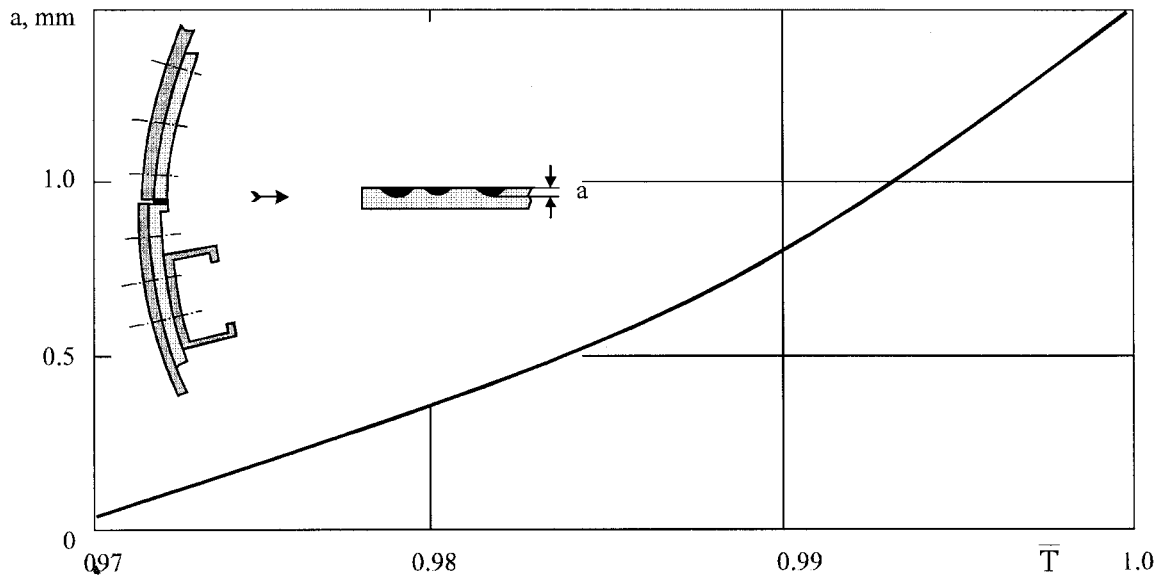


Figure 24. Relative Crack Growth Duration for Multisite Cracks in Strip Coupling the Pressurized Fuselage Skin Sheet Near Sheet Longitudinal Splices During Aircraft Tests; D16T Alloy.

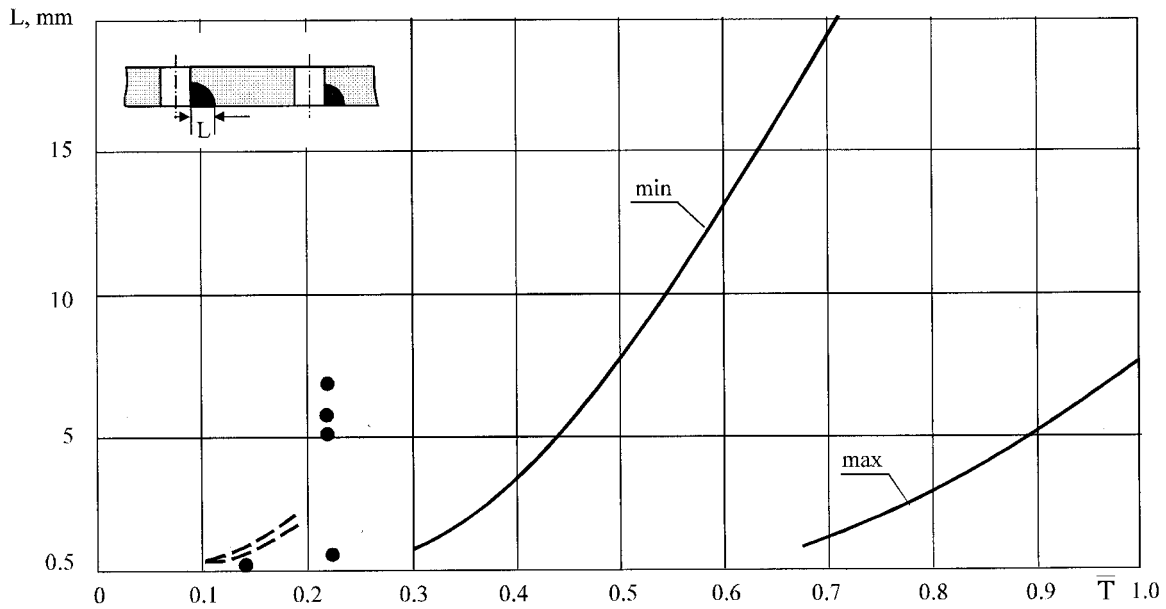


Figure 25. Relative Crack Growth Duration for Multisite Cracks in Attachment Parts of Wing Lower Surface During Full-Scale Aircraft Tests (Solid Curves) and In Service (Points and Dashed Curves Obtained by Fractography Methods); V93T1 Alloy.

Inspection and repair intervals were defined on the basis of analyzing multisite crack growth during both full-scale tests and operation (Figures 13-25) as well as on the basis of the data on residual strength of structures with multisite cracks (Figures 1-12). The analysis of multisite crack growth duration (Figures 13-25) has shown that different structures have very different ratios of

- duration ΔT of crack growth from lengths of 0.1-0.5 mm to failure to
- accumulated duration $T + \Delta T$ (life before crack initiation plus crack growth time). This ratio is in the range $\Delta T / (T_0 + \Delta T) = 0.03-0.8$. In general this ratio decreases with the ratio of local bending stresses to gross tensile stresses.

It follows from the results that when defining inspection intervals for the structures with possible multisite fatigue damage, the reliability factor η should be 2–3. This factor is applied to the average values of in-service multisite crack growth duration.

The study of failures due to multisite fatigue damage, as given in this paper as well as in Refs. [7-12, 17], is anticipated to help designers to solve the problem of multisite fatigue damage in aircraft structures at the design and service stages.

STUDY OF STRUCTURAL FATIGUE STRENGTH DEGRADATION

Fatigue testing of aircraft operated for a long time allows us to evaluate the effect of long operation on structural fatigue strength. Figure 26 compares life duration for new aircraft and high-time aircraft. All of these were fatigue tested to the same variable loading programs (specific to a flight vehicle type).

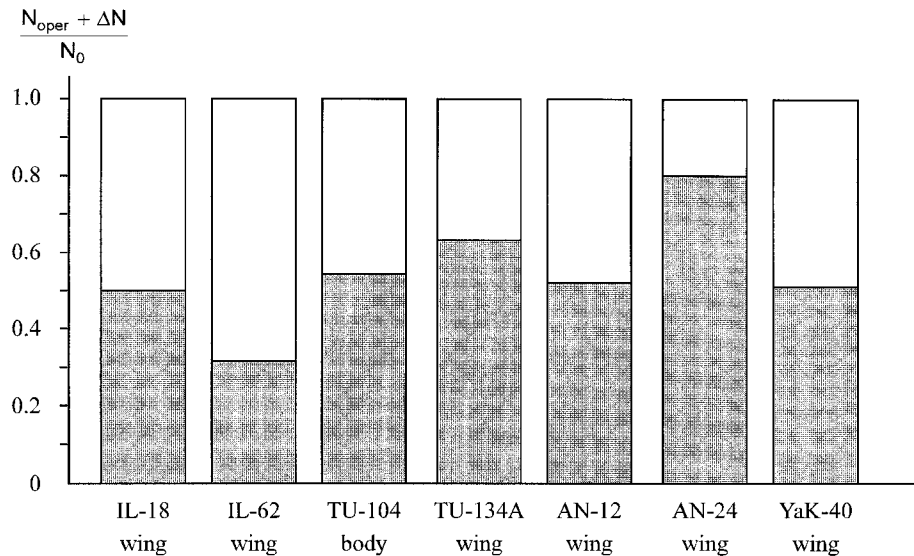


Figure 26. Relative Fatigue Strength of Aircraft Structures Before (Light Plus Dark Zones) and After (Dark Zones) Service.

The life of new aircraft is N_0 ; the life of high-time aircraft is the sum of operational time N_{oper} and laboratory fatigue test time ΔN . The comparison takes into account the equivalent fatigue damage rate for both the tests and operation. The data make it clear that operation decreases structural fatigue strength. Test data in Figure 25 suggest that the aging aircraft structures suffer from earlier initiation of multisite cracks and their faster in-service growth than during full-scale testing of a new structure.

STUDY OF MATERIAL CRACK RESISTANCE DEGRADATION

TsAGI conducted some specialized experiments on specimens cut from reinforced panel skins from high-time aircraft [18]. Figure 27 presents test data on material crack resistance for the wing skin of airplanes whose period of operation exceeded 20 years. It also shows test data on material crack resistance for the same alloys but manufactured later. All the data were obtained by testing the skin sheets with no bulging restraints (with no guides installed). As compared to new materials, old ones have fracture toughness values lower by some 20% and crack growth rates higher by a factor of 2 to 4. The degradation of crack resistance in old materials may be due to both imperfect manufacture processes and the effect of long-time operation.

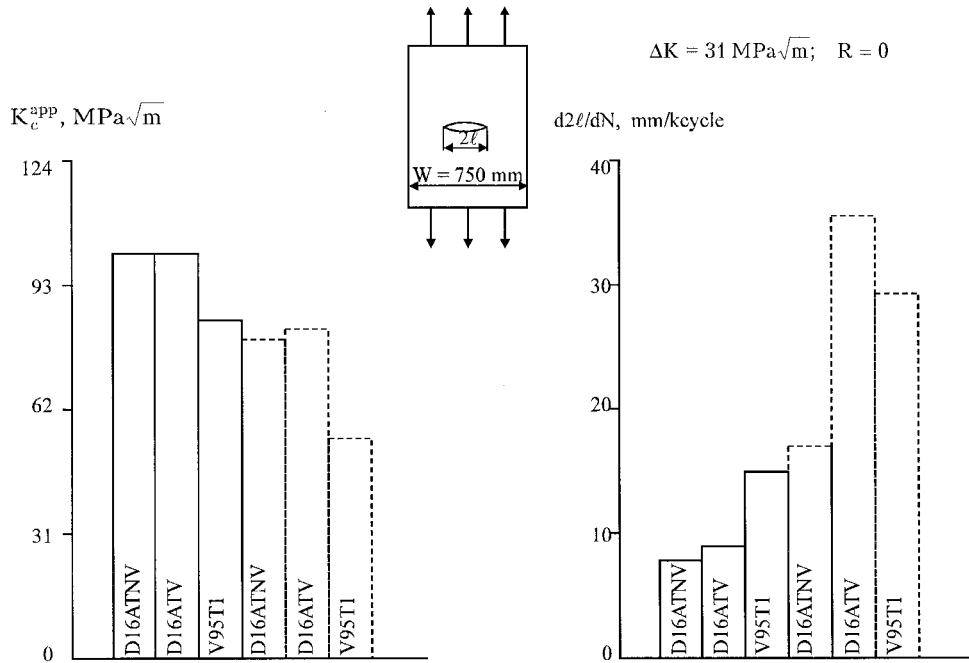


Figure 27. Crack Resistance of Aircraft Materials Before (Solid Lines) and After (Dashed Lines) Service.

In-service inspection intervals for aging aircraft structures in Russia are corrected on the basis of data from damage tolerance testing of full-scale, high-time aircraft structures. In so doing, the analysis of structural damage tolerance takes into account the results of studying crack resistance degradation.

CONCLUSION

In the 1950-70s the only concept to ensure safe aircraft operation in the USSR was the safe-life concept. In 1976, along with this concept, the philosophy including fail-safe and damage-tolerant design was introduced.

Full-scale structures of all aircraft types in the USSR were tested for fatigue resistance over time much longer than the design service life. In many cases several copies of the structures have been tested including those with a long time in service.

Russian specialists have developed a plan to prolong serviceability of aging aircraft. The planned values exceed the design values by a factor of over 1.5. Appropriate measures have been developed for each type of aging airplanes as well as for major categories of operation being common to all the aircraft types.

One of the principal concerns with aging aircraft is the multisite damage problem. In the USSR and in Russia this problem is being solved on the basis of experimental

investigation into damage behavior of full-scale airframes in both the tests and operation. Crack growth duration and residual strength were evaluated for various structural types with multisite damages. After summarization and analysis of these data the inspection threshold and intervals and in-service structural repair time were defined; thereafter some recommendations have been developed for designers.

When considering the aging aircraft problem, the issue of degradation of fatigue strength and crack resistance arises. To clarify this matter, the lifetimes of new and high-time airplanes were compared by testing in laboratory conditions to the same program of variable loading. Fatigue strength of high-time structures was observed to be degraded; as well, crack resistance of old materials turned out to be degraded. The results of these studies are taken into account in predicting the damage tolerance characteristics for aging Russian airframes.

REFERENCES

1. Nesterenko, G. I.: Discussion on Aging Aircraft. The 8th International Conference on Fracture (ICF-8), Kiev, Ukraine, June 8-12, 1993. Published at TsAGI.
2. Yablonsky, I. S.; Ol'kin, S. I.; Yegorshev, A. V.; Zaveryukha, G. G.: Strength of Sheet with Transverse Row of Holes Damaged by Fatigue Cracks. In: *Residual Strength of Wing Structures*. Trudy TsAGI, issue 1607, Moscow, 1974, pp. 11-15.
3. Yegorshev, A. V.; Nesterenko, G. I.: Some Features of Fatigue Fracture of Structures and their Components. In: *Residual Strength of Wing Structures*. Trudy TsAGI, issue 1607, Moscow, 1974, pp. 3-6.
4. Nesterenko, G. I.: On the Multicomponent Structure Residual Strength Calculation. In: *Residual Strength of Wing Structures*. Trudy TsAGI, issue 1607, Moscow, 1974, pp. 23-31.
5. Nesterenko, G. I.: Damage Tolerance of Aircraft Structures. In: *Strength, Reliability and Service Life of Aircraft Structures*. Proceedings of Kiev Institute of Civil Aviation Engineers (KIIGA), issue 2, Kiev, 1976, pp. 60-70.
6. Nesterenko, G. I.: Requirements to Ensuring Damage Tolerance of Passenger and Transport Aircraft Airframes at the Stage of Design. In: Collection of Reports at the Conference "Systems Approach to Aircraft Structure Service Life Requirements." TsAGI, 1984, book 1, pp. 199-207.
7. Swift, T.: The Influence of Slow Growth and Net Section Yielding on the Residual Strength of Stiffened Structure. Federal Aviation Administration. Presented at the 13th Symposium of International Committee on Aeronautical Fatigue, Pisa, Italy, May 22-24, 1985, pp. 2.10/7-2.10/46.

8. Goranson, U. G.: Damage Tolerance: Facts and Fiction. Boeing Commercial Airplane Group, USA. Presented at the 17th Symposium of International Committee on Aeronautical Fatigue, Stockholm, Sweden, June 9, 1993.
9. Hoggard, A. W.: Maintaining the Safety of an Aging Fleet of Aircraft. Proceedings of 16th Symposium of International Committee on Aeronautical Fatigue, May 22-24, 1991, Tokyo, Japan, pp. 113-136.
10. Tong, P.; Sampath, S. G.; and Broek, D.: Aging Aircraft. Detection of Multiple-Site Damage and the Risk of Failure. Proceedings of 16th Symposium of International Committee on Aeronautical Fatigue, May 22-24, 1991, Tokyo, Japan, pp. 237-254.
11. Lehrke, H. P.; and Schopfel, A.: Analysis of Multiple-Crack Propagation in Stiffened Sheet. Proceedings of 16th Symposium of International Committee on Aeronautical Fatigue, May 22-24, 1991, Tokyo, Japan, pp. 255-276.
12. Nakata, M.; Nishimura, T.; and Naba, K.: Damage Tolerance Assessment on the Multisite Cracks for the YS-11 Aircraft. Proceedings of 16th Symposium of International Committee on Aeronautical Fatigue, May 22-24, 1991, Tokyo, Japan, pp. 355-374.
13. Raikher, V. L.; Dubinsky, V. S.; Nesterenko, G. I.; Stuchalkin, Yu. A.: The Features of Aircraft Structure Fatigue Resistance Certification and Continued Airworthiness in Contemporary Conditions. Test Facilities and Aircraft Certification. International Symposium Proceedings, Zhukovsky, Russia, Aug. 22-25, 1995, pp. 233-245.
14. Nesterenko, G. I.: Multiple-Site Fatigue Damages of Aircraft Structures. AGARD CP-568. Widespread Fatigue Damage in Military Aircraft, 1995, pp. 11-1-11-8.
15. Stoyda, Yu. M.; Yekimenkov, L. N.: Method for Marking Cracks in Aluminum Airframe Elements During Fatigue Resistance Tests. Proceedings of the Third Sino-Russian Symposium on Aircraft Structure Strength. CAE, Beijing, China, Jan. 5-7, 1994, pp. 60-71.
16. Senik, V. Ya.: Analyzing Fatigue Crack Growth Characteristics of Aircraft Structural Elements on the Basis of In-Service Data. Trudy TsAGI, issue 1671, Moscow, 1975, pp. 17-27.
17. AGARD CP-568. Widespread Fatigue Damage in Military Aircraft. North Atlantic Treaty Organization, 1995.
18. Nesterenko, G. I.: Predicting the Structural Damage Tolerance on the Basis of Fracture Mechanics. *Fiziko-Khimicheskaya Mekhanika Metallov*, 1983, no. 1, pp. 12-23.

FATIGUE GROWTH OF SMALL CORNER CRACKS IN ALUMINUM 6061-T651

R.L. Carlson, D. L. Steadman,
D.S. Dancila, and G. A. Kardomateas
School of Aerospace Engineering
Georgia Institute of Technology
Atlanta, Georgia

SUMMARY

Results of an experimental investigation of the fatigue growth of small corner cracks emanating from small flaws are presented. A three-point bending state of loading was used and by virtue of the orientation of the square cross section of the specimen, the maximum tensile stress was developed at the middle of the gage section and on a corner edge. A growth-arrest behavior was observed and the increases in crack length during growth periods were of the order of the transverse grain size, so it is inferred that grain boundaries acted as barriers to continuing growth.

INTRODUCTION

The discovery by Pearson [1] that the growth of small fatigue cracks differed from that of long cracks has served as an impetus for the initiation of many subsequent research investigations. Early papers by Miller [2], Suresh [3], Lankford and Davidson [4], and Suresh and Ritchie [5] identified some of the important parameters and provided classification schemes which emphasized the importance of crack size scale relative to microstructural features. The importance of microstructural features has been further established in research conducted by Chan and Lankford [6], Navarro and de Los Rios [7], and Tannaka and Akiniwa [8]. Some of the investigations conducted have focused on the development of analytical methods for predicting growth histories. Edwards and Newman [9] have suggested that the anomalous growth of small cracks is caused by either an absence or a reduction in obstruction to closure. They have proposed the use of an effective range of stress-intensity factor which is formulated to account for a reduction in closure obstruction.

The objective of the studies to be presented here was to introduce a new experimental procedure for investigating small fatigue crack growth. Several test specimens and experimental procedures have been proposed for conducting small fatigue crack investigations. These have been described in ASTM Test Method E647 [10]. The specimen used is shown in Figure 1. The specimen had circular cross sections at the ends and a gage cross section which was square. The loading state applied to the specimen of Figure 1 is

shown in Figure 2. By virtue of the orientation of the square cross section of the specimen and the application of three-point bending, the maximum tensile stress is developed at the middle of the gage section and on a corner edge, i.e., the neutral axis of bending coincides with a diagonal of the square cross section.

The procedures described were developed under Contract No. F09603-G-0096-0013 with the Warner Robins Air Force Base. Mr. Gary Chamberlain was the Project Monitor.

EXPERIMENTAL RESULTS

During manufacturing and maintenance, flaws such as gouges or nicks are sometimes introduced, and these can serve as sites for crack initiation. Pickard, Brown, and Hicks [11] conducted an investigation in which the growth of corner cracks emanating from small notches were monitored. They used tensile loading for their tests which were modeled to represent gas turbine components. For the initial tests using the specimen and loading state described in Figures 1 and 2, a small corner notch was introduced at the location of maximum tensile stress to serve as a site for crack initiation. The test material for the investigation was the aluminum alloy 6061-T651 and specimens were machined from 16-mm-diameter bar stock. The 0.2 percent offset yield strength was 283 MPa and the ultimate strength was 293 MPa. The average transverse grain size was 200 microns. The longitudinal grains were elongated and varied widely about an average of 350 microns. Corner notches with a 60-degree included angle were cut at the midpoint of the specimen's cross section by use of a digitally controlled slitting saw. The faces adjacent to the notch were then polished with five grades of abrasive paper ranging from 600 to 2000 grit. Final polishing was performed by use of a three- and then a one-micron diamond paste. By polishing after notching, it is possible to obtain very small notches.

Experiments were conducted on an Instron servo-hydraulic testing machine which applied sinusoidal loading at 10 Hz. For the data reported, the load ratio $R = 0.0625$. A telemicroscope with a video camera and a monitor were used to measure crack length growth. Details of this system have been described previously [12]. Crack lengths were measured at fixed intervals to obtain data for records of crack length versus loading cycle. Cracks which started from notches were initiated by the application of a nominal maximum stress which was 0.9 of the yield strength. Small cracks were initiated after about 200,000 cycles of loading. The load was then reduced to produce a maximum stress of about 0.5 of the yield strength. Two types of experiments were conducted. In one test the growth of a moderately long crack was monitored to establish the near threshold region. In the second test the growth of a small crack was monitored. Notch depths for these tests were about 150 microns.

Although the use of the stress-intensity factor as a correlation parameter for small-crack growth has been questioned, its use does provide a means of comparing long- and small-crack growth. It is, therefore, used for that purpose here. Its incorporation as a parameter for design for small-crack growth is another issue which is discussed in a

subsequent section. The stress-intensity factor used is based on results for a corner crack in a bar with a rectangular cross section in the NASA/FLAGRO [13] computer program. The test specimen had a square cross section and in the application of the computer program results equal bending moments were superimposed to provide a resultant bending moment about the neutral axis (a cross section diagonal) of the test specimen.

Results for a long-crack test are presented on the log-log plot of Figure 3 for the near threshold region. A straight line through the data points can be represented by the equation

$$da/dN = 10^{-8}[\Delta K/6.7]^{28} \quad (1)$$

The exponent in Equation 1 is not to be confused with the exponent of the Paris equation for region II growth rate behavior. The large value of this exponent is the result of the fact that the da/dN versus ΔK curve in region I, the threshold region, is much steeper than that for region II.

Data obtained from small crack experiments are presented in Figures 4(a) and (b). The load applied at the midpoint of the test specimens was 854N and crack length values shown include the notch depth. The growth-arrest behavior which has been reported previously by other investigators is clearly evident.

Miller [2] has given a qualitative description of crack growth history by using crack length on a left-hand ordinate and sizes of microstructural features on a right-hand ordinate. This provides a perspective for comparing the length of a growing crack with such features as inclusions and grain size. If, for the corner crack, it is assumed that the arc of the crack front is circular and centered at the crack corner, the number of grains, on the average, along a crack front for a given crack length can be determined from the equation

$$n = \pi a / 2D \quad (2)$$

where a is the crack length (or radius to the crack front from the corner), n is the number of grains along the crack front, and D is the transverse grain size. Equation 2 has been used to determine the scale of the right-hand ordinates of Figures 4(a) and (b). Comparisons of the two ordinates, then, indicate the number of grains encountered, on the average, for a given crack length.

An examination of the initial growth-arrest features in Figure 4(a) would indicate that an elaborate scheme for computing growth rates is not warranted. Nevertheless, continuing growth is occurring and a growth trend is indicated. A simple method for representing the growth rates has been adopted. A trend curve has been developed by connecting successive inner corners of the steps. The rates so determined are represented by round data points on the Cartesian coordinate plot of Figure 5 for both faces of the corner. The small-crack growth data are to the left of the near threshold curve. Thus, for a given ΔK , the small-crack growth rates are greater than those for long cracks.

Data for a second small-crack growth experiment for the same loading conditions are presented in Figure 4(b). These data reveal that the crack length versus cycles histories for the two tests differ significantly. Also, the data of Figure 4(b) exhibit an abrupt increase in crack length at a value of about 420,000 cycles. This may be attributed to the nature of crack initiation for this test. Cracks were initiated at the intersection of the root surface of the notch and the outer faces. On each face, the direction of the initial crack deviated from a normal to the corner edge by about 40 degrees. The crack on one face was above a plane normal to the corner edge whereas the crack on the other face was below the normal plane. It has been inferred from this observation, and from the abrupt crack length increase, that the initial microcrack planes associated with the observed surface cracks were distinct and not connected, i.e., they were separated by an uncracked ligament which introduced a bridging mechanism. It is suggested that when this ligament was fractured, the observed sudden increase in crack length occurred.

In view of the initial behavior indicated in Figure 4(b), no attempt was made to calculate growth rates for this phase of growth, since the use of a stress-intensity factor here is not considered reasonable. Growth rates beyond 420,000 cycles were, however, calculated, and these results are represented on the growth rate versus range of stress-intensity factor plot of Figure 5 by square data points. Clearly, a comparison of these data with those for the growth data from Figure 4(a) again indicate a lack of reproducibility.

The crack lengths used for this latter computation ranged from about 800 to 1300 microns. These crack lengths may appear to exceed limits used to define small cracks. It has, however, been observed [14] that small crack behavior can extend to crack lengths which are about ten times the grain size. Since the grain size in the plane of crack growth is about 200 microns, the growth range for which the calculations were made is within this size limitation. Consequently, the results reaffirm the importance of grain size.

DISCUSSION OF RESULTS

Results from a number of investigations have indicated that low-load ratio tests on small cracks appear to correlate well with long-crack data for high-load ratio tests. It has been suggested [9] that either an absence or a reduction in obstruction to closure for these test conditions provides an explanation for the anomalous small crack behavior. The observed early deviations from planar growth could, however, promote obstruction to closure for small cracks. Also, the difference observed here between the orientations of the crack planes on the two corner surfaces suggests that, initially at least, there may be an internal, unfractured ligament between the crack surfaces which are on different planes. This could introduce a bridging mechanism which would result in an effect which would be counter to the absence or reduction of closure obstruction hypotheses. It is also of interest to note that Vasudevan and Sadananda [15] have suggested that the effects of obstruction to closure are not significant.

Just after crack initiation, a crack front encounters a small number of grains. Microstructural features such as grain size, orientation, and inclusions may be expected to affect crack growth [2, 4, 6, 7, 8, 16, and 17]. By contrast, the number of grains encountered by the crack front of a long crack can generally be expected to be relatively large. For corner and thumbnail cracks this number increases with increasing crack depth, i.e., as the small crack grows and becomes a long crack. An examination of Figure 4 indicates that over the range for which growth-arrest behavior has occurred, the number of grains encountered by the crack front is small. Thus, when four grains are encountered, two, or one-half of the grains, have free surfaces. Thus, only the two internal grains are completely surrounded and constrained. It has been suggested [18] that when the number of grains is small, the effect of the surface grain contributions to crack extension may be expected to be greater than when the surface grains are a small fraction of the total number of grains along the crack front. If this conjecture is correct, there could be, for the same alloy and crack depth, differences in crack growth rates for small corner cracks, small thumbnail cracks, and short cracks. Note that for the alloy tested a short, through edge crack in a 5-mm-thick sheet would encounter about 25 grains. The stress-intensity factor is insensitive to these details, so it cannot be expected to account for behaviors which may result from these differences.

It has been suggested here that the anomalous small-crack growth behavior may be due at least in part to the fact that the ratio of the total number of grains on the crack front to the number of partially constrained, surface grains is small. This ratio increases, of course, with increasing crack size or decreasing grain size. An alternative to previous proposals for crack growth rate could be to introduce a function of this ratio. Thus let,

$$da/dN = f[n_t/n_s]F[\Delta K, \Delta K_{th}, R, K_{IC}] \quad (3)$$

where n_t is the total number of grains intersected by the crack front, and n_s is the number of surface grains crossed by the crack front. The value of n_s will here be taken as 2.

A form of f which could be used is

$$f = [1 + g(n_t/2)] \quad (4)$$

where the function g should be constructed so that f is large for small cracks and approaches unity for long cracks. A function of g which satisfies these requirements is

$$g = C_1 \exp[-C_2(n_t/2)] \quad (5)$$

Note that since the number of grains on a crack front depends upon the size of the grains, grain size is explicitly included in Equation 3.

The data of Figure 4 indicate that the increases in crack length during the growth periods were of the order of the grain size. This supports the contention [19, 20, 21] that grain boundaries introduce barriers to continuing growth. Since it may be inferred that the use of grain boundary describes a two-dimensional encounter, it may be more descriptive to

visualize a three-dimensional geometry in which the advancing crack encounters a grain boundary wall. When there are only a few grains on the crack front, the growth-arrest phenomenon can be expected to be readily detectable. This is illustrated in Figure 6(a) in which a hexagonal array has been chosen to represent grains on the crack plane. The size of the hexagons corresponds to the transverse grain size of the 6061-T651 aluminum alloy tested. When the crack is passing through the first few grains near the corner, the grain size is a large percentage of the crack length and few grains are encountered by the crack front. If crack lengths of this order are detectable, the role of grain boundary barriers to growth can be easily detected. When the crack front reaches a depth along which there are more than, for example, eight grains, the grains boundaries can still act as barriers to growth, but continuing growth can be expected to be smoothed out. This probably occurs as the size of grains becomes a small fraction of the crack front length. Thus, although the crack front may have a local waviness, the amplitudes of the waves may be of the order of the grain size, and they in turn are also a small fraction of the measured crack depth.

The grain pattern of Figure 6(a) is symmetric with respect to a line which bisects the corner angle. Figure 6(b) represents a somewhat more realistic, nonsymmetric arrangement of grains, and it can be seen that, initially, crack growth on the right side of the top corner grain could be retarded by the inclined grain boundary. Again, however, when the crack depth is large compared to the grain size, the crack front would encounter a relatively large number of grains and differences in growth rates could be expected to diminish; i.e., although local differences in crack advance may persist, the dimensions of the differences become a small fraction of the crack length.

CONCLUSIONS

Crack extensions during the growth periods of the growth-arrest behavior of the small corner cracks were of the order of the grain size for the 6061-T651 aluminum alloy tested. This supports the contention that grain boundary walls may introduce local barriers to continuing growth. Small cracks were observed to grow below the threshold for the small load ratio, R , used. The initial crack growth behaviors of small cracks and short cracks may differ because of the large difference in grains along their crack fronts. Also, since small thumbnail cracks can, for the same crack depth, be expected to have about twice as many grains along their fronts as small corner cracks, their growth behaviors may differ. The stress-intensity factor is insensitive to these differences. The anomalous growth rate observed for small cracks may be due in part to the fact that surface grains, which are a large fraction of the total number of grains along the crack front of a small crack, do not have the complete constraint that interior grains have. The form of a modified crack growth rate equation which incorporates an effect of a difference in internal and surface grain constraints on initial, small-crack growth is described.

REFERENCES

1. Pearson, S.: Investigation of Fatigue Cracks in Commercial Al Alloys and Subsequent Propagation of Very Short Cracks, *Eng. Fract. Mech.*, Vol. 8, 1975, pp. 235-247.
2. Miller, K. J.: The Short Crack Problem, *J. Fatigue and Fracture of Eng. Mtls. and Structures*, Vol. 5, 1982, pp. 223-232.
3. Suresh, S.: Crack Deflection: Implications for the Growth of Long and Short Fatigue Cracks, *Metallurgical Trans.*, Vol. 14A, 1983, pp. 2375-2385.
4. Lankford, J. and Davidson, D. L.: Near Threshold Crack Tip Strain and Crack Opening for Large and Small Fatigue Cracks, Fatigue Crack Growth Threshold Concepts, D. L. Davidson and S. Suresh, (eds.), *Metallurgical Soc. of Amer. Inst. Mining Mineral Petroleum Engrs.*, Warrendale, PA, 1984, pp. 447-463.
5. Suresh, S. and Ritchie, R. O.: Propagation of Short Fatigue Cracks, *International Metals Reviews*, Vol. 29, 1984, pp. 445-476.
6. Chan, L. S. and Lankford, J.: The Role of Microstructural Dissimilitude in Fatigue and Fracture of Small Cracks, *Acta Metall.*, Vol. 36, 1988, pp. 193-206.
7. Navarro, A. and de Los Rios, E. R.: Short and Long Crack Growth: A Unified Model, *Phil. Mag.*, Vol. 57, 1988, pp. 15-36.
8. Tanaka, K. and Akiniwa, Y.: Propagation and Nonpropagation of Small Fatigue Cracks, *Advances in Fracture Research*, Proc. ICF 7, Vol. 2, 1989, pp. 869-889.
9. Edwards, P. R. and Newman, J. C.: An AGARD Supplemental Test Programme on the Behavior of Short Cracks Under Constant Amplitude and Aircraft Spectrum Loading, *Short-Crack Growth in Various Aircraft Materials*, AGARD Report 767, 1990.
10. American Society for Testing and Materials Proposed Small Cracks Appendix to Test Method, E 647, 1993.
11. Pickard, A. C., Brown, C. W., and Hicks, M. A.: The Development of Advanced Specimen Testing and Analysis Techniques Applied to Fracture Mechanics Lining of Gas Turbine Components, *Advances in Life Prediction Methods*, D. A. Woodward and J. R. Whitehead, (eds.), 1983, pp. 173-178.

12. Carlson, R. L., Dancila, D. S., and Kardomateas, G. A.: An Investigation of the Growth of Small Corner Cracks From Small Flaws in 6061-T651 Aluminum, *Proc. Sixth International Fatigue Congress*, G. Lütjering and H. Nowack, (eds.), Pergamon, 1996, pp. 289-293.
13. NASA/FLAGRO Fatigue Crack Growth Computer Program, 1989.
14. Taylor, D. and Knott, J. F.: Fatigue Crack Propagation Behavior of Short Cracks; The Effect of Microstructure, *Fatigue Engineering Mtls. and Structures*, Vol. 4, 1981, pp. 147-155.
15. Vasudevan, A. K. and Sadananda, K.: Fatigue Crack Growth in Advanced Materials, *Proc. Sixth International Fatigue Congress*, G. Lütjering and H. Nowack, (eds.), Pergamon, 1996, pp. 473-478.
16. Miller, K. J.: Materials Science Perspective of Metal Fatigue Resistance, *Mtls. Sci. Tech.*, Vol. 9, 1993, pp. 453-462.
17. Hussain, K., de Los Rios, E. R., and Navarro, A.: A Two-Stage Micromechanics Model for Short Fatigue Cracks, *Eng. Fract. Mech.*, Vol. 44, 1993, pp. 426-436.
18. Leis, B. N., Topper, A. T., Ahmad, J., Brock, D., and Kanninen, M. F.: Critical Review of the Fatigue Growth of Short Cracks, *Eng. Fract. Mech.*, Vol. 23, 1986, pp. 883-898.
19. Morris, W. L.: Microcrack Closure Phenomena for Al 2219-T851, *Met. Trans.*, Vol. 10A, 1979, pp. 5-11.
20. Tanaka, K., Nakai, Y., and Yamashita, M.: Fatigue Growth Threshold of Small Cracks, *Int. J. of Fracture*, Vol. 17, 1981, pp. 519-533.
21. Lankford, J.: The Growth of Small Fatigue Cracks in 7075-T6 Aluminum, *Fatigue Eng. Mtls. and Structures*, Vol. 5, 1982, pp. 233-248.

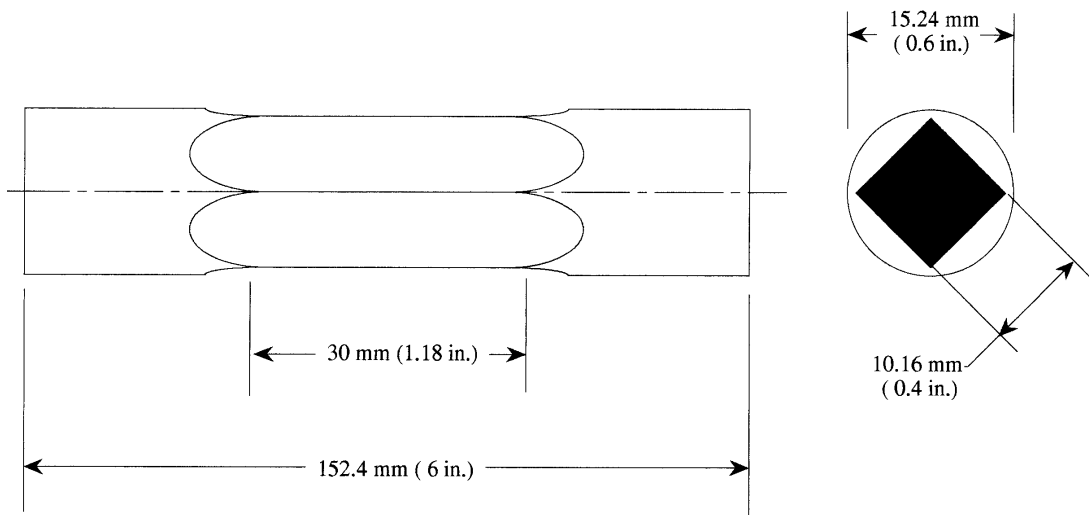


Figure 1. Test Specimen.

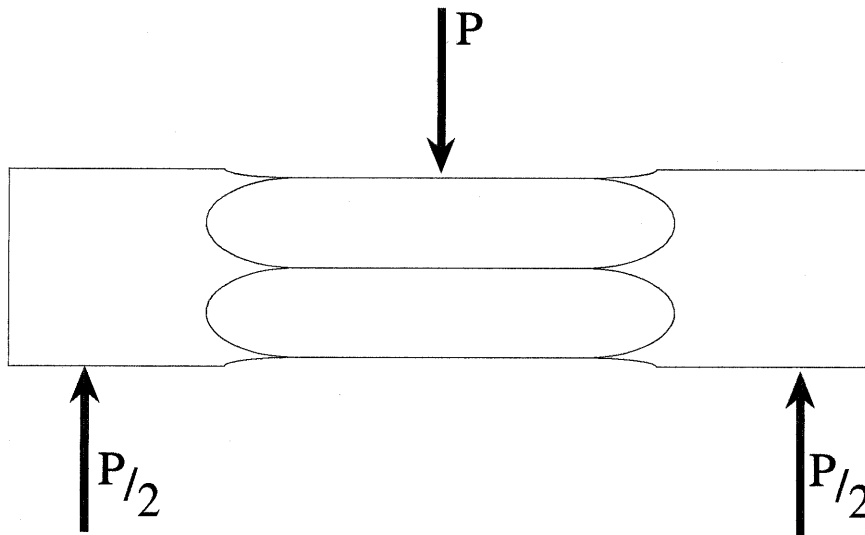


Figure 2. Loading State.

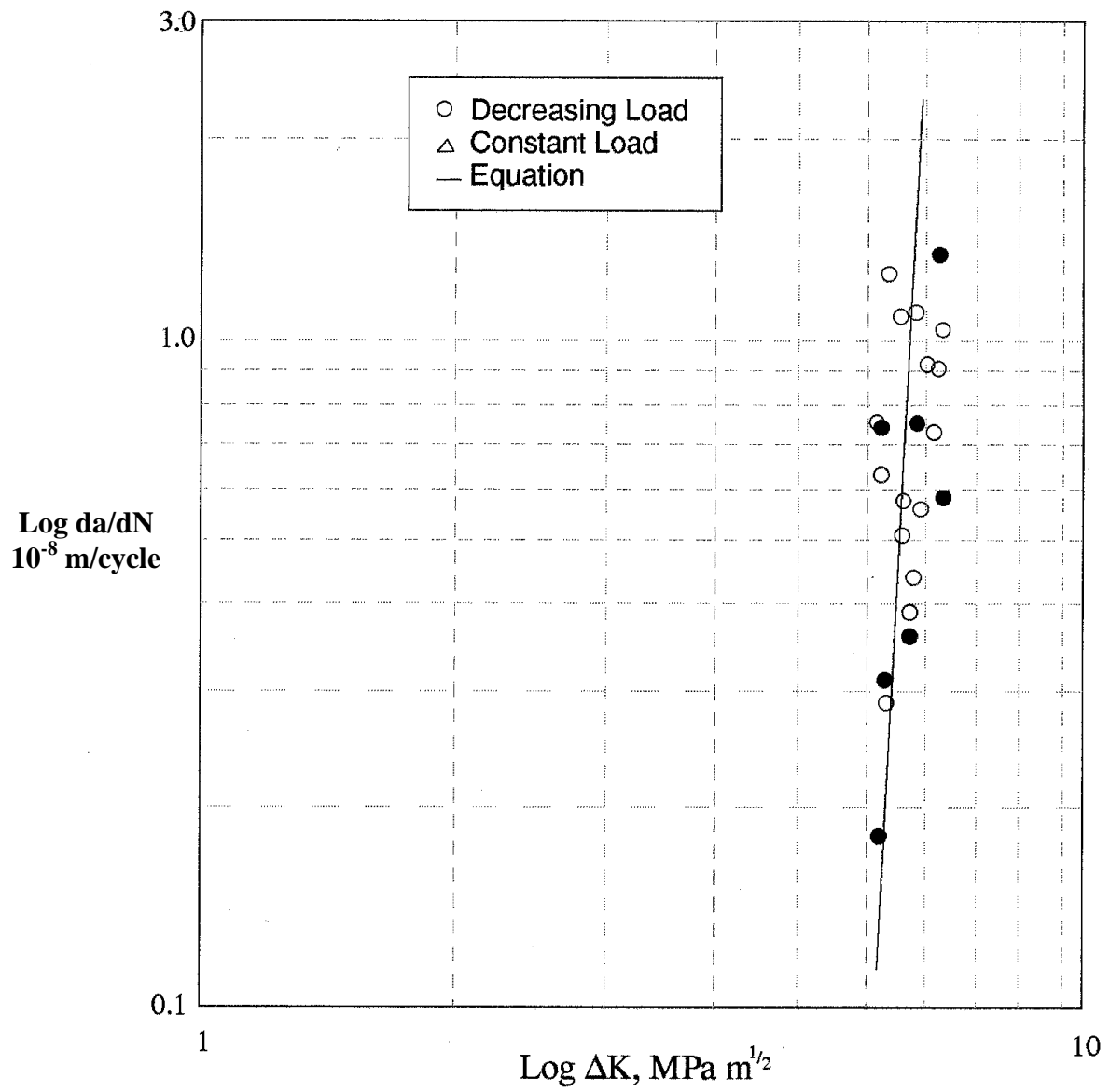
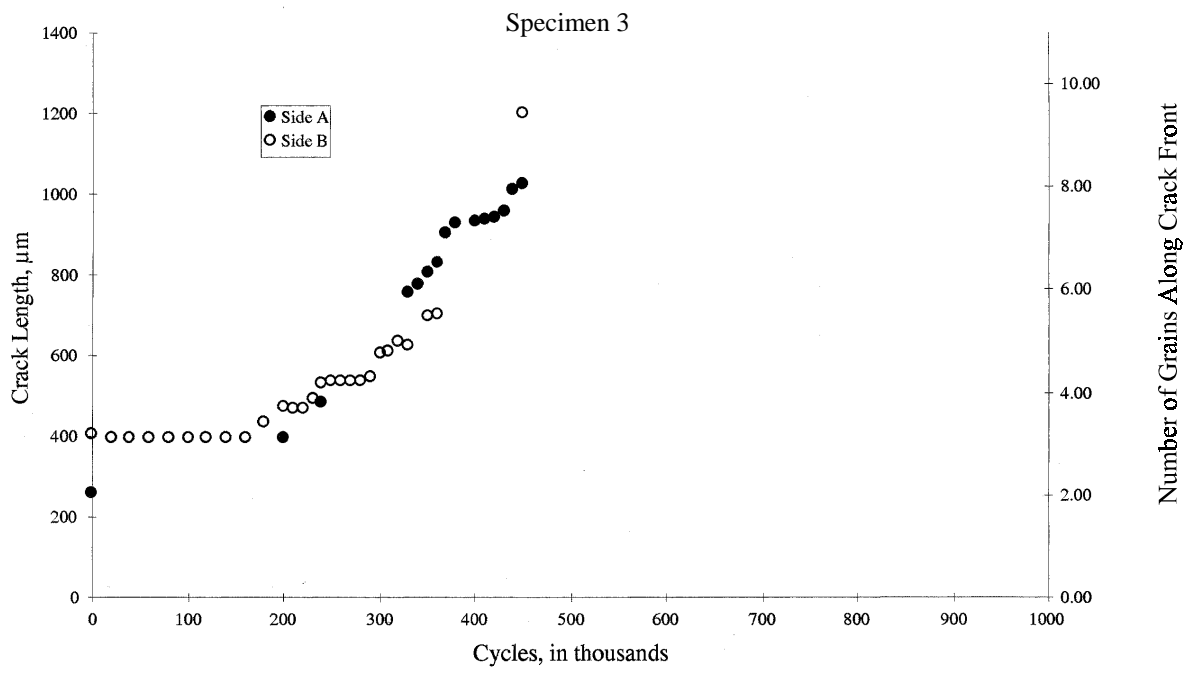
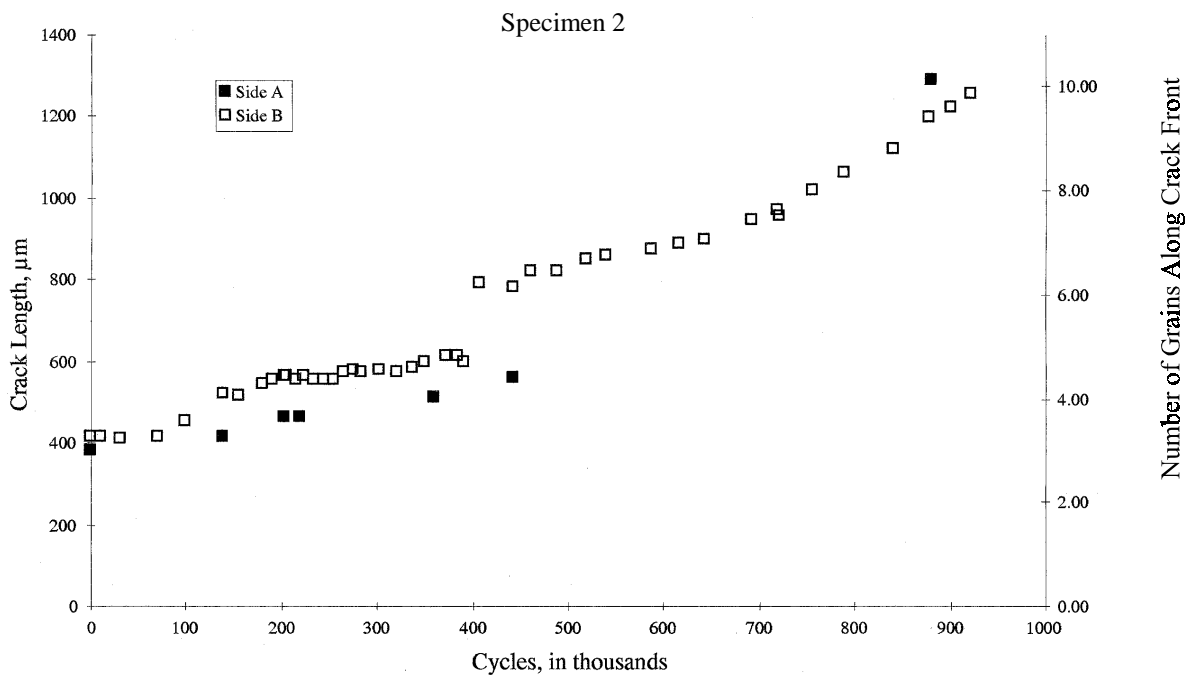


Figure 3. Growth Rate in Near Threshold Region.



(a)



(b)

Figure 4. Growth Data for Small Crack Tests.

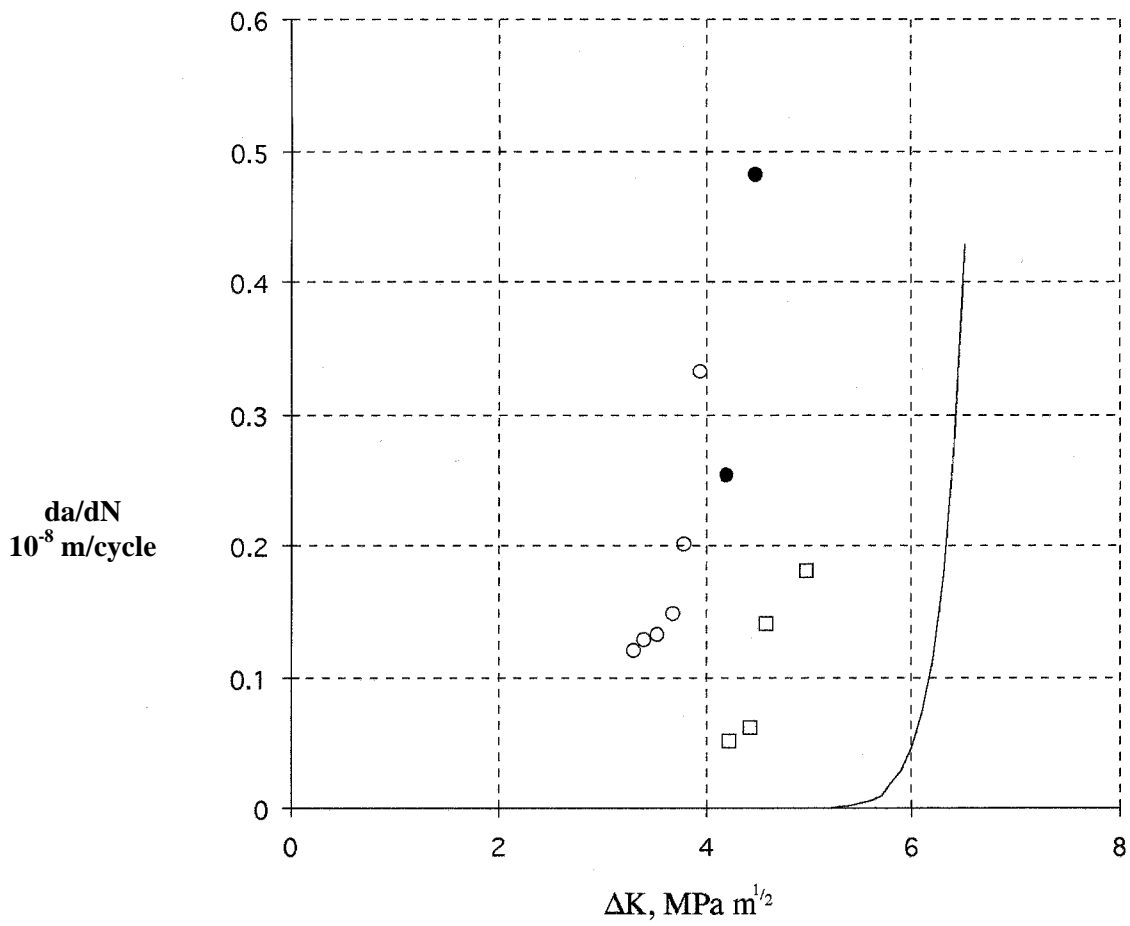


Figure 5. Cartesian Plot of Near Threshold Curve and Small Crack Data.

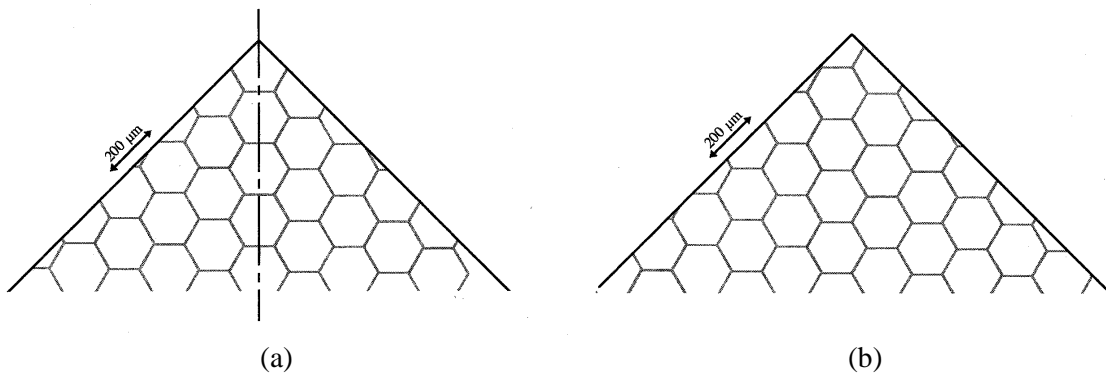


Figure 6. Models of Grains on Crack Plane.

FATIGUE STUDIES RELATED TO CERTIFICATION OF COMPOSITE CRACK PATCHING FOR PRIMARY METALLIC AIRCRAFT STRUCTURE

Dr. Alan Baker
Airframes and Engines Division
Defense Science and Technology Organization
Aeronautical and Maritime Research Laboratory
Australia

SUMMARY

This paper reports on part of a study which has the long-term aim of developing a predictive capability for the growth of patched fatigue cracks under spectrum loading. The first phase is to conduct fatigue-crack growth experiments under constant amplitude loading to validate an analytical model developed by Rose for the estimation of ΔK , in patched cracks. A simple Paris-type crack growth relationship is assumed between da/dN and ΔK for the patched crack.

The patching system under study consisted of edge-cracked 2024 T3 aluminum test panels (~3 mm thick) repaired with boron/epoxy patches, bonded with adhesive FM 73 and the variables evaluated were: a) patch disbond size, b) applied stress, c) patch thickness, d) R-ratio, and e) temperature.

Generally, ΔK estimated using the model provided reasonable correlation with observed da/dN , but there were anomalies in the case of temperature and R-ratio.

INTRODUCTION

Crack patching technology^{1,2} - repair of fatigue-cracked components with adhesively bonded advanced fiber composite reinforcements - pioneered in Australia since the mid 1970s has been extensively deployed on Royal Aeronautical Air Force (RAAF) aircraft and more recently on military aircraft in the US and Canada. These repairs have proved to be highly efficient and cost effective.

In Australia the composite generally used for the reinforcement or patch material is boron/epoxy (b/ep) because of its high Young's Modulus ($3 \times$ aluminum) and strength, resistance to fatigue, immunity to corrosion, and its low electrical conductivity. The patches are bonded with an aerospace grade structural epoxy-nitrile film adhesive, usually Cytec® FM 73. Special prebonding surface treatments, based on the use of silane coupling agents, were developed to ensure that highly durable bonds can be produced under field repair conditions.³

Figures 1a and b highlight some of the major disadvantages of mechanical repairs and advantages of bonded repairs. The important point is that bonded repairs provide a far more effective reinforcement than mechanical repairs so that “live” (untreated) cracks can be left in the structure. Mechanical repairs require the removal of the cracked region and also the introduction of extra fastener holes. Both of these requirements are costly, highly intrusive, and potentially damaging to the structure and substructure.

CERTIFICATION ISSUES

Application of critical repairs to primary structure is restrained by the difficult problem of certification. A critical repair is defined here as one in which the static strength of the (unrepaired) component would be reduced below design ultimate if the crack were to grow in service. Certification requirements are more demanding if the (unrepaired) crack has reduced the strength of the component below ultimate or, even worse, below limit load.

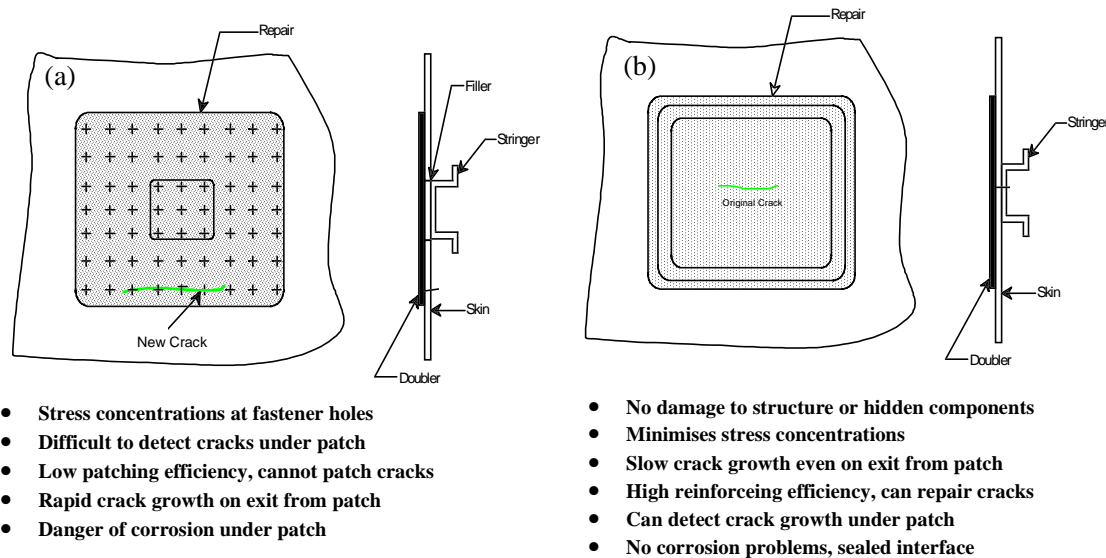


Figure 1. a) Some Disadvantages of Standard Mechanically Fastened Repairs and b) Advantages of Bonded Composite Repairs.

One approach to certification proposed² is to consider the repaired region to be new structure and demonstrate by analysis and/or by test that it can meet the strength⁴ damage tolerance⁵ and durability requirements. Ensuring the reliability of adhesive bond durability through high level quality control is the most critical requirement.

It has been demonstrated⁶ with bonded repairs that residual strength can be restored to a design ultimate capability, largely independent of crack length, as long as the crack is within the confines of the patched region. Thus an ability to estimate the length of time for the crack to grow through the patched region will allow prediction of repair safe life or the setting of inspection intervals for safety by inspection management.

Following a long history of successful bonded composite repairs to RAAF aircraft, confidence in Australia has grown to the extent that a composite repair was recently developed for a fatigue crack in the primary wing box of an F-111⁶ aircraft. This is the first known application where flight critical structure having a crack with potential to reduce strength below a limit load capability has been repaired by a composite repair.

Certification of this repair has followed a rigorous and extensive program of testing of structural details and subcomponents under representative spectrum loading conditions. However, the work required could have been dramatically reduced if suitable generic information were available. Thus studies, described in this paper, are in progress to develop a capability for predicting crack propagation behavior under spectrum loading, initially for a simple (generic) repair geometry.

For the design of less critical repairs a bonded repair manual (C5033) has been developed for RAAF; the background to this is discussed by Davis⁷.

AIMS OF PROGRAM

The primary aim of this program is to develop a predictive capability for the growth of patched cracks under spectrum loading. This study is based on an estimate of stress intensity K , using the analytical patching model described in the next section and experimental fatigue studies on a standard patched specimen. Since experimental results are limited at this stage the aim of this paper is essentially to illustrate the approach taken and reach tentative conclusions.

The aim is a) to obtain the crack growth constants under constant amplitude loading and b) to calibrate an appropriate model for load sequence or crack growth retardation effects.

The stress variables under constant amplitude stressing that must be assessed include:

- Stress range: $\Delta\sigma_{\infty} = \sigma_{\max} - \sigma_{\min}$ where σ_{\min} and σ_{\max} are respectively the minimum and maximum stress
- Stress Ratio: $R = \sigma_{\min}/\sigma_{\max}$

It is assumed that, as for unpatched cracks, a Paris-type relationship $da/dN = f(\Delta K, R) = A_R \Delta K^{n_R}$ holds, where a is crack size, N is number of constant amplitude cycles, and A_R and n_R are assumed to constants for a given R . More advanced models based on ΔK effective, taking into account crack closure effects, are not considered at this stage because of complications due to residual stresses.

For patched cracks, it will be shown later that K and R are functions of temperature. This is because of a) the sensitivity of the mechanical properties of the patching adhesive to

temperature and b) the development of residual stresses. Residual stresses arise from the difference in thermal coefficient of expansion between the metal structure and composite patch¹, this is a major disadvantage of composite compared with metallic patches. Tensile residual stresses increase the effective values for both σ_{min} and σ_{max} and therefore R and K_{max} and K_{min} the maximum and minimum value of K .

Recently, Fredel⁸ proposed the use of GLARE (glass fiber reinforced aluminum alloy laminate) patches for repairs to thin-skin fuselage structure, primarily to avoid the (possible) deleterious effect of residual stresses. GLARE has similar expansion coefficient to aluminum alloys and excellent fatigue properties compared to normal aluminum sheet; however, it is less stiff than aluminum and much weaker than the fiber composites.

To allow for load sequence effects a commonly used approach⁹ is to calibrate one of the retardation models, such as Wheeler's, from crack growth measurements made under an appropriate spectrum, such as FALSTAFF for a fighter aircraft or TWIST for a civil aircraft. However, since da/dN in patched panels is likely to be very low it may be reasonable to neglect load sequence effects and still produce a conservative estimate suitable for certification requirements and the setting of inspection intervals.

Early work on spectrum (FALSTAFF) loading was undertaken in collaboration with the Institute for Aerospace Research Canada.^{10,11} Further work on this topic is in progress, including F111 and F/A-18 spectrums and will be published elsewhere .

REPAIR DESIGN/ANALYSIS

The aim of the analysis¹ is to estimate a) K (and R) as a function of the various geometrical, physical, and stress parameters and b) the corresponding stresses in the patch system. Generally, the minimum patch thickness is chosen to obtain the desired stress intensity in the patched crack without exceeding the strength or fatigue strain allowables for the patch system (patch, tensile strain and adhesive, shear strain) to avoid excessive patch stiffness and to minimize residual stress. The parameters other than applied stress in determining K for a patched panel configuration, as shown in Figure 1b, are:

- Metallic Structure: thickness t_P , Young's modulus E_P , shear modulus G_P and thermal expansion coefficient α_P
- Patch Reinforcement: thickness t_R , Young's modulus E_R , and thermal expansion coefficient α_R
- Adhesive: thickness t_A , shear modulus G_A , shear yield stress τ_p under the operating conditions of temperature, humidity and loading rate.
- Disbonds (if any) over the cracked region: length normal to the crack, $2b$.

The model used here is described in the next section.

Model for Estimating Patching Efficiency

In the model developed by Rose¹² to estimate stress intensity in the patched crack a two-step approach, as illustrated in Figure 2, is used.

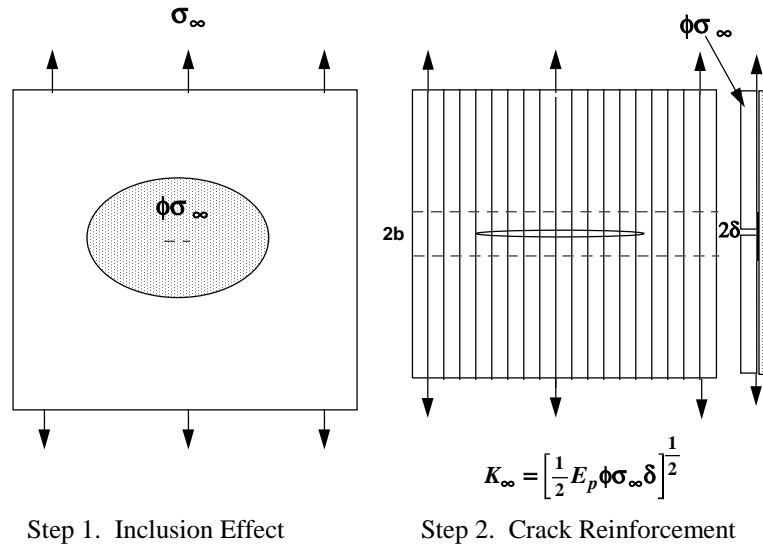


Figure 2. Schematic Illustration of the Analytical Approach to Crack Patching. The Parallel Lines Represent a Disbond, Width $2b$.

In the step 1, Figure 2, the patch is modeled as an inclusion in a large plate; the crack is assumed to be very small compared to the patch. The stress in the metallic component remote from the crack is then given by $\phi\sigma_\infty$, where σ_∞ is the applied stress and ϕ a factor which accounts for the stiffness and shape of the patch. Because the patch attracts load the stress reduction is usually significantly less than predicted simply on the basis of ratio of patch stiffness to plate stiffness.

In the step 2, Figure 2, the region under the patch is modeled; the crack is considered to be semi-infinite in length and is bridged by the patch. The stress intensity K_∞ is then as given by the equation in Figure 2, where δ is the “crack” opening displacement. Since δ is estimated from an overlap joint that would be obtained by cutting a strip through the panel normal to the crack, δ and therefore K_∞ are upper-bound estimates.

Under the cyclic stress range $\Delta\sigma_\infty$ the stress-intensity range ΔK_∞ is given by:

$$\Delta K_\infty = \left[\frac{1}{2} E_p \phi \Delta\sigma_\infty \Delta\delta \right]^{\frac{1}{2}} \quad (1)$$

Note that the crack length a does not feature in equation 1.

The displacement range $\Delta\delta$ is dependent on the thicknesses and stiffnesses of the patch and of the cracked component and on the thickness, shear modulus, and effective shear yield stress of the adhesive. It is important to note that the adhesive properties are highly temperature and strain-rate dependent and will also depend on the level of absorbed moisture. $\Delta\delta$ is also dependent on the residual stress level since this affects the level of external stress at which the adhesive will yield. Calculation of δ is described in reference 1.

Equation 1 is strictly correct only for linear behavior (no yielding of the adhesive) but provides a good estimate of ΔK_∞ provided shear yielding in the adhesive is limited, say, to a strain of less than 0.2.

The assumption that the crack growth behavior follows the relationship:

$$da/dN = A_R (\Delta K_\infty)^{n_R} \quad (2)$$

leads to the conclusion that da/dN will be independent of a . Thus a should be linearly related to N .

Finally, the relationship between crack length a and the number of cycles N can be obtained from:

$$a = A_R \int_0^N (\Delta K_\infty)^{n_R} dN \quad (3)$$

Extension of the Model for Growth of Disbond Damage in the Patch System

The above analysis was used in reference 13 to allow for the reduction in patching efficiency with disbond growth in the patch system. It is assumed in this simple extension to Rose's analysis that a parallel disbond, size $2b$, traverses the specimen, as illustrated in Figure 2.

Then the opening of the gap is increased by $2be$, where e is the estimated strain in the reinforcement.

Equation 1 then becomes:

$$\Delta K_\infty = \left[\frac{1}{2} E_p \Phi \Delta \sigma_\infty (\delta + 2be) \right]^{\frac{1}{2}} \quad (4)$$

If it is assumed as a first approximation (based on previous fatigue tests on double-overlap joints¹) that db/dN is a constant for given stressing conditions, then:

$$b = N \left(\frac{db}{dN} \right) \quad (5)$$

Thus the effect of disbond growth on crack growth behavior can be estimated using equation 4. If the disbond size is constant, b remains constant in equation 4.

With disbond growth ΔK_{∞} no longer remains constant but follows a square root relationship as a function of $b = f(N)$. Thus, for expected values of n_R a parabolic relationship between a and N is predicted from equations 3 and 4.

Rose^{14,15} has developed a much more sophisticated treatment of the effect of damage growth in the patch system, leading, however, to similar conclusions.

FATIGUE STUDIES

In the initial fatigue studies the approach was to use crack growth as a method of estimating the stress intensity following patching. As a result of the disbonding damage found in these experiments the follow-up study was to evaluate the effect of disbond growth in the patch system over the cracked region. Since more recently it was found possible to reduce markedly the amount of disbond damage it became feasible to attempt to quantify the effect of the variables of stress range, patch thickness, R -ratio and temperature, and this work is reported here.

EXPERIMENTAL PROCEDURE

Fatigue crack propagation tests were conducted on 2024 T3 specimens 3.14 mm thick having starting cracks about 5 mm long repaired with unidirectional boron/epoxy (Textron 5521/4) patches (unless otherwise mentioned) 7 plies (0.9 mm) thick. In later studies a layer of FM 73 adhesive was cocured onto the boron/epoxy bonding surface. The patches were then bonded with adhesive FM 73 at 120°C, following surface treatment of the metal using the silane process³ and the boron/epoxy patches by blasting with alumina grit, either directly onto boron/epoxy (in the early studies) or (in the later studies) onto the cocured adhesive layer.

In the fatigue tests, two similar panels are simultaneously tested, joined together as a honeycomb sandwich panel, Figure 3.

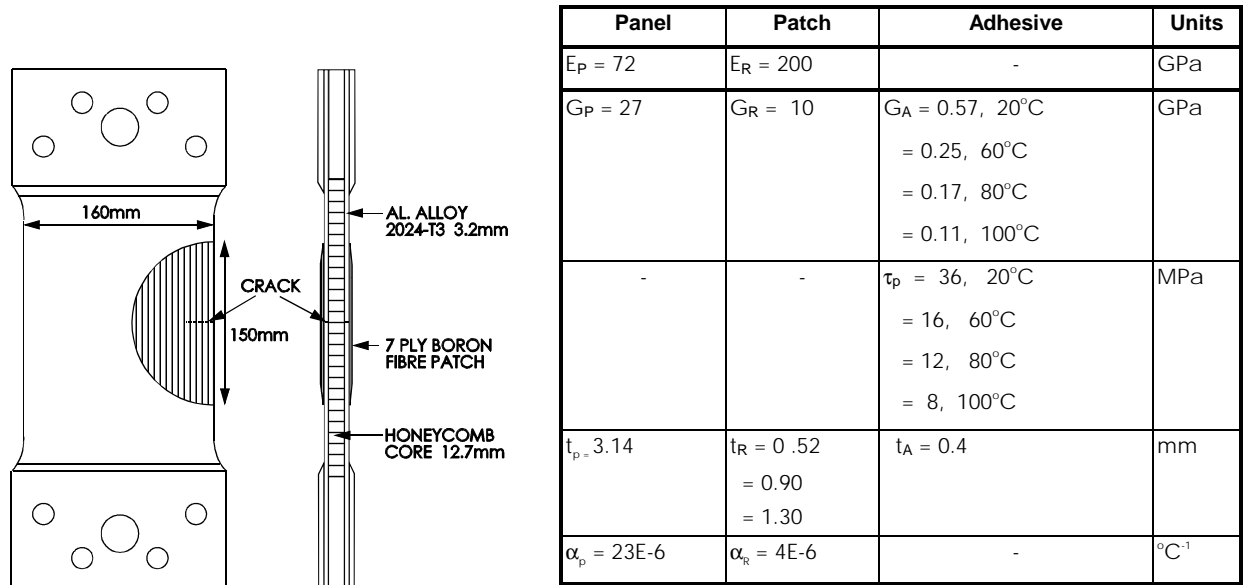


Figure 3. Illustration of the Test Configuration Used to Evaluate Patching Efficiency in Patched Panels. Note that two cracked-patched panels are tested simultaneously in this configuration. A 7-ply patch is standard but 4- and 10-ply patches were also evaluated. The table provides properties assumed in the calculations based on Cytec short-overlap shear data.

There are two reasons for using this configuration: The first is to minimize curvature following patching due to the residual stress σ_T which, as mentioned earlier, arises from the mismatch in thermal expansion coefficient between the patch material and the metal panel. Thus, the patches were bonded to the panels at the same time as the panels were bonded to the honeycomb core. The second reason is to minimize the secondary bending of the panels which would otherwise occur during testing. The bending moments arise from the displacement of the neutral plane by the patch. The resistance to bending resulting from the honeycomb core (substantial but not perfect) is considered to be a reasonable simulation of the level of support that would be provided by typical military aircraft structure. In almost all tests, similar rates of crack growth were observed for the two panels in the combination.

Tests were conducted under constant amplitude stressing to a maximum of 240 MPa at a range of temperatures up to 100°C and applied R values to 0.64. However, a stress of 138 MPa and nominal R of 0.1 and ambient temperature was standard. Crack length under the patch was measured within about ± 0.5 mm using standard eddy-current nondestructive inspection.

After testing, the patches were heated to 190°C for 2 hours and stripped from the test specimen (at the elevated temperature). This discolors any disbonded regions by oxidation, making them clearly visible.

EARLY STUDIES ON VALIDATION OF THE PATCHING MODEL

In early studies the aim was to validate the model by measuring the effective (experimental) value of ΔK_{∞} called ΔK_R (the effective stress intensity range following patching) from measurements of da/dN . The method used was as follows:

- a) Establish for the unpatched cracked panel the empirical relationship between $(da/dN)_a$ and ΔK_a the estimated stress intensity range and crack-growth rate. For the edge-notched configuration used

$$\Delta K_a = 1.1\Delta\sigma\sqrt{\pi a} \quad (6)$$

- b) Find da/dN from a versus N plots for the patched panels at $R = 0.1$ applied value and $R = 0.6$, allowing for residual stress, as discussed later.
- c) From comparison of da/dN with $(da/dN)_a$ estimate ΔK_R

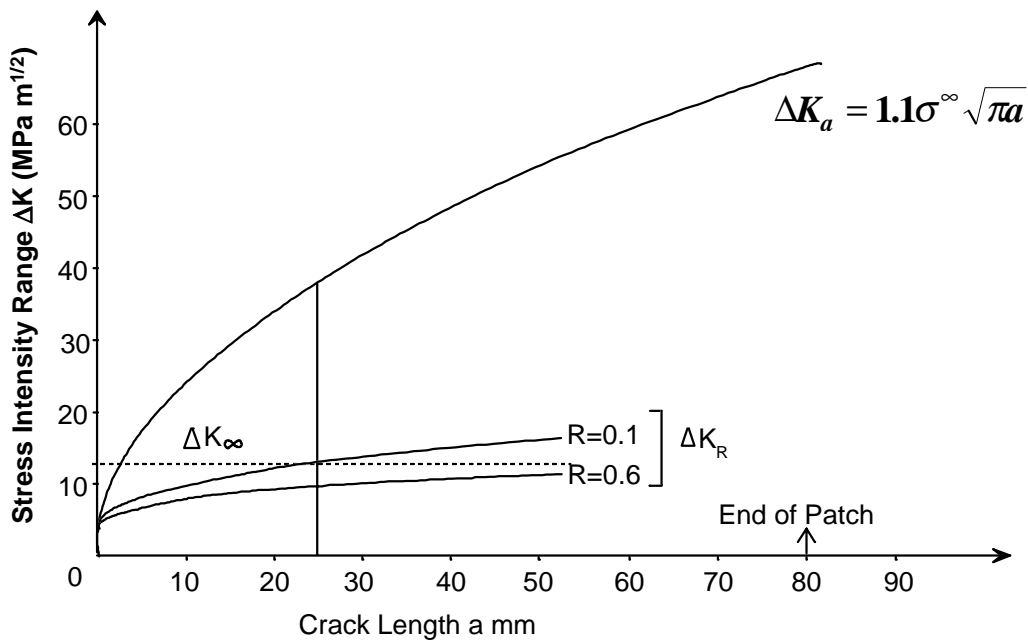


Figure 4. Plots of ΔK_R versus a . Also Shown is the Calculated Relationship Between ΔK_a and a and the Theoretical Values for ΔK_{∞} , Taken From Equation 4. Applied σ_{\max} Was 138 MPa and $R = 0.1$.

Generally, as shown in Figure 4, it was found that the estimate of ΔK_{∞} obtained from equation 4 (even though an upper bound estimate) agreed reasonably well with the experimentally determined value ΔK_R .

This method of validating ΔK_{∞} cannot be claimed to be other than approximate because of the sensitivity of da/dN to many variables including: alloy batch, residual stress, and stress intensity level; environmental isolation of the panel by the patch may also have an effect. To validate the model an independent direct method of measuring ΔK_{∞} is required based on direct stress measurement using, for example, X-ray diffraction or special stress-intensity (K) gauges.

Figure 4 shows that ΔK_R increases with a suggesting (section 0) the development of disbonding damage in the patch system so this aspect was the subject of the follow-on studies, described in the next section.

DISBOND DAMAGE IN THE PATCH SYSTEM

In these studies^{2,13} the aim was to evaluate the effect of disbond growth over the cracked region. The disbonds did not occur in the adhesive but within the surface layer of the boron/epoxy, which consists of a very light scrim of glass cloth, impregnated with the matrix epoxy resin.

A series of specimens were made with artificial disbonds (using thin PTFE sheet inserts) of length $2b$ ranging from 10 to 60 mm. Tests were conducted at a peak stress of 138 MPa and $R = 0.1$. The crack-growth results, Figure 5a, show that, as expected, patching efficiency falls dramatically with increasing disbond size.

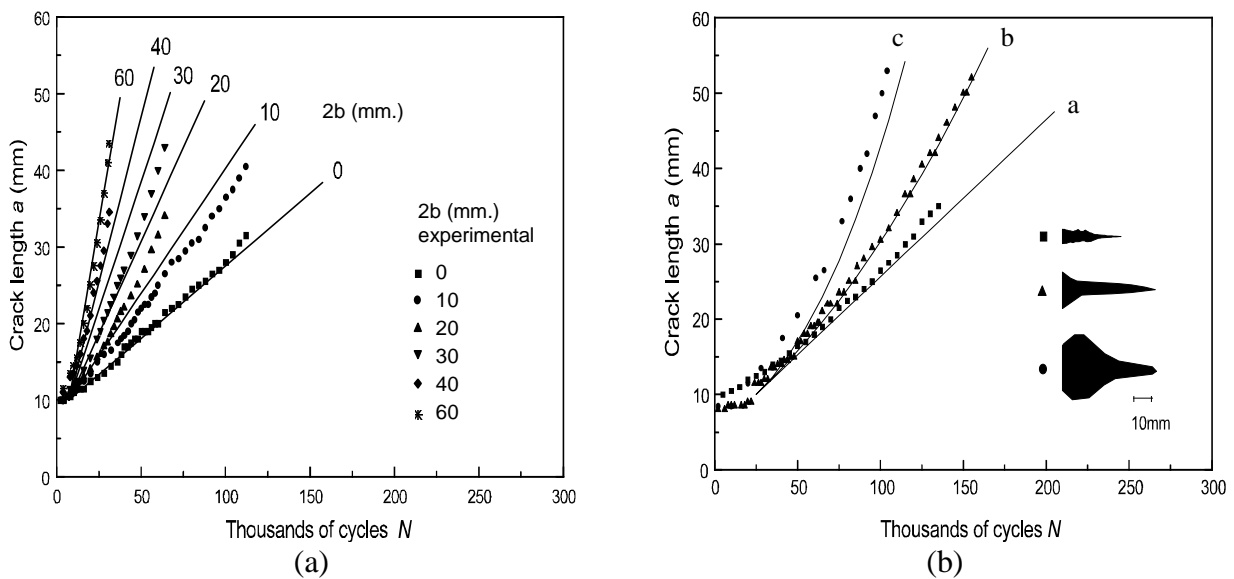


Figure 5. a) Plot of Crack Length (a) Versus Cycles (N) for a Patched Specimen Having Artificial Disbonds of Various Lengths; Solid Lines are Theoretical Estimates, Based on Estimated A_R and n_R . b) Plot of Crack Length (a) Versus Cycles (N) for Patched Panels Tested at a Peak Stress of 138 MPa and Nominal $R = 0.1$.

Figure 5b plots crack length a versus N at a peak stress of 138 MPa and $R = 0.1$ for three test panels. The observed final disbond shapes ($2b$) are shown inset in the figure. As seen in Figure 5, the greater the final disbond size the greater crack growth rate and the more parabolic the curve of a versus N ; for a small disbond a versus N is linear. These observations are in quantitative agreement with predictions of the patching model described in section 0.

Figure 5 also shows, as solid curves, labeled a to c, the predicted behavior based on the foregoing analysis and the final disbond growth rates respectively of 0 , 6×10^{-5} , and 20×10^{-5} mm/cycle. To produce these curves an Excel spreadsheet was developed to estimate da/dN and thus a versus N based on equations (2), (3), (4), and (5); where A_R and n_R for equation (2) are determined experimentally from patched panels with artificial disbonds. Using the method described in reference 2, this data was used to estimate A_R which was found to be around 5×10^{-11} and n_R around 3.

The estimates for the disbond growth rates, db/dN , for use in equation 5 are obtained from the observed *maximum* disbond size observed in the tests divided by N . Thus the disbond growth rates assumed in producing the theoretical curves, although an overestimate, are a reasonable approximation.

On the basis of the results provided here (and more fully in reference 2) the tentative conclusion reached is that the model outlined in section 0 can account for the influence of disbond growth in the patch system on patching efficiency.

A major input to this model is the relationship between db/dN and cyclic stress or strain level. This relationship can be obtained empirically from tests on equivalent double-overlap joint specimens representing the repair configuration. However, to estimate db/dN generically from repair design data, stress patch geometry etc., a suitable damage criterion for the adhesive is required. In the preliminary tests on representative joints¹ the effective shear strain range in the adhesive ($\Delta\gamma_A$) was used as the damage criterion, alternative criteria based on energy release rate are currently under investigation.

In the studies briefly described in the following sections the patch was formed with a cocured layer of adhesive. This produces a patch system more resistant to disbond damage, resulting in a change in the locus of the disbond damage from the patch/adhesive interface into cohesive failure in the adhesive.

STRESS RANGE

Figure 6a plots the results for a versus N for a 7-ply specimen for $R = 0.1$ at σ_{max} levels ranging from 80 to 244 MPa. The highest stress level corresponds to a limit load capability for this alloy and was thus very close to the level (248 MPa) used for the peak stresses in the FALSTAF studies¹⁰. Limit load is nominally experienced only once in the life of an aircraft.

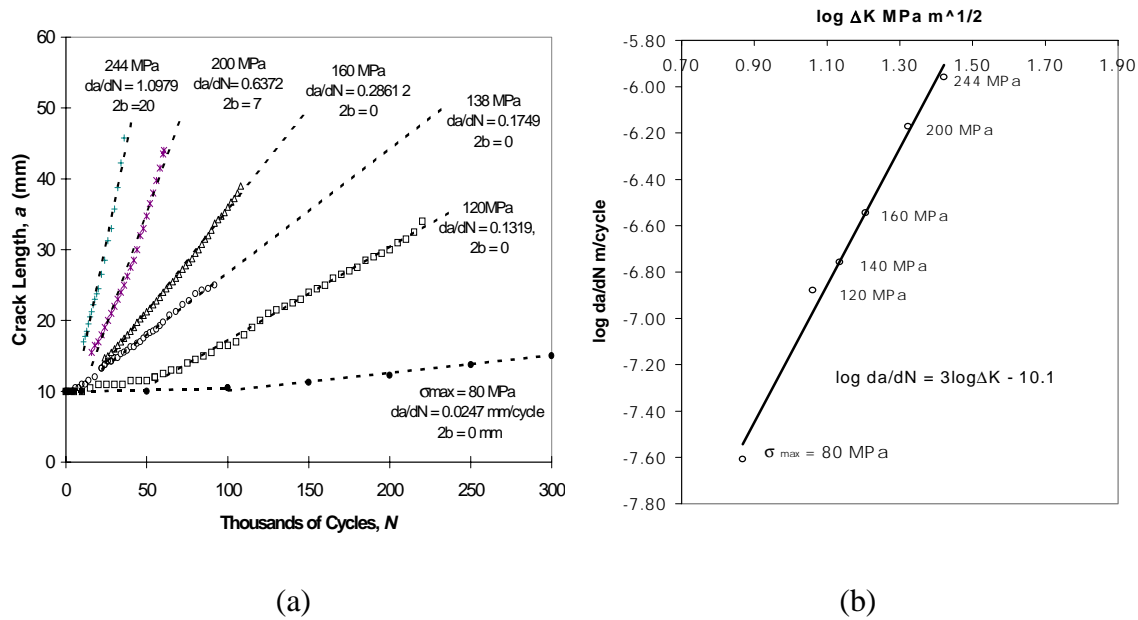


Figure 6. a) Plots of Crack Length a Versus Cycles N for a Standard 7-Ply Patched Specimen for Applied $R = 0.1$. b) Plot of $\log da/dN$ Versus $\log \Delta K_{\infty}$ for the Results in 6(a).

The change from a linear relationship to a parabolic relationship occurs above $\sigma_{max} = 138$ MPa and results from the development of damage in the adhesive layer, as indicated as a $2b$ value in the figure. For the standard 138 MPa stress level damage in the adhesive system is negligible, so as expected, patching efficiency is comparable to the best of the previous series, Figure 5.

A linear least squares fit was used to obtain da/dN for all the stress levels, despite the disbond damage found at the two highest stresses. The high stress values at small crack lengths are included since they fit well with the other results; however, if only the large crack da/dN values at these high stresses are considered these lie well to the left of the curve, as expected for damage. Using these results, Figure 6 b) plots $\log da/dN$ versus $\log \Delta K_{\infty}$ for these test specimens which confirms that the results fit the expected Paris-type relationship. The relationship thus obtained is $da/dN = 7.9 \times 10^{-11} \Delta K_{\infty}^3$ m/cycle, which is close to the results for the damage series mentioned in the previous section.

PATCH THICKNESS

Figure 7 plots $\log da/dN$ versus $\log \Delta K_{\infty}$ for test panels with 4, 7, or 10-ply-thick patches, at an R value of 0.1. The results for the 7-ply panel are as plotted in Figure 6 b); the results for the 4- and 10-ply panels were obtained from single test panels stressed at several levels.

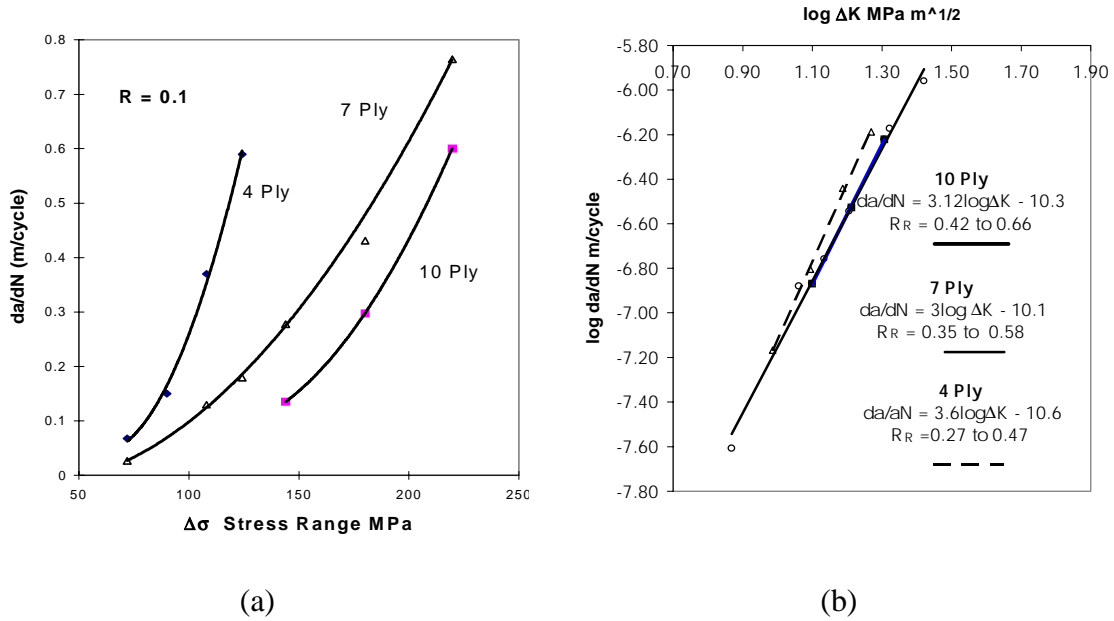


Figure 7. Plots a) of da/dN Versus $\Delta\sigma$ and b) Log da/dN Versus Log ΔK_∞ for Test Panels Having 4-, 7- or 10-Ply Patches. R is 0.1, R_R is as Indicated on b) and t_A is About 0.5 mm..

It can be seen from Figure 7 that the model using the da/dN relationship for the 7-ply panel would have given quite reasonable predictions for the 4- and 10-ply panels. However, the values obtained are: 4 Ply: $n_R = 3.6$, $A_R = 2.3 \times 10^{-11}$; 7 ply: $n_R = 3$, $A_R = 7.7 \times 10^{-11}$; 10 ply: $n_R = 3.12$, $A_R = 5 \times 10^{-11}$. While these results appear very promising further experimental results are needed before any firm conclusions can be made.

R-RATIO

For an unpatched specimen $R = \sigma_{\min}^\infty / \sigma_{\max}^\infty$, whereas for a patched specimen due to residual stress R_R the effective ratio is given by

$$R_R = (R\phi\sigma_\infty + \sigma_T) / (\phi\sigma_\infty + \sigma_T) \quad (7)$$

where σ_T is the thermal residual stress, which has a maximum value of

$$\sigma_T = t_R E_R E_P \Delta T (\alpha_P - \alpha_R) / (t_P E_P + t_R E_R) \quad (8)$$

where ΔT = (adhesive cure temperature - operating temperature).

Thus $R_R > R$ and varies with stress level for a constant R . For the standard 7-ply patched panel at $\sigma_{\max} = 138$ MPa and $R = 0.1$, $R_R = 0.58$.

To evaluate the effect of R standard 7-ply panel tests were conducted at R values of 0.1 (standard), 0.4, 0.55, and 0.64 at $\Delta\sigma = 72$ MPa. Stresses were kept fairly low to avoid adhesive damage which would have complicated the outcome of the tests. Figure 8 shows the results of a) a versus N and b) $\log da/dN$ versus $\log \Delta K_{\infty}$.

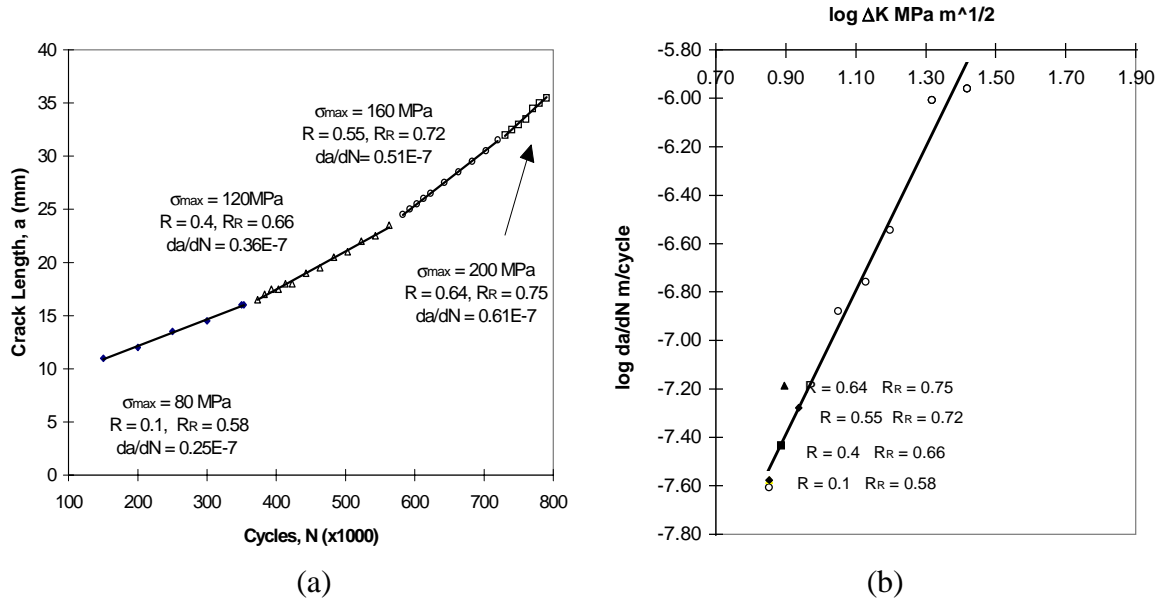


Figure 8. a) Plot of a Versus N for R Values as Shown for a Standard 7-Ply Test Specimen and b) Plot of Log da/dN Versus Log ΔK_{∞} for the Data From the 7-Ply Specimen ($R=0.1$) of Figure 6b, Including, as Solid Data Points the Corresponding Results for Different R -Ratios From 8(a).

As seen in Figure 8b, the data points for $R > 0$ fall close to the curve for $R = 0.1$ which is pleasing but unexpected since a higher crack growth rate would be expected at the higher R level so that these data points should lie to the left of the curve. However, studies at low temperatures² (-40°C) where R_R is also high (0.55) showed no observable change in crack growth rate compared to ambient so also suggest an insensitivity to R .

One possible explanation is that due to residual stresses the crack does not experience closure so that the effective K is insensitive to mean stress and crack growth is a function of ΔK only. If the behavior of composite patched cracks does turn out to be insensitive to R , prediction of crack growth behavior under spectrum loading would be greatly simplified.

TEMPERATURE

The influence of temperature on crack propagation behavior in patched specimens is quite complex^{2, 13} since the following changes occur:

- A change in R since residual stress reduces as temperature increases

- A change in patching efficiency:
 - ΔK_{∞} is increased as temperature increases because of a decrease in adhesive shear modulus G_A and shear yield stress τ_p ,
 - ΔK_{∞} is increased if the rate of disbond damage increases with increasing temperature
- A change in the crack propagation properties of the alloy itself

To investigate the influence of temperature, tests were conducted on a standard 7-ply specimen at a stress level of 138 MPa at 20, 60, 80, and 100°C. Estimations of ΔK_{∞} for the log plots against da/dN were based on the temperature values of G_A and τ_p provided in the table with Figure 3. Figure 9 shows the results of a) a versus N and b) $\log da/dN$ versus $\log \Delta K_{\infty}$.

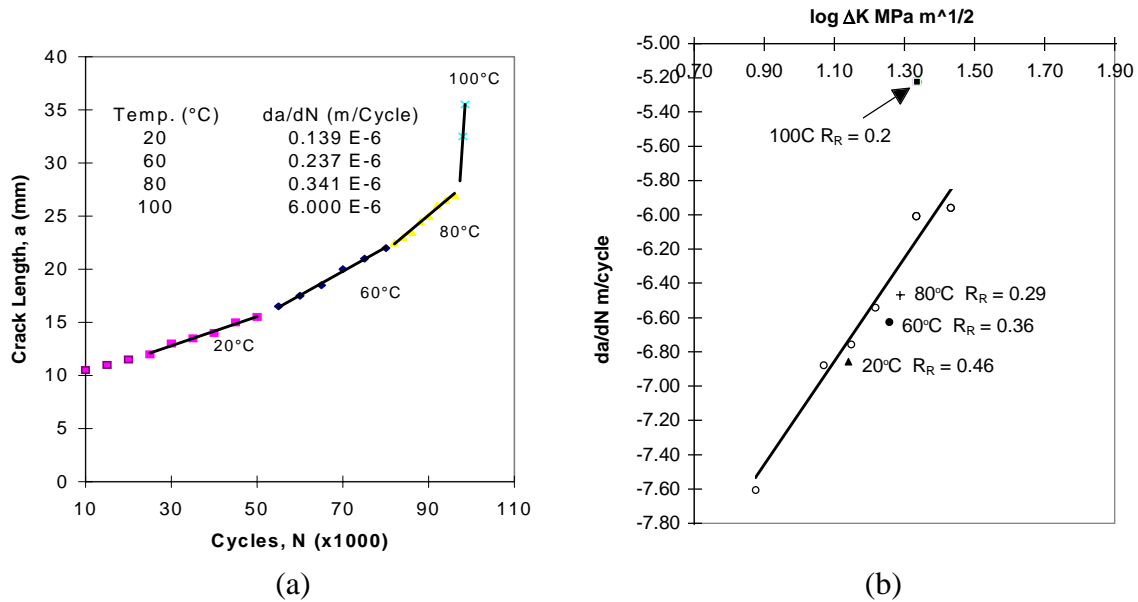


Figure 9. a) Plot of a Versus N at Various Temperature and b) Plot of $\log da/dN$ Versus $\log \Delta K_{\infty}$ for the Data From the Standard 7-Ply Specimen of Figure 6 ($R = 0.1$ at 20°C), Including, as Separate Data Points, the Corresponding Results From 9(a).

Based on these approximate values Figure 9b shows that the data points for temperatures up to 80°C lie below those for the standard 7-ply specimen, suggesting that the patching model or the input data is in error. The main problem using the model is to know what values to take for the adhesive properties at elevated temperature because both temperature and strain rate have to be taken into account; the values used (Table in Figure 3) for G_A and τ_p were based on static measurements and so will be low compared to dynamic values appropriate to the fatigue test conditions.¹⁶

CONCLUSIONS

The tentative findings of this study are as follows:

1. Patch Disbond Damage: A simple modification was made to the model to allow for disbond growth. The (modified) model predicts the correct form of the a versus N crack growth relationship for disbond growth in the patch system - linear for little disbond growth changing to parabolic for significant growth and, based on few results, produces reasonable quantitative predictions.
2. Applied Stress: Using the model (no disbond damage) to estimate ΔK (for a 7-ply boron/epoxy patch, $R = 0.1$), a straight line relationship was obtained between $\log da/dN$ and $\log \Delta K$ having A and n constants of the correct order for aluminum alloy 2024 T3.
3. Patch Thickness: The $\log da/dN$ and $\log \Delta K$ relationship for 4-, 7-, and 10-ply patches were similar suggesting that the model can give satisfactory predictions for patch stiffness variations over this range.
4. R -ratio: The results indicate an insensitivity to R for values from 0.1 to 0.64, since points (for 7-ply patches) at high R fall on the $\log da/dN$ and $\log \Delta K$ curve for $R = 0.1$. This may be a feature of patched cracks since low-temperature results (-40°C), where due to residual stresses R is very high, have no observable effect on da/dN .
5. Temperature: On the basis of the $\log da/dN$ and $\log \Delta K$ relationship for the 7-ply patched panels at 20°C , the model appears to overcompensate somewhat for temperatures of 60 , and 80°C . For both R and temperature, the problem could be related to the use of static rather than dynamic values for the adhesive shear modulus and shear yield properties; this issue is under investigation.

ACKNOWLEDGMENTS

The author would like to thank Onofrio Beninati and Paul Chapman for conducting the experimental work and Drs Francis Rose, Richard Chester, and Chun Wang for comments on the manuscript.

REFERENCES

1. A. A. Baker, "Crack Patching: Experimental Studies, Practical Applications," Chapter 6 in *Bonded Repair of Aircraft Structures*, Editors A. A. Baker and R. Jones, Martinus Nijhoff, pp. 107-173, 1988.
2. A. A. Baker, "Bonded Composite Repair of Metallic Aircraft Components", Paper 1 in *AGARD-CP-550 Composite Repair of Military Aircraft Structures*, 1994.
3. A. A. Baker and R. J. Chester, "Minimum Surface Treatments For Adhesively Bonded Repairs," *International Journal of Adhesives and Adhesion* **12** (1992), pp. 73-78.
4. C. Torkington "The Regulatory Aspects of the Repair of Civil Aircraft Metallic Structures," International Conference on Aircraft Damage and Repair, Australian Institute of Engineers, (1991) Melbourne.
5. J. W. Lincoln, "Challenges for the Aircraft Structural Integrity Program," FAA/NASA International Symposium on Advanced Structural Integrity Methods for Airframe Durability and Damage Tolerance, NASA Publication 3274, pp. 409-423.
6. A. A. Baker, L. R. F. Rose, K. F. Walker, and E. S. Wilson: "Repair Substantiation for a Bonded Composite Repair to a F-111 Lower Wing Skin," Proceedings of the Air Force 4th Aging Aircraft Conference, Colorado, July 1996.
7. M. Davis, "The Development of an Engineering Standard for Composite Repairs," Paper 24 in *AGARD-CP-550 Composite Repair of Military Aircraft Structures*, 1994.
8. R. S. Fredell, W. van Barnveld and A. Vlot, "Analysis of Composite Crack Patching of Fuselage Structures: High Patch Modulus Isn't the Whole Story", SAMPE International Symposium 39, April 1994.
9. D. Broek "Crack Growth Analysis Concepts," Chapter 5 in *The Practical Use of Fracture Mechanics*, Kluwer "Bonded Composite Repair of Thin Metallic Materials."
10. M. D. Raizenne, J. B. R. Heath, and T. Benak (1988) "TTCP PTP4 Collaborative Test Program - Variable Amplitude Loading of Thin Metallic Materials Repaired with Composite Patches," *LTR-ST-1662, National Aeronautical Establishment*, National Research Council Canada.
11. M. D. Raizenne, T. J. Benak, J. B. R. Heath, D. L. Simpson, and A. A. Baker, "Bonded Composite Repair of Thin Metallic Materials: Variable Load and Temperature Cycling Effects," Paper 5 in *AGARD-CP-550 Composite Repair of Military Aircraft Structures*, 1994.

12. L. R. F. Rose, "A Cracked Plate Repaired by Bonded Reinforcements," *International Journal of Fracture* **18** (1982) pp. 135-144.
13. A. A. Baker, "Repair Efficiency in Fatigue-Cracked Panels Reinforced with Boron/Epoxy Patches," *Fatigue and Fracture of Engineering Materials and Structures* **16** (1993), pp. 753-765.
14. L. R. F. Rose, "Influence of Disbonding on the Efficiency of Crack Patching," *Theoretical Applied Fracture Mechanics* **7** (1987) pp. 125-132.
15. B. N. Cox and L. R. F. Rose, "Time-or Cycle-Dependent Crack Bridging," *Mechanics of Materials* **19** (1994) pp. 39-57.
16. P. Chalkley and W. K. Chiu, "An Improved Method for Testing the Shear Stress/Shear Strain Behaviour of Adhesives," *International Journal on Adhesion and Adhesives* **13** (1993). pp. 237-242.